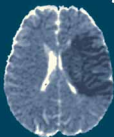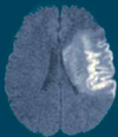T. MORITANI
S. EKHOLM
P.-L. WESTESSON

Diffusion-
Weighted
MR Imaging
of the
Brain

Springer

Diffusion-Weighted MR Imaging of the Brain

Moritani · Ekholm · Westesson

T. Moritani
S. Ekholm
P.-L. Westesson

Diffusion-Weighted MR Imaging of the Brain

With 661 Figures and 11 Tables

Springer

Foreword

Few advances in MR imaging have had the impact that diffusion-weighted imaging (DWI) has had in the evaluation of brain. From the time of the early descriptions by LeBihan and colleagues of the ability to image and measure the micromovement of water molecules in the brain to the present time, diffusion imaging and its derivatives have made an impact in the evaluation of multiple disease processes, primarily in ischemia, but also in other conditions of the brain. In most medical centers diffusion imaging is no longer considered a sequence to be used in special circumstances but rather it is employed as part of routine MR imaging of the brain. Because the information derived from diffusion measurements can improve our understanding of pathologic processes and can influence patient care, knowledge of the principles and applications of DWI is critical.

It is therefore of great interest that the group from the University of Rochester (Drs. Moritani, Ekholm, and Westesson) have assembled under one cover a collection of material which covers all the clinical aspects of diffusion-weighted imaging. Those who have attended recent meetings of the ASNR know the quality of the exhibits and presentations which have come from this group. They, early on, demonstrated the wide spectra of diseases which can cause restricted diffusion and they warned us of mimickers of infarction and ischemia.

In this richly illustrated volume the authors take the reader from the basic principles of DWI, through the pulse sequences used, to mathematical concepts behind the derivation of apparent diffusion coefficients. Following explanations of the different types of edema which can effect the brain and the appearance of DW images, this book allows the reader to see the variety of conditions which alter diffusion, including infarction, hemorrhage, cerebral infections, degenerative neurologic disorders, white matter diseases, toxic/metabolic disorders, and tumors. As one can easily see from the table of contents, the authors have systematically covered all major areas of neuroradiology. This will allow cross-referencing to problematic cases which one may encounter. Additionally, knowledge of what represents a normal brain in adults and in the developing brain along with an explanation of artifacts seen in DWI makes this a valuable book. It is noteworthy that the authors have chosen to abundantly illustrate the clinical material, drawing on pathologic correlations in a number of areas.

I believe that this book will benefit not only those who deal routinely with neuro-MR imaging, but also those who want to establish a basis for understanding of diffusion images in the hope of taking these principles of diffusion further into more exotic areas of neuroimaging such as white matter tract mapping with diffusion tensor imaging, analyzing alterations in highly organized structures with fractional anisotropy, or delving into macromolecular alterations with ever-higher b values. The authors are to be congratulated for putting their considerable experience together in this form, and I am sure that the collection of cases herein will serve to educate not only those who are just entering the clinical neurosciences, but also those who daily use diffusion imaging to arrive at a proper clinical diagnosis.

Robert M. Quencer, M.D.
Chairman, Department of Radiology
The Robert Shapiro, M.D. Professor of Radiology
University of Miami/Jackson Memorial
Medical Center
Miami, Florida, USA
Editor-in-Chief
American Journal of Neuroradiology

Preface

This book is the result of many years of clinical and academic interest in diffusion-weighted MR (DW) imaging of the brain. Researchers and clinicians at the University of Rochester started to collect DW images of a spectrum of abnormalities affecting the brain immediately after this technique became available. Several case series with clinical and radiographic correlations have been presented at the annual meetings of the American Society of Neuroradiology and the Radiological Society of North America via posters and scientific reports. Over time it became quite clear that we had a collection of DW images representing the majority of conditions that affect the brain and we felt a need to put them all together under one cover.

MR imaging has evolved dramatically since its introduction into clinical work in the mid-1980s. Looking back, there are several major steps that took MR imaging of the central nervous system to the next level. One of the first steps was the introduction of the clinical usefulness of contrast agents. Other steps were the development of fat suppression techniques, fast spin echo imaging, and, more recently, the development of a clinically useful DW imaging technique. DW imaging has revolutionized the imaging diagnosis of acute infarction in the brain. It is, however, quite clear from the series of cases shown in this book that DW imaging is useful for many other conditions. The time it takes to obtain a DW image is so short that in many institutions it is now being used as a routine part of any MR imaging of the brain.

The initial chapters on principles of DW imaging, normal DW appearance, and pitfalls and artifacts provide the bases for understanding DW imaging. This technique is complex and is associated with many pitfalls and artifacts. The following chapter on brain edema provides the basis for understanding the pathophysiology of signal alterations in DW images related to various pathological conditions. The images are correlated to corresponding neuropathologic slides and aid the understanding of the DW imaging representation of various types of brain edema.

Chapters 5–13 cover DW imaging characteristics of different pathologic conditions and in Chap. 14 (pediatrics) we have collected DW images of pediatric conditions.

The book is organized according to major disease categories. This brings structure to the book, but is not optimal for the clinician sitting in front of a set of images and wondering what they might represent. For that reason we have a summary chapter entitled "How to Use This Book" (Chap. 15), which is organized from the opposite perspective. Thus, in Chap. 15 we have started with DW images and grouped them according to imaging characteristics. In each table we have listed differential diagnoses for each specific set of DW imaging characteristics and added thumbnail images with references to the corresponding chapters. The clinician can go directly to Chap. 15, determine the signal on the DW imaging, combine it with the T2 and ADC signal characteristics, and get a list of the conditions that match these imaging characteristics. The thumbnail images, the reference to corresponding chapter and knowledge about the patient's clinical presentation should allow the clinician to formulate a relatively narrow differential diagnosis for most clinical conditions. We think that this "reversed" chapter will make the book very useful for everyday work with DW imaging of the brain.

We are grateful for many pathological slides and fruitful discussions with Barbara Germin, MD, Department of Pathology, University of Rochester. We acknowledge the case contribution from the Department of Radiology, Showa University, Japan, collected during the primary author's time at Showa University. We would also like to thank Masahiro Ida, MD, Department of Radiology, Ebara Municipal Hospital, Japan; Minoru Morikawa, MD, Department of Radiology, Nagasaki University, Japan; R. Nuri Sener, MD, Department of Radiology, Ege University Hospital, Turkey; and Ryutarou Ukisu, MD, Department of Radiology, Showa University, Japan, all of whom contributed case studies. Our deepest gratitude goes to Ms Margaret Kowaluk and Ms Theresa Kubera, Med-

ical Graphic Designers, Department of Radiology, University of Rochester, and Ms Belinda De Libero for her secretary work. We also wish to thank Yuji Numaguchi, MD, PhD, Department of Radiology, University of Rochester and St. Luke's Hospital, Japan, who gave us encouragement and support.

We want to thank the editorial staff at Springer-Verlag, without whose guidance, skills and knowledgeable advice this book would not have become a reality. We would also like to thank our colleagues, fellows and coworkers at the University of Rochester. Finally, but not least, we thank our families for giving us the time to complete this project.

It is our hope that our readers will find this book on "Diffusion-Weighted Imaging of the Brain" instructional and clinically useful.

October 2003   Toshio Moritani
                      Sven Ekholm
                      Per-Lennart Westesson

Authors

Toshio Moritani, MD, PhD
Assistant Research Professor
Division of Diagnostic
and Interventional Neuroradiology
Department of Radiology
University of Rochester
School of Medicine and Dentistry
Rochester, New York, USA

Sven Ekholm, MD, PhD
Professor of Radiology and Director of Research
Division of Diagnostic
and Interventional Neuroradiology
Department of Radiology
University of Rochester
School of Medicine and Dentistry
Rochester, New York

Professor of Radiology
University of Gothenburg
Gothenburg, Sweden

Per-Lennart Westesson, MD, PhD, DDS
Professor of Radiology
and Director of Division of Diagnostic
and Interventional Neuroradiology
Department of Radiology and
Professor of Clinical Dentistry
University of Rochester
School of Medicine and Dentistry
Rochester, New York, USA

Professor of Oral Diagnostic Sciences
State University of New York at Buffalo
Buffalo, New York, USA

Associate Professor of Oral Radiology
University of Lund
Lund, Sweden

Akio Hiwatashi, MD
Assistant Research Professor
Division of Diagnostic
and Interventional Neuroradiology
Department of Radiology
University of Rochester
School of Medicine and Dentistry
Rochester, New York, USA

Ramon R. de Guzman, MD
Fellow, Division of Diagnostic
and Interventional Neuroradiology
Department of Radiology
University of Rochester Medical Center
Rochester, New York, USA

Fellow, Philippine College of Radiology
Philippines

Jianhui Zhong, PhD
Associate Professor of Radiology,
Biomedical Engineering, and Physics
Director of MR Imaging Research
Department of Radiology
University of Rochester
School of Medicine and Dentistry
Rochester, New York, USA

Associate Professor of Radiology
Yale University School of Medicine
New Haven, Connecticut, USA

Contents

Basics of Diffusion Measurements by MRI

In collaboration with J. Zhong

Diffusion occurs as a result of the constant movement of water molecules. Water makes up 60–80% of our body weight. The heat associated with our body temperature energizes the water molecules, causing them to "jerk" around randomly. This phenomenon is called "Brownian motion" after the scientist who first described it [1, 2]. It can be demonstrated by adding a few drops of ink to a still bucket of water. Initially, the ink will be concentrated in a very small volume, but it will quickly spread out (diffuse) and mix with the rest of the water. The speed of this process of diffusion gives physicists a measure of the property of water. Similarly, if we could put some "magic ink" into the brain tissue and follow its progress, we would gain knowledge about the brain tissue itself, as well as the kind of changes that may occur in the brain when it is affected by various disease processes.

1.1 Diffusion Imaging in MR

In the measurement of diffusion by MR, the "magic ink" is created by the magnetic field gradients [3]. When the patient enters the large tunnel of a static magnetic field, nuclear spins (small magnets inside each proton nucleus) are lined up along the direction of the big magnet. Magnetic field gradients of certain duration will then add a smaller magnetic field to spins located in different regions within the tissue. This is similar to marking the spins with "magic ink". By applying another gradient pulse at a later time, information is obtained about how much the spins have spread (diffused) during this time. This is analogous to comparing two snapshots, one taken at the moment when the ink is dropped into the water and one taken later, to obtain information about how the ink has spread in the water. However, the analogy of ink in water and what happens in the brain stops here.

1.2 Diffusion Imaging of the Brain

The brain is complex and full of fibrous, globular and other structures and membranes, which may or may not allow water to move freely. Because water spins will run into constituents of cells of different concentrations in different cellular compartments, they will spread at different rates when labeled with the "magic ink". In addition, they will not behave in the same way when they are moving in different directions. As described below, the former is measured as the diffusion rate, diffusion coefficient, or simply diffusivity, depending on the unit used, and the latter is more formally described as diffusion anisotropy, with a variety of parameters defined [4–7].

1.3 Magnetic Resonance Principles of Diffusion Imaging

In order to perform diffusion studies, one needs to apply field gradients in addition to the radiofrequency and gradient pulses used for conventional MR imaging. A simplified version of the most commonly used pulse-gradient spin-echo pulse sequence for diffusion imaging is shown in Fig. 1.1. During the time evolution (TE), a pair of field gradients is used to perform "diffusion-encoding." Each gradient in this gradient pair will last a time δ, with strength G (usually in units of mT/m), and the pair is separated by a time Δ. A more formal analysis will tell us that the intensity of the signal will depend on all these parameters, given by

$$S = S_0 \exp(-b\,ADC), \tag{1}$$

where ADC is the apparent diffusion coefficient, and b is the gradient factor, sometimes simply called the b-factor. S_0 is the signal intensity obtained when no diffusion gradients are used. The diffusion coefficient

calculated in this way is usually called "apparent" because it is often an average measure of much more complicated processes in the tissues, as discussed below. The b-factor is related to the gradient parameters δ, G and Δ (Fig. 1.1), usually in the form $b \propto (\delta G)^2$ $(\Delta - \delta / 3)$, and is set by the experimenter. The formula for the b-factor tells us that we can increase diffusion weighting (DW) by increasing either gradient timing, δ or Δ, or gradient strength, G.

Equation 1.1 suggests that there is a reduction in the measured signal intensity when DW is applied, b≠0, which can be understood with some simple reasoning. As the diffusing spins are moving inside the field gradient (an additional magnetic field varying in intensity from location to location), each spin is affected differently by the field. The alignment of the spins with each other is thus destroyed. Since the measured signal is a summation of tiny signals from all individual spins, the misalignment, or "dephasing", caused by the gradient pulses results in a drop in signal intensity; the longer the diffusion distance, the lower the signal (more dephasing; Fig. 1.2).

1.4 Apparent Diffusion Coefficient

From Eq. 1.1 it can be seen that when a fixed DW b-factor is used, tissues with a higher ADC value produce a lower signal intensity. Since brain cerebrospinal fluid (CSF) contains water that can move around freely, its ADC value is much higher than that of other brain tissues (either gray matter or white matter), which contain many more cellular structures and constituents. Consequently, in a DW image one typically sees dark CSF space (pronounced dephasing) and brighter tissue signals (less dephasing). It is also clear from Eq. 1.1 that if we collect a series of DW images with different b-values, we can calculate according to the expression for every pixel and obtain a parametric map of ADC values. The result is sometimes referred to as an ADC map. The calculated ADC map would have image pixel intensities reflecting the strength of diffusion in the pixels. Regions of CSF will therefore have higher intensity than other brain tissues – a reversal of DW images. There are several reasons why it is sometimes desirable to calculate an ADC map instead of just using DW images. One is the so-called T2-shine-through effect, which will be discussed in a later chapter. It can also be noted that S_0 in Eq. 1.1 is equal to the signal when no DW is used.
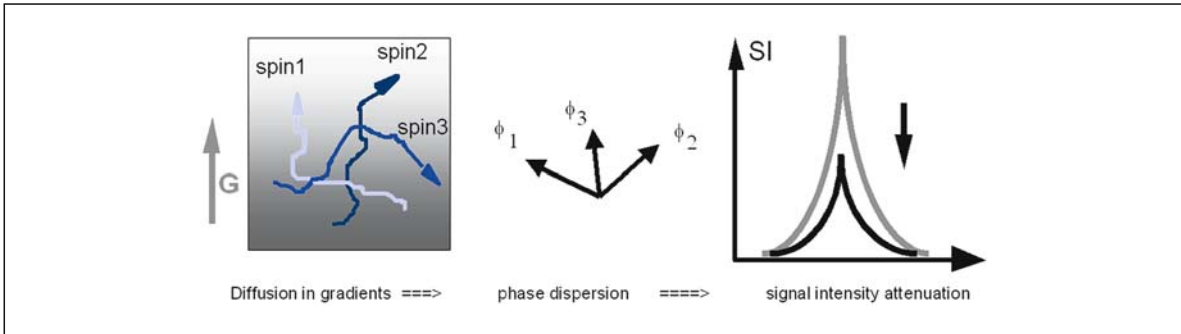
Figure 1.2

Effects of gradients on diffusing spins. Diffusion in the gradient causes dephasing of spins and therefore reduction in the measured signal intensity

Figure 1.1 suggests that this is actually the same as would be obtained from a simple spin-echo sequence. In most clinical scanners, a long TE time (tens of milliseconds) is needed to accommodate the diffusion pulses, so S_0 is often T2-weighted.

1.5 Diffusion Represents a Molecular Event

Even though an image pixel size in the order of millimeters is used in most clinical MR imaging, the information provided by diffusion imaging reflects cellular or molecular events in much smaller scales. This is because the molecular diffusion process is highly modulated by these events. It can be shown that water spins diffuse about tens of micrometers during a typical MR imaging measurement time, which coincides with the dimension of typical cellular structures. If spins experience minimal obstruction from cellular structures during this time (such as for spins in the CSF space), the measured diffusion is "free" and "isotropic", and ADC is just the intrinsic molecular diffusion coefficient. On the other hand, when diffusing spins run into cellular constituents and membranes, the value of ADC will be reduced when compared with the value in free space. What happens at the cellular level is represented schematically in Fig. 1.3. For patients with neurological abnormalities that change the water distribution in various cellular compartments, or change the ability of water to pass through cell membranes, the measured ADC values will also be altered [4–7]. Therefore the MR diffusion measurement offers a unique opportunity to obtain information about morphology otherwise inaccessible to conventional MR imaging methods. A wide range of pathological conditions can be explored with water diffusion measurements, as described later in this book. The measured ADC may also vary depending on the duration of the diffusion process, the direction in which diffusion is measured, and other factors. For diffusion in an anisotropic environment (such as in brain white matter, where bundles of axons with myelin layers wrapped around them make diffusion along the bundle much easier than across the bundle), diffusion becomes more complicated and a complete description of the process relies on what is called tensor analysis [8, 9].
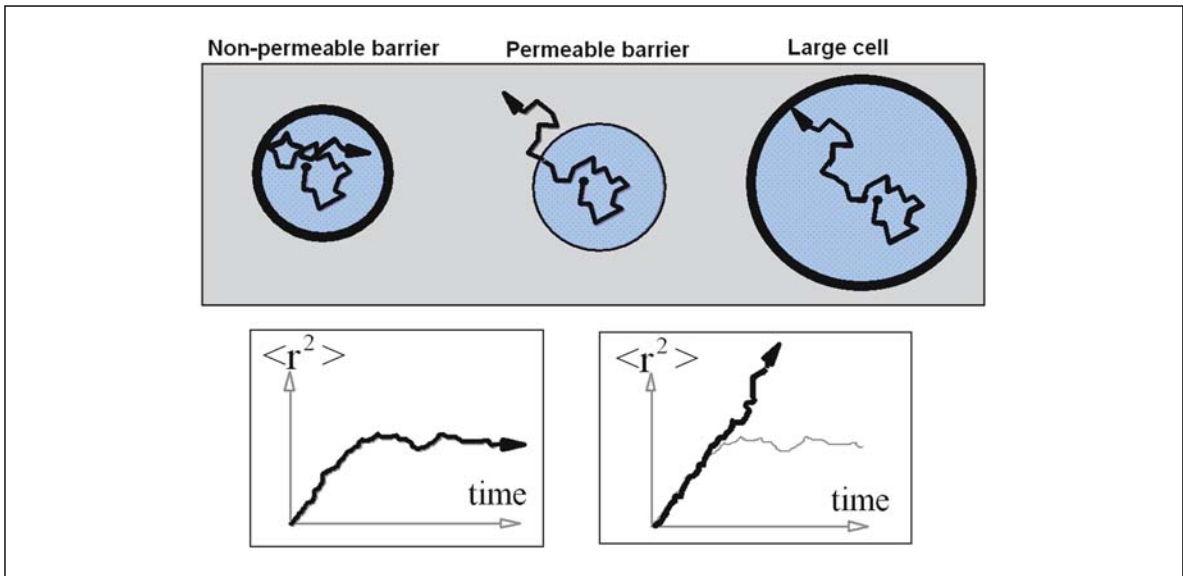
Figure 3.1

When water spins are diffusing among cellular structures, depending on the mean displacement ($<r^2>$) during the measurement time and the size of the cellular structure, their behavior can be quite different. Water inside a non-permeable cell (*top* and *bottom left*) experiences restriction or hindrance to diffusion. Diffusion barrier effects are minimal for water inside a permeable cell, or in a cell that is much larger than the mean displacement during diffusion (*top middle* and *right*, and *bottom right*)

1.6 Requirements in Clinical Diffusion Imaging

In a clinical environment, certain requirements are imposed for diffusion studies. A reasonable imaging time is often limited to several minutes for each type of measurement (T1 W, T2 W, diffusion, and others). Multiple slices (15–20) are required to cover most of the brain. A good spatial resolution (~5–8 mm thick, 1–3 mm in-plane) is required. A reasonably short TE (120 ms) to reduce T2 decay, and an adequate diffusion sensitivity (ADC ~0.2–1×10^{-3} mm^2/s for brain tissues) are also needed. However, most essential is the almost complete elimination of sensitivity to subject motion during scanning. The best compromise so far in most clinical practices of diffusion imaging is the use of the multi-directional (x,y,z), 2 b-factor (b=0, and b~1/ADC) single-shot echo-planar imaging technique. Sometimes fluid attenuation with inversion recovery (FLAIR) is used to eliminate signal in the highly diffusive CSF space. Separation from relaxation effects is achieved with calculation of ADC

instead of just using DW, and elimination of anisotropic diffusion is achieved by averaging the diffusion measurements from three orthogonal directions.

1.7 Setting the b-Value in Clinical DW Imaging

In a clinical setting it is advisable to maintain the same b-value for all examinations, making it easier to learn to interpret these images and become aware of the appearance of findings in various disease processes. The studies and discussions presented in this book are limited to DW imaging using b-factors of 0 and 1,000. An upper b-factor around 1,000 has been available for most clinical scanners until now and DW imaging at these standard values has been shown to be a sensitive tool in detecting and delineating restricted diffusion, e.g. in acute ischemic lesions of the brain. However, this technique has become clinically important in many other disease processes, which will be discussed in this book.

1.8 Future Trends in Clinical DW Imaging

Newer DW imaging techniques are using even higher b-values: 8.000 and more. Some recent articles that explore the use of higher b-values imply that they will simplify clinical diffusion imaging [10]. The increased b-values may free up routine DW imaging from its most pressing problem, "T2 shine-through". At high b-values more attention will be focused on the actual physiological basis of restricted and facilitated diffusion. Clearly, much of the advantage of increased b-values may lie not with the diagnosis of lesions with restricted diffusion, especially acute infarcts, but with allowing a more complete understanding of other types of diseases.

The benefits of improved diffusion contrast at high b values come with the complication of prescription dependent measures of apparent diffusion. The ADC is conventionally derived from images taken at two different b-values. Because tissues are described by fast and slow components, the results of a two-point measurement will depend on the specific b-values chosen. If the lower b-value is set to 0 (a T2-weighted image) and the upper value is allowed to vary, the ADC will vary as a function of the upper value. Specifically, one would expect the measured ADC to decrease as the upper b-value increases.

Another area of DW imaging that will evolve over the next few years is diffusion tensor imaging, which is becoming available in many modern clinical scanners. When these and other techniques become more accessible and technically more mature, they may provide more specific measurements.

References

1. Brown R (1928) A brief account of microscopical observations made in the months of June, July, and August, 1827, on the particles contained in the pollen of plants; and on the general existence of active molecules in organic and inorganic bodies. Phil Mag 4:161–173
2. Doob JL (1942) The Brownian movement and stochastic equations. Ann Math 43:351–369
3. Stejeskal EO, Tanner JE (1965) Spin diffusion measurements: spin echoes in the presence of time-dependent field gradient. J Chem Phys 42:288–292.
4. Le Bihan D, Breton E, Lallemand D, Grenier P, Cabanis E, Laval-Jeantet M (1986) MR imaging of intravoxel incoherent motions: application to diffusion and perfusion in neurologic disorders. Radiology Nov; 161(2):401–407
5. Moseley ME, Kucharczyk J, Mintorovitch J (1990) Diffusion-weighted MR imaging of acute stroke: correlation with T2-weighted and magnetic susceptibility-enhanced MR imaging in cats. AJNR Am J Neuroradiol 11:423
6. Moonen CT, Pekar J, Vleeschouwer de MHM, Gelderen van P, Zijl van PCM, DesPres D (1991) Restricted and anisotropic displacement of water in healthy cat brain and in stroke studied by NMR diffusion imaging. Magn Reson Med 19:327
7. Zhong J, Petroff OAC, Prichard JW, Gore JC (1993) Changes in water diffusion and relaxation properties of rat cerebrum during status epilepticus. Magn Reson Med 30:241
8. Basser PJ, Mattiello J, Le Bihan D (1994) Estimation of the effective self-diffusion tensor from the NMR spin-echo. J Magn Reson 103:247–254
9. Le Bihan D, Van Zijl P (2002) From the diffusion coefficient to the diffusion tensor. NMR Biomed Nov-Dec; 15(7–8):431–434
10. Clark CA, Le Bihan D (2000) Water diffusion compartmentation and anisotropy at high b values in the human brain. Magn Reson Med Dec; 44(6):852–859

Diffusion-Weighted Imaging of the Normal Brain

In collaboration with A. Hiwatashi and J. Zhong

2.1 Introduction

Diffusion-weighted (DW) images are usually obtained in three orthogonal orientations using spin-echo type single-shot DW echo-planar imaging with b-values around 0 and 1,000 s/mm². These three planes are combined into isotropic DW images, and apparent diffusion coefficient (ADC) maps are calculated on a pixel-by-pixel basis (Fig. 2.1). To avoid misinterpretations, it is important to recognize the normal findings on DW images and ADC maps.

2.2 Adult Brain

2.2.1 Low Signal in Basal Ganglia

Isotropic DW imaging in adult brain often shows low signal intensity in the basal ganglia (Fig. 2.1). This low signal is caused by normal iron deposition. The hypointensity on DW images of these areas is essentially related to T2 contrast, which is also shown on b_0 images. ADC maps usually show the areas as iso-intense, but it can be hyper- or hypointense depending on the paramagnetic susceptibility artifact of iron deposition.

2.2.2 Diffusion-Weighted Imaging of Gray and White Matter

Gray matter on DW images is generally hyperintense when compared with white matter. ADC of gray ($0.76 \pm 0.13 \times 10^{-3}$ mm²/s) and white matter ($0.77 \pm 0.18 \times 10^{-3}$ mm²/s) are, however, identical in the adult brain [1]. There are several reports about ADC increasing with age [2–7], but this increase is minimal and has been observed in all parts of the brain. It is usually more apparent in the white matter and lentiform nucleus than in the rest of the brain. Focal areas of DW hyperintensities are often seen in posterior limbs of internal capsule, corticospinal tracts, medial lemniscus and the decussation of the superior cerebellar peduncles (Fig. 2.1). These DW hyperintensities are caused by T2 contrast and represent normal findings without clinical significance. ADC maps are usually isointense in these areas.

2.2.3 Choroid Plexus

The choroid plexus occasionally shows prominent hyperintensity on DW imaging associated with mild elevation of ADC. In these situations the ADC is often higher than in white matter, but lower than in cerebrospinal fluid. The high DW signal is believed to represent gelatinous cystic changes of the choroid plexus, which can occur with age (Fig. 2.2).
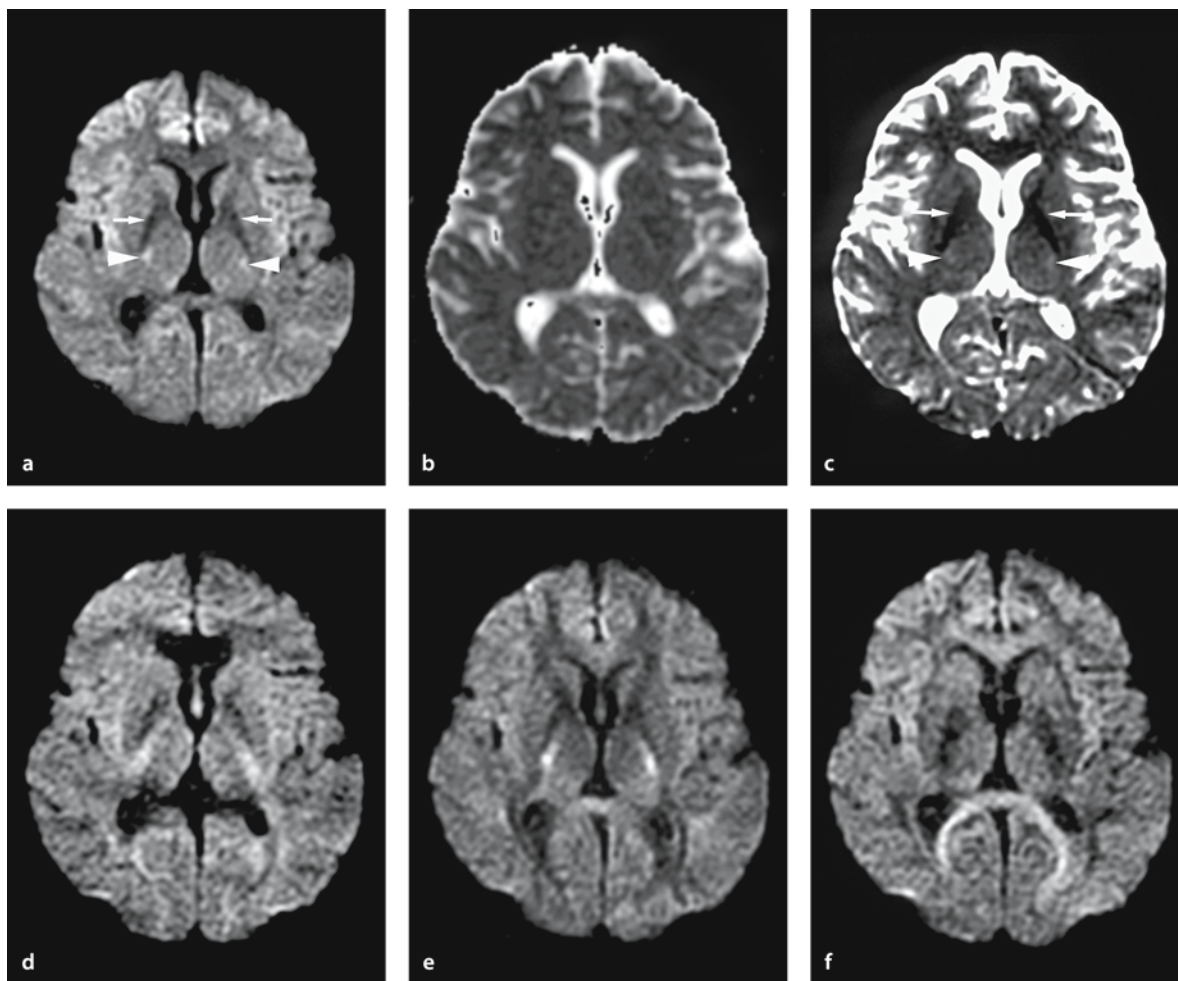
Figure 2.1 a–f

Normal adult brain of a 40-year-old male without neurological deficits. **a** Isotropic DW image is obtained by combining b_0 image and three orthogonal unidirectional images (*x, y, z* axis). The bilateral globi pallidi have low signal on DW image as a result of physiological iron deposition (*arrows*). Corticospinal tracts have mildly high signal on DW image (*arrowheads*). Gray matter shows mildly high signal compared to white matter. These signal changes on isotropic DW imaging are normal and are caused by T2 contrast. **b** ADC map shows homogeneous ADC values in globi pallidi, corticospinal tracts, gray and white matter. **c** b_0 image shows low signal in globi pallidi (*arrows*), high signal in corticospinal tracts (*arrowheads*), and the gray–white matter contrast. **d–f** Diffusion weighting is applied in *x* axis (**d**), *y* axis (**e**), and *z* axis (**f**)

Figure 2.2 a–d

Cystic changes in the choroid plexus. **a** DW image shows hyperintensity in cystic changes of the left choroid plexus (*arrow*). **b** ADC values of the cystic changes are lower than those of the CSF, which may represent viscous gelatinous materials, but higher than those of brain parenchyma (*arrow*). **c** T2-weighted image shows the cystic changes as hyperintensity (*arrow*). **d** Gadolinium-enhanced T1-weighted image with magnetization transfer contrast reveals no enhancement in it (*arrow*)
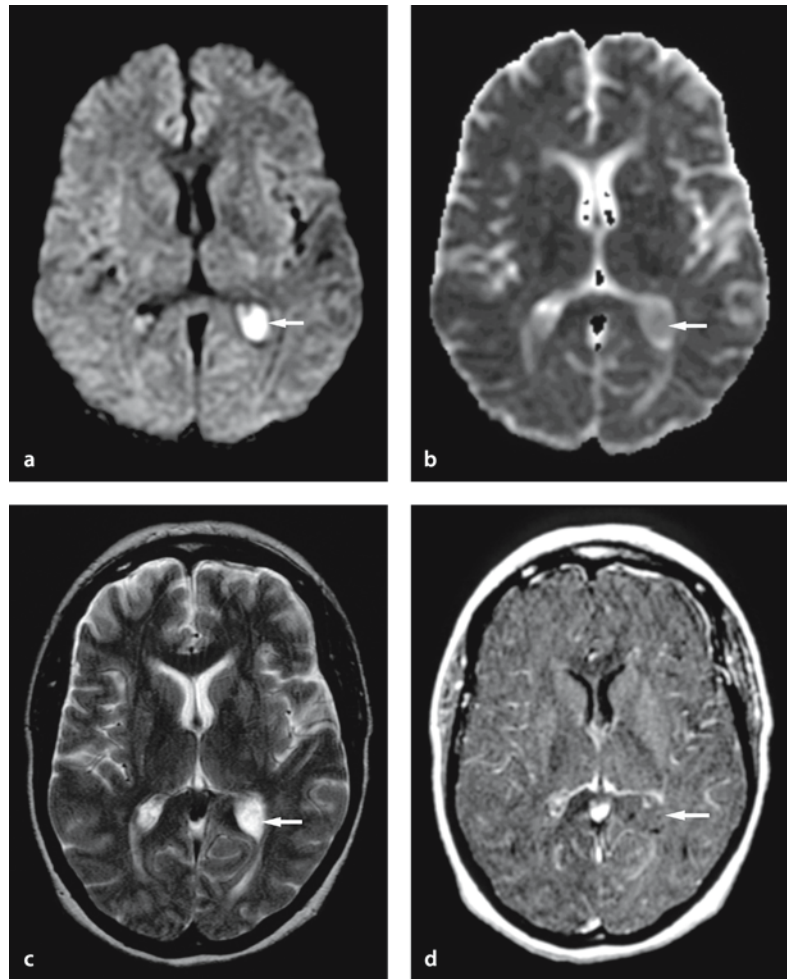
2.3 Pediatric Brain

2.3.1 Diffusion-Weighted Imaging and ADC of the Pediatric Brain

The normal brain of neonates and infants has significantly higher ADC values than the adult brain [8–13] (Fig. 2.3). ADC in neonates and infants varies markedly within different areas of the brain and is higher in white matter (1.13×10^{-3} mm^2/s) than in gray matter (1.02×10^{-3} mm^2/s) [13]. ADC at birth is higher in subcortical white matter (1.88×10^{-3} mm^2/s) than in both the anterior (1.30×10^{-3} mm^2/s) and posterior limbs of the internal capsule (1.09×10^{-3} mm^2/s). It is also higher in cortex and the caudate nucleus (1.34×10^{-3} mm^2/s) than in the thalamus and the lentiform nucleus (1.20×10^{-3} mm^2/s) [13]. With the exception of the cerebrospinal fluid (CSF), there is a trend of decreasing ADC with increasing maturation in most areas of the pediatric brain. These ADC changes seem to reflect a combination of different factors, including a reduction of overall water content, cellular maturation and white matter myelination. In neonates and infants, ischemia is usually global and can therefore resemble the normal image with elevated DW signal and decreased ADC. White matter diseases can also be mimicked by the normal, age-related appearance of DW imaging and ADC. Out of necessity, the ADC values will therefore have to be age related for a correct interpretation of the DW images of the pediatric brains.
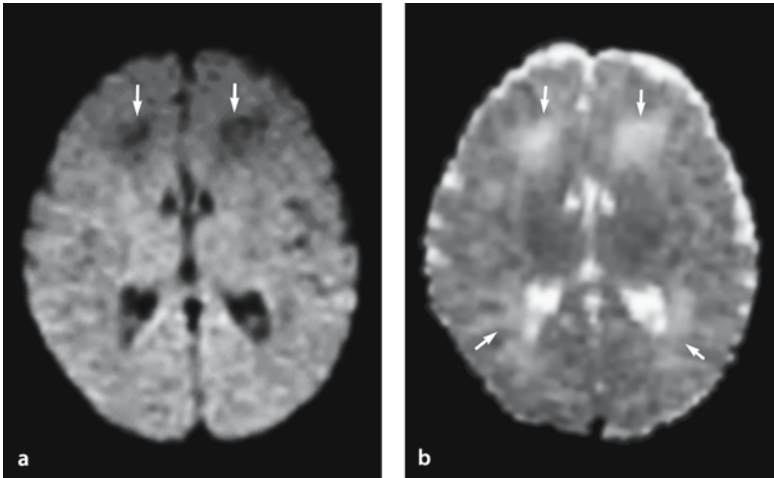
Figure 2.3 a, b

Normal neonatal brain. **a** The appearance of the pediatric brain on DW images varies with age. In neonates it is normal to have low DW signal intensities in the frontal deep white matter (*arrows*). **b** ADC values of the corresponding areas are high in neonatal brain, especially in the white matter (*arrows*). These ADC changes seem to reflect a combination of factors, including a reduction of overall water content, cellular maturation, and white matter myelination

2.4 Conclusion

Good knowledge of the DW appearance of the normal adult and pediatric brain and variations is necessary to avoid misinterpretation. In children it is also important to match the findings with those of normal children of the same age.

References

1. Yoshiura T, Wu O, Sorensen AG (1999) Advanced MR techniques: diffusion MR imaging, perfusion MR imaging, and spectroscopy. Neuroimaging Clin N Am 9:439–453
2. Chun T, Filippi CG, Zimmerman RD, Ulug AM (2000) Diffusion changes in the aging human brain. Am J Neuroradiol 21:1078–1083
3. Engelter ST, Provenzale JM, Petrella JR, DeLong DM, MacFall JR (2000) The effect of aging on the apparent diffusion coefficient of normal-appearing white matter. Am J Roentgenol 175:425–430
4. Helenius J, Soinne L, Perkio J (2002) Diffusion-weighted MR imaging in normal human brains in various age groups. Am J Neuroradiol 23:194–199
5. Gideon P, Thomsen C, Henriksen O (1994) Increased self-diffusion of brain water in normal aging. J Magn Reson Imaging 4:185–188
6. Nusbaum AO, Tang CY, Buchsbaum MS, Wei TC, Atlas SW (2001) Regional and global changes in cerebral diffusion with normal aging. Am J Neuroradiol 22:136–142
7. Abe O, Aoki S, Hayashi N, et al. (2002) Normal aging in the central nervous system: quantitative MR diffusion-tensor analysis. Neurobiol Aging 23:433–441
8. Sakuma H, Nomura Y, Takeda K, et al. (1991) Adult and neonatal human brain: diffusional anisotropy and myelination with diffusion-weighted MR imaging. Radiology 180:229–233
9. Morriss MC, Zimmerman RA, Bilaniuk LT, Hunter JV, Haselgrove JC (1999) Changes in brain water diffusion during childhood. Neuroradiology 41:929–934
10. Tanner SF, Ramenghi LA, Ridgway JP, et al. (2000) Quantitative comparison of intrabrain diffusion in adults and preterm and term neonates and infants. Am J Roentgenol 174:1643–1649
11. Neil JJ, Shiran SI, McKinstry RC, et al. (1998) Normal brain in human newborns: apparent diffusion coefficient and diffusion anisotropy measured by using diffusion tensor MR imaging. Radiology 209:57–66
12. Engelbrecht V, Scherer A, Rassek M, Witsack HJ, Modder U (2002) Diffusion-weighted MR imaging in the brain in children: findings in the normal brain and in the brain with white matter diseases. Radiology 222:410–418
13. Forbes KP, Pipe JG, Bird CR (2002) Changes in brain water diffusion during the 1st year of life. Radiology 222:405–409

Pitfalls and Artifacts of DW Imaging

In collaboration with A. Hiwatashi and J. Zhong

3.1 Introduction

There are many inherent artifacts and pitfalls in diffusion-weighted (DW) imaging of the brain that are important to recognize to avoid misinterpretations.

3.2 Influence of ADC and T2 on the DW Appearance

Diffusion-weighted images are inherently T2 weighted and changes in T2 signal characteristics will thus influence the appearance of DW images independent of tissue diffusibility [1–16]. The effect of T2 prolongation, so-called "T2 shine-through", is well known. Less well known is the balance between apparent diffusion coefficient (ADC) and T2, sometimes called T2 washout. Also the effect of T2 shortening, or T2 blackout, and magnetic susceptibility effects will influence the DW appearance in many situations. This chapter will illustrate and discuss the effects of T2 and ADC on DW images.

3.2.1 Concepts

The signal intensity (SI) on DW images is influenced by T2, ADC, the b factor, the spin density (SD) and the echo time (TE), and is calculated as follows:

$$SI=SI_{b=0}e^{-bADC}$$

However,

$$SI_{b=0}=kSD(1-e^{-TR/T1})e^{-TE/T2}$$

For TR >>T1

$$SI=kSDe^{-TE/T2}e^{-bADC}$$

where k is a constant, TR is repetition time, and $SI_{b=0}$ is the signal intensity on the spin-echo echo-planar image (b_0 image) [1, 2, 5, 7, 8, 10, 12, 16].

To evaluate the tissue T2 and ADC, we should pay attention to the images discussed below as well as isotropic DW images and b_0 images [3–5, 7, 8, 10, 11, 13–16].

3.2.2 Apparent Diffusion Coefficient Maps

To evaluate the diffusibility, ADC is calculated as:

$$ADC=-ln\,(SI/SI_{b=0})/b$$

Subsequently, increased ADC causes decreased SI on DW images, and decreased ADC causes increased SI on DW images [3–5, 7, 10, 15, 16].

3.2.3 Exponential Images

To remove the T2-weighted contrast, the DW image can be divided by the b_0 image to create an "exponential image" [4, 7, 10, 15].

The signal intensity (SI_{eDWI}) on the exponential image is calculated as:

$$SI_{eDWI}=SI/SI_{b=0}=e^{-bADC}$$

Therefore, this image can eliminate the effect of T2. Contrary to ADC maps, hyperintensity on exponential DW images means decreased ADC, and hypointensity means increased ADC.

3.3 Clinical Conditions

3.3.1 T2 Shine-through

This is a well-known phenomenon that causes hyperintensity on DW images by means of T2 prolongation [3–5, 7, 8, 10, 11, 15, 16]. If ADC is decreased at the same time, this can result in an accentuation of the hyperintensity on DW images (Figs. 3.1, 3.2 and 3.3).
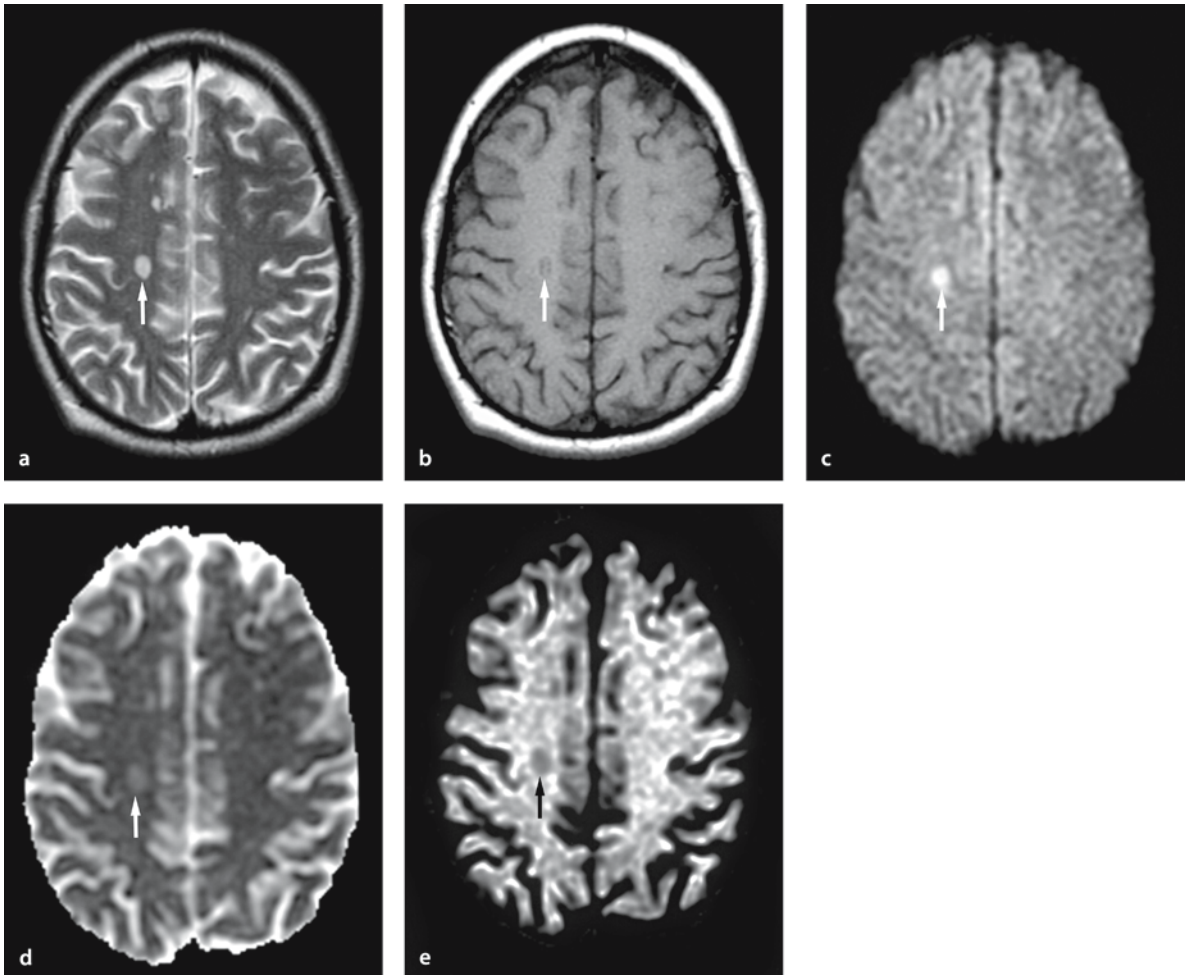
Figure 3.1 a–e

T2 shine-through in a 35-year-old female with multiple sclerosis and weakness of the lower extremities. **a** T2-weighted image shows several hyperintense lesions, with the largest one in the right frontal lobe (*arrow*). **b** On T1-weighted image the lesion was hypointense (*arrow*) and did not enhance with contrast (not shown). **c** On DW image the lesion is hyperintense (*arrow*). **d** ADC map also shows hyperintensity in the lesion (1.2×10^{-3} mm^2/s; *arrow*). **e** Exponential image eliminates the T2 effect and shows the lesion to be hypointense (*arrow*). This confirms that the hyperintensity on DW image is due to a T2 shine-through
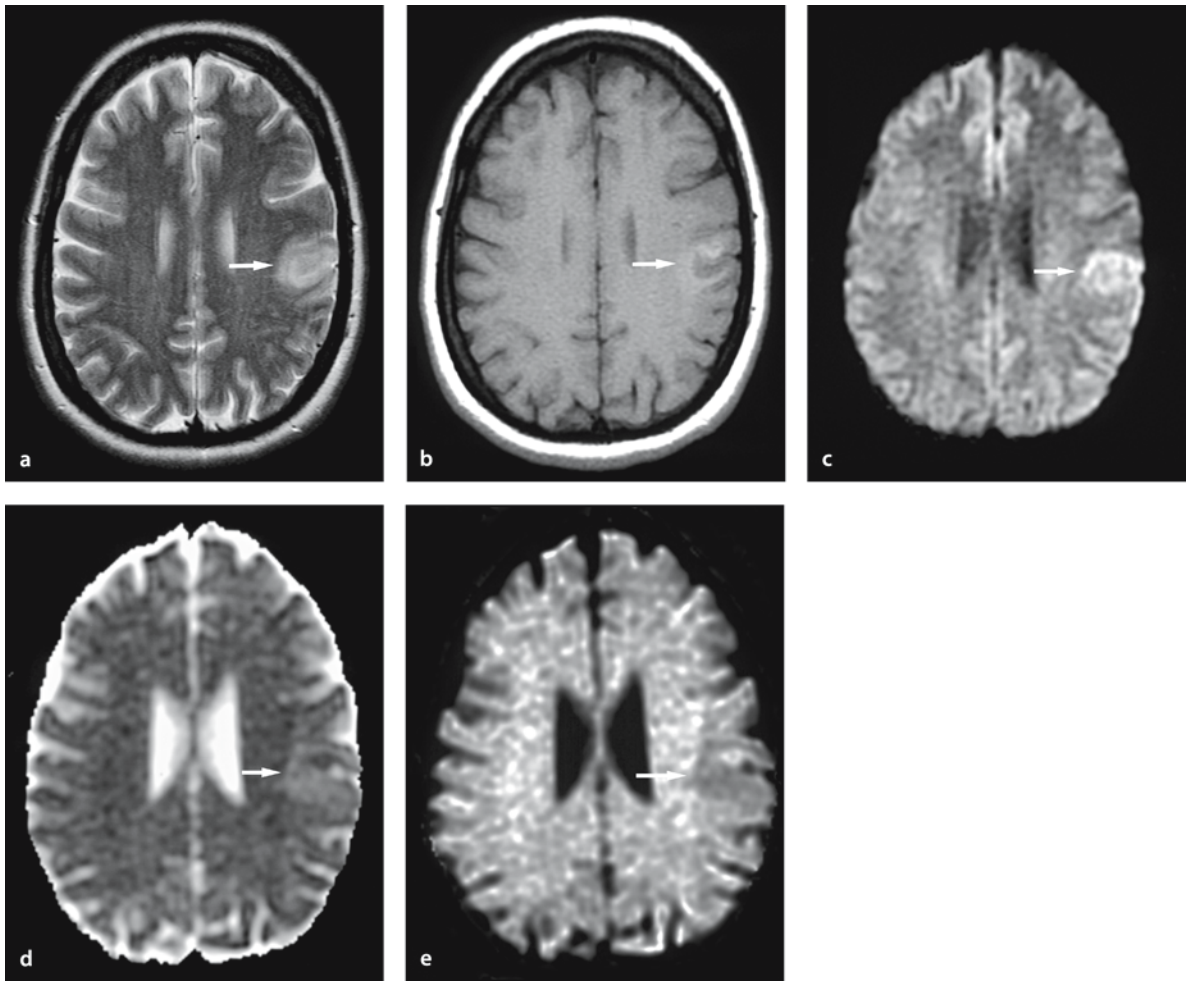
Figure 3.2 a–e

T2 shine-through in a 45-year-old female with seizures caused by anaplastic astrocytoma. **a** T2-weighted image shows a hyperintense lesion in the left frontal lobe (*arrow*). **b** On T1-weighted image the lesion is hypointense with peripheral hyperintense area (*arrow*). The lesion did not enhance with contrast (not shown). **c** DW image shows hyperintensity (*arrow*). **d** ADC map also shows hyperintensity in the lesion (0.98–1.35×10^{-3} mm^2/s; *arrow*). **e** Exponential image eliminates the T2 effect and shows the lesion to be hypointense (*arrow*). This confirms that the hyperintensity on DW image is due to a T2 shine-through
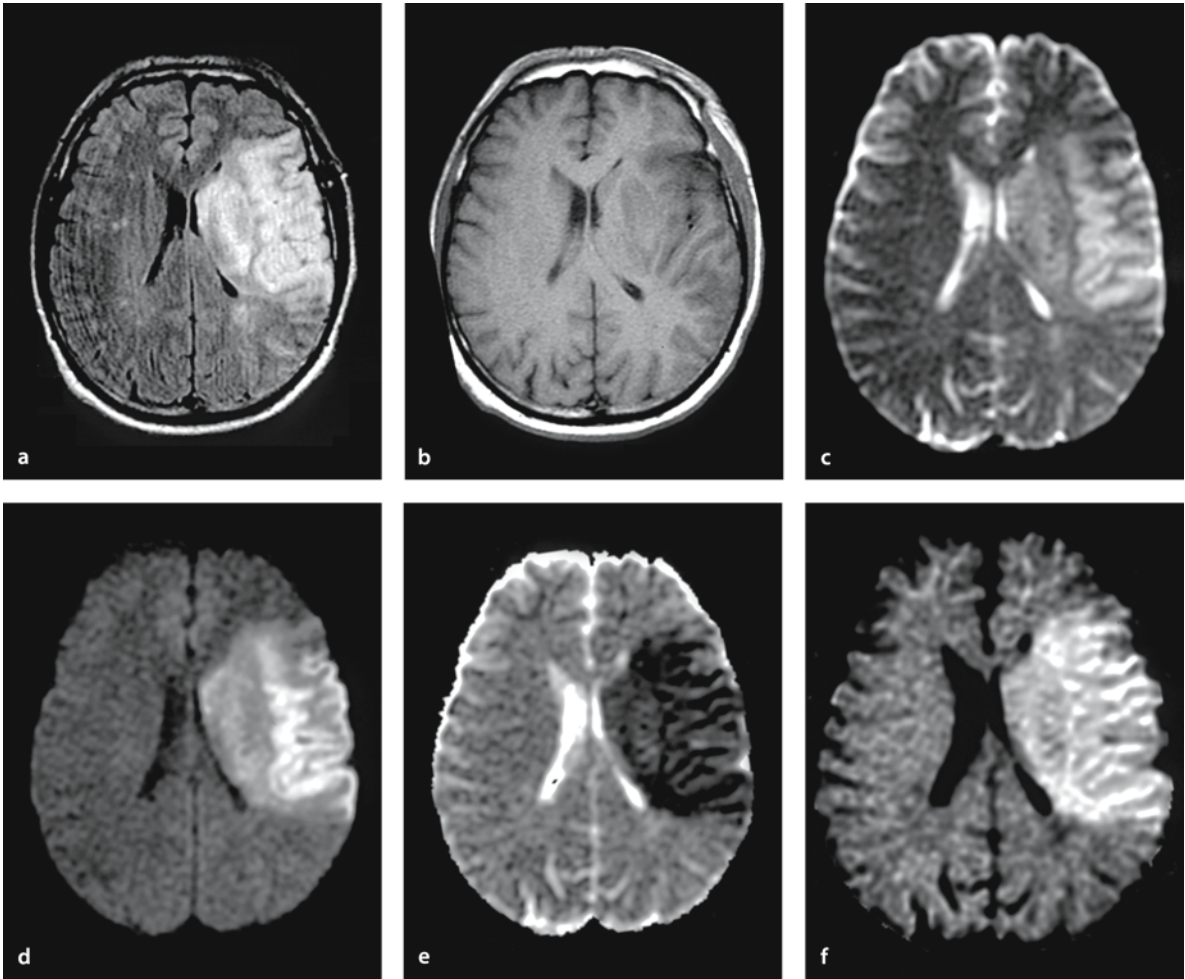
Figure 3.3 a–f

T2 shine-through and restricted diffusion in a 56-year-old male with right-sided weakness due to acute infarction. MR imaging obtained 24 hours after the onset of symptoms. **a** FLAIR image shows a hyperintense lesion in the left middle cerebral artery territory. **b** On T1-weighted image the lesion is hypointense. **c** On T2-weighted image (b_0) the lesion is hyperintense. **d** DW image also shows hyperintensity in the lesion. **e** ADC map shows hypointensity in the lesion $(0.27–0.45\times10^{-3}$ mm^2/s). **f** On the exponential image, which eliminates the T2 effect, the lesion remains hyperintense. This confirms that the DW hyperintensity is due to both restricted diffusion and T2 prolongation

3.3.2 T2 Washout

This implies that isointensity on DW images is the result of a balance between hyperintensity on T2-weighted images and increased ADC [13, 14, 16]. This is often seen in vasogenic edema, where the combination of increased ADC and hyperintensity on T2-weighted images will result in isointensity on DW images (Fig. 3.4).

To the best of our knowledge there have been no systematic reports on pathological conditions with isointensity on DW images, caused by a balance of hypointensity on T2-weighted images and decreased ADC.

Figure 3.4 a–d

T2 washout in a 45-year-old female with hypertension, seizures and posterior reversible encephalopathy syndrome. **a** FLAIR image shows hyperintense lesions in the bilateral occipital lobe (*arrows*). **b** T2-weighted image (b$_0$) also shows hyperintensity of the lesions (*arrows*). **c** DW image shows mild hyperintensity in the lesions. **d** ADC map shows hyperintensity of the lesions (1.18–1.38×10^{-3} mm^2/s; *arrows*). With the strong T2 prolongation one would expect more hyperintensity on the DW image, but the T2 shine-through effect is reduced by the hyperintensity on the ADC, resulting in a balance between increased diffusibility and hyperintensity on the T2-weighted image (T2 wash-out)
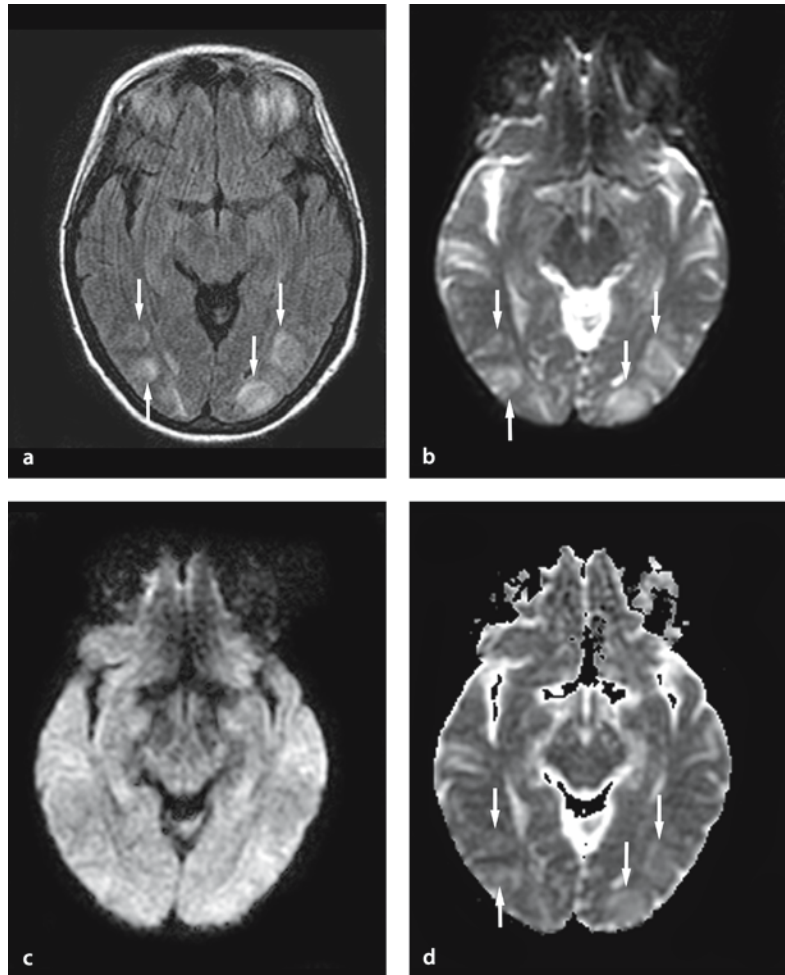
3.3.3 T2 Blackout

This indicates hypointensity on DW images caused by hypointensity on T2-weighted images and is typi-

cally seen in some hematomas [9,16]. Paramagnetic susceptibility artifacts may occur in this situation (Figs. 3.5 and 3.6).
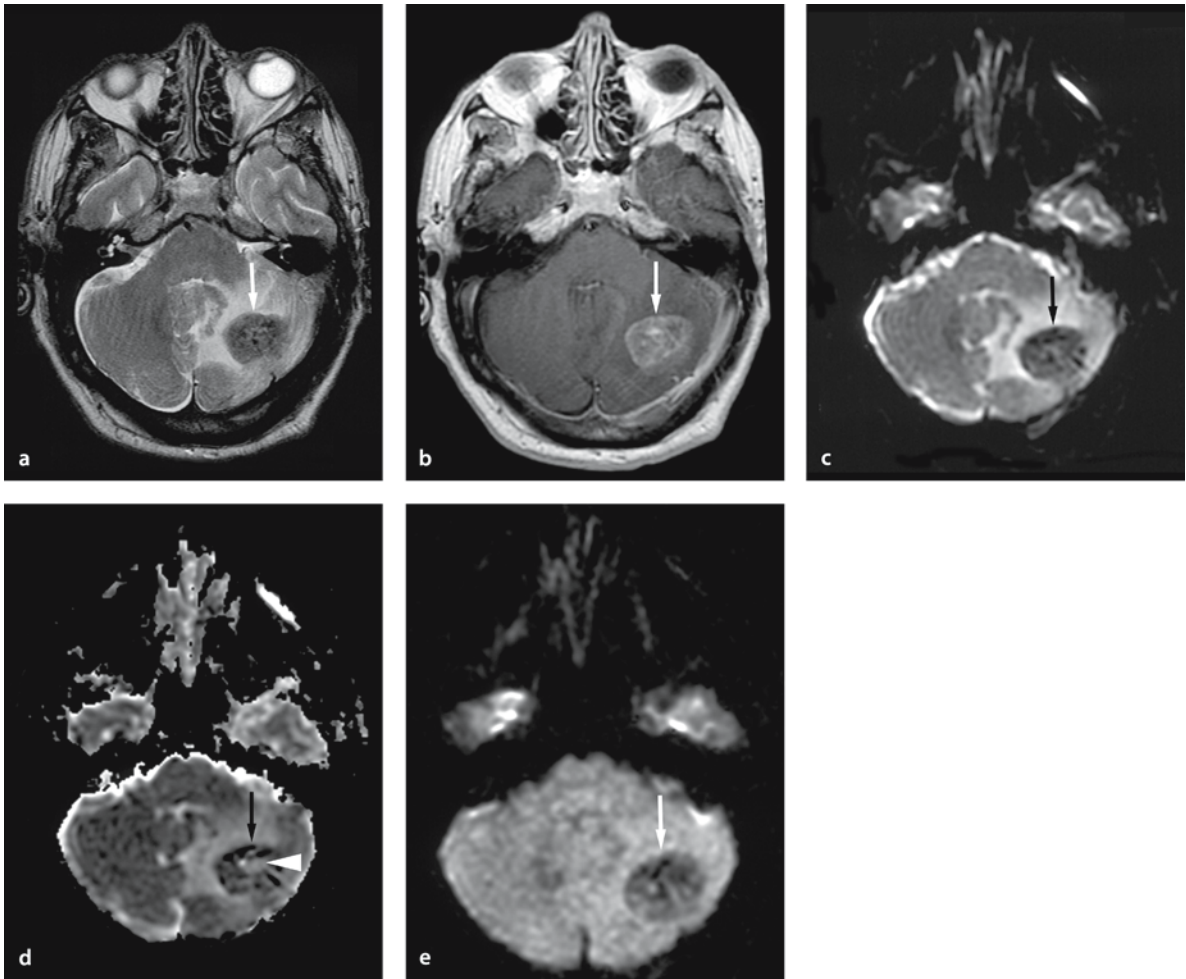
Figure 3.5 a–e

T2 blackout in lung cancer metastasis in a 62-year-old male with adenocarcinoma of the lung. **a** T2-weighted image shows a hypointense mass (*arrow*) with surrounding edema in the left cerebellar hemisphere. **b** Gadolinium-enhanced T1-weighted image shows heterogeneous enhancement of the mass (*arrow*). **c** T2-weighted image (b_0) also shows hypointensity in the lesion with surrounding hyperintense edema (*arrow*). **d** ADC map shows central hyperintensity ($1.63–2.35\times10^{-3}$ mm^2/s; *arrowhead*) and peripheral hypointensity ($1.13–1.38\times10^{-3}$ mm^2/s; *arrow*) of the mass. There is also hyperintensity of the surrounding tissue, consistent with vasogenic edema. **e** DW image shows heterogeneous hypointensity of the mass (*arrow*) and isointensity of the surrounding edema. The DW hypointensity of the mass (*arrow*) is due to the increased diffusibility and hypointensity on T2-weighted image. The isointensity in the surrounding edema is due to the balance between the increased diffusibility and hyperintensity on T2-weighted image (T2 washout)
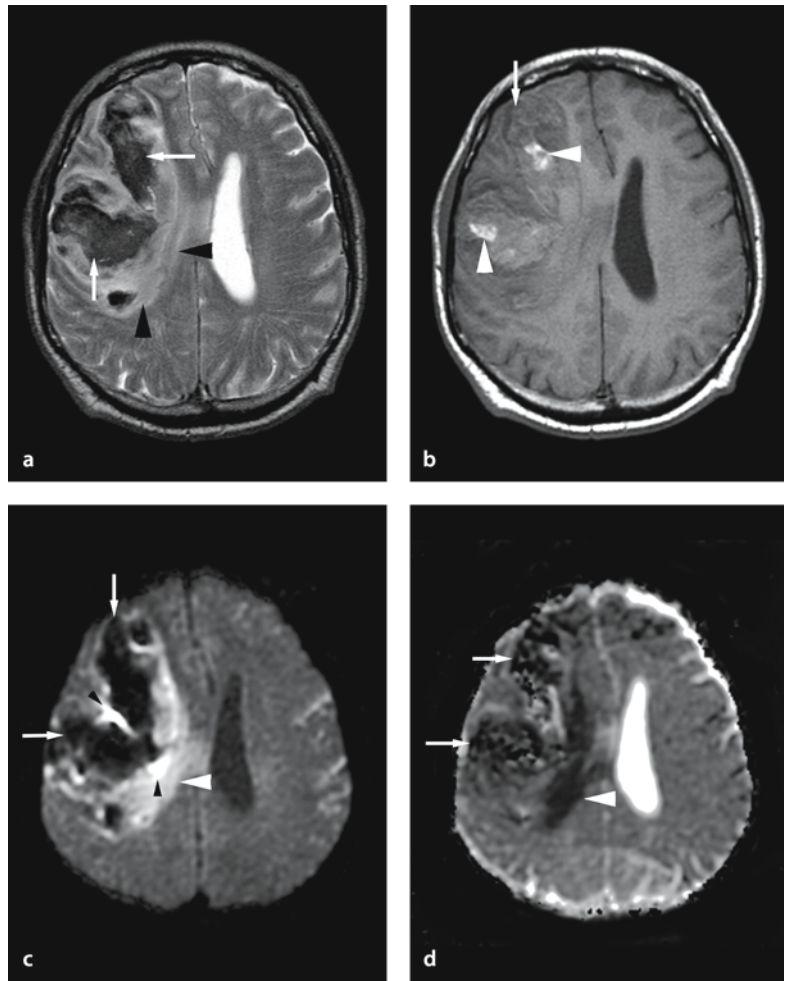
Figure 3.6 a–d

T2 blackout from susceptibility artifacts in acute hemorrhage (deoxyhemoglobin and intracellular met-hemoglobin) in a 74-year-old male with left-sided weakness. MR imaging was obtained 24 hours after the onset of symptoms. **a** T2-weighted image shows hypointense lesions in the right frontoparietal lobes (*arrows* deoxyhemoglobin and intracellular met-hemoglobin) with areas of surrounding hyperintensity consistent with edema (*arrowheads*). **b** T1-weighted image shows the heterogeneous lesion with hypointensity (*arrow* deoxyhemoglobin) and hyperintensity (*arrowheads* intracellular met-hemoglobin). **c** DW image shows hypointensity (*arrows* deoxy-hemoglobin and intracellular met-hemoglobin) and hyperintensity in region of edema (*arrowhead*). The surrounding hyperintense rims (*small arrowheads*) are due to magnetic susceptibility artifacts. **d** ADC could not be calculated accurately in the T2 "dark" hematoma due to magnetic susceptibility artifacts (*arrows*). The surrounding areas of hypointensity (*arrowhead*) probably correspond to cytotoxic edema surrounding the hematoma. This example shows how T2 hypointensity from susceptibility effects can produce a complex appearance in and around cerebral hemorrhage

3.4 Artifacts

Numerous artifacts can be generated during acquisition of DW images. There are five main artifacts of single-shot DW echo-planar imaging:

1. Eddy current artifacts due to echo-planar imaging phase-encode and readout gradients, and motion-probing gradient pulses for diffusion weighting
2. Susceptibility artifacts
3. N/2 ghosting artifacts
4. Chemical shift artifacts
5. Motion artifacts

We will discuss each artifact separately.

3.4.1 Eddy Current Artifacts

Eddy currents are electrical currents induced in a conductor by a changing magnetic field. Eddy currents can occur in patients and in the MR scanner itself, including cables or wires, gradient coils, cryoshields and radiofrequency shields [17]. Eddy currents are particularly severe when gradients are turned on and off quickly, as in echo-planar imaging pulse sequences. Gradient waveforms are distorted due to eddy currents, which results in image artifacts, including spatial blurring and misregistration. In single-shot DW echo-planar imaging, eddy currents are due to both echo-planar imaging gradients and motion-probing gradients, which lead to image distortions (Fig. 3.7). Correction of image distortion is essential to calculate ADC values and especially to quantify anisotropy with diffusion tensor imaging. **Correction methods:** (1) correction of distortion by using post-processing [18–21], (2) pre-emphasis or pre-compensation, purposely distorting the gradient-driving currents [22, 23], (3) shielded gradients, redesigning the magnet to incorporate shielding coils between the gradient coils and main windings [24].

3.4.2 Susceptibility Artifacts

Single-shot echo-planar imaging is sensitive to susceptibility artifacts, especially frequency and phase errors due to paramagnetic susceptibility effects. These artifacts are seen near the skull base, especially near the air in the sinus and mastoid (Fig. 3.8). Susceptibility artifacts are more severe along the phase-encoding direction and phase encoding should thus be along the anterior–posterior direction for axial DW images. Coronal and sagittal DW images are helpful in detecting lesions in certain locations, such as the hippocampus and brain stem, and to identify susceptibility artifacts (Fig. 3.9). Increased matrix size leads to elongation of readout time, which causes even larger image distortions.

Correction methods: (1) multi-shot echo-planar imaging (to reduce the readout time, to enable high-resolution scan) [25, 26], (2) line scan [27,28], (3) single-shot fast spin echo (SSFSE) [29, 30], (4) periodically rotated overlapping parallel lines with enhanced reconstruction (PROPELLER) [31, 32], (5) sensitive encoding (SENSE)/array spatial and sensitivity-encoding technique (ASSET), undersampling of k-space enables effective band width and shortens readout time, providing thin section and high-resolution matrix [33].
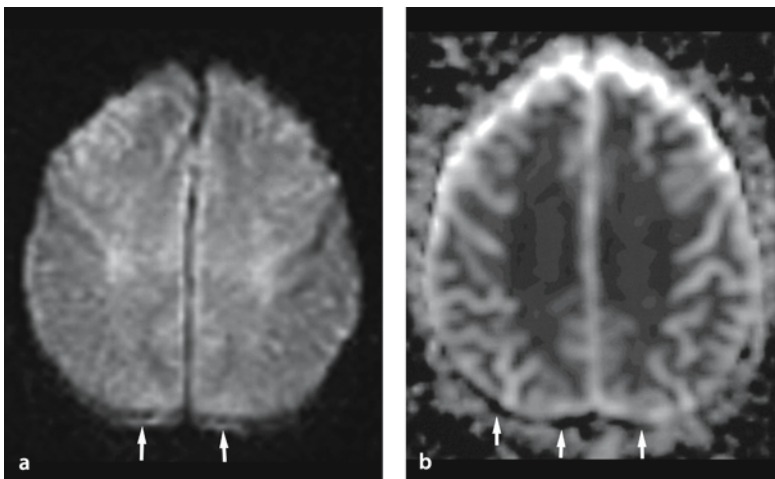
Figure 3.7 a,b

Misregistration due to eddy current artifact. **a, b** Misregistration artifact is noted in the occipital regions (*arrows*) on DW image (**a**) and the ADC map (**b**). Gradient waveforms are distorted due to eddy currents, which results in this misregistration

Figure 3.8

Susceptibility artifact. Susceptibility artifacts are seen near the air content of the mastoids (*arrows*). This is generally prominent in echo-planar sequences
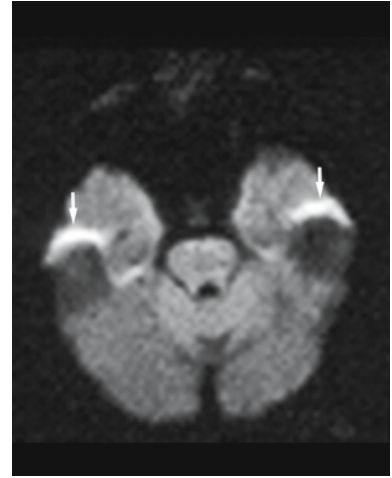
Figure 3.9 a–d

Susceptibility artifact in coronal and sagittal plane DW images. Coronal DW image (**a**) and the ADC map (**b**) are used to evaluate the hippocampus, but susceptibility artifacts distort the image near the mastoids. Sagittal DW image (**c**) and the ADC map (**d**) show a pontine infarct as hyperintense with decreased ADC (*arrowhead*). Susceptibility artifacts are caused by air in the ethmoid and sphenoid sinuses (*arrows*)
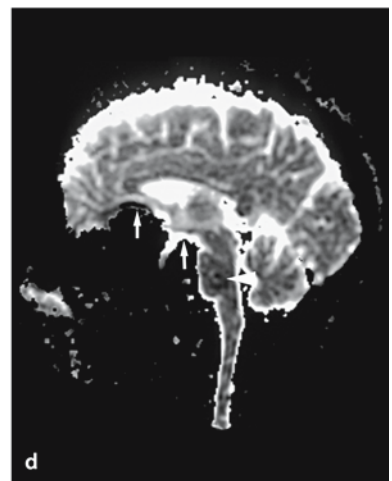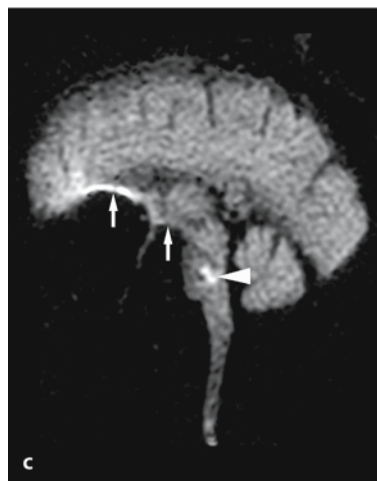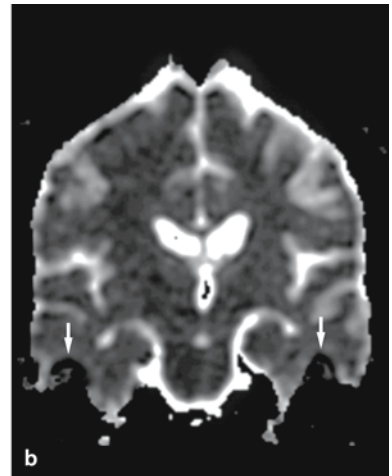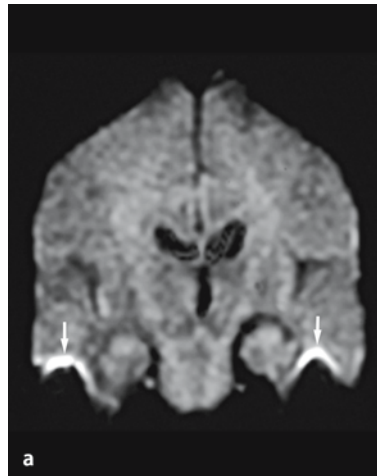
3.4.3 N/2 Ghosting Artifact (Nyquist Ghost)

N/2 ghosting artifact occurs when there are differences between the even and odd lines of the k-space. Phase error is due to hardware imperfections (eddy currents, imperfect timing of even and odd echo, imperfect gradients, and magnetic field inhomogeneity), which can be produced by on-off switching during readout gradients. The ghosts in this artifact are always shifted by half of the field of view in the phase-encoding direction (Fig. 3.10). This ghost can produce severe artifacts when ADC maps are calculated. **Correction methods:** (1) reduce eddy currents, (2) adjust gradients and magnetic field homogeneity, (3) high b-value, (4) fluid-attenuated inverse-recovery (FLAIR) DW imaging (reduce cerebrospinal fluid signal) [33, 34].

3.4.4 Chemical Shift

In echo-planar DW imaging, chemical shift artifacts due to the different resonance frequencies in water and fat are produced along the phase-encoding direction, while they are along the frequency-encoding direction in conventional spin-echo type MR imaging. This artifact is more severe in echo-planar imaging than in conventional spin-echo type MR imaging. Effective fat suppression techniques, such as the chemical shift selective (CHESS) method and the spectral selective radiofrequency excitation method are necessary.

Correction methods: appropriate fat suppression techniques.

3.4.5 Motion Artifacts

The sources of motion artifacts include gross head motion, respiratory motions, cardiac-related pulsations and patient bed vibration due to gradient pulses. Single-shot DW echo-planar imaging has relatively low sensitivity to patient motion, because each image is acquired in about 100–300 ms and the total acquisition time is less than 40 s. If one of the x, y, z or b_0 images is corrupted by motion artifacts during a scan, or if patient head motion occurs between scans, the isotopic DW images and the ADC maps will have these artifacts (Figs. 3.11 and 3.12). In those cases, unidirectional and b_0 images from the raw data of DW imaging can be free from the motion artifacts and remain diagnostically useful. Long (tens of ms) gradient pulses to reach sufficient diffusion weighting often increase sensitivity to motion.

Correction methods: (1) For a fixed b-factor, use high-gradient amplitude but reduce gradient pulse duration to minimize the sensitivity to motion, (2) post-processing to correct for phase error (Navigator method) [35–37], (3) elimination of phase-encode step (line scan method, projection reconstruction), (4) minimize time for phase error accumulation (single-shot echo-planar imaging, hybrid method with multishot echo-planar imaging), (5) SSFSE, (6) PROPELLER [38], (7) SENSE.
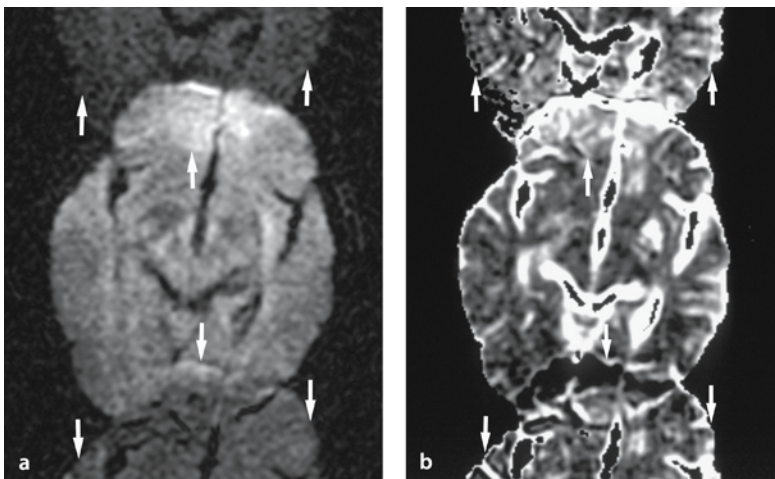
Figure 3.10 a,b

N/2 ghosting artifact. **a** DW image shows N/2 ghosting artifacts (*arrows*), which are always shifted by half of the field of view in the phase-encoding direction. **b** On the ADC map severe N/2 ghosting artifacts are also seen (*arrows*)

Figure 3.11 a–d

Motion artifacts due to head motion during the scan of a patient with status epilepticus. **a** It is difficult to evaluate the DW image because of severe motion artifacts. **b** In the raw data of the DW imaging, the *x* axis image is corrupted by head motion during the scan. **c** The *y* axis image is free from the artifacts. This image shows a hyperintense lesion in the left hippocampus (*arrow*). **d** ADC map of *y* axis image also shows decreased ADC of the lesion (transferred to a workstation for image processing, using a home-made code, which is based on the numerical computation software)
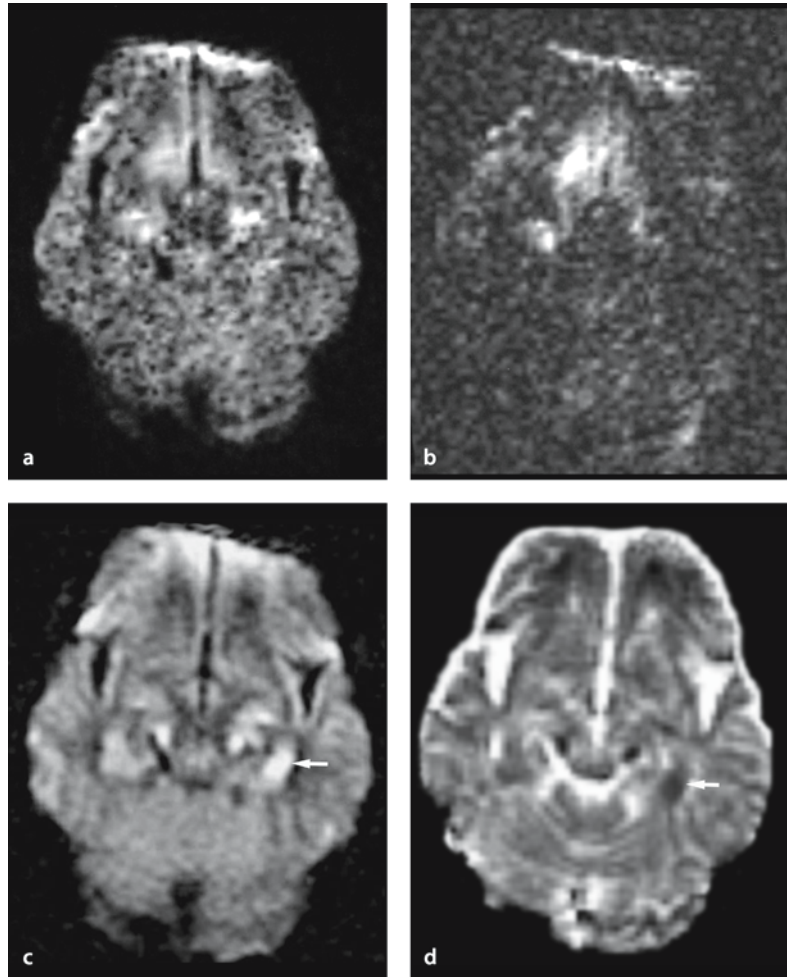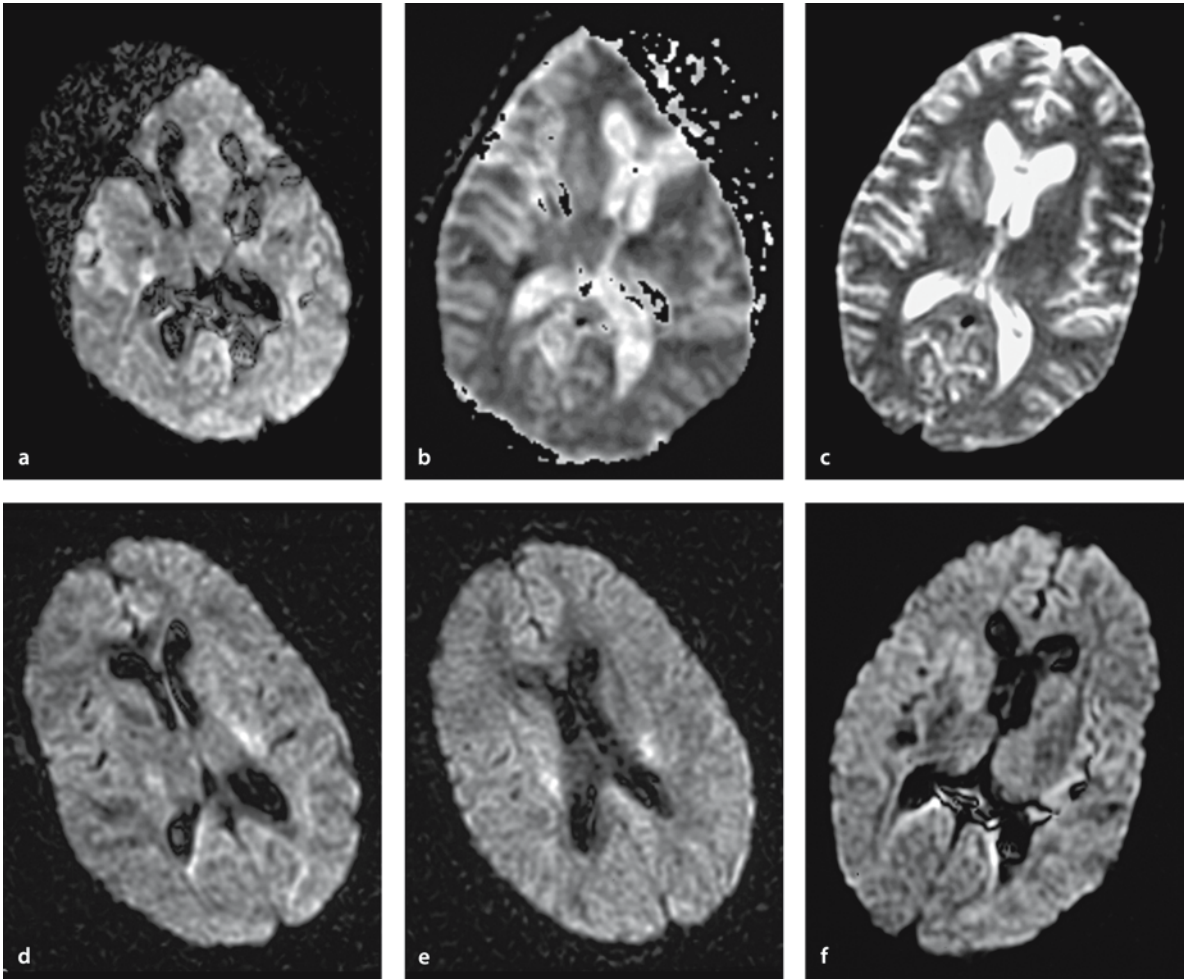
Figure 3.12 a–f

Motion artifacts due to head motion between the scans. Chronic infarcts in the right basal ganglia. **a** DW image has motion artifacts due to head motion between the scans. This image appears overlapping of b_0, and x, y, z axis images. **b** ADC map also shows severe motion artifacts. **c** b_0, **d** x axis, **e** y axis, **f** z axis. b_0 and unidirectional images are all free from the artifacts

3.5 Conclusion

Diffusion-weighted images are inherently T2 weighted and the interpretation of signal intensity on DW images requires a correlation between b_0 images, ADC maps and exponential images to uncover the underlying pathophysiologic condition. It is also important to understand a variety of artifacts to avoid misinterpreting the DW images. Understanding inherent artifacts and the way to reduce the artifacts on DW imaging will improve the quality and accuracy of DW imaging.

References

1. Stejkal EO, Tanner J (1965) Spin diffusion measurements: spin echoes in the presence of a time-dependent field gradient. J Chemical Phys 42:288–292
2. LeBihan D, Breton E, Lallemand D, Grenier P, Cabanis E, Laval-Jeantet (1986) MR imaging of intravoxel incoherent motions: application to diffusion and perfusion in neurologic disorders. Radiology 161:401–407
3. Warach S, Gaa J, Siewert B, Wielopolski P, Edelman RR (1995) Acute human stroke studied by whole brain echo planar diffusion-weighted magnetic resonance imaging. Ann Neurol 37:231–241
4. Provenzale JM, Engelter ST, Petrella JR, Smith JS, MacFall JR (1999) Use of MR exponential diffusion-weighted images to eradicate T2 "shine-through" effect. AJR Am J Roentgenol 172:537–539
5. Burdette JH, Elster AD, Ricci PE (1999) Acute cerebral infarction: quantification of spin-density and T2 shine-through phenomena on diffusion-weighted MR images. Radiology 212:333–339
6. Coley SC, Porter DA, Calamante F, Chong WK, Connelly A (1999) Quantitative MR diffusion mapping and cyclosporine-induced neurotoxicity. AJNR Am J Neuroradiol 20:1507–1510
7. Schaefer PW, Grant PE, Gonzalez RG (2000) Diffusion-weighted MR imaging of the brain. Radiology 217:331–345
8. Field A (2001) Diffusion and perfusion imaging. In: Elster AD, Burdette JH (eds). Questions and answers in magnetic resonance imaging. Mosby, St. Louis, Missouri pp 194–214
9. Maldjian JA, Listerud J, Moonis G, Siddiqi F (2001) Computing diffusion rates in T2-dark hematomas and areas of low T2 signal. AJNR Am J Neuroradiol 22:112–128
10. Engelter ST, Provenzale JM, Petrella JR, Alberts MJ, DeLong DM, MacFall JR (2001) Use of exponential diffusion imaging to determine the age of ischemic infarcts. J Neuroimaging 11:141–147
11. Chen S, Ikawa F, Kurisu K, Arita K, Takaba J, Kanou Y (2001) Quantitative MR evaluation of intracranial epidermoid tumors by fast fluid-attenuated inversion recovery imaging and echo-planar diffusion-weighted imaging. AJNR Am J Neuroradiol 22:1089–1096
12. Geijer B, Sundgren PC, Lindgren A, Brockstedt S, Stahlberg F, Holtas S (2001) The value of b required to avoid T2 shine-through from old lacunar infarcts in diffusion-weighted imaging. Neuroradiology 43:511–517
13. Casey S (2001) "T2 washout": an explanation for normal diffusion-weighted images despite abnormal apparent diffusion coefficient maps. AJNR Am J Neuroradiol 22:1450–1451
14. Provenzale JM, Petrella JR, Cruz LC Jr, Wong JC, Engelter S, Barboriak DP (2001) Quantitative assessment of diffusion abnormalities in posterior reversible encephalopathy syndrome. AJNR Am J Neuroradiol 22:1455–1461
15. Eastwood JD, Engelter ST, MacFall JF, Delong DM, Provenzale JM (2003) Quantitative assessment of the time course of infarct signal intensity on diffusion-weighted images. AJNR Am J Neuroradiol 24:680–687
16. Hiwatashi A, Kinoshita T, Moritani T, et al. (2003) Hypointensity on diffusion-weighted MRI related to T2 shortening and susceptibility effects. AJR Am J Roentgenol (in press)
17. Elster AD, Burdette JH (2001) Scanner hardware. In: Elster AD, Burdette JH (eds). Questions and answers in magnetic resonance imaging. Mosby, St. Louis, Missouri pp 54–71
18. Haselgrove JC, Moore JR (1996) Correction for distortion of echo-planar images used to calculate the apparent diffusion coefficient. Magn Reson Med 36:960–964
19. Horsfield MA (1999) Mapping eddy current induced fields for the correction of diffusion-weighted echo planar images. Magn Reson Imaging 17:1335–1345
20. Jezzard P, Barnett AS, Pierpaoli C (1998) Characterization of and correction for eddy current artifacts in echo planar diffusion imaging. Magn Reson Med 39:801–812
21. Calamante F, Porter DA, Gadian DG, Connelly A (1999) Correction for eddy current induced Bo shifts in diffusion-weighted echo-planar imaging. Magn Reson Med 41:95–102
22. Schmithorst VJ, Dardzinski BJ (2002) Automatic gradient preemphasis adjustment: a 15-minute journey to improved diffusion-weighted echo-planar imaging. Magn Reson Med 47:208–212
23. Papadakis NG, Martin KM, Pickard JD, Hall LD, Carpenter TA, Huang CL (2000) Gradient preemphasis calibration in diffusion-weighted echo-planar imaging. Magn Reson Med 44:616–624
24. Chapman BL (1999) Shielded gradients. And the general solution to the near field problem of electromagnet design. MAGMA 9:146–151
25. Robson MD, Anderson AW, Gore JC (1997) Diffusion-weighted multiple shot echo planar imaging of humans without navigation. Magn Reson Med 38:82–88
26. Brockstedt S, Moore JR, Thomsen C, Holtas S, Stahlberg F (2000) High-resolution diffusion imaging using phase-corrected segmented echo-planar imaging. Magn Reson Imaging 18:649–657
27. Maier SE, Gudbjartsson H, Patz S, et al. (1998) Line scan diffusion imaging: characterization in healthy subjects and stroke patients. AJR Am J Roentgenol 171:85–93
28. Robertson RL, Maier SE, Mulkern RV, Vajapayam S, Robson CD, Barnes PD (2000) MR line-scan diffusion imaging of the spinal cord in children. AJNR Am J Neuroradiol 21:1344–1348

29. Lovblad KO, Jakob PM, Chen Q, et al. (1998) Turbo spin-echo diffusion-weighted MR of ischemic stroke. Am J Neuroradiol 19:201–208
30. Alsop DC (1997) Phase insensitive preparation of single-shot RARE: application to diffusion imaging in humans. Magn Reson Med 38:527–533
31. Forbes KP, Pipe JG, Karis JP, Farthing V, Heiserman JE (2003) Brain imaging in the unsedated pediatric patient: comparison of periodically rotated overlapping parallel lines with enhanced reconstruction and single-shot fast spin-echo sequences. AJNR Am J Neuroradiol 24:794–798
32. Bammer R, Keeling SL, Augustin M, et al. (2001) Improved diffusion-weighted single-shot echo-planar imaging (EPI) in stroke using sensitivity encoding (SENSE). Magn Reson Med 46:548–554
33. Porter DA, Calamante F, Gadian DG, Connelly A (1999) The effect of residual Nyquist ghost in quantitative echo-planar diffusion imaging. Magn Reson Med 42:385–392
34. Bastin ME (2001) On the use of the FLAIR technique to improve the correction of eddy current induced artefacts in MR diffusion tensor imaging. Magn Reson Imaging 19:937–950
35. Anderson AW, Gore JC (1994) Analysis and correction of motion artifacts in diffusion weighted imaging. Magn Reson Med 32:379–387
36. Ordidge RJ, Helpern JA, Qing ZX, Knight RA, Nagesh V (1994) Correction of motional artifacts in diffusion-weighted MR images using navigator echoes. Magn Reson Imaging 12:455–460
37. Dietrich O, Heiland S, Benner T, Sartor K (2000) Reducing motion artefacts in diffusion-weighted MRI of the brain: efficacy of navigator echo correction and pulse triggering. Neuroradiology 42:85–91
38. Pipe JG (1999) Motion correction with PROPELLER MRI: application to head motion and free-breathing cardiac imaging. Magn Reson Med 42:963–969

Brain Edema

4.1 Characterization and Classification of Brain Edema

Brain edema is defined as accumulation of excess fluid in cells or in the extracellular space. Brain edema can be classified as cytotoxic (cellular), vasogenic [1] or interstitial. Cytotoxic and vasogenic edema usually coexist in pathological conditions such as infarction, hypoxic ischemic encephalopathy, trauma, or multiple sclerosis. The edema may primarily be either vasogenic or cytotoxic, but as the process evolves over time, the injury leads to a combination of cellular swelling and vascular damage. Interstitial edema occurs with hydrocephalus, water intoxication, or plasma hyposmolarity.

Conventional MR imaging does not always allow distinction between the different forms of edema. However, diffusion-weighted (DW) imaging, which is based on the microscopic movement of water molecules in brain tissue, can differentiate cytotoxic edema from vasogenic and interstitial edema [2].

4.2 Definition and Classification of Cytotoxic Edema

Cytotoxic or cellular edema is an abnormal uptake of fluid in the cytoplasm due to abnormal cellular osmoregulation. This kind of edema may accompany various processes that damage cells, such as ischemia, trauma, toxic metabolic disease, demyelina-tion, and even the early phase of degeneration. Classification of the involved cell types may explain the pathophysiology and different prognosis of these conditions.

In normal brain tissues, the gray and white matters are mainly composed of neurons, glial cells, axons, and myelin sheaths (Fig. 4.1). In the gray matter, cytotoxic edema occurs mainly in neurons and glial cells (Fig. 4.2). In the white matter, however, cytotoxic edema occurs in glial cells, axons (axonal swelling) (Fig. 4.3) and myelin sheaths (intramyelinic edema) (Fig. 4.4) [1].

4.3 Pathophysiology of Cytotoxic Edema

4.3.1 Energy Failure

In ischemia or hypoxia, cytotoxic edema is mainly caused by energy failure [3]. The insult initiates substrate depletion, which leads to a decrease in intracellular ATP used for oxidative phosphorylation, and a failure of the sodium–potassium pump. This will cause an influx of sodium and calcium into the cells, subsequently increasing the osmotic gradient and the transport of water into the cells, resulting in cellular swelling. Moreover, in an attempt to produce ATP, the cells switch from oxidative phosphorylation to anaerobic glycolysis, resulting in intracellular lactate. This will further increase the osmotic gradient across the cell membrane, which exacerbates the cytotoxic edema.
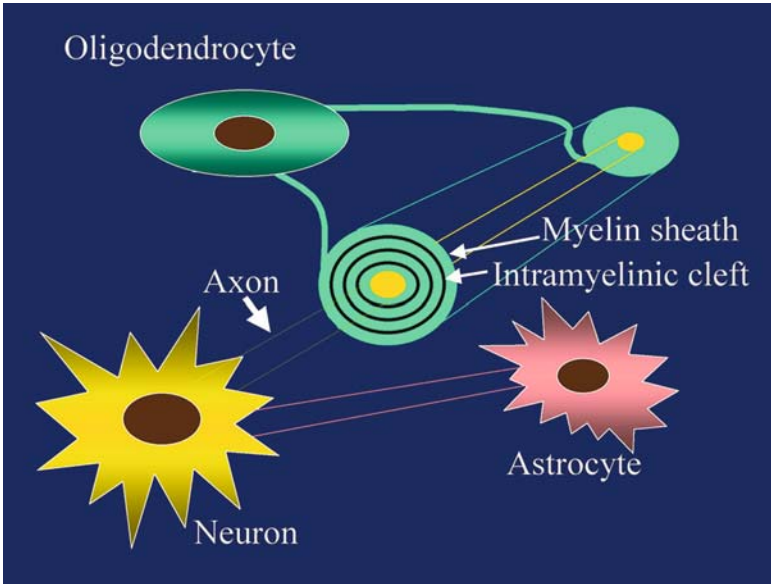
Fig. 4.1. Normal brain tissue is mainly composed of neurons, glial cells (astrocytes or oligodendrocytes), axons and myelin sheaths surrounded by an extracellular space
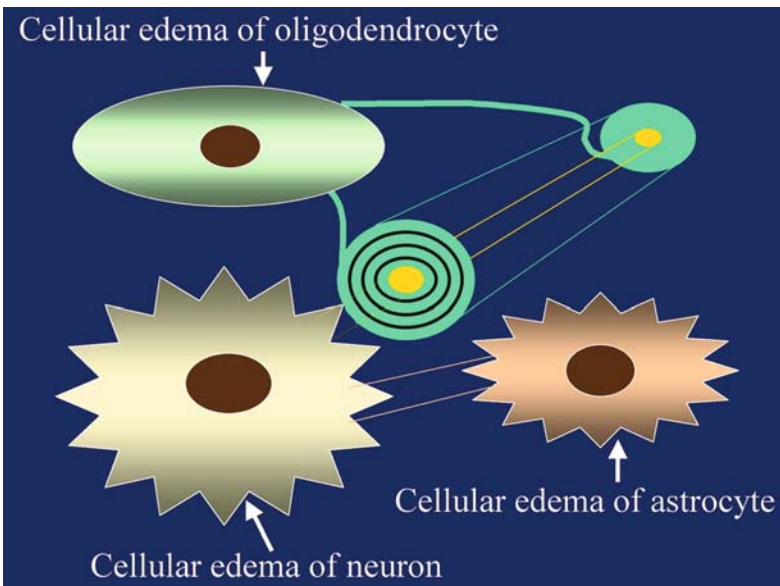
Cytotoxic edema occurs in neurons and glial cells (astrocytes and oligodendrocytes). These cells are vulnerable to ischemia. As cells increase in size, there is a shift of water from extracellular to intracellular compartments, which can occur without a net gain in water (compared with Fig. 4.1). Cytotoxic edema results in increased intracellular space and decreased extracellular space, which may cause a decrease in ADC
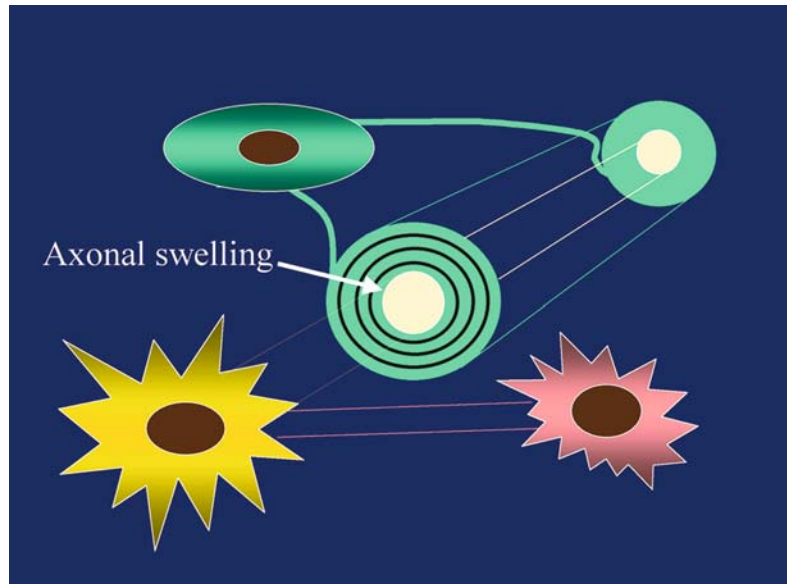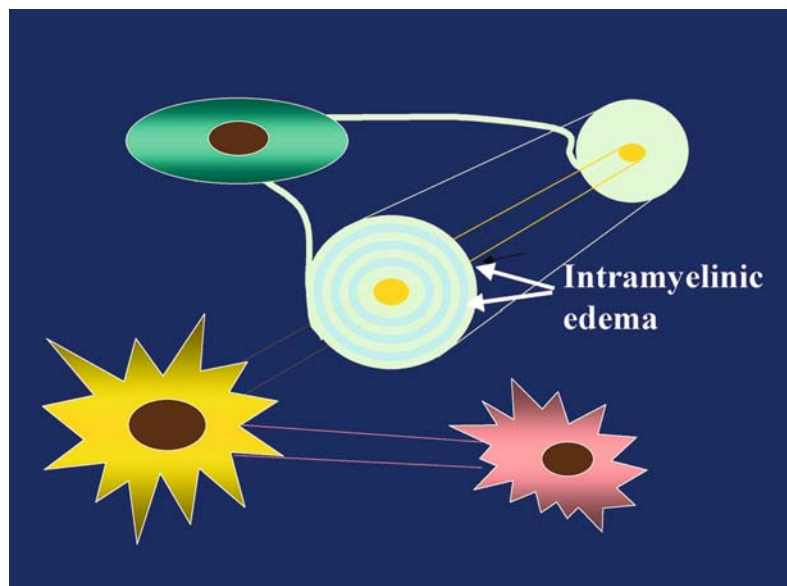
Figure 4.3

Cytotoxic edema can occur in axons

Axonal swelling

Figure 4.4

Cytotoxic edema can occur in myelin sheaths in which edema is found in either the myelin sheath itself or in the intramyelinic cleft

Intramyelinic edema

4.3.2 Excitotoxic Brain Injury

Energy failure is not the only mechanism responsible for the cytotoxic edema [3]. Membrane transporters can be triggered or inhibited by a range of excitatory neurotransmitters, such as glutamate and aspartate, but also other agents such as cytokines and free radicals [4]. Any cell, including neuron, glia, axon and myelin sheath can be a target of these toxic sub-stances; however, reactive astrocytes play a significant role in cellular and tissue repair by detoxifying various noxious substances (such as glutamate, free radical, ammonia and metals). Neuropathologic examination shows that the acutely reactive astrocytes have swollen cytoplasm and neutrophil, consistent with cytotoxic edema [5].

High glutamate in the synaptic and extracellular space is one of the important mechanisms associated
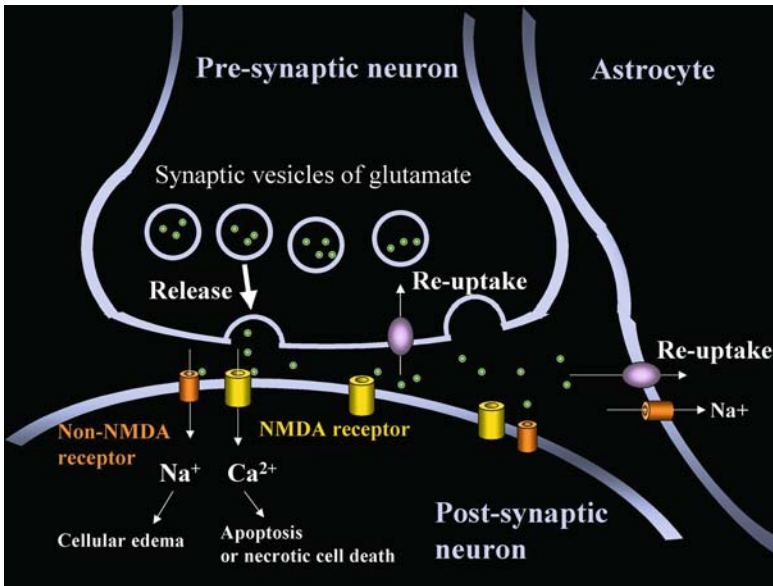
Excitotoxic mechanisms in the neuron and astrocyte. In the neuron, glutamate is released from the pre-synaptic terminal into the synaptic cleft. The glutamate binding to NMDA receptors allows entry of Ca^{2+} into the post-synaptic neuron, which can result in necrotic cell death or apoptosis. The glutamate binding to non-NMDA receptors allows entry of Na^+ into the post-synaptic neuron, resulting in cytotoxic edema of the neuron. Re-uptake of extracellular glutamate takes place at the pre-synaptic terminals and in adjacent astrocytes. Similar mechanisms also cause cytotoxic edema in the astrocyte

with cytotoxic edema of various diseases, including infarction, hypoxic ischemic encephalopathy, status epilepticus, and traumatic brain injury, such as diffuse axonal injury, contusion and shaken baby syndrome [6, 7]. Increased extracellular glutamate is a direct cause of excitotoxic brain injury. In acute excitotoxic injury, increased extracellular glutamate results from an increased release/ leakage of glutamate or a decreased re-uptake (Fig. 4.5). Neuronal glutamate is released from the pre-synaptic terminal into the synaptic cleft. The glutamate binding to N-methyl-D-aspartate (NMDA) receptors allows entry of Ca^{2+} into the post-synaptic neuron, which results in necrotic cell death or apoptosis. The glutamate binding to non-NMDA receptors allows entry of Na^+ into the post-synaptic neuron, resulting in cytotoxic edema. Apoptosis is defined as a programmed cell death and is histologically characterized by fragmentation of DNA in the nucleus of the cell. Re-uptake of extracellular glutamate takes place at the pre-synaptic terminals and in adjacent glial cells, which may cause cytotoxic edema (acute phase of reactive astrocytosis).

Whatever the cause, cytotoxic edema can result in necrosis or delayed neuronal death, or degeneration similar to apoptosis with various amounts of reactive gliosis. Whether necrosis or apoptosis ensues, it may neurochemically depend on the levels of adenosine triphosphate or cytosol calcium ions that trigger protease and lipase production [8].

4.4 Diffusion-Weighted Imaging and Cytotoxic Edema

Cytotoxic edema characteristically shows hyperintensity on DW images associated with decreased apparent diffusion coefficient (ADC). The precise mechanisms underlying the reduction in ADC are unknown. The most common explanation is a shift of extracellular water to the intracellular space. However, the observed 40% reduction of ADC cannot be explained by an increase in intracellular water alone, even if all extracellular fluid went intracellular [9]. There must be a reduction in diffusivity of water molecules in the intracellular space which may be explained by the large number of intracellular organelles, that may act as obstacles for diffusion. A decrease in intracellular ADC could also be due to a decrease in the energy-dependent intracellular circulation or an increase in cytoplasmic viscosity from a swelling of intracellular organelles [10].

Tumors, hemorrhages, abscesses and coagulative necrosis also result in a decrease in ADC. The mechanisms underlying the reduction in ADC in those lesions are also unknown, but can be related to hypercellularity or hyperviscosity of the pathological tissue [11, 12].

## 4.4.1 Conditions that Cause Cytotoxic Edema, and Reversibility

Cytotoxic edema of neuron and glial cells may accompany infarction [13–16], hypoxic ischemic encephalopathy [17, 18], traumatic brain injury [19, 20], status epilepticus [6, 21, 22], encephalitis [23] and Creutzfeldt–Jakob disease [24, 25].

Neurons and glial cells are the cells most vulnerable to ischemia and hypoxia, but if the ischemia is severe, myelin sheaths and axons may also be involved [3]. These differences among cell types for cytotoxic edema can explain the different time courses of DW abnormalities between gray and white matter in cerebral infarction and hypoxic ischemic encephalopathy. In arterial infarction, the area of cytotoxic edema
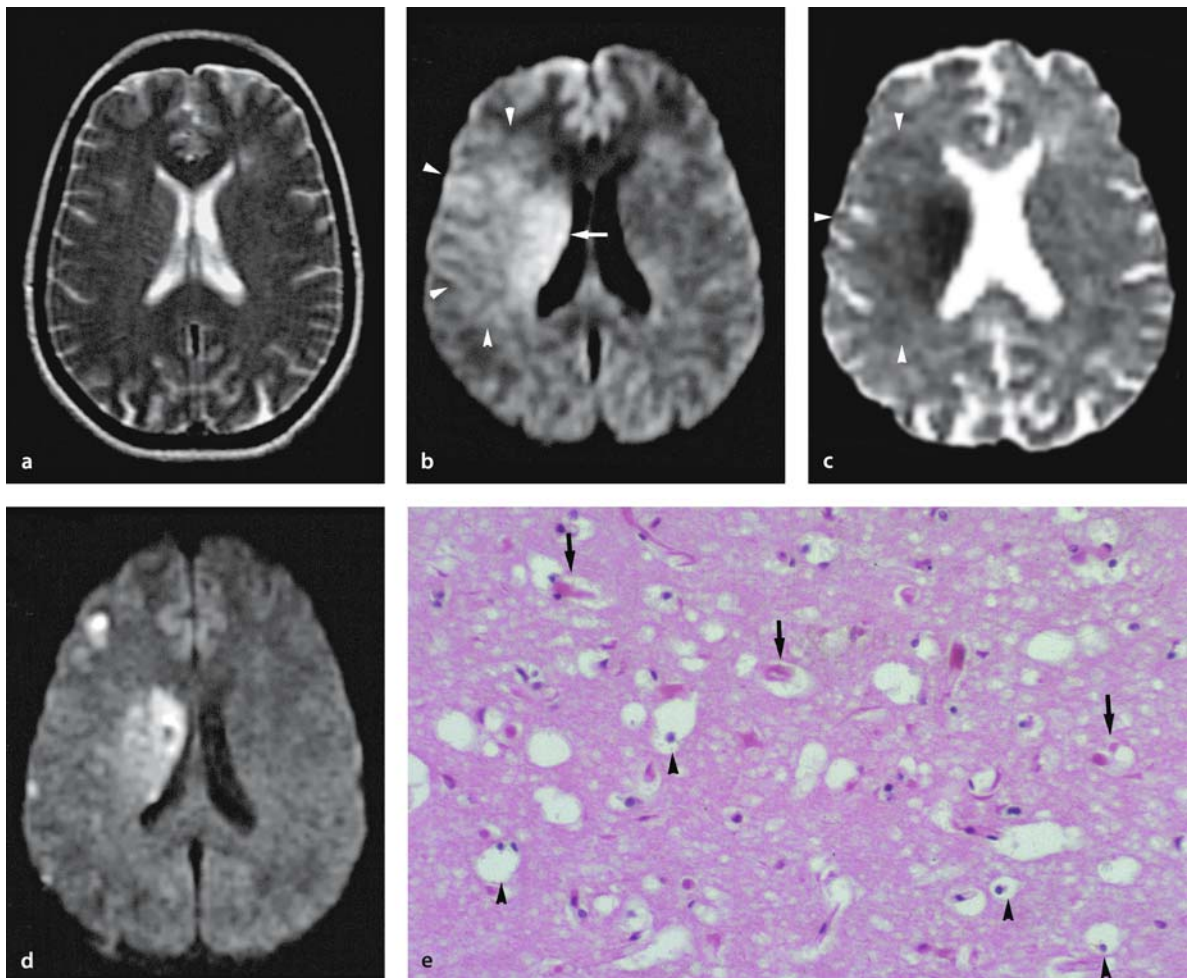
Figure 4.6 a–e

Hyperacute cerebral infarction (3 h after onset) in a 39-year-old woman with decreased consciousness. Her neurologic functions improved after intra-arterial thrombolytic therapy. **a** T2-weighted image appears normal. **b** DW image shows a hyperintense lesion in the right corona radiata (*arrow*) and a slightly hyperintense lesion in the right middle cerebral artery (MCA) territory, which may correspond to ischemic penumbra (*arrowheads*). **c** ADC map shows a definite decrease in ADC in the corona radiata and slightly decreased ADC in the right MCA territory (*arrowheads*). **d** On DW image after fibrinolytic therapy (3 days after onset), the hyperintense lesion in the cortical area is largely resolved, with remaining small, peripheral infarcts. Early cytotoxic edema with slightly decreased ADC does not always result in infarction. **e** Another case. Pathological specimen of cytotoxic edema in the cortex in an acute stroke shows swelling of neurons (*arrows*) and glial cells (*arrowheads*) (hematoxylin–eosin stain, original magnification ×200). (From [36])
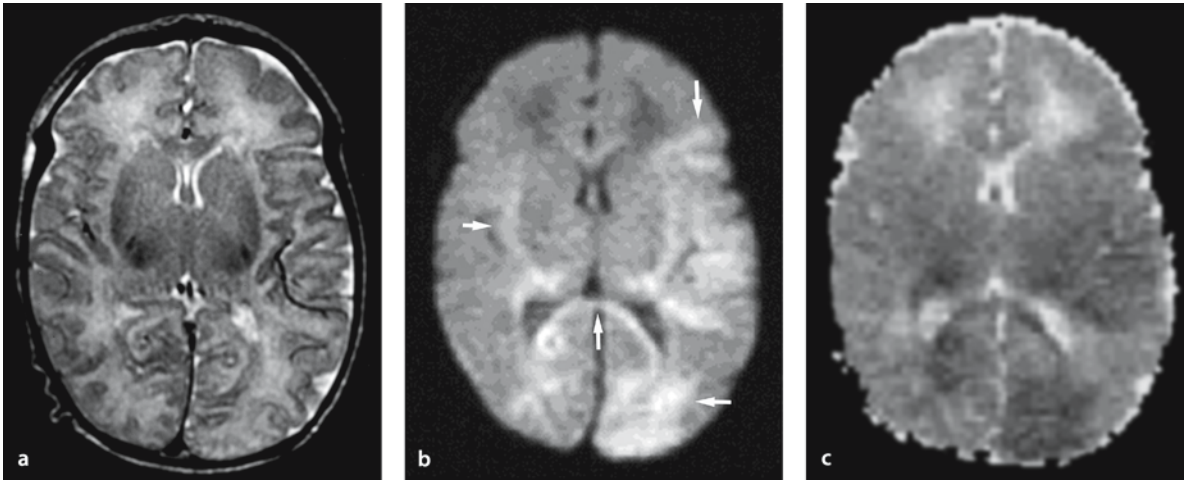
Figure 4.7 a–d

A 2-day-old term girl with hypoxic ischemic encephalopathy due to perinatal hypoxia–ischemia event. **a** T2-weighted image appears normal. **b** DW image shows hyperintense lesions in the temporo-occipital gray and white matter including the corpus callosum (*arrows*). Low intensity in bilateral frontal deep white matter (*arrowheads*) is a normal finding in a patient of this age. **c** ADC map shows these lesions as decreased ADC representing cytotoxic edema. Increased ADC in the frontal deep white matter is also a normal finding in a patient of this age. These ischemic lesions are more clearly seen on DW imaging than on the ADC map because DW imaging depicts subtle T2 contrast abnormalities (T2 shine-through effect) in addition to the contrast of diffusion restriction of these lesions

on DW imaging seems to be irreversibly damaged tissue, resulting in coagulative or liquefactive necrosis. However, mild decreased ADC in the ischemic penumbra can be reversible after intra-arterial or intravenous fibrinolytic therapy (Fig. 4.6). In transient ischemic attacks and venous infarctions, an initially abnormal signal on DW imaging has occasionally been reversed, partially or completely, on follow-up MR images. Hypoxic ischemic encephalopathy (Fig. 4.7) and traumatic brain injury are usually related to irreversible brain damage.

In status epilepticus, cytotoxic edema is often reversed, partially or completely, but may result in selective necrosis, brain atrophy or gliosis (Fig. 4.8). A cytotoxic edema of reactive astrocytes in the acute phase can be responsible for the reversible signal abnormalities [6].

In Creutzfeldt–Jakob disease, the area of cytotoxic edema will eventually develop into prominent brain atrophy (Fig. 4.9). Axonal swelling can also accompany diffuse axonal injury (Fig. 4.10) and the early phase of wallerian degeneration (Fig. 4.11) [26].

Intramyelinic edema may accompany the acute phase of multiple sclerosis (Fig. 4.12) [27, 28], toxic or metabolic leukoencephalopathy (Fig. 4.13) [29–31] and osmotic myelinolysis [32]. Partially or completely reversible lesions are also seen in these diseases. The explanation for this reversibility may be an intramyelinic edema where the edema is often primarily located in the intramyelinic cleft [1].

Figure 4.8 a–d

Status epilepticus in a 2-year-old girl 24 hours after onset. **a** T2-weighted image shows diffuse cortical hyperintensity in the entire left hemisphere cortex. **b** DW image shows diffuse hyperintensity mainly in the gray matter of the left hemisphere. **c** ADC map shows decreased ADC of these lesions. **d** Diffuse brain atrophy and hyperintense lesions in the left hemisphere are seen on a 5-month follow-up T2-weighted image
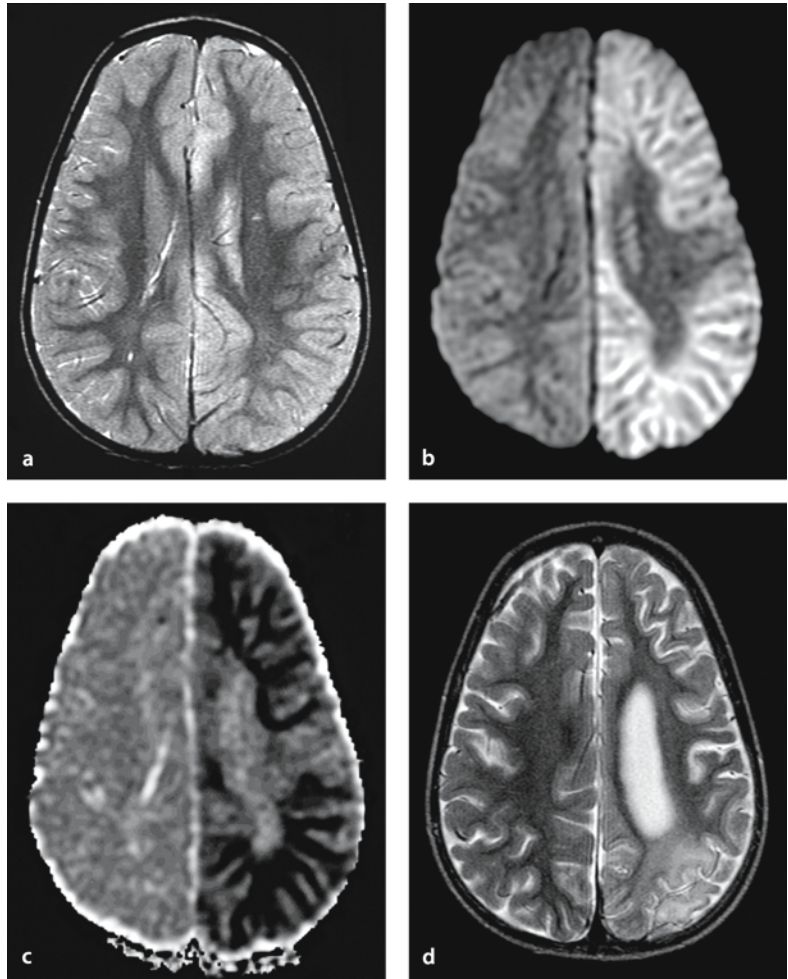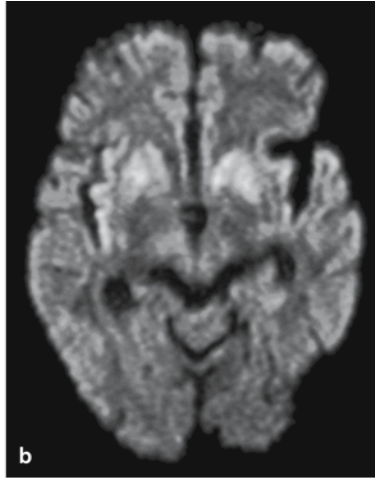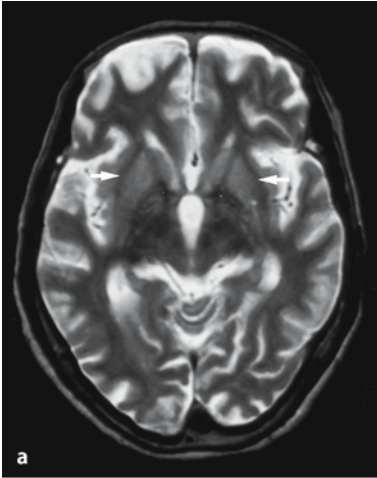
Figure 4.9 a–d

Creutzfeldt–Jakob disease in a 72-year-old woman with progressive dementia. **a** T2-weighted image demonstrates mildly increased signal bilaterally in the caudate nuclei and putamina (*arrows*). **b** DW image clearly demonstrates bilateral, symmetrical increase in signal intensity in the caudate nuclei and putamina. **c** ADC map shows these lesions as decreased ADC. **d** 4-month follow-up MRI shows prominent brain atrophy. (From [37])
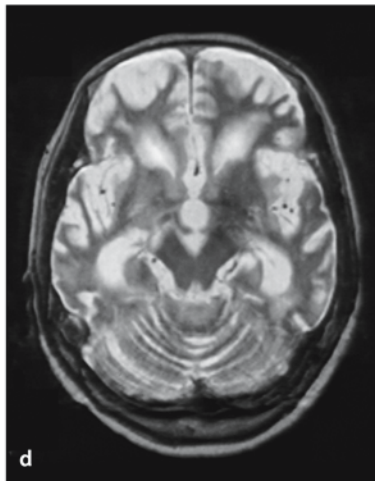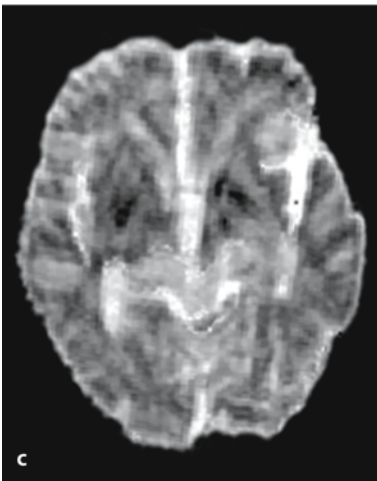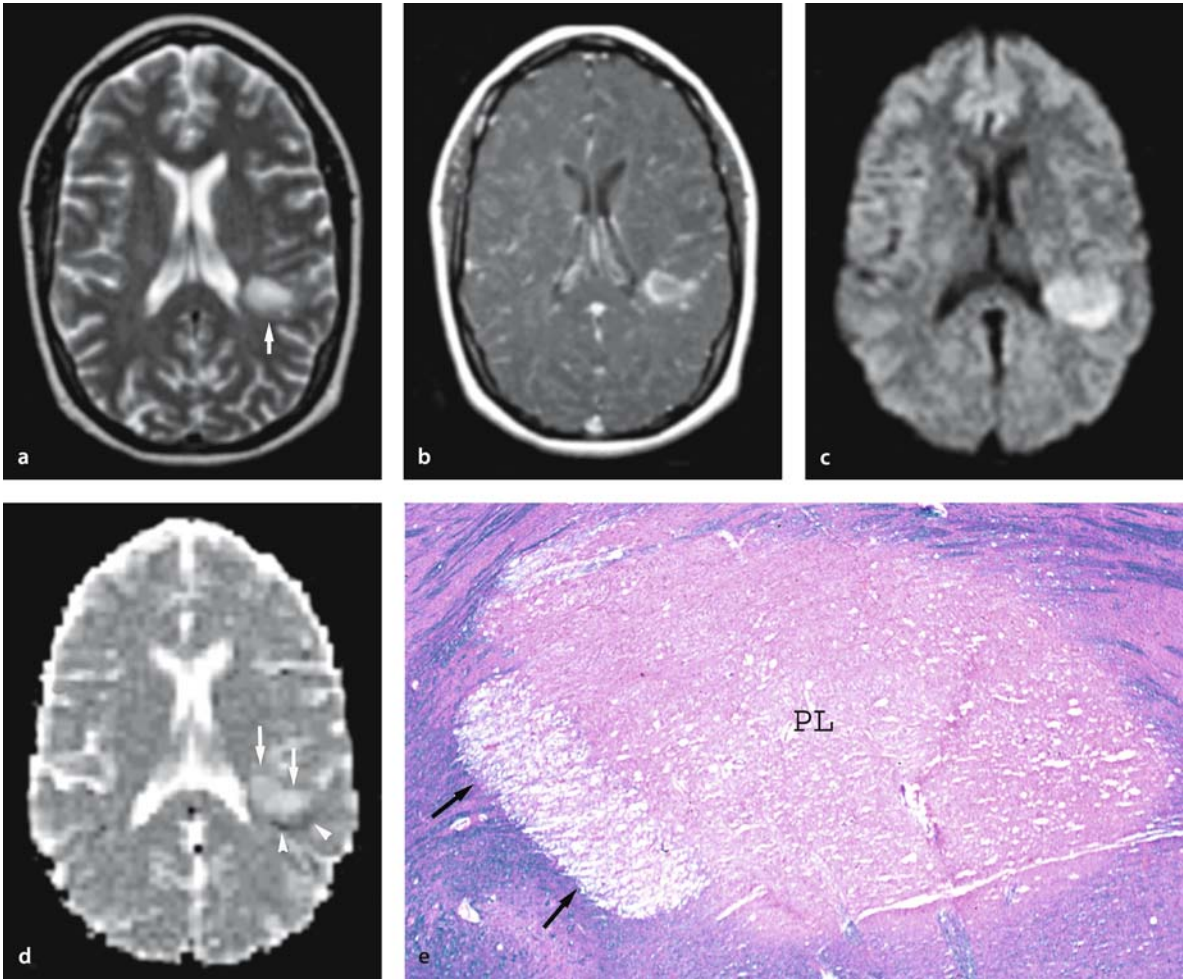
Figure 4.10 a–c

Diffuse axonal injury in an 18-year-old female 48 h after motor vehicle accident. **a** T2-weighted image shows mildly hyperintense lesions in the corpus callosum and the white matter of bilateral frontal lobes (*arrows*). **b** DW image demonstrates diffuse axonal injury as high signal intensity, representing cytotoxic edema (*arrows*). **c** ADC map shows decreased ADC lesions in the anterior to posterior corpus callosum and the frontal deep white matter (*arrows*). (From [37])
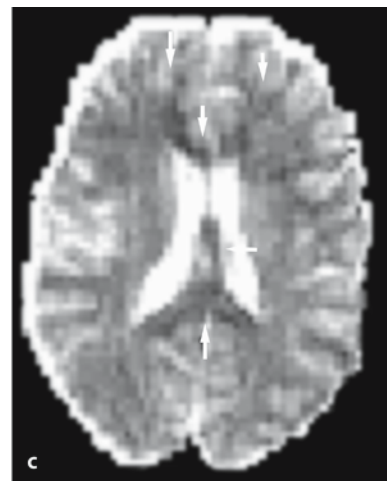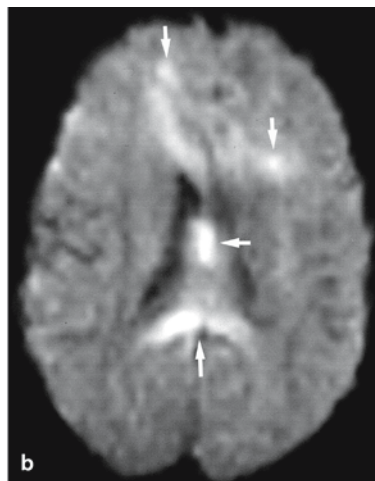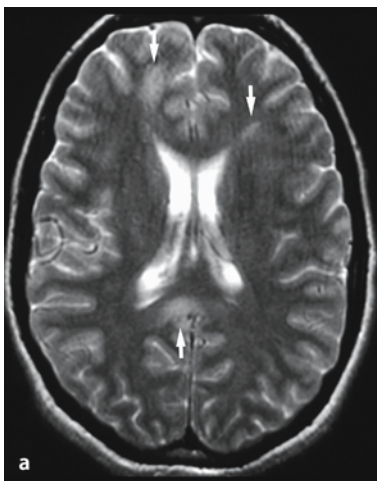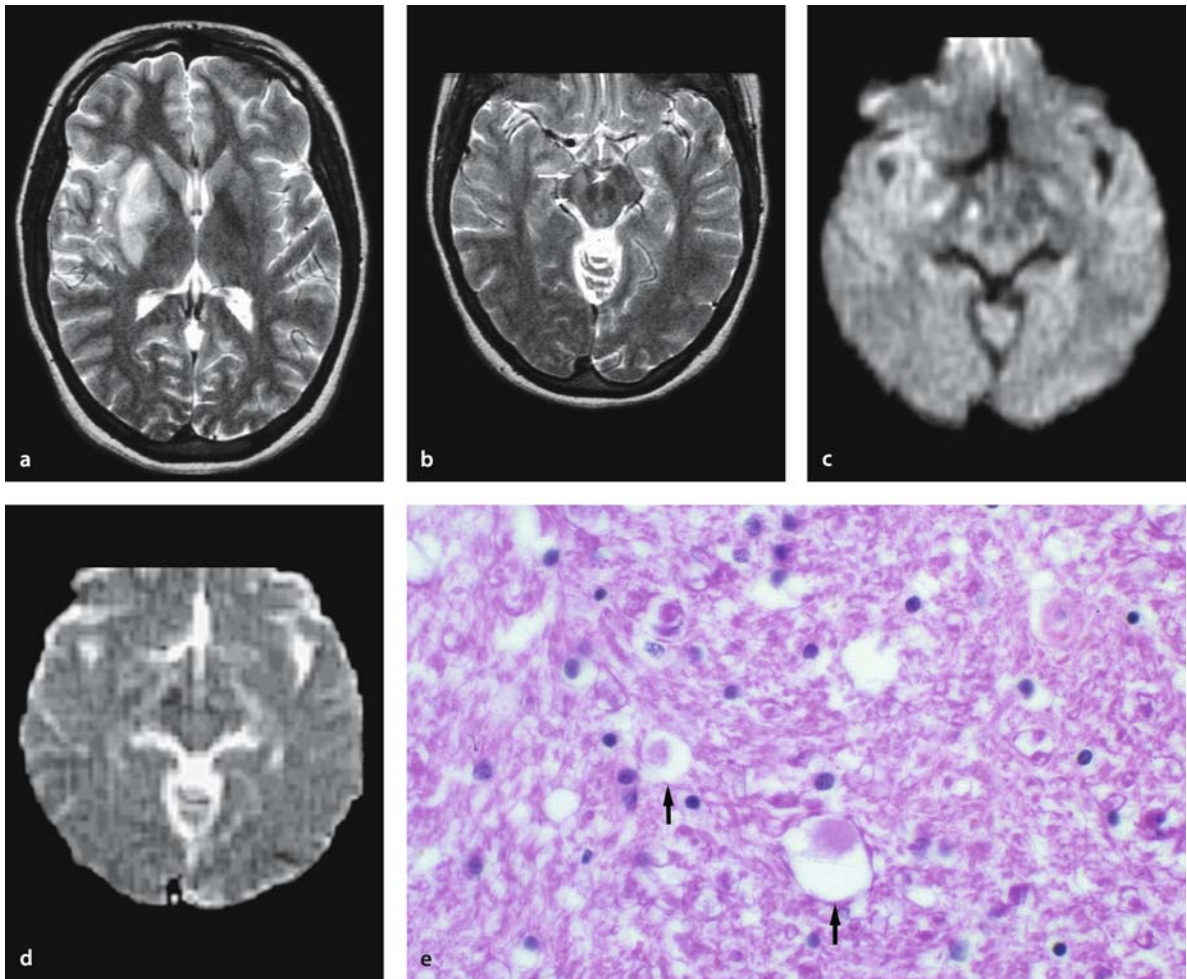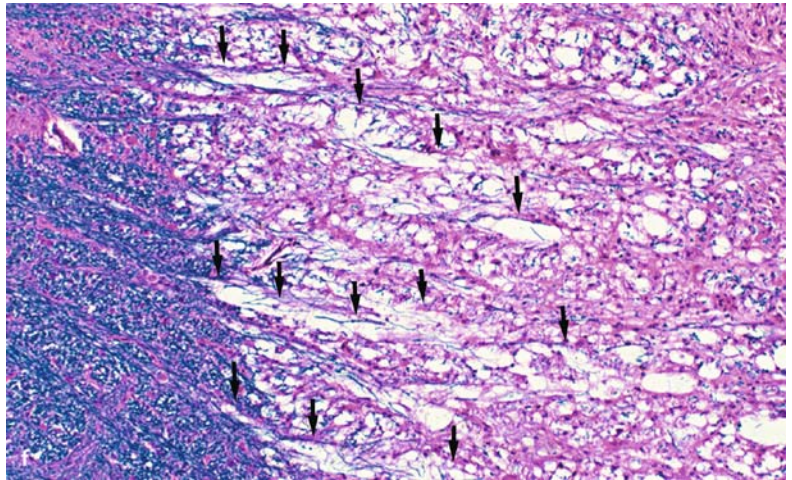
Figure 4.11 a–e

An early phase of wallerian degeneration in a 20-year-old woman with subacute infarction (72 h after onset). **a** T2-weight-ed image shows hyperintense lesion involving the right basal ganglia, the posterior limb of the internal capsule and co-rona radiata, representing an acute infarct. **b** T2-weighted image shows hyperintense lesion along the ipsilateral corti-cospinal tract (*arrow*) and substantia nigra (*arrowheads*) in the cerebral peduncle, which represents wallerian and transneuronal degeneration secondary to the infarction in the right basal ganglia and corona radiata. **c d** DW image shows a hyperintense spot in the right cerebral peduncle associated with decreased ADC, which may represent axonal swelling in the early phase of wallerian degeneration. **e** Another case of the early phase of wallerian degeneration. Histopathology shows axonal swelling as an enlarged axon in the corticospinal tract in the brain stem (*arrows*) (hema-toxylin–eosin stain, original magnification ×200)

Multiple sclerosis in a 36-year-old woman with subacute onset of progressive aphasia. **a** T2-weighted image shows a hyperintense lesion in the periventricular white matter (*arrow*). **b** Gadolinium T1-weighted image with magnetization transfer contrast shows rim enhancement of this lesion. **c** DW image shows a combination of moderately hyperintense and significantly hyperintense lesions. **d** On ADC, the moderately hyperintense lesion on DW image has an increased ADC, which may represent demyelination (*arrows*), while the markedly hyperintense lesion on the DW image, with decreased ADC, may represent intramyelinic edema (*arrowheads*). **e** Another case. Histopathology shows that intramyelinic edema (*arrows*) is located in the periphery of a plaque (*PL*) (Luxol fast blue PAS stain, original magnification ×40). **f** Magnification of (**e**). Intramyelinic edema is seen along the myelin sheaths (*arrows*) (Luxol fast blue PAS stain, original magnification ×200). (From [36])

Figure 4.13 a–d

Phenylketonuria in a 36-year-old male. **a** T2-weighted image shows hyperintense lesions in the periventricular white matter (*arrows*). **b** DW image shows these lesions as hyperintense. **c** These hyperintense lesions have decreased ADC, representing cytotoxic edema, especially intramyelinic edema. **d** 3-month follow-up MRI shows complete resolution of these lesions with clinical improvement
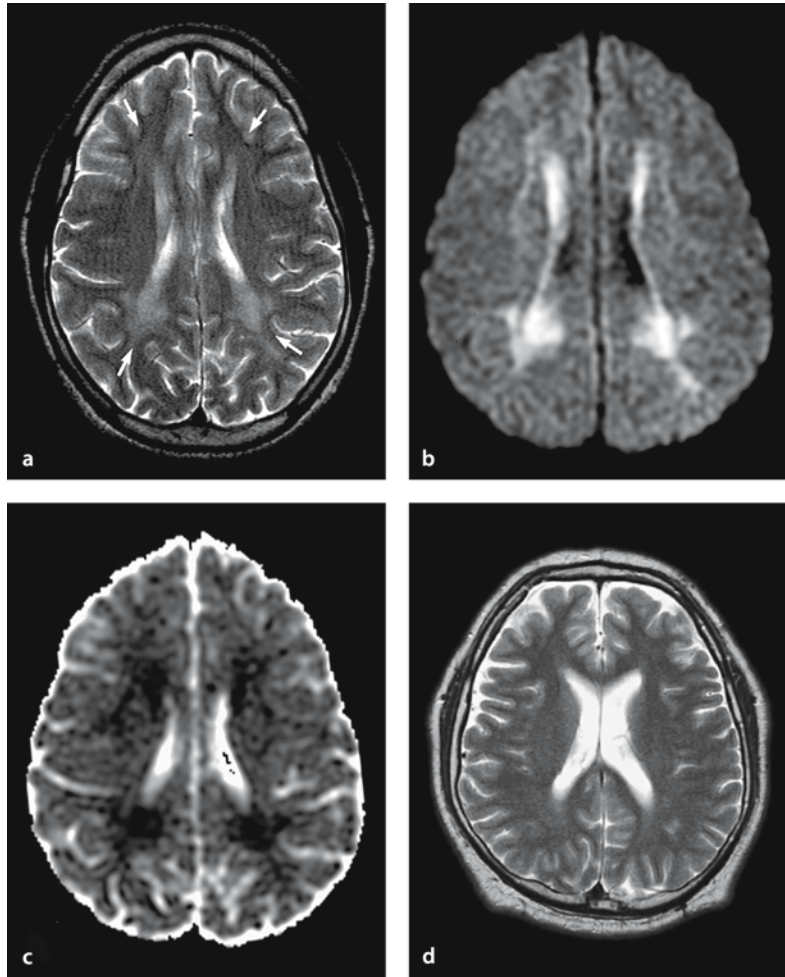
4.5 Vasogenic or Interstitial Edema

Vasogenic edema is characterized by dysfunction of the blood–brain barrier, allowing an abnormal passage of proteins, electrolytes and water into the extracellular compartments. Fluid leaving the capillaries enlarges the extracellular space, predominantly in the white matter. Osmotic and hydrostatic gradients will also cause interstitial edema, increasing the extracellular space as water shifts from blood vessels and/or ventricles. Intracellular components are rela-

tively preserved (Fig. 4.14), although some swelling of myelin sheaths and astrogliosis may be seen histologically [3].

In vasogenic and interstitial edema, electron microscopy has shown an increase of interstitial spaces in white matter amounting to 1000 nm, versus 60 nm in normal white matter [33]. These enlarged extracellular spaces, with free water, may be the dominant source for the total brain water signal, resulting in increased ADC.

Figure 4.14

Vasogenic or interstitial edema. There is enlarged extracellular space as water shifts from the blood vessels and/or ventricles. Intracellular compartments are relatively preserved
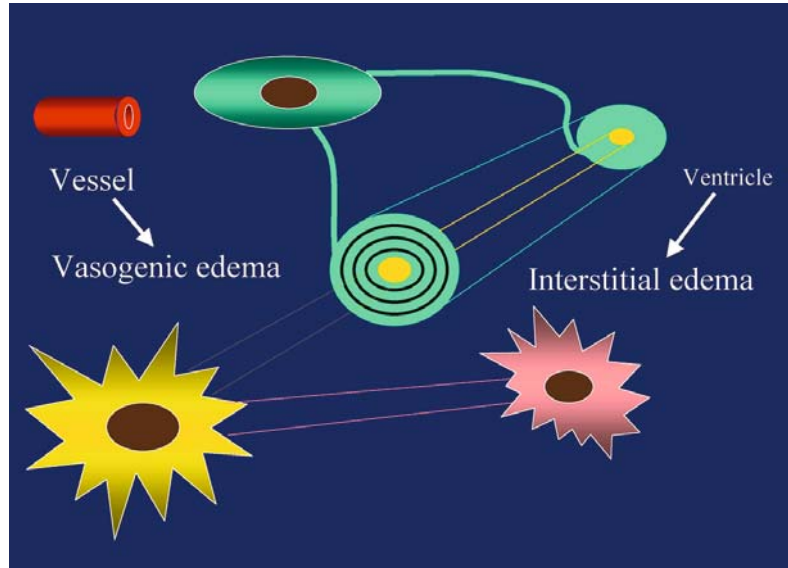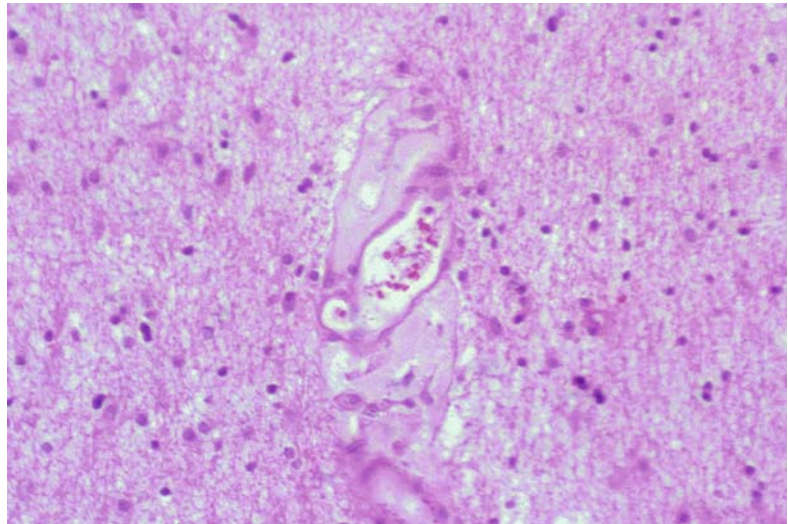

Figure 4.15

Vasogenic edema, as shown on this tissue stain of a trauma case (*arrows*), is the result of plasma leakage through the blood vessel walls. The increase in extracellular space osmolarity will result in a marked increase in extracellular water, i.e. vasogenic edema (hematoxylin–eosin stain, original magnification ×200). (From [36])

### 4.5.1 Conditions that Cause Vasogenic Edema

Vasogenic edema is related to multiple pathological conditions. It typically occurs in the vicinity of brain tumors, intracerebral hematomas, infarctions, cerebral abscesses, contusions and in the reversible posterior leukoencephalopathy syndrome [34]. Venous ischemia at first shows a vasogenic edema due to venous congestion and a breakdown of the normal blood–brain barrier. Progressive venous ischemia results in reduced capillary perfusion pressure and cytotoxic edema [35].

Pathological specimens of vasogenic edema show leakage of plasma from the vessel and diffuse expansion of the extracellular space in the white matter (Fig. 4.15).

Diffusion-weighted images show low signal intensity, isointensity or slightly increased intensity, depending on T2 contrast, and an increase in ADC that reflects free water in the enlarged extracellular space (Fig. 4.16).
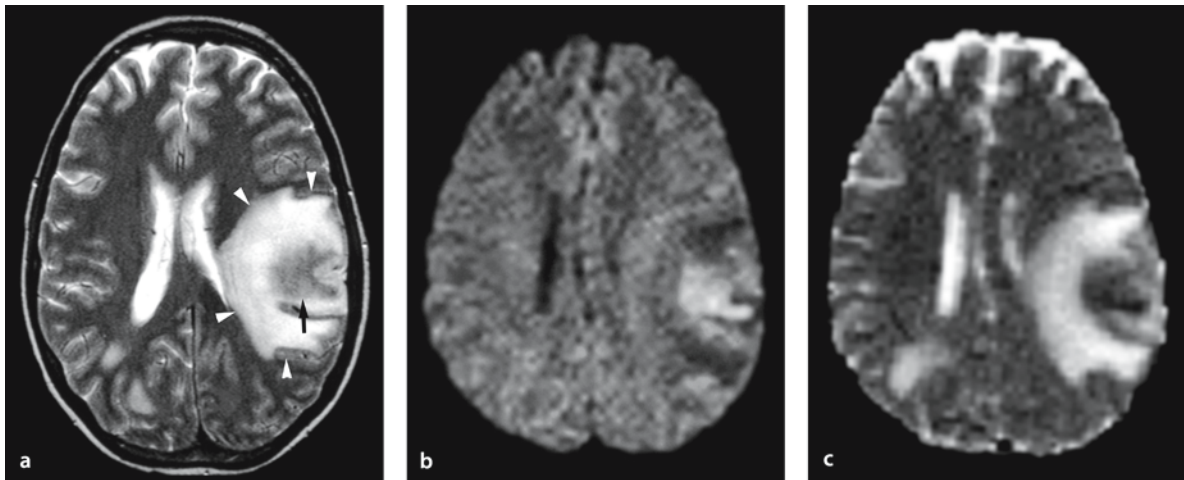
Figure 4.16 a–c

Cerebral toxoplasmosis and vasogenic edema in an 18-year-old woman with headache. **a** T2-weighted image shows central necrosis as slightly hyperintense (*arrow*) and peripheral vasogenic edema as very hyperintense in the left hemisphere (*arrowheads*). Multiple lesions of toxoplasmosis are also seen in the right occipital and left periventricular areas. **b** DW image reveals vasogenic edema as hypointense, while the central necrosis shows hyperintensity on DW image. **c** ADC map shows increased ADC from the vasogenic edema. Decreased ADC of the central necrosis is probably due to hyperviscosity of the coagulative necrosis

4.6 Conclusion

4.6.1 Cytotoxic or Cellular Edema

Cytotoxic or cellular edema is hyperintense on DW images and associated with decreased ADC. It can occur in neurons, glial cells, axons (axonal swelling) and myelin sheaths (intramyelinic edema). Cytotoxic edema may be present not only in infarction/ischemia and trauma, but also in status epilepticus, the acute phase of multiple sclerosis, toxic or metabolic leukoencephalopathy, osmotic myelinolysis, encephalitis, and presumably in the early phase of transneuronal or wallerian degeneration and Creutzfeldt–Jakob disease. The differential diagnosis for hyperintense DW images also includes tumor, abscess and hemorrhage, conditions that also may have decreased ADC. The decreased ADC in these latter conditions may be due to hypercellularity and/or hyperviscosity rather than the cytotoxic edema.

4.6.2 Vasogenic Edema

Vasogenic edema has a variable appearance on DW images, with increased ADC. It is reversible but occasionally associated with cytotoxic edema, which usually is not reversible. DW images and ADC maps are useful for understanding MR images of various diseases with cytotoxic and/or vasogenic edema. These images are more sensitive than conventional MRI to determine the extent of edema in both gray and white matter.

References

1. Milhorat TH (1992) Classification of the cerebral edemas with reference to hydrocephalus and pseudotumor cerebri. Child's Nerv Syst 8:301–306
2. Ebisu T, Naruse S, Horikawa Y, et al. (1993) Discrimination between different types of white matter edema with diffusion-weighted MR imaging. J Magn Res Imaging 3:863–868
3. Ironside JW, Pickard JD (2002) Raised intracranial pressure, oedema and hydrocephalus. In: Graham DI, Lantos PL (eds) Greenfield's neuropathology, 7th edn, pp 193–231

4. Lipton SA, Rosenberg PA (1994) Excitatory amino acids as a final common pathway for neurologic disorders. N Engl J Med 330:613–622

5. Chan S, et al. (1996) Reversible signal abnormalities in the hippocampus and neocortex after prolonged seizures. AJNR Am J Neuroradiol 17:1725–1731

6. Mark LP, Prost RW, Ulmer JL, et al. (2001) Pictorial review of glutamate excitotoxicity: fundamental concepts for neuroimaging. AJNR Am J Neuroradiol 22:1813–1824

7. Moritani T, Shrier D, Wang H, et al. (2002) Excitotoxic mechanism in pediatric brain. Neurographics Vol. 2, Article 1, http://foundation.asnr.org/neurographics/

8. Sharp FR, Swanson RA, Honkaniemi J, et al. (1998) Neurochemistry and molecular biology. In: Barnett HJM, Mohr JP, Stein BM, et al. (eds) Stroke pathophysiology, diagnosis, and management, pp 54–56

9. Duong TO, Ackerman JJH, Ying HS, et al. (1998) Evaluation of extra- and intracellular apparent diffusion in normal and globally ischemic rat brain via ^{19}F NMR. Magn Reson Med 40:1–13

10. van der Toorn A, Sykova EDRM, Vorisek I, et al. (1996) Dynamic changes in water ADC, energy metabolism, extracellular space volume, and tortuosity in neonatal rat brain during global ischemia. Magn Reson Med 36:52–56

11. Tien RD, Felsberg GJ, Friedman H, et al. (1993) MR imaging of high-grade cerebral gliomas: value of diffusion weighted echoplanar pulse sequence. AJR Am J Roentgenol 162:671–677

12. Desprechins B, Stadnik T, Koerts G, et al. (1999) Use of diffusion-weighted MR imaging in differential diagnosis between intracerebral necrotic tumors and cerebral abscesses. AJNR Am J Neuroradiol 20:1252–1257

13. Desmond PM, Lovell AC, Rawlinson AA, et al. (2001) The value of apparent diffusion coefficient maps in early cerebral ischemia. AJNR Am J Neuroradiol 22:1260–1267

14. Burdette JH, Ricci PE, Petitti N, et al. (1998) Cerebral infarction: Time course of signal intensity changes on diffusion-weighted MR images. AJR Am J Roentgenol 171:791–795

15. Kamal AK, Segal AZ, Ulug AM (2002) Quantitative diffusion-weighted MR imaging in transient ischemic attacks. AJNR Am J Neuroradiol 23:1533–1538

16. Forbes KP, Pipe JG, Heiserman JE (2001) Evidence for cytotoxic edema in the pathogenesis of cerebral venous infarction. AJNR Am J Neuroradiol 22:450–455

17. Arbelaez A, Castillo M, Mukheri SK (1999) Diffusion-weighted MR imaging of global cerebral anoxia. AJNR Am J Neuroradiol 20:999–1007

18. Wolf RL, Zimmerman RA, Clancy R, et al. (2001) Quantitative apparent diffusion coefficient measurements in term neonates for early detection of hypoxic-ischemic brain injury: initial experience. Radiology 218:825–833

19. Barzo P, Marmarou A, Fatouros P, et al. (1997) Contribution of vasogenic and cellular edema to traumatic brain swelling measured by diffusion-weighted imaging. J Neurosurg 87:900–907

20. Liu AY, Maldjian JA, Bagley LJ, Sinson GP, et al. (1999) Traumatic brain injury: diffusion-weighted MR imaging findings. AJNR Am J Neuroradiol 20:1636–1641

21. Kim JA, Chung JI, Yoon PH, et al. (2001) Transient MR signal changes in patients with generalized tonicoclonic seizure or status epilepticus: periictal diffusion-weighted imaging. AJNR Am J Neuroradiol 22:1149–1160

22. Men S, Lee DH, Barron JR, et al. (2000) Selective neuronal necrosis associated with status epilepticus; MR findings. AJNR Am J Neuroradiol 21:1837–1840

23. Tsuchiya K, Katase S, Yoshino A, et al. (1999) Diffusion-weighted MR imaging of encephalitis. AJR Am J Roentgenol 173:1097–1099

24. Demaerel P, Baert AL, Vanopdenbosch L, et al. (1997) Diffusion-weighted magnetic resonance imaging in Creutzfeldt–Jakob disease. Lancet 349:847–848

25. Bahn MM, Parchi P. (1999) Abnormal diffusion-weighted magnetic resonance images in Creutzfeldt–Jakob disease. Arch Neurol 56:577–583

26. Castillo M, Mukheriji SK (1999) Early abnormalities related to postinfarction wallerian degeneration: evaluation with MR diffusion-weighted imaging. JCAT 23:1004–1007

27. Verity MA (1997) Toxic disorders. In: Graham DI, Lantos PL (eds) Greenfield's neuropathology, 6th edn, pp 755–811

28. Tievsky AL, Ptak T, Farkas J (1999) Investigation of apparent diffusion coefficient and diffusion tenser anisotropy in acute and chronic multiple sclerosis lesion. AJNR Am J Neuroradiol 20:1491–1499

29. Matsumoto S, Nishizawa S, Murakami S, et al. (1995) Carmofur-induced leukoencephalopathy: MRI. Neuroradiology 37:649–652

30. Phillips MD, McGraw P, Lowe MJ, et al. (2001) Diffusion-weighted imaging of white matter abnormalities in patients with phenylketonuria. AJNR Am J Neuroradiol 22:1583–1586

31. Sener RN (2002) Metachromatic leukodystrophy: diffusion MR imaging findings. AJNR Am J Neuroradiol 23:1424–1426

32. Cramer SC, Stegbauer KC, Schneider A, et al. (2001) Decreased diffusion in central pontine myelinolysis. AJNR Am J Neuroradiol 22:1476–1479

33. Gonatas NK, Zimmerman HM, Levine S (1963) Ultrastructure of inflammation with edema in the rat brain. Am J Pathol 42:455–469

34. Mukherjee P, McKinstry RC (2001) Reversible posterior leukoencephalopathy syndrome: evaluation with diffusion-tensor MR imaging. Radiology 219:756–765

35. Keller E, Flancke S, Urbach H, et al. (1999) Diffusion- and perfusion-weighted magnetic resonance imaging in deep cerebral venous thrombosis. Stroke 30:1144–1146

36. Moritani T (2002) Classification of brain edema. In Koredewakaru Diffusion MRI, Tokyo: Shujunsha pp 128–137

37. Moritani T, Shrier DA, (2000) Numaguchi Y, et al. Diffusion-weighted echo-planar MR imaging: clinical applications and pitfalls – a pictorial essay. Clin Imaging 24:181–92

Infarction

In collaboration with R. de Guzman

5.1 Clinical Significance and Therapeutic Considerations for Brain Infarcts

Stroke is the third leading cause of death in the USA, and cerebral infarction is the most common cause of disability among adult Americans. Until recently these patients were mainly imaged with computed tomography (CT) to establish if the cause of stroke was ischemic or hemorrhagic. Treatment was above all aimed to reduce the risk for further embolic events. In a few instances intra-arterial or intravenous thrombolysis has been instituted, but in most cases this is not feasible because of the narrow therapeutic window. Thrombolytic treatment has a risk of hemorrhagic complications, which is why it has become important to establish the potential benefit of thrombolysis for the individual patient. CT as well as conventional MR imaging have sensitivities below 50% with regard to detection of infarcts in the hyperacute stage, within 6 hours.

5.1.1 Stroke Mimickers

There is a long list of conditions that mimic the symptoms of an acute ischemic stroke. The most common ones include intracranial hemorrhage, migraines, seizures, functional and metabolic disorders, and also vasogenic edema syndromes. It is important to visualize and verify that an ischemic lesion is indeed the cause of the clinical symptoms before therapy is initiated, as these non-ischemic stroke mimickers should not be treated with thrombolysis and such therapy could actually be harmful. Moreover, in older patients it is not uncommon to detect older lesions with prolonged T2 that are indistinguishable from acute lesions using conventional MR imaging.

5.1.2 Diffusion-Weighted Imaging

In recent years, diffusion-weighted (DW) imaging has been proven as the most sensitive MR imaging technique to diagnose hyperacute cerebral infarction. The detection of acute ischemic lesions is based on alterations in motion of water molecules. It is a very sensitive technique, which is not significantly affected by patient motion. DW imaging of the brain can usually be accomplished in less than 2 minutes.

The ischemic event results in restricted diffusion of the affected tissue, which can be seen as early as 30 minutes after ictus. A few rare cases of false-negative DW imaging have been reported [1, 2]. These infarcts were seen on perfusion-weighted images and later on DW imaging [1, 2].

5.2 Diffusion-Weighted Imaging and Pathophysiology of Cerebral Infarction

The abnormal imaging finding of cerebral and cerebellar infarctions is an area of hyperintensity on DW imaging of the involved vascular territory. This hyperintensity is presumed to be caused by cytotoxic edema as a result of cessation of ATP production. Under normal circumstances, ATP maintains the Na^+/K^+ pump activity and other intracellular energy-related processes. When the Na^+/K^+ pump is not functioning properly, an inability to remove excess water from the cells develops, resulting in intracellular edema. The outcome of this on DW imaging is restriction of water diffusion, which results in a signal increase on DW imaging and a decrease in diffusion shown as a reduced apparent diffusion coefficient (ADC) [3]. These findings in acute stroke usually represent irreversible damage of brain tissue, or infarction [4].

5.3 Apparent Diffusion Coefficient

The ADC is used to determine whether the signal abnormality on DW images is caused by restricted diffusion or a T2 shine-through effect, as seen in subacute–chronic infarctions. ADC represents the degree of diffusibility of water molecules and aids in detecting subtle fluid changes in the hyperacute–acute stages of ischemic stroke. Reduced diffusion is seen as an area of low signal intensity on ADC maps.

5.3.1 Explanation for Restricted Diffusion

Several mechanisms have been proposed to explain the restricted diffusion in ischemia. These include cellular necrosis, shift of fluid from extra- to intracellular spaces causing a reduction in size and increase in tortuosity of the extracellular space, but there is also rather strong evidence that at least parts of these findings relate to a reduction in intracellular diffusion [5].

Regions of decreased or restricted diffusion are best seen on DW imaging, while ADC maps will verify the findings by eliminating the T2 shine-through effect as a cause of the increased signal intensity on DW imaging. DW imaging and ADC can also show changes in diffusion that vary for the different stages of a stroke [6], and they can possibly distinguish between multiple strokes over time versus a single, progressive stroke by determining the time course of a cerebral infarction.

Apparent diffusion coefficient values may also be of help in the future to assist in selecting patients with salvageable tissue within an ischemic penumbra for thrombolysis. Intermediate ADC values are noted in the ischemic penumbra, indicating tissue at risk of infarction [7]. An approach that is used more often to select patients who may benefit from thrombolysis is by comparing DW imaging and perfusion MR imaging to look for hypoperfused but not diffusion-restricted regions. The mismatch between DW imaging and perfusion demonstrates affected tissue that is still salvageable and not yet infarcted: the penumbra.

5.4 Time Course of Infarction

Infarctions may be classified as hyperacute (less than 6 hours from time of onset of symptoms), acute (6 hours to 3 days), subacute (3 days to 3 weeks), or chronic (3 weeks to 3 months), each having its characteristic signal abnormalities (Table 5.1).

5.4.1 Hyperacute (< 6 Hours)

One of the main clinical applications of DW imaging is to detect a hyperacute cerebral infarction. This information is critical, particularly in cases of territorial thromboembolic infarction, as thrombolytic therapy can be started within the golden period of 3 hours from onset of symptoms. Such treatment can result in early reperfusion and reduce the extension of the infarction [3, 8]. The DW signal intensity is increased during the hyperacute stage (<6 hours), with corresponding low ADC, manifested as a dark area on the ADC map (Fig. 5.1).

Table 5.1. Time course of thromboembolic infarction of the middle cerebral artery [7]

	< 6 hours	3 days	7 days	30 days
T2	Isointense	Bright	Bright	Bright
DW imaging	Bright	Very bright	Bright	Isointense
ADC	Dark	Very dark	Dark	Bright

Figure 5.1 a–d

Hyperacute infarction (2 hours after onset) in a 39-year-old woman with decreased consciousness. The symptoms improved after intra-arterial fibrinolytic therapy. **a** T2-weighted image appears normal. **b** DW image shows a hyperintense lesion in the right corona radiata (*arrows*) and a slightly hyperintense lesion in the right middle cerebral artery (MCA) territory (*arrowheads*). **c** ADC map shows decreased ADC in the corona radiata (*arrows*) and slightly decreased ADC in the cortical area of the MCA territory (*arrowheads*). **d** On DW image after fibrinolytic therapy (3 days after onset), the hyperintense lesion in the cortical area mostly resolved with peripheral small infarcts. Early cytotoxic edema with mild decreased ADC does not always result in infarction after treatment
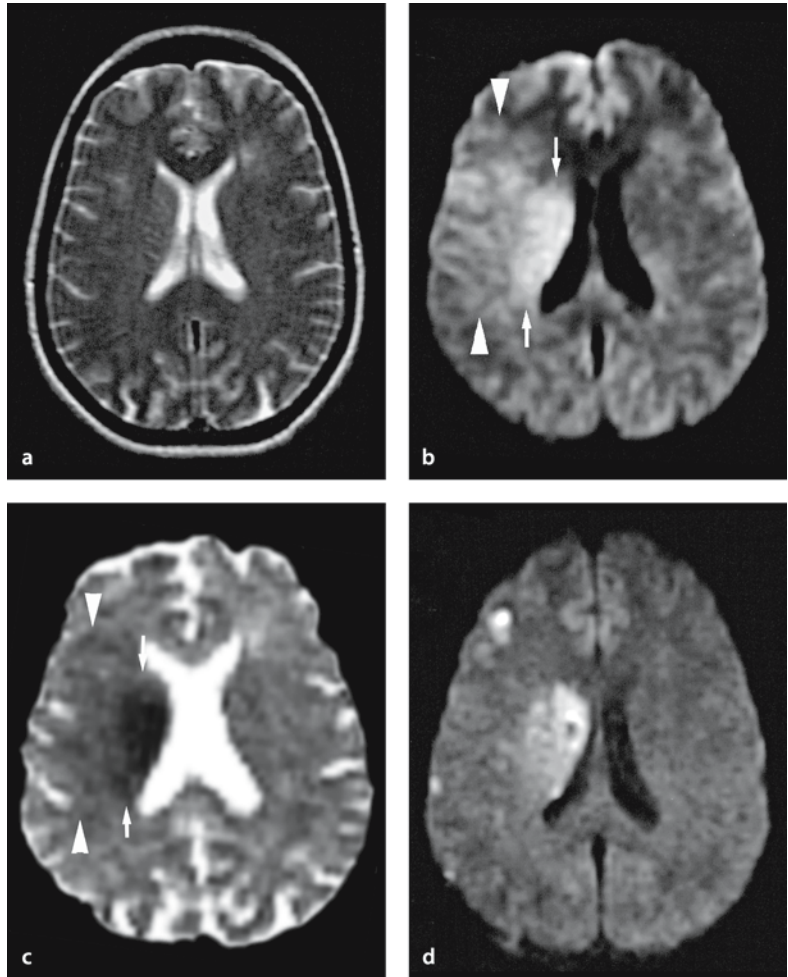
5.4.2 Acute (6 Hours to 3 Days)

Almost all acute (6 hours to 3 days) stroke patients examined within 24 hours of onset of symptoms show abnormal signal intensity on DW imaging [9]. At this stage the infarctions show a further increase in DW signal intensity and also a lower ADC than in the hyperacute stage (Fig. 5.2).
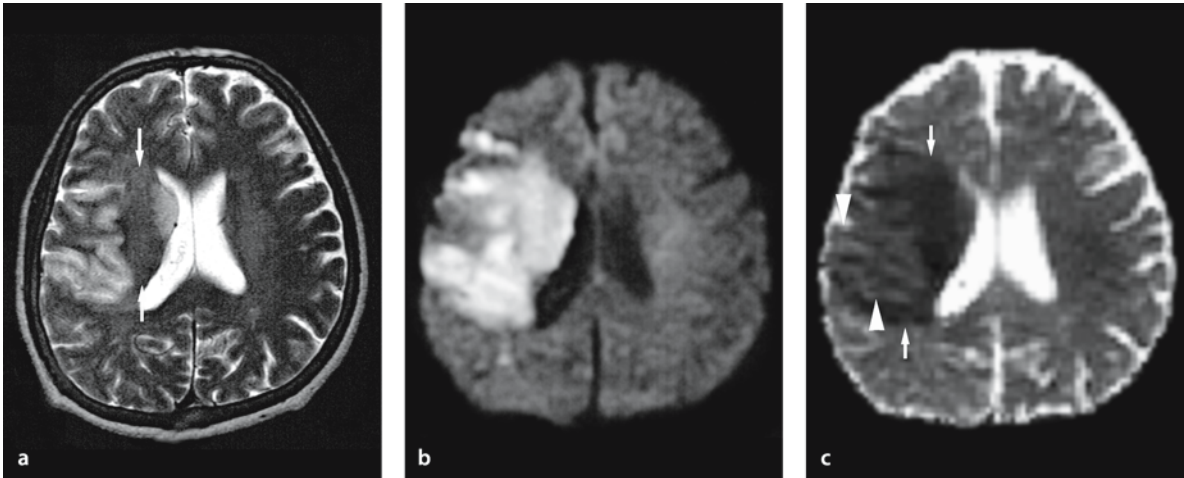
Figure 5.2 a–c

Acute infarction (24 hours after onset) in a 56-year-old man with left hemiparesis. **a** T2-weighted image shows hyperintense lesions preferentially involving the right posterior frontal cortex and the right caudate region, sparing the right corona radiata (*arrows*). This finding is consistent with a relatively greater involvement of gray matter in the early infarction. **b** DW image shows the entire right MCA territory as hyperintense. **c** Decreased ADC is seen in the right MCA territory (*arrows*). However, some cortical lesions seem to be isointense or have a slightly increased ADC (*arrowheads*). This may reflect relative vulnerability for brain tissue. Hyperintensity on DW image of these cortical lesions is due to a T2 shine-through effect. DW images and ADC maps are more sensitive than conventional MRI for showing both gray and white matter involvement. ADC maps precisely reflect diffusion restrictions of the lesion within the gray and white matter

5.4.3 Subacute (3 Days to 3 Weeks)

As the infarct continues to evolve into the subacute stage (3 days to 3 weeks), there is pseudo-normalization of the ADC, most likely attributed to a combination of (a) persistence of cytotoxic edema, and (b) development of vasogenic edema and cell membrane disruption, which results in increased amounts of extracellular water. The hyperintensity on DW imaging usually decreases within 1–2 weeks [10], but is still slightly hyperintense, while ADC is usually normalized within 10 days [11]. This time gap is thought to result from T2 shine-through effects on DW imaging in the late subacute infarction (Fig. 5.3).

Figure 5.3 a–d

Subacute infarction (10 days after onset) in a 19-year-old woman with loss of consciousness due to cerebral embolism after cardiac surgery for endocarditis. **a** T2-weighted image shows hyperintense lesions in the gray (*arrowheads*) and white matter (*arrows*) in the right hemisphere and left frontal region. **b** Gadolinium T1-weighted image with magnetization transfer contrast shows gyral enhancement in the cortical lesions, representing subacute infarcts. **c** DW image also shows hyperintense lesions in the right deep white matter (*arrows*), and gray matter of both frontal and right parieto-occipital regions (*arrowheads*). **d** The ADC map shows decreased ADC in the right deep white matter lesion (*arrows*), and normal or slightly increased ADC in the gray matter lesions (*arrowheads*). The prolonged decreased ADC in the white matter may reflect edema of myelin sheaths or axons
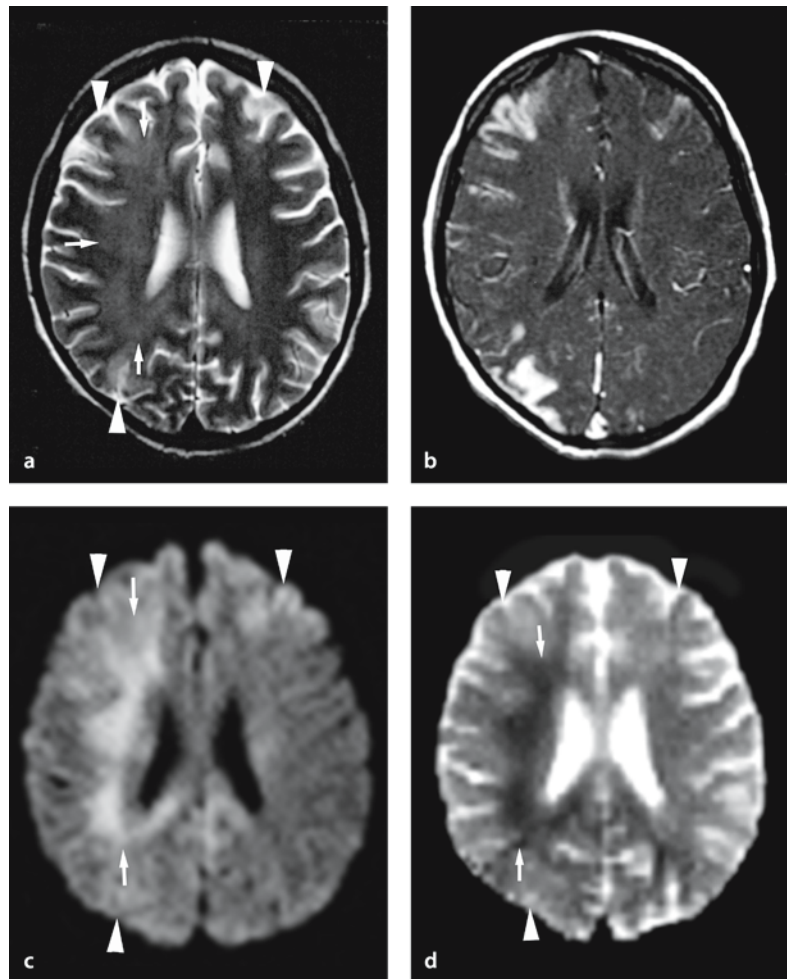
5.4.4 Chronic (3 Weeks to 3 Months)

In the chronic stage (3 weeks to 3 months) of infarction, there is a more or less complete necrosis of the cells and at this stage there is an increase in ADC with a bright signal on the ADC map. On T2-weighted imaging the infarction is seen as a bright signal and this, in combination with the increased ADC, will result in a decrease in the signal on DW imaging; the infarction is isointense with surrounding tissue (Fig. 5.4).
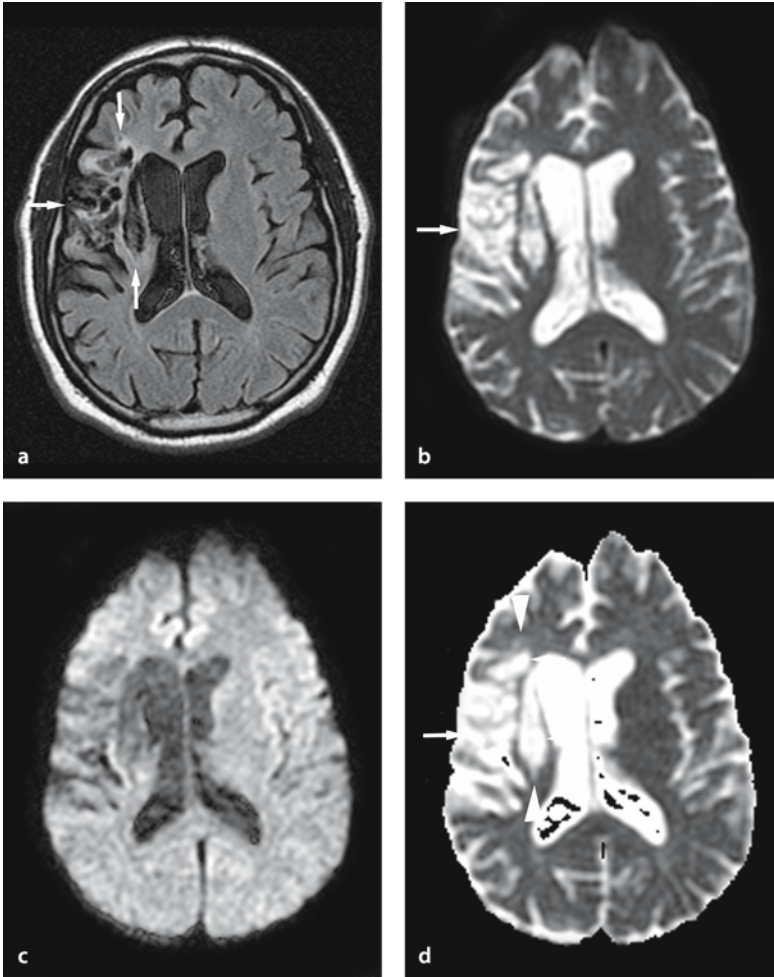
Figure 5.4 a–d

Chronic infarction (10 months after onset) in a 54-year-old man with numbness and weakness of the left lower extremity. **a** Fluid-attenuated inversion-recovery (FLAIR) image shows chronic infarction in the right MCA territory as a cystic lesion with low signal intensity (cystic necrosis) and peripheral mild hyperintensity (gliosis) with atrophy (*arrows*). **b** b$_0$ image shows the hyperintense cystic lesion (*arrow*). **c** DW image shows chronic infarction as hypointense cystic areas, and iso- or slightly hyperintense areas representing gliosis. **d** The ADC map shows marked increased ADC in the cystic necrosis (*arrow*), and slightly increased ADC in the gliotic periphery of the lesion (*arrowheads*)

5.5 Diffusion-Weighted Imaging and ADC Characteristics of Gray and White Matter Ischemia

Diffusion-weighted imaging and ADC maps are more sensitive than conventional MR imaging in demonstrating both gray and white matter ischemia (Figs. 5.1, 5.2 and 5.3). Changes in ADC values in acute infarctions seem to be different for gray matter and white matter. Thus, there is a more prominent decrease in ADC in white matter than in gray matter. This decrease also remains for a longer period than in gray matter (Figs. 5.2 and 5.3). One of the explanations for these phenomena is that necrosis may be completed earlier in gray matter infarctions than in white matter infarctions. Another explanation is that the prominent and prolonged decrease in ADC in white matter may reflect cytotoxic edema in different cell types, such as myelin sheaths, axons and glial cells [5, 6, 11].

5.5.1 Relative ADC

The time course of relative ADC is slightly different in gray matter when compared with the relative ADC in white matter [6]. Fiebach et al. observed a decrease in the relative ADC up to 3 days after the stroke and an increase in relative ADC from the third to the tenth day. The relative ADC increased slightly faster in gray matter than in white, which may be due to the variability between these two tissue types at any stage in the ischemic process, which leads to an altered diffusion. The observed diffusion contrast in gray and white matter could be caused by differences in the mismatch between blood supply and metabolic demand, the type and/or severity of the histopathologic response to ischemic injury (vulnerability) or mechanisms by which histopathologic changes lead to altered diffusion [12]. Regarding the histopathologic response, gray matter has traditionally been considered to be more vulnerable than white matter to early ischemia. More recent findings in experimental models of stroke have demonstrated that ischemic damage to white matter occurs earlier and with greater severity than previously appreciated [13]. However, if this is true for humans as well is to our knowledge, not yet established.

5.6 Reversibility and Treatment

Reversible ADC is rare but can be found in cases of transient ischemic attack in which imaging was performed within 4 hours, venous infarction, hemiplegic migraine and transient global amnesia. In these rare clinical settings, ischemia does not progress to complete necrosis but a minor subclinical, irreversible injury cannot be ruled out [5].

Clinically, the area of cytotoxic edema with bright DW signal seems to be irreversibly damaged resulting in permanent infarction. In early cerebral ischemia, mildly decreased ADC in the ischemic penumbra is indicative of viable tissue, but hypoperfused tissue at risk of infarction [14]. After intra-arterial or intravenous fibrinolytic therapy, or spontaneous lysis of a clot, abnormal signal in such areas is occasionally reversed, partially or completely (Figs. 5.4 and 5.5).
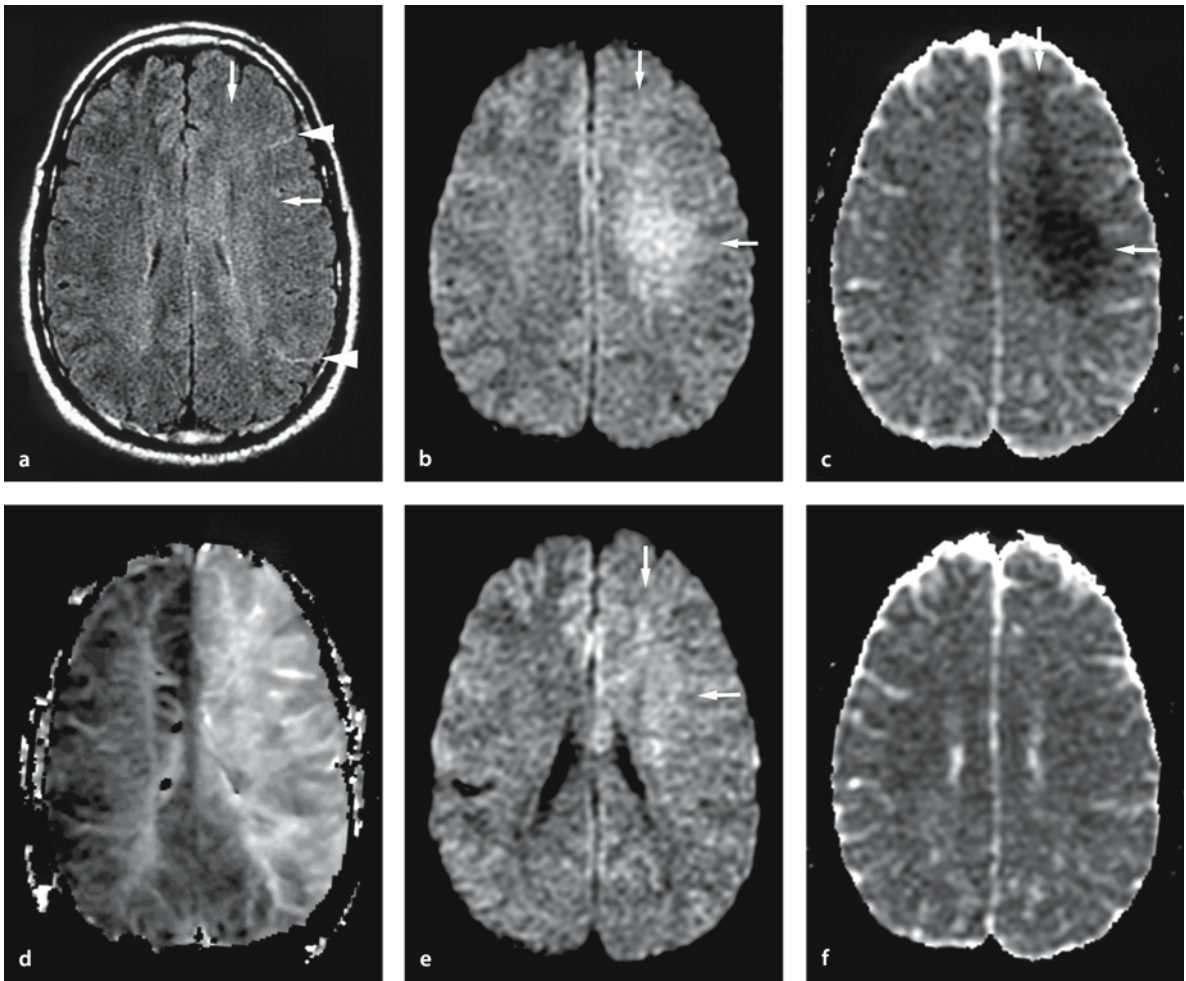
Figure 5.5 a–f

Reversible ischemia with cytotoxic edema (2 h from onset) in a 39-year-old man with left internal carotid artery dissection, presenting with right-sided weakness. **a** FLAIR image shows a subtle hyperintensity in the left frontoparietal white matter (*arrows*), and linear hyperintensity representing slow flow in the peripheral arteries (*arrowheads*). **b, c** DW image (**b**) shows a hyperintense lesion with decreased ADC (**c**) in the left frontoparietal white matter, representing cytotoxic edema (*arrows*). **d** Perfusion-weighted image shows increase in mean transit time of the entire left anterior and MCA territories. **e** Follow-up DW image 2 days later shows only a very subtle hyperintensity in the left frontal white matter (*arrows*). **f** ADC was normalized, which is in accordance with clinical improvement. Early ischemia with cytotoxic edema may have spontaneously resolved

5.7 Watershed Infarction

Watershed infarction may develop between two major vascular territories or within a single territory in the supraganglionic white matter, a border zone of the superficial and deep penetrating arterioles (Fig. 5.6). As mentioned above, thrombolytic therapy within the first 3 hours from acute onset of symptoms can be effective to limit the size of the infarct under those circumstances. This is, however, not the case in watershed infarctions, as the basic etiology for these lesions is a significant reduction in perfusion secondary to an overall decrease in cerebral blood flow with subsequent poor perfusion pressure distally [7].

There is a difference in the evolution time of ADC between watershed and thromboembolic infarction, the latter having an earlier normalization (Table 5.2). However, T2 signal intensity is the same for both types of infarction. The reason for this difference most likely lies in the different pathophysiologic features and cerebral perfusion of the two stroke subtypes. It is important to note that strokes with different pathogenetic, hemodynamic mechanisms may have different evolution in the ADC courses as well [7].
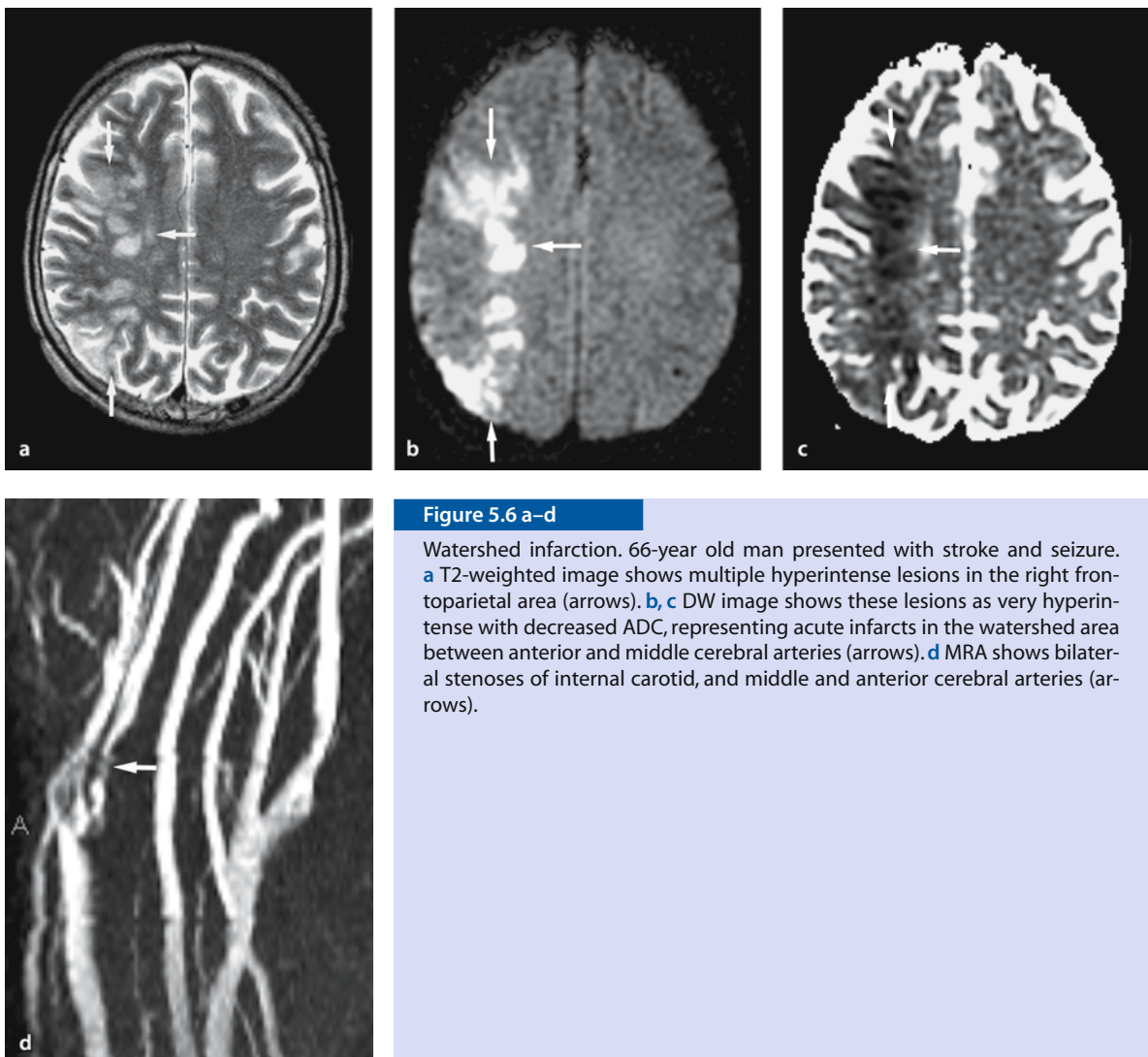
Figure 5.6 a–d

Watershed infarction. 66-year old man presented with stroke and seizure. **a** T2-weighted image shows multiple hyperintense lesions in the right frontoparietal area (arrows). **b, c** DW image shows these lesions as very hyperintense with decreased ADC, representing acute infarcts in the watershed area between anterior and middle cerebral arteries (arrows). **d** MRA shows bilateral stenoses of internal carotid, and middle and anterior cerebral arteries (arrows).

Table 5.2. Time course of watershed infarction of middle cerebral arterial territory [7]

	3 days	7 days	14 days	30 days
T2	Bright	Bright	Bright	Bright
DW imaging	Bright	Bright	Bright	Bright
ADC	Dark	Dark	Dark	Less dark

5.8 Perfusion Versus Diffusion Imaging

Perfusion MR imaging may be more sensitive than DW imaging in the detection of a hyperacute cerebral infarction, but it currently entails extensive post-processing to create interpretable perfusion maps (Figs. 5.5 and 5.6). Moreover, MR perfusion determines the degree of blood flow reduction at the level of the cerebral microvasculature, but it will not tell if a hypoperfused area represents an area of infarction or severe hypoperfusion. Perfusion MR can, however, be matched with the infarcted area on DW images and can demonstrate the area of hypoperfusion outside the infarction – the so-called penumbra. This is the area where neural tissue is at risk for infarction if perfusion is not re-established and ischemic penumbra is assumed to be salvageable by means of thrombolysis.

5.9 Venous Infarction

Cerebral venous sinus thrombosis accounts for only a small percentage of cerebral infarctions in general. Because of its non-specific presentation, cerebral venous sinus thrombosis can be difficult to diagnose. In about 50% of cases, cerebral venous sinus thrombosis results in cerebral venous infarction. This usually presents as a hemorrhagic infarction or focal edema in regions that are not typical for an arterial vascular distribution, usually occurring within the white matter or at the gray–white matter junction (Fig. 5.7).

5.9.1 Predisposing Factors

There are several predisposing factors for thrombus formation within the cerebral venous sinuses. These include pregnancy, infection, extrinsic compression or local invasion by tumor, dehydration, oral contraceptives, hypercoagulable state, trauma, drug abuse. It may also be idiopathic. Thrombus initially forms within the venous sinuses, eventually extending to the veins draining into the sinuses, leading to infarction.

5.9.2 Pathophysiology

The pathophysiological mechanisms that lead to cerebral venous infarction are unclear. It has been postulated that: (1) retrograde venous pressure may cause breakdown of the blood–brain barrier, with leakage of fluid (vasogenic edema) and hemorrhage into the extracellular space or, (2) retrograde venous pressure may cause a decrease in cerebral blood flow, causing tissue damage similar to that seen in arterial infarctions. Restricted water diffusion suggesting cytotoxic edema is found in patients with acute cerebral venous infarction [2]. However, in cases with only vasogenic edema, ADC is increased with variable DW signals (Fig. 5.7). Preferred imaging modalities when suspecting cerebral venous sinus thrombosis are conventional MR imaging combined with MR venography.
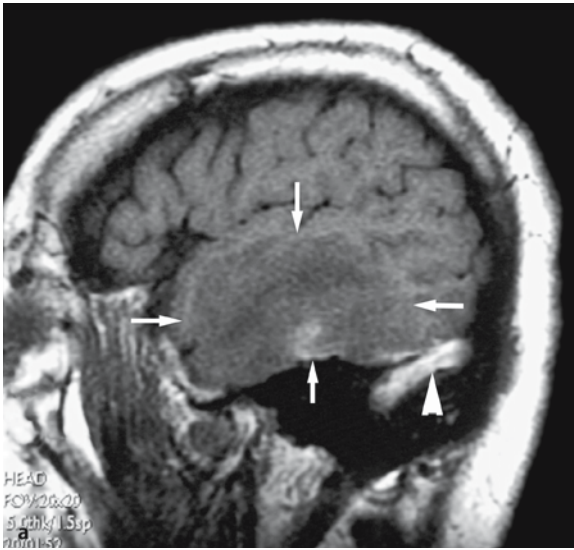
Figure 5.7 a–d

Venous infarction in a 57-year-old man with dysarthria. **a** Sagittal T1-weighted image shows a large area of hyperintensity in the left temporal lobe (arrows) with a small area (hemorrhage). The hyperintensity in the left transverse sinus represents sinus thrombosis (arrowhead). **b** T2-weighted image shows a hyperintense lesion in the left temporal lobe (*arrow*). **c** DW image reveals this lesion as mildly hyperintense. **d** ADC is increased, representing vasogenic edema. On DW image, the lesion is overlapped with diamagnetic susceptibility artifacts from air in the mastoid cells
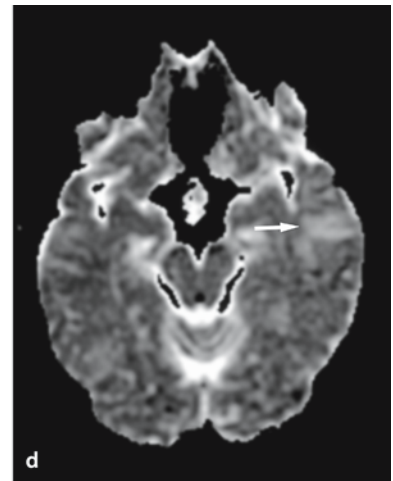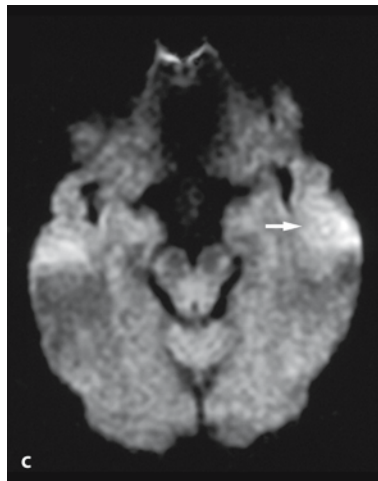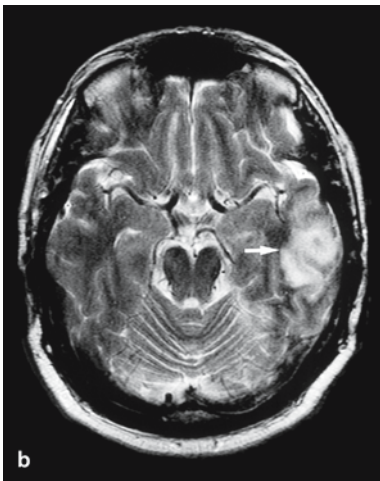
5.10 Small Vessel Infarcts

These are small infarcts measuring approximately 5–15 mm, usually seen in the basal ganglia, internal capsule, thalamus, pons and corona radiata. They account for about 20% of all infarctions and are secondary to an embolus, thrombus or atheromatous lesion within long, single, penetrating end arterioles.

These infarcts show increased signal in DW imaging with low ADC values (Fig. 5.8). However, unlike the usual time course of cerebral infarctions, they may show a prolonged increase in DW imaging signal and decrease in ADC values, sometimes seen beyond 60 days after onset of symptoms [15].

Differential diagnoses include widened perivascular spaces (Virchow–Robin spaces) and subependymal myelin pallor.
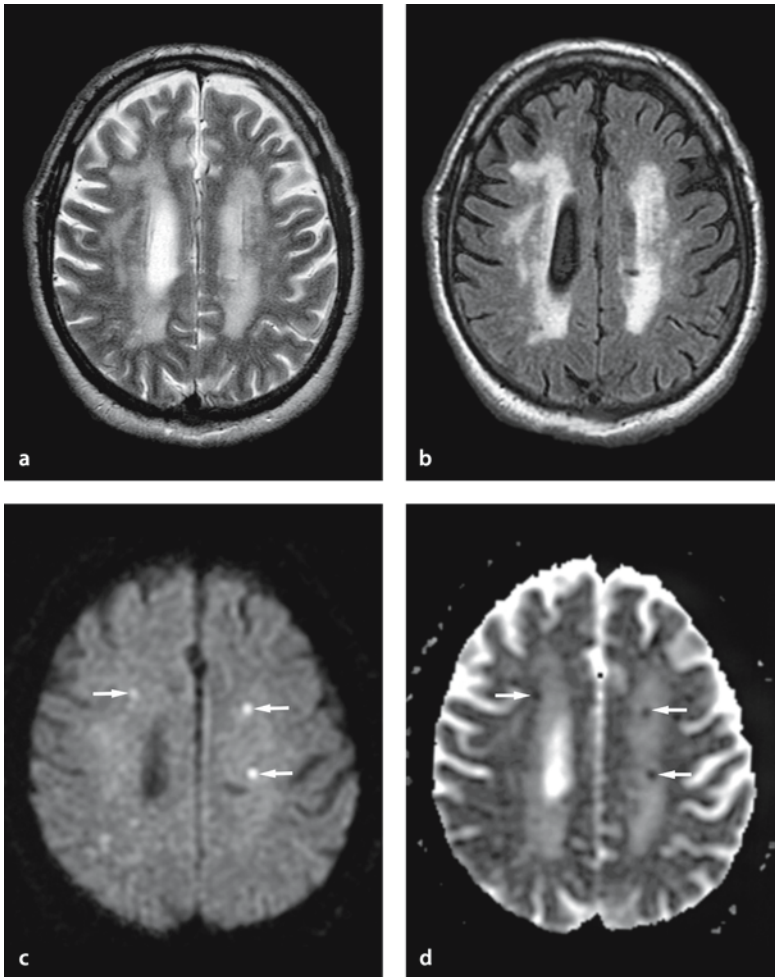
Figure 5.8 a–d

Small vessel infarcts in a 69-year-old man. **a, b** T2-weighted and FLAIR images show periventricular hyperintensities; however, it is difficult to detect acute small infarcts. **c** DW image clearly shows multiple hyperintensity spots in the white matter, representing the acute phase of small vessel infarcts. **d** ADC

5.11 Brain Stem and Cerebellar Infarcts

Cerebellar infarction is caused by occlusion of one of the major posterior circulation branches, which include the superior cerebellar, the anterior and posterior inferior cerebellar arteries, and the basilar artery. The posterior inferior cerebellar artery (PICA) supplies the postero-inferior portions of the cerebellum and is the most commonly obstructed cerebellar artery. The size of the infarct is important because a large infarct may cause a significant mass effect on the fourth ventricle and lead to hydrocephalus as well as brain stem compression. PICA infarctions can also result in the so-called lateral medullary (Wallenberg) syndrome, manifested by ipsilateral Horner's syndrome, ataxia, dysphagia, vertigo, nystagmus, hiccups and contralateral numbness, diminished pain and temperature sensation. The brain stem and cerebellar infarcts behave similar to cerebral infarcts on DW imaging and ADC maps (Fig. 5.9).
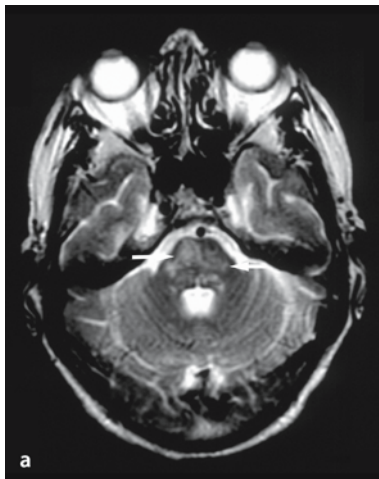
Figure 5.9 a–c

Brain stem infarction in an 83-year-old woman with slurred speech and gait difficulties. **a** T2-weighted image show hyperintense lesions in the pons (*arrows*). **b** DW image clearly shows a hyperintense lesion. **c** ADC is decreased in the right side of the pons, representing acute infarction (*arrow*)
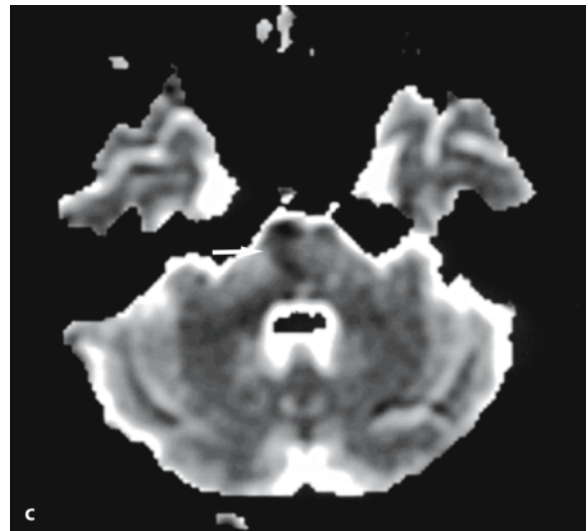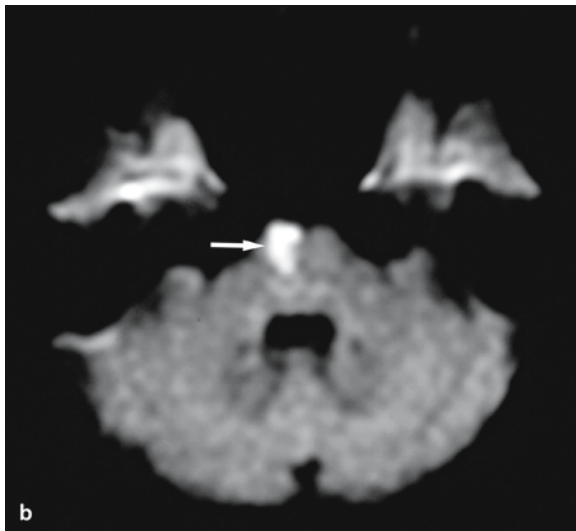
5.12 Corpus Callosum Infarcts

Isolated corpus callosum infarction due to pericallosal artery disease is rare, but can present as an alien hand syndrome. These patients fail to recognize the ownership of one hand when placed in certain positions or situations [16]. These lesions are readily detected by DW imaging and have signal characteristics similar to cerebral infarcts (Fig. 5.10).
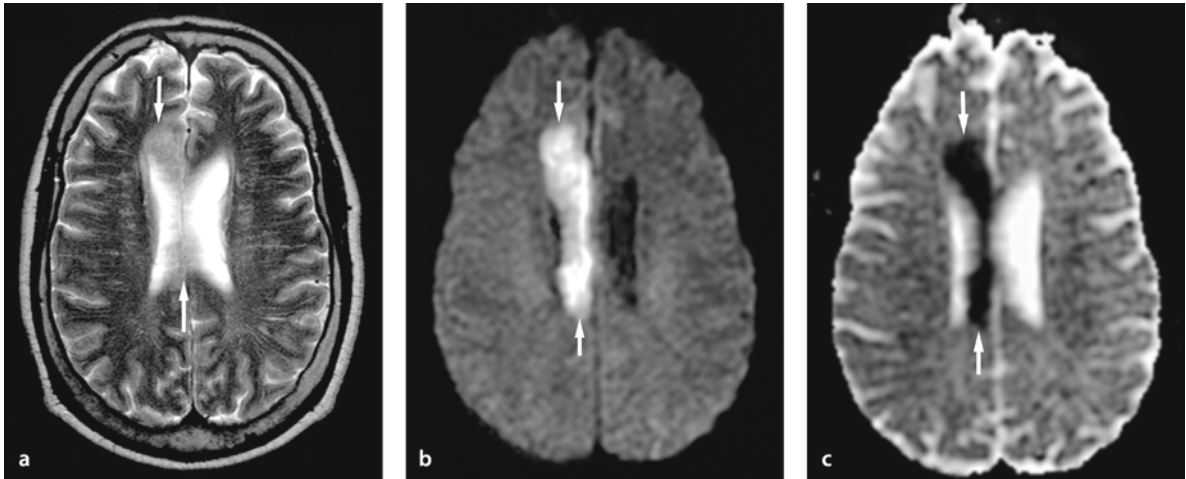
Figure 5.10 a–c

Corpus callosum infarction in a 64-year-old man with left-sided weakness. **a** T2-weighted image shows a hyperintense lesion in the anterior part and body of the corpus callosum extending into right frontal white matter (*arrows*). **b** DW image clearly shows this lesion as hyperintense. **c** ADC is decreased, representing acute infarction (*arrows*)

5.13 Hemorrhagic Infarcts

About 40–50% of all stroke patients develop hemorrhagic transformation of their infarcts (Fig. 5.11). This usually occurs during the first week after onset of symptoms. The cause may be a spontaneous lysis of an embolus, which took place at a time when endothelial cells of the vessel had also been damaged by the ischemia, thus resulting in a breakthrough hemorrhage into the infarcted region. The incidence of hemorrhage is increased with use of thrombolytic therapy, as well as in the presence of certain clinical conditions, such as hypertension, embolic etiology, use of anticoagulant therapy and increasing stroke severity.

Studies have shown that neuroimaging can predict which lesions are prone to progress into a hemorrhagic infarction [17]. Thus, ischemic lesions with a significantly greater percentage of low ADC values have a higher risk for hemorrhagic transformation than lesions with a smaller proportion of low ADC [17].
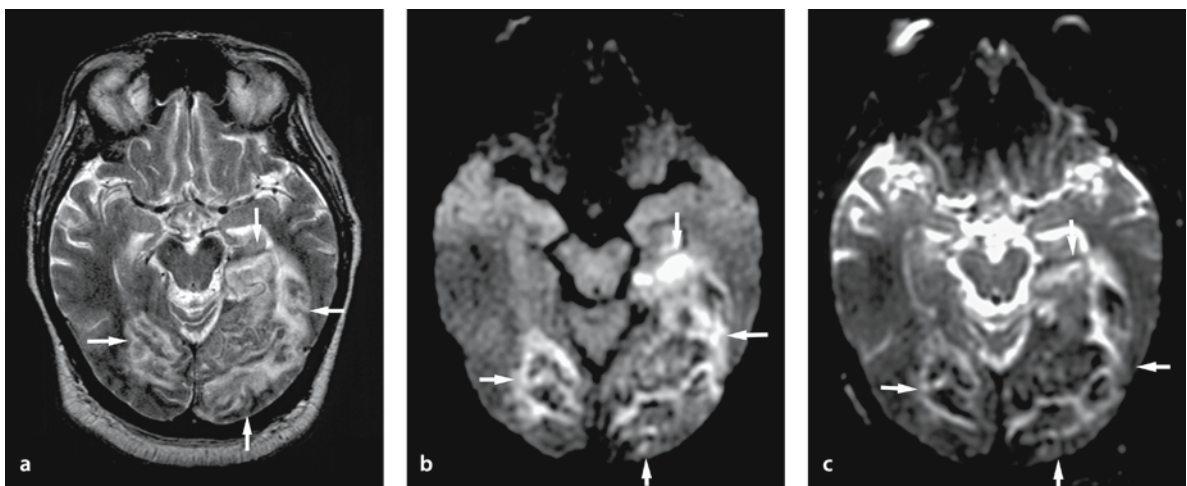
Figure 5.11 a–c

Hemorrhagic infarction in a 64-year-old man with mental status change. **a** T2-weighted image shows mixed hyper- and hypointense lesions in bilateral occipital lobes (*arrows*). **b** DW image shows these lesions as mixed hyper-, hypo- and isointense, representing acute hemorrhagic infarction (*arrows*). **c** ADC is decreased with areas of hyperintensities

References

1. Lefkowitz D, LaBenz M, Nudo Sr, et al. (1999) Hyperacute ischemic stroke missed by diffusion-weighted imaging. AJNR Am J Neuroradiol 20:1871–1875

2. Wang PYK, Barker PB, Wityk RJ, et al. (1999) Diffusion-negative stroke: a report of two cases. AJNR Am J Neuroradiol 20:1876–1880

3. Provenzale JM, Sorensen AG (1999) Diffusion-weighted MR imaging in acute stroke: theoretic considerations and clinical applications. AJR Am J Radiol 173:1459–1467

4. Keller E, Flacke S, Urbach H, Schild H. (1999) Diffusion- and perfusion-weighted magnetic resonance imaging in deep cerebral venous thrombosis. Stroke 30:1144–1146

5. Grant PE, He J, Halpern EF, Wu O, Schaefer PW, et al. (2001) Frequency and clinical context of decreased apparent diffusion coefficient reversal in the human brain. Radiology 221:43–50

6. Fiebach, JB, Jansen O, Schellinger PD, et al. (2002) Serial analysis of the apparent diffusion coefficient time course in human stroke. Neuroradiology 44:294–298

7. Desmond PM, Lovell AC, Rawlinson AA, et al. (2001) The value of apparent diffusion coefficient maps in early cerebral ischemia. AJNR Am J Neuroradiol 22:1260–1267

8. Huang II, Chen CY, Chung HW, et al. (2001) Time course of cerebral infarction in the middle cerebral arterial territory: deep watershed versus territorial subtypes on diffusion-weighted MR images. Radiology 221:35–42

9. Burdette JH, Ricci PE, Petitti N, et al. (1998) Cerebral infarction: time course of signal intensity changes on diffusion-weighted MR images. Am J Radiol 171:791–795

10. Mukherjee P, Bahn MM, McKinstry RC, et al. (2000) Differences between gray and white matter water diffusion in stroke: diffusion-tensor MR imaging in 12 patients. Radiology 215:211–220

11. Krueger K, Kugel H, Grond M, et al. (2000) Late resolution of diffusion-weighted MRI changes in a patient with prolonged reversible ischemic neurological deficit after thrombolytic therapy. Stroke 31:2715–2718

12. Fitzek C, Tintera J, Muller-Forell W, et al. (1998) Differentiation of recent and old cerebral infarcts by diffusion-weighted MRI. Neuroradiology 40:778–782

13. Pan Foni L, Garcia GH, Gutierreg JA (1996) Cerebral white matter is highly vulnerable to ischemia Strole 27:1641–1647.

14. Kuroiwa T, Nagaoka T, Ueki M, et al. (1998) Different apparent diffusion coefficient: water content correlations of gray and white matter during early ischemia. Stroke 29:859–865

15. Geijer B, Lindgren A, Brockstedt S, et al. (2001) Persistent high-signal on diffusion-weighted MRI in the late stages of small cortical and lacunar ischemic lesions. Neuroradiology 43:115–122

16. Suwanwela NC, Leelacheavasit N (2002) Isolated corpus callosal infarction secondary to pericallosal artery disease presenting as alien hand syndrome. J Neurosurg Psychiatry 72:533–536

17. Tong DC, Adami A, Moseley ME, et al. (2000) Relationship between apparent diffusion coefficient and subsequent hemorrhagic transformation following acute ischemic stroke. Stroke 31:2378–2384

Intracranial Hemorrhage

In collaboration with A. Hiwatashi

6.1 Introduction

Intracranial hemorrhages are often characterized according to their location, such as intraparenchymal, subarachnoid, subdural, epidural and intraventricular hemorrhages. The etiology of these hemorrhages includes a variety of heterogeneous conditions, such as trauma, hypertension, infarction, infection, neoplasm, vascular malformations, vasculitis, vasculopathy, coagulopathy, and drugs. This chapter will describe diffusion-weighted (DW) imaging characteristics of intracranial hemorrhages in relation to their location and evolutionary stage.

6.2 Intraparenchymal Hemorrhages: Appearance and Evolution

The classic pattern for the temporal evolution of intracerebral hematomas on MRI at 1.5 T is well known [1–38]. However, determination of the age of a hemorrhage is often inaccurate because of variations between individual patients. The change in signal intensity over time depends on many factors, such as the oxygenation state of hemoglobin, the status of red blood cell membranes, hematocrit, proteins and clot formation [1–34, 37, 38]. Among these, the evolution of hemoglobin and the red cell membrane integrity are the most important [1–23, 25, 28, 30, 31, 33, 34]. The transition of oxy-hemoglobin to deoxy-hemoglobin and thereafter to met-hemoglobin depends primarily upon the oxygen tension in the vicinity of the lesion as well as inside the hematoma itself. In the hyperacute stage, oxy-hemoglobin will dominate initially, but transformation into deoxy-hemoglobin will soon take place and deoxy-hemoglobin will dominate after a few days – the acute hematoma [7, 11, 14, 19, 22, 23, 25, 28, 29, 33, 34]. After approximately one week, deoxy-hemoglobin will transform to met-hemoglobin [3, 4, 7, 10, 11, 14, 19, 22, 23, 28–30,

33, 34]. However, the rate of this oxidation to met-hemoglobin will depend on the oxygen tension in the tissue, which may further complicate the temporal pattern of expected signal changes. Initially, met-hemoglobin will be found within intact red blood cells (the early subacute stage), but when the red cell membranes start to rupture, met-hemoglobin will be found in the extracellular fluid space (the late subacute stage), which takes place about two weeks following hemorrhage [7, 11, 14, 19, 22, 23, 28, 29, 33, 34]. The final stage, the chronic stage, is the result of continuous phagocytation of the breakdown products of hemoglobin, ferritin and hemosiderin, which starts about one month following hemorrhage. The products, ferritin and hemosiderin, will remain within the phagocytic cells, which accumulate in the periphery of the hematoma, where they may remain for years, maybe indefinitely, as a marker of an old hemorrhage [6, 7, 11, 14, 17, 19–23, 27, 33, 34].

6.2.1 Hyperacute Hematoma

In the early stage of a hyperacute hematoma (Figs. 6.1 and 6.2), oxygenated hemoglobin within intact red blood cells is dominant. Oxy-hemoglobin is a diamagnetic substance and will, as such, generate an opposing magnetic field that reduces the applied magnetic field, as in most normal tissues in the body. Since there are no unpaired electrons in the iron of oxygenated hemoglobin, both longitudinal and transverse relaxation will be created by the so-called proton–proton, dipole–dipole interactions. At this stage, hematomas will have shorter relaxation times than water due to their protein content and will be slightly hypo- or iso-intense when compared with brain parenchyma on T1-weighted images. On T2-weighted images, oxy-hemoglobin will be seen as a slightly hyperintense region because of the high water content [7, 11, 14, 19, 22, 23, 25, 28, 29, 33, 34].
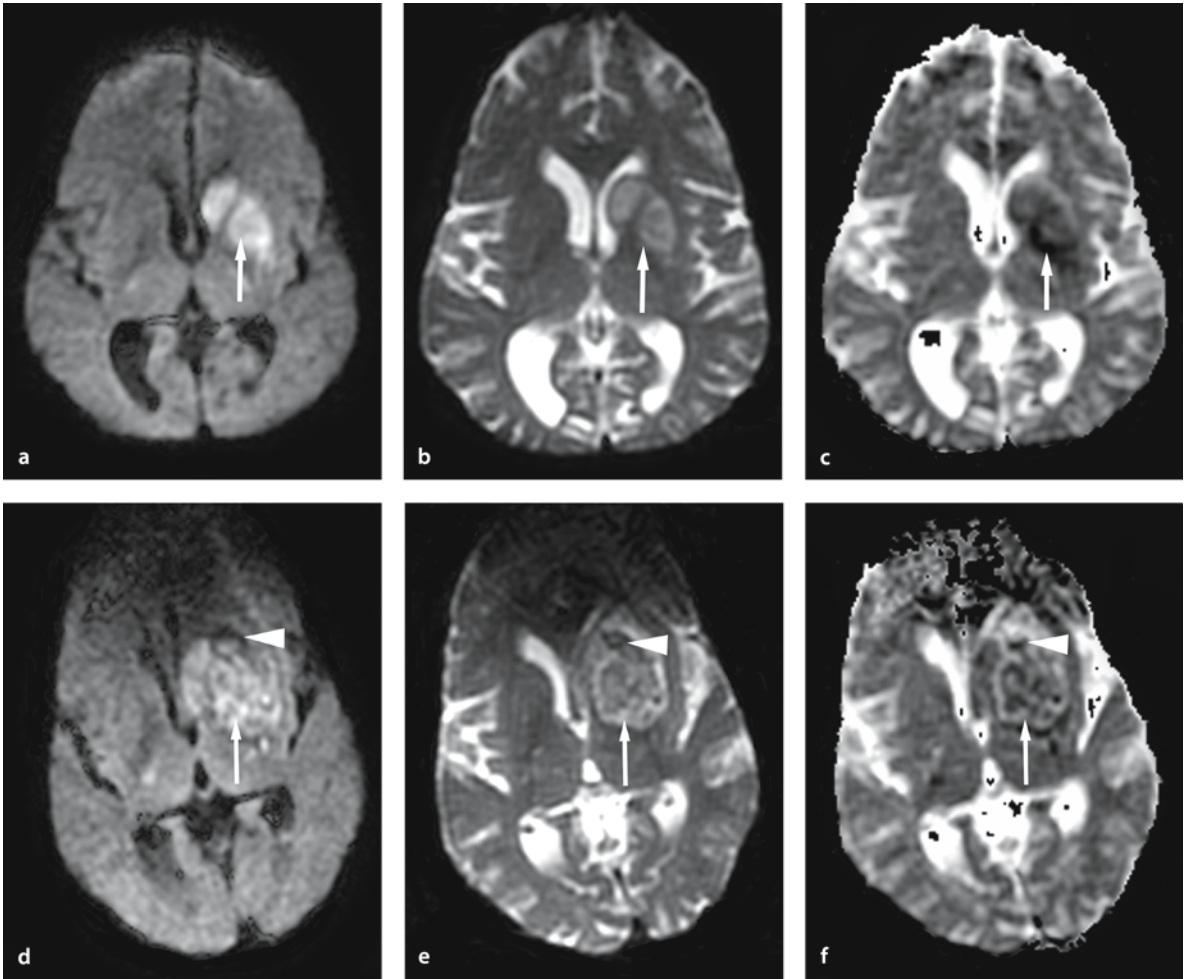
Figure 6.1 a–f

Acute infarction with hyperacute hemorrhage (oxy-hemoglobin/deoxy-hemoglobin). A 72-year-old woman suffered from a right-sided weakness. MR imaging 30 hours after the onset of symptoms (**a–c**) showed a lesion in the right basal ganglia (*arrow*) that is hyperintense on DW (**a**) and b_0 images (**b**). On the ADC map (**c**) the lesion is hypointense (*arrow*), indicating that this is a non-hemorrhagic acute infarction. During the end of the MR scanning, 30.5 hours after the onset of symptoms (**d–f**), the patient suddenly lost consciousness. The study was repeated, showing the increased size of the basal ganglia lesion. On the DW image (**d**) there is now a heterogeneous hyperintensity (*arrow*), consistent with oxy-hemoglobin. The b_0 image (**e**) also shows the lesion as heterogeneous, hyperintense (*arrow*), supporting oxy-hemoglobin. Note the new regions of hypointensity around the lesion (*arrowhead*), indicating deoxy-hemoglobin (**d–f**). The ADC map (**f**) shows the lesions as heterogeneously hypointense, consistent with oxy-hemoglobin (*arrow*). However, it is difficult to calculate the ADC due to the presence of paramagnetic deoxy-hemoglobin (*arrowhead*).

Results of DW imaging of hematomas at this stage have not been well characterized. In our experience, however, a hyperacute intraparenchymal hemorrhage is hyperintense on DW images, with a decreased apparent diffusion coefficient (ADC). This is in accordance with observations of other authors [28, 33]. The possible causes for the decreased ADC are shrinkage of extracellular space due to clot retraction, changes in the concentration of hemoglobin and a high viscosity [13, 19, 22–24, 28, 33–35].
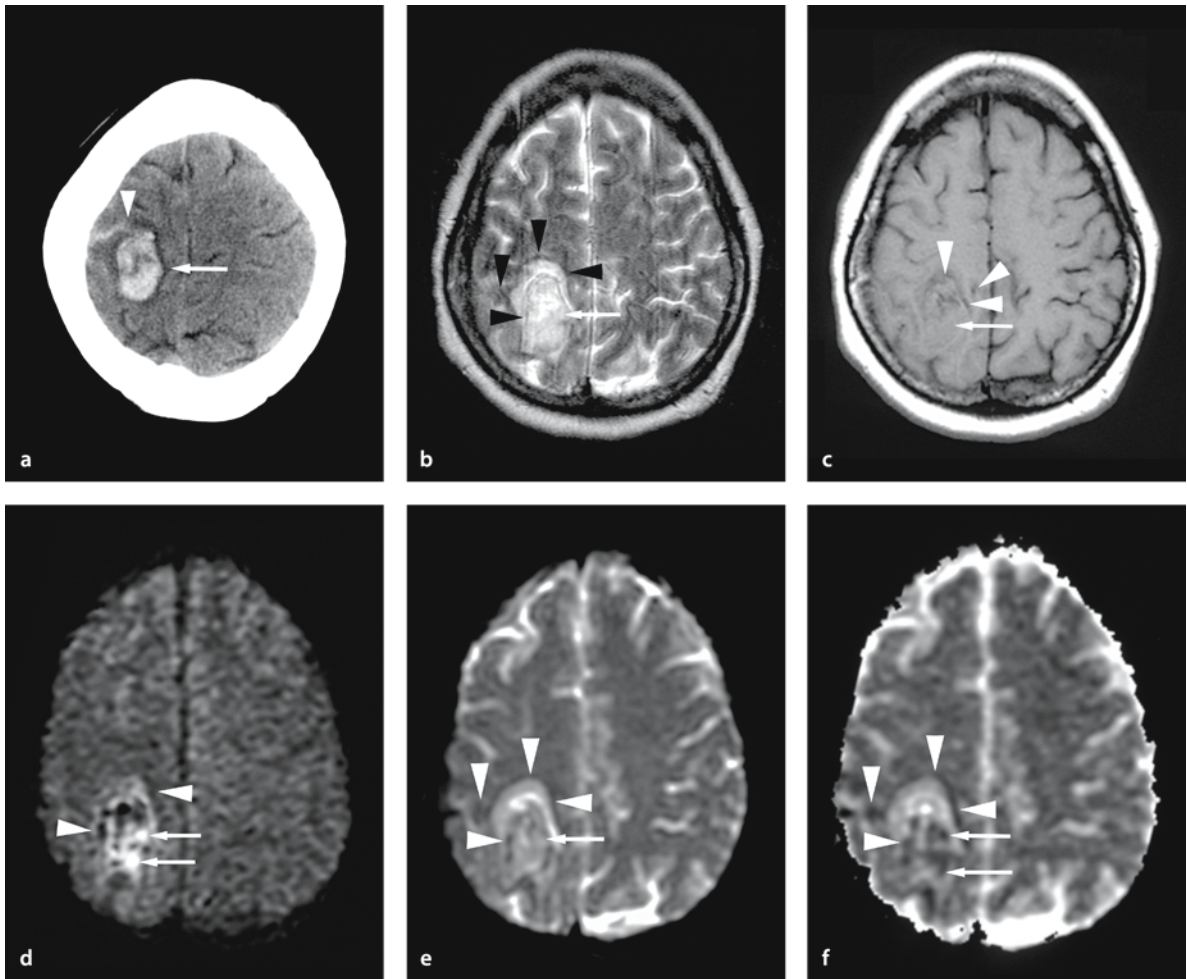
Figure 6.2 a–f

Hyperacute and chronic hemorrhage (oxy-hemoglobin/deoxy-hemoglobin, met-hemoglobin and hemosiderin/ferritin). A 40-year-old woman developed an acute left-sided weakness. A non-enhanced CT scan 6 hours after the onset of symptoms (a) shows a hyperdense lesion (*arrow*) in the right frontoparietal region associated with a small amount of subarachnoid hemorrhage (*arrowhead*). MR imaging 12 hours after the onset of symptoms (b–h) shows a heterogeneous lesion with areas of central hyperintensity on the T2-weighted image (b) (*arrow*; oxy-hemoglobin) with a peripheral hypointensity from the susceptibility influence of paramagnetic material (*arrowheads*; deoxy-hemoglobin). The T1-weighted image (c) shows the lesion as heterogeneous with areas of isointensity (*arrow*; oxy-hemoglobin) and hypointensity (*arrowheads*; deoxy-hemoglobin). Both the DW (d) and b_0 images (e) show the lesion as heterogeneous with areas of hyperintensity (*arrows*; oxy-hemoglobin) and hypointensity (*arrowheads*; deoxy-hemoglobin). The hypointensity is more prominent on these sequences than on the T2-weighted image (b). The ADC map (f) has a similar appearance of a heterogeneous lesion with areas of hypointensity (*arrows*; oxy-hemoglobin and *arrowheads*; deoxy-hemoglobin). As usual, when there is a strong susceptibility influence, it is difficult to calculate ADC.

▶
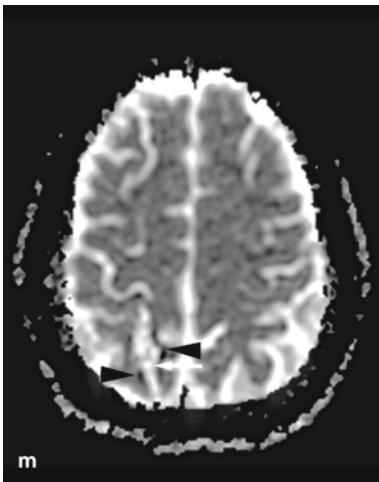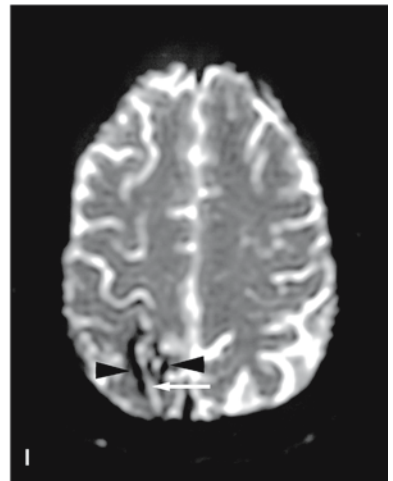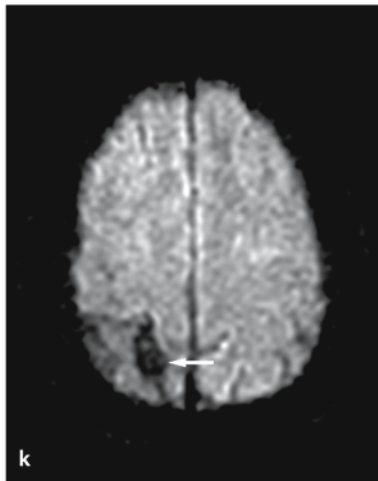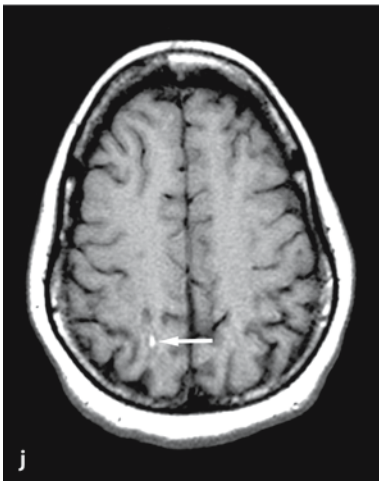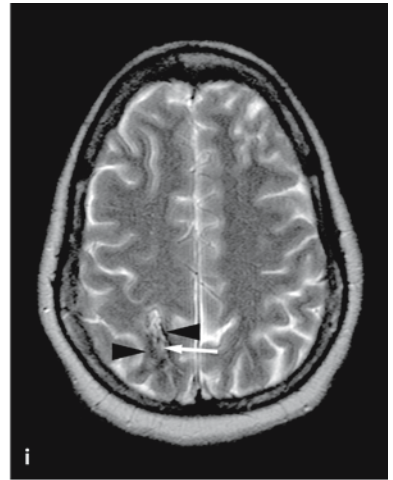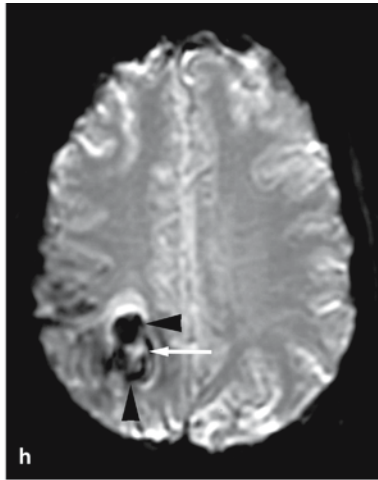
Figure 6.2 g–n

The coronal GRE image (**g**) and the GRE–echo-planar image (**h**) are more sensitive in depicting the susceptibility effect from deoxy-hemoglobin (*arrowheads*). The diamagnetic oxy-hemoglobin will, as expected, show an isointense signal (*arrow*), similar to the other sequences. Four months after the onset of symptoms (**i–n**), the patient had a new MR examination. On a T2-weighted image (**i**), the lesion is still heterogeneous, but there are now areas of hyperintensity (extracellular met-hemoglobin; *arrow*) and hypointensity (*arrowheads*; hemosiderin/ferritin). The T1-weighted image (**j**) shows the heterogeneous lesion with areas of hyperintensity (*arrow*; extracellular met-hemoglobin) and hypointensity (hemosiderin/ferritin). The DW image (**k**) show the lesion as hypointense overall and the same is seen on the b_0 image (**l**), but this "T2-weighted" image has a small hyperintense zone in the center of the hematoma, probably due to extracellular met-hemoglobin (*arrow*). The hypointensity (*arrowheads*) on the b_0 image (**l**) is more pronounced than on the conventional T2-weighted image (**i**), demonstrating the higher sensitivity to susceptibility with this imaging sequence. The susceptibility effect will make it difficult to calculate ADC accurately, but the ADC map (**m**) will demonstrate the susceptibility from hemosiderin/ferritin as peripheral hypointense areas (*arrowheads*). In the center there are hyperintense areas (*arrow*), probably containing extracellular met-hemoglobin. The hypointensity on the DW image (**k**) is probably a combined effect of T2 shortening, magnetic susceptibility and increased diffusibility. A marked peripheral hypointensity from hemosiderin/ferritin will also be seen when a GRE technique (**n**) is used (*arrowheads*)

◄

6.2.2 Acute Hematoma

Following hemorrhage there is normally a gradual oxygen desaturation of hemoglobin transforming oxy-hemoglobin into deoxy-hemoglobin (Fig. 6.3) [7, 11, 14, 19, 22, 23, 25, 28, 29, 33, 34]. The loss of oxygen will change the binding geometry of iron from a six-ligand system to a five-ligand system, leaving four unpaired electrons and making it paramagnetic. When exposed to a magnetic field, paramagnetic substances will enhance the applied field locally. This will influence image contrast by means of so-called magnetic susceptibility-induced relaxation, which only effects transverse relaxation (T2* effect). The susceptibility effects create local field inhomogeneities, with a rapid loss of transverse magnetization of protons within this region resulting in signal loss on T2-weighted images. Deoxy-hemoglobin will therefore demonstrate a marked hypointensity on T2-weighted images [1, 3, 7–9, 11–15, 19, 22–25, 30–34]. Besides the concentration of deoxy-hemoglobin, red blood cell concentration and/or clot formation may also contribute to this T2 hypointensity. Since this is an effect of magnetic susceptibility, gradient-echo (GRE) images will be more sensitive than DW- and T2-weighted images for the detection of acute, as well as chronic hematomas [19, 26, 27, 32]. The T1 relaxivity effect is related to dipole–dipole relaxation, in this case the dipoles of water and unpaired electrons of the paramagnetic center. This would normally result in a shortening of relaxation time; however, the molecular configuration of deoxy-hemoglobin will act as a shield for such a close approach of water molecules to the unpaired electrons of the paramagnetic, ferrous iron. The acute hematoma containing deoxy-hemoglobin will thus show an iso- to hypointense signal on T1-weighted images, similar to oxy-hemoglobin [5, 22, 23, 34].

Diffusion-weighted images of an acute hematoma show a marked hypointensity [28–31, 33], caused by the magnetic field inhomogeneity created by the paramagnetic deoxy-hemoglobin [6, 7, 14, 18, 22, 23, 25, 33]. Although the ADC has been reported to be decreased, accurate calculations are often difficult [28–30, 33, 36].

6.2.3 Early Subacute Hematoma

In the early stage of the subacute hematoma (Figs. 6.2 and 6.3), there is a decline in the energy state of the red blood cell and hemoglobin is oxidized to met-hemoglobin [3, 4, 7, 10, 11, 14, 19, 22, 23, 28–30, 33, 34]. In met-hemoglobin the iron is still bound to the heme moiety within the globin protein, but it is now in the ferric state with five unpaired electrons. This transformation normally starts in the periphery of the hemorrhage and gradually evolves to the center. In the transition to met-hemoglobin, conformational changes will take place in the molecule and water protons will now have access to the unpaired electrons of iron in met-hemoglobin, creating a proton–electron, dipole–dipole interaction. Dipolar relaxation enhancement will then take place, making met-hemoglobin appear hyperintense on T1-weighted images. Met-hemoglobin, as a paramagnetic sub-

stance, will induce magnetic susceptibility relaxation affecting the transverse relaxation (T2* effect), which results in a marked hypointensity on T2-weighted images [3, 6, 7, 10, 14, 22–24, 28–31, 33, 34].

On DW imaging, intracellular met-hemoglobin shows hypointensity due to these paramagnetic susceptibility effects and ADC measurements are not reliable due to the susceptibility effects [28–30, 33].
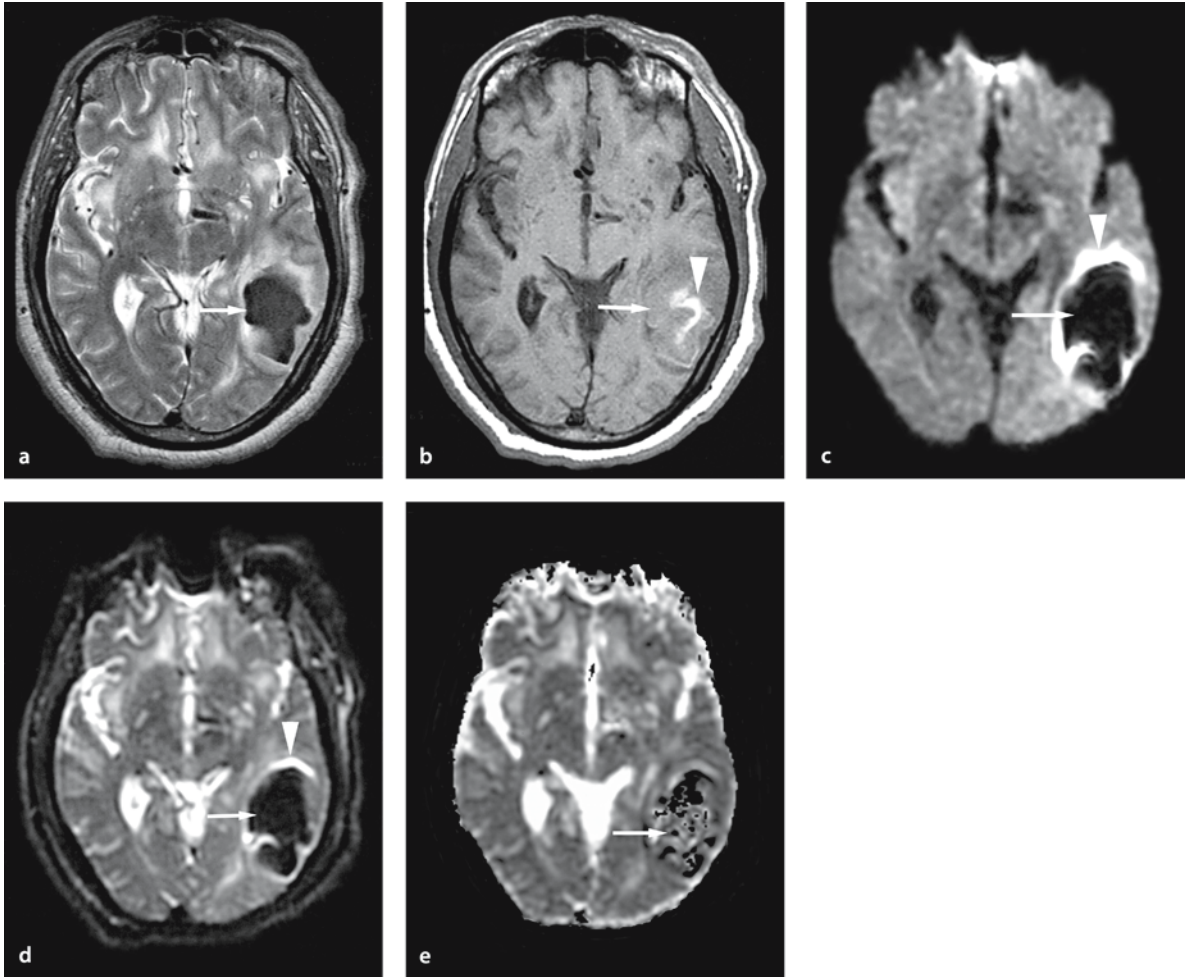
Figure 6.3 a–e

Acute to early subacute hemorrhage (deoxy-hemoglobin and intracellular met-hemoglobin). A 49-year-old man with headache and aphasia was referred for MR imaging 24 hours after the onset of symptoms (**a–e**). This study shows a left temporal lobe lesion that is hypointense on the T2-weighted image (**a**) (*arrow*; deoxy-hemoglobin and intracellular met-hemoglobin) with surrounding edema. On the T1-weighted image (**b**) the lesion is heterogeneous with areas of hypointensity (*arrow*; deoxyhemoglobin) and hyperintensity (*arrowhead*; intracellular met-hemoglobin). The DW image (**c**) demonstrates hypointensity (*arrow*; deoxy-hemoglobin and intracellular met-hemoglobin). The surrounding hyperintense rim (*arrowhead*) is a magnetic susceptibility artifact. This peripheral artifact is also seen around the hypointensity (*arrow*) created by deoxy-hemoglobin and intracellular met-hemoglobin on the b_0 image (**d**). ADC cannot be calculated accurately, which is easy to understand when looking at the extremely heterogeneous lesion depicted on the ADC map (**e**)
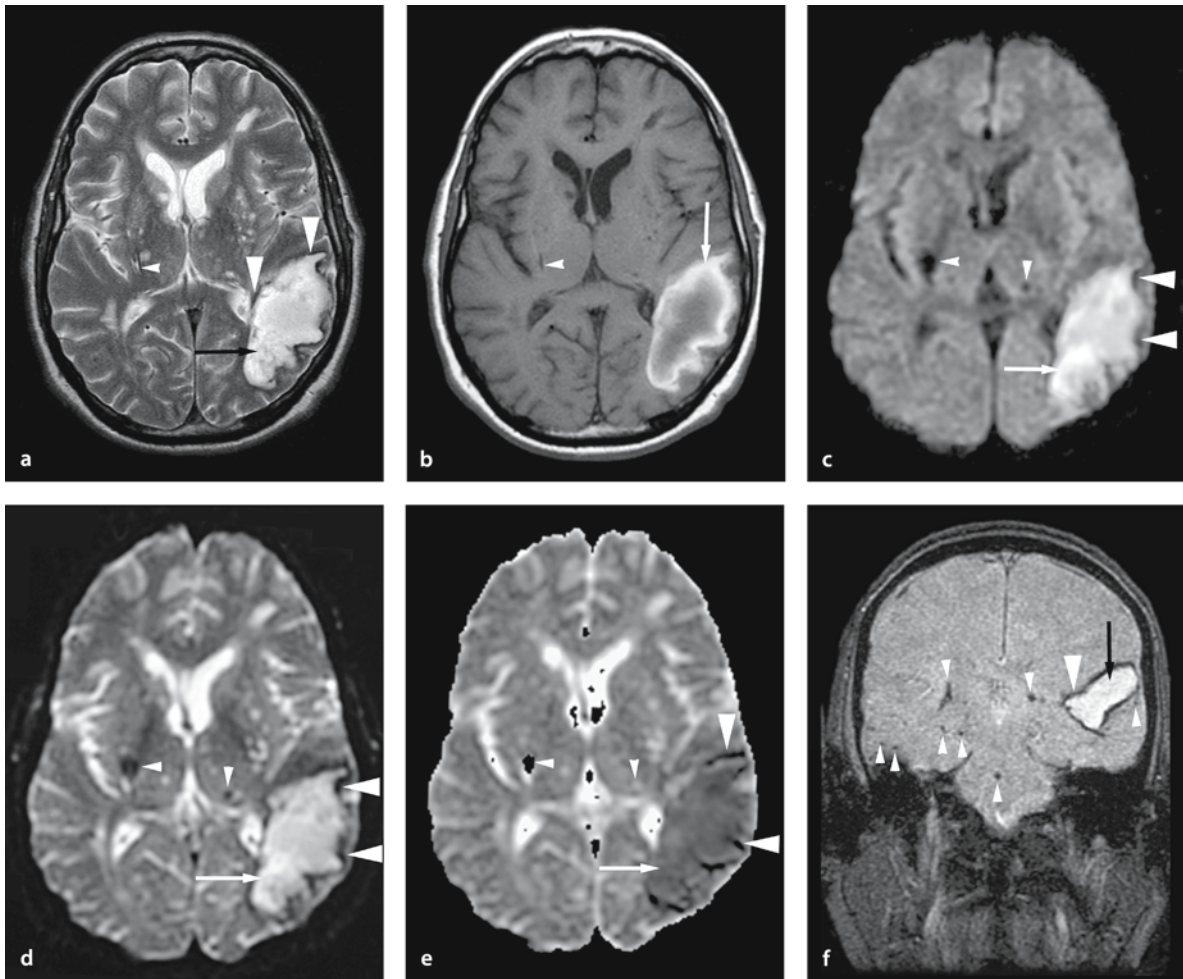
Figure 6.4 a–f

Late subacute-chronic hemorrhage (extracellular met-hemoglobin and hemosiderin/ferritin). A 52-year-old man with a history of chronic hypertension complained of headache and aphasia. MR examination 2 months after the onset of symptoms shows a left temporal lobe lesion that is hyperintense on the T2-weighted image (**a**) (*arrow*; extracellular met-hemoglobin) and surrounded by a hypointense rim (*arrowheads*; hemosiderin/ferritin). Another hypointense lesion is visualized in the right basal ganglia (*small arrowhead*; hemosiderin/ferritin), compatible with chronic hemorrhage secondary to hypertension. The T1-weighted image (**b**) shows the temporal lobe lesion as hyperintense (*arrow*; extracellular met-hemoglobin). The lesion in the right basal ganglia is also hypointense on this sequence (*small arrowhead*; hemosiderin/ferritin). On the DW image (**c**) the temporal lobe lesion is hyperintense (*arrow*; extracellular met-hemoglobin) with a hypointense rim (*arrowheads*; hemosiderin/ferritin). The basal ganglia lesion remains hypointense, but the signal void is more extensive than on the conventional T2-weighted image (**a**), since GRE does not compensate for signal loss due to local magnetic field inhomogeneities and is thus more sensitive than regular spin-echo imaging. This increased susceptibility sensitivity revealed a second, old hemorrhagic lesion in the left thalamus (small *arrowhead*; hemosiderin/ferritin). The b_0 image (**d**) also shows the hyperintense lesion (*arrow*; extracellular met-hemoglobin) with the hypointense rim (*arrowheads*; hemosiderin/ferritin) as well as the older lesions in the basal ganglia and thalamus (*small arrowheads*; hemosiderin/ferritin). On the ADC map (**e**) the temporal lesion is somewhat hypointense (*arrow*; extracellular met-hemoglobin) with a hypointense rim (*arrowheads*; hemosiderin/ferritin). The other lesions are also visualized (*small arrowheads*); however, ADC cannot be calculated. Finally, the coronal GRE image (**f**) shows the temporal lesion as hyperintense (*arrow*; extracellular met-hemoglobin) with a hypointense rim (*arrowhead*; hemosiderin/ferritin). The GRE sequence is the most sensitive and shows multiple small hypointense lesions (old hemorrhagic breakdown products) in the cerebral hemispheres and in the pons (*small arrowheads*; hemosiderin/ferritin)

6.2.4 Late Subacute Hematomas

The decline in energy state of the red blood cell will eventually damage the integrity of the red cell membrane, releasing the intracellular content to the extracellular fluid space (Figs. 6.2 and 6.4). Subsequently, there will be a dilution of the paramagnetic met-hemoglobin in extracellular fluid, reducing the susceptibility effect of met-hemoglobin [7, 11, 14, 19, 22, 23, 28, 29, 33, 34]. The signal intensity on T2-weighted images will thus relate to the water content, creating a hyperintense signal on T2-weighted images. Extracellular met-hemoglobin will, however, still have high signal intensity on T1-weighted images created by the same proton–electron, dipole–dipole relaxation as described in early subacute hematomas [5–7, 10, 14, 22, 23].

It has been reported that late subacute hematomas are hyperintense on DW imaging [28, 29]. The ADC value for late subacute hematoma is controversial. Ebisu et al. [24] reported decreased ADC in hematomas of hemorrhagic infarctions, whereas Atlas et al. reported ADC values higher than normal white matter in late subacute hematomas and suggested this was due to increased diffusibility [28]. Finally, Kang et al. reported decreased ADC in late subacute hematomas and thought this was due to high viscosity and cellularity [33].

6.2.5 Chronic Hematomas

Over time, met-hemoglobin will be resorbed or degraded and the effect on T1 enhancement will be reduced (Figs. 6.2 and 6.4). The high water content in the chronic stage will result in prolonged T1 as well as T2 relaxation. From the start of the hemorrhage there is a continuous phagocytation of heme proteins. Ferritin and hemosiderin, the final breakdown products of hemoglobin, will remain within the phagocytic cells, which accumulate in the periphery of the hematoma, where they may remain indefinitely as a marker of an old hemorrhage [6, 7, 11, 14, 17, 19–23, 27, 33, 34, 37, 38]. Ferritin and hemosiderin within these cells will have no access to water protons and thus there are no relaxivity effects. Magnetic susceptibility is the only factor influencing the signal, creating a marked signal loss on T2-weighted images. As mentioned earlier, the magnetic susceptibility effects are most prominent on T2*-weighted images [7, 17, 22, 23, 34].

Diffusion-weighted images are also hyperintense in chronic hematomas [29, 33]. The ADC value has been reported to be increased, but is often difficult to measure accurately due to magnetic susceptibility artifacts [28–30, 33, 36].

6.3 Subarachnoid Hemorrhage

Computed tomography (CT) is still essential in the diagnosis of acute subarachnoid hemorrhages (Fig. 6.5), as the sensitivity and usefulness of MR imaging is controversial [4, 5, 9, 34, 39–45]. Fluid-attenuated inversion-recovery (FLAIR) imaging has a high sensitivity for subarachnoid hemorrhage [46–49]. However, the specificity is low because there are several other causes for the appearance of subarachnoid hemorrhage on FLAIR imaging, such as high proton concentration, mass effect, vascular disease, contrast medium and use of specific intravenous anesthetic agents [50–53].

It is often difficult to detect subarachnoid hemorrhage on DW images [31, 54]. Lin et al. detected subarachnoid hemorrhage in two of four cases on GRE imaging, but it could not be detected on b_0 images [31]. Wiesmann et al. reported that proton density and FLAIR images could detect subarachnoid hemorrhage, but T2-weighted and DW images could not [54].

However, DW images may be useful to visualize parenchymal injuries secondary to subarachnoid hemorrhage. Ischemic changes, probably related to subarachnoid hemorrhage, have shown hyperintensity on DW images in both clinical and animal studies [55–60]. This finding depends on the timing of imaging and the severity of injury.
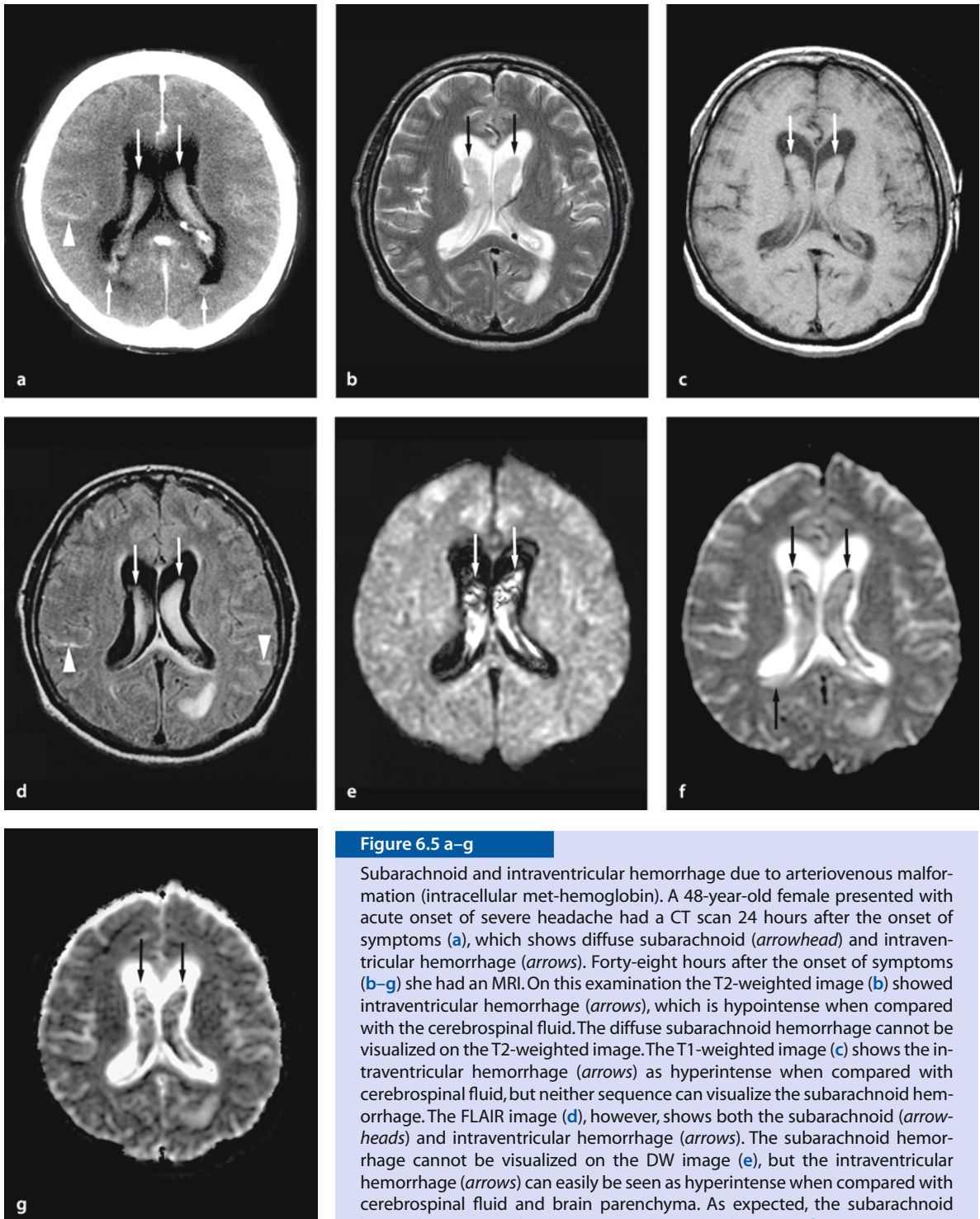
Figure 6.5 a–g

Subarachnoid and intraventricular hemorrhage due to arteriovenous malformation (intracellular met-hemoglobin). A 48-year-old female presented with acute onset of severe headache had a CT scan 24 hours after the onset of symptoms (**a**), which shows diffuse subarachnoid (*arrowhead*) and intraventricular hemorrhage (*arrows*). Forty-eight hours after the onset of symptoms (**b–g**) she had an MRI. On this examination the T2-weighted image (**b**) showed intraventricular hemorrhage (*arrows*), which is hypointense when compared with the cerebrospinal fluid. The diffuse subarachnoid hemorrhage cannot be visualized on the T2-weighted image. The T1-weighted image (**c**) shows the intraventricular hemorrhage (*arrows*) as hyperintense when compared with cerebrospinal fluid, but neither sequence can visualize the subarachnoid hemorrhage. The FLAIR image (**d**), however, shows both the subarachnoid (*arrowheads*) and intraventricular hemorrhage (*arrows*). The subarachnoid hemorrhage cannot be visualized on the DW image (**e**), but the intraventricular hemorrhage (*arrows*) can easily be seen as hyperintense when compared with cerebrospinal fluid and brain parenchyma. As expected, the subarachnoid hemorrhage cannot be demonstrated on either b_0 image (**f**) or ADC maps (**g**), but both sequences will depict the intraventricular hematoma as hypointense (*arrows*)

6.4 Subdural and Epidural Hemorrhages

Subdural and epidural hematomas (Fig. 6.6) are well demonstrated on T1- and T2-weighted images. In the acute and subacute stages, the signal intensity is often similar to intraparenchymal hematomas. In the chronic stage, MR images often show hyperintensity of the hematoma, which may be iso- to hypodense on CT [34, 61–67].

Diffusion-weighted imaging findings of subdural and epidural hematomas have not been well described. Lin et al. reported that all three lesions could be detected on b_0 images, but GRE images were better at detecting lesions [31]. The benefit of DW imaging is probably for the detection of underlying or associated parenchymal lesions [68, 69].
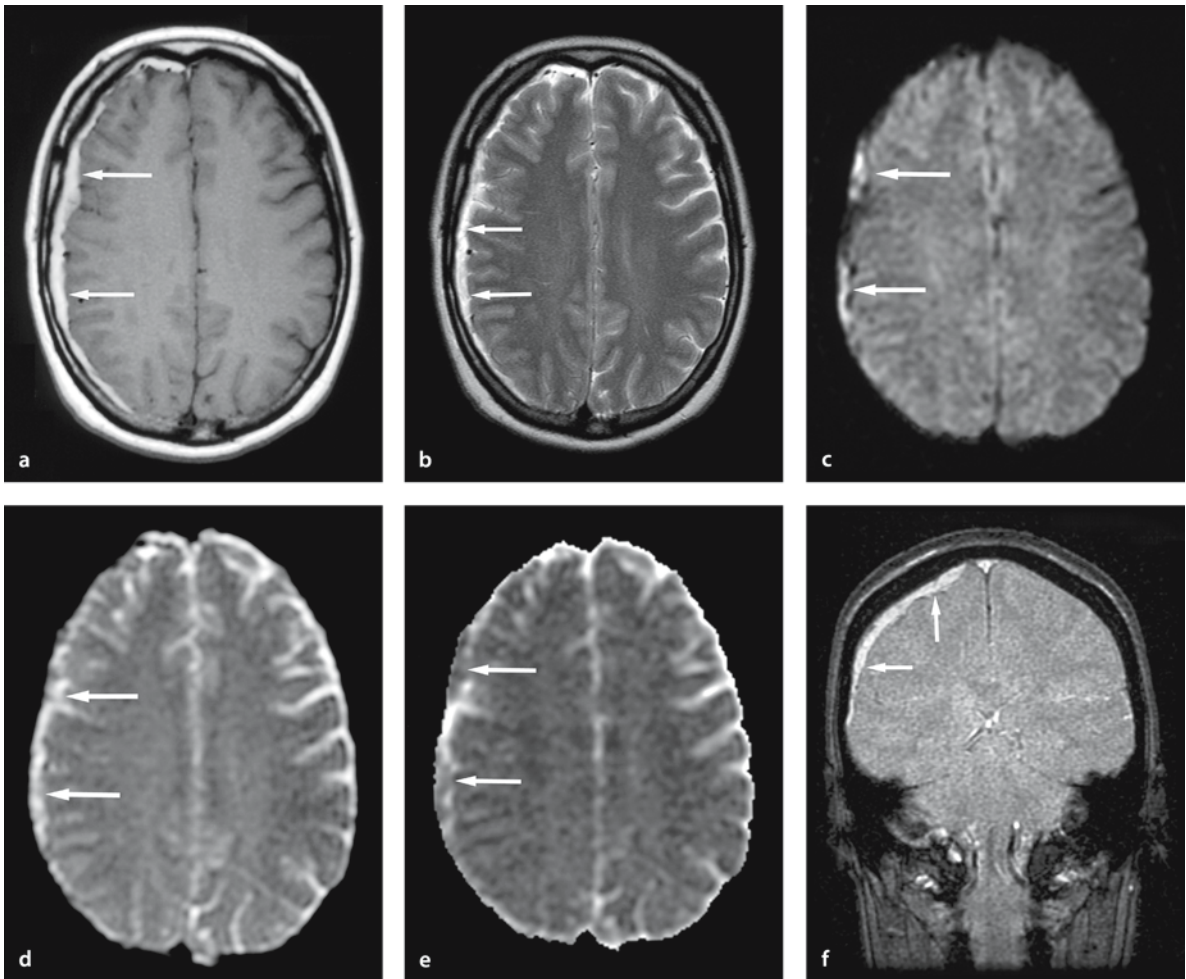
Figure 6.6 a–f

Subacute subdural hemorrhage (extracellular met-hemoglobin). A 49-year-old woman with headache following head trauma had an MR examination 2 weeks after the trauma, which shows right subdural hemorrhage as a hyperintense lesion (*arrows*) on the T1-weighted (**a**) and T2-weighted (**b**) images. The lesion was hyperintense on the DW (**c**) and the b_0 (**d**) images (*arrows*). On the ADC map (**e**) there are hypointense lesions (*arrows*), which correspond to the hyperintense lesions on the DW image (**c**). The coronal GRE image (**f**) shows the subdural hemorrhage to be hyperintense (*arrows*)

6.5 Intraventricular Hemorrhage

Intraventricular hemorrhages (Figs. 6.5 and 6.7) are well demonstrated on FLAIR, T1-, T2- and proton density-weighted images [34, 59, 70–72]. FLAIR has been reported to have the highest sensitivity for detection of intraventricular hematomas [71]. DW images can demonstrate intraventricular hemorrhages, but in general the GRE images have a higher sensitivity [31].
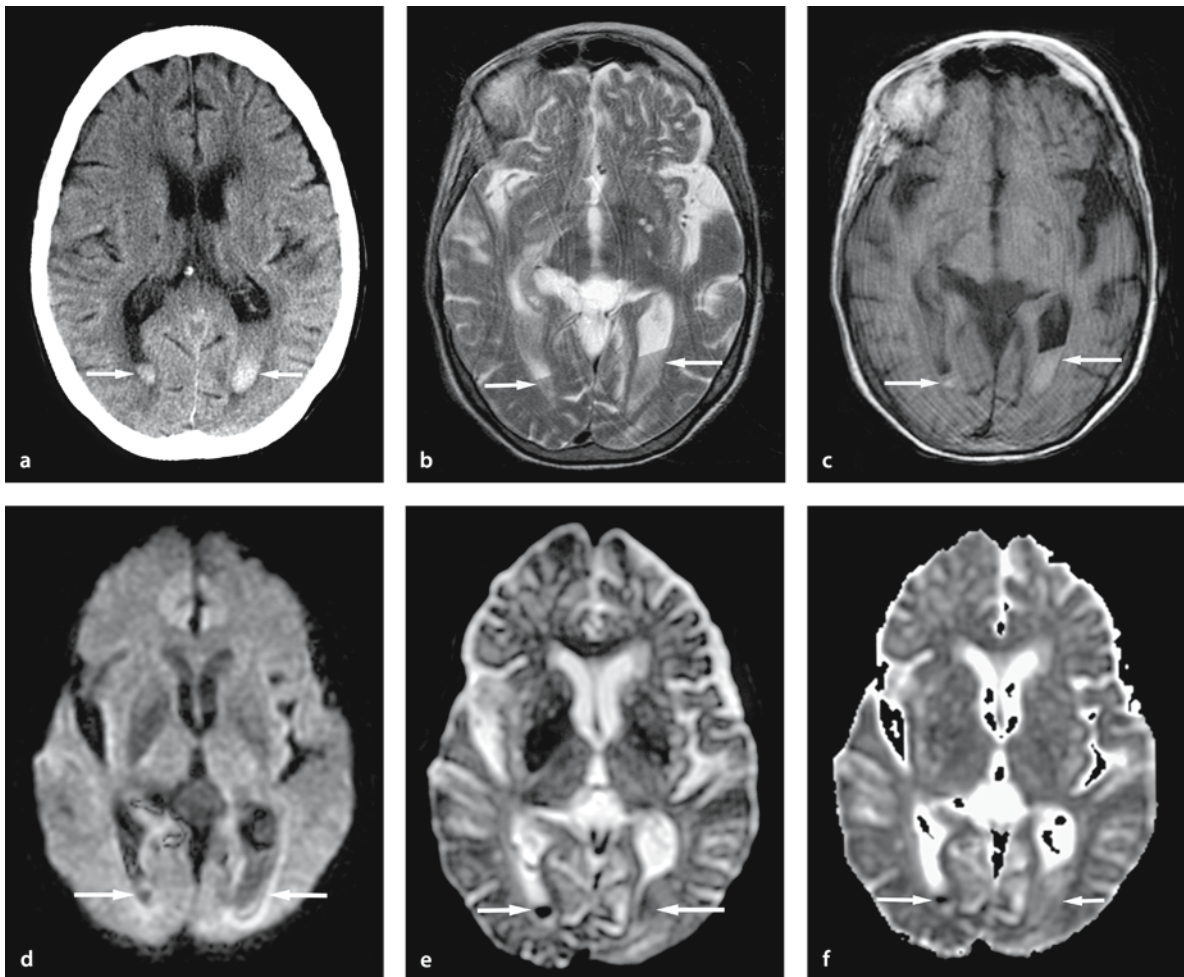
Figure 6.7 a–f

Intraventricular hemorrhage (intracellular met-hemoglobin). A 78-year-old woman with headache after thrombolytic therapy for femoral artery occlusion had a CT scans 6 hours after surgery (**a**). This shows intraventricular hemorrhage in the bilateral lateral ventricles (*arrows*). Three days after surgery (**b–f**), the T2-weighted image (**b**) shows hypointense lesions in the bilateral lateral ventricles with fluid–fluid levels (*arrows*) and the T1-weighted image (**c**) shows hyperintense lesions in the same distributions (*arrows*). The DW image (**d**) shows hypointense lesions (*arrows*) with surrounding hyperintensities. These are ascribed to magnetic susceptibility artifacts. The b_0 image (**e**) also shows hypointense lesions (*arrows*). These hypointensities are more prominent than on the T2-weighted images (**b**). The ADC map (**f**) shows hypointense lesions (*arrows*)

6.6 Intra-tumoral Hemorrhage

Many primary brain tumors and metastases can bleed [34, 73–78]. The signal intensity of intra-tu-moral hemorrhage (Fig. 6.8) tends to be more complex and its evolution tends to be delayed when compared with non-neoplastic hemorrhages [34, 78]. DW and b_0 images are useful to detect the hemorrhage in tumors [31].
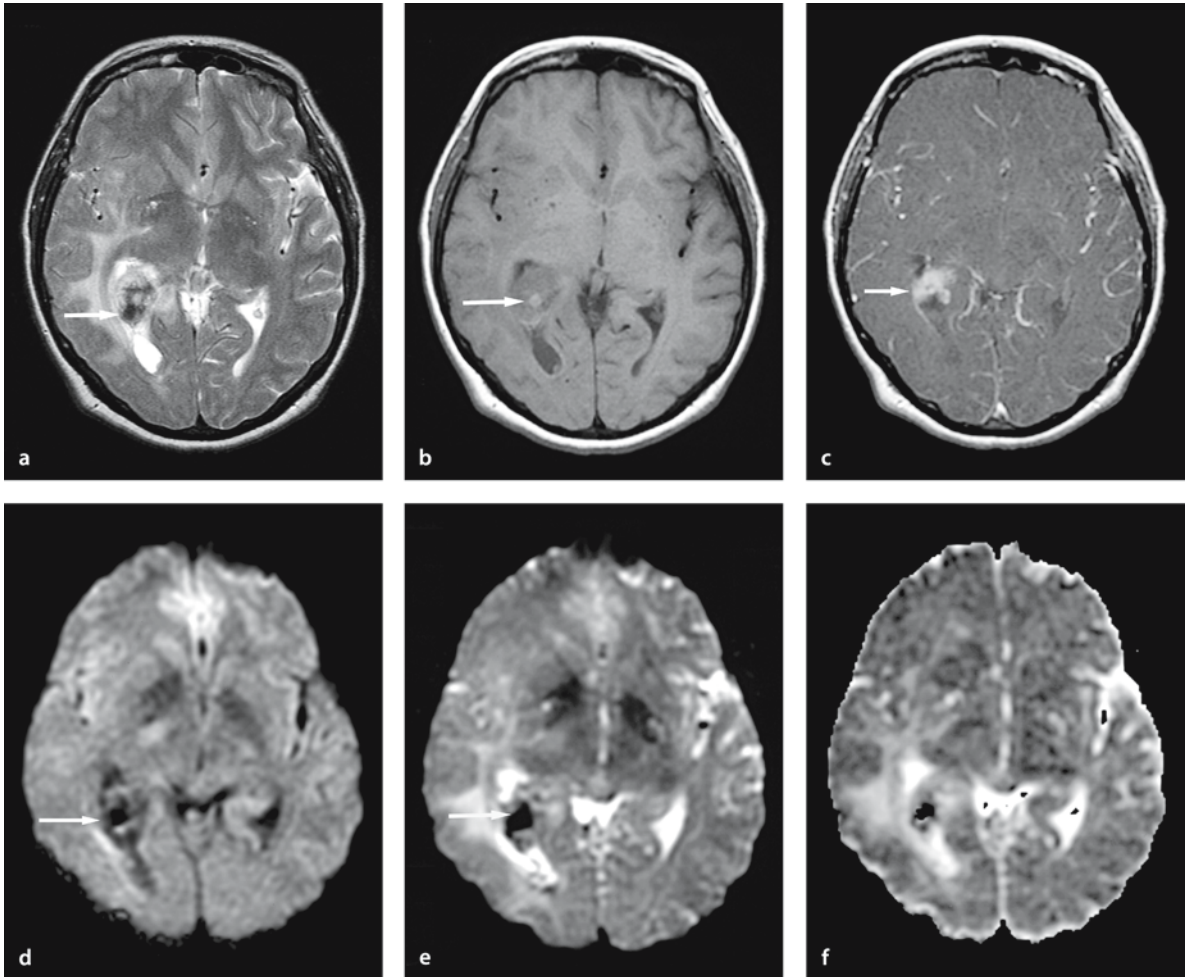
Figure 6.8 a–f

Hemorrhagic tumor. The T2-weighted MR image (**a**) in a 54-year-old woman with glioblastoma shows a mass lesion with heterogeneous intensity near the right lateral ventricle. The irregular hypointensities centrally in the lesion (*arrow*) indicate hemorrhage. The T1-weighted image (**b**) shows the heterogeneous hypointense to isointense mass, with a central area of higher signal intensity consistent with hemorrhage (*arrow*). The gadolinium-enhanced T1-weighted image (**c**) shows heterogeneous enhancement (*arrow*). On the DW image (**d**) the hemorrhage is heterogeneously hypointense (*arrow*). The b_0 image (**e**) shows the hemorrhage to be more hypointense (*arrow*) than on the T2-weighted image (**a**). The ADC (**f**) cannot be calculated due to magnetic susceptibility artifacts

6.7 Hemorrhage Related to Vascular Malformation

Vascular malformations can also cause intracranial hemorrhages (Fig. 6.9). Cavernous angioma is a vascular malformation that contains blood cavities surrounded by a single layer of endothelium [79–83]. MR imaging findings are well known and characterized as a central reticulated core with a peripheral rim of hypointensity due to the deposition of hemosiderin [79, 82, 83]. DW and b_0 images are useful for detecting hemorrhages related to vascular malformations.
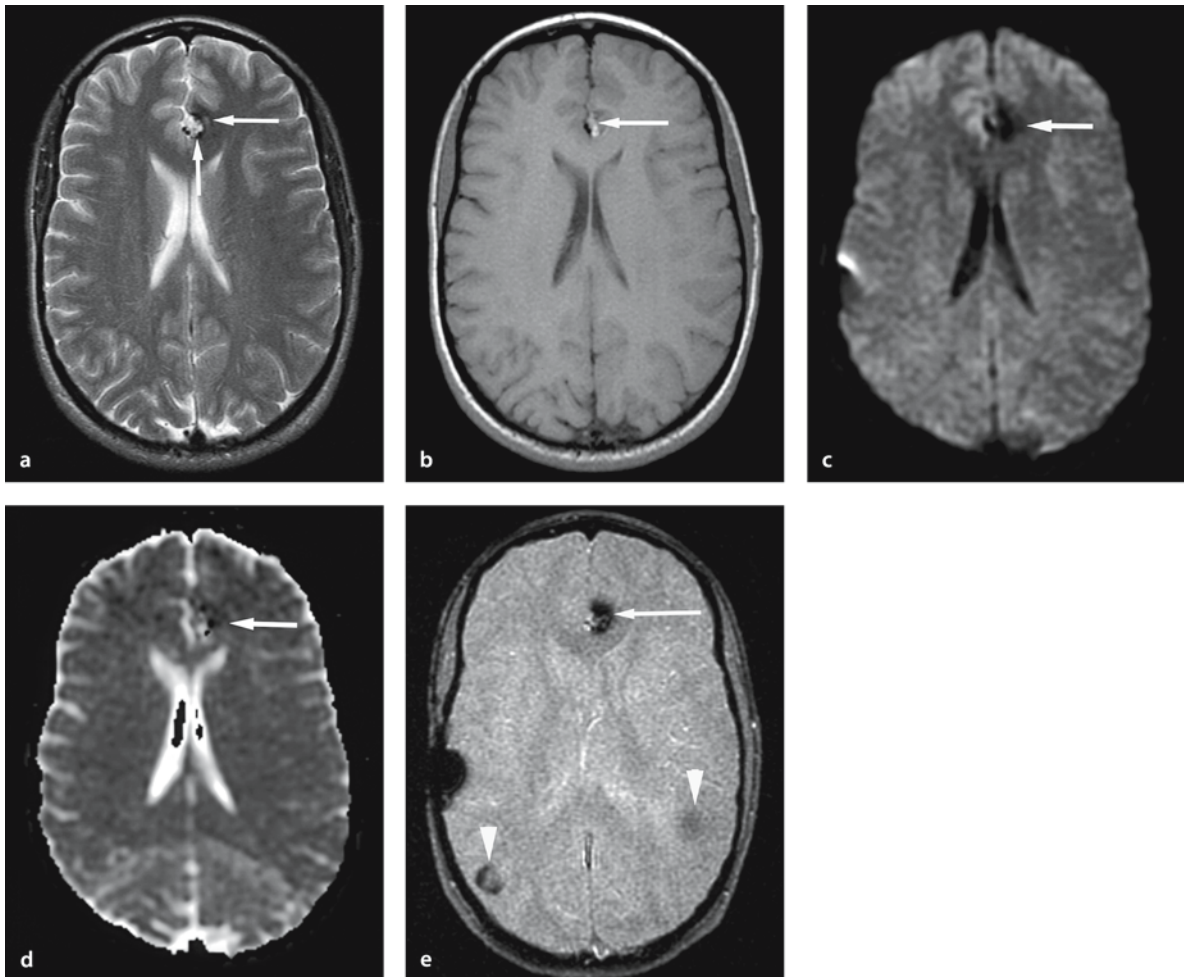
Figure 6.9 a–e

Multiple cavernous angiomas. The T2-weighted MR image (**a**) in a 30-year-old woman with seizures shows a hyperintense lesion in the left frontal lobe with a surrounding hypointense rim (*arrows*). This is a characteristic finding for a cavernous angioma. The lesion is hyperintense on the T1-weighted image (**b**) (*arrow*) and hypointense on the DW image (**c**) (*arrow*). The ADC map (**d**) shows heterogeneous intensity and the GRE image (**e**) shows marked hypointensity in the left frontal lobe (*arrow*). The hypointensities in the right and left temporo-occipital region (*arrowheads*) suggest multiple cavernous angiomas

6.8 Hemorrhage Related to Trauma

Trauma is one of the most common causes of intracranial hemorrhages in younger patients (Fig. 6.10). MR imaging is valuable in detecting intracranial injuries. DW and b_0 images and an ADC map can be more sensitive than conventional MR images to detect whether the abnormality includes diffuse axonal injury [84].

6.9 Conclusions

Diffusion-weighted imaging is often of limited value for diagnosis and staging of intracranial hemorrhages because accurate ADC measurements are only possible in the hyperacute stage, which contains diamagnetic oxy-hemoglobin, and in the late subacute phase, which contains extracellular met-hemoglobin, whose paramagnetic susceptibility artifacts are diminished by the dilution of extracellular fluid. CT and routine MR imaging continue to be the mainstay in diagnosing and characterizing intracranial hemorrhages. A thorough understanding of DW imaging characteristics is important, however, in order to avoid misinterpretations and inaccurate conclusions.
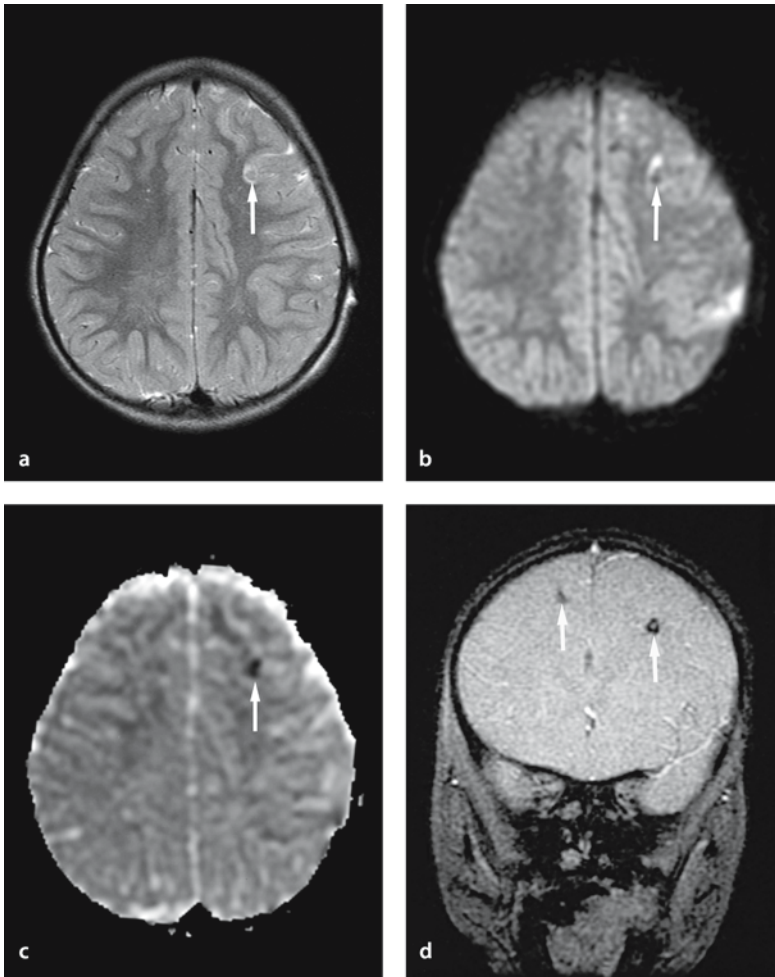
Figure 6.10 a–d

Trauma with hemorrhagic diffuse axonal injury. MR imaging of a 2-year-old girl 12 hours after a motor vehicle accident shows (**a**) a hyperintense lesion in the left frontal lobe on T2-weighted image (*arrow*). The corresponding area on the DW image (**b**) is hypointense with surrounding hyperintensity (*arrow*). The ADC map (**c**) shows hypointensity (*arrow*). The coronal GRE (**d**) image shows hypointense lesions in the bilateral frontal lobes (*arrows*)

References

1. Thulborn KR, Waterton JC, Matthews PM, Radda GK (1982) Oxygenation dependence of the transverse relaxation time of water protons in whole blood at high field. Biochim Biophys Acta 714:265–270

2. Fullerton GD, Potter JL, Dornbluth NC (1982) NMR relaxation of protons in tissues and other macromolecular water solutions. Magn Reson Imaging 1:209–226

3. Sipponen JT, Sepponen RE, Sivula A (1983) Nuclear magnetic resonance (NMR) imaging of intracerebral hemorrhage in the acute and resolving phases. J Comput Assist Tomogr 7:954–959

4. DeLaPaz RL, New PF, et al. (1984) NMR imaging of intracranial hemorrhage. J Comput Assist Tomogr 8:599–607

5. Bradley WG Jr, Schmidt PG (1985) Effect of methemoglobin formation on the MR appearance of subarachnoid hemorrhage. Radiology 156:99–103

6. Gomori JM, Grossman RI, Bilaniuk LT, Zimmerman RA, Goldberg HI (1985) High-field MR imaging of superficial siderosis of the central nervous system. J Comput Assist Tomogr 9:972–975

7. Gomori JM, Grossman RI, Goldberg HI, Zimmerman RA, Bilaniuk LT (1985) Intracranial hematomas: imaging by high-field MR. Radiology 157:87–93

8. Sipponen JT, Sepponen RE, Tanttu JI, Sivula A (1985) Intracranial hematomas studied by MR imaging at 0.17 and 0.02 T. J Comput Assist Tomogr 9:698–704

9. Grossman RI, Kemp SS, Ip CY, et al. (1986) Importance of oxygenation in the appearance of acute subarachnoid hemorrhage on high field magnetic resonance imaging. Acta Radiol Suppl 369:56–58

10. Di Chiro G, Brooks RA, Girton ME, et al. (1986) Sequential MR studies of intracerebral hematomas in monkeys. AJNR Am J Neuroradiol 7:193–199

11. Gomori JM, Grossman RI, Yu-Ip C, Asakura T (1987) NMR relaxation times of blood: dependence on field strength, oxidation state, and cell integrity. J Comput Assist Tomogr 11:684–690

12. Zimmerman RD, Heier LA, Snow RB, Liu DP, Kelly AB, Deck MD (1988) Acute intracranial hemorrhage: intensity changes on sequential MR scans at 0.5 T. AJR Am J Roentgenol 150:651–661

13. Hayman LA, Ford JJ, Taber KH, Saleem A, Round ME, Bryan RN (1988) T2 effect of hemoglobin concentration: assessment with in vitro MR spectroscopy. Radiology 168:489–491

14. Brooks RA, Di Chiro G, Patronas N (1989) MR imaging of cerebral hematomas at different field strengths: theory and applications. J Comput Assist Tomogr 13:194–206

15. Hayman LA, McArdle CB, Taber KH, et al. (1989) MR imaging of hyperacute intracranial hemorrhage in the cat. AJNR Am J Neuroradiol 10:681–686

16. Hayman LA, Taber KH, Ford JJ, et al. (1989) Effect of clot formation and retraction on spin-echo MR images of blood: an in vitro study. AJNR Am J Neuroradiol 10:1155–1158

17. Hardy PA, Kucharczyk W, Henkelman RM (1990) Cause of signal loss in MR images of old hemorrhagic lesions. Radiology 174:549–555

18. Bryant RG, Marill K, Blackmore C, Francis C (1990) Magnetic relaxation in blood and blood clots. Magn Reson Med 13:133–144

19. Clark RA, Watanabe AT, Bradley WG Jr, Roberts JD (1990) Acute hematomas: effects of deoxygenation, hematocrit, and fibrin-clot formation and retraction on T2 shortening. Radiology 175:201–206

20. Thulborn KR, Sorensen AG, Kowall NW, et al. (1990) The role of ferritin and hemosiderin in the MR appearance of cerebral hemorrhage: a histopathologic biochemical study in rats. AJNR Am J Neuroradiol 11:291–297

21. Bizzi A, Brooks RA, Brunetti A, et al. (1990) Role of iron and ferritin in MR imaging of the brain: a study in primates at different field strengths. Radiology 177:59–65

22. Bradley WG Jr (1993) MR appearance of hemorrhage in the brain. Radiology 189:15–26

23. Ekholm S (1996) Intracranial hemorrhages. Rivista di Neuroradiologia 9 (Suppl 1):17–21

24. Ebisu T, Tanaka C, Umeda M, et al. (1997) Hemorrhagic and nonhemorrhagic stroke: diagnosis with diffusion-weighted and T2-weighted echo-planar MR imaging. Radiology 203:823–828

25. Atlas SW, Thulborn KR (1998) MR detection of hyperacute parenchymal hemorrhage of the brain. AJNR Am J Neuroradiol 19:1471–1477

26. Liang L, Korogi Y, Sugahara T, et al. (1999) Detection of intracranial hemorrhage with susceptibility-weighted MR sequences. AJNR Am J Neuroradiol 20:1527–1534

27. Kinoshita T, Okudera T, Tamura H, Ogawa T, Hatazawa J (2000) Assessment of lacunar hemorrhage associated with hypertensive stroke by echo-planar gradient-echo T2*-weighted MRI. Stroke 31:1646–1650

28. Atlas SW, DuBois P, Singer MB, Lu D (2000) Diffusion measurements in intracranial hematomas: implications for MR imaging of acute stroke. AJNR Am J Neuroradiol 21:1190–1194

29. Schaefer PW, Grant PE, Gonzalez RG (2000) Diffusion-weighted MR imaging of the brain. Radiology 217:331–345

30. Maldjian JA, Listerud J, Moonis G, Siddiqi F (2001) Computing diffusion rates in T2-dark hematomas and areas of low T2 signal. AJNR Am J Neuroradiol 22:112–128

31. Lin DD, Filippi CG, Steever AB, Zimmerman RD (2001) Detection of intracranial hemorrhage: comparison between gradient-echo images and b(0) images obtained from diffusion-weighted echo-planar sequences. AJNR Am J Neuroradiol 22:1275–1281

32. Hermier M, Nighoghossian N, Derex L, et al. (2001) MRI of acute post-ischemic cerebral hemorrhage in stroke patients: diagnosis with T2*-weighted gradient-echo sequences. Neuroradiology 43:809–815

33. Kang BK, Na DG, Ryoo JW, Byun HS, Roh HG, Pyeun YS (2001) Diffusion-weighted MR imaging of intracerebral hemorrhage. Korean J Radiol 2:183–191

34. Atlas SW, Thulborn KR (2002) Intracranial hemorrhage. In: Magnetic resonance imaging of the brain and spine. Lippincott Williams & Wilkins, Philadelphia, pp 773–832

35. Latour LL, Svoboda K, Mitra PP, Sotak CH (1994) Time-dependent diffusion of water in a biological model system. Proc Natl Acad Sci USA 91:1229–1233

36. Does MD, Zhong J, Gore JC (1999) In vivo measurement of ADC change due to intravascular susceptibility variation. Magn Reson Med 41:236–240

37. Harrison PM, Fischbach FA, Hoy TG, Haggis GH (1967) Ferric oxyhydroxide core of ferritin. Nature 216:1188–1190

38. Munro HN, Linder MC (1978) Ferritin: structure, biosynthesis, and role in iron metabolism. Physiol Rev Apr;58(2):317–396

39. Chakeres DW, Bryan RN (1986) Acute subarachnoid hemorrhage: in vitro comparison of magnetic resonance and computed tomography. AJNR Am J Neuroradiol 7:223–228

40. Jenkins A, Hadley DM, Teasdale GM, Condon B, Macpherson P, Patterson J (1988) Magnetic resonance imaging of acute subarachnoid hemorrhage. J Neurosurg 68:731–736

41. Satoh S, Kadoya S (1988) Magnetic resonance imaging of subarachnoid hemorrhage. Neuroradiology 30:361–366

42. Atlas SW (1993) MR imaging is highly sensitive for acute subarachnoid hemorrhage ... not! Radiology 186:319–322

43. Ogawa T, Uemura K (1993) MR imaging is highly sensitive for acute subarachnoid hemorrhage ... not! Reply. Radiology 186:323

44. Ogawa T, Inugami A, Shimosegawa E, et al. (1993) Subarachnoid hemorrhage: evaluation with MR imaging. Radiology 186:345–351

45. Griffiths PD, Wilkinson ID, Mitchell P, et al. (2002) Multimodality MR imaging depiction of hemodynamic changes and cerebral ischemia in subarachnoid hemorrhage. AJNR Am J Neuroradiol 22:1690–1697

46. Noguchi K, Ogawa T, Inugami A, Toyoshima H, Okudera T, Uemura K (1994) MR of acute subarachnoid hemorrhage: a preliminary report of fluid-attenuated inversion-recovery pulse sequences. AJNR Am J Neuroradiol 15:1940–1943

47. Noguchi K, Ogawa T, Inugami A, et al. (1995) Acute subarachnoid hemorrhage: MR imaging with fluid-attenuated inversion recovery pulse sequences. Radiology 196:773–777

48. Noguchi K, Ogawa T, Seto H, et al. (1997) Subacute and chronic subarachnoid hemorrhage: diagnosis with fluid-attenuated inversion-recovery MR imaging. Radiology 203(1):257–262

49. Noguchi K, Seto H, Kamisaki Y, Tomizawa G, Toyoshima S, Watanabe N (2000) Comparison of fluid-attenuated inversion-recovery MR imaging with CT in a simulated model of acute subarachnoid hemorrhage. AJNR Am J Neuroradiol 21:923–927

50. Melhem ER, Jara H, Eustace S (1997) Fluid-attenuated inversion recovery MR imaging: identification of protein concentration thresholds for CSF hyperintensity. AJR Am J Roentgenol 169:859–862

51. Singer MB, Atlas SW, Drayer BP (1998) Subarachnoid space disease: diagnosis with fluid-attenuated inversion-recovery MR imaging and comparison with gadolinium-enhanced spin-echo MR imaging – blinded reader study. Radiology 208:417–422

52. Dechambre SD, Duprez T, Grandin CB, Lecouvet FE, Peeters A, Cosnard G (2000) High signal in cerebrospinal fluid mimicking subarachnoid haemorrhage on FLAIR following acute stroke and intravenous contrast medium. Neuroradiology 42:608–611

53. Taoka T, Yuh WT, White ML, Quets JP, Maley JE, Ueda T (2001) Sulcal hyperintensity on fluid-attenuated inversion recovery mr images in patients without apparent cerebrospinal fluid abnormality. AJR Am J Roentgenol 176:519–524

54. Wiesmann M, Mayer TE, Yousry I, Medele R, Hamann GF, Bruckmann H (2002) Detection of hyperacute subarachnoid hemorrhage of the brain by using magnetic resonance imaging. J Neurosurg 96:684–689

55. Busch E, Beaulieu C, de Crespigny A, Moseley ME (1998) Diffusion MR imaging during acute subarachnoid hemorrhage in rats. Stroke 29:2155–2161

56. Rordorf G, Koroshetz WJ, Copen WA, et al. (1999) Diffusion- and perfusion-weighted imaging in vasospasm after subarachnoid hemorrhage. Stroke 30:599–605

57. Domingo Z, Bradley JK, Blamire AM, Brindle K, Styles P, Rajagopalan B (2000) Diffusion weighted imaging and magnetic resonance spectroscopy in a low flow ischaemia model due to endothelin induced vasospasm. NMR Biomed 13:154–162

58. Condette-Auliac S, Bracard S, Anxionnat R, et al. (2001) Vasospasm after subarachnoid hemorrhage: interest in diffusion-weighted MR imaging. Stroke 32:1818–1824

59. Hadeishi H, Suzuki A, Yasui N, Hatazawa J, Shimosegawa E (2002) Diffusion-weighted magnetic resonance imaging in patients with subarachnoid hemorrhage. Neurosurgery 50:741–747

60. Leclerc X, Fichten A, Gauvrit JY, et al. (2002) Symptomatic vasospasm after subarachnoid haemorrhage: assessment of brain damage by diffusion and perfusion-weighted MRI and single-photon emission computed tomography. Neuroradiology 44:610–616

61. Fobben ES, Grossman RI, Atlas SW, Hackney DB, Goldberg HI, Zimmerman RA, Bilaniuk LT (1989) MR characteristics of subdural hematomas and hygromas at 1.5 T. AJR Am J Roentgenol 153:589–595

62. Ebisu T, Naruse S, Horikawa Y, Tanaka C, Higuchi T (1989) Nonacute subdural hematoma: fundamental interpretation of MR images based on biochemical and in vitro MR analysis. Radiology 171:449–453

63. Wilms G, Marchal G, Geusens E, et al. (1992) Isodense subdural haematomas on CT: MRI findings. Neuroradiology 34:497–499

64. Ashikaga R, Araki Y, Ishida O (1997) MRI of head injury using FLAIR. Neuroradiology 39:239–242

65. Williams VL, Hogg JP (2000) Magnetic resonance imaging of chronic subdural hematoma. Neurosurg Clin N Am Jul;11(3):491–498

66. Tsui EY, Fai Ma K, Cheung YK, Chan JH, Yuen MK (2000) Rapid spontaneous resolution and redistribution of acute subdural hematoma in a patient with chronic alcoholism: a case report. Eur J Radiol 36:53-57

67. Lee Y, Lee KS, Hwang DH, Lee IJ, Kim HB, Lee JY (2001) MR imaging of shaken baby syndrome manifested as chronic subdural hematoma. Korean J Radiol 2:171–174

68. Biousse V, Suh DY, Newman NJ, Davis PC, Mapstone T, Lambert SR (2002) Diffusion-weighted magnetic resonance imaging in Shaken Baby Syndrome. Am J Ophthalmol Feb;133(2):249–255

69. Mesiwala AH, Goodkin R (2002) Reversible ischemia detected by diffusion-weighted magnetic resonance imaging. Case illustration. J Neurosurg 97:230

70. Bakshi R, Kamran S, Kinkel PR, et al. (1999) MRI in cerebral intraventricular hemorrhage: analysis of 50 consecutive cases. Neuroradiology 41:401–409

71. Bakshi R, Kamran S, Kinkel PR, et al. (1999) Fluid-attenuated inversion-recovery MR imaging in acute and subacute cerebral intraventricular hemorrhage. AJNR Am J Neuroradiol 20:629–636

72. Nakai Y, Hyodo A, Yanaka K, Nose T (2002) Fatal cerebral infarction after intraventricular hemorrhage in a pregnant patient with moyamoya disease. J Clin Neurosci 9:456–458

73. Scott M (1975) Spontaneous intracerebral hematoma caused by cerebral neoplasms. Report of eight verified cases. J Neurosurg 42:338–342

74. Mandybur TI (1977) Intracranial hemorrhage caused by metastatic tumors. Neurology 27:650–655

75. Little JR, Dial B, Belanger G, Carpenter S (1979) Brain hemorrhage from intracranial tumor. Stroke 10:283–288

76. Zimmerman RA, Bilaniuk LT (1980) Computed tomography of acute intratumoral hemorrhage. Radiology 135:355–359

77. Leeds NE, Elkin CM, Zimmerman RD (1984) Gliomas of the brain. Semin Roentgenol 19:27–43

78. Atlas SW, Grossman RI, Gomori JM, et al. (1987) Hemorrhagic intracranial malignant neoplasms: spin-echo MR imaging. Radiology 164:71–77

79. Brunereau L, Labauge P, Tournier-Lasserve E, Laberge S, Levy C, Houtteville JP (2000) Familial form of intracranial cavernous angioma: MR imaging findings in 51 families. French Society of Neurosurgery. Radiology 214:209–216

80. Tagle P, Huete I, Mendez J, del Villar S (1986) Intracranial cavernous angioma: presentation and management. J Neurosurg 64:720–723

81. Zabramski JM, Wascher TM, Spetzler RF, et al. (1994) The natural history of familial cavernous malformations: results of an ongoing study. J Neurosurg 80:422–432

82. Gomori JM, Grossman RI, Goldberg HI, Hackney DB, Zimmerman RA, Bilaniuk LT (1986) Occult cerebral vascular malformations: high-field MR imaging. Radiology 158:707–713

83. Sigal R, Krief O, Houtteville JP, Halimi P, Doyon D, Pariente D (1990) Occult cerebrovascular malformations: follow-up with MR imaging. Radiology 176:815–819

84. Liu AY, Maldjian JA, Bagley LJ, Sinson GP, Grossman RI (1999) Traumatic brain injury: diffusion-weighted MR imaging findings. AJNR Am J Neuroradiol 20:1636–1641

Vasculopathy and Vasculitis

7.1 Definition

Vasculopathy is a general term used to describe any disease affecting blood vessels [1]. It includes vascular abnormalities caused by degenerative, metabolic and inflammatory conditions, embolic diseases, coagulative disorders, and functional disorders such as posterior reversible encephalopathy syndrome. The etiology of vasculopathy is generally unknown and the condition is frequently not pathologically proven. Vasculitis, on the other hand, is a more specific term and is defined as inflammation of the wall of a blood vessel [2]. However, the term vasculopathy is also used for "vasculitis" that has not been pathologically established.

7.2 Clinical Presentation

Vasculitis and vasculopathy of the central nervous system (CNS) often have similar clinical and radiological characteristics. Both result in ischemia, which can be reversible or develop into infarction. The reversibility of a lesion is related to the size and location of vessels involved and the severity of ischemia. Diffusion-weighted (DW) imaging has been useful in the early detection of cytotoxic edema in hyperacute or acute infarctions and can distinguish cytotoxic edema from vasogenic edema and chronic infarctions [3]. Some specific types of vasculitis or vasculopathy demonstrate primarily vasogenic edema [4–8].

7.3 Treatment

Vasculitis and vasculopathy of the CNS caused by an abnormal immune reaction are often treated with immunosuppressant agents. If, on the other hand, the vascular changes are caused by thrombosis or embolism, they are treated with anticoagulants. Prompt

characterization of the nature of CNS vasculitis and vasculopathy, by imaging and/or biopsy, is thus necessary to institute appropriate management.

7.4 Vasculitis of the CNS

The term vasculitis encompasses a heterogeneous group of multisystemic disorders characterized pathologically by inflammation and necrosis of the blood vessel wall. Cerebral ischemia, which may result in focal infarction, is the major neurological manifestation of CNS vasculitis. The clinical manifestations include headache, transient ischemic attacks (TIAs), altered mental status, seizures, cranial nerve palsies and localized neurologic deficits.

7.4.1 Characterization of CNS Vasculitis

Vasculitis of the CNS is characterized by the size of the affected vessel, as illustrated in Fig. 7.1 [2]. Determining size and location of the predominantly affected vessels is useful to obtain an optimal tissue biopsy and establish appropriate treatment [9]. Large artery vasculitis usually responds well to steroids alone, while small and medium-sized vessel vasculitis respond better to a combination of cytotoxic agents and steroids. Therefore, a clear understanding of the size of the vessels involved and the pathophysiologic mechanisms are useful for the treatment decision [10, 11].

Digital subtraction catheter angiography and brain biopsy are the diagnostic foundations in establishing the diagnosis. However, angiography has a false-negative rate of 20–30%, as small arteries with a diameter of less than 100–200 μm are beyond the limit of resolution of digital subtraction angiography [2]. Good-quality MR angiography can demonstrate stenosis or occlusion of large to middle-sized arteries, but the resolution is not sufficient to detect abnormalities of small arteries. MR imaging, on the
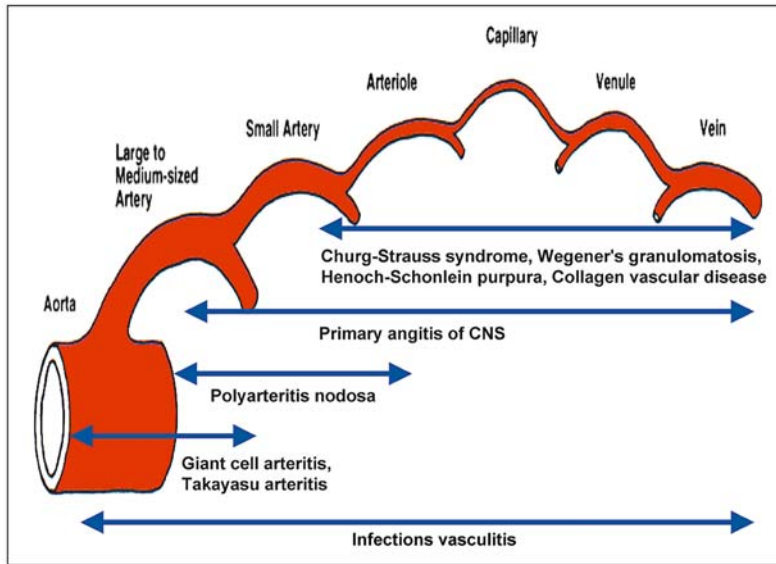
Figure 7.1

Classification of CNS vasculitis (modified from [10])

other hand, is sensitive to detect gray and white matter lesions in CNS vasculitis, but the appearance of these lesions is usually not specific [12].

Whether the lesions on MR imaging are reversible or irreversible depends on the severity of ischemia and seems to be related to size and location of the vessels involved. Occlusion or stenosis involving large, medium or small arteries mainly results in infarction, whereas lesions involving arterioles, capillaries, venules or veins predominantly cause vasogenic edema or gliosis. DW imaging can be useful to differentiate an acute or subacute infarction from vasogenic edema or gliosis, which is important both for choice of treatment and to predict the long-term prognosis.

Multifocal and multiphasic ischemia are some of the characteristic sequelae of CNS vasculitis. DW imaging can differentiate the phases of cerebral infarction as hyperacute, acute, subacute or chronic. The hyperacute phase of an infarction usually has a decreased apparent diffusion coefficient (ADC) and a normal or subtle increase in signal intensity on T2-weighted or fluid-attenuated inversion-recovery (FLAIR) images. The acute phase has a decreased ADC with hyperintensity on T2-weighted images. In the subacute phase, ADC values are normalized; in the chronic phase, DW imaging shows hypointensity with increased ADC.

7.4.2 Primary Angitis of the Central Nervous System

Primary angitis of the central nervous system is a non-infectious granulomatous angitis, pathologically characterized by infiltration of the vessel walls with lymphocytes, histiocytes, and/or multinucleated giant cells, with a variable degree of fibrinoid necrosis [13]. The pathogenesis is probably related to T cell-mediated inflammation. Primary angitis of the central nervous system tends to affect small to medium-sized vessels of the brain parenchyma and meninges, but can affect vessels of any size. Angiography typically shows a "string-of-beads" appearance, but it has a false-negative rate of 20–30% [14]. Brain and meningeal biopsies are diagnostic in only 50–72% of patients with primary angitis of the central nervous system.

Magnetic resonance imaging findings in primary angitis of the central nervous system are highly variable, ranging from multiphasic cerebral infarction, vasogenic edema and gliosis, to hemorrhage and leptomeningeal enhancement [15, 16]. The lesions caused by occlusion of large or medium-sized arteries affect the cortical or deep gray matter. If the vessels involved are small, MR imaging may show discrete or diffuse lesions in the deep or subcortical white matter. On follow-up MR imaging, the lesions may change with regard to number and size, and they may even disappear. DW imaging is useful in differentiating an acute or subacute infarction from re-

versible vasogenic edema (Fig. 7.2) and can demonstrate multiphasic infarctions (Fig. 7.3). Prompt diagnosis is important, as primary angitis of the central nervous system is often fatal if not treated with aggressive immunosuppression [17].

7.4.3 Giant Cell (Temporal) Arteritis

The criteria of the American College of Rheumatology for the diagnosis of giant cell arteritis (Fig. 7.4) include at least three of the following: (1) age at disease onset >50 years, (2) new onset of headache, (3) claudication of jaw or tongue, (4) tenderness of the temporal artery on palpation or decreased pulsation, (5) erythrocyte sedimentation ratio >50 mm/h and
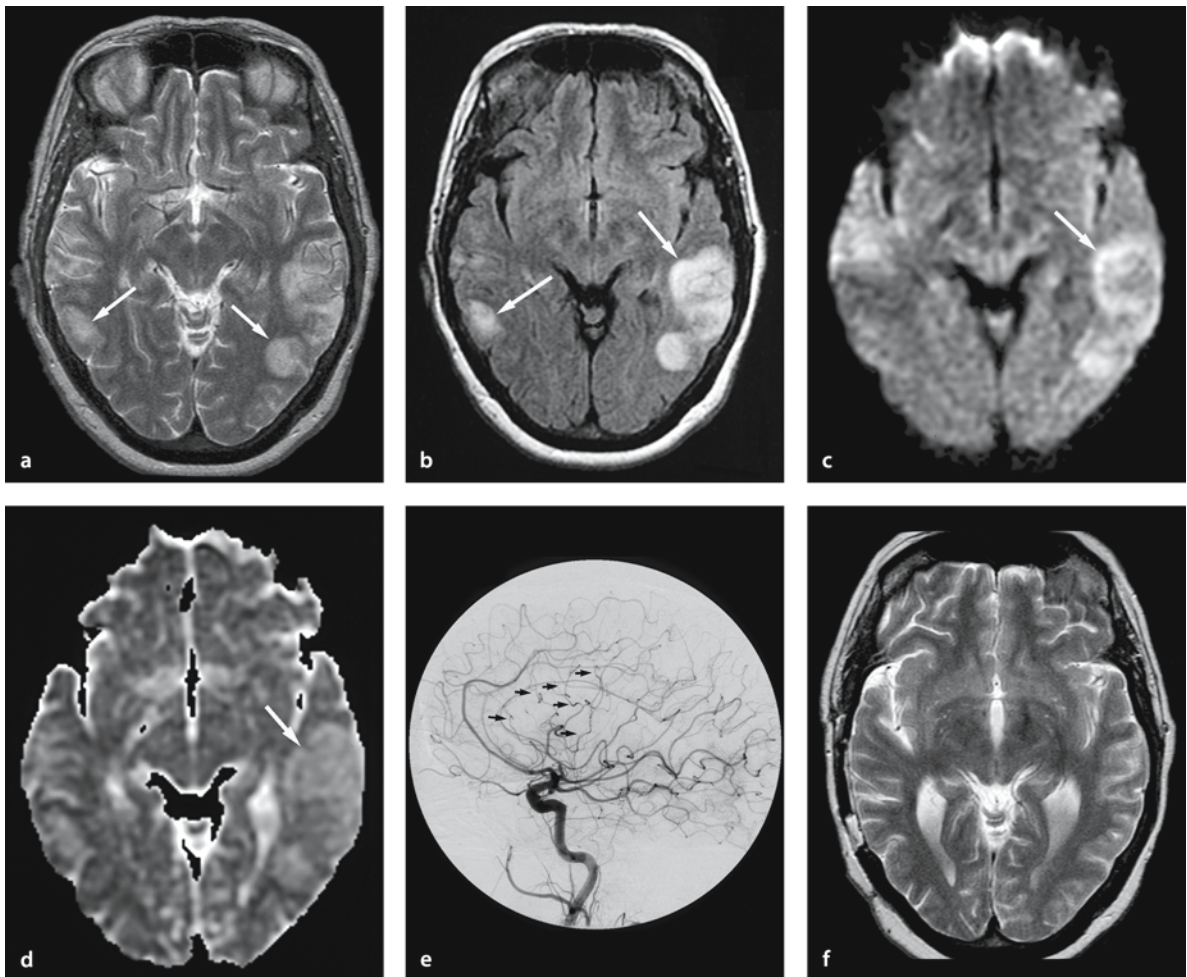
Figure 7.2 a–f

Primary angitis of central nervous system (proven by biopsy) in a 60-year-old woman with dizziness and speech difficulties. **a** T2-weighted image shows hyperintense lesions in the bilateral tempo-occipital cortices (*arrows*). **b** FLAIR image shows hyperintense lesions in the bilateral tempo-occipital cortices (*arrows*). **c** DW image shows slightly high signal in the lesions (*arrow*) with increased ADC (**d**), mainly representing vasogenic edema (*arrow*). **e** DSA shows multiple focal stenoses of distal branches of left middle cerebral arteries (*arrows*). **f** Two-month follow-up T2-weighted image shows no infarction in the bilateral tempo-occipital areas. (From [49])
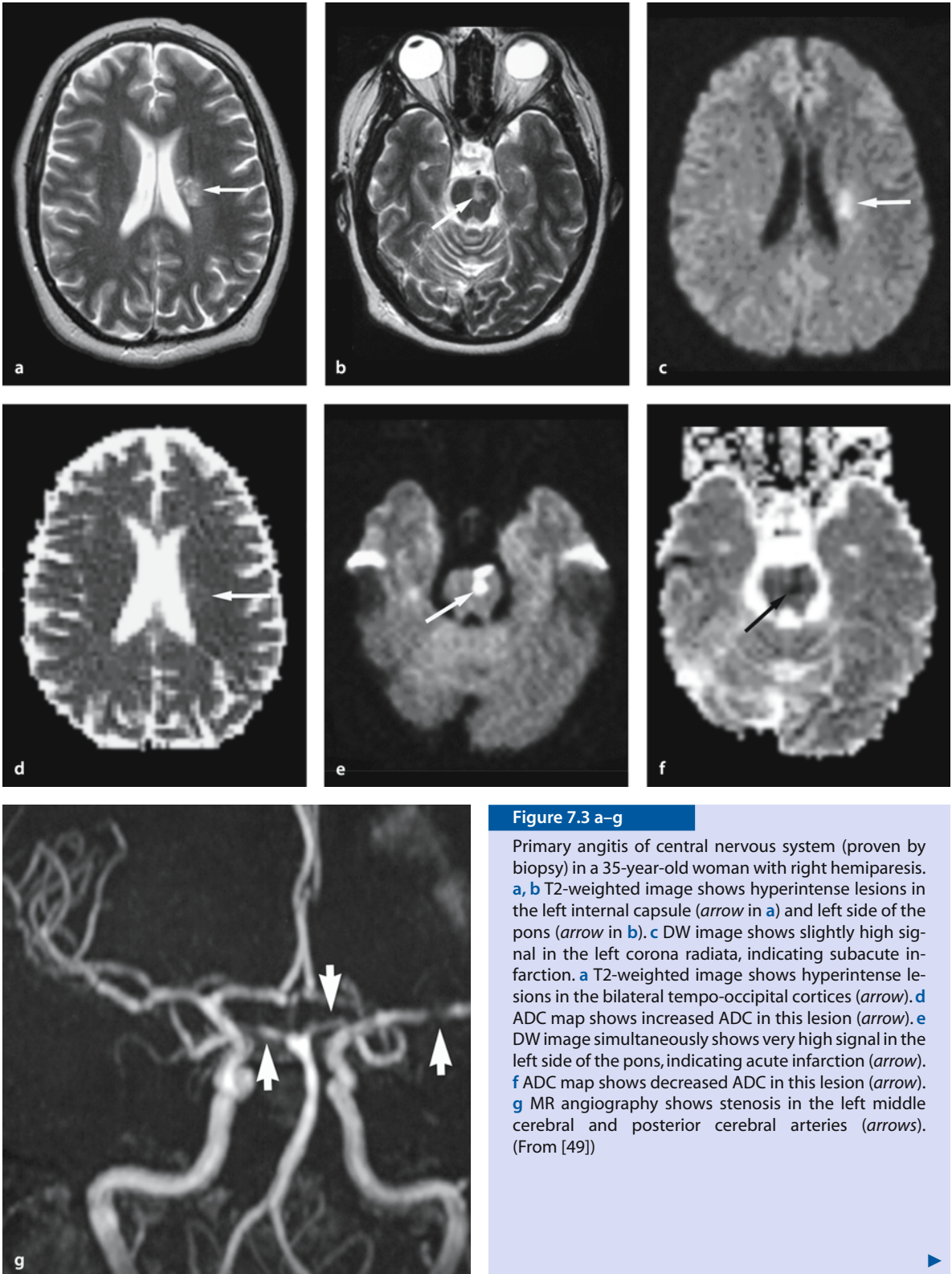
Figure 7.3 a–g

Primary angitis of central nervous system (proven by biopsy) in a 35-year-old woman with right hemiparesis. **a, b** T2-weighted image shows hyperintense lesions in the left internal capsule (*arrow* in **a**) and left side of the pons (*arrow* in **b**). **c** DW image shows slightly high signal in the left corona radiata, indicating subacute infarction. **a** T2-weighted image shows hyperintense lesions in the bilateral tempo-occipital cortices (*arrow*). **d** ADC map shows increased ADC in this lesion (*arrow*). **e** DW image simultaneously shows very high signal in the left side of the pons, indicating acute infarction (*arrow*). **f** ADC map shows decreased ADC in this lesion (*arrow*). **g** MR angiography shows stenosis in the left middle cerebral and posterior cerebral arteries (*arrows*). (From [49])

▶
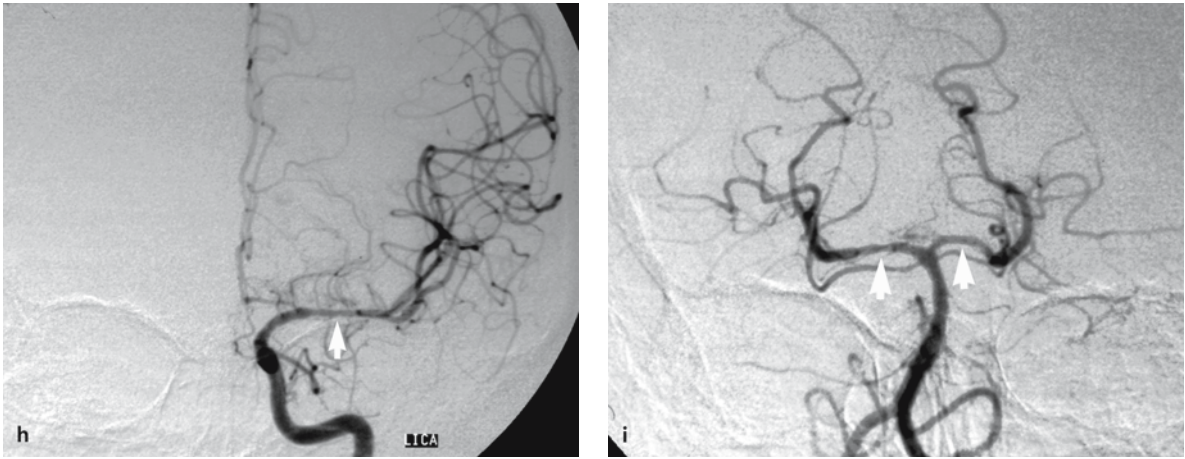
Figure 7.3 h–j

h, i Digital subtraction angiography (DSA) confirms the stenosis in the left middle cerebral (*arrow* in **h**) and posterior cerebral arteries (**i**) (*arrows* in **i**). **j** Pathological specimen by meningeal biopsy shows infiltration of the vessel walls with lymphocytes and multinucleated giant cells, with intramural granulomatous tissue formation (*arrows*). (From [49])
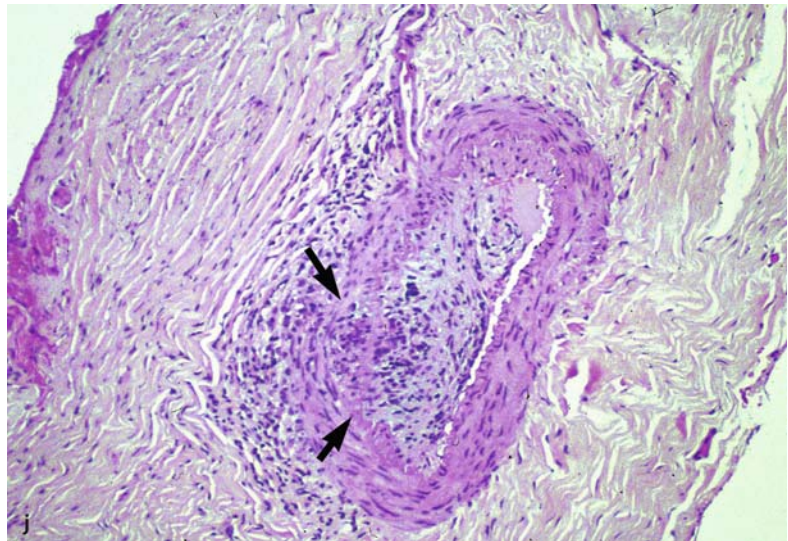
(6) temporal artery biopsy showing vasculitis with multinucleated giant cells.

Giant cell arteritis is probably a T cell-mediated vasculitis and it can affect medium to large arteries. The superficial temporal, vertebral and ophthalmic arteries are more commonly involved than the internal carotid arteries, while the intracranial arteries are rarely involved (Fig. 7.4) [18]. Abrupt and irreversible visual loss is the most dramatic complication of giant cell arteritis, while a TIA and stroke are rare (7%), but when present most often involve the vertebrobasilar territory. Steroids are effective, and giant cell arteritis is usually self-limited and rarely fatal.

7.4.4 Takayasu's Arteritis (Aortitis Syndrome)

Takayasu's arteritis (Fig. 7.5) is a primary arteritis of unknown cause but probably also related to T cell-mediated inflammation. Takayasu's arteritis commonly affects large vessels including the aorta and its major branches to the arms and the head. It is more commonly seen in Asia and usually affects young women [19]. Pulseless upper extremities and hypertension are the common clues to suggest the diagnosis. Most patients are treated with steroids alone to reduce the inflammation. The prognosis is relatively good and 90% of patients are still alive after 10 years. TIA or stroke is rare but can occasionally occur in severe cases with significant stenosis of arteries supplying the CNS (Fig. 7.5).
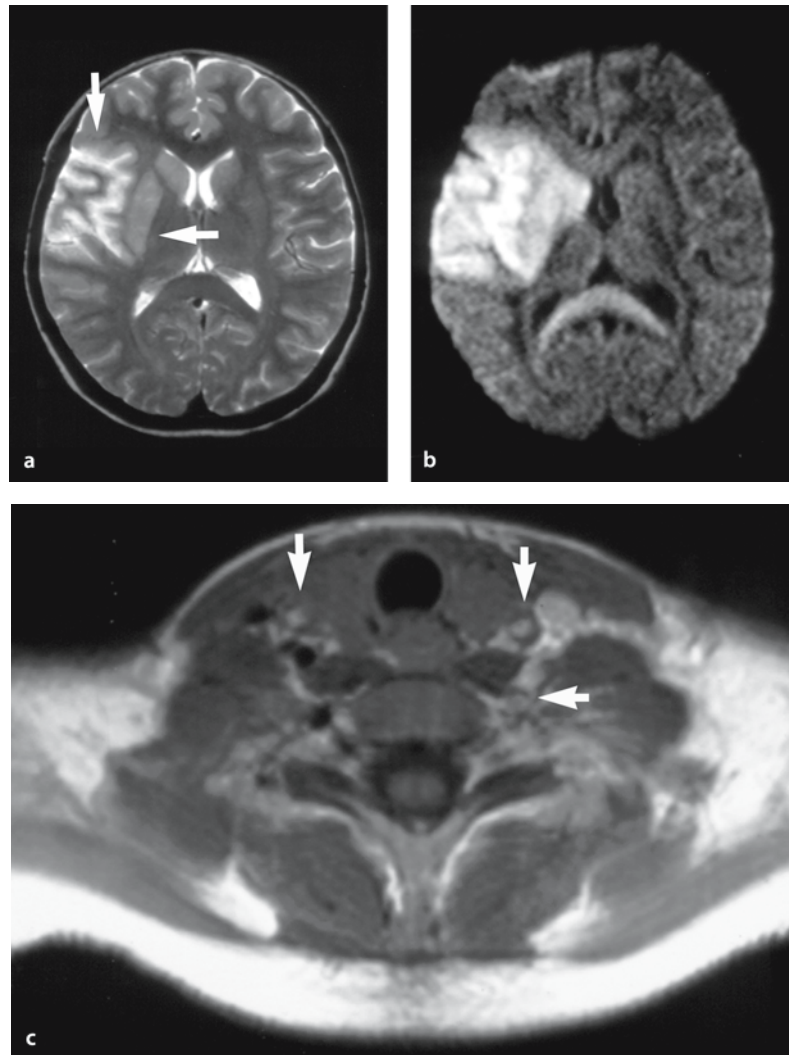
Figure 7.5 a–d

Takayasu's arteritis in an 18-year-old woman with left hemiparesis. **a** T2-weighted image shows a hyperintense lesion in the right basal ganglia and temporal lobe (*arrows*). **b** DW image shows a very high signal lesion, indicating an acute infarct. **c** T1-weighted axial image shows occlusion of internal carotid arteries bilaterally and the left vertebral artery, with thickening of the wall and thrombosis (*arrows*). **d** DSA shows occlusion of both carotid arteries, and stenosis of the brachiocephalic and left subclavian arteries (*arrows*)
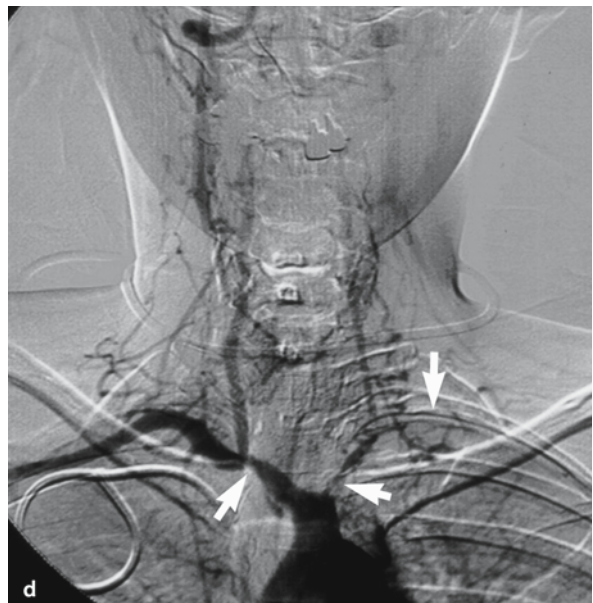
7.4.5 Polyarteritis Nodosa

The criteria of the American College of Rheumatology for the diagnosis of polyarteritis nodosa include at least three of the following: (1) weight loss >4 kg, (2) livedo reticularis, (3) testicular pain or tenderness, (4) myalgias, weakness or leg tenderness, (5) mono- or polyneuropathy, (6) hypertension, (7) elevated blood creatinine or blood urea nitrogen, (8) hepatitis B antigen or antibodies in the serum, (9) aneurysm or occlusion of the visceral arteries and (10) granulocytes in small or medium-sized arteries on vessel wall biopsy. Neurologic abnormalities occur in 25–50% of cases. Ischemic stroke can result from vasculitis, severe hypertension or embolism secondary to cardiac involvement [20]. The treatment usually requires both cytotoxic agents and steroids.

7.4.6 Churg–Strauss Disease

This is an antineutrophil cytoplasmic autoantibody-mediated vasculitis, defined by at least four of the following: (1) asthma, (2) history of allergy, (3) eosinophilia (>10%), (4) mono- or polyneuropathy, (5) migratory or transitory pulmonary infiltrates and (6) sinusitis. A biopsy of affected organs, including small arteries, arterioles or venules shows extravascular eosinophils, which confirms the diagnosis. Neurological involvement occurs in 62% of cases, including stroke and intracerebral hemorrhage (Fig. 7.6) [21, 22]. Steroids usually stabilize this condition, but treatment with cyclophosphamide may be required. A normal angiogram does not exclude this form of

vasculitis, as affected vessels are often smaller than the resolution of angiography.

7.4.7 Other Small Vessel Vasculitis

The incidence of CNS involvement in Wegener's granulomatosis varies from 11 to 44%, but stroke is a very rare complication [23]. Involvement of the CNS in other forms of small vessel vasculitis (microscopic polyangitis, Henoch–Schönlein purpura, essential cryoglobulinemia and hypersensitivity vasculitis) is rare, but Henoch–Schönlein purpura may show reversibility of lesions on MRI [7].

7.4.8 Collagen Vascular Diseases

Behçet's disease is a multisystem vasculitis of unknown origin. It is especially common in Middle Eastern and Mediterranean countries. CNS involvement has been described in 4–49% of cases [6]. The parenchymal distribution of lesions, especially at the mesodiencephalic junction (46%) supports small vessel vasculitis involving both the arterial and venous systems; mainly venules. The lesions are occasionally reversible on MRI, which mainly represents vasogenic edema, which is why DW imaging is useful in distinguishing them from infarction (Fig. 7.7). The treatment is usually a combination of cytotoxic agents and steroids. In other types of collagen diseases, such as scleroderma or rheumatoid arthritis, involvement of the CNS is very rare.
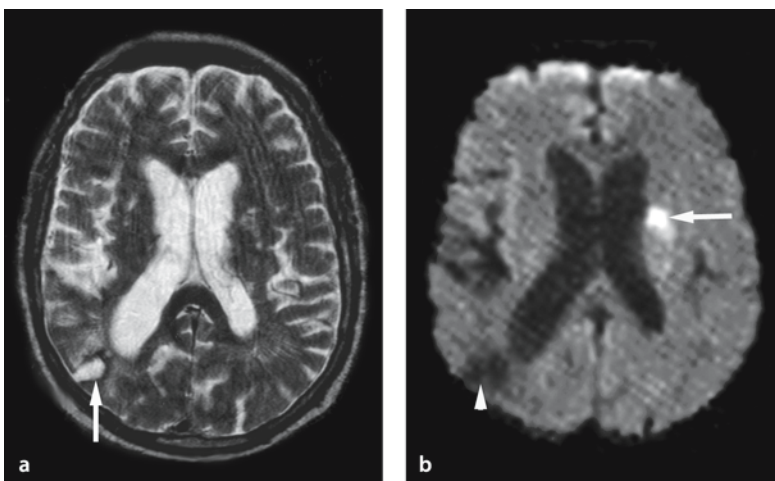
Figure 7.6 a,b

Churg–Strauss disease in a 65-year-old man with seizures. **A** T2-weighted image shows multiple hyperintense lesions in both corona radiata and right parieto-occipital area, the latter with a hemosiderin rim, representing old hemorrhage (*arrow*). **b** DW image shows a hyperintense lesion (*arrow*) in the left corona radiata, representing an acute infarct. An old hemorrhage shows hypointensity (*arrowhead*) on DW image. MR and DS angiography revealed no abnormalities (not shown). (From [49])

Figure 7.7 a–d

Neuro-Behçet's disease in a 24-year-old male. **a** T2-weighted image shows a hyperintense lesion in the left midbrain extending into the left temporal lobe, with enlargement of the left cerebral peduncle (*arrow*). **b** Gadolinium-enhanced T1-weighted image shows enhancement in this lesion (*arrow*). **c** DW image shows a hyperintense lesion with increased signal intensity in the left cerebral peduncle, probably representing vasogenic edema (*arrow*). **d** ADC map shows increased ADC in this lesion (*arrow*). (From [50])
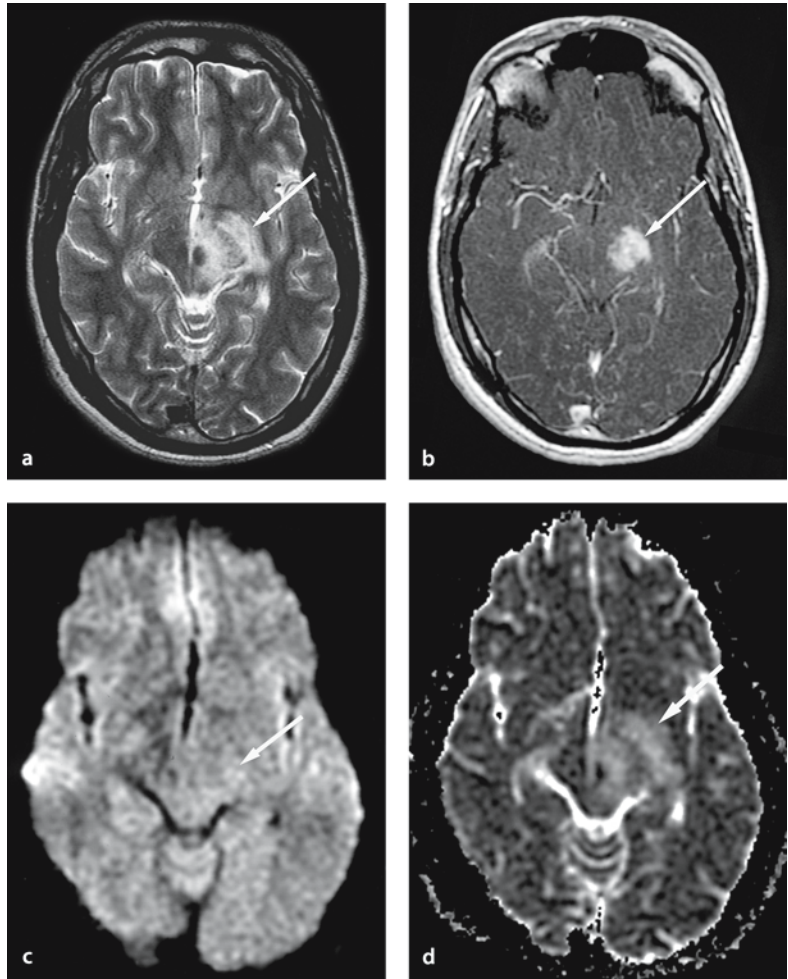
7.4.9 Infectious Vasculitis

Infections can cause vasculitis both by direct invasion of the vessel walls and by an immune-mediated response to the pathogens. Bacterial, fungal and some viral vasculitis (e.g. herpes virus) cause a direct invasion of the vessel walls, usually resulting in infarction (Fig. 7.8) [2, 24]. Vasculitis with aseptic meningitis is probably related to an immunologic reaction, which can show reversible lesions. Aspergillus infiltrates and destroys the internal elastic lamina of major cerebral arteries, which results in infarction, abscess formation and hemorrhage [25] (Fig. 7.9). Infection of the infarcted tissue may be aggressive, and direct extension into the surrounding brain may progress quickly.
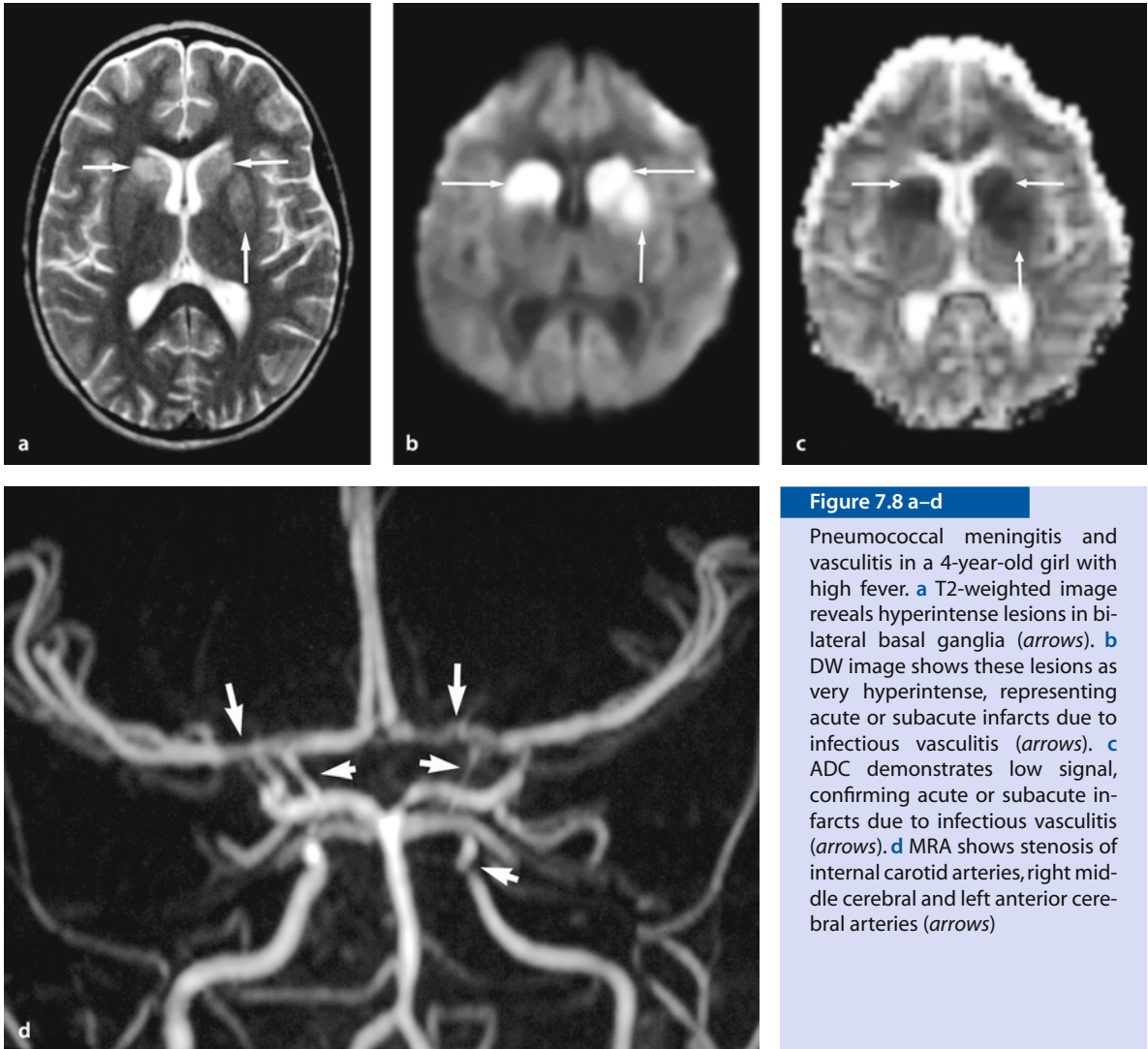
Figure 7.8 a–d

Pneumococcal meningitis and vasculitis in a 4-year-old girl with high fever. **a** T2-weighted image reveals hyperintense lesions in bilateral basal ganglia (*arrows*). **b** DW image shows these lesions as very hyperintense, representing acute or subacute infarcts due to infectious vasculitis (*arrows*). **c** ADC demonstrates low signal, confirming acute or subacute infarcts due to infectious vasculitis (*arrows*). **d** MRA shows stenosis of internal carotid arteries, right middle cerebral and left anterior cerebral arteries (*arrows*)

Figure 7.9 a–d

Disseminated aspergillosis in a 48-year-old female presenting with altered mental status and a history of acute lymphoblastic leukemia, post recent bone marrow transplant. **a** T2-weighted image shows a high signal intensity lesion (*arrow*) at the corticomedullary junction in the medial left frontal lobe. A hypointense spot in this lesion represents a hemorrhagic component (*arrowhead*). **b** Gadolinium-enhanced T1-weighted image reveals no enhancement within this lesion (*arrows*). **c** DW image shows this lesion containing areas of very high signal intensity (*arrows*), indicating a vasculitis-mediated acute septic infarction. **d** ADC shows heterogeneous decreased signal (*arrows*) in the lesion, confirming a conglomerate of acute septic infarctions. (From [49])
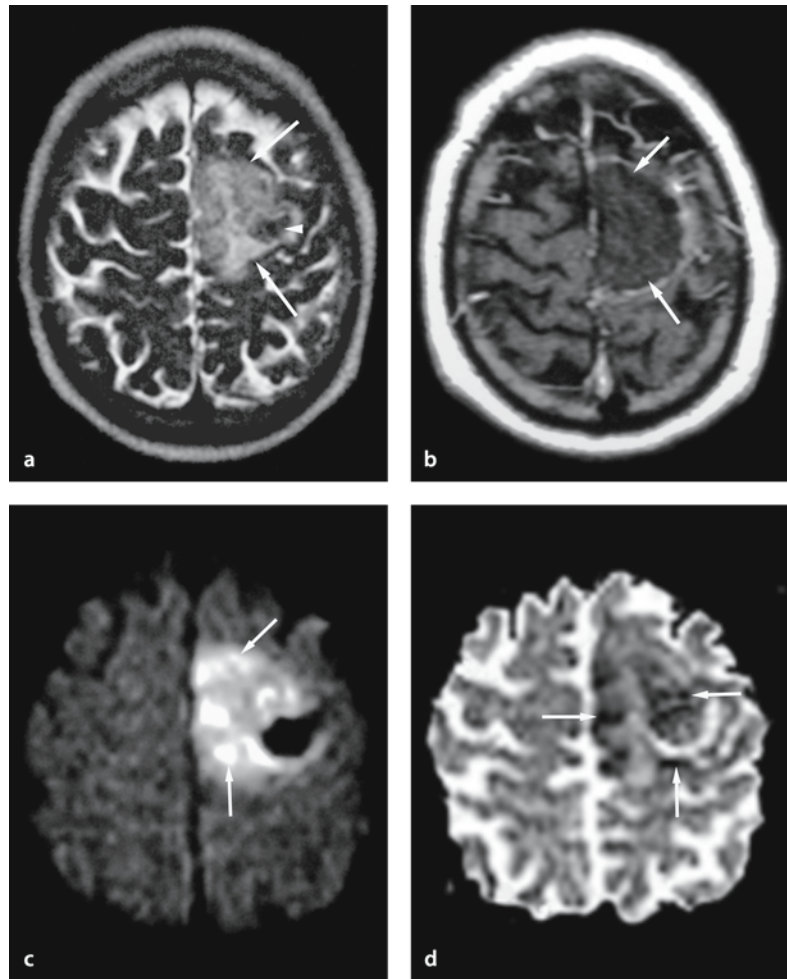
7.4.10 Drug-Induced Vasculitis, Including Illicit Drugs

Some drugs, such as chemotherapeutic agents (e.g. sulfonamide, thiouracil) and illicit drugs (e.g. cocaine), can cause vasculitis [26]. Stroke can occur soon after administration of illicit drugs by an intravenous, oral or nasal route. Cocaine, heroin, amphetamine and other sympathomimetic drugs are most commonly implicated. The diagnosis of "vasculitis" depends on the pathological findings, not on the angiographic findings, which are usually non-specific and may simply indicate vasospasm induced by these drugs.

Cocaine use has emerged as an important cause of cerebrovascular events in young adults [27]. Vasculitic changes can be present on angiography, but the significance of these changes has been debated. However, elevated sedimentation rate and biopsy changes of vasculitis have been documented. MR angiography may reveal irregularity of the intracerebral vessels and DW imaging is useful for the detection of acute ischemic changes (Fig. 7.10).
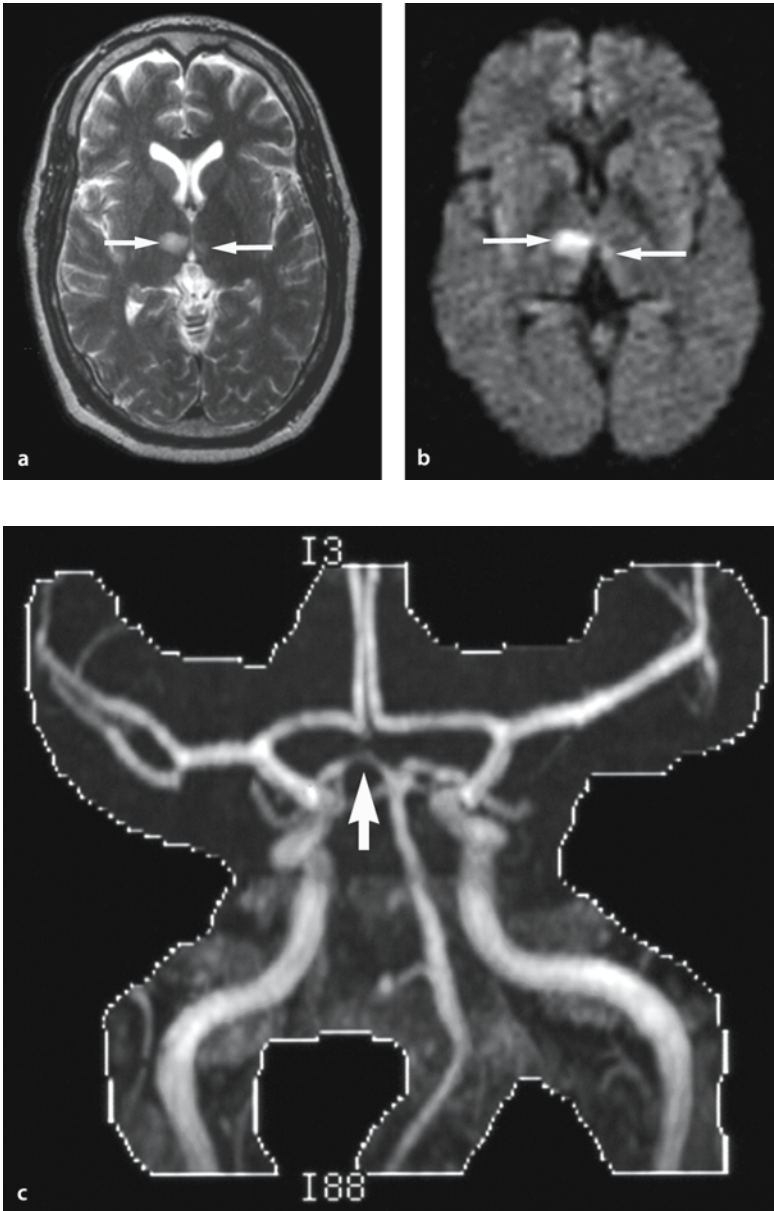
Cocaine-induced vasculopathy in a 41-year-old man with dysarthria. **a** T2-weighted image shows bilateral hyperintense lesions in medial thalami (*arrows*). **b** DW image shows the lesion in the right thalamus as hyperintense, indicating an acute infarct. **c** MR angiography shows stenosis of the right posterior cerebral artery (*arrow*). Biopsy was not performed and therefore the term cocaine-induced vasculopathy was used. (From [49])

7.5 Vasculopathy of the CNS

Vasculopathy is caused by a wide variety of underlying conditions such as degenerative, metabolic, inflammatory, embolic, coagulative and functional disorders [1]. This presentation focuses on vasculopathies that mimic vasculitis, but have no inflammation in the wall of the blood vessel (Fig. 7.11).

7.5.1 Systemic Lupus Erythematosus

Involvement of the CNS occurs in 14–75% of patients with systemic lupus erythematosus (SLE) [4]. Pathologically, microinfarcts and small vessel vasculopathy are the most common. Vasculopathy affects predominantly the arterioles and capillaries, resulting in vessel tortuosity, vascular hyalinization, endothelial proliferation and perivascular inflammation or gliosis.

Figure 7.11

Spectrum of CNS vasculopathy. (Modified from [10])
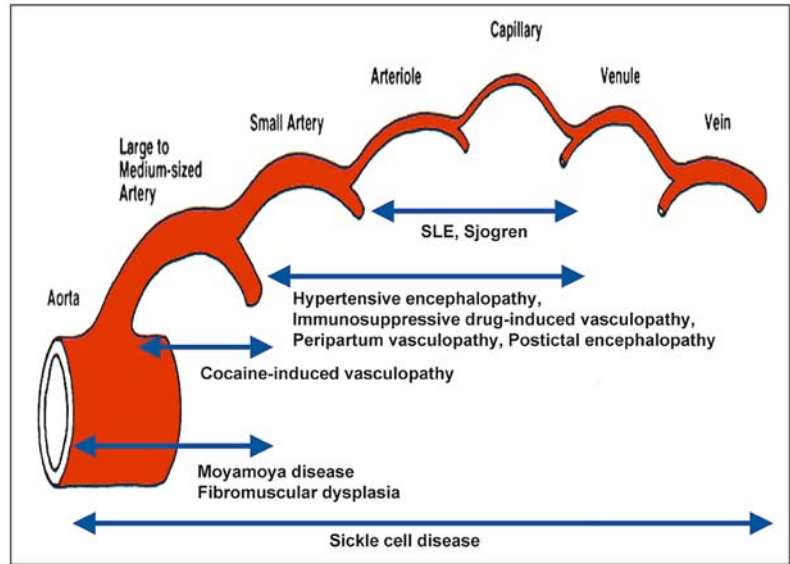
Figure 7.12 a–d

Systemic lupus erythematosus in a 39-year-old woman with recurrent episodes of stroke, who presented with fever and disturbance of consciousness. **a** T2-weighted image shows hyperintense lesions in the right thalamus, internal capsule, putamen, subcortical white matter, and the left internal capsule (*arrows*). **b** Gadolinium-enhanced T1-weighted image reveals marked enhancement of the lesion in the right side, suggesting blood–brain barrier breakdown (*arrows*). **c** DW image shows a slightly hyperintense lesion in the right thalamus but an isointense lesion in the right putamen and white matter (*arrows*). There is a linear hyperintense lesion in the right internal capsule (*long thin arrow*). A subtle hyperintense lesion in the left internal capsule is also seen (*arrowhead*). **d** The ADC map shows increased ADC of the lesion in the right side (*short thick arrows*), representing vasogenic edema. Increased ADC of the lesion in the left internal capsule (*arrowhead*) represents an old infarct. Decreased ADC is seen in the lesion in the right internal capsule (*long thin arrow*), presumably representing acute microinfarcts. (From [51])
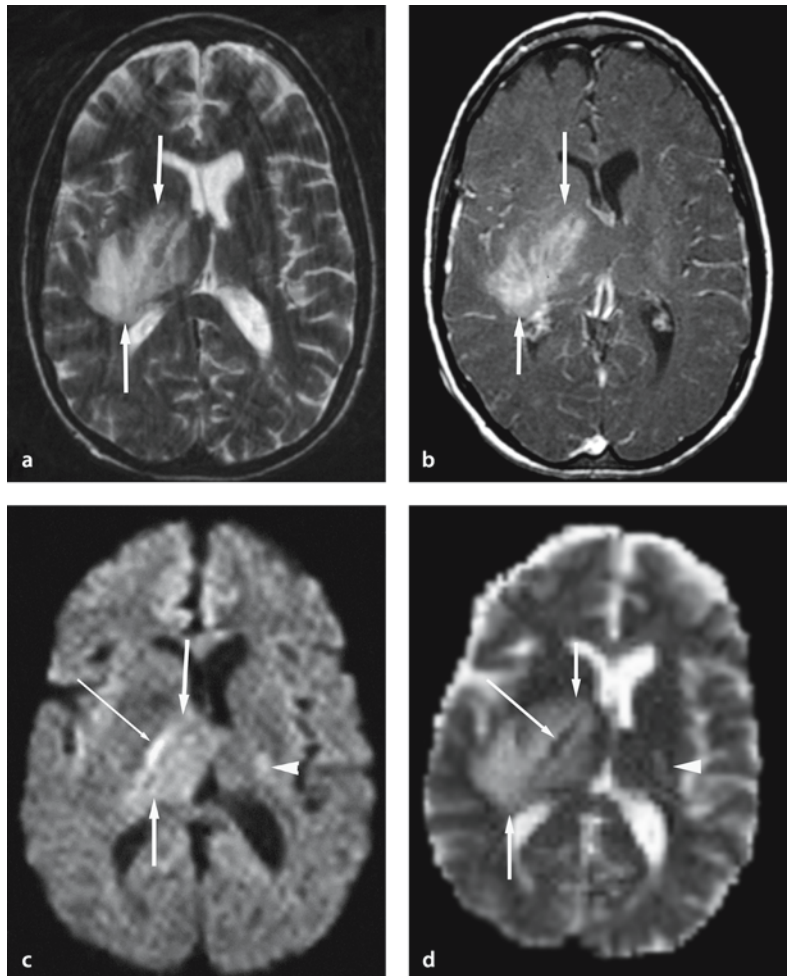
True vasculitis is very rare (0–7%). This vasculopathy may be related to both acute inflammation and ischemia [28]. In recent reports, the mechanism of vasculopathy in CNS involvement of SLE has been attributed to intravascular activation of a complement, which leads to adhesion between neutrophils and/or platelets and endothelium, resulting in leukothrombosis in the microvasculature (Shwartzman phenomenon) [29].

In this vasculopathy, despite widespread microvascular occlusions, parenchymal damage is minimal and potentially reversible. Sibbit et al. reported that up to 38% of CNS lesions in SLE were potentially reversible on MR imaging [30]. MR angiography and conventional angiography may provide additional information concerning vascular abnormalities. DW imaging shows primarily two patterns of parenchymal lesions with acute or subacute CNS symptoms: one is an acute or subacute infarction, and the other is vasogenic edema with or without microinfarcts (Fig. 7.12) [5]. CNS involvement in SLE is also due to associated uremia, hypertension, infection, Libman–Sacks endocarditis, and corticosteroid or immunosuppressive therapy.

7.5.2 Moyamoya Disease

Moyamoya disease is a rare, non-inflammatory vasculopathy of the intracranial vessels of unknown cause, which is found predominantly in East Asia. It has a bimodal age presentation, the first in childhood (first decade) and the second in adults (fourth decade). Endothelial thickening of the cellular fibrous tissue, the main pathological finding, leads to chronic progressive arterial stenosis of the circle of Willis and eventually to infarctions. In the adult form, the presenting symptom is often intracranial hemorrhage, usually intraparenchymal. The stenosis or occlusion of the supraclinoid portion of the internal carotid artery should be bilateral, but unilateral lesions can be included as "probable" cases of Moyamoya disease. DW imaging is useful in evaluating cerebral ischemia in Moyamoya disease (Fig. 7.13) [31].

7.5.3 Sickle Cell Disease

About 5–8% of patients with sickle cell disease develop symptomatic cerebrovascular disease. The risk of stroke is greatest during thrombotic crises and during the first 15 years of life [32]. Approximately 75% of strokes are the result of an occlusion of the large arteries at the base of the brain. Cortical and white matter watershed ischemia is common. This vasculopathy can be similar to Moyamoya disease. Occlusion of the small cortical branches, which leads to ischemia of deep white matter, accounts for 25% of cerebral infarctions. These lesions are thought to be related to peripheral vaso-occlusive events in which the arteriole or postcapillary venule is the major site of sickle cell adhesion [32]. If progression is associated with neurologic dysfunction, strong consideration should be given to place the patient on a long-term transfusion program. DW imaging is useful in detecting active ischemic changes and in differentiating them from chronic ischemic changes (Fig. 7.14).

7.5.4 Posterior Reversible Encephalopathy Syndrome

Posterior reversible encephalopathy syndrome is a remarkably heterogeneous group of disorders, related to hypertensive encephalopathy, severe preeclampsia/eclampsia, immunosuppressive drug or interferon neurotoxicity, uremia and thrombotic thrombocytopenic purpura [33]. The clinical symptoms are headache, altered mental status, seizures and visual loss. Posterior reversible encephalopathy syndrome is due to dysfunction of a cerebrovascular autoregulatory system, and a vasculopathy of small vessels, the arterioles. Brain perfusion is maintained by the autoregulatory system of the small arteries and arterioles that have myogenic and neurogenic components. Since the vertebrobasilar system and posterior cerebral arteries are sparsely innervated by sympathetic nerves, the occipital lobes and other posterior brain regions are susceptible to a breakthrough of the autoregulation in case of a sudden elevation of the systemic blood pressure. Endothelial damage, which can attenuate the myogenic response of the autoregulatory system, is hypothesized to be the cause of the posterior reversible encephalopathy syndrome.

Other names for the posterior reversible encephalopathy syndrome are reversible posterior leukoencephalopathy syndrome, or posterior leukoencephalopathy syndrome [34, 35]. The lesion can also involve the cerebral cortex and another name for posterior reversible encephalopathy syndrome is occipital parietal encephalopathy [36]. Similar lesions can also be seen in the frontal lobes, basal ganglia, brain stem

Probable Moyamoya disease in a 7-year-old girl with left hemiparesis. **a** T2-weighted image shows mild high signal lesions in the right basal ganglia and parieto-occipital cortex. **b** DW image clearly shows these lesions as high signal intensity, representing acute infarcts. **c** MR angiography shows occlusion of the right middle cerebral artery and stenosis of the right internal carotid artery and bilateral posterior cerebral arteries (*arrows*).
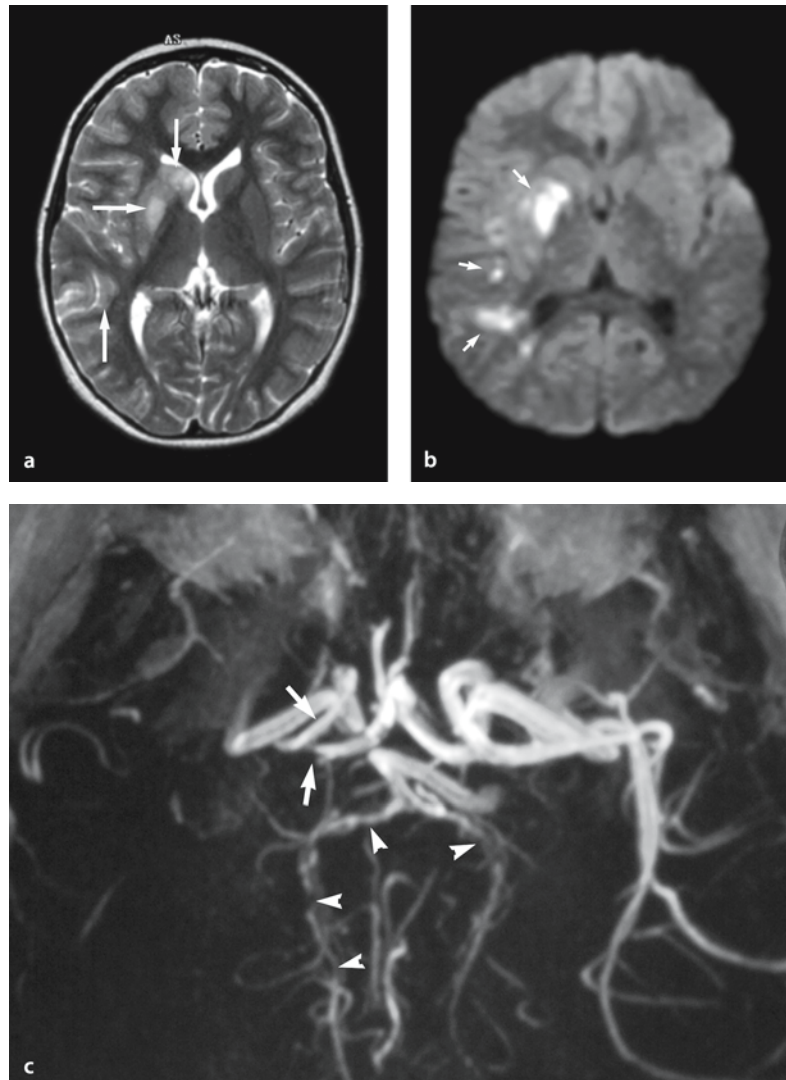
and cerebellum. In addition, the posterior reversible encephalopathy syndrome may not be entirely reversible, as infarction and hemorrhage may develop.

7.5.5 Hypertensive Encephalopathy

The primary cause of hypertensive encephalopathy is thought to be fluid extravasation through the interstitium, resulting from overdistension of the distal small cerebral vessels (breakthrough of autoregulation) causing vasogenic edema [37]. Ischemic processes can be triggered by vasospasm of the cerebral arteriole in response to a severe increase in blood pressure (overregulation). This will usually result in infarctions. Hypertensive encephalopathy is a clinical syndrome in which morphological and clinical phenomena are not correlated to each other. However, plasma proteins, including fibrin, are deposited in the walls of small arteries (hypertensive vasculopathy). This process leads to destruction of smooth muscle cells (fibrinoid necrosis).

The most common abnormality is seen in bilateral parieto-occipital subcortical white matter. However, these lesions can occur in the gray matter but can also involve the frontal lobes, basal ganglia, thalamus, cerebellum and brain stem. They are potentially reversible; however, if left untreated, permanent neurologic deficits or even death may occur as a result of ensuing cerebral infarction or hemorrhage. The prognosis probably depends on the extent of cytotoxic edema, which may be seen in severe cases. DW im-
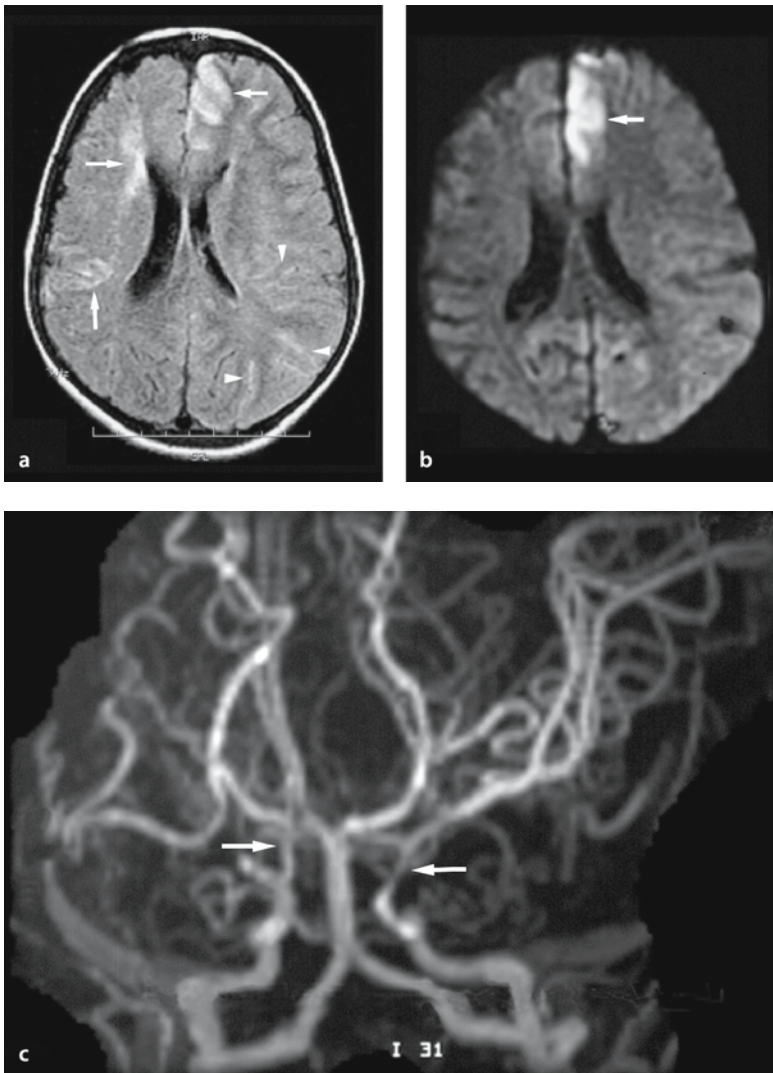
Figure 7.14 a–c

Sickle cell disease. 3-year-old boy presented with right side weakness as a recurrent stroke. He has been non-compliant to transfusion therapy. **a** FLAIR image shows multiple hyperintense lesions in the left frontal and right frontotemporal regions (arrows). FLAIR image also shows multiple curvilinear hyperintensity along the peripheral vessels that probably reflects the slow flow in the collateral circulation (arrowheads). **b** DW image shows the left frontal lesion as very hyperintense representing an acute infarct (arrow). **c** MRA shows bilateral stenoses of internal carotid, and middle and anterior cerebral arteries (arrows). (From [52])

aging can distinguish irreversible ischemic changes from reversible conditions with vasogenic edema alone (Fig. 7.15) [37].

7.5.6 Preeclampsia/Eclampsia

Preeclampsia is characterized by hypertension, abnormal peripheral edema, and proteinuria that can progress to eclampsia, which also involves seizures. Although CNS changes in severe preeclampsia and eclampsia represent a form of hypertensive encephalopathy, they also occur in normotensive individuals. The precise pathogenesis remains unclear. However, endothelial dysfunction due to circulating endothelial toxins or antibodies against the endothe-

lium can be the primary cause [38]. MR findings in patients with severe preeclampsia/eclampsia are often similar to those with hypertensive encephalopathy. However, intracranial hemorrhage and infarction (Fig. 7.16) are common [39]. Bilateral external capsule or basal ganglia lesions are also common [40]. DW imaging can discriminate a cytotoxic edema from vasogenic edema [41].

Hemolysis, elevated liver enzymes and low platelets (HELLP syndrome) is a thrombotic microangiopathic vasculopathy in pregnancy. Fatalities are attributable to intracranial hemorrhage, which may occur either in isolation or as part of the HELLP syndrome. The DW imaging findings are similar to those in eclampsia/preeclampsia.

7.5.7 Immunosuppressive Drug-Induced Vasculopathy

Cyclosporine, tacrolimus (FK506) and interferon-α are effective immunosuppressive agents for the treatment of organ transplant rejection. Previous theories regarding the mechanism of neurotoxicity include neuropeptide-mediated ischemia and high-pressure failure of cerebral autoregulation [42]. Neurotoxicity usually coexists with hypertensive crisis; however, it also occurs in normotensive individuals. These drugs have profound effects directly on the endothelium and cause release of potent vasoconstrictors such as endothelin. Disruption of the blood–brain barrier with possible focal loss of vascular autoregulation causes extravasation of fluid, which leads to vasogenic edema.
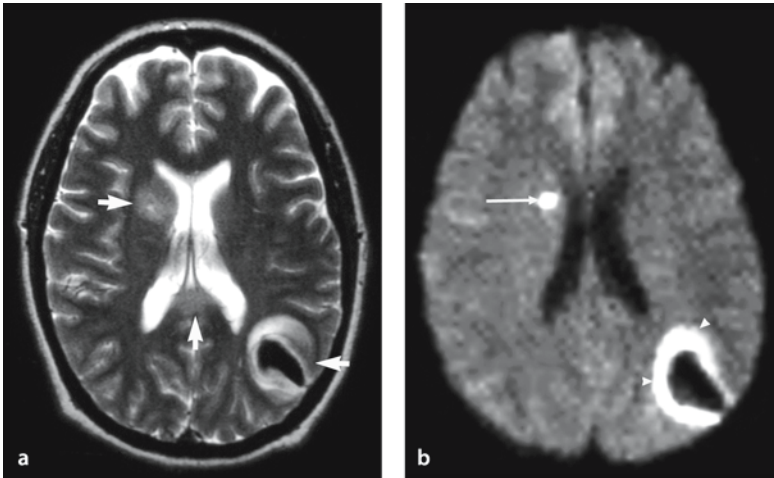
Figure 7.16 a,b

Eclampsia in a 30-year-old woman with seizures. **a** T2-weighted image shows high signal intensity lesions in the right corona radiata, posterior corpus callosum and left parieto-occipital region (*arrows*). The lesion in the left parieto-occipital region has a central very low signal intensity, representing hemorrhage. **b** On DW image, a small infarct in the right corona radiata (*arrow*) and a hemorrhagic infarct in the left parieto-occipital region (*arrowheads*) are shown as hyperintense associated with decreased ADC (not shown). The lesion in the posterior corpus callosum represents vasogenic edema
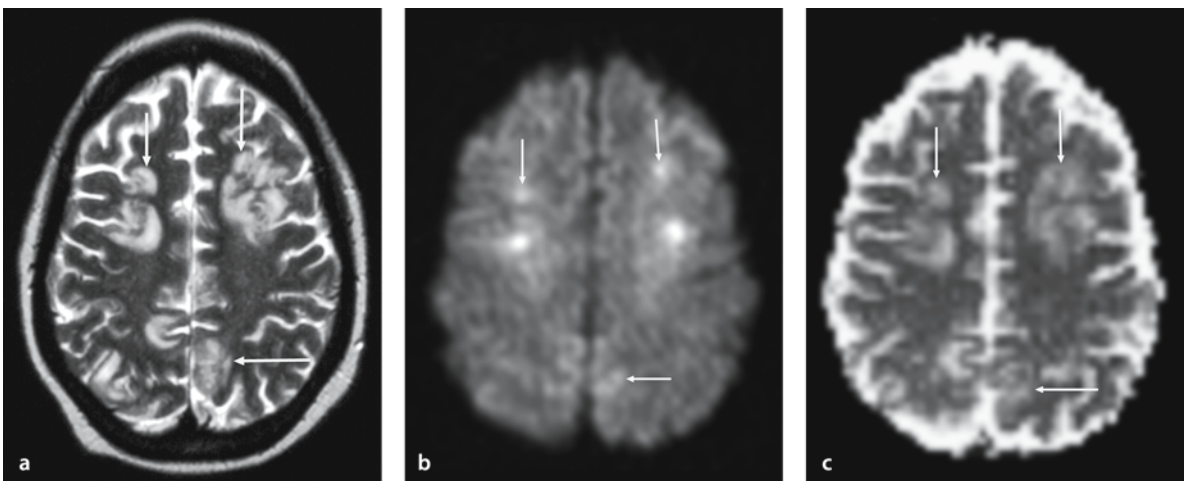
Figure 7.17 a–c

Tacrolimus neurotoxicity in a 42-year old woman with confusion after liver transplantation. **a** T2-weighted image shows high signal intensity lesions in the bilateral fronto-parieto-occipital subcortical white matter (*arrows*). **b** On DW image, these lesions show slightly hyperintense or isointense signal intensity (*arrows*). **c** ADC map shows increased ADC, which with hyperintense lesions (*arrows*) on DW image indicates T2 shine-through effect. These lesions were resolved on follow-up MRI (not shown)

Magnetic resonance imaging shows signal changes within the cortex and subcortical white matter in the occipital, posterior temporal, parietal and frontal lobes (Fig. 7.17). Non-transplant patients or those with total body irradiation develop white matter lesions, whereas those conditioned with chemotherapy develop mixed cortical and white matter lesions [43].

7.5.8 Uremic Encephalopathy and Hemolytic Uremic Syndrome

Uremic encephalopathy is the name given to a brain syndrome that occurs in patients with renal failure. The pathogenesis is unknown, but it has been hypothesized that it may be caused by various toxins associated with uremia (elevated parathyroid hormone level, hypercalcemia, and other metabolic abnormalities) [44]. MR imaging usually shows reversible bilateral symmetric white matter lesions. The lesions can also involve the basal ganglia or cortex. DW imaging usually shows iso- or slightly hyperintense lesions with increased ADC, mainly representing vasogenic edema (Fig. 7.18). Follow-up MRI can show cortical laminar necrosis on T1-weighted images.

Hemolytic uremic syndrome is defined as a multiorgan disease characterized by the triad of microangiopathic hemolytic anemia, thrombocytopenia and uremia. CNS complications are commonly seen (20–50%) [45]. Hemolytic uremic syndrome caused by O-157 *Escherichia coli* enterocolitis can potentially result in fatal CNS complications in infants and children. MR imaging sometimes shows irreversible lesions in the basal ganglia or cortex, representing infarction or cortical laminar necrosis. DW imaging can show these lesions as hyperintense with decreased ADC (Fig. 7.19).
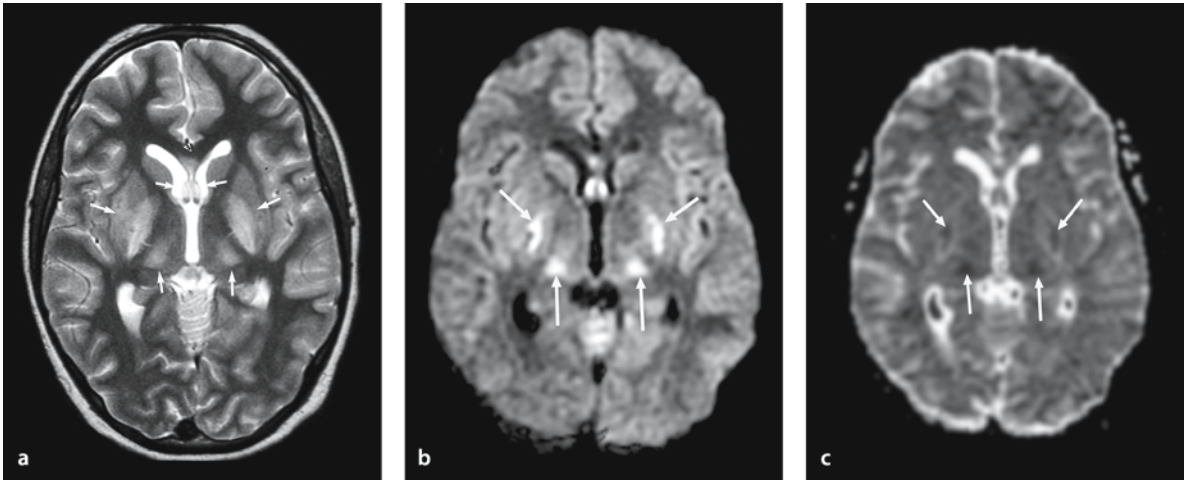
Figure 7.19 a–c

Hemolytic uremic syndrome in a 12-year-old girl with bloody diarrhea. **a** T2-weighted image shows high signal intensity lesions in the bilateral basal ganglia, thalami and fornices (*arrows*). **b** DW image shows these lesions as hyperintensity. **c** ADC map shows these lesions as decreased ADC

7.5.9 Thrombotic Thrombocytopenic Purpura

Thrombotic thrombocytopenic purpura is a multisystem vasculopathy characterized by microangiopathic hemolytic anemia, thrombocytopenia, renal involvement, fluctuating neurologic manifestations and fever [46]. Neuropathology shows hyaline thrombosis and occlusion of capillaries and arterioles without surrounding inflammatory reaction, which results in infarcts and petechial hemorrhages. MR findings are variable, ranging from punctate white matter lesions to posterior reversible encephalopathy syndrome, multifocal gray matter edema, infarction and hemorrhage. DW imaging can differentiate between these lesions (Fig. 7.20), which is important since some of the lesions seen on T2-weighted images may disappear following treatment with plasma exchange [47].

7.5.10 Cerebral Amyloid Angiopathy

Cerebral amyloid angiopathy is characterized by deposition of homogeneous eosinophilic material in the media and adventitia of arterioles and small arteries of the cortex and leptomeninges. The usual neurolog-

ic presentation is spontaneous hemorrhage. Gardientecho T2*-weighted image is sensitive to detect microangiopathy-related microbleeds. DW image and the b0 image can show such micobleeds as low signal intensity spots [48].

7.6 Conclusion

Diffusion-weighted imaging is useful in detecting acute infarctions and in differentiating diseases that show a cytotoxic edema from those with vasogenic edema in patients with CNS vasculitis and vasculopathy. Overall, lesions demonstrating cytotoxic edema are usually irreversible and those with vasogenic edema are often reversible. Thus, DW imaging is an important tool to establish a prognosis and to determine the best treatment.

Thrombotic thrombocytopenic purpura in a 53-year-old woman with altered mental status and seizures. **a** Computed tomography shows a hemorrhage in the right parieto-occipital area (*arrow*) and a wedged-shaped area of low density more peripherally in the right occipito-parietal area (*arrowheads*). **b** T2-weighted and **c** FLAIR images show corresponding hyperintense lesions in the deep white matter and right occipito-parietal area (*arrowheads*). Hemorrhage is seen as a hypointense lesion (*arrow*). **d** On DW image, deep white matter lesions are isointense, mainly representing vasogenic edema, while a cortical lesion in the right occipito-parietal area is hyperintense, representing acute infarction (*arrowheads*). Hemorrhage is hypointense with a hyperintense rim (*arrow*)
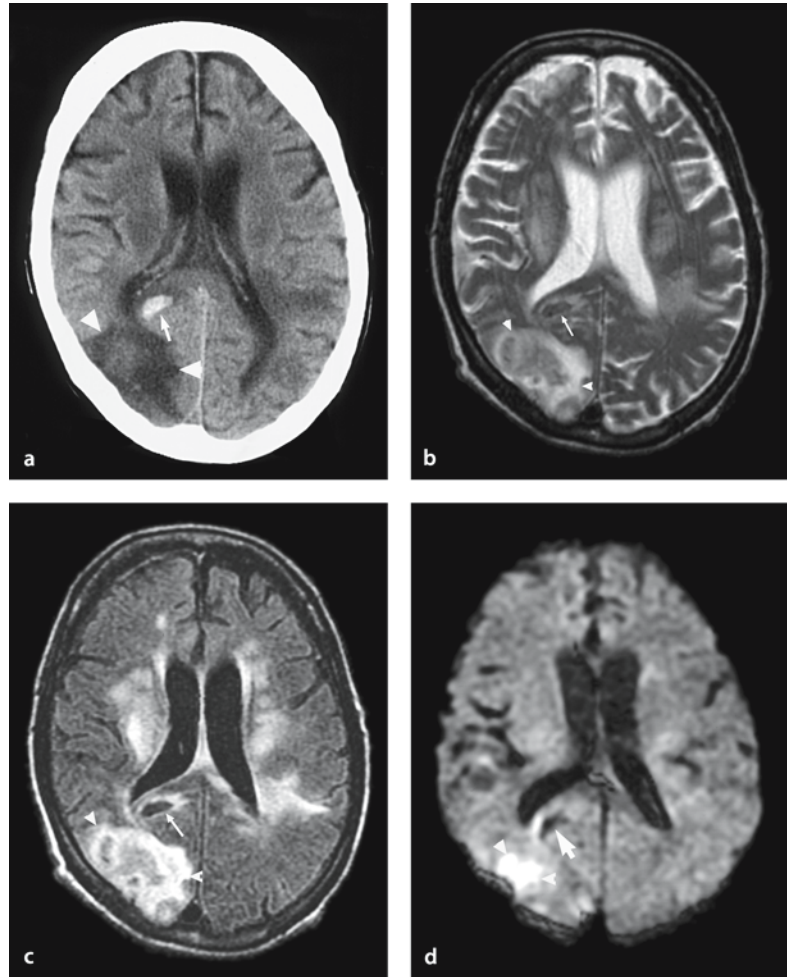
References

1. Berlit P (1994) The spectrum of vasculopathies in the differential diagnosis of vasculitis. Semin Neurol 14:370–379
2. Lie JT (1997) Classification and histopathologic spectrum of central nervous system vasculitis. Neurologic Clinics 15:805–819
3. Ebisu T, Naruse S, Horikawa Y, Ueda S, Tanaka C, Uto M, Umeda M, Higuchi T (1993) Discrimination between different types of white matter edema with diffusion-weighted MR imaging. J Magn Res Imaging 3:863–868
4. Aisen AM, Gabrielsen TO, McCune WJ (1985) MR imaging of systemic lupus erythematosus involving the brain. AJR Am J Roentgenol 144:1027–1031
5. Moritani T, Shrier DA, Numaguchi Y, Takahashi C, Yano T, Nakai K, Zhong J, Wang HZ, Shibata DK, Naselli SM (2001) Diffusion-weighted MR imaging of CNS involvement in systemic lupus erythematosus. Academic Radiology 8:741–753
6. Kocer N, Islak C, Siva A, Saip S, Akman C, Kantarci O, Hamuryudan V (1999) CNS involvement in neuro-Behçet syndrome: an MR study. AJNR Am J Neuroradiol 20:1015–1024
7. Woolfenden AR, Hukin J, Poskitt KJ, Connolly MB (1998) Encephalopathy complicating Henoch–Schonlein purpura: reversible MRI changes. Pediatr Neurol 19:74–77
8. Hinchey J, Chaves C, Appignani B, Breen J, Pao L, Wang A, Pessin MS, Lamy C, Mas JL, Caplan LR (1996) A reversible posterior leukoencephalopathy syndrome. N Engl J Med 334:494–500
9. Parisi JE, Moore PM (1994) The role of biopsy in vasculitis of the central nervous system. Semin Neurol 14:341–347
10. Jennette JC, Falk RJ, Milling DM (1994) Pathogenesis of vasculitis. Semin Neurol 14:291–299
11. Valente RM, Conn DL (1994) Current therapies for systemic vasculitis. Semin Neurol 14:380–386
12. Pomper MG, Miller TJ, Stone JH, et al. (1999) CNS vasculitis in autoimmune disease: MR imaging findings and correlation with angiography. AJNR Am J Neuroradiol 20:75–85
13. Lie JT (1994) Primary (granulomatous) angiitis of the central nervous system: a clinicopathologic analysis of 15 new cases and a review of the literature. Hum Pathol 23:164–171
14. Harris KG, Tran DD, Sickels WJ, Cornell SH, Yuh WT (1994) Diagnosing intracranial vasculitis: the role of MR and angiography. AJNR Am J Neuroradiol 15:317–330

15. Campi A, Benndorf G, Filippi M, Reganati P, Martinelli V, Terreni MR (2001) Primary angiitis of the central nervous system: serial MRI of brain and spinal cord. Neuroradiology 43:599–607

16. Ay H, Sahin G, Saatci I, Soylemezoglu F, Saribas O (2002) Primary angiitis of the central nervous system and silent cortical hemorrhages. AJNR Am J Neuroradiol 23:1561–1563

17. Moore P (1989) Diagnosis and management of isolated angitis of the central nervous system. Neurology 39:167–173

18. Brack A, Martinez-tabada V, Stanson A, et al. (1999) Disease pattern in cranial and large-vessel giant cell arteritis. Arthritis Rheum 42:311–317

19. Yamada I, Nakagawa T, Himeno Y, et al. (1998) Takayasu arteritis: evaluation of the thoracic aorta with CT angiography. Radiology 209:103–109

20. Provenzale JM, Allen NB (1996) Neurologic findings in polyarteritis nodosa. AJNR Am J Neuroradiol 17:1119–1126

21. Sehgal M, Swanson JW, DeRemee RA, et al. (1995) Neurologic manifestations of Churg-Strauss syndrome. Mayo Clin Proc 70:337–341

22. Liou HH, Liu HM, Chiang IP, et al. (1997) Churg-Strauss syndrome presented as multiple intracerebral hemorrhage. Lupus 6:279–282

23. Murphy JM, Gomez-Anson FB, Gillard JH, et al. (1999) Wegener granulomatosis: MR imaging findings in brain and meninges. Radiology 213:794–799

24. Castillo M (1994) Magnetic resonance imaging of meningitis and its complications. Top Magn Reson Imaging 6:53–58

25. DeLone DR, Goldstein RA, Petermann G, et al. (1999) Disseminated aspergillosis involving the brain: distribution and imaging characteristics. AJNR Am J Neuroradiol 20: 1597–1604

26. Lexa FJ (1995) Drug-induced disorders of the central nervous system. Semin Roentgenol 30:7–17

27. Gradon JD, Wityk R (1995) Diagnosis of probable cocaine-induced cerebral vasculitis by magnetic resonance angiography. South Med J 88:1264–1266

28. Hess DC (1997) Cerebral lupus vasculopathy. Mechanism and clinical relevance. Ann NY Acad Sci 823:154–168

29. Belmont HM, Abramson SB, Lie JT (1996) Pathology and pathogenesis of vascular injury in systemic lupus erythematosus. Interactions of inflammatory cells and activated endothelium. Arthritis Rheum 39:9–22

30. Sibbit WL, Sibbit RR, Griffey RH, et al. (1989) Magnetic resonance and computed tomographic imaging in the evaluation of acute neuropsychiatric disease in systemic lupus erythematosus. Ann Rheum Dis 48:1014–1022

31. Yamada I, Himeno Y, Nagaoka T, et al. (1999) Moyamoya disease: evaluation with diffusion-weighted and perfusion echo-planar MR imaging. Radiology 212:340–347

32. Moran CJ, Siegel MJ, DeBaun MR (1998) Sickle cell disease: imaging of cerebrovascular complications. Radiology 206:311–321

33. Casey SO, Sampaio RC, Michel E, et al. (1998) Posterior reversible encephalopathy syndrome: utility of fluid-attenuated inversion recovery MR imaging in the detection of cortical and subcortical lesions. AJNR Am J Neuroradiol 21:1199–1206

34. Hinchey J, Chaves C, Appignani B, et al. (1996) A reversible posterior leukoencephalopathy syndrome. N Engl J Med 334:494–500

35. Ay H, Buonanno FS, Schaefer PW, Le DA, et al. (1998) Posterior leukoencephalopathy without severe hypertension: utility of diffusion-weighted MRI. Neurology 51:1369–1376

36. Pavlakis SG, Frank Y, Kalina P, et al. (1997) Occipital-parietal encephalopathy: a new name for an old syndrome. Pediatr Neurol Feb;16:145–148

37. Schwartz RB, Mulkern RV, Gudbjartsson H, et al. (1998) Diffusion-weighted MR imaging in hypertensive encephalopathy: clues to pathogenesis. AJNR Am J Neuroradiol 19:859–862

38. Schwartz RB, Feske SK, Polak JF, et al. (2000) Preeclampsia-eclampsia: clinical and neuroradiographic correlates and insights into the pathogenesis of hypertensive encephalopathy. Radiology 217:371–376

39. Ursell MR, Marras CL, Farb R, et al. (1998) Recurrent intracranial hemorrhage due to postpartum cerebral angiopathy: implications for management. Stroke 29:1995–1998

40. Digre KB, Varner MW, Osborn AG, et al. (1993) Cranial magnetic resonance in severe preeclampsia vs eclampsia. Arch Neurol 50:399–406

41. Schaefer PW, Mulkern RV, Gudbjartsson H, et al. (1997) Diffusion-weighted imaging discriminates between cytotoxic and vasogenic edema in a patient with eclampsia. Stroke 28:1082–1085

42. Coley SC, Porter DA, Calamante F, et al. (1999) Quantitative MR diffusion mapping and cyclosporine-induced neurotoxicity. AJNR Am J Neuroradiol 20:1507–1510

43. Bartynski WS, Zeigler Z, Spearman MP, Lin L, Shadduck RK, Lister J (2001) Etiology of cortical and white matter lesions in cyclosporin-A and FK-506 neurotoxicity. AJNR Am J Neuroradiol 22:1901–1914

44. Okada J, Yoshikawa K, Matsuo H, et al. (1991) Reversible MRI and CT findings in uremic encephalopathy. Neurodiology 33:524–526

45. Schmidt S, Gudinchet F, Meagher-Villemure K, et al. (2001) Brain involvement in haemolytic-uraemic syndrome: MRI features of coagulative necrosis. Neuroradiology Jul;43(7):581–585

46. Bakshi R, Shaikh ZA, Bates VE, et al. (1999) Thrombotic thrombocytopenic purpura: brain CT and MRI findings in 12 patients. Neurology 52:1285–1288

47. D'Aprile P, Farchi G, Pagliarulo R, et al. (1994) Thrombotic thrombocytopenic purpura: MR demonstration of reversible brain abnormalities. AJNR Am J Neuroradiol 15:19–20

48. Fazekas F, Kleinert R, Roob G, et al. (1999) Histopathologic analysis of foci of signal loss on gradient-echo T2*-weighted MR images in patients with spontaneous intracerebral hemorrhage: evidence of microangiopathy-related microbleeds. AJNR Am J Neuroradiol. 20: 637–42.

49. Moritani T, Hiwatashi A, Shrier DA, et al. (2003) CNS vasculitis and vasculopathy Efficacy and usefulness of diffusion-weighted echo-planar MR imaging. Clinn Imaging. In press.

50. Hiwatashi A, Garber T, Moritani T, Kinoshita T, Westesson P-L (2003) Diffusion-weighted MR Imaging of neuro_Behcet disease: a case report Neuroradiology 45: 468–471.

51. Moritani T, Shrier DA, Numaguchi Y, et al. (2001) Diffusion-weighted MR imaging of CNS involvement in systemic lupus erythematosus. Academic Radiology 8: 741–753

52. Moritani T, Numaguchi Y, Lerner NB, et al. (2003) Sickle Cell Cerebrovascular Disease: usual and unusual findings on MR Imaging and MR Angiography. Clin Imaging. In press

53. Kinoshita T, Moritani T, Shrier DA, et al. (2003) Diffusion-weighted MR imaging of posterior reversible leukoencephalopathy syndrome. A pictorial essay. Clin Imaging. 27: 307–15.

Epilepsy

8.1 Definition

Epilepsy is a chronic brain disorder, which has a wide spectrum of underlying causes. It is characterized by recurrent seizures due to excessive discharge of cerebral neurons (epileptic seizures) and is associated with a variety of clinical and laboratory manifestations [1]. Epileptic seizures are defined as the clinical manifestation of abnormal excessive neuronal activity in cerebral gray matter.

8.2 Classification

The international classification of epileptic seizures is useful to describe the patients' symptoms, but this is often only the first step in the diagnostic process (Table 8.1) [2]. If the clinical characteristics are associated with a recognizable group of features, such as age of onset, genetic background and course, they may constitute an epileptic syndrome. The international classification of the epilepsy and epileptic syndromes classifies epilepsy as localized or generalized, and idiopathic or symptomatic (Table 8.2) [2].

Table 8.1. Classification of epileptic seizures

1. Partial (focal, local) seizures
   Simple partial seizures
   Complex partial seizures
   Partial seizures evolving to secondary generalized seizures

2. Generalized seizures (convulsive or non-convulsive)
   Absence seizures
   Myoclonic seizures
   Clonic seizures
   Tonic seizures
   Tonic–clonic seizures
   Atonic seizures

3. Unclassified epileptic seizures

Table 8.2. Classification of epilepsies and epileptic syndromes

1. Localization-related epilepsies and syndromes
   Idiopathic with age-related onset
   Symptomatic (temporal, frontal, parietal or occipital epilepsy)

2. Generalized epilepsies and syndromes
   Idiopathic with age-related onset
   Idiopathic or symptomatic
   (West syndrome, Lennox–Gestaut syndrome)
   Symptomatic
   (early myoclonic encephalopathy, specific syndromes)

3. Epilepsies and syndromes undetermined as to whether they are focal or generalized
   Neonatal seizures

4. Special syndromes
   Febrile convulsions
   Drug-induced seizures
   Eclampsia
   Chronic progressive epilepsia partialis continua of childhood

8.3 Mechanisms and Pathophysiology of Epilepsy

The fundamental mechanisms of epilepsy can be studied at the basic level of the molecular environment of the cell. This involves cellular systems such as membrane channels, neuronal systems, cell populations and cell-to-cell interactions.

Several neurotransmitter systems are important for the mechanisms of epilepsy [3]. Glutamate is an excitatory synaptic transmitter in cerebral cortex and hippocampus. The primary receptors are divided into two groups: N-methyl-D-aspartate (NMDA) receptors and non-NMDA receptors [4]. Excessive release of glutamate activates the NMDA receptor, depolarizes the postsynaptic terminals, and induces changes in membrane function and ionic homeosta-

sis. NMDA receptors, which have a high density in the hippocampus and other parts of the limbic system, can be related to regions that are susceptible to excitotoxic damage [5]. In some models of epileptogenesis it has been possible to block bursts of discharges by NMDA channel antagonists [6].

Another neurotransmitter related to epilepsy is gamma-aminobutyric acid (GABA), which is an inhibitor of discharges. Loss of GABAergic inhibition can generate epileptiform activity, which is believed to be important in chronic epilepsy [3].

The onset of epileptiform activity presupposes that an epileptic focus must exist where the seizure originates. The epileptic focus may exist in a discrete group of neurons, such as the CA1 pyramidal cells in the hippocampus, or over a larger region, including hippocampus and entorhinal cortex [5]. The seizure attack is associated with abnormal discharges in populations of synchronously active neurons. The spread of the seizure may be associated with an accumula-

tion of extracellular substances, such as potassium ions or excitotoxic amines, and electrical gating mechanisms among neurons.

8.4 Magnetic Resonance Imaging of Epilepsy

Magnetic resonance imaging is widely used to evaluate patients with seizures and can detect structural brain abnormalities that may give rise to the epileptic disorder, e.g. stroke, anoxic injury, trauma, tumor, infections, demyelination and congenital anomalies. The most common cause of seizures in patients older than 45 years is stroke [7]. Intracranial tumors are often associated with epileptic seizures, and trauma is the most common cause of seizures in patients aged 15–24 years [8]. Up to 5% of epilepsy cases have a history of central nervous system infections [9].

Magnetic resonance imaging has become very useful for the diagnosis of an important cause of
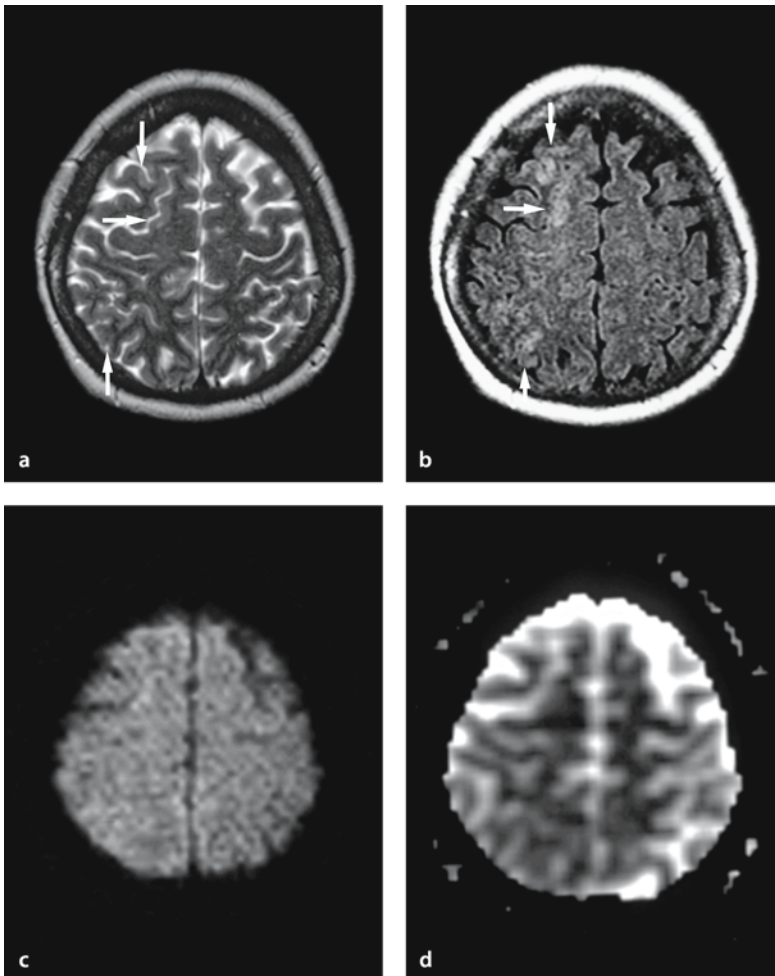
Figure 8.1 a–d

Postictal cerebral lesion following partial seizure evolving to generalized seizure in a 60-year-old woman. **a** T2-weighted and **b** FLAIR images 24 h after seizures show hyperintense lesions (*arrows*) in the right fonto-parietal cortex. **c** DW image and **d** ADC map show these lesions as isointense, probably representing mild vasogenic edema. These lesions were resolved on the 20-day follow-up MRI (not shown)

seizure, namely mesial temporal (hippocampal) sclerosis [10–14]. Most seizure activity resolves within a few minutes without persistent neurologic deficits. However, transient hemiparesis (Todd's paralysis), sensory loss, persistent altered mental status, or aphasia occasionally occurs in epilepsy. MR imaging can show secondary effects of seizures on the brain [15–26]. For example, mesial temporal sclerosis, which may occur as a primary lesion, may also arise as a lesion secondary to status epilepticus [19, 21].

8.4.1 Diffusion-Weighted Imaging in Epilepsy

On routine MR imaging, signal alterations related to ictal or postictal status can be misdiagnosed as infarctions, tumorous conditions, inflammatory diseases or demyelinating diseases. This may occur because routine MR sequences will not separate vasogenic edema from cytotoxic edema. Such misdiagnoses may result in unnecessary invasive treatment. Diffusion-weighted (DW) imaging is helpful in eval-
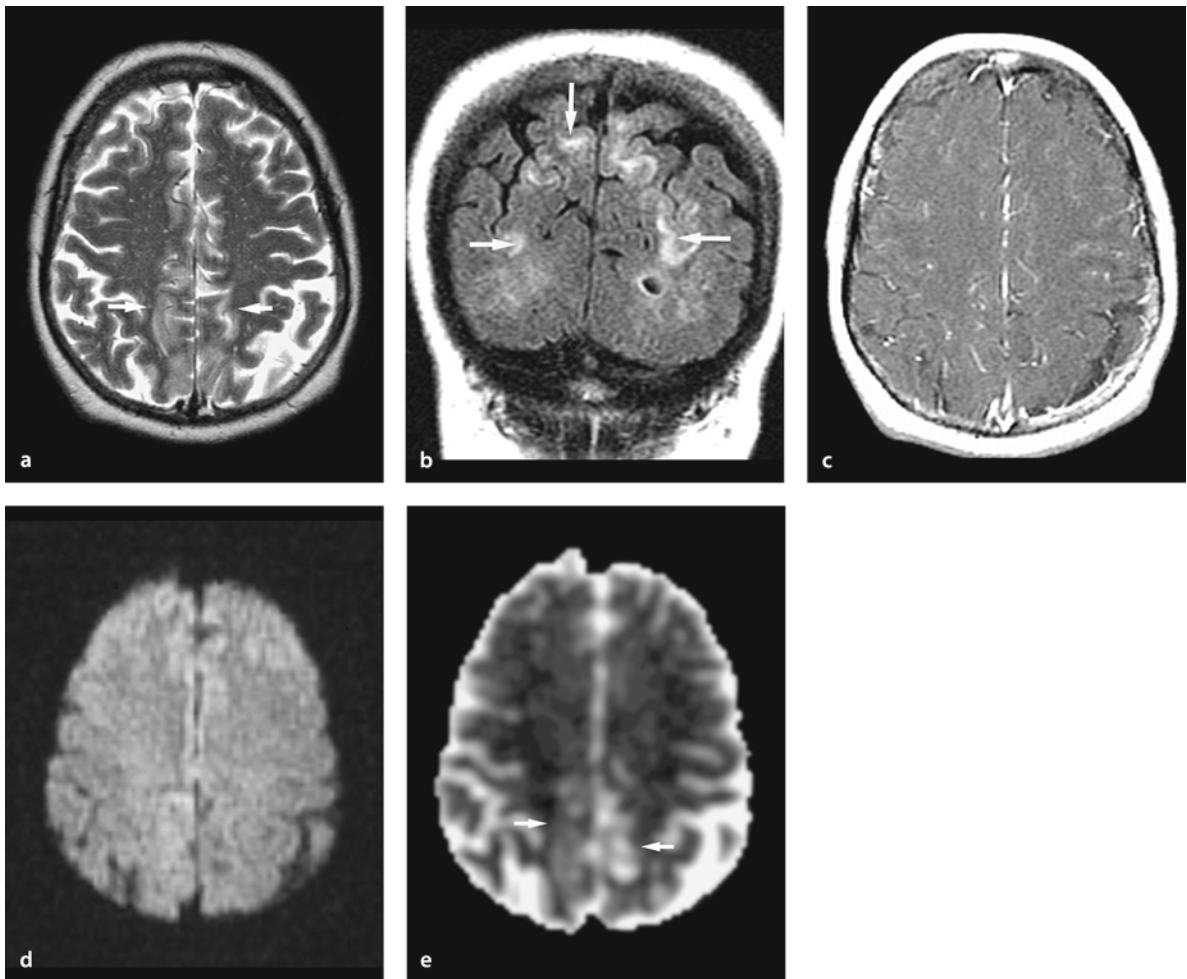
Figure 8.2 a–e

Postictal cerebral lesion following partial seizure in a 64-year-old woman with generalized seizure secondary to hyperglycemia. **a** T2-weighted image 24 h after seizures shows hyperintense lesions in bilateral medial fronto-parietal cortex (*arrows*). **b** Coronal FLAIR image also shows cortical and subcortical hyperintense lesions (*arrows*). **c** Gadolinium-enhanced T1-weighted image shows no abnormal enhancement. **d** DW image shows these lesions as isointense with increased ADC (**e**) (*arrows*), representing vasogenic edema
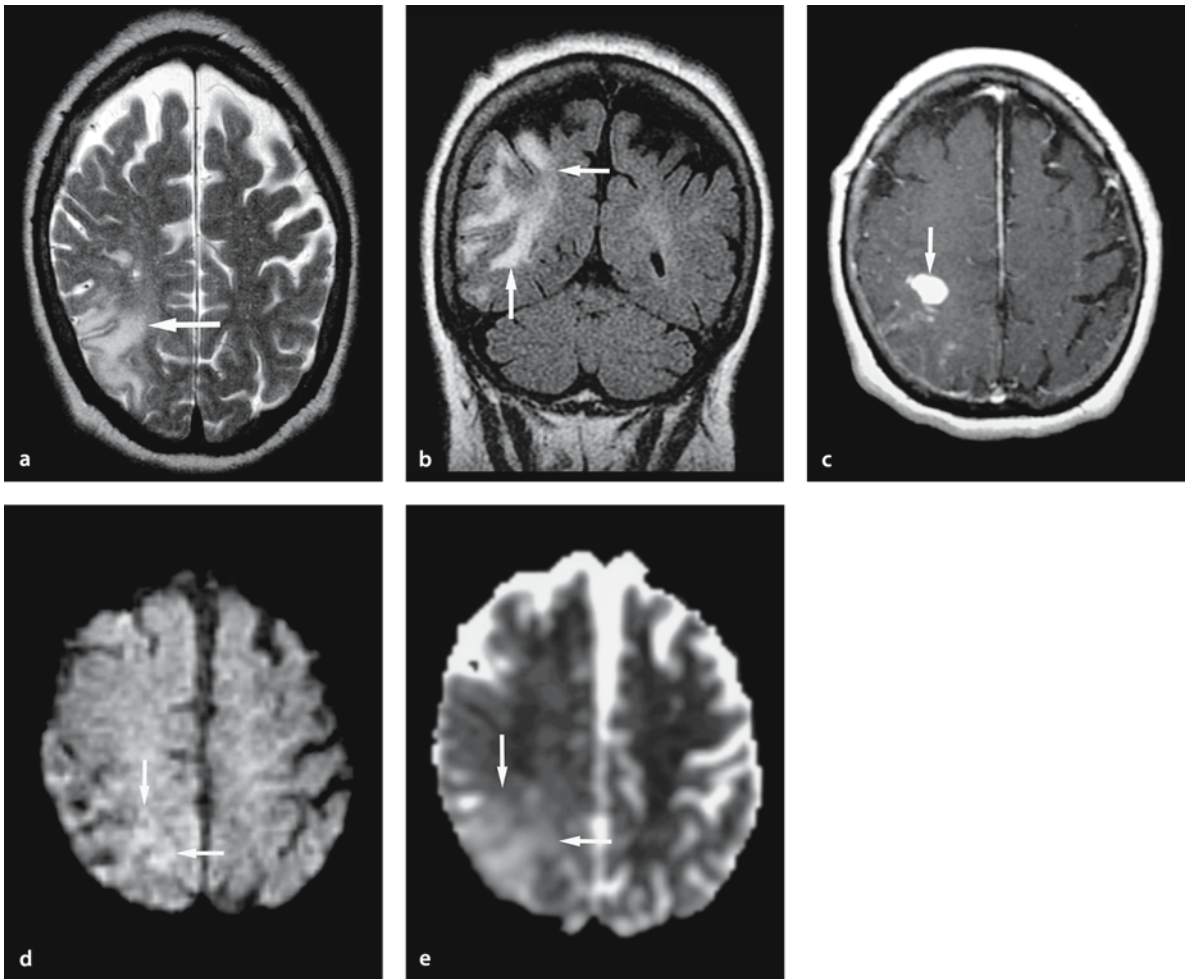
Figure 8.3 a–e

Postictal cerebral lesion following partial seizures with or without secondary generalization in a 75-year-old woman. **a** T2-weighted image at 4 days after seizures shows hyperintense lesions in the right fronto-parietal region (*arrow*). **b** Coronal FLAIR image shows cortical and subcortical hyperintense lesions (*arrows*). **c** Gadolinium-enhanced T1-weighted image shows a dense enhancing nodule (*arrow*) and leptomeningeal enhancement. **d** DW image shows these lesions as isointense to slightly hyperintense (*arrows*), with increased ADC (*arrows*) (**e**). Brain biopsy was performed and proved the lesions to be acute ischemic changes

uating epilepsy, as it will detect cytotoxic edema and can differentiate between cytotoxic and vasogenic edema in ictal and postictal lesions of the brain.

8.4.2 Magnetic Resonance Signal Alterations in Epilepsy

Variable MR findings have been reported in the brain in the ictal or postictal stage [15–26]. These findings include transient increase in T2 signal and swelling of the cerebral cortex, subcortical white matter and medial temporal lobe (including hippocampus), thalamus, claustrum and cerebellar hemispheres (Figs.
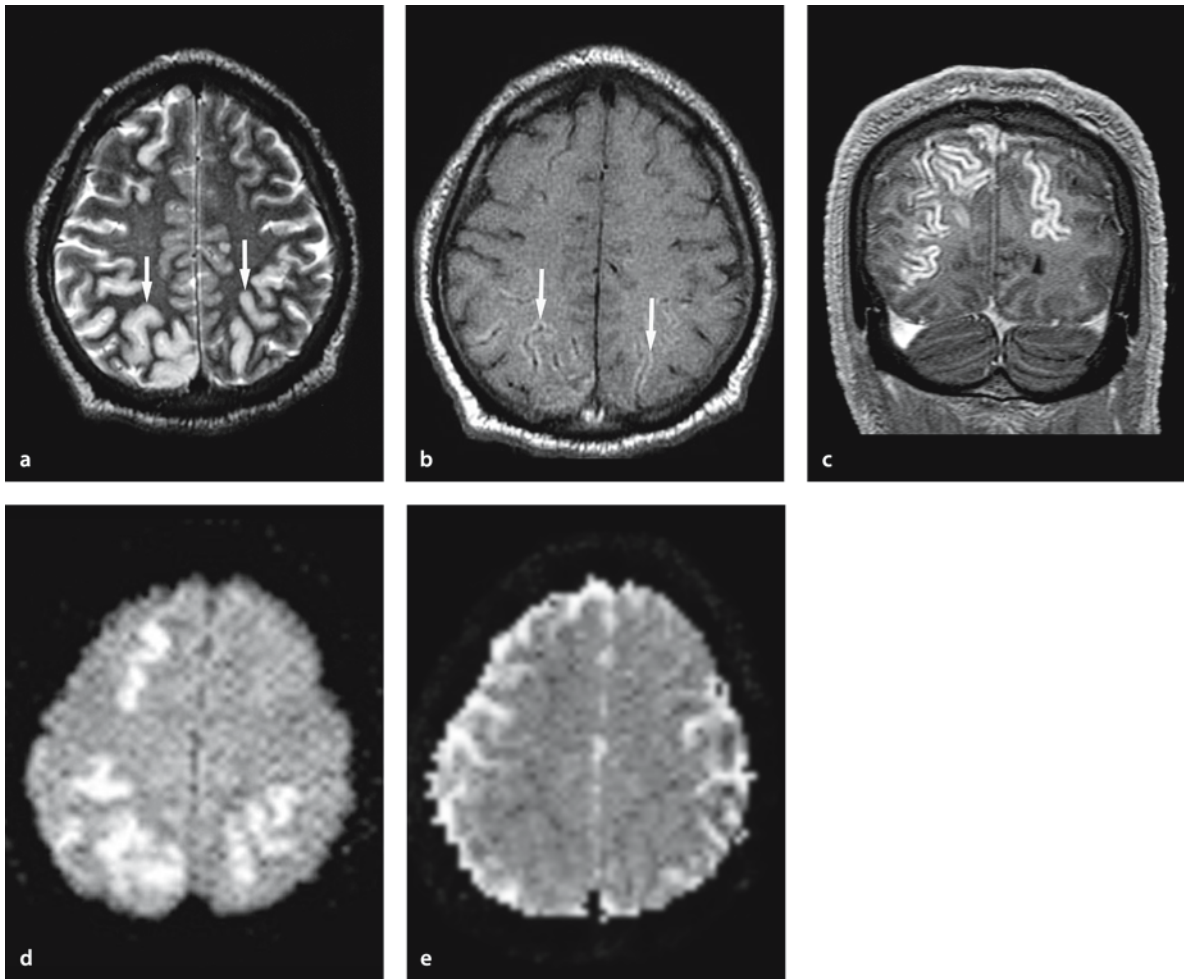
Figure 8.4 a–e

Postictal cerebral lesion following generalized tonic–clonic seizure in a 42-year-old male with alcohol withdrawal. **a** T2-weighted image shows hyperintense lesions (*arrows*) in bilateral fronto-parietal cortex. **b** T1-weighted image 8 days after the seizure shows gyriform high signal intensity in these lesions, representing cortical laminar necrosis (*arrows*). **c** Coronal gadolinium-enhanced T1-weighted image shows gyriform enhancement of these lesions. **d** DW image shows corresponding regions of hyperintensity. **e** ADC map shows almost normal ADC values of these lesions, suggesting a subacute phase of ischemia

8.1, 8.2, 8.3, 8.4, 8.5, 8.6 and 8.7). Cortical or subcortical lesions can be uni- or bilateral and they are predominantly found in the fronto-parietal regions. Whether periictal lesions are reversible or irreversible on MR imaging seems to depend on the duration and/or severity of the seizures.

8.4.3 Ictal Stage to Periictal Stage

During ictus there is an increase in metabolism (oxygen and glucose) in the seizure focus. This hypermetabolic state results in consumptive hypoxia, hypercarbia and lactic acidosis, which impair vascular autoregulation in the affected areas of cortex, leading to vasogenic edema and disruption of the blood–brain barrier [22]. If the seizures are not too prolonged, the
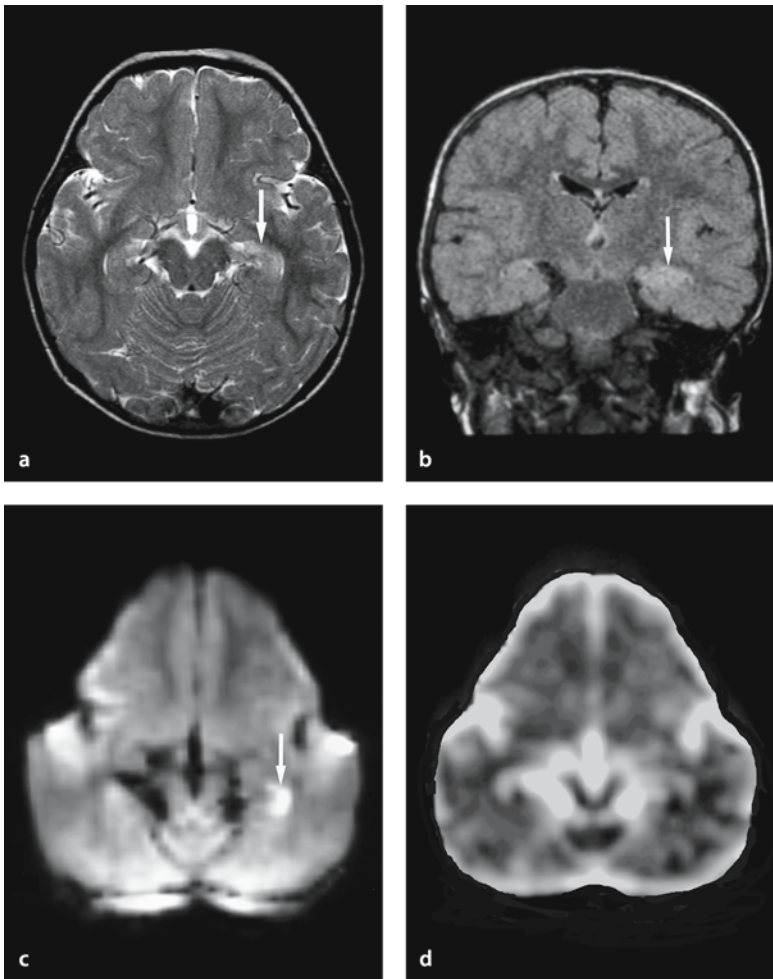
Figure 8.5 a–d

Hippocampal lesion following generalized tonic–clonic seizure in a 2-year-old female with febrile seizure leading to generalized tonic–clonic seizure. **a** T2-weighted and **b** FLAIR images 3 days after seizure show hyperintensity in the left hippocampus (*arrows*). **c** DW image shows increased signal in the left hippocampus (*arrows*) associated with normal or slightly decreased ADC (**d**), suggesting a subacute phase of the postictal hippocampal lesion

periictal brain lesions will only show transient T2 hyperintensity, mainly representing vasogenic edema. However, if the seizures are severe or prolonged, cytotoxic edema can develop. This is often seen in patients with generalized tonic–clonic seizure or status epilepticus (Figs. 8.4, 8.5, 8.6 and 8.7). Whether these lesions show enhancement or not depends on the degree of blood–brain barrier disruption (Figs. 8.2 and 8.3).

Vasogenic edema in periictal brain lesions has variable signal intensity on DW imaging, which is associated with an increase in ADC (Figs. 8.1, 8.2 and 8.3). As mentioned above, DW imaging is useful in detecting and differentiating cytotoxic from vasogenic edema.

8.4.4 Status Epilepticus

Status epilepticus is defined as continuous seizure activity that lasts longer than 30 minutes, or two or more sequential seizures that together last longer than 30 minutes and without full recovery of consciousness between the seizure attacks [28]. This is a serious event and should be treated aggressively, as the mortality associated with status epilepticus is about 8% in children and 30% in adults [28, 29].

In status epilepticus, neuronal injury is thought to result primarily from an excitotoxic mechanism mediated by intrinsic neuronal seizure activity. This is supported by the effect of kainic acid (an excitotoxic analog of glutamate), as shown in animal studies [30, 31]. Neuronal seizure activity will increase the release of glutamate from the pre-synaptic terminal of neuronal axons. The released glutamate crosses the

Figure 8.6 a–d

Hippocampal lesion following status epilepticus in a 55-year-old male with prolonged seizures associated with tacrolimus toxicity. **a** FLAIR image at 2 days after seizure shows high signal areas in the bilateral frontal deep white matter and the left hippocampus (*arrows*). **b** DW image (*y axis*) shows high signal in the left hippocampus (*arrow*). **c** ADC (*y axis*) shows low signal intensity (*arrow*) consistent with cytotoxic edema. **d** 7 months follow-up coronal FLAIR image shows the resolution of white matter changes and residual high signal intensity with atrophy in the left hippocampus (*arrow*)
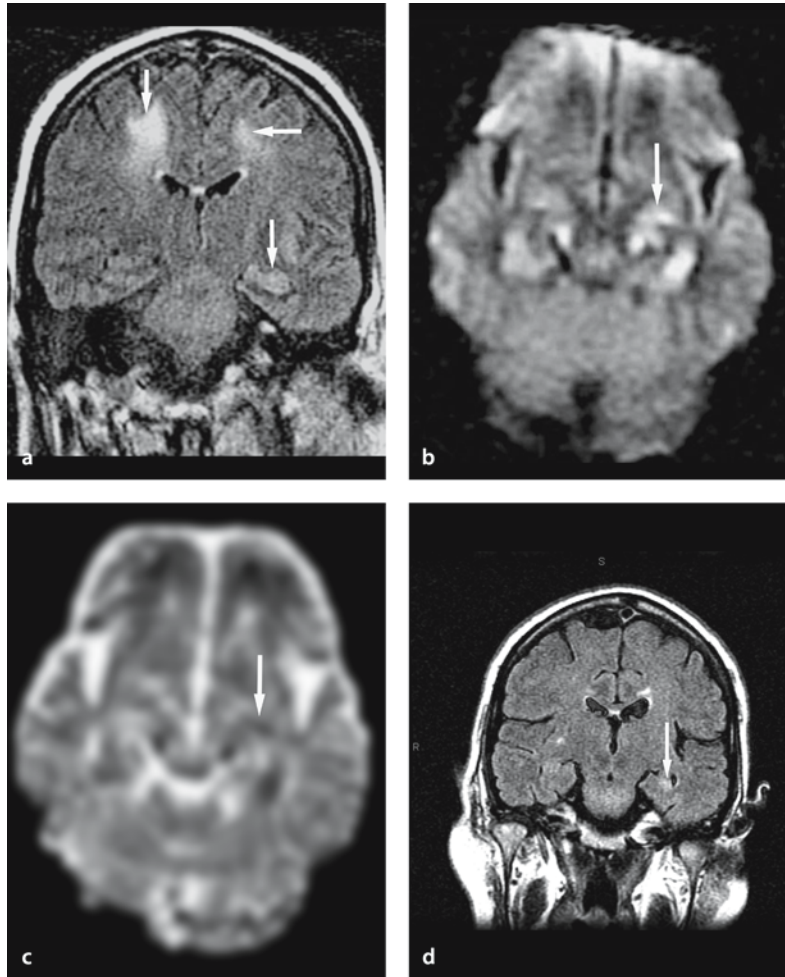
synaptic cleft to bind to NMDA receptors of the post-synaptic neurons, resulting in cytotoxic edema. Cytotoxic edema is also seen in the astrocytes as an acute phase of reactive astrocytosis [21].

8.4.5 Cytotoxic Edema in Status Epilepticus

Cytotoxic edema following status epilepticus can be at least partially reversible [22], as compared to cerebral ischemia, where these changes are usually irreversible. In cerebral ischemia, a significant compromise of blood supply leads to irreversible failure of energy metabolism. In sustained seizures, there is an increased cerebral metabolism with an increase in cerebral blood flow. This will maintain the energy state of the neuron provided there is sufficient oxygen supply.

The parts of the human brain that are most vulnerable include parts of the hippocampus (the CA1 and CA3 segments, and the hilus), amygdala, pyriform cortex, thalamus, cerebellum, and cerebral cortex. NMDA receptors are predominantly located in the CA1 of the hippocampus and layers 3 and 4 in the cerebral cortex [32, 33]. The Purkinje cell loss of the cerebellum, seen in severe epilepsy, may be explained by an increased demand for inhibition, resulting in GABA depletion and subsequent influx of calcium into neurons [34]. Unilateral hemispheric involvement is occasionally seen in status epilepticus.

Transient and reversible MR signal changes have been reported in patients following status epilepticus [16, 19–23]. On the other hand, other lesions have been proven irreversible, resulting in selective neuronal necrosis, gliosis and delayed neuronal death with subsequent atrophy [24–26] (Figs. 8.6 and 8.7). Following
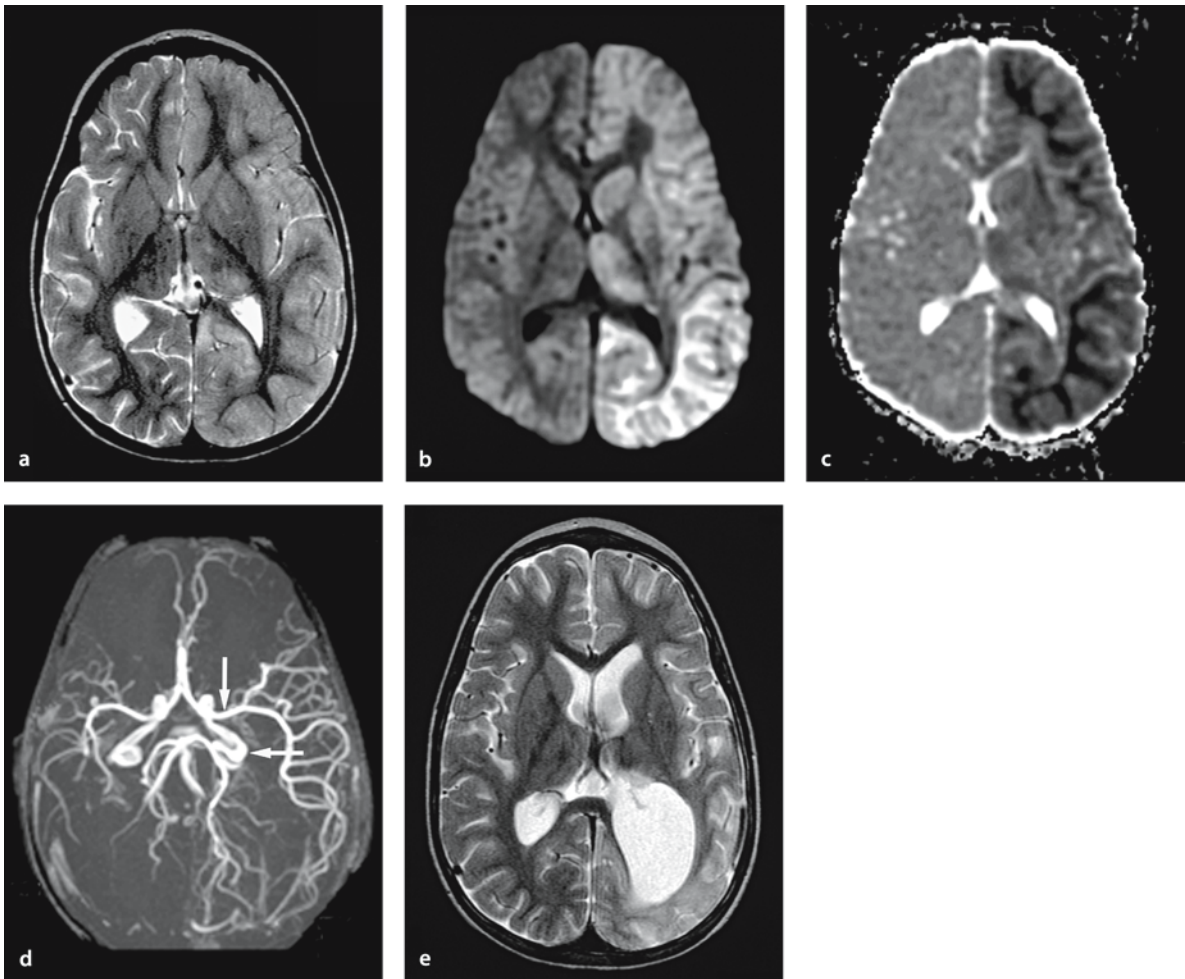
Figure 8.7 a–e

Hemiplegic hemiconvulsion epilepsy syndrome in a 2-year-old girl with partial status epilepticus involving the right face and hand. **a** T2-weighted image 24 h after seizure shows diffuse cortical hyperintense lesions in the entire left cerebral hemisphere, including the basal ganglia, and thalamus. **b** DW image shows diffuse left-sided cortical and subcortical hyperintense lesions with decreased ADC (**c**), representing cytotoxic edema. **d** MR angiography reveals dilatation of the left middle cerebral and posterior cerebral artery branches (*arrows*), representing hyperperfusion. **e** Diffuse atrophy with ventricular dilatation and hyperintense lesions in the left hemisphere seen on 5 months follow-up T2-weighted image.

status epilepticus, there has also been reported acute neuronal loss in the hippocampus accompanied by intense astrocytic reactions, called mesial temporal gliosis. This is pathologically different from mesial temporal sclerosis [16, 35, 36] (Fig. 8.6). However, these lesions may be the first step in the development of mesial temporal sclerosis [19, 21]. Increased apparent diffusion coefficient (ADC) in the hippocampus has been reported in mesial temporal sclerosis [27].

Diffusion-weighted imaging and ADC maps are more sensitive than conventional MR imaging to show both gray and white matter involvement, and discriminate between cytotoxic and vasogenic edema following status epilepticus [22]. In experimental status epilepticus models, ADC decrease was first seen at about 3 hours and lasted until 48 hours after the onset of seizures, after which time it normalized or even increased [37–42]. The definite time course of DW

imaging changes in humans is unknown, but areas of signal abnormalities on DW imaging and ADC are seen in cytotoxic edema following status epilepticus, although they are sometimes reversible, as mentioned above [22].

8.4.6 Other Imaging Techniques for Epilepsy

Several other newer MR imaging techniques have been used in epilepsy. These include MR angiography [20], perfusion-weighted imaging [23], single-photon emission computed tomography (SPECT) [43], xenon CT [44] and positron emission tomography (PET) [45]. MR spectroscopy can show metabolic changes such as decreased *N*-acetyl aspartate (NAA), and increased lactate and glutamate/glutamine peaks [46].

8.5 Hemiconvulsion–Hemiplegia Epilepsy Syndrome

Hemiconvulsion–hemiplegia epilepsy syndrome is one of the recognized sequelae of convulsive status epilepticus [47, 48] in infancy and early childhood. Epilepsia partialis continua (Rasmussen syndrome) is excluded on clinical grounds. In hemiconvulsion–hemiplegia epilepsy syndrome, DW imaging shows diffuse cytotoxic edema confined to one hemisphere (Fig. 8.7).

8.6 Focal Lesion in the Splenium of the Corpus Callosum in Epileptic Patients

The cause of the focal lesion sometimes seen in the splenium of the corpus callosum is not known. It has been speculated to represent transient focal edema, related to the transhemispheric connection and secondary generalized seizure activity [49]. Interhemi-

spheric propagation of the seizure activity is via the splenial callosal fibers. The splenium contains decussating fibers originating in the temporal lobe, which are likely to be involved in a secondarily generalized seizure. The lesion may be related to toxic effects of antiepileptic drugs such as dilantin, carbamazepine and vigabatrin [50]. Abrupt withdrawal and dose reduction of antiepileptic drugs may contribute to the transient edema, mediated by the influence of these drugs on fluid balance systems, namely arginine–vasopressin [51]. Conventional MRI shows a non-hemorrhagic, hyperintense lesion on T2-weighted and fluid-attenuated inversion-recovery (FLAIR) images, which is slightly hypointense on T1-weighted images (Fig. 8.8). There is no enhancement after administration of intravenous gadolinium. DW imaging shows an acute, hyperintense lesion in the splenium of the corpus callosum, with decreased ADC. This finding indicates that the lesion represents a cytotoxic edema in myelinated tracts (intramyelinic edema) in the corpus callosum, which can be a reversible lesion.

8.7 Conclusion

Routine MR imaging is widely used to evaluate various primary brain diseases that cause seizures. These include stroke, anoxic injury, trauma, tumor, infections, demyelination, congenital anomaly and many others. The typical MR finding in a seizure patient is an area of T2 hyperintensity, often located in the cerebral cortex, subcortical white matter, hippocampus, thalamus and/or cerebellum. DW imaging can provide additional information concerning the brain edema and tell whether it is primarily cytotoxic or vasogenic. This is important since cytotoxic edema following seizures indicates a more serious injury and, although often reversible, may result in brain atrophy and necrosis.
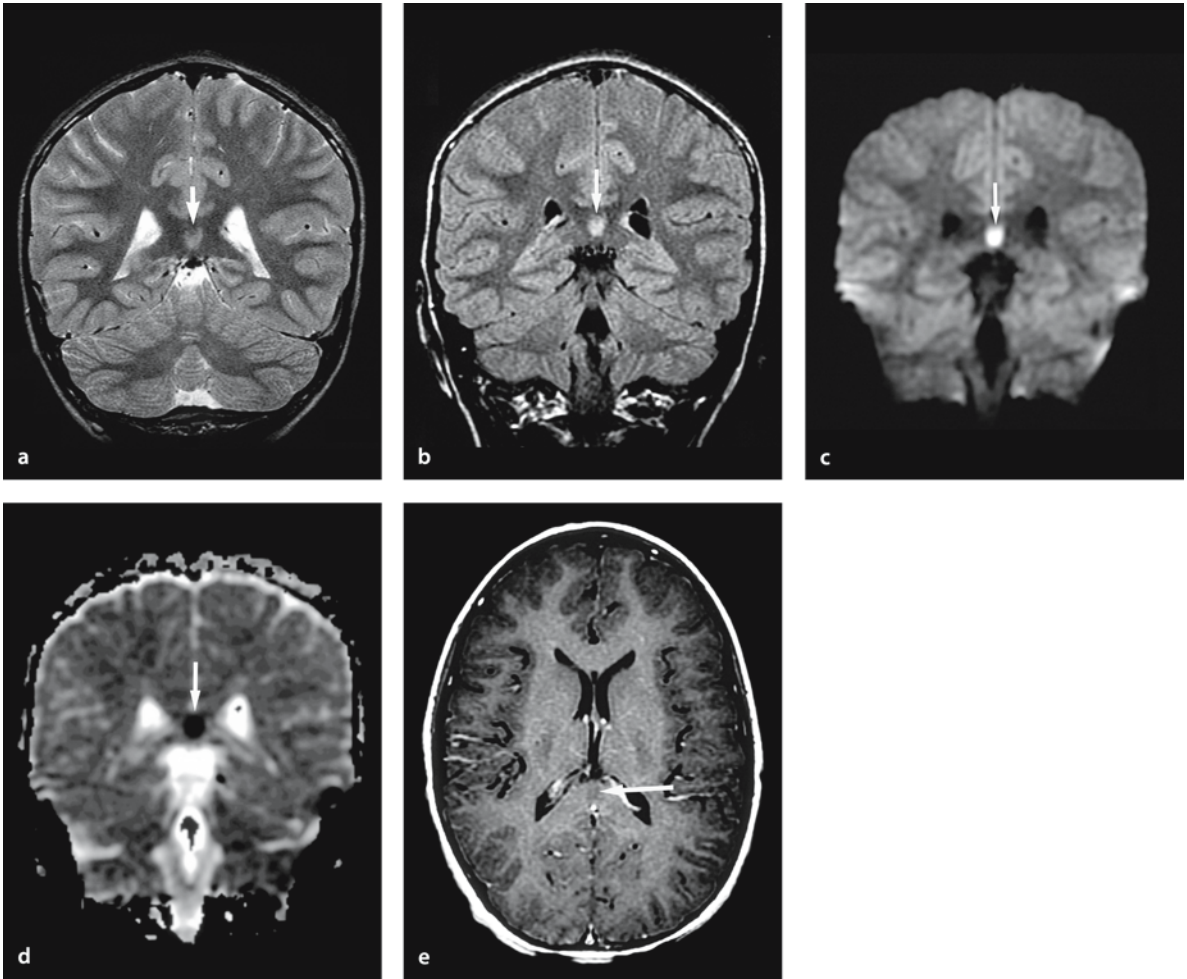
Figure 8.8 a–e

Focal lesion in the splenium of the corpus callosum in epilepsy in a 9-year-old presenting with intractable partial seizures since the age of 4 years. **a** Coronal T2-weighted and **b** FLAIR images 3 days after seizure show a focal hyperintense lesion in the central portion of the splenium of the corpus callosum (*arrow*). **c** Coronal DW image shows this lesion (*arrow*) as hyperintense associated with decreased ADC (**d**). **e** Gadolinium-enhanced T1-weighted image reveals mild hypointense lesion with no abnormal enhancement (*arrow*)

References

1. Gestaut H (1973) Dictionary of epilepsy, part 1: definitions. Geneva: World Health Organization

2. Commission on Classification and Terminology of the International League Against Epilepsy (1989) Proposal for revised classification of epilepsies and epileptic syndromes. Epilepsia 30:389–399

3. Wasterlain CG, et al. (1993) Pathophysiological mechanisms of brain damage from status epilepticus. Epilepsia 34(Suppl 1):S37–S53

4. Rothman SM, et al. (1987) Excitotoxicity and NMDA receptor. Trends Neurosci 10:301–304

5. Babb TL, Lieb JP, Brown WJ, Pretorius J, Crand PH (1984) Distribution of pyramidal cell density and hyperexcitability in the epileptic human hippocampal formation. Epilepsia 25:721–728

6. Herron CE, Williamson R, Collingridge GL (1985) A selective N-methyl-D-aspartate antagonist depresses epileptiform activity in rat hippocampal slices. Neurosci Lett 61:255–260

7. Aminoff MJ, Simon RP, Wiedemann E (1980) Status epilepticus. Causes, clinical features and consequences in 98 patients. Am J Med 69:657–666

8. Annegers JF, Hauser WA, Lee JR, Rocca WA (1995) Incidence of acute symptomatic seizures in Rochester, Minnesota, 1935–1984. Epilepsia 36:327–333

9. Durack DT, Whitly RJ, Scheld WM (1991) Approach to the patient with central nervous system infection. In: Sheld WM (eds). Infections of the central nervous system. New York: Raven Press, pp 41–86

10. Maertens PM, Machen BC, Williams JP, Evans O, Bebin J, Bassam B, Lum GB (1987) Magnetic resonance imaging of mesial temporal sclerosis: case reports. J Comput Tomogr 11:136–139

11. Heinz ER, Crain BJ, Radtke RA, Burger PC, Friedman AH, Djang WT, Wilkinson WE (1990) MR imaging in patients with temporal lobe seizures: correlation of results with pathologic findings. AJNR Am J Neuroradiol 11:827–832

12. Meiners LC, van Gils A, Jansen GH, de Kort G, Witkamp TD, Ramos LM, Valk J, Debets RM, van Huffelen AC, van Veelen CW, et al (1994) Temporal lobe epilepsy: the various MR appearances of histologically proven mesial temporal sclerosis. AJNR Am J Neuroradiol 15:1547–1555

13. Jack CR Jr, Rydberg CH, Krecke KN, Trenerry MR, Parisi JE, Rydberg JN, Cascino GD, Riederer SJ (1996) Mesial temporal sclerosis: diagnosis with fluid-attenuated inversion-recovery versus spin-echo MR imaging. Radiology 199:367–373

14. Lee DH, Gao FQ, Rogers JM, Gulka I, Mackenzie IR, Parrent AG, Kubu CS, Munoz DG, McLachlan RS, Blume WT, Girvin JP (1998) MR in temporal lobe epilepsy: analysis with pathologic confirmation. AJNR Am J Neuroradiol 19:19–27

15. Silverstein AM, Alexander JA (1998) Acute postictal cerebral imaging. AJNR Am J Neuroradiol 20:1485–1488

16. Chan S, et al. (1996) Reversible signal abnormalities in the hippocampus and neocortex after prolonged seizures. AJNR Am J Neuroradiol 17:1725–1731

17. Horowitz SW, et al. (1992) Complex partial seizure-induced transient MR enhancement. J Comput Assist Tomogr 16:814–816

18. Kassem-Moussa H, et al. (2000) Early diffusion-weighted MR imaging abnormalities in sustained seizure activity. AJR Am J Roentgenol 174:1304–1306

19. Cox JE, Mathews VP, Santos CC, Elster AD (1995) Seizure-induced transient hippocampal abnormalities on MR: correlation with positron emission tomography and electroencephalography. AJNR Am J Neuroradiol 16:1736–1738

20. Lansberg MG, et al. (1999) MRI abnormalities associated with partial status epilepticus. Neurology 52:1021–1027

21. Tien RD, Felsberg GJ (1995) The hippocampus in status epilepticus: demonstration of signal intensity and morphologic changes with sequential fast spin-echo MR imaging. Radiology 194:249–256

22. Kim JA, Chung JI, Yoon PH, et al. (2001) Transient MR signal changes in patients with generalized tonicoclonic seizure or status epilepticus: periictal diffusion-weighted imaging. AJNR Am J Neuroradiol 22:1149–1160

23. Flacke S, Wullner U, Keller E, Hamzei F, Urbach H (2000) Reversible changes in echo planar perfusion- and diffusion-weighted MRI in status epilepticus. Neuroradiology 42:92–95

24. Men S, et al. (2000) Selective neuronal necrosis associated with status epilepticus: MR findings. AJNR Am J Neuroradiol 21:1837–1840

25. Soffer D, Melamed E, Assaf Y, et al. (1986) Hemispheric brain damage in unilateral status epilepticus. Ann Neurol 20:737–740

26. Walker MT, et al. (1999) Profound neocortical atrophy after prolonged, continuous status epilepticus. AJR Am J Roentgenol 173:1712–1713

27. Yoo SY, Chang KH, Song IC, Han MH, Kwon BJ, Lee SH, Yu IK, Chun CK (2002) Apparent diffusion coefficient value of the hippocampus in patients with hippocampal sclerosis and in healthy volunteers. AJNR Am J Neuroradiol 23:809–812

28. Dodson WE, DeLorenzo RJ, Pedley TA, et al. (1993) Treatment of convulsive status epilepticus. Recommendations of the Epilepsy Foundation of America's Working Group on Status Epilepticus. JAMA 270:854–859

29. Hauser WA (1990) Status epilepticus: epidemiologic considerations. Neurology 40(5 Suppl 2):9–13

30. Sperk G, Lassmann H, Baran H, Kish SJ, Seitelberger F, Hornykiewicz O (1983) Kainic acid induced seizures: neurochemical and histopathological changes. Neuroscience 10:1301–1315

31. Siesjo BK, Wieloch T (1986) Epileptic brain damage: pathophysiology and neurochemical pathology. Adv Neurol 44:813–847

32. DeGiorgio CM, Tomiyasu U, Gott PS, Treiman DM (1992) Hippocampal pyramidal cell loss in human status epilepticus. Epilepsia 33:23–27

33. Ingvar M, Morgan PF, Auer RN (1988) The nature and timing of excitotoxic neuronal necrosis in the cerebral cortex, hippocampus and thalamus due to flurothyl-induced status epilepticus. Acta Neuropathol (Berl) 75:362–369

34. Dam AM, Dam M (1991) Neuropathology. In: Dam M, Gram L (eds) Comprehensive epileptology. New York: Raven Press, pp 43–55

35. Bruton CJ (1988) The neuropathology of temporal lobe epilepsy. New York: Oxford University Press
36. Corsellis JAN, Bruton CJ (1983) Neuropathology of status epilepticus in humans. In: Delgado-Escuta AV, Wasterlain CG, Treiman DM, Porter RJ (eds) Advances in neurology: status epilepticus. New York: Raven Press, 34:129–139
37. Zhong J, Petroff OA, Prichard JW, Gore JC (1993) Changes in water diffusion and relaxation properties of rat cerebrum during status epilepticus. Magn Reson Med 30:241–246
38. Zhong J, Petroff OA, Prichard JW, Gore JC (1995) Barbiturate-reversible reduction of water diffusion coefficient in flurothyl-induced status epilepticus in rats. Magn Reson Med 33:253–256
39. Righini A, Pierpaoli C, Alger JR, Di Chiro G (1994) Brain parenchyma apparent diffusion coefficient alterations associated with experimental complex partial status epilepticus. Magn Reson Imaging 12:865–871
40. Nakasu Y, Nakasu S, Morikawa S, Uemura S, Inubushi T, Handa J (1995) Diffusion-weighted MR in experimental sustained seizures elicited with kainic acid. AJNR Am J Neuroradiol 16:1185–1192
41. Christopher JW, et al (2000) Rapid alterations in diffusion-weighted images with anatomic correlates in a rodent model of status epilepticus. AJNR Am J Neuroradiol 21:1841–1852
42. Wang Y, et al. (1996) Postictal alteration of sodium content and apparent diffusion coefficient in epileptic rat brain induced by kainic acid. Epilepsia 37:1000–1006
43. Wichert-Ana L, Velasco TR, Terra-Bustamante VC, et al. (2001) Typical and atypical perfusion patterns in periictal SPECT of patients with unilateral temporal lobe epilepsy. Epilepsia 42:660–666
44. Johnson DW, Hogg JP, Dasheiff R, Yonas H, Pentheny S, Jumao-as A (1993) Xenon/CT cerebral blood flow studies during continuous depth electrode monitoring in epilepsy patients. AJNR Am J Neuroradiol 14:245–252
45. Theodore WH (1999) Cerebral blood flow and glucose metabolism in human epilepsy. Adv Neurol 79:873–881
46. Fazekas F, Kapeller P, Schmidt R, Stollberger R, Varosanec S, Offenbacher H, Fazekas G, Lechner H (1995) Magnetic resonance imaging and spectroscopy findings after focal status epilepticus. Epilepsia 36:946–949
47. Salih MA, Kabiraj M, Al-Jarallah AS, El Desouki M, Othman S, Palkar VA (1997) Hemiconvulsion-hemiplegia-epilepsy syndrome. A clinical, electroencephalographic and neuroradiological study. Childs Nerv Syst 13:257–263
48. Freeman JL, Coleman LT, Smith LJ, Shield LK (2002) Hemiconvulsion-hemiplegia-epilepsy syndrome: characteristic early magnetic resonance imaging findings. J Child Neurol 17:10–16
49. Cohen-Gadol AA, Britton JW, Jack CR Jr, Friedman JA, Marsh WR (2002) Transient postictal magnetic resonance imaging abnormality of the corpus callosum in a patient with epilepsy. Case report and review of the literature. J Neurosurg 97:714–717
50. Kim SS, Chang KH, Kim ST, Suh DC, Cheon JE, Jeong SW, Han MH, Lee SK (1999) Focal lesion in the splenium of the corpus callosum in epileptic patients: antiepileptic drug toxicity? AJNR Am J Neuroradiol 20:125–129
51. Polster T, Hoppe M, Ebner A (2001) Transient lesion in the splenium of the corpus callosum: three further cases in epileptic patients and a pathophysiological hypothesis. J Neurol Neurosurg Psychiatry 70: 459–463

Demyelinating and Degenerative Disease

In collaboration with J. Zhong

9.1 Demyelinating Disease

9.1.1 Multiple Sclerosis

T2-weighted and fluid-attenuated inversion-recovery (FLAIR) images are sensitive for depicting focal lesions in patients with multiple sclerosis (MS), but lack histopathologic specificity. Other lesions such as inflammation, edema, demyelination, remyelination, reactive gliosis and axonal loss have an MR appearance similar to MS lesions and can often not be distinguished from MS [1]. Hypointense T1 lesions in MS are usually caused by matrix destruction and loss of axons [2]. These lesions, which are hypointense on T1-weighted images and have a low magnetization transfer ratio (MTR), correlate better with clinical disability than proton density/T2 lesions. A low MTR in hypointense lesions on T1-weighted images has in one study been related to clinically more severe MS [3]. Decreased magnetization transfer ratio is, however, also observed in normal-appearing white matter in MS patients [4].

Increased apparent diffusion coefficient (ADC) values and decreased fractional anisotropy can be seen in normal-appearing white matter of patients with MS. This is clearly different from healthy control subjects, where these abnormalities are not seen [5, 6]. The ADC and fractional abnormalities may represent occult small MS plaques, gliosis or wallerian degeneration.

Multiple sclerosis plaques usually show hyper- or isointensity on diffusion-weighted (DW) images, with increased ADC, in both contrast-enhancing active plaques (Fig. 9.1) and chronic plaques (Fig. 9.2). MS plaques are reported to have decreased anisotropy [6, 7]. The increased ADC and decreased anisotropy in MS plaques are thought to be related to an increase in the extracellular space due to demyelination, perivascular inflammation with vasogenic edema, and gliosis. An enhancing portion of MS plaques has slightly increased ADC, histologically representing prominent inflammation with mild demyelination, while the non-enhancing portions tend to have more increased ADC, representing scarring with mild inflammation and myelin loss [8]. ADC values of MS plaques seem to be related to the severity of MS. The ADC values in secondary-progressive MS are higher than those in relapsing-remitting MS [9].

In the acute phase of MS, decreased ADC can also be observed in plaques, although it is rare [10] (Figs. 9.3 and 9.4). Decreased ADC of plaques is presumably caused by intramyelinic edema, which may be located in the periphery of a plaque. Intramyelinic edema occurs in the myelin sheath itself and/or in the intramyelinic cleft. Some of the intramyelinic edema is reversible, probably because the edema is mainly located in the intramyelinic cleft.
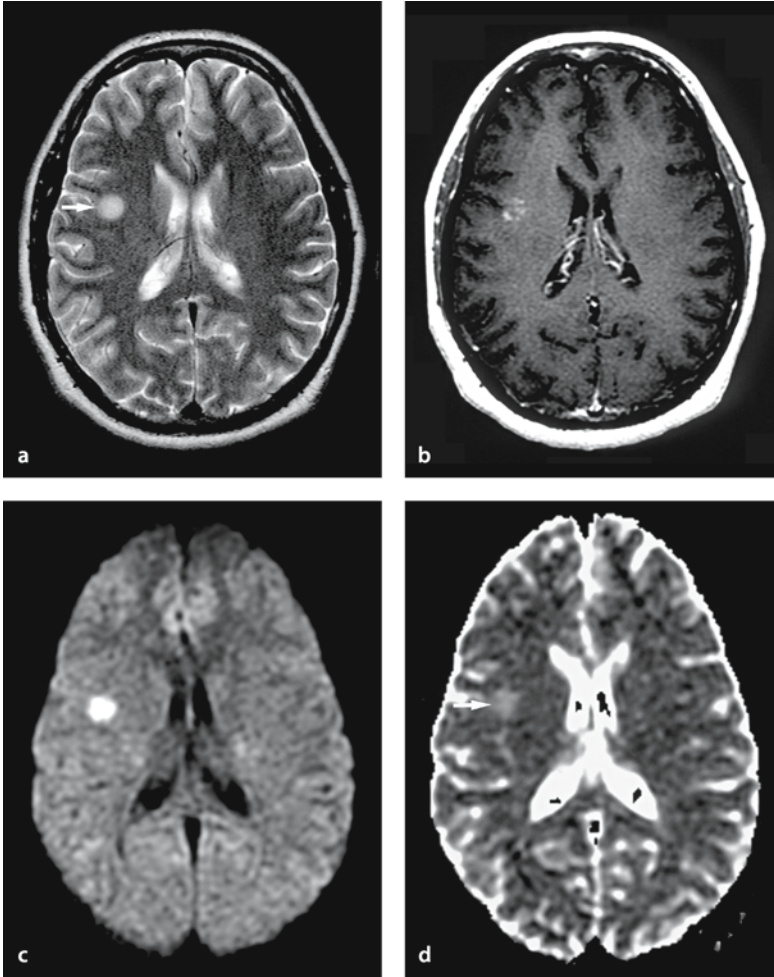
Figure 9.1 a–d

Multiple sclerosis in a 28-year-old man presenting with visual problems. **a** T2-weighted image shows a hyperintense lesion in the right frontotemporal region (*arrow*). **b** Gadolinium T1-weighted image shows mild enhancement of this lesion, representing an active plaque. **c, d** DW image (**c**) shows a hyperintense lesion associated with increased ADC (**d**), T2 shine-through (*arrow*)
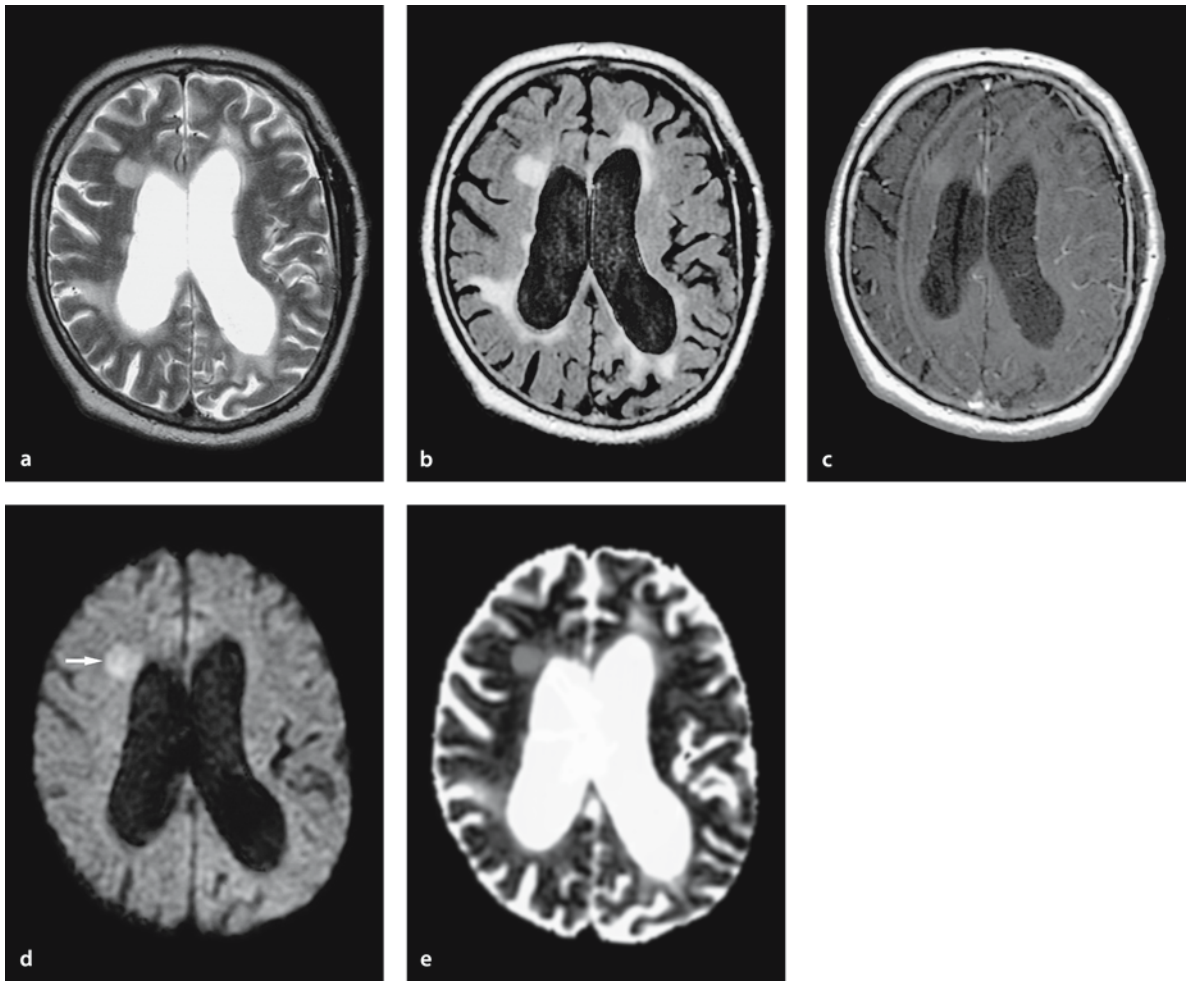
Figure 9.2 a–e

Multiple sclerosis in a 59-year-old man with a long history of recurrent seizures. T2-weighted (**a**) and FLAIR (**b**) images show multiple periventricular hyperintense lesions with ventricular dilatation. **c** On gadolinium T1-weighted image with magnetization transfer contrast, there is no enhancement of these lesions, representing relatively chronic plaques. **d** DW image shows a right frontal lesion as mildly hyperintense (*arrow*). **e** ADC is increased (T2 shine-through) and the other periventricular lesions are isointense with increased ADC (T2 washout)
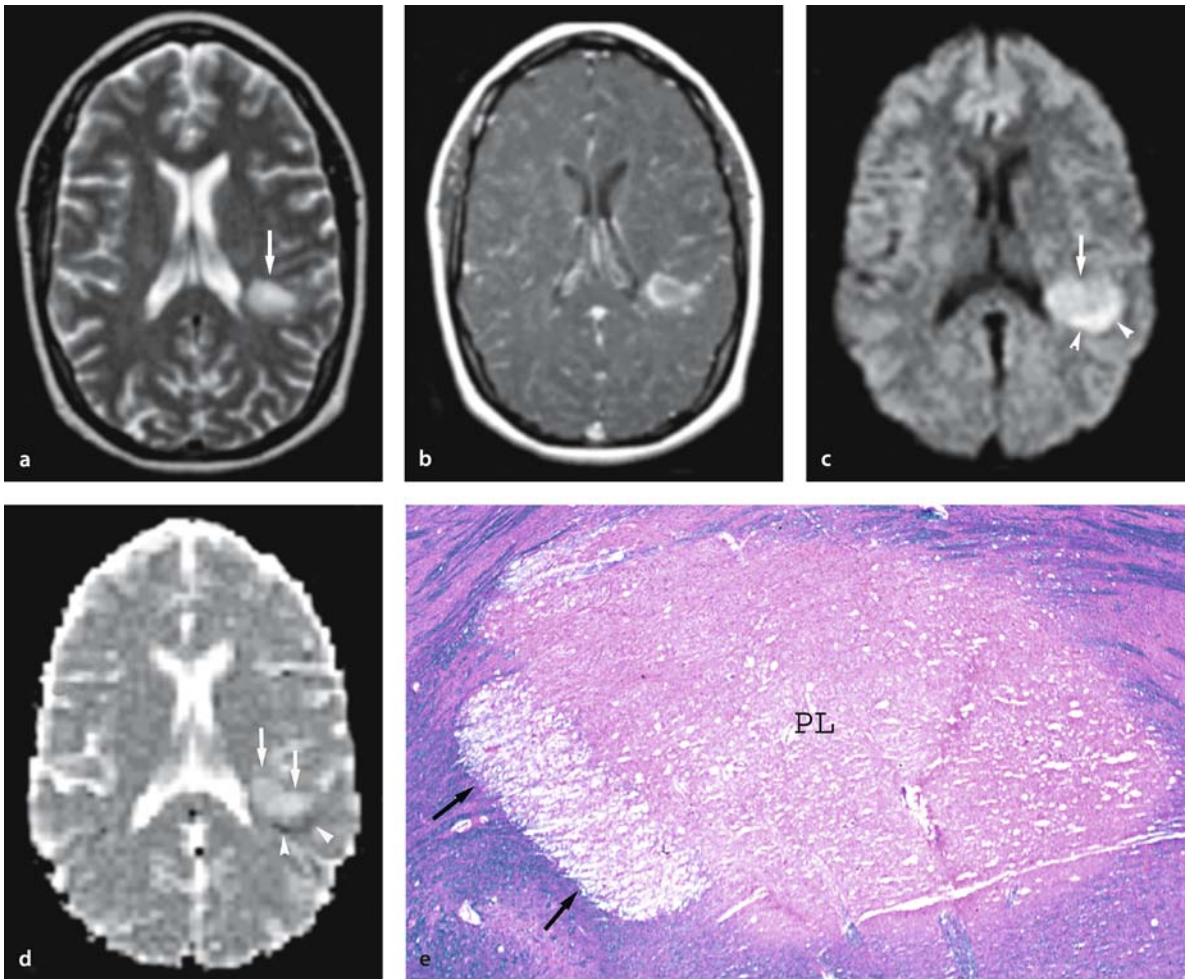
Figure 9.3 a–e

Multiple sclerosis in a 36-year-old woman presenting with subacute onset of progressive aphasia. **a** T2-weighted image shows a hyperintense lesion in the left periventricular white matter (*arrow*). **b** Gadolinium T1-weighted image with magnetization transfer contrast shows rim enhancement of this lesion. **c** DW image shows combination of a moderately hyperintense (*arrow*) and a significantly hyperintense lesion (*arrowheads*). **d** The moderately hyperintense lesion on DW image with increased ADC may represent demyelination (*arrows*), and the very hyperintense lesion on DW image with decreased ADC may represent intramyelinic edema (*arrowheads*). **e** Histopathology of another case shows that intramyelinic edema (*arrows*) is located in the periphery of a plaque (*PL*) (Luxol fast blue PAS stain, original magnification ×40). (From [33])
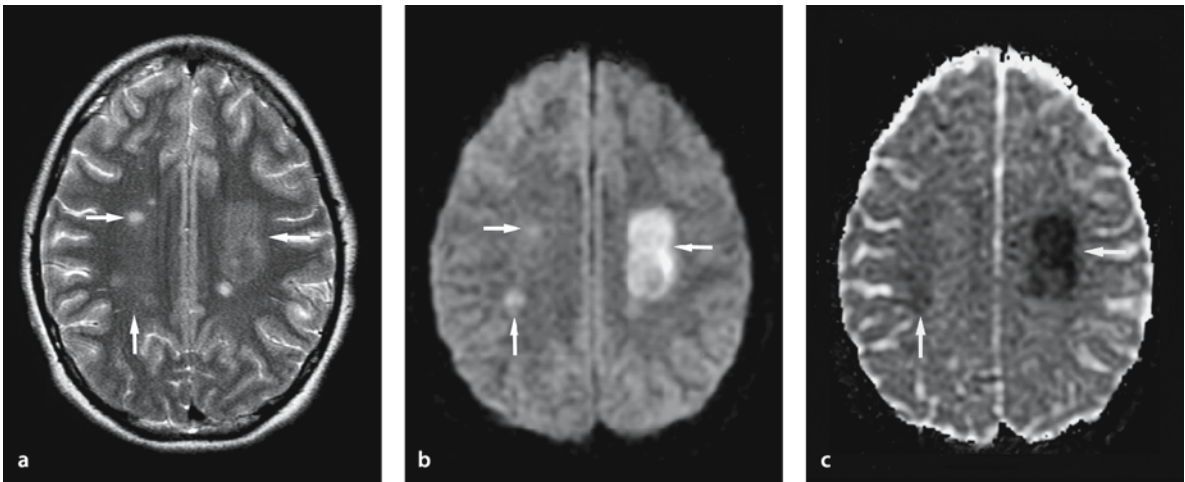
Figure 9.4 a–c

Multiple sclerosis in a 13-year-old female presented with acute-onset right-sided weakness and dysarthria. **a** T2-weighted image shows multiple hyperintense lesions in the bilateral centrum semiovale (arrows). **b** DW image shows some lesions as hyperintense (arrows). **c** ADC is decreased representing acute cytotoxic plaques (arrows)

Figure 9.5 a–d

Acute disseminated encephalomyelitis in a 15-year-old male presenting with right hemiparesis. **a** T2-weighted image shows multiple hyperintense lesions in the left frontal lobe (*arrows*) **b** Gadolinium T1-weighted image with magnetization transfer contrast shows inhomogeneous enhancement of these lesions. **c** DW image shows left frontal lesions as hyperintense due to T2 shine-through. **d** ADC is increased
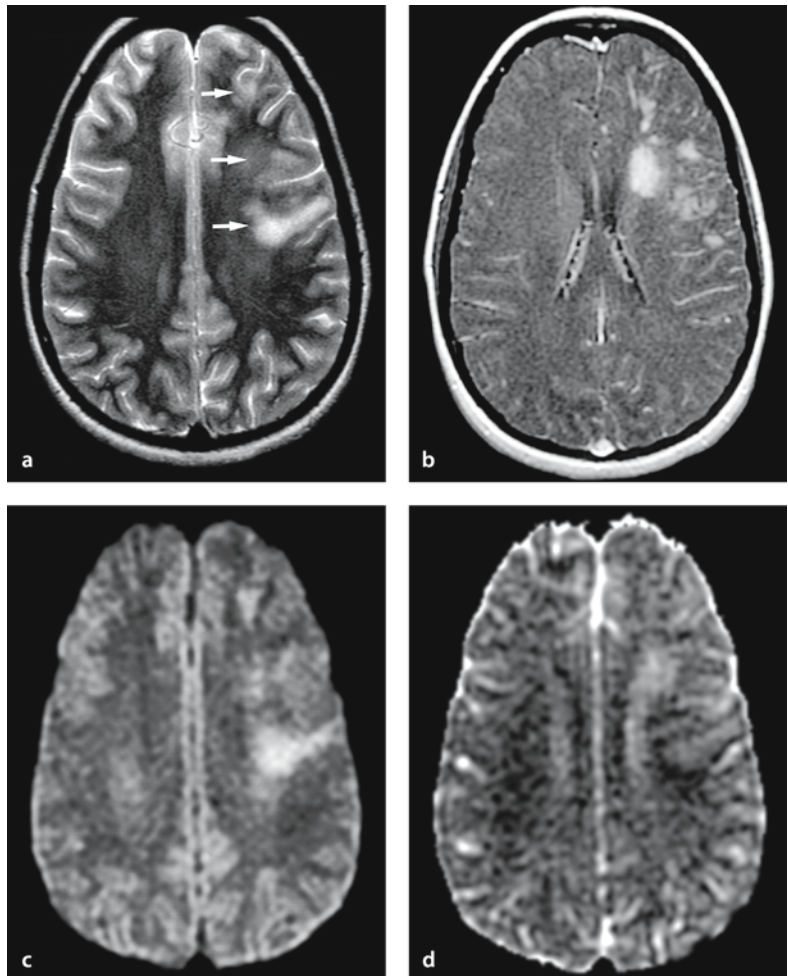
9.1.2 Acute Disseminated Encephalomyelitis

The neurologic picture of acute disseminated encephalomyelitis (ADEM) usually reflects a multifocal but monophasic involvement, while MS is characterized by recurrent episodes in both time and space. ADEM lesions tend to resolve, partially or completely, and new lesion formation rarely occurs.

Magnetization transfer ratio and ADC values in normal-appearing white matter of ADEM patients are similar to those of healthy control subjects [11]. DW imaging usually shows hyperintense lesions with increased ADC in the white matter [12] (Fig. 9.5). The ADC values of the ADEM lesions have been reported to be decreased or normal, but this seems to be very rare [13].

9.1.3 Progressive Multifocal Leukoencephalopathy

Progressive multifocal leukoencephalopathy (PML) is a fatal demyelinating disease of the central nervous system occurring in immunocompromised patients. Demyelination in PML results from the lytic infection of oligodendrocytes by JC virus, spreading to adjacent oligodendrocytes. DW imaging is usually hyperintense with increased ADC, but occasionally it shows hyperintensity with decreased ADC, especially at the margin of the lesion, which may represent JC virus-infected swollen oligodendrocytes [14] (Fig. 9.6).
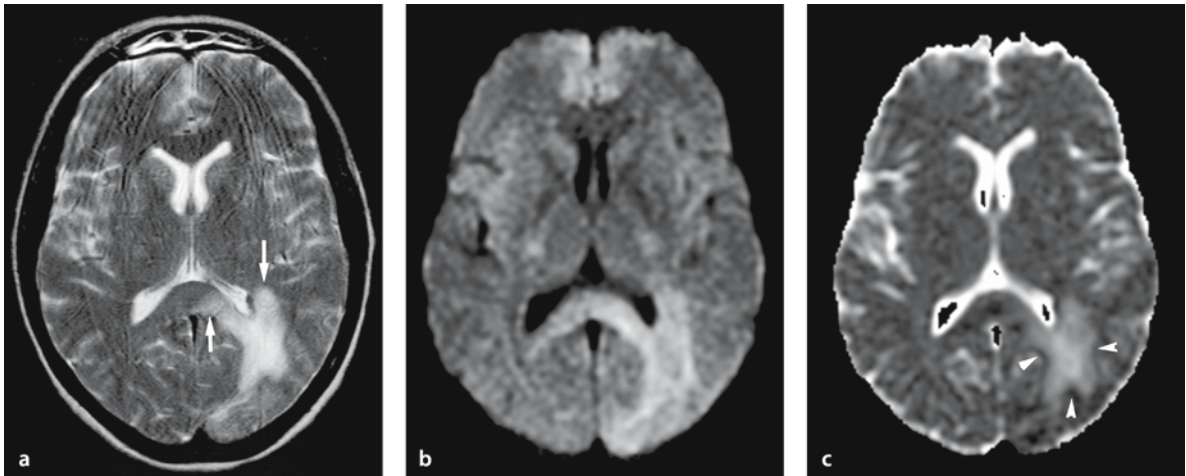
Figure 9.6 a–c

Progressive multifocal leukoencephalopathy in a 50-year-old female presenting with right hemianopsia after chemotherapy for chronic lymphocytic leukemia. Progressive multifocal leukoencephalopathy caused demyelination in this patient. **a** T2-weighted image shows a hyperintense lesion in the left occipital white matter extending into the posterior corpus callosum (*arrows*). **b** DW image shows the lesion as hyperintense due to T2 shine-through. **c** ADC is increased. The peripheral area of the lesion seems to have relatively decreased ADC (*arrowheads*).

9.2 Degenerative Disease

9.2.1 Wallerian or Transneuronal Degeneration

Wallerian degeneration is an antegrade degeneration of the axons and myelin sheath resulting from injury of the proximal portion of the axons or cell bodies. It is most commonly recognized in the corticospinal tract secondary to middle cerebral artery infarction. DW imaging shows the acute phase of wallerian degeneration as hyperintense associated with decreased ADC, presumably representing axonal or astrocytic swelling [15, 16] (Fig. 9.7).

Transneuronal (trans-synaptic) degeneration in the substantia nigra can occur secondary to striatal infarction [17]. This neuronal injury may be related to an excitotoxic mechanism via synapses resulting from loss of inhibitory GABA-ergic input. DW imaging shows hyperintensity associated with decreased ADC in the substantia nigra (Fig. 9.7) [18]. The decreased ADC of these lesions is thought to represent cellular edema of astrocytes or neurons in the substantia nigra. Astrocytic swelling, which is related to this degeneration, has been reported in an experimental study [19].

Figure 9.7 a–d

Wallerian and transneuronal degeneration in a 76-year-old man with a large infarct in the right middle cerebral artery (MCA) territory (6 days after onset). **a** T2-weighted image shows a right MCA infarct as hyperintense, including the left putamen. **b** T2-weighted image at the level of the midbrain reveals slightly a hyperintense lesion in the right cerebral peduncle including the substantia nigra (*arrows*), as well as a right MCA infarct in the temporal area. **c** DW image shows a hyperintense lesion. **d** ADC is decreased involving both the right cerebral peduncle and the right substantia nigra (*arrows*)
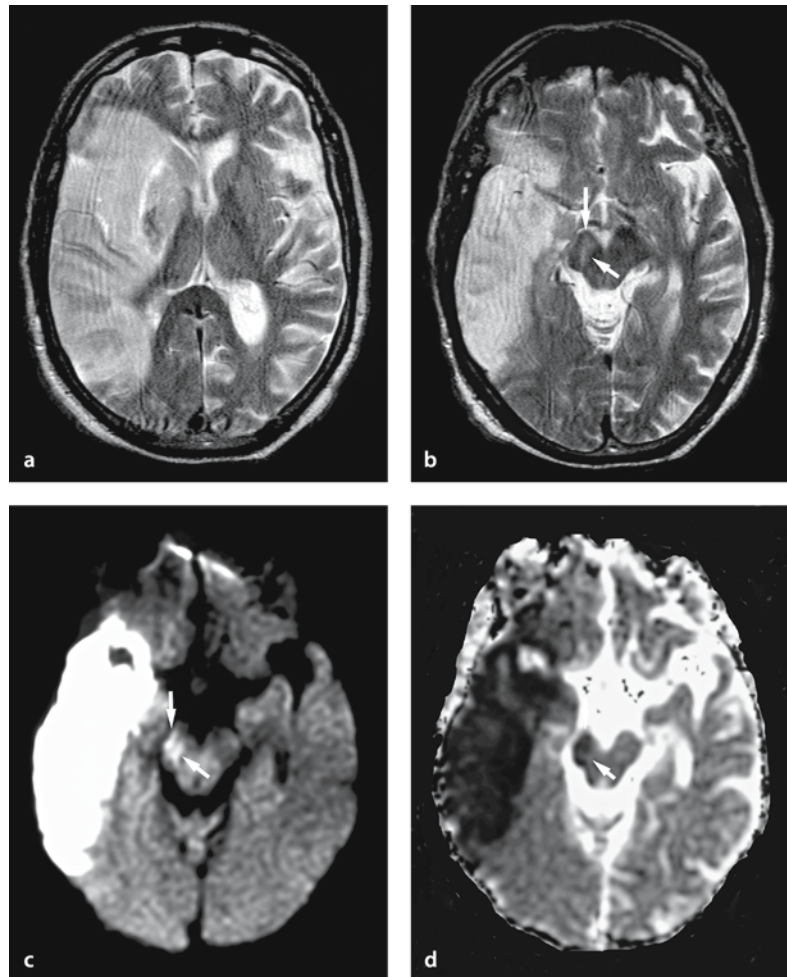
9.2.2 Creutzfeldt–Jakob Disease

Creutzfeldt–Jakob disease (CJD) is one of the prion diseases characterized by rapidly progressive degenerative dementia, myoclonus and ataxia. There are four forms: sporadic, iatrogenic, familial and variant [20]. Iatrogenic cases include contaminated neurosurgical instruments, administration of human growth hormone, cadaver-derived gonadotrophin, and dura matter (Fig. 9.8) and corneal grafts [21]. Histological features include spongiform degeneration of the gray matter, characterized by clustered, 5–25 micrometer large prion protein-containing vacuoles in the neuronal and glial elements, and neuronal loss, presumably due to apoptosis [22].

T2-weighted and FLAIR images show hyperintense lesions in the cerebral cortex and bilateral basal ganglia in patients with CJD. The lesions often involve bilateral thalami (pulvinar sign) and periaqueductal areas in patients with variant CJD [23, 24], but this finding is also seen in sporadic CJD [25] (Fig. 9.9). DW imaging is more sensitive than conventional MRI in detecting abnormalities in CJD. The lesions are hyperintense on DWI and often associated with decreased ADC [26–29] (Figs 9.8 and 9.9). Electron microscopy shows these vacuoles as focal swelling of neuritic processes, both axonal and dendritic swelling (cellular edema), which may cause decreased ADC [30]. In the late stages, abnormal hyperintense signals disappear with prominent brain atrophy, histologically representing neuronal loss and marked fibrillary gliosis [31].

Figure 9.8 a,b

Creutzfeldt–Jakob disease in a 57-year-old woman with progressive dementia 10 years after surgery using cadaver dura matter. **a** T2-weighted image shows postoperative change in the left temporo-occipital region with mild ventricular dilatation. **b** DW image reveals bilateral hyperintensity in the caudate nuclei (*arrows*) and mild increased signal diffusely in the left hemisphere
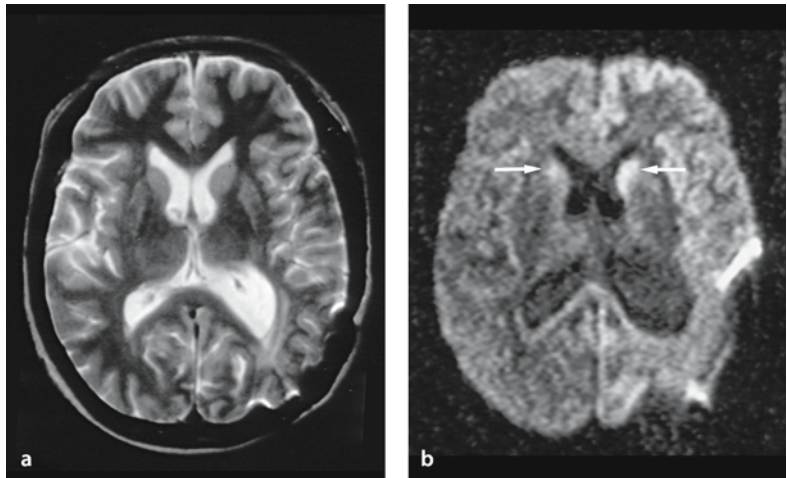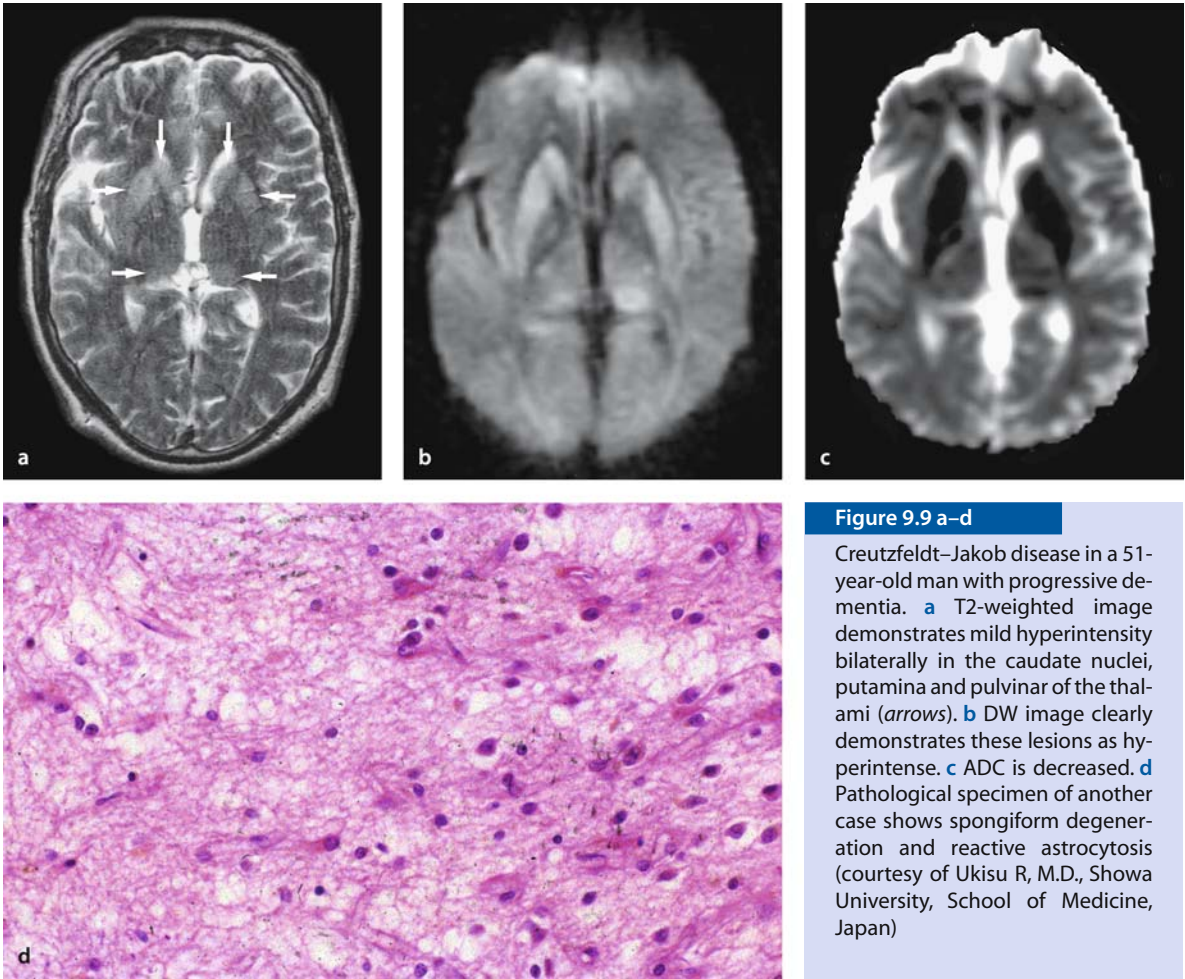
Figure 9.9 a–d

Creutzfeldt–Jakob disease in a 51-year-old man with progressive dementia. **a** T2-weighted image demonstrates mild hyperintensity bilaterally in the caudate nuclei, putamina and pulvinar of the thalami (*arrows*). **b** DW image clearly demonstrates these lesions as hyperintense. **c** ADC is decreased. **d** Pathological specimen of another case shows spongiform degeneration and reactive astrocytosis (courtesy of Ukisu R, M.D., Showa University, School of Medicine, Japan)

9.2.3 Amyotrophic Lateral Sclerosis

Amyotrophic lateral sclerosis affects middle-aged patients and is characterized by progressive muscle weakness, limb and truncal atrophy associated with bulbar signs and symptoms. The disease progression is relentless and half of the patients are dead within 3 years. MR images of amyotrophic lateral sclerosis are characterized by high T2 signal along the large myelinated pyramidal tract fibers in the posterior limb of the internal capsule and cerebral peduncles. On DW imaging there is typically increased ADC and decreased fractional anisotropy in the corticospinal tracts [32]. Diffusion tensor MR imaging may be useful in analyzing the extent and severity of axonal degeneration in amyotrophic lateral sclerosis (Fig. 9.10).

9.3 Conclusion

Magnetic resonance imaging with DW and ADC is useful in characterizing demyelinating and degenerative lesions of the brain. These imaging techniques can increase specificity and improve our understanding of the pathophysiology of these diseases.
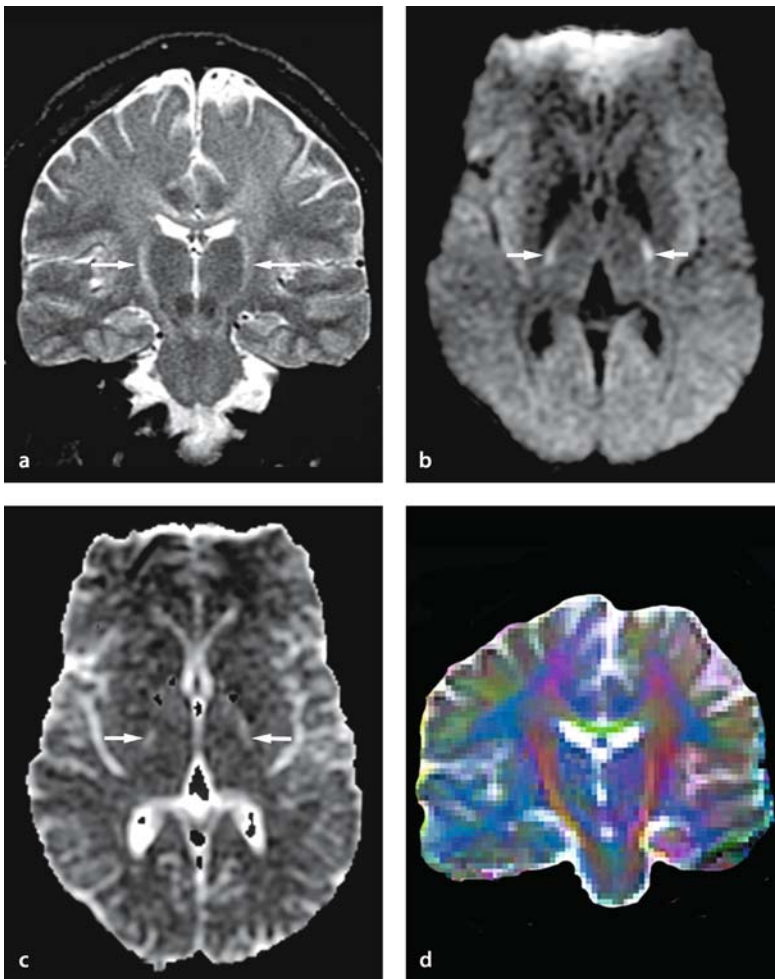
Figure 9.10 a–d

Amytrophic lateral sclerosis in a 27-year-old male with progressive weakness and dysphagia. **a** Coronal spin-echo T2-weighted image shows bilateral symmetrical hyperintensity along the corticospinal tract (*arrows*), extending into the white matter of the motor area. **b** DW image shows mild hyperintensity in bilateral corticospinal tracts. **c** ADC is increased (*arrows*). Hyperintensity and distortion in the frontal region is due to susceptibility artifact from air in the frontal sinuses. **d** Coronal diffusion tensor image with color mapping reveals decreased anisotropy along bilateral corticospinal tracts

References

1. Filippi M, Inglese M (2001) Overview of diffusion-weighted magnetic resonance studies in multiple sclerosis. J Neurol Sci 186 Suppl 1:S37–S43
2. van Walderveen MA, Lycklama A Nijeholt GJ, et al. (2001) Hypointense lesions on T1-weighted spin-echo magnetic resonance imaging: relation to clinical characteristics in subgroups of patients with multiple sclerosis. Arch Neurol 58:76–81
3. Loevner LA, Grossman RI, McGowan JC, Ramer KN, Cohen JA (1995) Characterization of multiple sclerosis plaques with T1-weighted MR and quantitative magnetization transfer. AJNR Am J Neuroradiol 16:1473–1479
4. Loevner LA, Grossman RI, Cohen JA, Lexa FJ, Kessler D, Kolson DL (1995) Microscopic disease in normal-appearing white matter on conventional MR images in patients with multiple sclerosis: assessment with magnetization-transfer measurements. Radiology 196:511–515
5. Horsfield MA, Larsson HB, Jones DK, Gass A (1998) Diffusion magnetic resonance imaging in multiple sclerosis. J Neurol Neurosurg Psychiatry 64 Suppl 1:S80–S84
6. Guo AC, MacFall JR, Provenzale JM (2002) Multiple sclerosis: diffusion tensor MR imaging for evaluation of normal-appearing white matter. Radiology 222:729–736
7. Tievsky AL, Ptak T, Farkas J (1999) Investigation of apparent diffusion coefficient and diffusion tensor anisotropy in acute and chronic multiple sclerosis lesion. Am J Neuroradiol 20:1491–1499
8. Roychowdhury S, Maldjian JA, Grossman RI (2000) Multiple sclerosis: comparison of trace apparent diffusion coefficients with MR enhancement pattern of lesions. AJNR Am J Neuroradiol 21:869–874
9. Castriota Scanderbeg A, Tomaiuolo F, Sabatini U, Nocentini U, Grasso MG, Caltagirone C (2000) Demyelinating plaques in relapsing-remitting and secondary-progressive multiple sclerosis: assessment with diffusion MR imaging. Am J Neuroradiol 21:862–868
10. Rovira A, Pericot I, Alonso J, Rio J, Grive E, Montalban X (2002) Serial diffusion-weighted MR imaging and proton MR spectroscopy of acute large demyelinating brain lesions: case report. Am J Neuroradiol 23:989–994
11. Inglese M, Salvi F, Iannucci G, Mancardi GL, Mascalchi M, Filippi M (2002) Magnetization transfer and diffusion tensor MR imaging of acute disseminated encephalomyelitis. Am J Neuroradiol 23:267–272
12. Harada M, Hisaoka S, Mori K, Yoneda K, Noda S, Nishitani H (2000) Differences in water diffusion and lactate production in two different types of postinfectious encephalopathy. J Magn Reson Imaging 11:559–563
13. Bernarding J, Braun J, Koennecke HC (2002) Diffusion- and perfusion-weighted MR imaging in a patient with acute demyelinating encephalomyelitis (ADEM). J Magn Reson Imaging 15:96–100
14. Ohta K, Obara K, Sakauchi M, Obara K, Takane H, Yogo Y (2001) Lesion extension detected by diffusion-weighted magnetic resonance imaging in progressive multifocal leukoencephalopathy. J Neurol 248:809–811
15. Castillo M, Mukheriji SK (1999) Early abnormalities related to postinfarction wallerian degeneration: evaluation with MR diffusion-weighted imaging. JCAT 23:1004–1007
16. Kang DW, Chu K, Yoon BW, Song IC, Chang KH, Roh JK (2000) Diffusion-weighted imaging in wallerian degeneration. J Neurol Sci 178:167–169
17. Ogawa T, Okudera T, Inugami A, et al. (1997) Degeneration of the ipsilateral substantia nigra after striatal infarction: evaluation with MR imaging. Radiology 204:847–851
18. Kinoshita T, Moritani T, Shrier DA, et al. (2002) Secondary degeneration of the Substantia Nigra and Corticospinal tract after hemorrhagic middle celebral artery infarction; Diffusion-weighted MR findings. Magnetic Resonance in Medical Sciences 1: 175–198
19. Nakase M, Tamura A, Miyasaka N, et al. (2001) Astrocytic swelling in the ipsilateral substantia niagra after occlusion of the middle cerebral artery in rats. Am J Neuroradiol 22:660–663
20. Johnson RT, Gibbs CJ Jr (1998) Creutzfeldt–Jakob disease and related transmissible spongiform encephalopathies. N Engl J Med 339:1994–2004
21. Brown P, Preece M, Brandel JP, et al. (2000) Iatrogenic Creutzfeldt–Jakob disease at the millennium. Neurology 55:1075–1081
22. Lucassen PJ, Williams A, Chung WCJ, et al. (1995) Detection of apoptosis in murine scrapie. Neuroscience Letters 198:185–188
23. Zeidler M, Sellar RJ, Collie DA, et al. (2000) The pulvinar sign on magnetic resonance imaging in variant Creutzfeldt–Jakob disease. Lancet 355:1412–1418
24. Molloy S, O'Laoide R, Brett F, Farrell M (2000) The "pulvinar" sign in variant Creutzfeldt–Jakob disease. Am J Roentgenol 175:555–556
25. Haik S, Brandel JP, Oppenheim C, et al. (2002) Sporadic CJD clinically mimicking variant CJD with bilateral increased signal in the pulvinar. Neurology 58:148–149
26. Demaerel P, Baert AL, Vanopdenbosch, et al. (1997) Diffusion-weighted magnetic resonance imaging in Creutzfeldt–Jakob disease. Lancet 349:847–848
27. Bahn MM, Parchi P (1999) Abnormal diffusion-weighted magnetic resonance images in Creutzfedlt–Jakob disease. Arch Neurol 56:577–583
28. Mittal S, Farmer P, Kalina P, Kingsley PB, Halperin J (2002) Correlation of diffusion-weighted magnetic resonance imaging with neuropathology in Creutzfeldt–Jakob disease. Arch Neurol 59:128–134
29. Murata T, Shiga Y, Higano S, Takahashi S, Mugikura S (2002) Conspicuity and evolution of lesions in Creutzfeldt–Jakob disease at diffusion-weighted imaging. AJNR Am J Neuroradiol 23:1164–1172
30. Dearmond MA, Kretzschmar HA, Prusiner SB (2002) Prion diseases. In: Graham DI, Lantos PL (eds) Greenfield's neuropathology, 7th edn, pp 273–323
31. Matoba M, Tonami H, Miyaji H, Yokota H, Yamamoto I (2001) Creutzfeldt–Jakob disease: serial changes on diffusion-weighted MRI. J Comput Assist Tomogr 25:274–277
32. Ellis CM, Simmons A, Jones DK, et al. (1999) Diffusion tensor MRI assesses corticospinal tract damage in ALS. Neurology 53:1051–1058
33. Moritani T (2002) Classification of brain edema. In Koredewakaru Diffusion MRI, Tokyo: Shujunsha. pp 128–137

Toxic and Metabolic Disease

In collaboration with J. Zhong

Computed tomography (CT) of patients with toxic and metabolic disease is generally non-specific, showing decreased attenuation of lesions in the white matter. Routine MR imaging is informative, but usually also non-specific, with T2 prolongation of those lesions. The white matter is often diffusely and symmetrically involved, as are the basal ganglia and/or brain stem. Diffusion-weighted (DW) imaging can add to the diagnostic information and improve the understanding of the pathophysiology of various white matter abnormalities, such as dysmyelination and demyelination in toxic and metabolic diseases.

10.1 Toxic Disease

10.1.1 Chemotherapy-Induced Leukoencephalopathy

Intrathecal or intravenous methotrexate, with or without radiation therapy, can cause diffuse white matter changes [1]. MR imaging shows diffuse or multifocal white matter lesions that are hyperintense on T2-weighted image. DW imaging show these white matter changes as diffuse hyperintensity with decreased apparent diffusion coefficient (ADC) in the white matter, even before conventional MR imaging can detect the lesions (Fig. 10.1). Pathologically these lesions represent intramyelinic and axonal swelling.

High-dose chemotherapy including carmustine (BCNU), cyclophosphamide, cisplatin, 5-fluorouracil (5-FU) and carmofur can also cause diffuse white matter disease. The lesions are hyperintense on T2-weighted images as well as on DW images, and ADC is decreased [2–4] (Fig. 10.2). Chemotherapeutic agents such as 5-FU and carmofur can have direct toxic effects on myelin, which causes intramyelinic edema [5]. Chemotherapy-associated leukoencephalopathy can be fatal and early diagnosis and discontinuation of the offending drug is therefore often necessary.

10.1.2 Heroin-Induced Spongiform Leukoencephalopathy

The inhalation of black-market heroin vapors (pyrolysate) as well as intravenous consumption of heroin can lead to toxic leukoencephalopathy [6]. The leukoencephalopathy is pathologically characterized by spongiform degeneration of the white matter as a result of fluid accumulation within the myelin sheaths (intramyelinic edema). Electron microscopy shows vacuoles between the myelin lamellae by splitting of the intraperiod lines [7]. CT and MR imaging show abnormalities in the cerebral and cerebellar white matter, cerebral peduncles, corticospinal tracts, lemniscus medialis and solitary tracts [8]. The accumulation of restricted fluid between the layers of myelin lamellae may cause hyperintensity on DW imaging with decreased ADC [9] (Fig. 10.3). Because the myelin itself and the blood–brain barrier are intact in cases of less severe heroin-induced leukoencephalopathy, one may expect the changes in the DW signal to be reversible on follow-up MR imaging [10].

10.1.3 Cocaine, Phencyclidine Hydrochloride, Amphetamines and Related Catecholaminergics

Cocaine, phencyclidine hydrochloride, amphetamines and related catecholaminergics can cause hemorrhage or infarction due to vasculitis, vasculopathy, or acute hypertensive effects [1]. DW imaging can be useful for the detection of these lesions (see also Chap. 7).
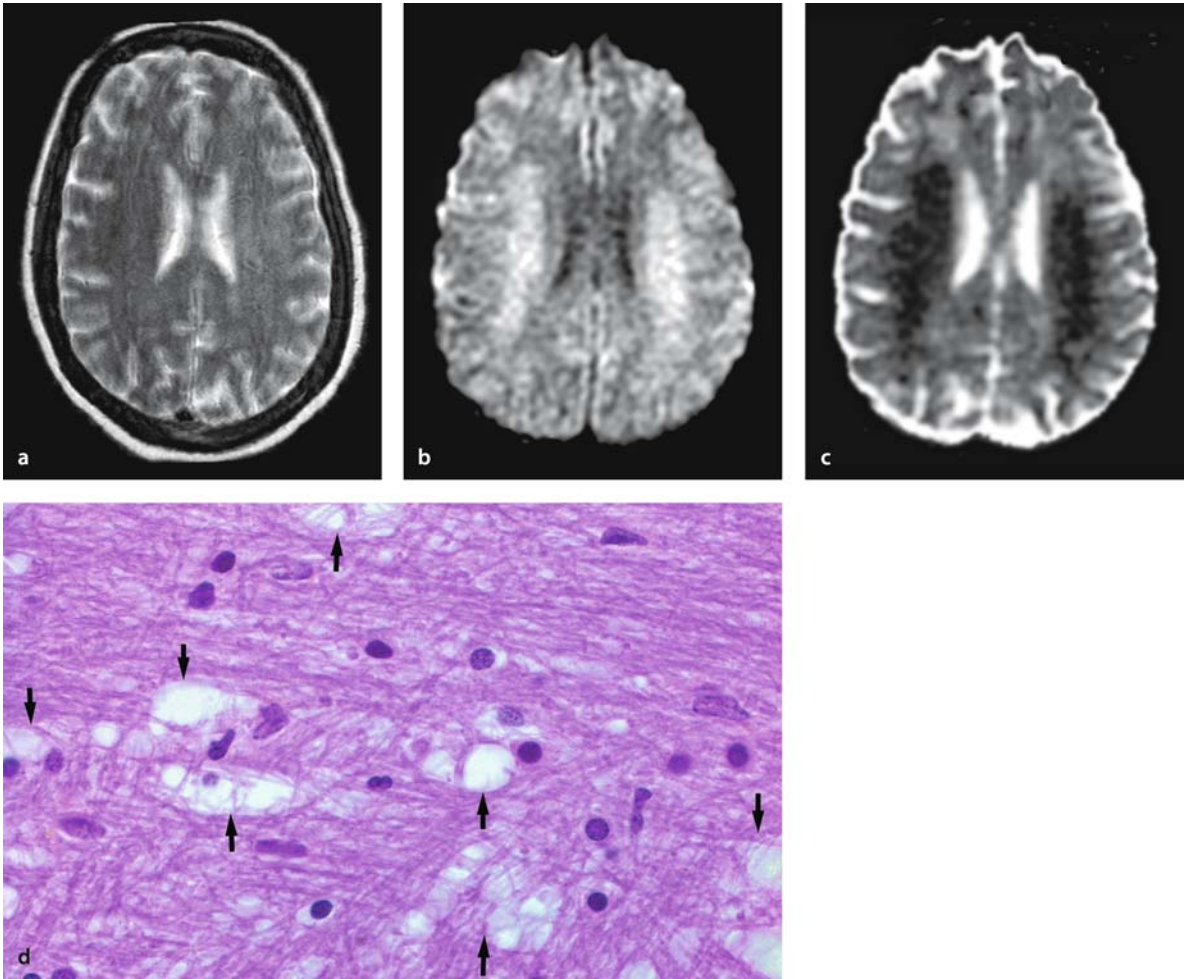
Figure 10.1 a–d

Methotrexate leukoencephalopathy in a 50-year-old female. **a** T2-weighted image does not demonstrate an appreciable abnormality in the white matter. **b** DW image shows diffuse hyperintensity in the bilateral corona radiata extending into the central semiovale. **c** ADC map shows diffuse white matter lesions as decreased ADC, which represents pure intramyelinic edema. **d** Pathological specimen shows spongiform change representing intramyelinic edema (*arrows*) diffusely in white matter. Astrocytes and axons are relatively spared (hematoxylin–eosin stain, original magnification ×200)
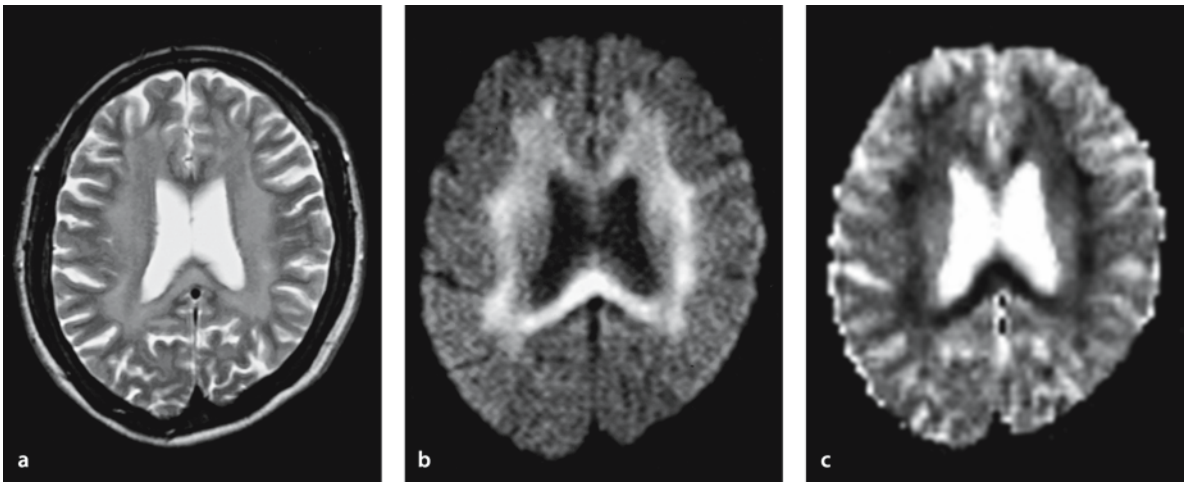
Figure 10.2 a–c

Carmofur leukoencephalopathy in a 58-year-old female. **a** T2-weighted image shows diffuse hyperintensity in the periventricular white matter including the corpus callosum. **b, c** DW image shows these lesions as hyperintense with decreased ADC, presumably related to intramyelinic edema
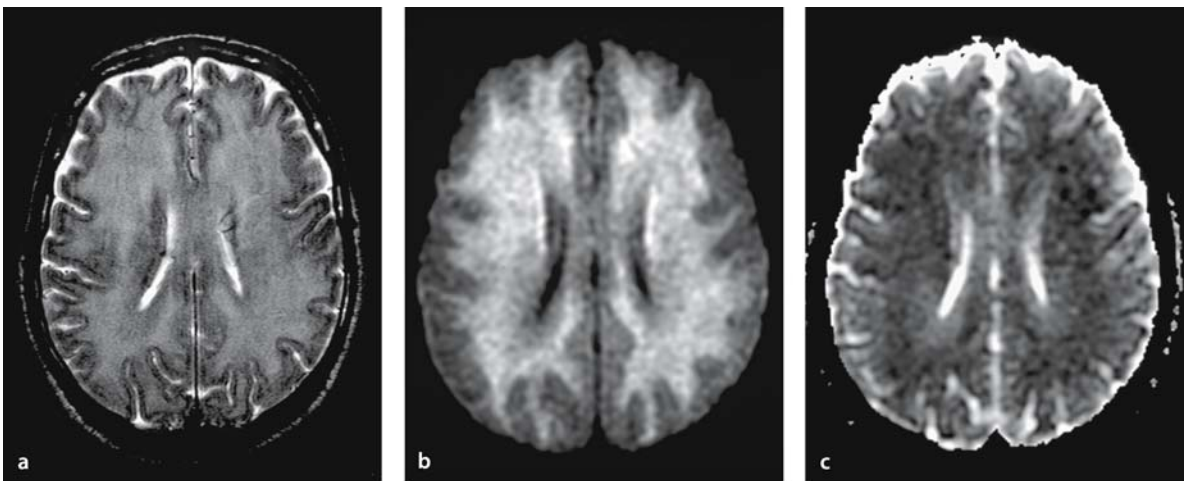
Figure 10.3 a–d

Heroin-induced leukoencephalopathy in a 55-year-old male. **a** T2-weighted image shows diffuse hyperintensity in the white matter including U fibers. **b, c** DW image shows these lesions as diffusely hyperintense with mildly decreased ADC. **d** Pathology shows intramyelinic edema and reactive astrogliosis, consistent with the subacute phase of heroin induced leukoencephalopathy (hematoxylin–eosin stain, original magnification ×200)
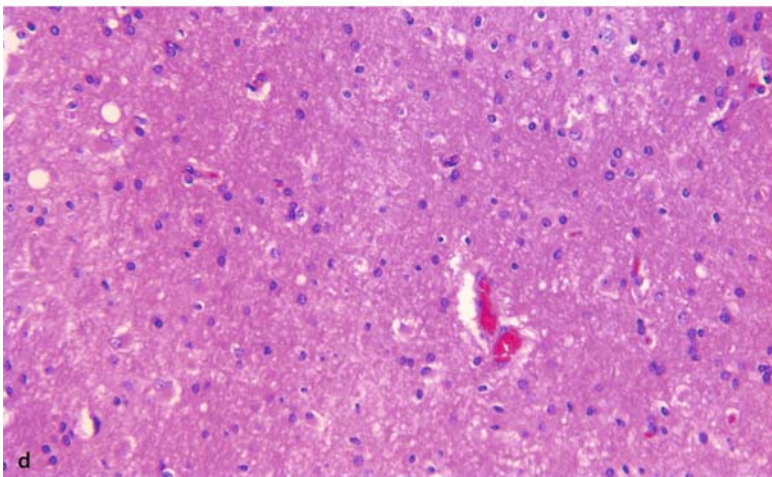
10.1.4 Central Pontine Myelinolysis and Extrapontine Myelinolysis

Central pontine myelinolysis (CPM) and extrapontine myelinolysis (EPM) represent destruction of myelin sheaths in characteristic places within the brain stem and cerebrum. The most common location is the central part of the basis pontis, followed by a combined type with central and extrapontine areas of myelinolysis. Isolated EPM is rare [11]. The basal ganglia, caudate nucleus, thalamus, geniculate bodies, internal and external capsules and gray–white matter junction are possible sites of EPM. The synonyms include osmotic myelinolysis and osmotic demyelination syndrome [12, 13].

Pathological findings include destruction of myelin sheaths, though the nerve cells and axons are relatively spared. The underlying etiology and pathogenesis are unknown, but the hypotheses include osmotic endothelial injury, excessive brain dehydra-
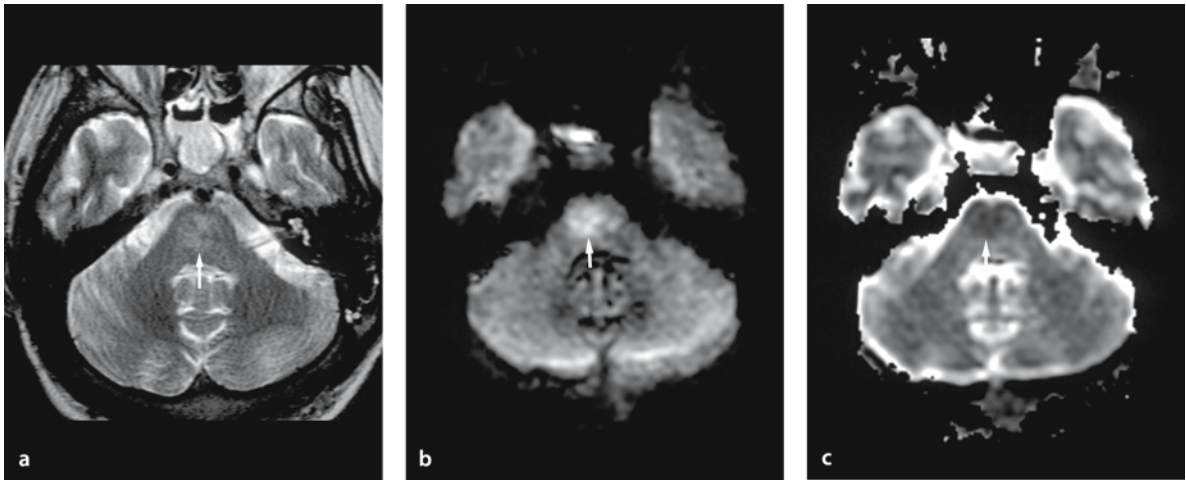
Figure 10.4 a–c

Central pontine myelinolysis in a 33-year-old male. **a** T2-weighted image shows a hyperintense lesion in the center of the pons (*arrow*). **b, c** DW image shows this lesion as hyperintense with decreased ADC
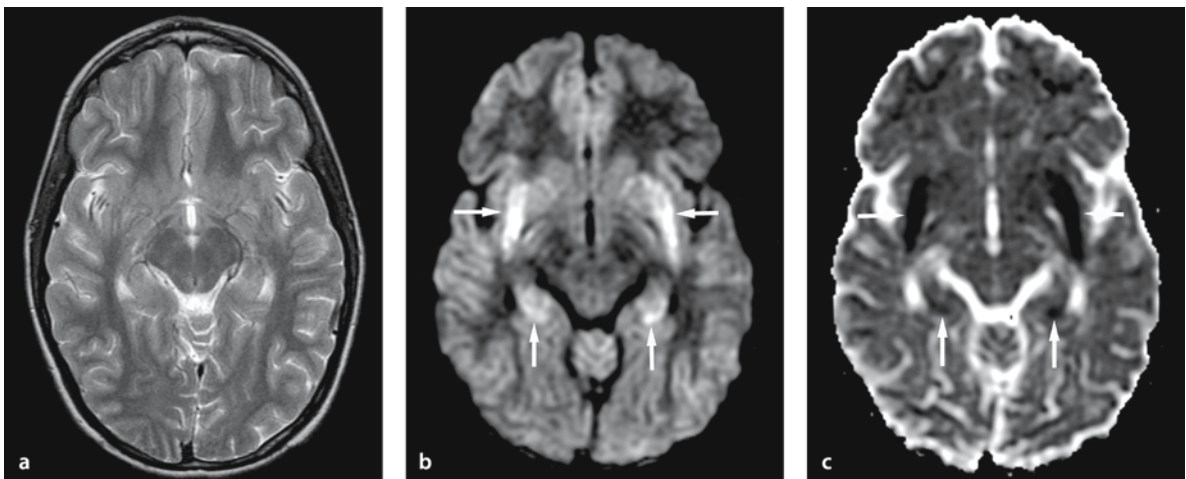
tion, and metabolic compromise [14]. The most common osmotic insult is a rapid correction of hyponatremia. However, CPM and EPM can also occur in normo- or hypernatremic states in patients with chronic alcoholism, post-liver transplantation, malnutrition and AIDS [15–17].

Magnetic resonance imaging has a fundamental role in the diagnosis and discloses hyperintense lesions on T2-weighted images, with or without enhancement on gadolinium-enhanced T1-weighted images. DW imaging can be useful in detecting the lesions in the early phase as hyperintense with decreased ADC, which represents cytotoxic edema (Figs. 10.4 and 10.5) [18]. Cytotoxic edema in CPM and EPM can occur not only in myelin sheaths, but also in neurons, axons and astrocytes [19]. The clinical outcome of CPM and EPM is highly variable, and both fatal and clinically reversible cases may be associated with this kind of cytotoxic edema.

10.1.5 Wernicke Encephalopathy

Thiamine (vitamin B1) deficiency can cause Wernicke encephalopathy, characterized by confusion, ataxia, and abnormal eye movements. Without thiamine, the Krebs and pentose phosphate cycles cannot metabolize glucose [20]. Cellular homeostasis will soon fail and the midline gray matter degenerates. Pathologic findings include decreased myelination, edema, astrocytic swelling, and necrosis in the mamillary bodies, thalamic and hypothalamic nuclei, periaqueductal gray matter, walls of the third and floor of the fourth ventricle, and less commonly, caudate, frontal, and parietal cortex.

Magnetic resonance imaging shows hyperintense lesions of these areas on T2-weighted images. They may or may not show enhancement on T1-weighted images following contrast agent injection [21]. With intravenous thiamine treatment, these lesions may
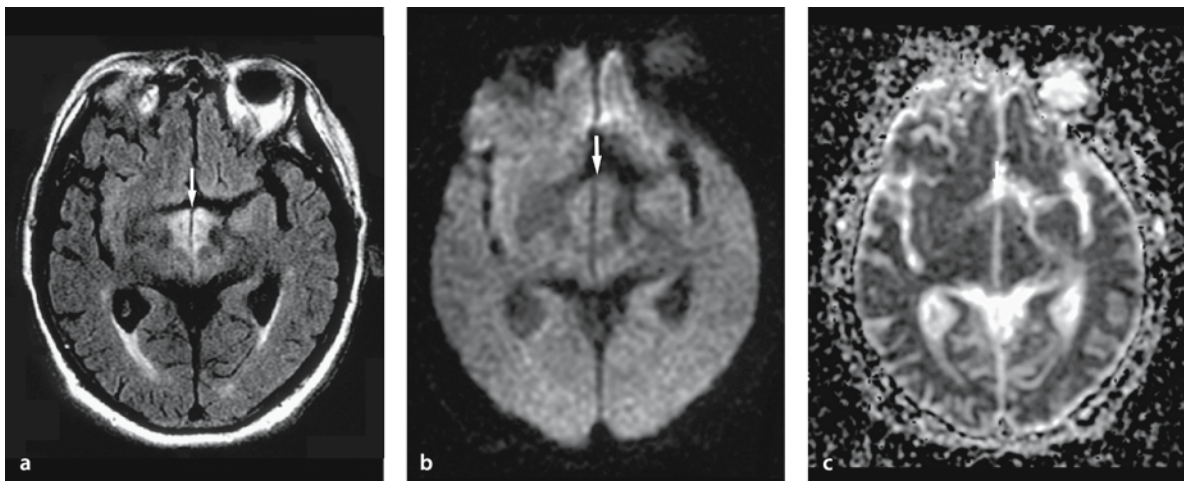
Figure 10.6 a–c

Wernicke encephalopathy in a 75-year-old male. **a** FLAIR shows a symmetrical hyperintense lesion in the hypothalamus (*arrow*). **b, c** DW image shows isointense lesions with increased ADC in the hypothalamus, which may represent vasogenic edema (*arrow*)

Figure 10.5 a–c

Extrapontine myelinolysis in an 11-year-old male. **a** On T2-weighted image shows no appreciable abnormality in the external capsules and hippocampi. **b, c** DW image demonstrates bilateral symmetrical hyperintense lesions with decreased ADC in the external capsules and hippocampi (*arrows*), representing cytotoxic edema

◄

dissipate. DW imaging shows these lesions as hyperintense with decreased or increased ADC. Lesions with decreased ADC are thought to represent cytotoxic edema of neurons or astrocytes, while lesions with increased ADC may represent vasogenic edema (Fig. 10.6) [22–24]. Both types of lesion can be reversible [25].

10.1.6 Marchiafava–Bignami Disease

Marchiafava–Bignami disease is a fatal disorder characterized by demyelination of the corpus callosum, often associated with chronic alcoholism [26]. The genu of the corpus callosum is more frequently involved, but the degeneration can extend throughout the entire corpus callosum. Occasionally, optic chiasm and the visual tracts, putamen, anterior commissure, cerebellar peduncles, cortical gray matter and U-fibers may be involved. Clinical signs include seizures, impairment of consciousness, and signs of interhemispheric disconnection, but they are nonspecific.

The corpus callosum appears hypoattenuated on CT and hyperintense on T2-weighted and fluid-attenuated inversion-recovery (FLAIR) images, which is essential to confirm the diagnosis. These lesions can be partially reversible with treatment [27]. DW imaging shows lesions in the early phase as hyperintense with decreased ADC [28] representing cytotoxic edema, mainly in the myelin sheaths (intramyelinic edema). In the subacute phase, the lesions are hyperintense on DW imaging with increased ADC representing demyelination or necrosis (Fig. 10.7).
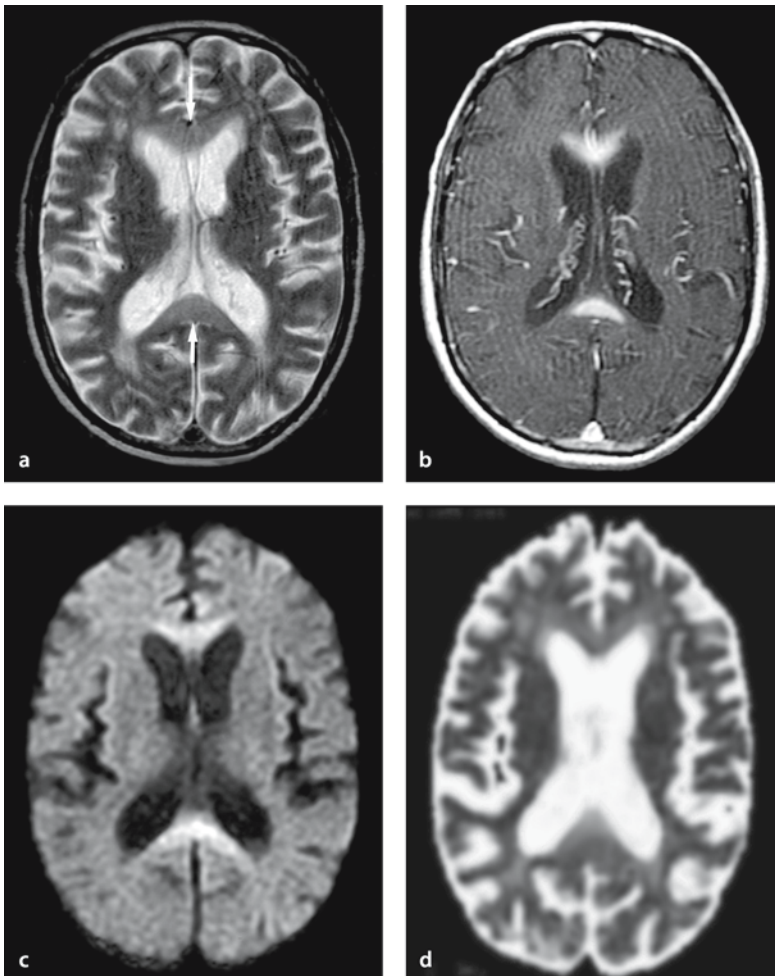
Figure 10.7 a–d

Marchiafava–Bignami disease in a 58-year-old male. **a** T2-weighted image shows hyperintensity in the anterior and posterior corpus callosum (*arrows*) and in the periventricular white matter. **b** Gadolinium-enhanced T1-weighted image with magnetization transfer contrast reveals enhancing lesions in the anterior and posterior corpus callosum. **c** DW image shows hyperintense lesions with increased ADC in the corpus cal-losum, representing demyelination and necrosis in the subacute phase

10.2 Metabolic Disease

10.2.1 Mitochondrial Encephalopathy

Mitochondrial encephalopathies are a heterogeneous group of disorders affecting primarily the central nervous system and skeletal muscles. Two main hypotheses attempt to explain the cerebral lesions: (1) metabolic damage of the endothelium, which leads to small-vessel occlusion and secondary neuronal death and (2) mitochondrial dysfunction, which results in anaerobic metabolism and neuronal death from acidosis [29].

T2-weighted images occasionally show increased signal intensity in the gray and white matter, which usually does not follow vascular territories. Proton MR spectroscopy is useful in the diagnosis by detecting elevated lactate peak. DW imaging often shows the stroke-like lesions in mitochondrial encephalopathy with lactic acidosis (MELAS) as hyperintense. They have increased or normal ADC, which presumably represents vasogenic edema [29–32] (Fig. 10.8). However, decreased ADC in these lesions representing cytotoxic edema can be observed [33–35] (Fig. 10.9).

Figure 10.8 a–d

Mitochondrial encephalopathy with lactic acidosis and stroke (MELAS) in a 27-year-old female. **a** T2-weighted and FLAIR images show a hyperintense lesion in the right temporal lobe (*arrow*). **b, c** DW image shows this lesion as hyperintense with increased ADC (*arrow*), mainly representing vasogenic edema
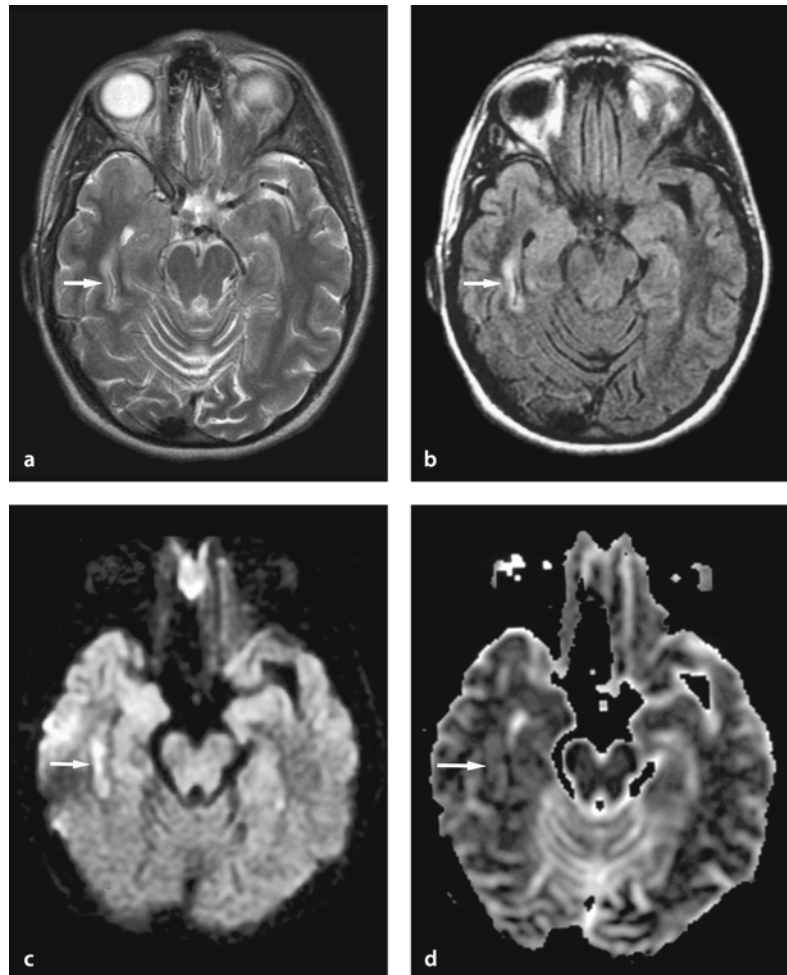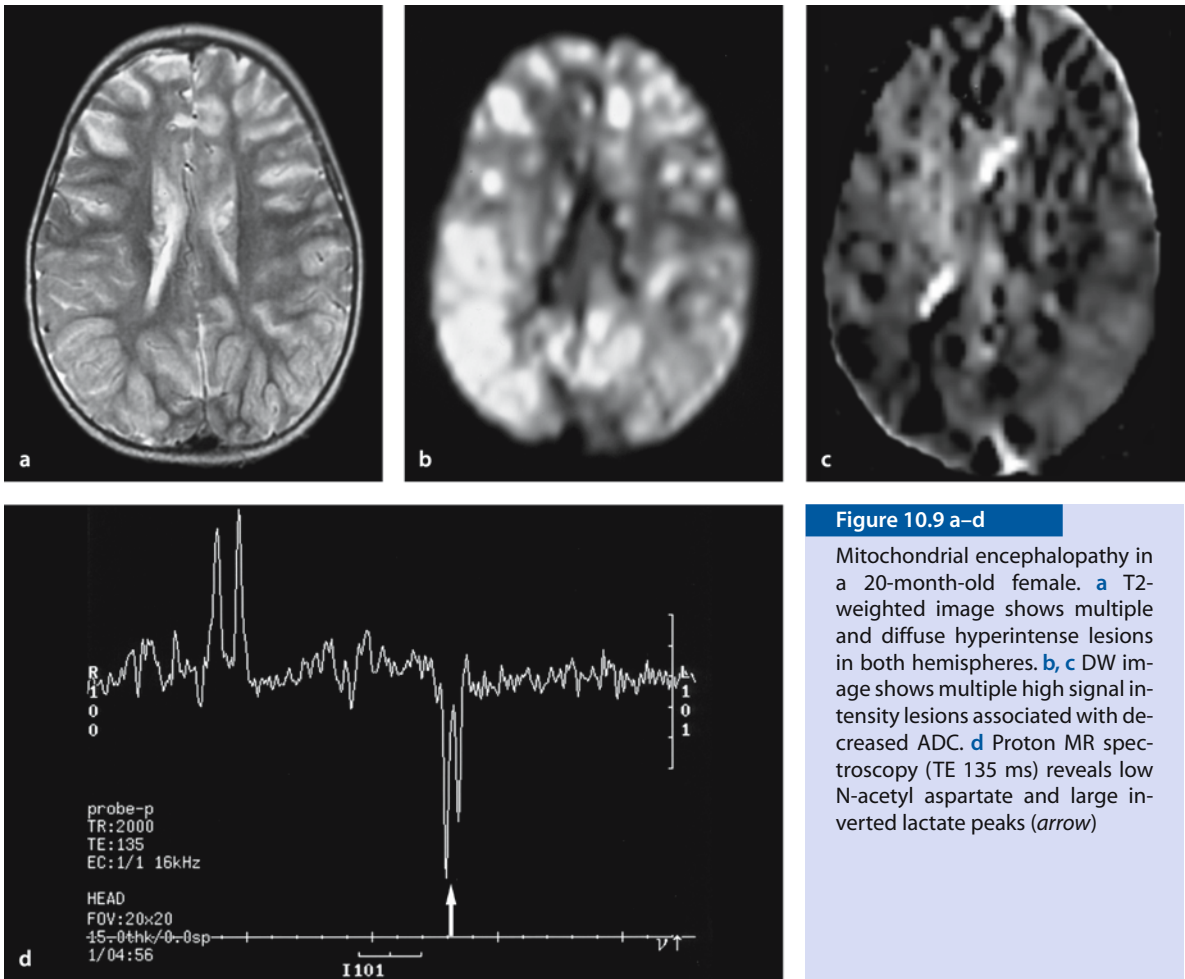
Figure 10.9 a–d

Mitochondrial encephalopathy in a 20-month-old female. **a** T2-weighted image shows multiple and diffuse hyperintense lesions in both hemispheres. **b, c** DW image shows multiple high signal intensity lesions associated with decreased ADC. **d** Proton MR spectroscopy (TE 135 ms) reveals low N-acetyl aspartate and large inverted lactate peaks (*arrow*)

10.2.2 Phenylketonuria

Phenylketonuria is an autosomal recessive disorder caused by a deficiency of phenylalanine hydroxylase. It is the most common congenital disorder of amino acid metabolism. Untreated patients typically develop mental retardation, seizures, growth retardation, hyper-reflexia, eczematous dermatitis, and hyperpigmentation. Pathologic findings include delayed or defective myelination, diffuse white matter vacuolation, demyelination, and gliosis [36].

Magnetic resonance imaging shows hyperintense lesions on T2-weighted images in the periventricular parietal and occipital regions, and in more severe cases extending to the frontal and subcortical white matter [37]. DW imaging shows these lesions as hyperintense with decreased ADC, which presumably represents intramyelinic edema and astrocytic swelling [38] (Fig. 10.10). These lesions can becompletely reversible on follow-up MRI when dietary control has been instituted.

10.2.3 Other Metabolic Diseases and Leukodystrophies

Diffusion-weighted imaging is thought to be useful to differentiate between demyelinating and dysmyelinating disorders [39, 40]. Decreased ADC in the white matter has been reported in Canavan disease [41] (Chap. 14), adrenoleukodystrophy [42], metachromatic leukodystrophy [43], L-2 hydroxyglutaric aciduria [44] (Fig. 10.11), and infantile neuronal dystrophy [45]. The cause of the decrease in ADC in these
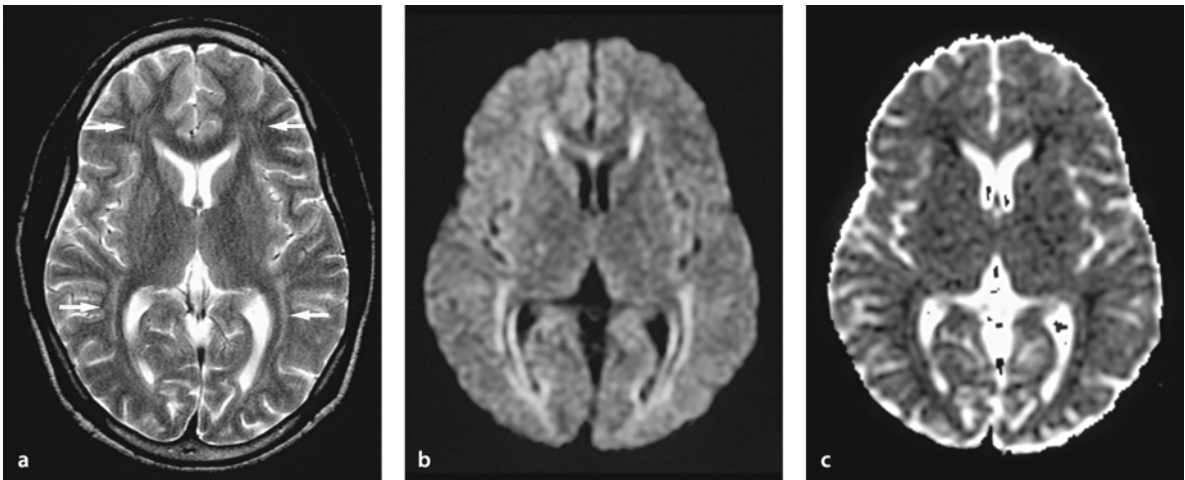
Figure 10.10 a–c

Phenylketonuria in a 36-year-old male. **a** T2-weighted image shows hyperintense lesions in the periventricular white matter (*arrows*). **b, c** DW image shows these lesions as hyperintense with decreased ADC, presumably representing intramyelinic edema
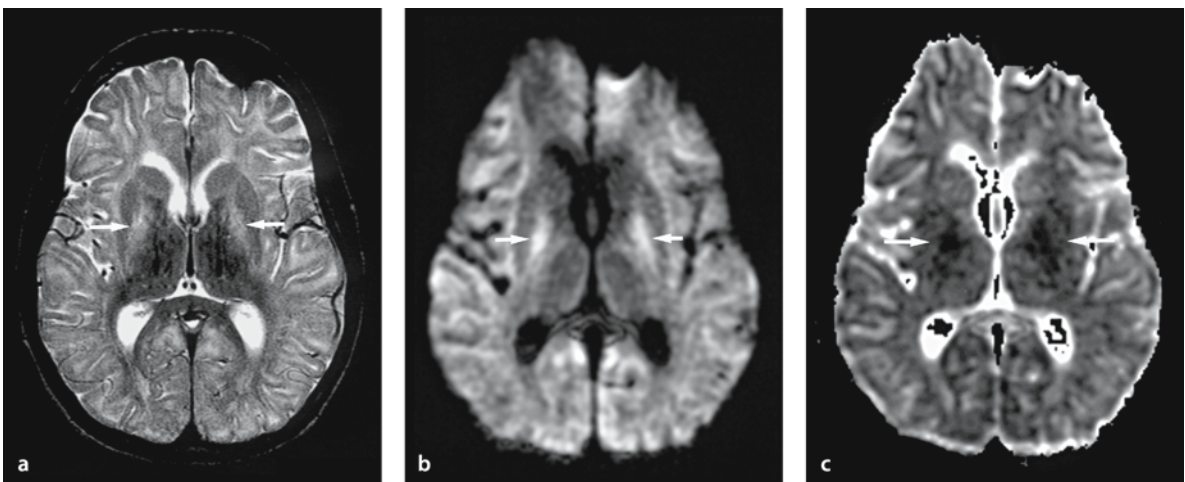
Figure 10.11 a–c

Glutaric aciduria in a 13-year-old male. **a** T2-weighted image shows symmetrical hyperintense lesions in bilateral globus pallidum (*arrows*) and diffusely in the white matter. **b, c** DW image shows these lesions as hyperintense; however, ADC is mildly decreased in the globus pallidum (*arrows*), and mildly increased in the white matter

diseases seems to be intramyelinic edema [46], or axonal swelling associated with impaired myelin sheaths or axons. On the other hand, increased or normal ADC in the white matter is seen on Pelizaeus–Merzbacher disease [47] (Chap. 14),

Krabbe disease, van de Knaap disease (Fig. 10.12) and leukoencephalopathy with vanishing white matter (Chap. 14). Diffusion tensor MR imaging can be useful in differential diagnosis of leukodystrophies [39, 42, 48].
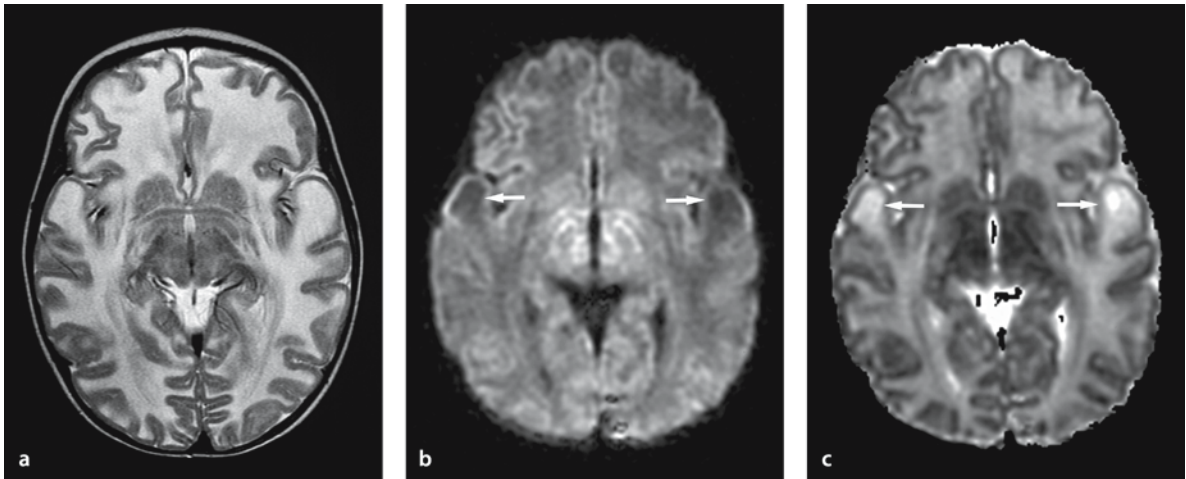
Figure 10.12 a–c

van der Knaap disease in a 10-month-old male with megalencephaly. **a** T2-weighted image shows diffuse hyperintensity in the white matter. **b, c** DW image shows diffuse hypointensity with increased ADC, especially prominent in symmetrical subcortical cysts in the temporal lobes (*arrows*)

References

1. Lexa FJ (1995) Drug-induced disorders of the central nervous system. Seminars in Roentgenol 30:7–17
2. Brown MS, Stemmer SM, Simon JH, et al. (1998) White matter disease induced by high-dose chemotherapy: longitudinal study with MR imaging and proton spectroscopy. AJNR Am J Neuroradiol 19:217–221
3. Fujikawa A, Tsuchiya K, Katase S, Kurosaki Y, Hachiya J (2001) Diffusion-weighted MR imaging of Carmofur-induced leukoencephalopathy. Eur Radiol 11:2602–2606
4. Tha KK, Terae S, Sugiura M, et al. (2002) Diffusion-weighted magnetic resonance imaging in early stage of 5-fluorouracil-induced leukoencephalopathy. Acta Neurol Scand 106:379–386
5. Matsumoto S, Nishizawa S, Murakami S, et al. (1995) Carmofur-induced leukoencephalopathy: MRI. Neuroradiology 37:649–652
6. Maschke M, Fehlings T, Kastrup O, Wilhelm HW, Leonhardt G (1999) Toxic leukoencephalopathy after intravenous consumption of heroin and cocaine with unexpected clinical recovery. J Neurol 246:850–851
7. Wolters EC, van Wijngaarden GK, Stam FC, et al (1982) Leucoencephalopathy after inhaling "heroin" pyrolysate. Lancet 2:1233–1237
8. Tan TP, Algra PR, Valk J, Wolters EC (1994) Toxic leukoencephalopathy after inhalation of poisoned heroin: MR findings. Am J Neuroradiol 15:175–178
9. Chen CY, Lee KW, Lee CC, Chin SC, Chung HW, Zimmerman RA (2000) Heroin-induced spongiform leukoencephalopathy: value of diffusion MR imaging. J Comput Assist Tomogr 24:735–737
10. Barnett MH, Miller LA, Reddel SW, Davies L (2001) Reversible delayed leukoencephalopathy following intravenous heroin overdose. J Clin Neurosci 8:165–167
11. Gocht A, Colmant HJ (1987) Central pontine and extrapontine myelinolysis: a report of 58 cases. Clin Neuropathol 6:262–270
12. Sterns RH, Riggs JE, Schochet SS Jr (1986) Osmotic demyelination syndrome following correction of hyponatremia. N Engl J Med 314:1535–1542
13. Ho VB, Fitz CR, Yoder CC, Geyer CA (1993) Resolving MR features in osmotic myelinolysis (central pontine and extrapontine myelinolysis. Am J Neuroradiol 14:163–167
14. Norenberg MD (1983) A hypothesis of osmotic endothelial injury. A pathogenetic mechanism in central pontine myelinolysis. Arch Neurol 40:66–69
15. Mascalchi M, Cincotta M, Piazzini M (1993) Case report: MRI demonstration of pontine and thalamic myelinolysis in a normonatremic alcoholic. Clin Radiol 47:137–138
16. Rodriguez J, Benito-Leon J, Molina JA, Ramos A, Bermejo F (1998) Central pontine myelinolysis associated with cyclosporin in liver transplantation. Neurologia 13:437–440
17. Miller RF, Harrison MJ, Hall-Craggs MA, Scaravilli F (1998) Central pontine myelinolysis in AIDS. Acta Neuropathol 96:537–540
18. Cramer SC, Stegbauer KC, Schneider A, Mukai J, Maravilla KR (2001) Decreased diffusion in central pontine myelinolysis. AJNR Am J Neuroradiol 22:1476–1479
19. Anderson AW, Zhong J, Petroff OA, et al (1996) Effects of osmotically driven cell volume changes on diffusion-weighted imaging of the rat optic nerve. Magn Reson Med 35:162–167
20. Victor M, Adams RD, Collins GH (1971) The Wernicke-Korsakoff syndrome. A clinical and pathological study of 245 patients, 82 with post-mortem examinations. Contemp Neurol Ser 7:1–206
21. Antunez E, Estruch R, Cardenal C, Nicolas JM, Fernandez-Sola J, Urbano-Marquez A (1998) Usefulness of CT and MR imaging in the diagnosis of acute Wernicke's encephalopathy. AJR Am J Roentgenol 171:1131–1137
22. Oka M, Terae S, Kobayashi R, et al. (2001) Diffusion-weighted MR findings in a reversible case of acute Wernicke encephalopathy. Acta Neurol Scand 104:178–181
23. Doherty MJ, Watson NF, Uchino K, Hallam DK, Cramer SC (2002) Diffusion abnormalities in patients with Wernicke encephalopathy. Neurology 58:655–657
24. Chu K, Kang DW, Kim HJ, Lee YS, Park SH (2002) Diffusion-weighted imaging abnormalities in wernicke encephalopathy: reversible cytotoxic edema? Arch Neurol 59:123–127
25. Rugilo CA, Roca MC, Zurru MC, Gatto EM (2003) Diffusion abnormalities and Wernicke encephalopathy. Neurology 60:727–728; author reply 727–728
26. Gambini A, Falini A, Moiola L, Comi G, Scotti G (2003) Marchiafava-Bignami disease: longitudinal MR imaging and MR spectroscopy study. Am J Neuroradiol 24:249–253
27. Gass A, Birtsch G, Olster M, Schwartz A, Hennerici MG (1998) Marchiafava-Bignami disease: reversibility of neuroimaging abnormality. J Comput Assist Tomogr 22:503–504
28. Inagaki T, Saito K (2000) A case of Marchiafava-Bignami disease demonstrated by MR diffusion-weighted image. No To Shinkei 52:633–637
29. Oppenheim C, Galanaud D, Samson Y, et al. (2000) Can diffusion weighted magnetic resonance imaging help differentiate stroke from stroke-like events in MELAS? J Neurol Neurosurg Psychiatry 69:248–250
30. Yoneda M, Maeda M, Kimura H, Fujii A, Katayama K, Kuriyama M (1999) Vasogenic edema on MELAS: a serial study with diffusion-weighted MR imaging. Neurology 53:2182–2184
31. Yonemura K, Hasegawa Y, Kimura K, Minematsu K, Yamaguchi T (2001) Diffusion-weighted MR imaging in a case of mitochondrial myopathy, encephalopathy, lactic acidosis, and strokelike episodes. AJNR Am J Neuroradiol 22:269–272
32. Ohshita T, Oka M, Imon Y, et al. (2000) Serial diffusion-weighted imaging in MELAS. Neuroradiology 42:651–656
33. Kim HS, Kim DI, Lee BI, et al. (2001) Diffusion-weighted image and MR spectroscopic analysis of a case of MELAS with repeated attacks. Yonsei Med J 42:128–133
34. Majoie CB, Akkerman EM, Blank C, Barth PG, Poll-The BT, den Heeten GJ (2002) Mitochondrial encephalomyopathy: comparison of conventional MR imaging with diffusion-weighted and diffusion tensor imaging: case report. AJNR Am J Neuroradiol 23:813–816
35. Flemming K, Ulmer S, Duisberg B, Hahn A, Jansen O (2002) MR spectroscopic findings in a case of Alpers-Huttenlocher syndrome. AJNR Am J Neuroradiol 23:1421–1423

36. Huttenlocher PR (2000) The neuropathology of phenylketonuria: human and animal studies. Eur J Pediatr Suppl 2:S102–S106

37. Pearsen KD, Gean-Marton AD, Levy HL, Davis KR (1990) Phenylketonuria: MR imaging of the brain with clinical correlation. Radiology 177:437–440

38. Phillips MD, McGraw P, Lowe MJ, Mathews VP, Hainline BE (2001) Diffusion-weighted imaging of white matter abnormalities in patients with phenylketonuria. AJNR Am J Neuroradiol 22:1583–1586

39. Ono J, Harada K, Mano T, Sakurai K, Okada S (1997) Differentiation of dys- and demyelination using diffusional anisotropy. Pediatr Neurol 16:63–66

40. Engelbrecht V, Scherer A, Rassek M, Witsack HJ, Modder U (2002) Diffusion-weighted MR imaging in the brain in children: findings in the normal brain and in the brain with white matter diseases. Radiology 222:410–418

41. Sener RN (2003) Canavan disease: diffusion magnetic resonance imaging findings. J Comput Assist Tomogr 27:30–33

42. Eichler FS, Itoh R, Barker PB, et al. (2002) Proton MR spectroscopic and diffusion tensor brain MR imaging in X-linked adrenoleukodystrophy: initial experience. Radiology 225:245–252

43. Sener RN (2002) Metachromatic leukodystrophy: diffusion MR imaging findings. AJNR Am J Neuroradiol 23:1424–1426

44. Sener RN (2003) L-2 hydroxyglutaric aciduria: proton magnetic resonance spectroscopy and diffusion magnetic resonance imaging findings. J Comput Assis Tomo 27:38–43

45. Sener RN (2003) Diffusion magnetic resonance imaging in infantile neuroaxonal dystrophy. J Comput Assis Tomo 27:34–37

46. Ellison D, Love S (1998) Toxic injury of the CNS. In: Neuropathology, 1st edn, section 8, chapter 25. Barcelona, Mosby, pp 25.1–25.22

47. Ono J, Harada K, Sakurai K, et al. (1994) MR diffusion imaging in Pelizaeus-Merzbacher disease. Brain Dev 16:219–223

48. Guo AC, Petrella JR, Kurtzberg J, Provenzale JM (2001) Evaluation of white matter anisotropy in Krabbe disease with diffusion tensor MR imaging: initial experience. Radiology 218:809–815

Infectious Diseases

11.1 Overview of Brain Infections

Infections of the brain are caused by bacteria, virus, fungi or parasites. Bacterial infections are often related to septic emboli and extracranial infections spreading intracranially and intra-axially. This can result in cerebritis and brain abscesses. Viral infections are more diffuse and cause encephalitis and vasculitis. Toxoplasmosis, which is the most common parasitic infection of the brain, causes encephalitis and abscesses, while disseminated aspergillosis causes vasculitis-mediated infarctions resulting in extensive cerebritis and/or abscess formation.

The pathophysiology and the imaging findings vary greatly depending on the organism causing the infection. Diffusion-weighted (DW) imaging is useful for diagnosis of infectious conditions of the brain by means of differentiating vasogenic edema from cytotoxic edema [1]. DW imaging can also separate abscesses from cystic and necrotic tumors [2–6].

11.2 Bacterial Brain Abscess

Bacterial brain abscesses are potentially fatal, but can often be medically and surgically treated if detected early. Symptoms are often non-specific and vague, and imaging is therefore necessary for detection and characterization.

A brain abscess begins as a focal area of microvascular injury, usually at the gray–white matter junction or deeper in the white matter. Pathologically the initial stage of a brain abscess is a focal area of cerebritis or presuppurative encephalitis. This is characterized by early necrosis of the cerebral parenchyma, vascular congestion, petechial hemorrhage, neutrophil infiltration and vasogenic edema [7–9].

Late cerebritis is characterized by a necrotic and purulent center. This evolves to frank abscess formation, which is characterized by central pus, inflammatory granulation tissue and a fibrous capsule. The pus usually consists of both dead and viable neutrophils. Even in the chronic phase of an abscess, there is both coagulative necrosis and bacteria (Fig. 11.1).

The early phase of the brain abscess has a homogeneous, bright signal on DW imaging associated with decreased apparent diffusion coefficient (ADC) (Fig. 11.1). On follow-up DW imaging, the chronic phase of an abscess can still show hyperintensity, but ADC values are partially increased [10]. A possible explanation for the high signal on DW imaging is restriction of water mobility due to the high viscosity of coagulative necrosis and the hypercellularity of polynucleated neutrophils in the pus.
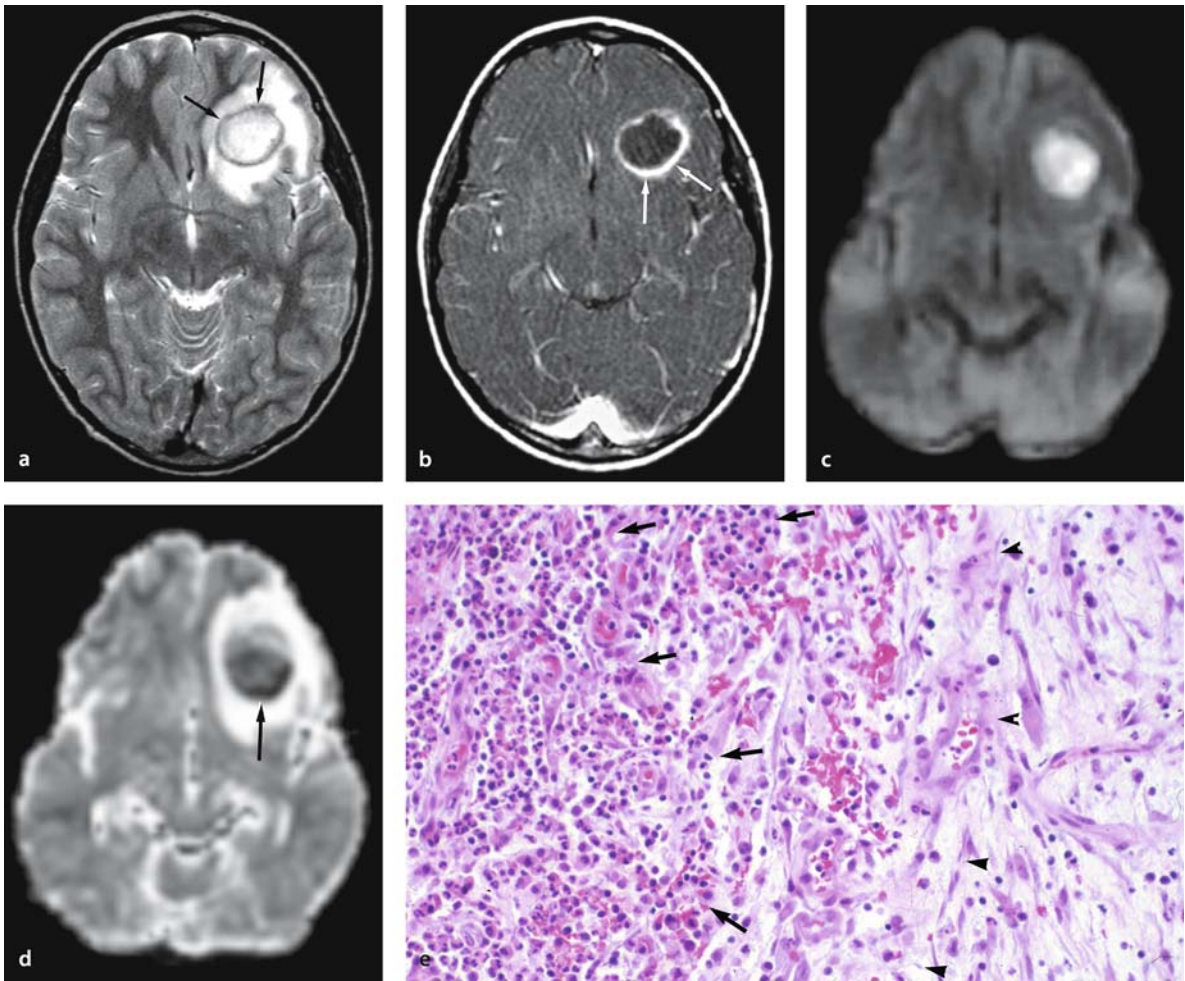
Figure 11.1 a–e

Chronic streptococcal brain abscess in a 7-year-old boy presenting with severe headache. **a** T2-weighted image shows a central hyperintense mass lesion with low signal rim (*black arrows*) and peripheral edema in the left frontal lobe. **b** Gadolinium-enhanced T1-weighted image with magnetization transfer contrast shows this mass with ring enhancement. **c** DW image shows a central cystic component as hyperintense. **d** ADC map shows decreased ADC of this component. **e** Specimen shows numerous neutrophils (*arrows*) in the pus and granulomatous fibrous capsules (*arrowheads*) in a chronic abscess

11.3 Septic Emboli

The main risk factors for brain abscesses are bacterial endocarditis and chronic suppurative intrathoracic infections [11]. If septic emboli of sufficient size are lodged in an intracerebral arterial vessel, infarction can occur. Infarctions are bright on DW imaging, with decreased ADC (Fig. 11.2). Septic infarctions usually occur in the distal cortical branch territories, while small septic emboli are characteristically found in the corticomedullary junction. It can take a few weeks and up to several months for septic emboli to develop into an abscess. Serial DW imaging is therefore often useful in patients at risk for septic encephalopathy. By means of repeated DW imaging, it is possible to identify the initial infarction and the subsequent cerebritis/abscess evolution [12]. This allows for early treatment.
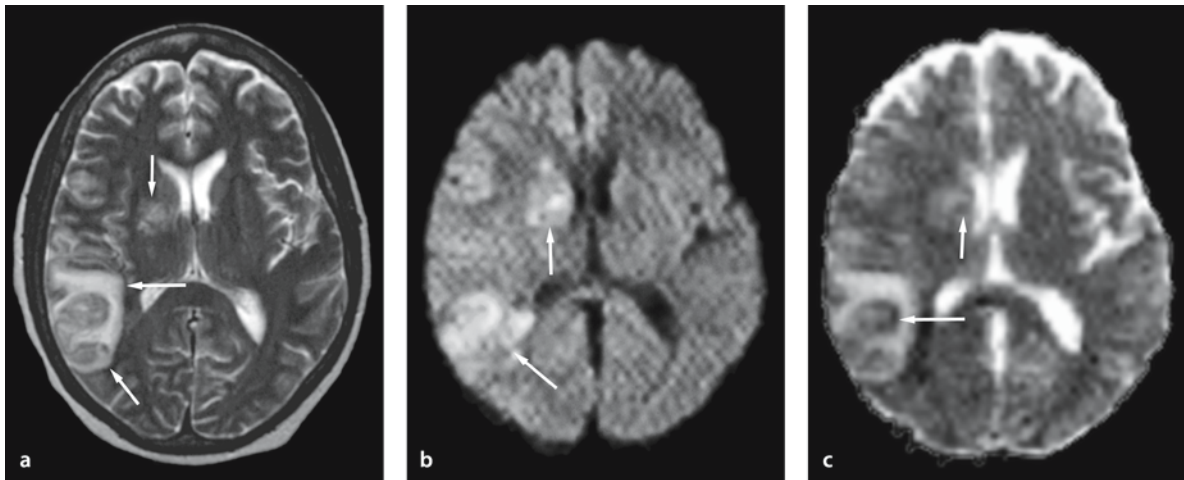
Figure 11.2 a–c

Septic emboli from staphylococcus endocarditis in a 44-year-old woman presenting with left hemiparesis of 3 days' duration. **a** T2-weighted image shows hyperintense lesions in the right basal ganglia and posteriorly in the middle cerebral artery territory (*arrows*). **b** DW image shows these lesions as hyperintense (*arrows*). **c** ADC map shows these lesions as decreased ADC, mainly representing infarcts (*arrows*)

11.4 Brain Abscess Caused by Unusual Bacteria

The classical finding in a brain abscess is a cystic lesion with marked enhancement following contrast medium injection. On DW imaging, the cyst shows a high signal and ADC is reduced. However, the characteristics of brain abscess appear to be related to the type of organism and the immunity of the host. Thus, in an immunodeficient patient with sepsis, multiple micro-abscesses are often observed. Multiple micro-abscesses of gram-negative rods may involve basal ganglia bilaterally and mimic small infarcts (Fig. 11.3) [13].

Listeria infection is often associated with parenchymal involvement, especially in the brain stem [14]. A central small abscess may be seen as high signal on DW imaging, with decreased ADC (Fig. 11.4).

11.4.1 Differential Diagnosis

Diffusion-weighted imaging can discriminate brain abscesses from cystic or necrotic tumors, which is often difficult with conventional MR imaging (Fig. 11.5) [2–6]. Abscesses and tumor necrosis are both generally bright on DW images, but the abscesses characteristically have low ADC, whereas the ADC in tumors varies. There are exceptions and central necrosis of a tumor or metastasis can occasionally show the same characteristics with hyperintensity on DW imaging with low ADC (Fig. 11.6) [15–17]. Sterile and liquefactive coagulative necrosis, hemorrhage and viscous mucinous components are possible causes for this finding.

Pure coagulative necrosis typically develops after radiofrequency thalamotomy [18]. The lesion often shows hyperintensity on DW imaging, with decreased ADC (Fig. 11.7). Although imaging characteristics are very similar to those of an abscess, the history of the patient and the symptomatology can usually help to differentiate post-surgical lesions from abscesses.
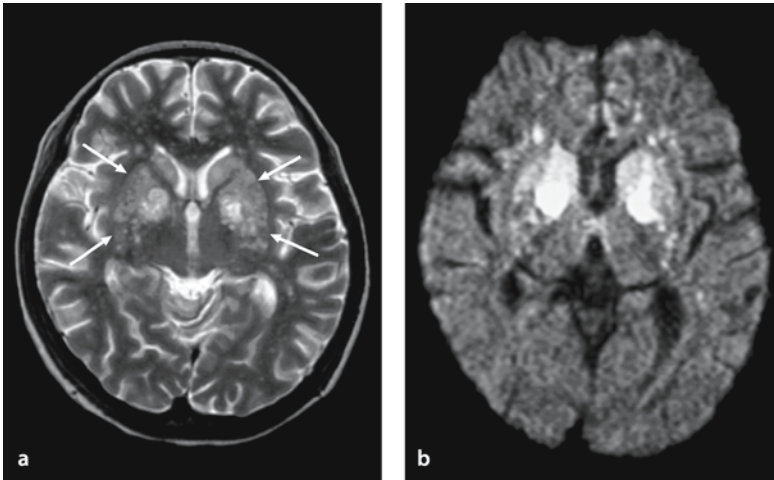
Figure 11.3 a,b

Brain abscesses due to gram-negative rods bacteria in a 28-year-old woman with Crohn's disease and long-term steroid use presenting with headache. Blood culture showed gram-negative rods. **a** T2-weighted image shows multiple small hyperintense lesions in bilateral basal ganglia (*arrows*) and white matter. **b** DW image shows these lesions as very hyperintense with decreased ADC (not shown). This finding mimics multiple small infarcts but it represents multiple small abscesses
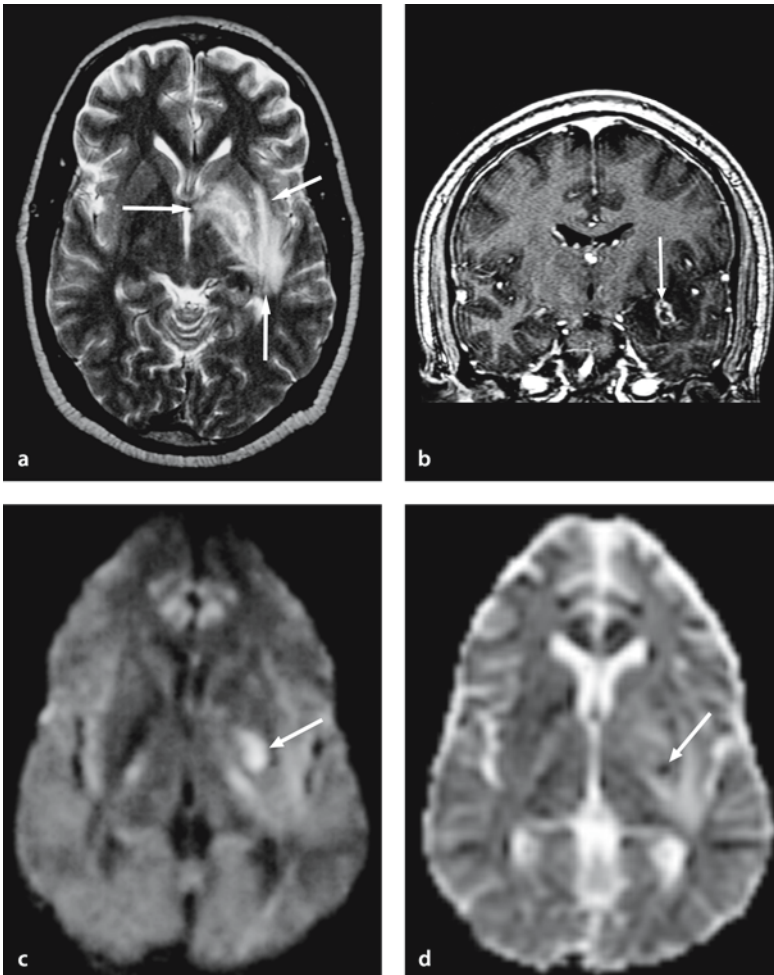
Figure 11.4 a–d

Listeria meningoencephalitis after bone marrow transplantation for chronic myeloblastic leukemia in a 31-year-old man presenting with a 2-day history of severe headache. **a** T2-weighted image shows hyperintense lesions in the left basal ganglia, internal capsule and white matter in the temporal lobe, representing encephalitis (*arrows*). **b** Coronal gadolinium-enhanced T1-weighted image shows an irregular ring-enhancing lesion (*arrow*). **c** DW image shows a central cystic component as hyperintense with decreased ADC (**d**) (*arrow*), representing an abscess

Figure 11.5 a–d

Glioblastoma multiforme in a 69-year-old woman. **a** T2-weighted image shows a central hyperintense mass lesion with low signal rim and peripheral edema in the right frontal lobe. **b** Gadolinium-enhanced T1-weighted image with magnetization transfer contrast shows this mass with irregular ring enhancement. **c** DW image shows a central cystic component as hypointense (*arrow*). **d** ADC map shows increased ADC of this cystic component (*arrow*)
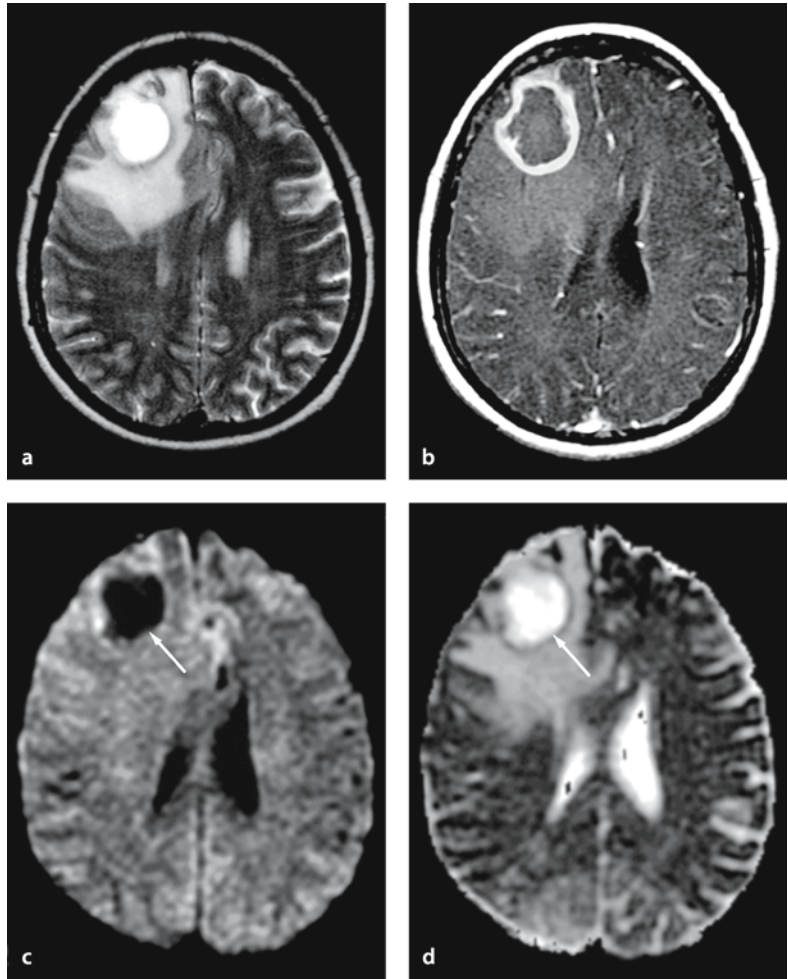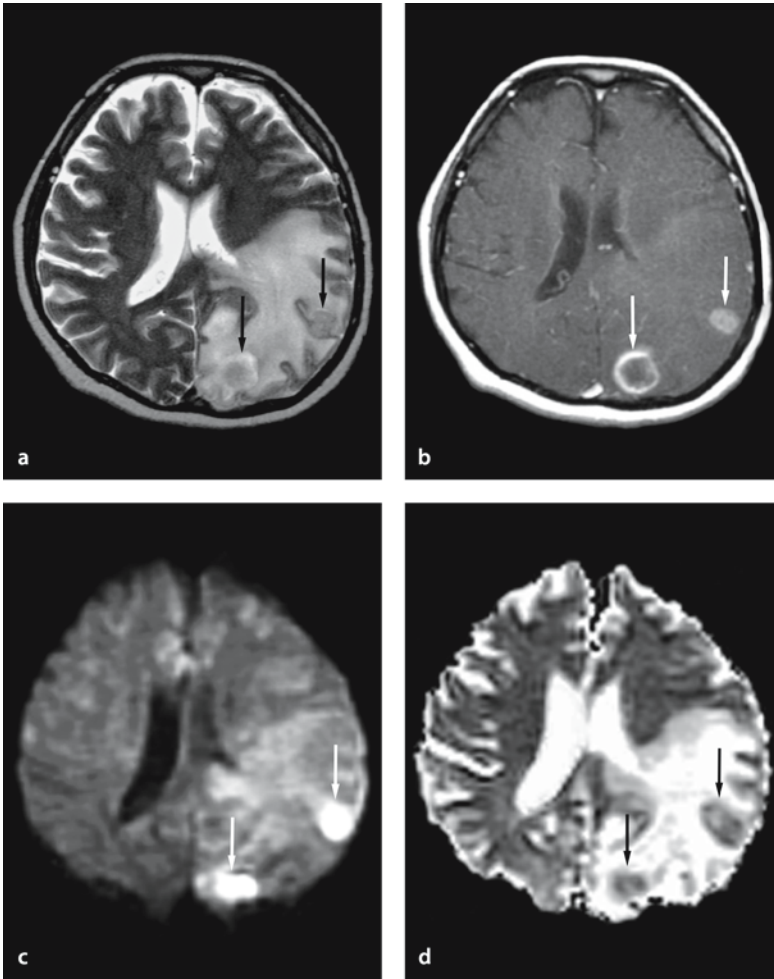
Figure 11.6 a–d

Brain metastasis from adenocarcinoma of the lung in a 44-year-old man. **a** T2-weighted image shows multiple mass lesions and peripheral edema in the left parieto-occipital lobe. **b** Gadolinium-enhanced T1-weighted image with magnetization transfer contrast shows these lesions with irregular ring enhancement (*arrows*). **c** DW image shows central cystic components as hyperintense (*arrows*). **d** ADC map shows relative low ADC values of cystic components, presumably representing coagulative necrosis or mucinous substance (*arrows*)
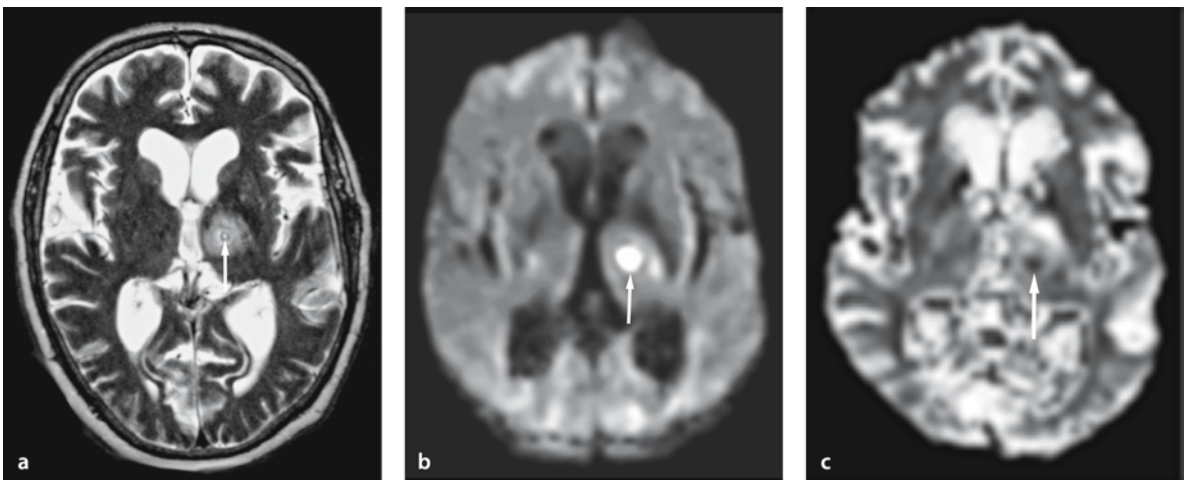
11.5 Bacterial Abscess in the Extra-Axial Space

Infections can enter the extra-axial spaces by a variety of mechanisms, including direct spread from an adjacent focus, retrograde septic thrombophlebitis, hematogenous seeding and sequela of purulent leptomeningitis [19]. Abscesses can occur in epidural, subdural (Fig. 11.8), leptomeningeal (Fig. 11.9) or intraventricular spaces (Fig. 11.10) [20, 21]. Wherever they occur, DW imaging shows pus in the abscess as hyperintense, with relatively low ADC values. An exception to the rule can be found in some cases of extraaxial pus collections where the ADC may from low to high. Regions of increased ADC may represent dilution of pus with CSF.

11.5.1 Differential Diagnosis

Hematomas and epidermoids occasionally have imaging characteristics similar to those of an extra-axial abscess on DW imaging. The hematomas often show hyperintensity with decreased ADC, probably because of the hypercellularity or hyperviscosity (Fig. 11.11) [22, 23]. Epidermoids also show an extra-axial hyperintense lesion on DW imaging (Fig. 11.12) caused by high viscosity keratohyalin- containing materials, which are arranged in layers, as in an onion bulb. Moreover, they are rich in cholesterol crystals. ADC maps usually show slightly increased ADC as compared with normal brain parenchyma [24].
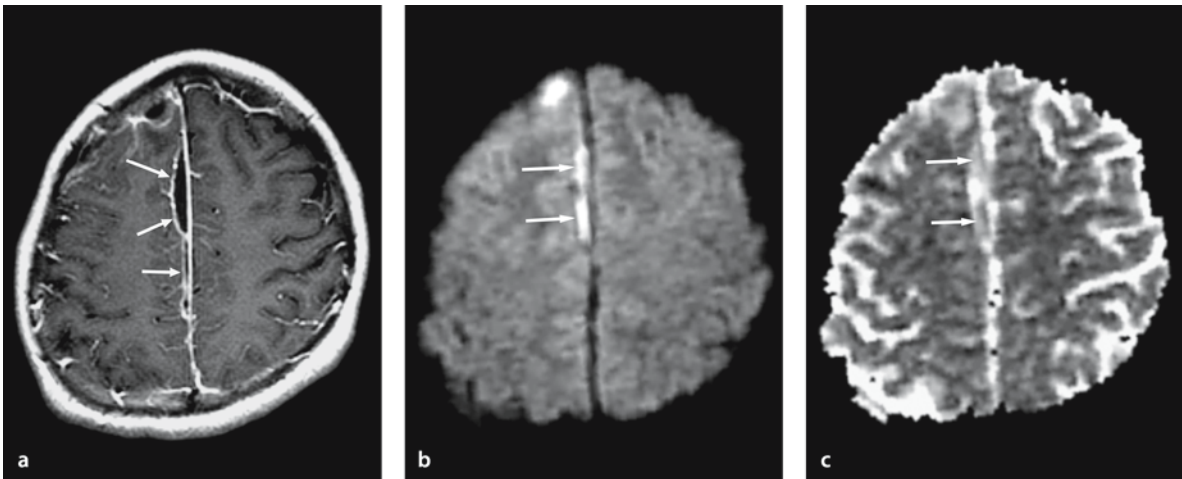
Figure 11.8 a–c

Subdural empyema in a 16-year-old male. a Gadolinium-enhanced T1-weighted image with magnetization transfer contrast shows rim-enhancing lesions along the falx (*arrows*). Mild meningeal enhancement is also seen. b DW image shows these lesions as hyperintense, representing subdural abscesses (*arrows*). c ADC map shows these lesions as relatively decreased ADC (*arrows*) compared with CSF (Courtesy of Morikawa M, M.D., Nagasaki University, School of Medicine, Japan)

Figure 11.7 a–c

Coagulative necrosis 4 weeks after radiofrequency thalamotomy for essential tremor in a 70-year-old man. a T2-weighted image shows a hyperintense lesion with mild peripheral edema in the left thalamus (*arrow*). b DW image shows a central cystic component as hyperintense. c ADC map shows this component as decreased ADC, probably representing coagulative necrosis. This lesion was decreased in size on follow-up MRI without antibiotic treatment

◀
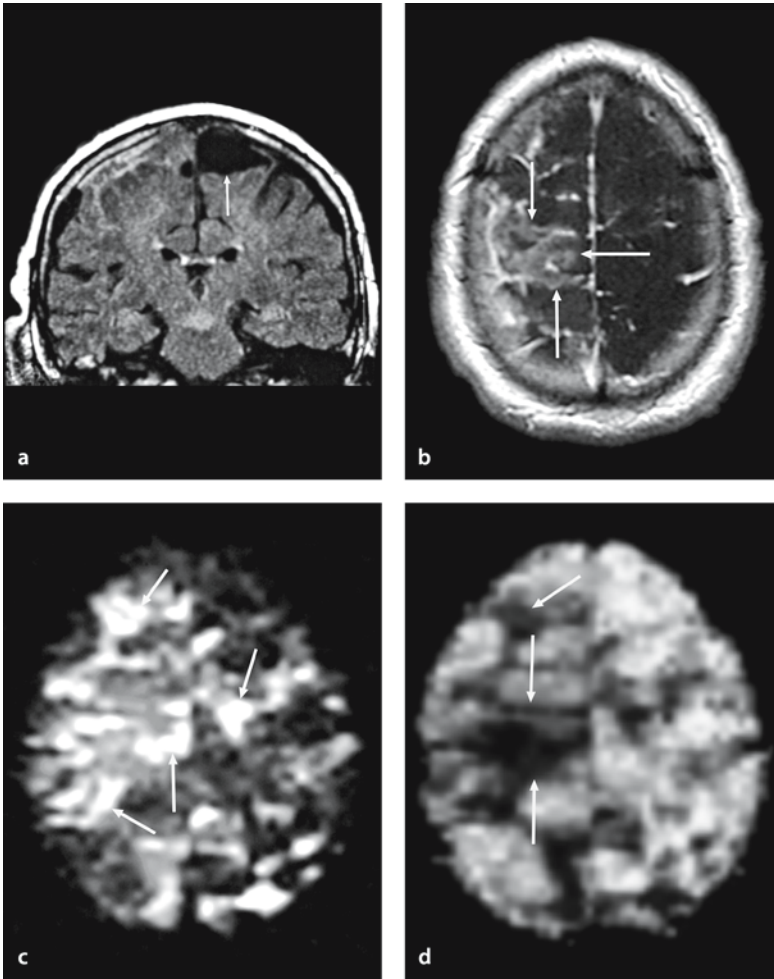
Figure 11.9 a–d

Purulent leptomeningitis in a 77-year-old man. Pneumococcus was proven by CSF examination. **a** Coronal fluid-attenuated inversion-recovery image shows hyperintense lesions in subarachnoid space in the right fronto-parietal region (*arrow*). **b** Gadolinium-enhanced T1-weighted image with magnetization transfer contrast shows irregular enhancement of these lesions (*arrows*). **c** DW image shows these lesions as hyperintense, representing purulent leptomeningitis (*arrows*). **d** ADC map shows these lesions as decreased ADC (*arrows*)

Figure 11.10 a–d

Purulent ventriculitis after surgery in a 60-year-old man. **a** Gadolinium-enhanced T1-weighted image with magnetization transfer contrast shows linear enhancement along the ventricle (*arrows*). There are post-surgical changes in the left frontal lobe and extracranially on the left. **b** T2-weighted image shows a fluid–fluid level in bilateral lateral ventricles (*arrows*) and postoperative changes in the left frontal lobe (*arrowhead*). **c** DW image shows the fluid (*arrows*) as hyperintense, representing purulent ventriculitis, and postoperative changes in the left frontal lobe (*arrowhead*). **d** ADC map shows these lesions as decreased ADC
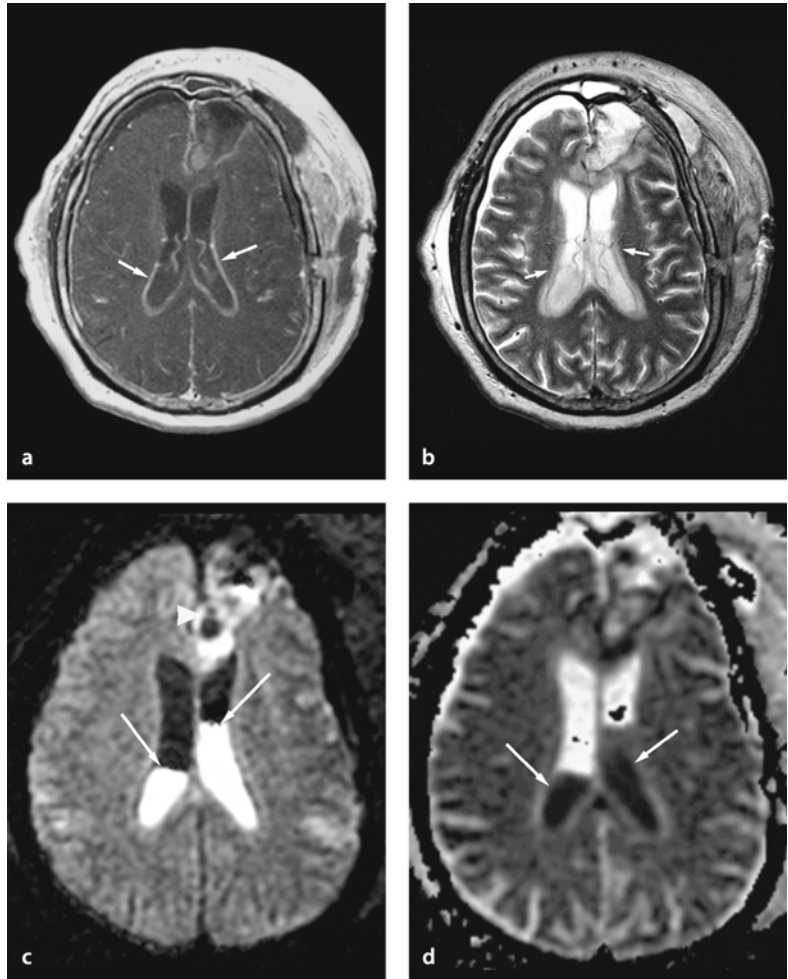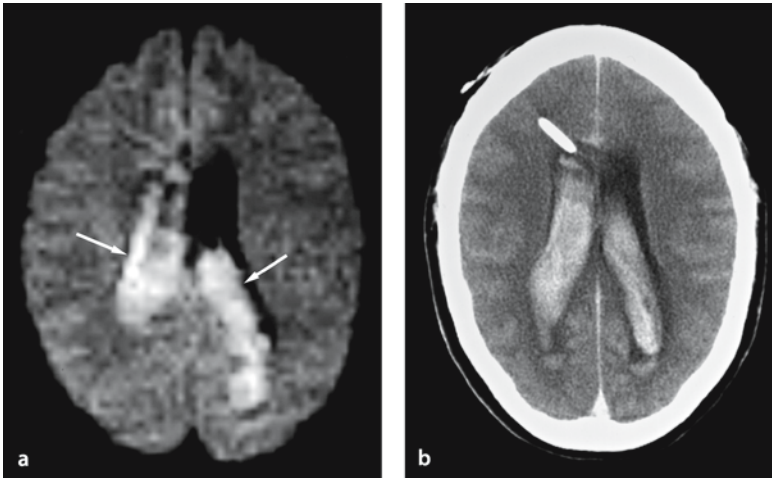
Figure 11.11 a,b

Intraventricular hemorrhage due to arteriovenous malformation in a 29-year-old man. **a** DW image shows hyperintense lesions (*arrows*) with decreased ADC (not shown), similar to the finding seen in purulent intraventriculitis. **b** Computed tomography shows the high density of intraventricular hemorrhage
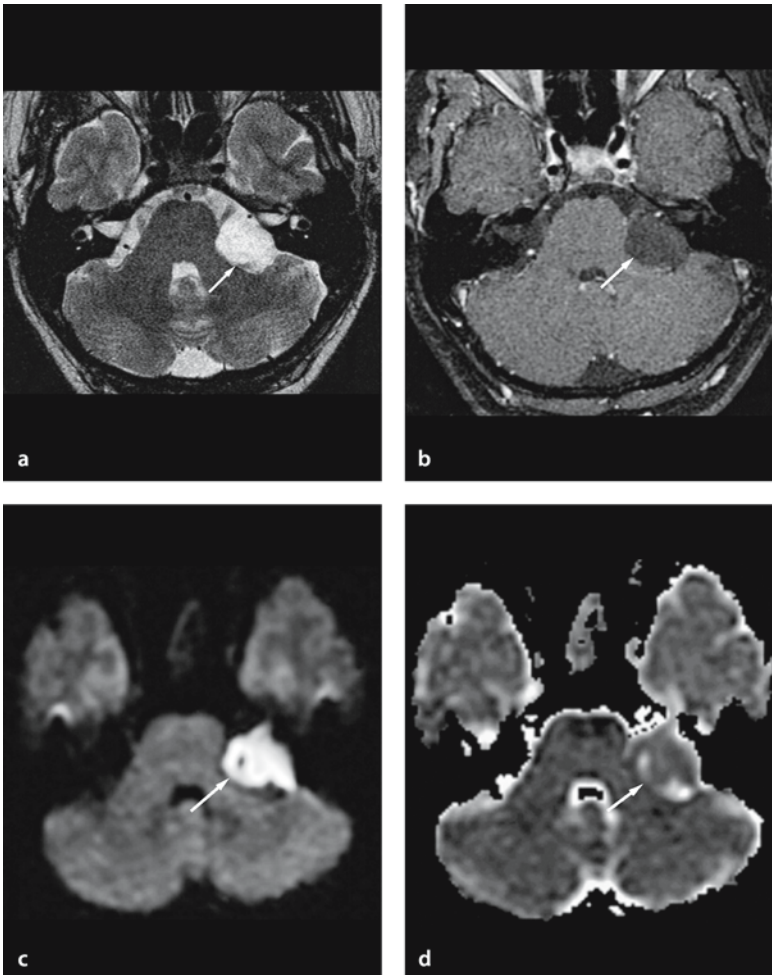
Figure 11.12 a–d

Epidermoid in a 29-year-old male. **a** T2-weighted image shows a hyperintense mass (*arrow*) in the left cerebello-pontine angle. **b** Gadolinium-enhanced T1 weighted image with magnetization transfer contrast shows the lesion (*arrow*) as hypointense with no enhancement. **c** DW image shows this lesion (*arrow*) as hyperintense. **d** ADC map shows almost similar ADC value to the cerebellar parenchyma

11.6 Bacterial Vasculitis

Cerebral infarctions secondary to meningitis are well documented in the pediatric age group. Thus, *Streptococcus* B meningitis in neonates can result in infarction, a condition that is rare in adults. The blood–brain/blood–cerebrospinal fluid (CSF) barrier and the mechanical integrity of meninges are immature in young infants, which may explain the preponderance for these changes to occur in babies and young infants [25]. Both arteries and veins can be involved by infection via the perivascular space. Pial arteriolar occlusion causes infarction of the subpial cortex (Fig. 11.13). Although vasculitic changes occur early, they only become prominent resulting in an infarction by the second to third week after onset of the meningeal infection. DW imaging is useful in early detection of the infarction, which is bright on DW imaging, with low ADC.

11.7 Toxoplasmosis

Toxoplasma abscesses consist of ischemic necrosis of the brain tissue associated with sclerosing endoarteritis and a variety of inflammatory reactions. Toxoplasma abscesses are more commonly seen in immunocompromised patients, such as patients with acquired immunodeficiency syndrome (AIDS). In fact, toxoplasma abscesses in AIDS patients were once so common that they were morphologically grouped into three subtypes: (1) poorly circumscribed areas of necrosis (necrotizing abscess), (2) a central area of coagulative necrosis surrounded by macrophages and organism (organizing abscess), and (3) well-demarcated cystic spaces (chronic abscess) [26].

Diffusion-weighted imaging of a toxoplasma abscess may show a variety of signal characteristics, which probably is a reflection of the different pathologic/morphologic subtypes (Fig. 11.14). Abscesses with different characteristics are often seen in the same patient. Central necroses in toxoplasma abscesses do not contain as many inflammatory cells as regular bacterial abscesses.
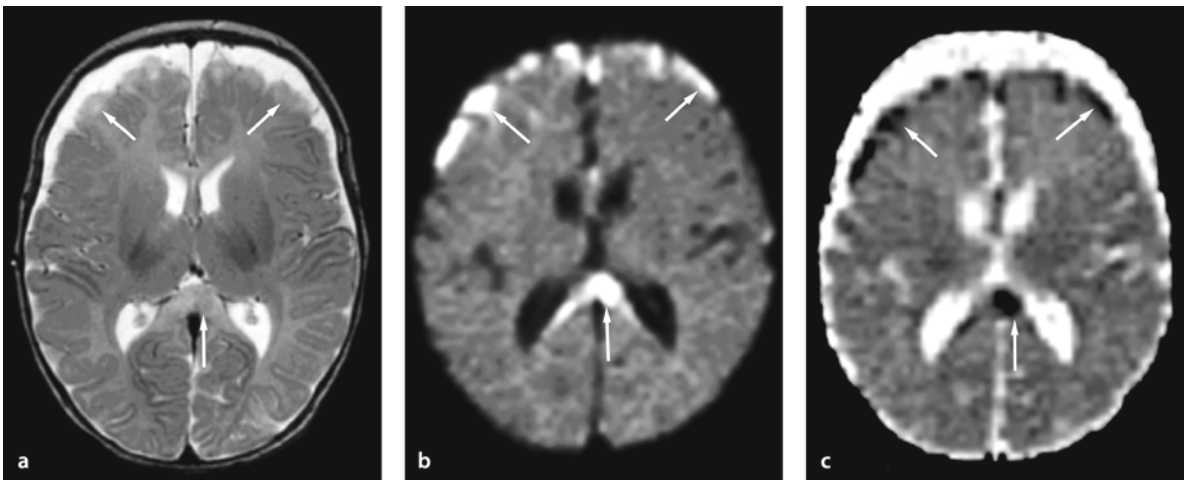
Figure 11.13 a–c

Group B *Streptococcus* meningitis in a 5-week-old boy. **a** T2-weighted image shows bifrontal subdural effusion and hyperintense lesions in bilateral frontal superficial cortices and posterior corpus callosum (*arrows*). **b** DW image shows these lesions (*arrows*) as hyperintense. **c** ADC map shows these lesions (*arrows*) as decreased ADC, representing acute infarcts of the subpial cortex
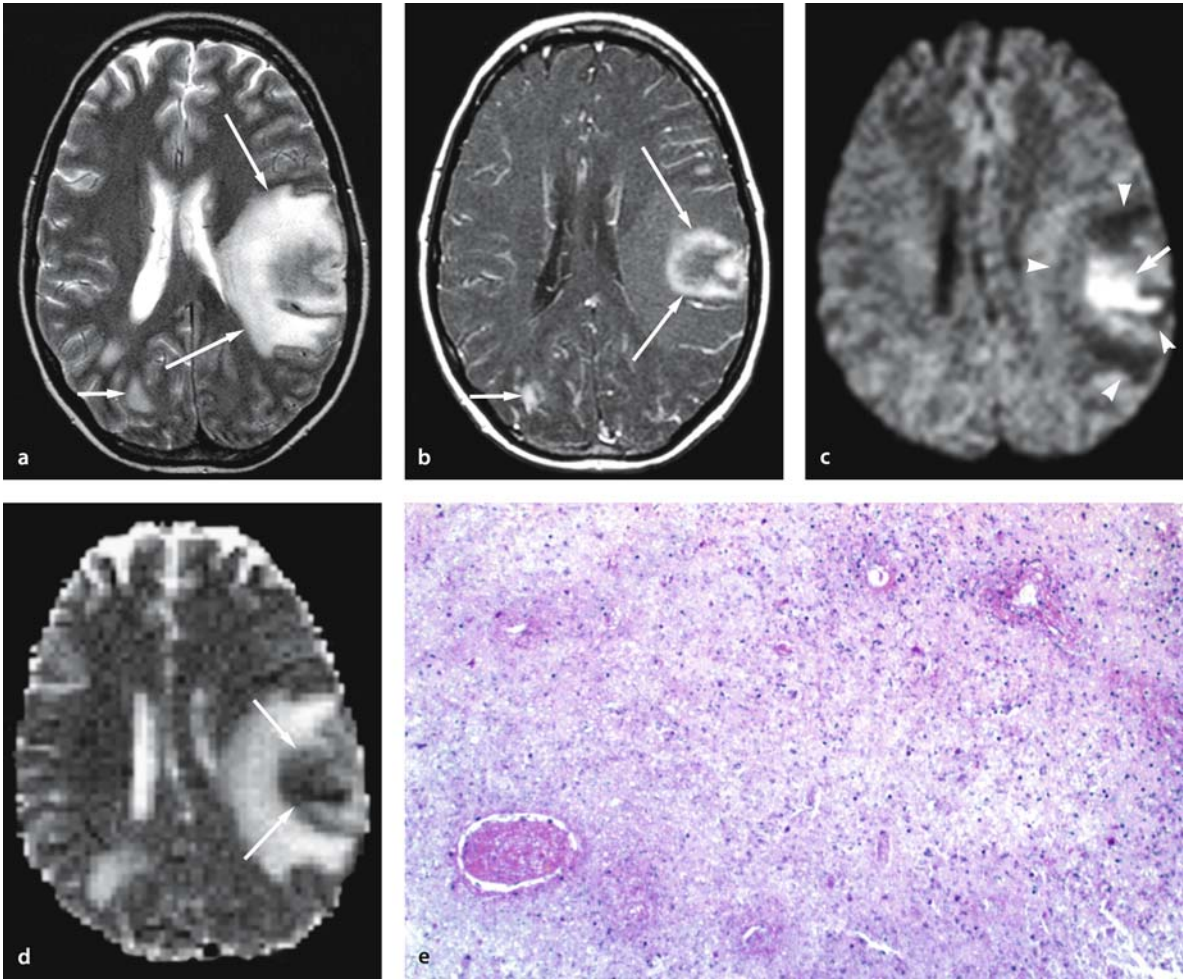
Figure 11.14 a–g

Toxoplasmosis in an 18-year-old woman with acute myeloblastic leukemia. **a** T2-weighted image shows a mass lesion with vasogenic edema in the left fronto-temporal region (*long arrows*). Hyperintense lesions are also seen in the right occipital area (*short arrow*). **b** Gadolinium-enhanced T1-weighted image with magnetization transfer contrast shows a ring-enhancing mass (*long arrows*) and an enhancing nodule (*short arrow*). **c** DW image shows a non-enhancing cystic central area as hyperintensity (*arrow*), and the enhancing rim and peripheral vasogenic edema as hypointensity (*arrowheads*). **d** ADC map shows decreased ADC of this cystic component (*arrows*). **e** Biopsy specimen shows coagulative necrosis of this cystic component (hematoxylin–eosin stain). **f, g** DW image shows a small cystic lesion (*arrow*) as hypointense with increased ADC (**g**) in the right caudate nucleus (*arrow*), which may indicate the different phase of toxoplasma abscess. Left fronto-temporal mass and multiple hyperintense nodules are also seen
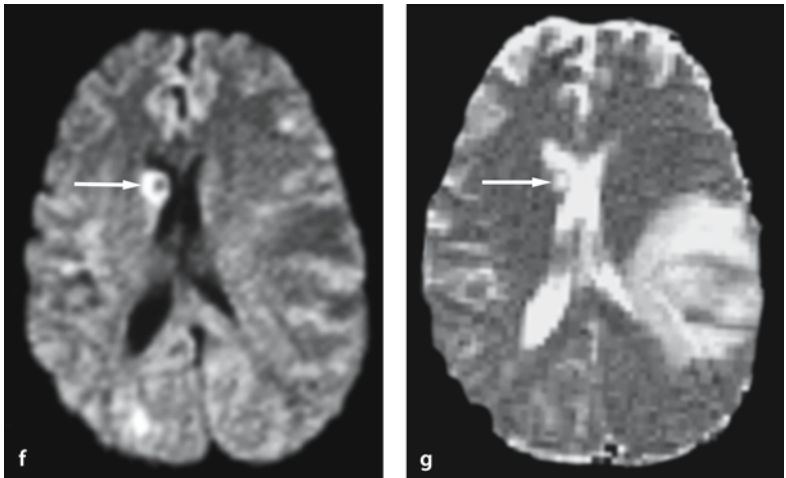
11.7.1 Differential Diagnosis

The main differential diagnosis is lymphoma. In AIDS patients, central nervous system lymphoma is often associated with central necrosis. This is occasionally liquefactive, presumably related to hypoxia or apoptosis of tumor cells. The enhancing portion of the lesion usually shows hyperintensity on DW imaging, with relatively low ADC due to hypercellularity of lymphomas (Fig. 11.15). A central necrosis usually shows hypointensity on DW imaging, with increased ADC.

Figure 11.15

AIDS-related lymphoma in a 23-year-old man. **a** T2-weighted image shows a necrotic mass in the left frontal lobe extending into the temporo-occipital lobe. **b** Gadolinium-enhanced T1-weighted image magnetization transfer contrast shows these lesions (*arrows*) with irregular ring enhancement. **c** DW image shows enhancing solid components as hyperintensity (*arrowheads*), and a necrotic component as hypointensity (*arrow*). **d** ADC map shows central necrosis as increased ADC (*long arrow*) and the solid components (*short arrows*) as relatively low ADC compared to the central necrosis
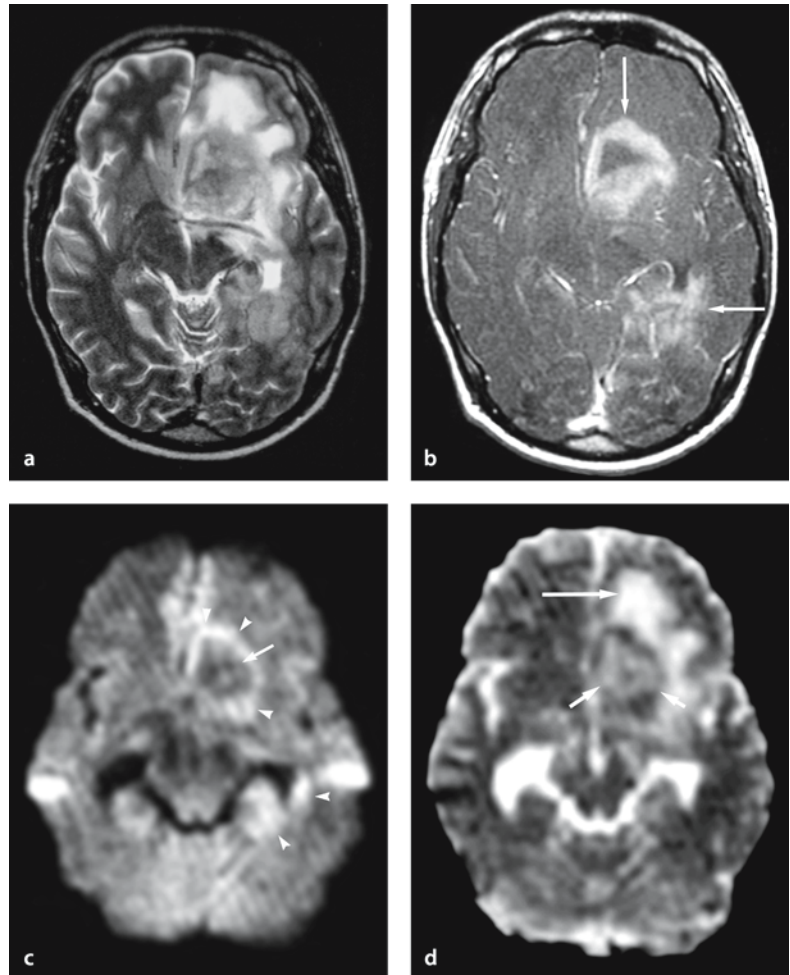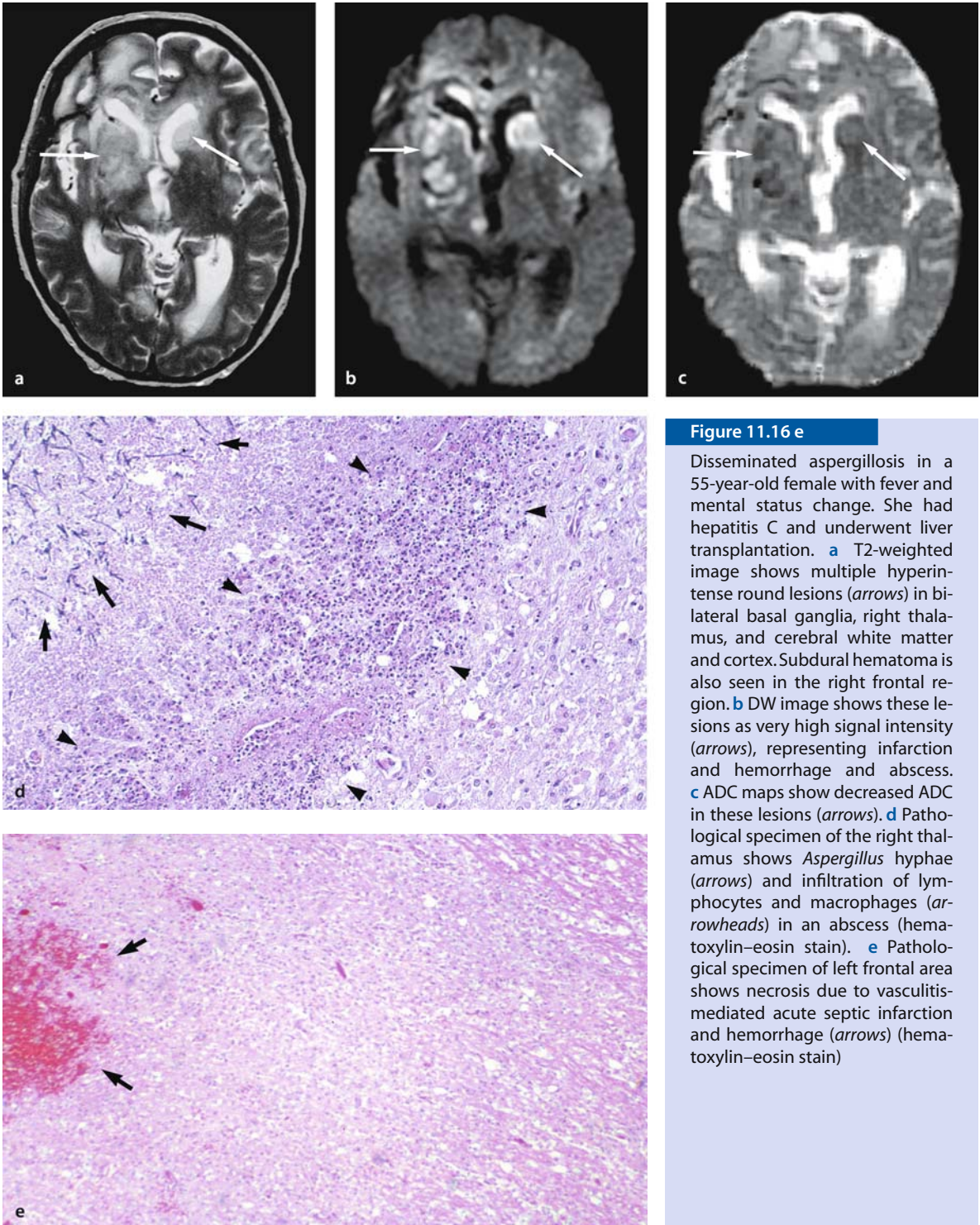
Figure 11.16 e

Disseminated aspergillosis in a 55-year-old female with fever and mental status change. She had hepatitis C and underwent liver transplantation. **a** T2-weighted image shows multiple hyperintense round lesions (*arrows*) in bilateral basal ganglia, right thalamus, and cerebral white matter and cortex. Subdural hematoma is also seen in the right frontal region. **b** DW image shows these lesions as very high signal intensity (*arrows*), representing infarction and hemorrhage and abscess. **c** ADC maps show decreased ADC in these lesions (*arrows*). **d** Pathological specimen of the right thalamus shows *Aspergillus* hyphae (*arrows*) and infiltration of lymphocytes and macrophages (*arrowheads*) in an abscess (hematoxylin–eosin stain). **e** Pathological specimen of left frontal area shows necrosis due to vasculitis-mediated acute septic infarction and hemorrhage (*arrows*) (hematoxylin–eosin stain)

11.8 Disseminated Aspergillosis

In disseminated aspergillosis, *Aspergillus* infiltrates and destroys the internal elastic lamina of cerebral arteries and causes vasculitis [27]. This leads initially to acute infarction or hemorrhage. Most of the process extends into the surrounding tissue as cerebritis and eventually evolves into an abscess. Infection of already infarcted brain tissue is often aggressive with rapid progression. DW imaging is useful for early detection of this vasculopathy-mediated septic infarction and abscess (Fig. 11.16). New antifungal therapies (triazole) have made effective treatment possible.

11.9 Herpes Encephalitis

Pathologically, herpes encephalitis has both cytotoxic and vasogenic edema associated with massive tissue necrosis and petechial or even confluent hemorrhage. DW imaging is more sensitive than conventional MR imaging in detecting early changes of herpes encephalitis (Fig. 11.17) [28, 29]. This is important for early diagnosis and treatment. Herpes encephalitis typically affects the temporal lobes, which occasionally can make the detection of lesions in the middle cranial fossa difficult on DW imaging because of susceptibility artifacts.
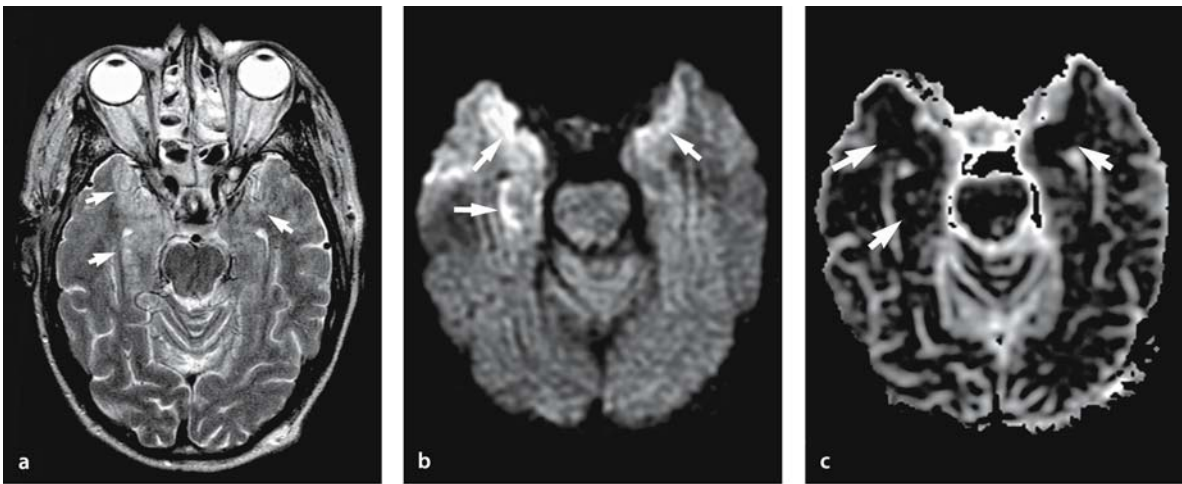
Figure 11.17 a–d

Herpes encephalitis in a 48-year-old man. **a** T2-weighted image shows hyperintense lesions in bilateral temporal lobes (*arrows*). **b** DW image shows these lesions as hyperintense. **c** ADC maps shows partially decreased ADC of these lesions (*arrows*). **d** In another patient with herpes encephalitis, pathological specimen shows cytotoxic edema and hemorrhage
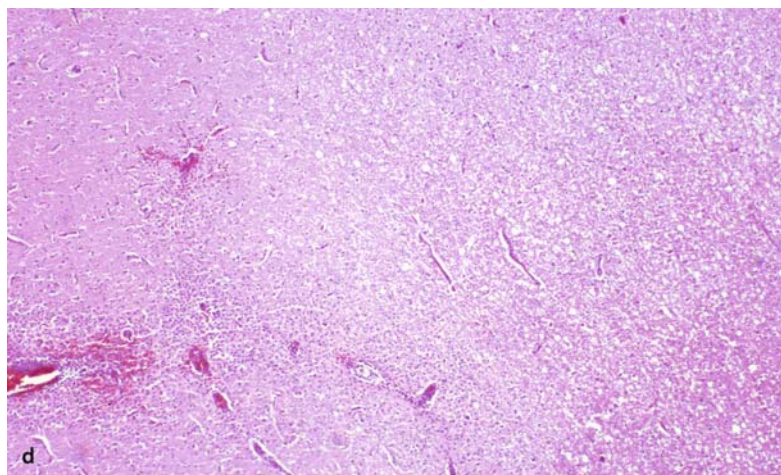
11.10 Human Immunodeficiency Virus Infection

The pathological hallmark of human immunodeficiency virus (HIV) encephalopathy is multinucleated giant cells in the white matter [30]. This results in myelin pallor and rarefaction. MR imaging typically shows diffuse periventricular white matter lesions, but brain stem and basal ganglia can also be involved. DW imaging usually shows mild hyperintensity with decreased ADC which is secondary to a T2 shine through effect (Fig. 11.18).

Cerebral infarction in HIV patients is common and has been seen on MR imaging in up to 18% of the patients [31]. The infarctions are caused by opportunistic infections, drug use and primary HIV vasculitis. AIDS-related bilateral basal ganglia lesions are reported to be numerous microinfarcts on postmortem neuropathological examination [32]. DW imaging can show numerous hyperintense lesions in bilateral basal ganglia, presumably representing microinfarcts (Fig. 11.19).
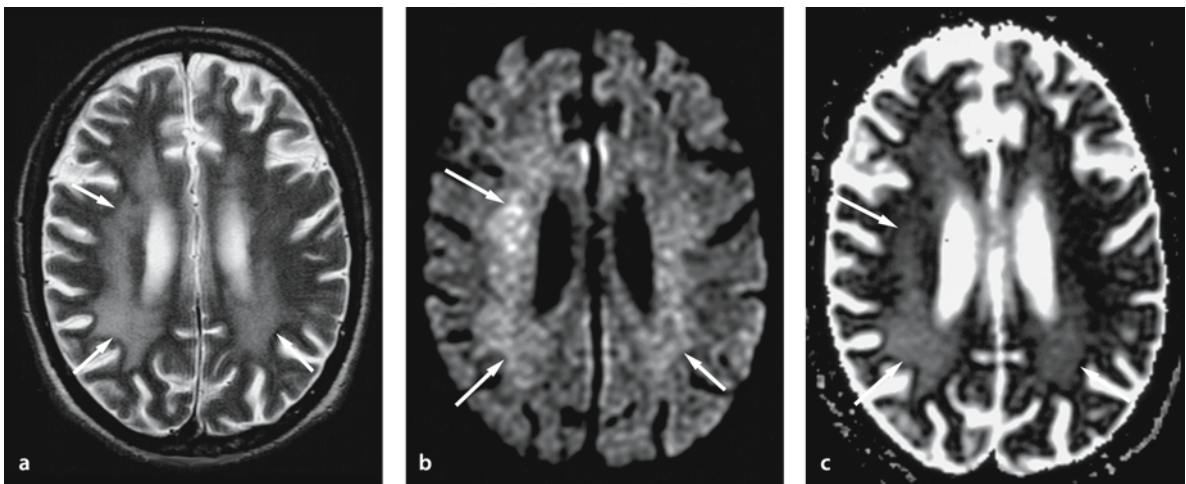
Figure 11.18 a–c

HIV encephalopathy in a 60-year-old man. **a** T2-weighted image shows periventricular hyperintense lesions (*arrows*). **b** DW image shows these lesions as mild hyperintensity (*arrows*). **c** ADC map shows these lesions as increased ADC. Mild hyperintensity on DW imaging is due to T2 shine-through effect (*arrows*)
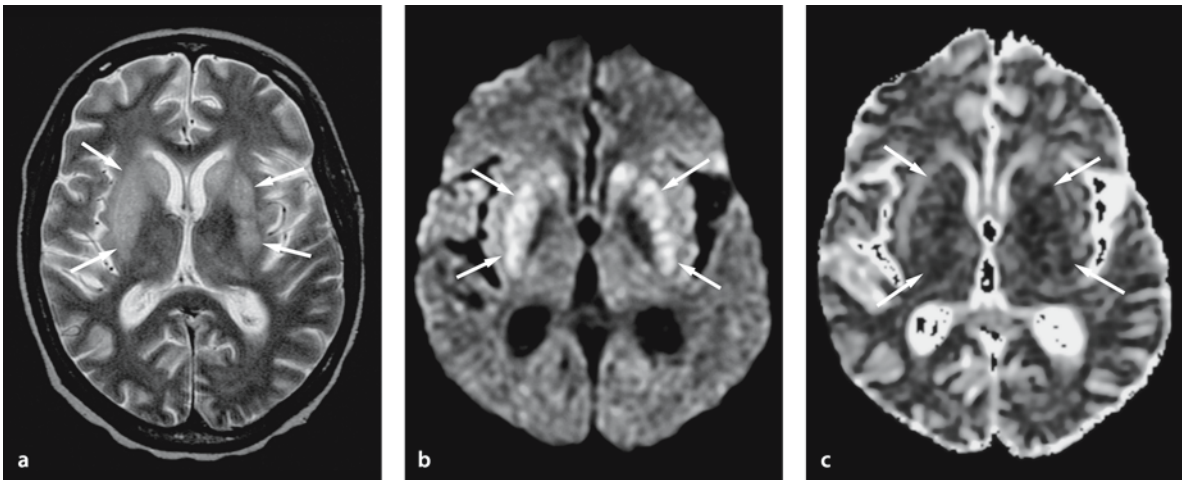
Figure 11.19 a–c

AIDS-related bilateral basal ganglia lesions in a 38-year-old female with multiple small infarcts, probably associated with HIV vasculitis. **a** T2-weighted image shows hyperintense lesions in bilateral caudate nuclei and putamina (*arrows*). **b** DW image demonstrates these lesions as numerous hyperintense spots, probably representing microinfarcts associated with HIV infection and/or drug abuse (*arrows*). **c** ADC map shows these lesions as partially decreased ADC (*arrows*)

References

1. Ebisu T, Naruse S, Horikawa Y, et al. (1993) Discrimination between different types of white matter edema with diffusion-weighted MR imaging. JMRI 3:863–868

2. Ebisu T, Tanaka C, Umeda M, et al. (1996) Discrimination of brain abscess from necrotic or cystic tumors by diffusion-weighted echo planar imaging. Magn Reson Imaging 14:1113–1116

3. Kim YJ, Chang KH, Song IC, et al. (1998) Brain abscess and necrotic or cystic brain tumor: discrimination with signal intensity on diffusion-weighted MR imaging. AJR Am J Roentgenol 171:1487–1490

4. Desprechins B, Stadnik T, Koerts G, et al. (1999) Use of diffusion-weighted MR imaging in differential diagnosis between intracerebral necrotic tumors and cerebral abscesses. AJNR Am J Neuroradiol 20:1252–1257

5. Noguchi K, Watanabe N, Nagayashi T, et al. (1999) Role of diffusion-weighted echo-planar MRI in distinguishing between brain abscess and tumor: a preliminary report. Neuroradiology 41:171–174

6. Castillo M (1999) Imaging brain abscess with diffusion-weighted and other sequences. AJNR Am J Neuroradiol 20:1193–1194

7. Gray F, Nordmann P (1997) Bacterial infections. In: Graham DI, Lantos PL (eds) Greenfield's neuropathology, vol 2, 6th edn, pp 114–129

8. Falcone S, Post MJD (2000) Encephalitis, cerebritis, and brain abscess: pathophysiology and imaging findings. Neuroimaging Clin North Am 10:333–353

9. Hatta S, Mochizuki H, Kuru Y, et al. (1994) Serial neurological studies in focal cerebritis. Neuroradiology 36:285–288

10. Ketelslegers E, Duprez T, Ghariani S, et al. (2000) Time dependence of serial diffusion-weighted imaging features in a case of pyogenic brain abscess. JCAT 24:478–481

11. Bakshi R, Wright PD, Kinkel PR, et al. (1999) Cranial magnetic resonance imaging findings in bacterial endocarditis: the neuroimaging spectrum of septic brain embolization demonstrated in twelve patients. J Neuroimaging 9:78–84

12. Höllinger P, Zürcher R, Schroth G, et al. (2000) Diffusion magnetic resonance imaging findings in cerebritis and brain abscess in a patient with septic encephalopathy. J Neurol 247:232–234

13. Nagase T, Wada S, Nakamura R, et al. (1995) Magnetic resonance imaging of multiple brain abscesses of bilateral basal ganglia. Internal Medicine 34:554–558

14. Southwick FS, Purich DL (1996) Intracellular pathogenesis of listeriosis. New Eng J Med 334:770–776

15. Holtås S, Geijer B, Strömblad LG, et al. (2000) A ring-enhancing metastasis with central high signal on diffusion-weighted imaging and low apparent diffusion coefficients. Neuroradiology 42:824–827

16. Hartman M, Jansen O, Heiland S, et al. (2001) Restricted diffusion within ring enhancement is not pathognomonic for brain abscess. AJNR Am J Neuroradiol 22:1738–1742

17. Tung GA, Evangelista P, Rogg JM, et al. (2001) Diffusion-weighted MR imaging of rim-enhancing brain masses: is markedly decreased water diffusion specific for brain abscess? AJR Am J Roentgenol 177:709–712

18. Fredman DP, Goldman HW, Flanders AE (1997) MR imaging of stereotaxic palidotomy and thalamotomy. AJR Am J Roentgenol 169:894–896

19. Ackerman LL, Traynelis VC (1999) Dural space infection: cranial subdural empyema and cranial epidural abscess. In: Osenbach RK, Zeidman SM, (eds) Infections in neurological surgery. Philadelphia: Lippincott-Raven, pp 85–99

20. Ramsay DW (2000) Diffusion-weighted imaging of cerebral abscess and subdural empyema. AJNR Am J Neuroradiol 21:1172

21. Rana S, Albayram S, Lin DDM, et al. (2002) Diffusion-weighted imaging and apparent diffusion coefficient maps in a case of intracerebral abscess with ventricular extension. AJNR Am J Neuroradiol 23:109–112

22. Ebisu T, Tanaka C, Umeda M, et al. (1997) Hemorrhagic and nonhemorrhagic stroke: diagnosis with diffusion-weighted and T2-weighted echo-planar MR imaging. Radiology 203:823–828

23. Atlas SW, Dubois P, Singer MB, et al. (2000) Diffusion measurements in intracranial hematomas: implications for MR imaging of acute stroke. AJNR Am J Neuroradiol 21:1190–1194

24. Tsuruda JS, et al. (1990) Diffusion-weighted MR imaging of the brain: value of differentiating between extraaxial cysts and epidermoid tumors. AJNR Am J Neuroradiol 11:925–931

25. Moodley M, Bullock MR (1985) Severe neurological sequelae of childhood bacterial meningitis. S Afr Med J 68:566–570

26. Navia BA, Petito CK, Gold JWM, et al. (1986) Cerebral toxoplasmosis complicating the acquired immune deficiency syndrome: clinical and neurological findings in 27 patients. Ann Neurol 19:224–238

27. DeLone DR, Goldstein RA, Petermann G, et al. (1999) Disseminated aspergillosis involving the brain: distribution and imaging characteristics. AJNR Am J Neuroradiol 20:1597–1604

28. Sener RN (2001) Herpes simplex encephalitis: diffusion MR imaging findings. Comput Med Imaging Graph 25:391–397

29. Tsuchiya K, Katase S, Yoshino A, et al. (1999) Diffusion-weighted MR imaging of encephalitis. AJR Am J Roentgenol 173:1097–1099

30. Flowers CH, Mafee MF, Crowell R, et al. (1990) Encephalopathy in AIDS patients: evaluation with MR imaging. AJNR Am J Neuroradiol 11:1235–1245

31. Connor MD, Lammie GA, Bell JE, et al. (2000) Cerebral infarction in adult AIDS patients: observations from the Edinburgh HIV autopsy cohort. Stroke 31:2117–2126

32. Meltzer CC, Wells SW, Becher MW, et al. (1998) AIDS-related MR hyperintensity of the basal ganglia. AJNR Am J Neuroradiol 19:83–89

Trauma

12.1 Introduction

Head injuries are the most common cause of death and permanent disability in the early decades of life. They vary widely in their etiology, pathophysiology, clinical presentation, and optimal treatment strategies. Traumatic brain injuries are classified in two main categories: focal and diffuse brain injuries [1]. Focal brain injuries usually result from direct impact force to the head, like cerebral contusions and epidural hematomas. Diffuse brain injuries are caused by sudden changes in movement of the head, usually rotational accelerations, which result in a variety of injuries, ranging from a brief cerebral concussion to extensive diffuse axonal injuries (DAI).

Computed tomography (CT) is imperative in patients with focal and diffuse injuries, especially when hemodynamically or neurologically unstable [2]. However, CT is often false negative or underestimates contusions shortly after trauma, and DAIs are often not detected. Conventional MR imaging has higher detection sensitivity with regard to these lesions because of its greater sensitivity for edema [3].

Once it was thought that edema following traumatic brain injury was vasogenic, but recent experimental studies using diffusion-weighted (DW) imaging have shown that edema after head trauma consists of both vasogenic and cytotoxic edema [4–9]. Since DW imaging is also very sensitive in detecting small lesions of cytotoxic edema and can differentiate cytotoxic from vasogenic edema, it has become especially useful in the evaluation and staging of patients with DAI.

12.2 Diffuse Axonal Injury

Diffuse axonal injury results from a diffuse shearing-strain deformation causing change in shape of brain tissue from unequal movement of adjacent tissues that differ in density and rigidity [1]. Patients with DAI more often than with other types of primary brain injuries show severe impairment of consciousness at impact.

Pathologically, injury related to DAI is always more extensive microscopically than at gross examination [10]. Microscopically, shearing injuries initially produce multiple, characteristic axonal bulbs, or retraction balls, as well as numerous foci of perivascular hemorrhages.

The origin behind cytotoxic edema in DAI seems to be related to an excitotoxic mechanism, in particular glutamate [1, 11, 12]. Damage at the node of Ranvier will result in a traumatic defect in the axonal membrane. This defect causes excessive neurotransmitter release with increase in intracellular calcium ions, as in brain ischemia, which leads to axonal and glial cell swelling (cytotoxic or neurotoxic edema). These changes can eventually lead to axonal degeneration or necrosis with microglial and astrocytic reactive changes. Accumulation of hemosiderin-laden macrophages is also seen in the chronic phase.

12.2.1 Location

Common locations of DAI are at the gray–white matter junctions (Fig. 12.1), in the corpus callosum (Fig. 12.2) and at the dorsolateral aspect of the upper brain stem (Fig. 12.3). DAI may be confined to the white matter of the frontal and temporal lobes in mild head trauma [13]. With more severe rotational acceleration, lesions are also seen in the lobar white matter as well as in the posterior half of the corpus callosum. In cases with even greater trauma, lesions will also be found in the anterior corpus callosum, and the dor-
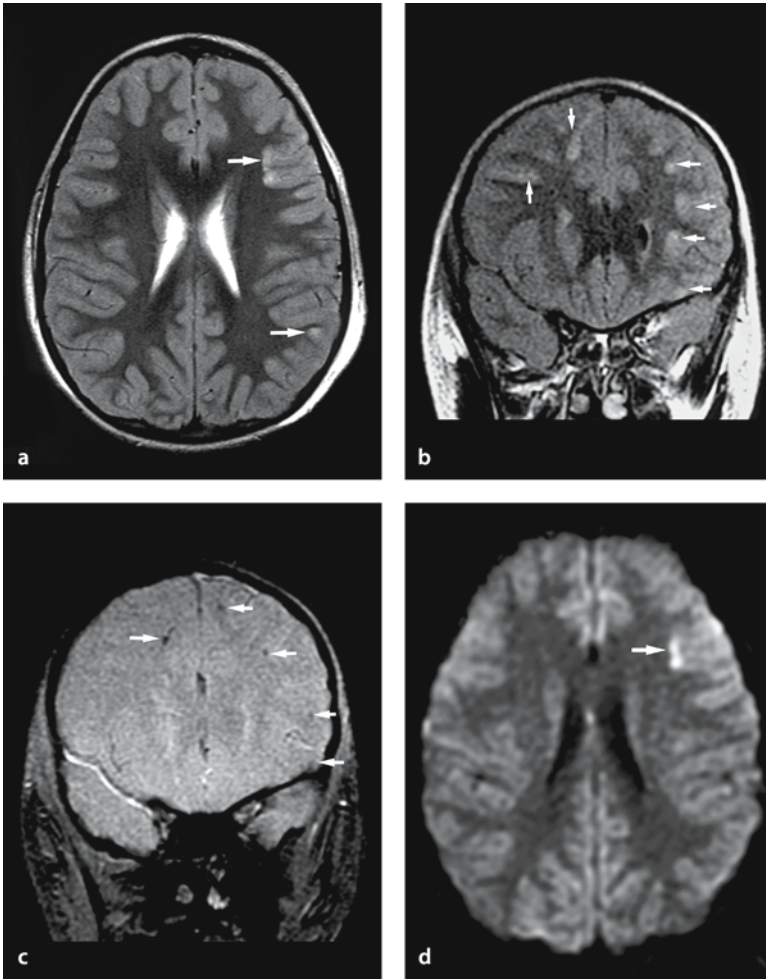
Figure 12.1 a–d

Fig. 12.1a–d. Diffuse axonal injury in gray–white matter junction in a 7-year-old male after a motor vehicle accident. T2-weighted (**a**) and coronal FLAIR (**b**) images show multiple hyperintense lesions in the gray–white matter junction of bilateral frontoparietal lobes (*arrows*). **c** Coronal GRE image shows multiple small hemorrhages as low signal in these lesions (*arrows*). **d** DW image demonstrates diffuse axonal injury as high signal intensity (*arrow*) with decreased ADC (not shown), representing cytotoxic edema

solateral aspects of the midbrain and upper pons. Occasionally, DAI lesions occur in the parietal and occipital lobes, internal and external capsules (Fig. 12.2), basal ganglia (Fig. 12.4), thalamus (Fig. 12.2), fornix (Fig. 12.5), septum pellucidum, and cerebellum (Fig. 12.6). Intraventricular hemorrhage can accompany these findings. They have the same mechanical origin and are due to disruption of the subependymal plexus of capillaries and veins that lie along the ventricular surface of the corpus callosum, fornix, and septum pellucidum [14].

Figure 12.3 a–c

Diffuse axonal injury in the brain stem in a 28-year-old male after a motor vehicle accident. **a** DW image shows a hypointense lesion with a hyperintense rim in the dorsolateral aspect of the midbrain, representing a hemorrhagic lesion of diffuse axonal injury (*arrow*). **b** ADC map shows decreased ADC of this lesion (*arrow*). This might be due to a paramagnetic susceptibility artifact. **c** Coronal GRE image clearly shows hemorrhagic lesions as hypointense in the brain stem (*arrow*) and in the right frontoparietal region

▶

Figure 12.2 a–d

Diffuse axonal injury in the corpus callosum, internal capsule and thalamus in a 29-year-old female after a motor vehicle accident. T2-weighted (**a**) and FLAIR (**b**) images show multiple hyperintense lesions in the anterior and posterior corpus callosum, internal capsules and left thalamus (*arrows*). **c** DW image demonstrates these lesions as high signal intensity with decreased ADC (**d**)
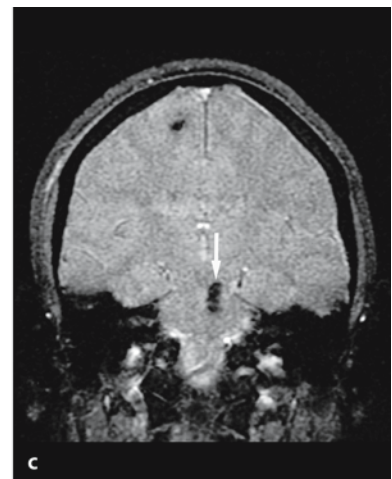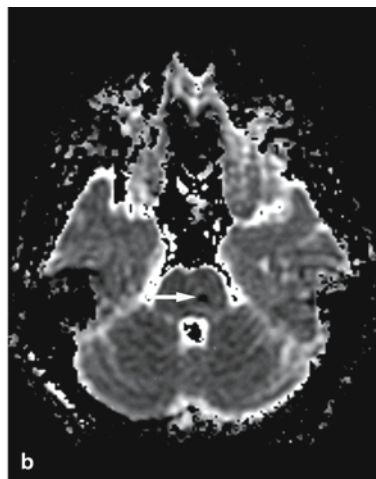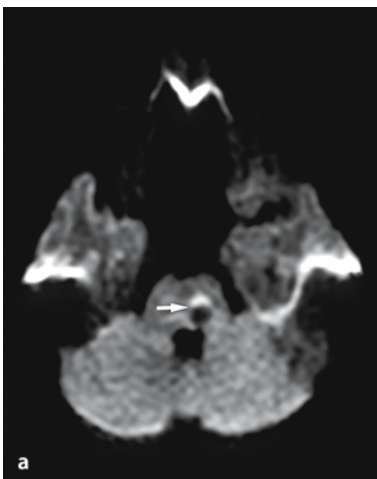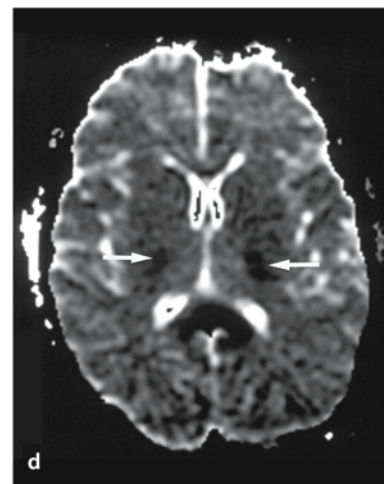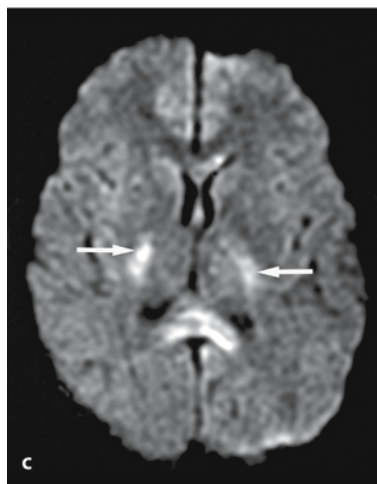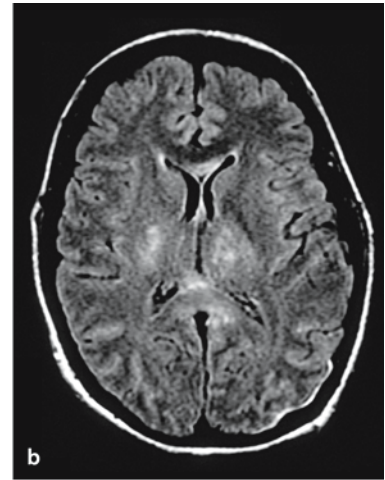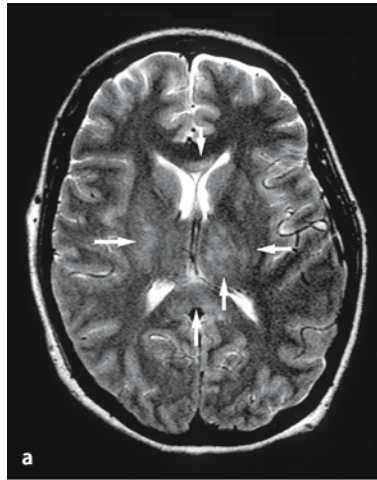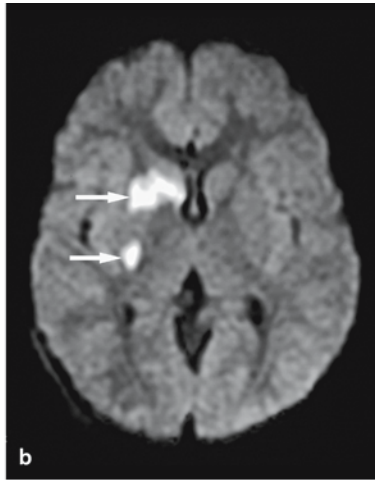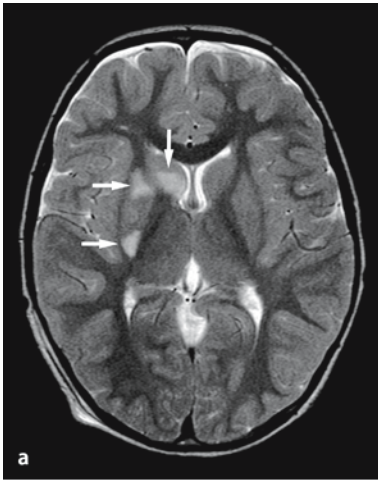
Figure 12.4 a–d

Diffuse axonal injury in the basal ganglia in a 3-year-old male after a motor vehicle accident. **a** T2-weighted image shows hyperintense lesions in the right lentiform and caudate nucleus (*arrows*). **b, c** DW imaging shows these lesions as hyperintense with decreased ADC (*arrows*). **d** Coronal GRE image clearly shows no hemorrhagic foci in these lesions
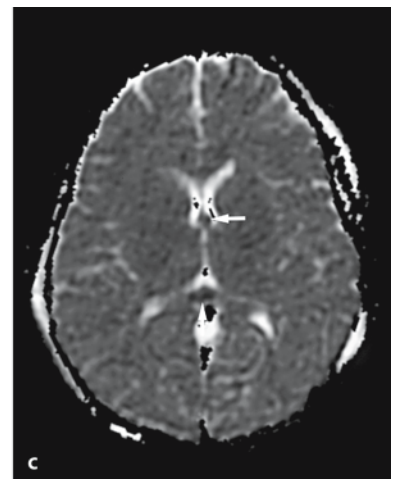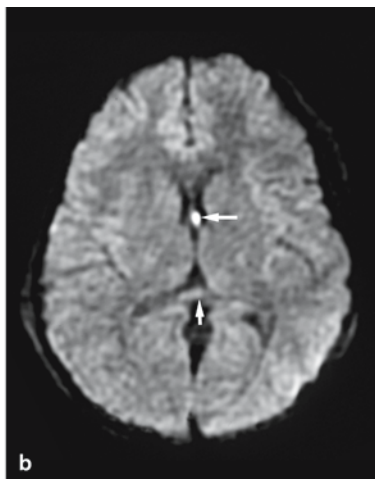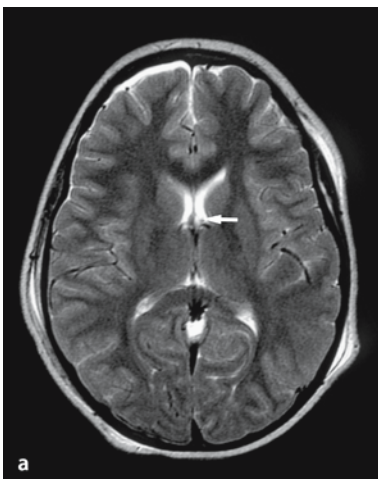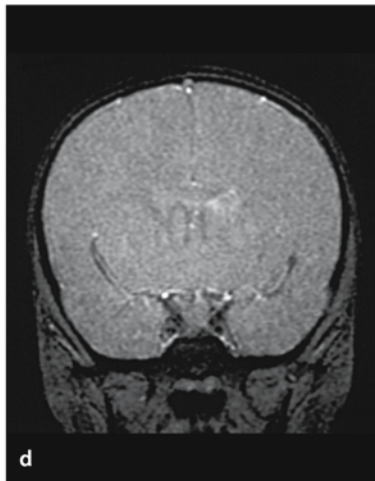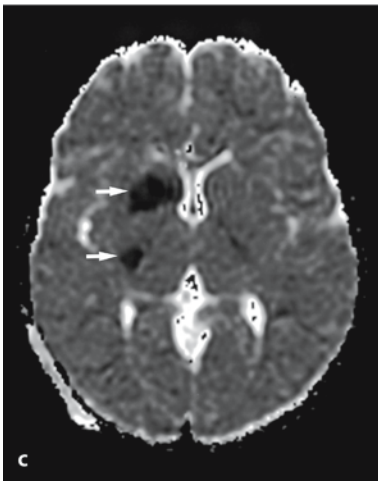
Figure 12.6 a–d

Diffuse axonal injury in the cerebellum of an 18-year-old male after a motor vehicle accident. **a** T2-weighted image shows a hypointense lesion in the right middle cerebellar peduncle (*arrow*). **b** DW image shows a hypointense lesion with a hyperintense rim, representing a hemorrhagic lesion (*arrow*). **c** ADC map reveals decreased ADC in this lesion (*arrow*). This may be due to a paramagnetic susceptibility artifact. **d** Coronal GRE image clearly demon- strates hemorrhagic lesions as hypointense (*arrow*)
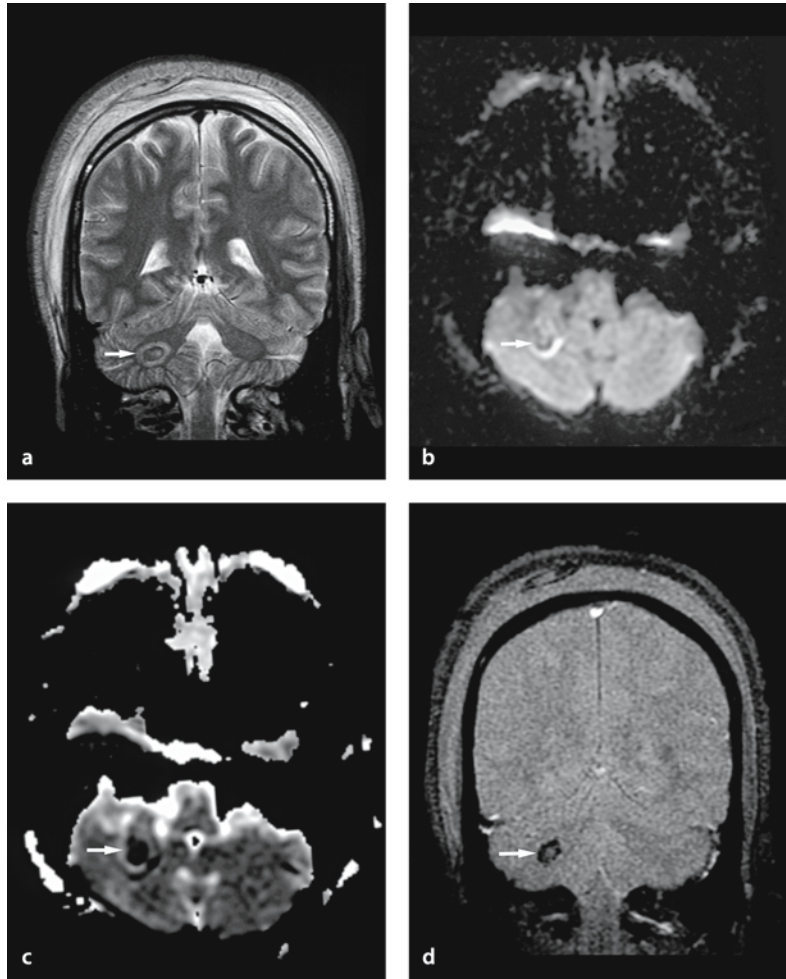
Figure 12.5 a–c

Diffuse axonal injury in the fornix of an 11-year-old female after a motor vehicle accident. **a** On T2-weighted image, it is difficult to detect a small hyperintense lesion in the fornix (*arrow*). **b, c** DW image shows the lesion in the fornix and posterior corpus callosum as hyperintense with decreased ADC (*arrows*)

◄

12.2.2 Computed Tomography and MR Imaging

Few DAI lesions are visible with CT. Only large lesions or those that are grossly hemorrhagic are seen. MR imaging has been proven to be more sensitive for detection as well as for characterization of DAI lesions [2]. Conventional MR imaging shows multiple, small, deeply situated elliptical lesions that spare the overlying cortex. Fluid-attenuated inversion-recovery (FLAIR) images are more sensitive than T2-weighted images to detect small hyperintense lesions adjacent to the cerebrospinal fluid, such as in the fornix and septum pellucidum [15]. These lesions are, moreover, often accompanied by small, petechial hemorrhages. They occur in 10–30% of all DAI lesions [16] and are best appreciated on T2*-weighted gradient-echo (GRE) images because of their susceptibility effects [17]. However, even these MRI sequences are thought to underestimate the true extent of DAI.

12.2.3 Diffusion-Weighted Imaging

Diffusion-weighted imaging measures a unique physiologic parameter, movement of water in the tissue, which allows for identification of DAI lesions that may not be visible on T2/FLAIR or T2*-weighted GRE images. DAI lesions on DW imaging are hyperintense and associated with decreased apparent diffusion coefficient (ADC) [17–22]. The precise mechanisms underlying the diffusion changes associated with DAI are unknown. Cytotoxic edema, which seems to be the cause of reduced ADC in ischemic brain injury, can also occur in the early phase of DAI. However, reduced ADC could also be due to the development of retraction balls and concomitant cytoskeletal collapse along the severed axons [21].

The time course of the ADC abnormality seems to be different from that of ischemic brain injury. Prolonged decrease in ADC, over 2 weeks, was occasionally observed in DAI [18], and cytotoxic edema in the corpus callosum can be partially reversible on follow-up imaging using T2-weighted sequences [22]. However, axonal and glial cell swelling in DAI is thought to be mainly due to excitotoxic mechanisms. It can be a slower or reversible form of cellular swelling than that seen in ischemic brain injuries [6]. Hemorrhagic components, which often accompany these brain injuries, will affect the signal intensity on DW images.

12.3 Brain Contusion

Brain contusions are defined as traumatic injuries to the cortical surface of the brain [1]. They are caused by direct contact between the skull and the brain parenchyma. Compared with DAI, contusions tend to be larger, more superficial, more ill defined and more likely to contain areas of hemorrhage. Cytotoxic edema in brain contusions is also related to excitotoxic mechanisms [23].

12.3.1 Location

Common locations of brain contusions are in the temporal and frontal lobes, especially along their anterior, lateral, and inferior surfaces (Fig. 12.7). The parietal occipital lobes, hippocampus (Fig. 12.8), cerebellar hemisphere, vermis and cerebellar tonsils (Fig. 12.9) are less frequently involved [2].

Figure 12.8 a–c

Brain contusion in the hippocampus in an 11-year-old female after a motor vehicle accident. **a** FLAIR image shows a hyperintense lesion in the left hippocampus (*arrow*). **b** DW image shows this lesion as hyperintense. **c** ADC is decreased in the left hippocampus and left side of the brain stem (*arrows*), representing mainly cytotoxic edema ▶

Figure 12.7 a–d

Brain contusion in the frontal lobe in a 37-year-old male after a motor vehicle accident. **a** On CT obtained after evacuation of epidural hematoma, it is difficult to delineate the extent of a mass lesion in the right frontal lobe (*arrows*). **b** T2-weighted image delineates the extent of the edematous brain contusion (*arrows*). **c** DW image shows heterogeneous signal intensity in these lesions, representing mixed vasogenic and cytotoxic edema with hemorrhagic necrotic tissues (*arrows*). **d** ADC map reveals mixed increase and relative decrease of ADC (*arrows*) in these lesions
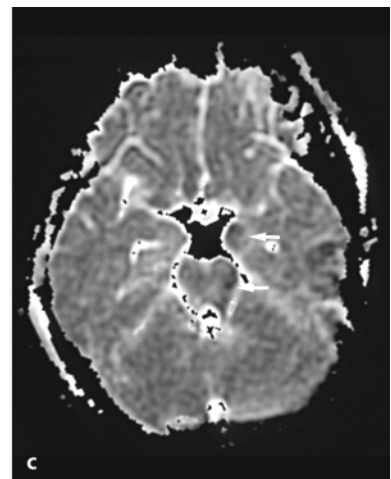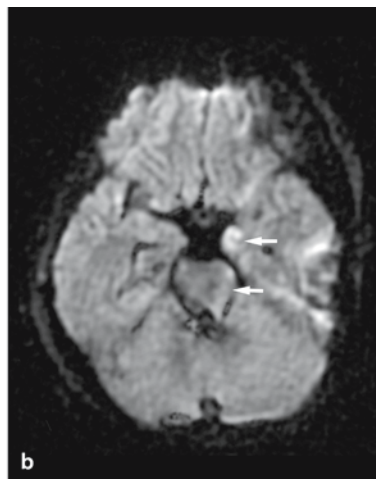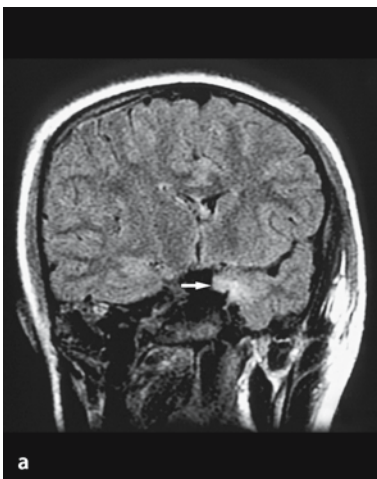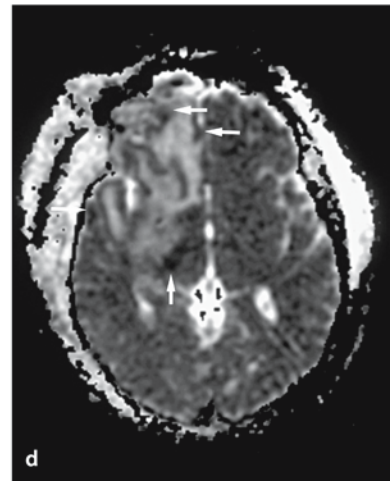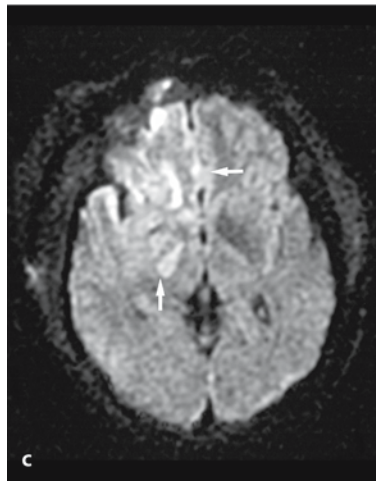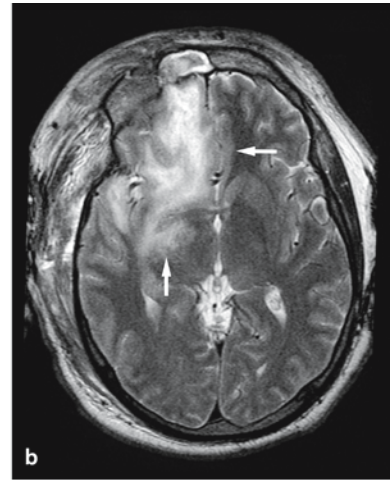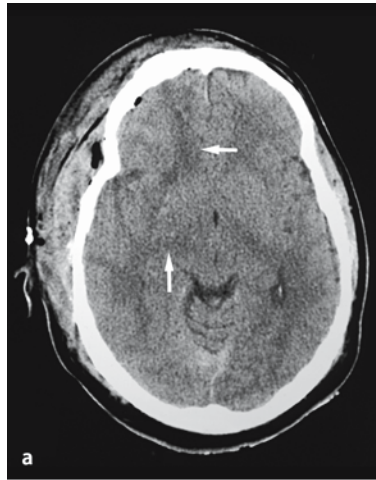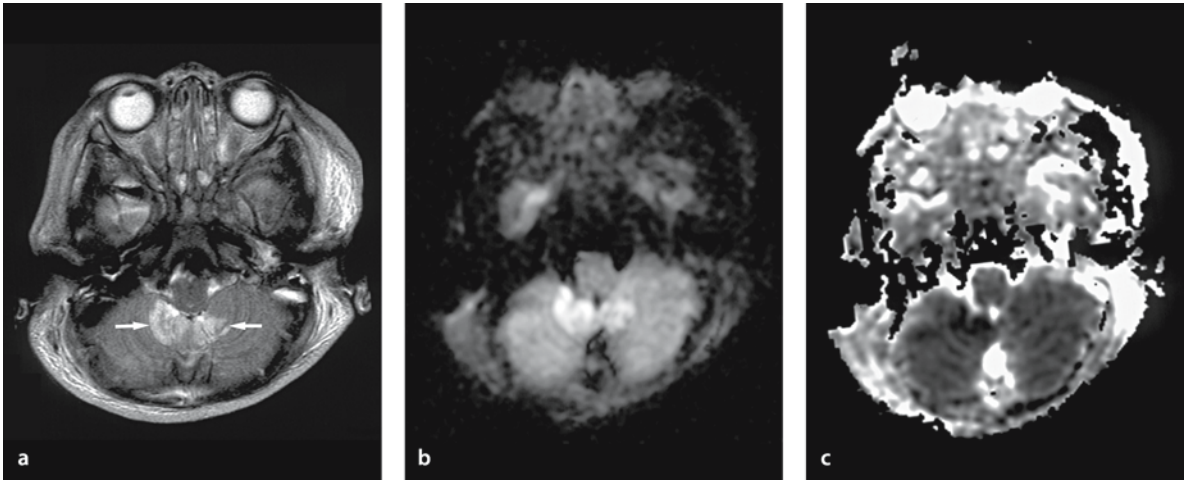
Figure 12.9 a–c

Brain contusion in the cerebellar tonsil in an 11-year-old female after a motor vehicle accident. **a** T2-weighted image shows hyperintense lesions in the cerebellar tonsils (*arrows*). **b** DW image shows this lesion as hyperintense. **c** ADC is partially decreased

12.3.2 Computed Tomography and MR Imaging

Contusions are often difficult to identify on CT obtained shortly after trauma unless they are large or contain areas of hemorrhage [2]. Initial CT will often show only faint areas of low attenuation, sometimes mixed with a few tiny areas of petechial hemorrhage. MRI is considerably more sensitive than CT for early detection and evaluation of their extent.

12.3.3 Diffusion-Weighted Imaging Findings

Brain contusions are sometimes associated with a non-hemorrhagic mass effect, which progresses rapidly after the trauma. Edema in brain contusions is heterogeneous, composed of cytotoxic and vasogenic edema [24], which can be demonstrated by DW imaging. Kawamata et al. reported a specific DW imaging finding of brain contusions [25, 26]. On DW imaging, the contusion is shown as a low intensity core, with increased ADC, surrounded by a rim of a high intensity, with decreased ADC. This suggests that intra- and extracellular components undergo disintegration and homogenization within the central area, whereas cellular swelling is predominant in the peripheral area.

12.4 Hemorrhage Related to Trauma

Traumatic hemorrhages result from injury to a cerebral vessel (artery, vein or capillary) [2]. Subdural hematomas originate from disruption of the bridging cortical veins, which are vulnerable to rapid stretching. Epidural hematoma can have either an arterial or a venous sinus origin, typically associated with a skull fracture. Traumatic intracerebral hematomas result from a shear-strain injury involving arteries, veins or capillaries. Traumatic subarachnoid hemorrhage is usually seen after severe head trauma and may as such accompany brain contusion or DAI. Hemorrhages can also represent a disruption of intracranial arteries, especially arteries of the vertebrobasilar system.

12.4.1 Computed Tomography and MR Imaging

Computed tomography is the modality of choice for the initial evaluation of traumatic brain hemorrhages, as it is a fast examination technique, is widely available, has no contraindications and relatively accurately depicts most hematomas [2].

Magnetic resonance imaging is usually not the primary imaging technique and findings will then depend on the stage of degradation of the hemoglobin at the time of examination. However, in most instances MR imaging is extremely helpful to detect hematomas, especially along the vertex and skull base, and can in certain questionable cases differentiate between subdural and epidural hematomas [2]. T2*-weighted GRE and FLAIR images seem to be more sensitive to detect hemorrhage than conventional spin-echo imaging [27–30].

12.4.2 Diffusion-Weighted Imaging

Diffusion-weighted imaging findings of subdural and epidural hematomas have not been well described in the literature. Depending on the age of the hematoma, DW imaging will vary in signal intensity (Fig. 12.10). Gradient-echo sequences are better in detecting hematomas, including subdural and epidural hematomas, than DW imaging [30]. Although often difficult to detect [31, 32], DW imaging can occasionally depict a subarachnoid hemorrhage as a hyperintense signal (Fig. 12.11). The benefit of DW imaging is probably for the detection of underlying or associated parenchymal lesions. For example, subarachnoid hemorrhage will often cause vasospasm of the intracranial arteries, which can result in brain ischemia. Mass effect secondary to subdural or epidural hematomas, which is closely related to morbidity and mortality, is due to a combination of the hematoma, underlying parenchymal edema and diffuse cerebral swelling.

Figure 12.10 a–d

Epidural and subdural hematoma in a 26-year-old male after a motor vehicle accident. **a** CT shows a left epidural hematoma (*arrow*) but it is difficult to depict the isodense small subdural hematoma in the right side (*arrowheads*). **b** T2-weighted image shows the left epidural hematoma (*arrow*) as a hypointense lesion and the right subdural hematoma as partially hypointense lesions (*arrowheads*). **c** DW image shows the epidural hematoma as very hypointense due to deoxy-hemoglobin, and the subdural hematoma as very hyperintense presumably due to high viscosity or hypercellularity of hematoma. **d** ADC map shows hypointensity due to loss of pixels with background masking in the left epidural hematoma (*arrow*). ADC map also shows decreased ADC in the right subdural hematoma (*arrowheads*)
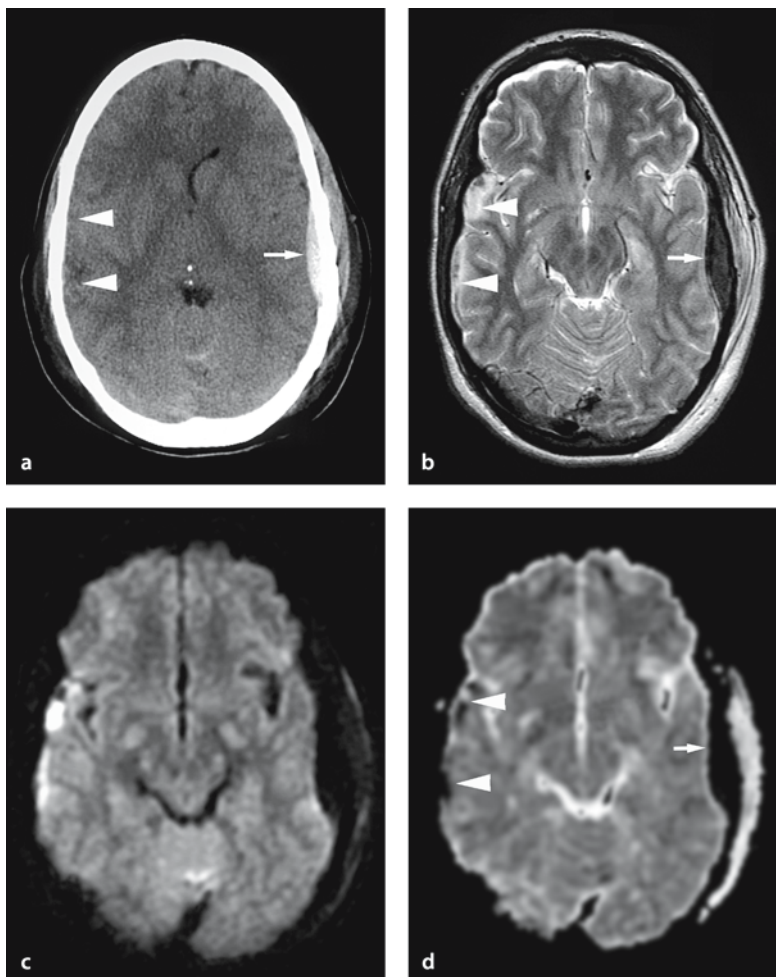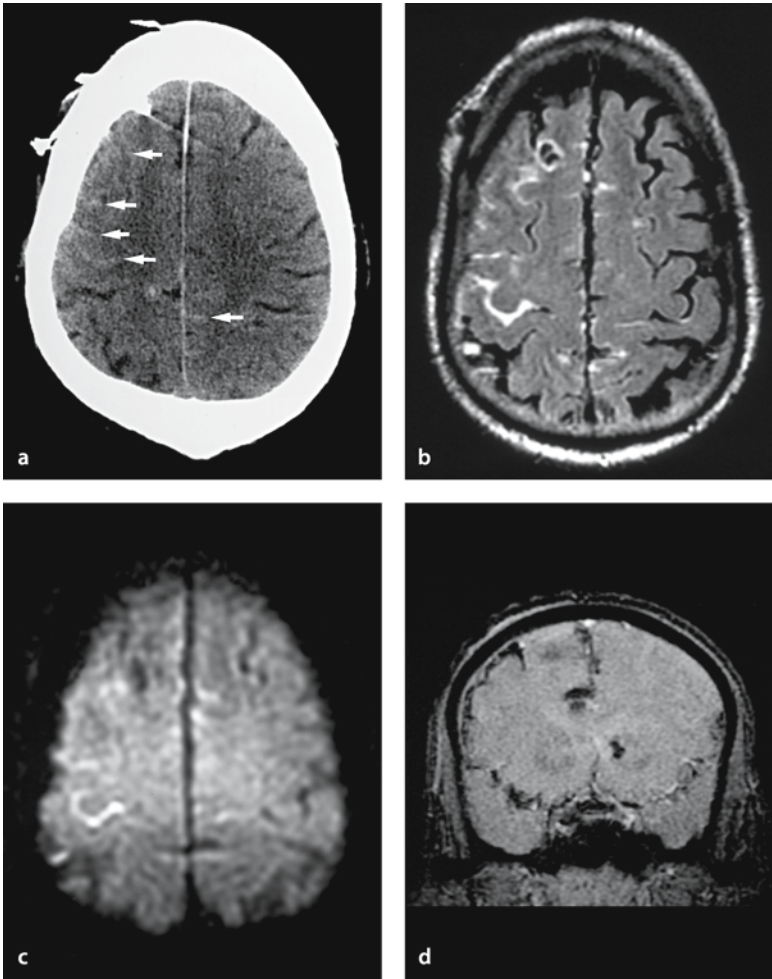
Figure 10.11 a–d

Subarachnoid hemorrhage in a 68-year-old male with ruptured aneurysm of the right middle cerebral artery bifurcation. **a** Postoperative CT shows subtle high density of subarachnoid space in the right frontoparietal area (*arrows*). **b** FLAIR image shows subarachnoid hemorrhage as hyperintensity. **c** DW image also shows subarachnoid hemorrhage as hyperintensity with mildly increased ADC (not shown). **d** Coronal GRE shows the hemorrhage as low signal intensity

12.5 Vascular Injuries

Traumatic arterial and venous injuries (dissections, lacerations, occlusions, pseudoaneurysm, arteriovenous fistulas) are more prevalent than generally believed [2]. Many asymptomatic lesions probably escape detection, and others are recognized several days to months after the injury (Fig. 12.12). CT is useful to detect skull base fractures and CT angiography may help to evaluate the vascular injuries. However, a combination of MR imaging and MR angiography is probably the most efficacious way to screen high-risk patients for traumatic vascular injuries, especially if combined with DW imaging, which is very sensitive to detect small and early ischemic lesions secondary to traumatic vascular injuries. Still, one has to acknowledge that conventional angiography continues to be the gold standard in the evaluation of known or suspected traumatic arterial lesions.
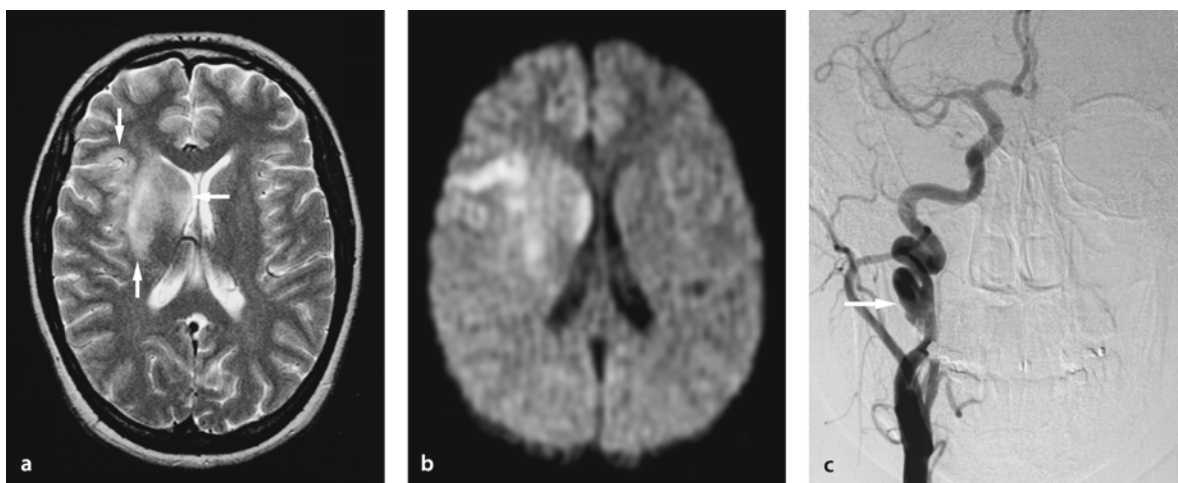
Figure 12.12 a–c

Cerebral infarction after carotid artery dissection with pseudoaneurysm in a 20-year-old female after a motor vehicle accident. **a** T2-weighted image shows hyperintense lesions in the right middle cerebral artery territory including the right basal ganglia (*arrows*). **b** DW image also shows these lesions as hyperintense with decreased ADC (not shown), representing acute infarction. **c** Conventional angiogram shows pseudoaneurysm of the right carotid artery (*arrow*)

References

1. Gennarelli TA (1993) Mechanisms of brain injury. J Emerg Med 11 Suppl 1:5–11
2. Gentry LR (1994) Imaging of closed head injury. Radiology 191:1–17
3. Kelly AB, Zimmerman RD, Snow RB, Gandy SE, Heier LA, Deck MD (1988) Head trauma: comparison of MR and CT-experience in 100 patients. AJNR Am J Neuroradiol 9:699–708
4. Alsop DC, Murai H, Detre JA, McIntosh TK, Smith DH (1996) Detection of acute pathologic changes following experimental traumatic brain injury using diffusion-weighted magnetic resonance imaging. J Neurotrauma 13:515–521
5. Hanstock CC, Faden AI, Bendall MR, Vink R (1994) Diffusion-weighted characterization, edema, diffusion aging differentiates ischemic tissue from traumatized tissue. Stroke 25:843–848
6. Barzo P, Marmarou A, Fatouros P, Hayasaki K, Corwin F (1997) Contribution of vasogenic and cellular edema to traumatic brain swelling measured by diffusion-weighted imaging. J Neurosurg 87:900–907
7. Ito J, Marmarou A, Barzo P, Fatouros P, Corwin F (1996) Characterization of edema by diffusion-weighted imaging in experimental traumatic brain injury. J Neurosurg 84:97–103
8. Albensi BC, Knoblach SM, Chew BG, O'Reilly MP, Faden AI, Pekar JJ (2000) Diffusion and high resolution MRI of traumatic brain injury in rats: time course and correlation with histology. Exp Neurol 162:61–72
9. Assaf Y, Beit-Yannai E, Shohami E, Berman E, Cohen Y (1997) Diffusion- and T2-weighted MRI of closed-head injury in rats: a time course study and correlation with histology. Magn Reson Imaging 15:77–85
10. Gennarelli TA, Graham DI (1998) Neuropathology of the head injuries. Semin Clin Neuropsychiatry 3:160–175
11. Faden AI, Demediuk P, Panter SS, Vink R (1989) The role of excitatory amino acids and NMDA receptors in traumatic brain injury. Science 244:798–800
12. Katayama Y, Becker DP, Tamura T, Ikezaki K (1990) Cellular swelling during cerebral ischaemia demonstrated by microdialysis in vivo: preliminary data indicating the role of excitatory amino acids. Acta Neurochir Suppl (Wien) 51:183–185
13. Mittl RL, Grossman RI, Hiehle JF, Hurst RW, Kauder DR, Gennarelli TA, Alburger GW (1994) Prevalence of MR evidence of diffuse axonal injury in patients with mild head injury and normal head CT findings. AJNR Am J Neuroradiol 15:1583–1589
14. Gentry LR, Thompson B, Godersky JC (1988) Trauma to the corpus callosum: MR features. Am J Neuroradiol 9:1129–1138
15. Ashikaga R, Araki Y, Ishida O (1997) MRI of head injury using FLAIR. Neuroradiology 39:239–242
16. Yanagawa Y, Tsushima Y, Tokumaru A, Un-no Y, Sakamoto T, Okada Y, Nawashiro H, Shima K (2000) A quantitative analysis of head injury using T2*-weighted gradient-echo imaging. J Trauma 49:272–277
17. Huisman TA, Sorensen AG, Hergan K, Gonzalez RG, Schaefer PW (2003) Diffusion-weighted imaging for the evaluation of diffuse axonal injury in closed head injury. J Comput Assist Tomo 27:5–11
18. Liu AY, Maldjian JA, Bagley LJ, Sinson GP, et al. (1999) Traumatic brain injury: diffusion-weighted MR imaging findings. AJNR Am J Neuroradiol 20:1636–1641
19. Rugg-Gunn FJ, Symms MR, Barker GJ, Greenwood R, Duncan JS (2001) Diffusion imaging shows abnormalities after blunt head trauma when conventional magnetic resonance imaging is normal. J Neurol Neurosurg Psychiatry 70:530–533
20. Hergan K, Schaefer PW, Sorensen AG, Gonzalez RG, Huisman TA (2002) Diffusion-weighted MRI in diffuse axonal injury of the brain. Eur Radiol 12:2536–2541
21. Arfanakis K, Haughton VM, Carew JD, Rogers BP, Dempsey RJ, Meyerand ME (2002) Diffusion tensor MR imaging in diffuse axonal injury. AJNR Am J Neuroradiol 23:794–802
22. Takayama H, Kobayashi M, Sugishita M, Mihara B (2000) Diffusion-weighted imaging demonstrates transient cytotoxic edema involving the corpus callosum in a patient with diffuse brain injury. Clin Neurol Neurosurg 102:135–139
23. Maeda T, Katayama Y, Kawamata T, Yamamoto T (1998) Mechanisms of excitatory amino acid release in contused brain tissue: effects of hypothermia and in situ administration of CO2+ on extracellular levels of glutamate. J Neurotrauma 15:655–664
24. Umeda M, Yamaki T, Tanaka C, et al. (1996) Analysis of brain edema in experimental cerebral contusion using diffusion weighted MRI and ADC value. Neurotraumatology 19:79–83
25. Kawamata T, Katayama Y, Mori T, Aoyama N, Tsubokawa T (2002) Mechanisms of the mass effect of cerebral contusion: ICP monitoring and diffusion MRI study. Acta Neurochir Suppl 81:281–283
26. Kawamata T, Katayama Y, Aoyama N, Mori T (2000) Heterogeneous mechanisms of early edema formation in cerebral contusion: diffusion MRI and ADC mapping study. Acta Neurochir Suppl 76:9–12
27. Melhem ER, Jara H, Eustace S (1997) Fluid-attenuated inversion recovery MR imaging: identification of protein concentration thresholds for CSF hyperintensity. Am J Roentgenol 169:859–862
28. Singer MB, Atlas SW, Drayer BP (1998) Subarachnoid space disease: diagnosis with fluid-attenuated inversion-recovery MR imaging and comparison with gadolinium-enhanced spin-echo MR imaging–blinded reader study. Radiology 208:417–422
29. Dechambre SD, Duprez T, Grandin CB, Lecouvet FE, Peeters A, Cosnard G (2000) High signal in cerebrospinal fluid mimicking subarachnoid haemorrhage on FLAIR following acute stroke and intravenous contrast medium. Neuroradiology 42:608–611
30. Taoka T, Yuh WT, White ML, Quets JP, Maley JE, Ueda T (2001) Sulcal hyperintensity on fluid-attenuated inversion recovery MR images in patients without apparent cerebrospinal fluid abnormality. AJR Am J Roentgenol 176:519–524
31. Lin DD, Filippi CG, Steever AB, Zimmerman RD (2001) Detection of intracranial hemorrhage: comparison between gradient-echo images and b0 images obtained from diffusion-weighted echo-planar sequences. AJNR Am J Neuroradiol 22:1275–1281
32. Wiesmann M, Mayer TE, Yousry I, Medele R, Hamann GF, Bruckmann H (2002) Detection of hyperacute subarachnoid hemorrhage of the brain by using magnetic resonance imaging. J Neurosurg 96:684–689

Brain Neoplasms

In collaboration with A. Hiwatashi

13.1 Introduction

Routine MR imaging is the most sensitive method of detecting tumors of the brain. It is, however, not specific enough to determine the histologic nature of most tumors. Diffusion-weighted (DW) imaging can differentiate between tumor and infection [1–51] and can provide information about tumor cellularity, thereby helping in the characterization and grading of brain tumors. This chapter will demonstrate DW imaging characteristics of intracranial tumors.

13.2 Gliomas

The signal intensity of gliomas on DW images is variable and depends mainly on their T2 and apparent diffusion coefficient (ADC) values [1–22]. Thus, some gliomas are hyperintense on DW images with decreased ADC, which reflects a reduced volume of the extracellular space. Other gliomas have a normal or increased ADC, that is the DW signal is a T2 shinethrough effect (Figs. 13.1, 13.2, 13.3, 13.4, 13.5, 13.6 and 13.7).

13.2.1 High-Grade Tumors

It has been reported that high-grade gliomas typically are hyperintense on DW images with decreased ADC [3, 8–10, 12, 13, 19]. High tumor cellularity is probably the major determinant of the decreased ADC values in high-grade brain tumors [3, 8, 12, 18].

Other studies have suggested that ADC correlates not only with tumor cellularity, but also with total nuclear area and tumor grade [8, 12, 13, 17, 19], with high-grade tumors having high cellular density and decreased ADC. Other studies have correlated areas of decreased ADC and found it to be associated with increased choline on MR spectroscopy. Choline is a marker for cell membrane turnover [7, 9].

Although there is a general principle of high-grade gliomas having high DW signal with decreased ADC, there are still controversies regarding how well DW imaging can differentiate between high-grade primary brain tumors, lymphoma and metastasis. Krabbe et al. reported that both the contrast-enhancing portions and the peritumoral edema of metastasis have higher ADC than high-grade gliomas [6]. In the individual case the distinction between metastasis and high-grade glioma is often difficult to make, as some high-grade gliomas also have high ADC [18, 46]. For lymphomas, Guo et al. reported that ADC was generally lower than in high-grade gliomas. This could be useful to differentiate the two [16], but in the clinical situation there is often overlap between lymphoma and high-grade lymphoma. In our experience, the ADC of lymphoma ranges between 0.51 and 0.71×10^{-3} mm^2/s, whereas that of high-grade gliomas ranges between 0.58 and 0.89×10^{-3} mm^2/s. Lymphomas tend to have lower ADC values because of a higher nuclear to cytoplasmic ratio [16]. These are general principles, but in practical clinical work it is often difficult to distinguish between lymphomas, metastasis and high-grade gliomas, even with the most sophisticated ADC maps [4, 10–13, 18].
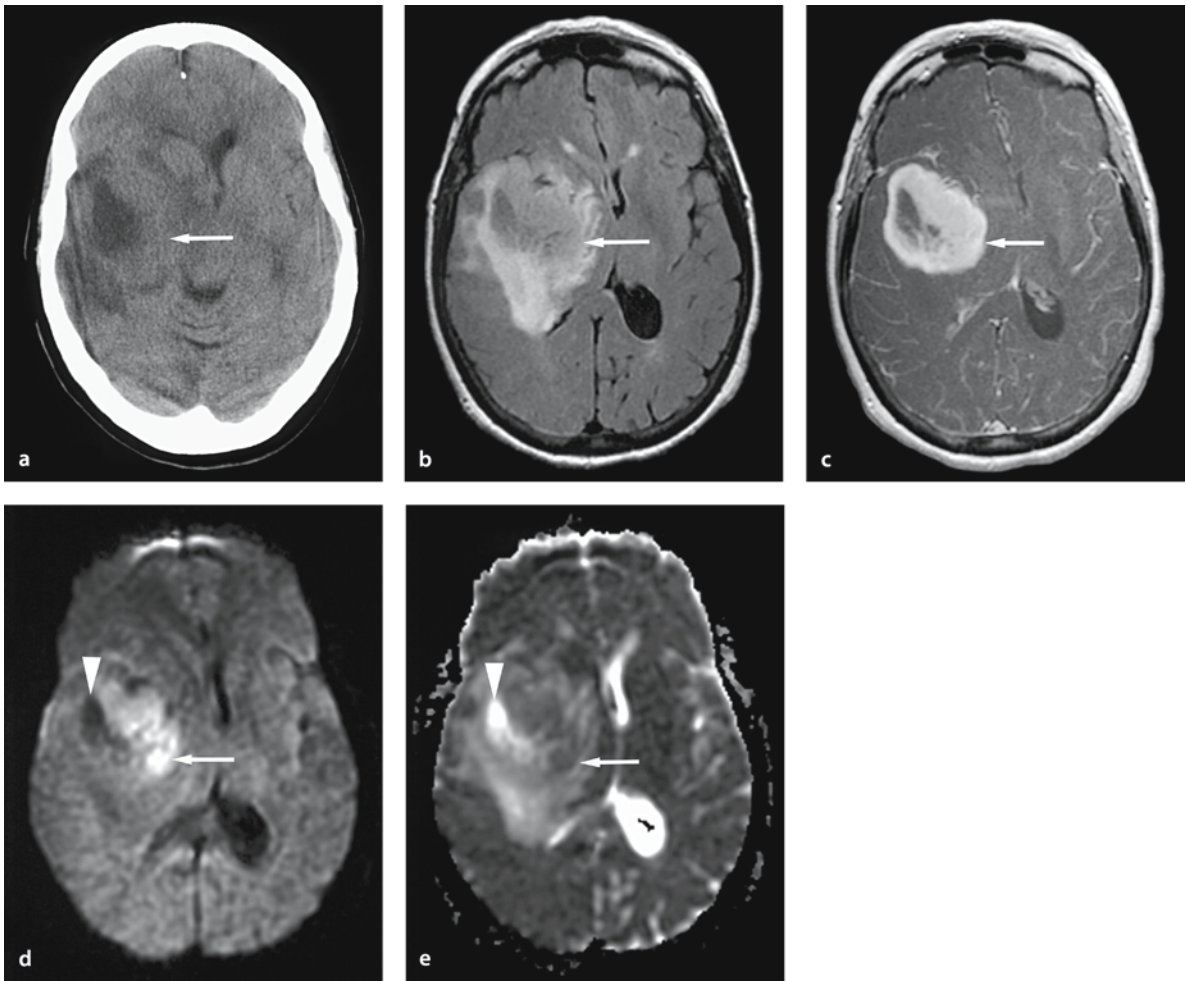
Figure 13.1 a–e

Glioblastoma multiforme in a 69-year-old female with left-side weakness. **a** Unenhanced computed tomography shows a heterogeneous iso- to hypodense lesion in the right temporal lobe (*arrow*). **b** Fluid-attenuated inversion-recovery image shows the heterogeneous hyperintense lesion in the right temporal lobe (*arrow*). **c** Gadolinium-enhanced T1-weighted image shows heterogeneous enhancement in the mass (*arrow*). **d** DW image shows hyperintensity in the enhancing portion of the mass (*arrow*) and hypointensity in the cystic/necrotic portion of the mass (*arrowhead*). **e** ADC map shows heterogeneous hypointensity (0.74–0.85×10^{-3} mm^2/s; *arrow*) in the enhancing portion of the mass compared to the surrounding vasogenic edema. Cystic/necrotic portion of the mass (*arrowhead*) is hyperintense. These findings may correspond to the high cellularity of the enhancing tumor and increased diffusibility of the cystic/necrotic portion
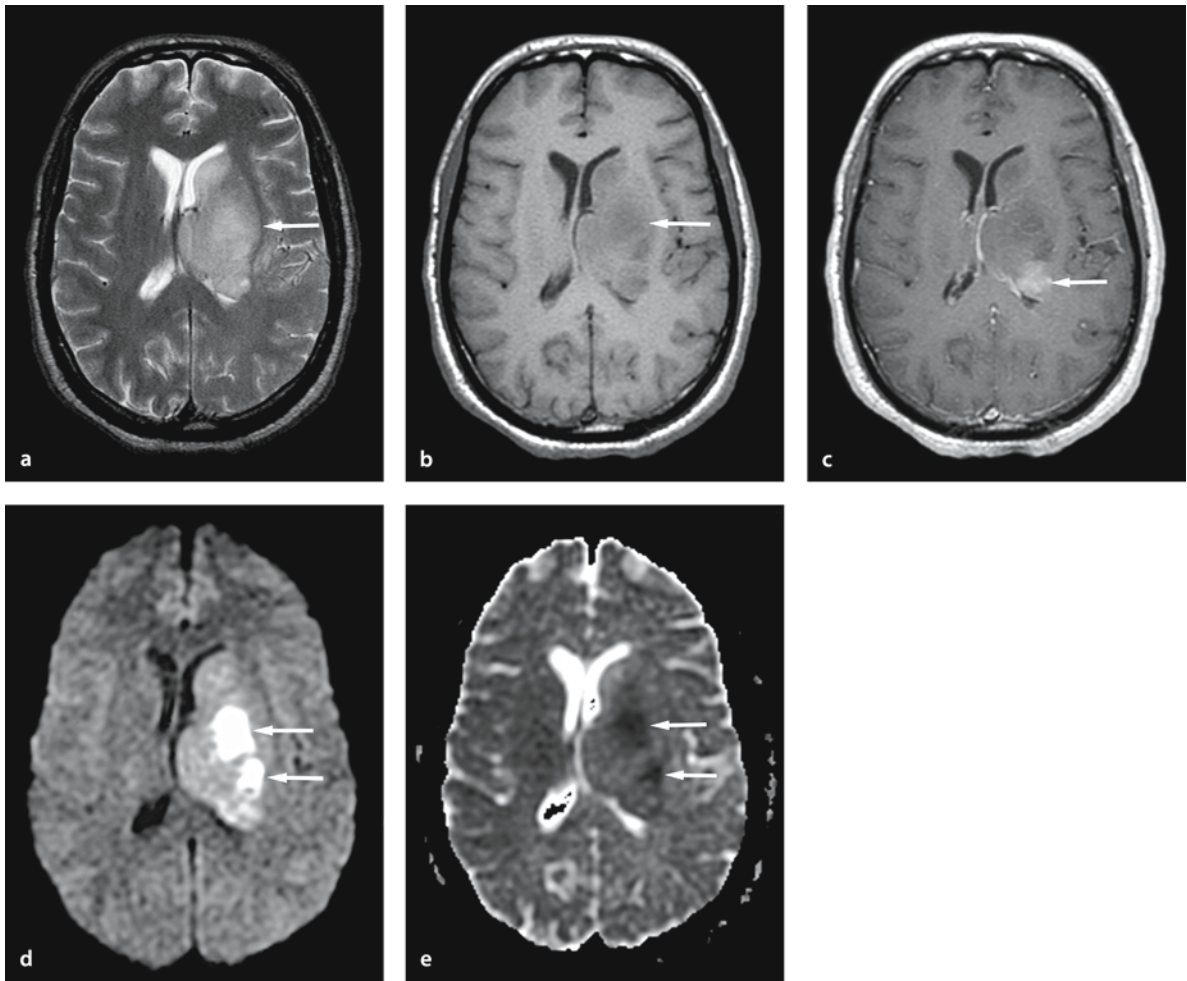
Glioblastoma multiforme in a 51-year-old male with right-side weakness. **a** T2-weighted image shows a hyperintense mass in the left basal ganglia and thalamus (*arrow*). **b** T1-weighted image shows hypointensity in the lesion (*arrow*). **c** Gadolinium-enhanced T1-weighted image shows heterogeneous enhancement in the posterior portion of the tumor (*arrow*). **d** DW image shows hyperintensities (*arrows*). The areas of marked hyperintensity on DW image does not show contrast enhancement in this patient. **e** ADC map shows heterogeneous hypointensity in the lesion ($0.58–0.89\times10^{-3}$ mm^2/s; *arrows*)
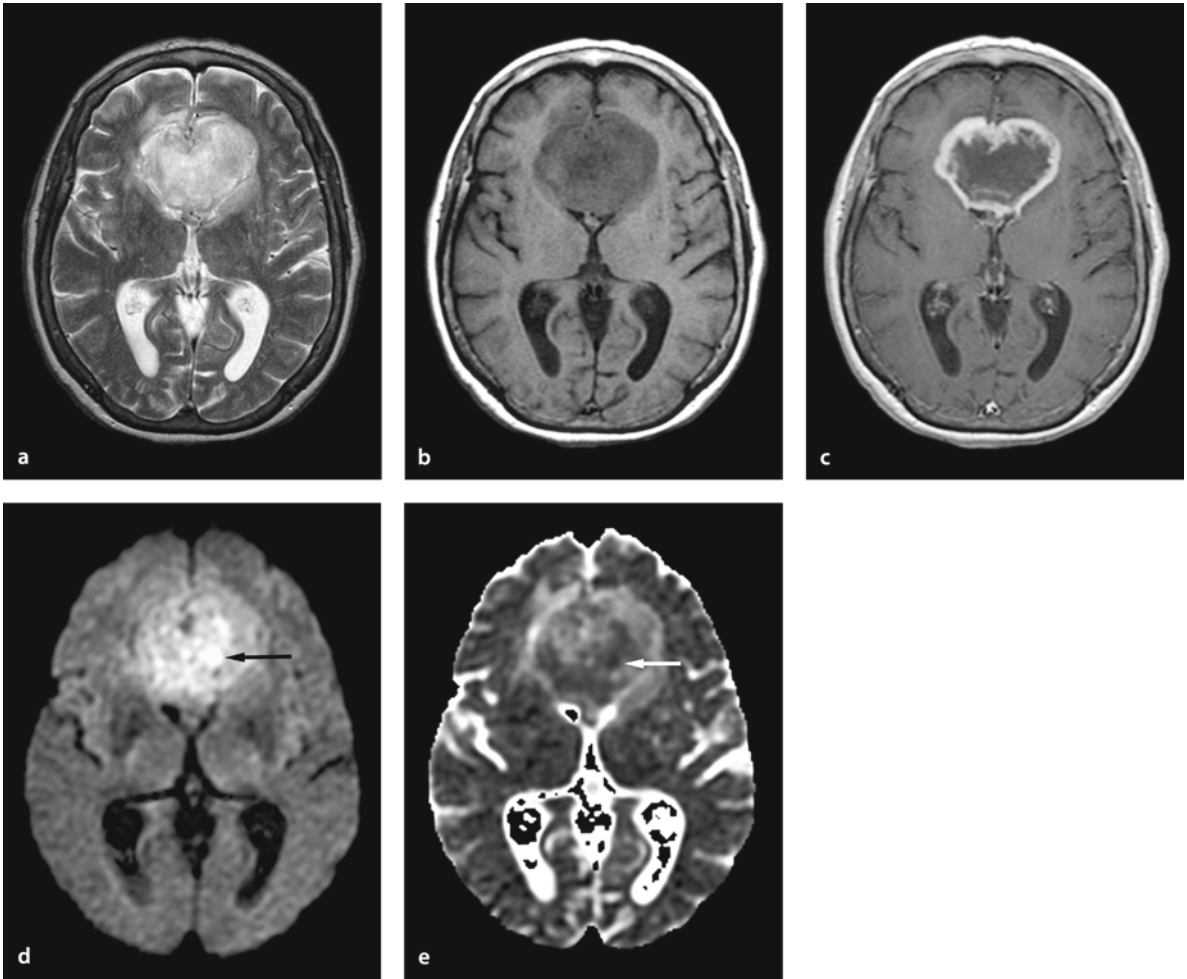
Figure 13.3 a–e

Glioblastoma multiforme in an 80-year-old female with personality change. **a** T2-weighted image shows a hyperintense mass, which involves the genu of corpus callosum (butterfly tumor). **b** T1-weighted image shows hypointensity in the lesion. **c** Gadolinium-enhanced T1-weighted image shows irregular ring-like enhancement of the tumor. **d** DW image shows hyperintensity (*arrow*). **e** ADC map shows heterogeneous intensity in the mass. Note the hypointensity in the center of the lesion (0.65×10^{-3} mm^2/s; *arrow*). These findings may correspond to the cellularity of the tumor

Figure 13.4 a–d

Juvenile pilocytic astrocytoma in a 14-year-old male with headache. **a** T2-weighted image shows a hyperintense mass in the cerebellum (*arrow*). There is a mural nodule in the tumor (*arrowhead*). **b** Gadolinium-enhanced T1-weighted image shows enhancement in the nodule (*arrowhead*). **c** DW image shows hypointensity in the cystic component (*arrow*) and mild hypointensity in the nodule (*arrowhead*). **d** ADC map shows hyperintensity in the cystic component (*arrow*) and mild hyperintensity in the nodule (1.18× 10^{-3} mm^2/s; *arrowhead*) of the mass
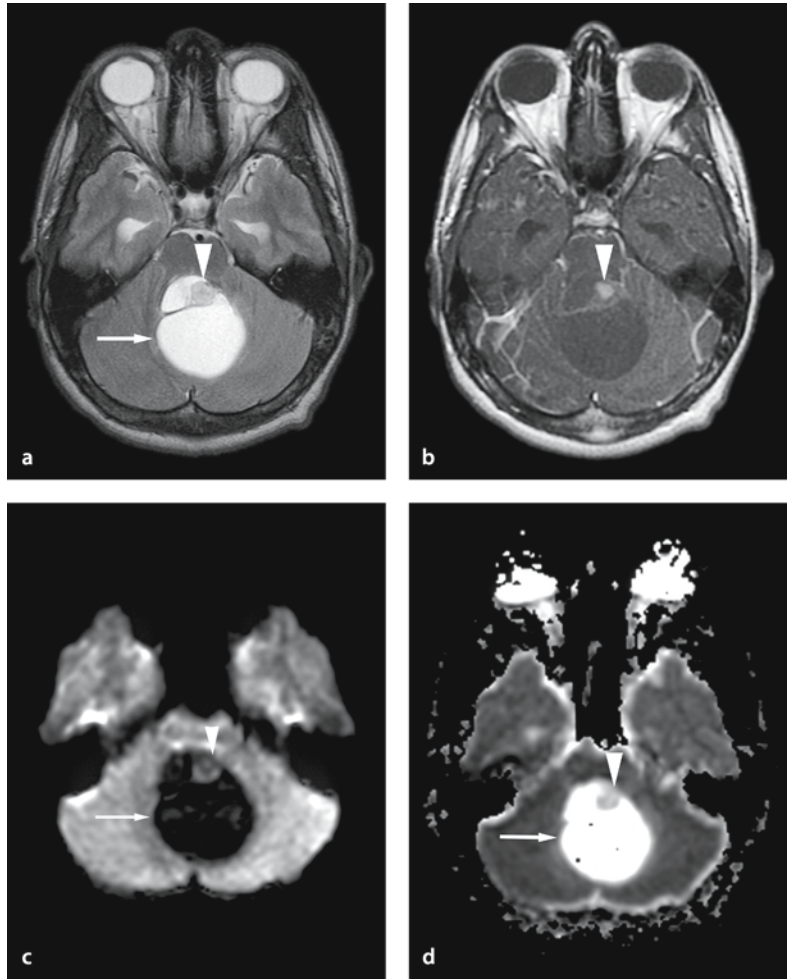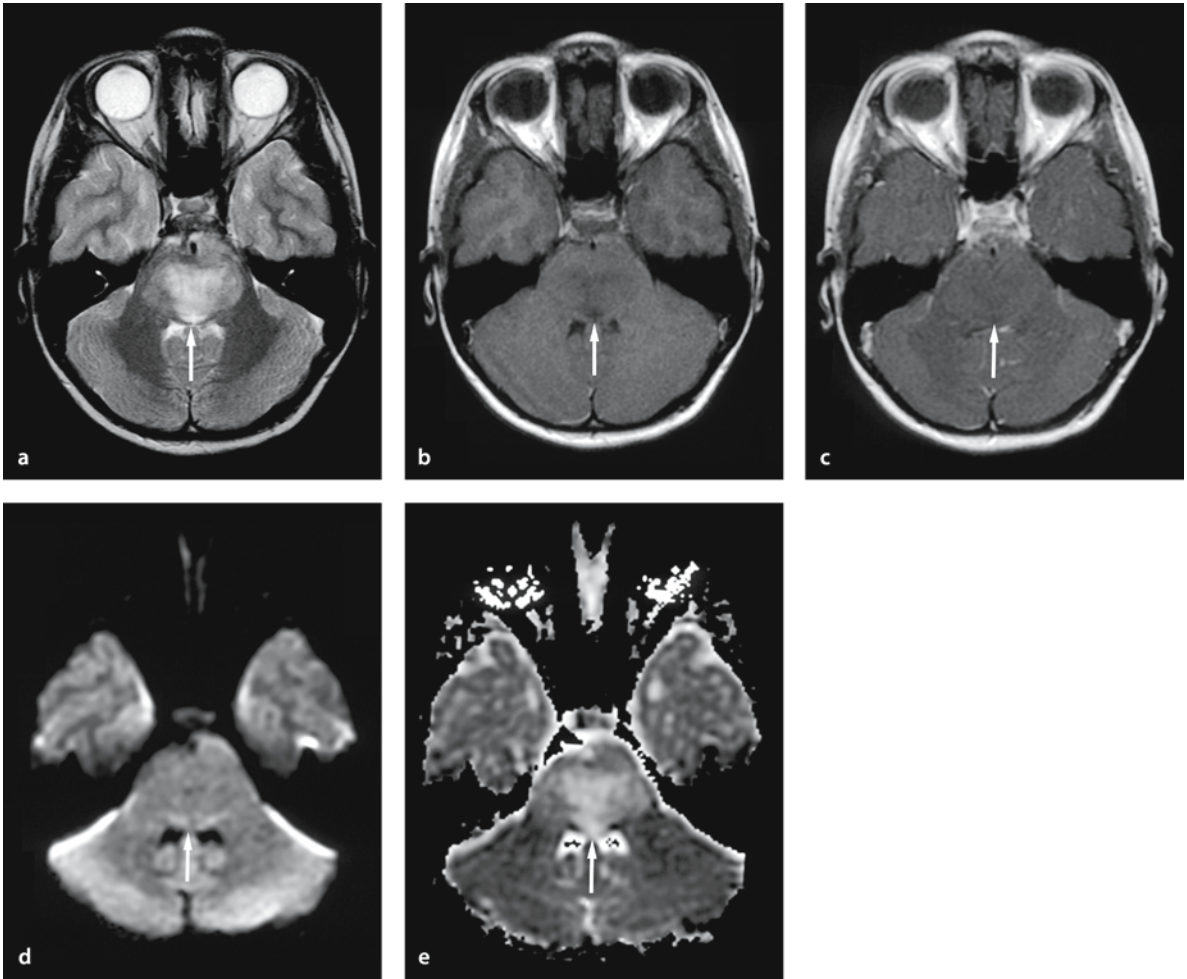
Figure 13.5 a–e

Brain stem glioma in an 8-year-old female with headache. **a** T2-weighted image shows a hyperintense lesion (*arrow*) with surrounding edema in pons. **b** T1-weighted image shows the hypointense lesion (*arrow*). **c** Gadolinium-enhanced T1-weighted image shows no significant enhancement. **d** DW image shows isointensity in the lesion (*arrow*). **e** ADC map shows hyperintensity in the lesion (0.85–1.17×10^{-3} mm^2/s; *arrow*). The isointensity on DW image is caused by a balance between increased T2 and ADC

Figure 13.6 a–d

Low-grade oligoastrocytoma in a 48-year-old female with seizures. **a** T2-weighted image shows a hyperintense lesion in the right temporal lobe (*arrow*). **b** Gadolinium-enhanced T1-weighted image shows a slightly hypointense lesion and no enhancement (*arrow*). **c** DW image shows hyperintensity (*arrow*). **d** ADC map shows hyperintensity in the lesion (0.98–1.19×10^{-3} mm^2/s; *arrow*)

13.2.2 Peritumoral Infiltration

The value of DW imaging for the delineation of peritumoral invasion in primary brain tumors is controversial. Some authors have suggested that ADC is useful to determine the extent of tumor invasion [3, 19], but most of the recent studies have shown that it is not possible to determine accurately the degree of peritumoral infiltration by DW imaging and ADC mapping [4, 10–12, 18, 19]. The poor delineation is probably due to the conjoined effects of T2 and ADC on DW images. For tumors that are biologically different, such as glioblastomas and meningiomas, it has been reported that ADC, T1 and fractional anisotropy of the enhancing tumor and its peritumoral edema are markedly different [15]. Future studies will show if diffusion tensor imaging can add more information about tumor infiltration.

13.2.3 Treatment Response

Diffusion-weighted imaging has been attempted to follow response to treatment and disease progress. For example, animal studies have shown a tendency to an increase in ADC during treatment, followed by a return to the pretreatment level during recurrent tumor growth [20–22]. There are no published human studies, but the preliminary reports have confirmed the observations in animals. Thus, recent studies have shown that radiation necrosis has a higher ADC than tumor recurrence [23].

13.3 Epidermoid Tumors and Arachnoid Cysts

Epidermoid tumors are benign neoplasms of ectodermal origin with stratified squamous epithelium and keratinaceous debris [13, 24–31]. They are hyperintense on DW images, with decreased ADC. The ADC of epidermoid tumors has been reported to be lower than that of cerebrospinal fluid and equal to or higher than that of brain parenchyma [24–26, 28, 29, 31]. Therefore, the hyperintensity of epidermoid tumors on DW images is primarily caused by a T2 shine-through effect (Fig. 13.8).

Arachnoid cysts have a similar appearance on routine MR imaging as epidermoid tumors, but it is well known that DW imaging can distinguish the two [24–31]. Arachnoid cysts are hypointense on DW images as a result of free diffusion and in general their DW signal characteristics are similar to those of cerebrospinal fluid (Fig. 13.9) [24–26].

Figure 13.8 a–d

Epidermoid tumor in a 9-year-old female without symptoms. **a** T2-weighted image shows a hyperintense mass near the falx. **b** T1-weighted image shows the hypointense lesion. **c** DW image shows hyperintensity in the lesion, which is caused by both increased T2 and restricted diffusibility. **d** ADC map shows heterogeneous hypointensity in the lesion, consistent with restricted diffusion. ADC was not calculated because raw data were not available
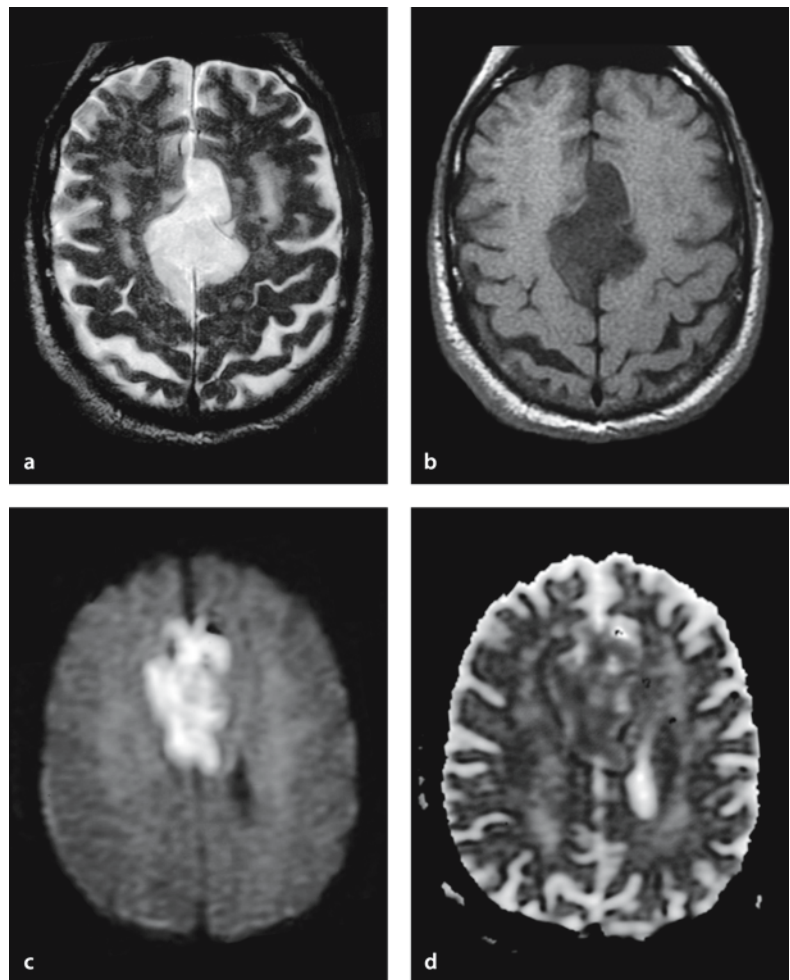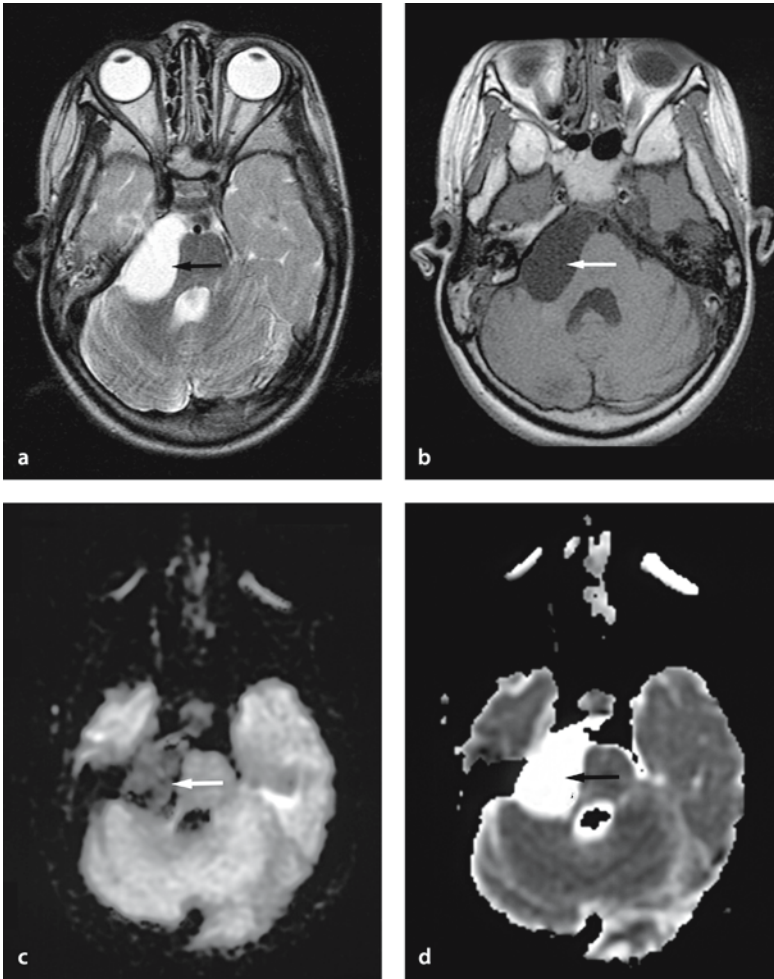
Figure 13.9 a–d

Arachnoid cyst in a 9-year-old female with developmental delay. **a** T2-weighted image shows a large hyperintense lesion in the right cerebellopontine angle (*arrow*). **b** T1-weighted image shows hypointensity in the lesion (*arrow*). **c** DW image shows hypointensity (*arrow*). **d** ADC map shows hyperintensity in the lesion due to increased diffusibility (3.07–3.12×10^{-3} mm^2/s; *arrow*)

13.4 Primitive Neuroectodermal Tumors

Primitive neuroectodermal tumors are a group of histologically similar tumors that occur mostly in children. They include embryonal, largely undifferentiated tumors, such as medulloblastoma, neurob-lastoma, pineoblastoma, ependymoblastoma and medulloepithelioma. These tumors have a high cellular density and are typically hyperintense on DW images, with decreased ADC [32–35]. The hyperintensity on DW images and decreased ADC is caused by their dense cellularity and high nuclear to cytoplasmic ratio (Fig. 13.10).

Figure 13.10 a–d

Primitive neuroectodermal tumor in a 20-month-old female with lethargy and nausea. **a** T2-weighted image shows a well-demarcated and heterogeneous intense mass in the right frontal lobe. **b** T1-weighted image shows heterogeneous hypointensity in the lesion. **c** DW image shows hyperintensity. **d** ADC map shows heterogeneous hypointensity (0.54–0.74×10^{-3} mm^2/s) in the lesion, which may represent hypercellularity
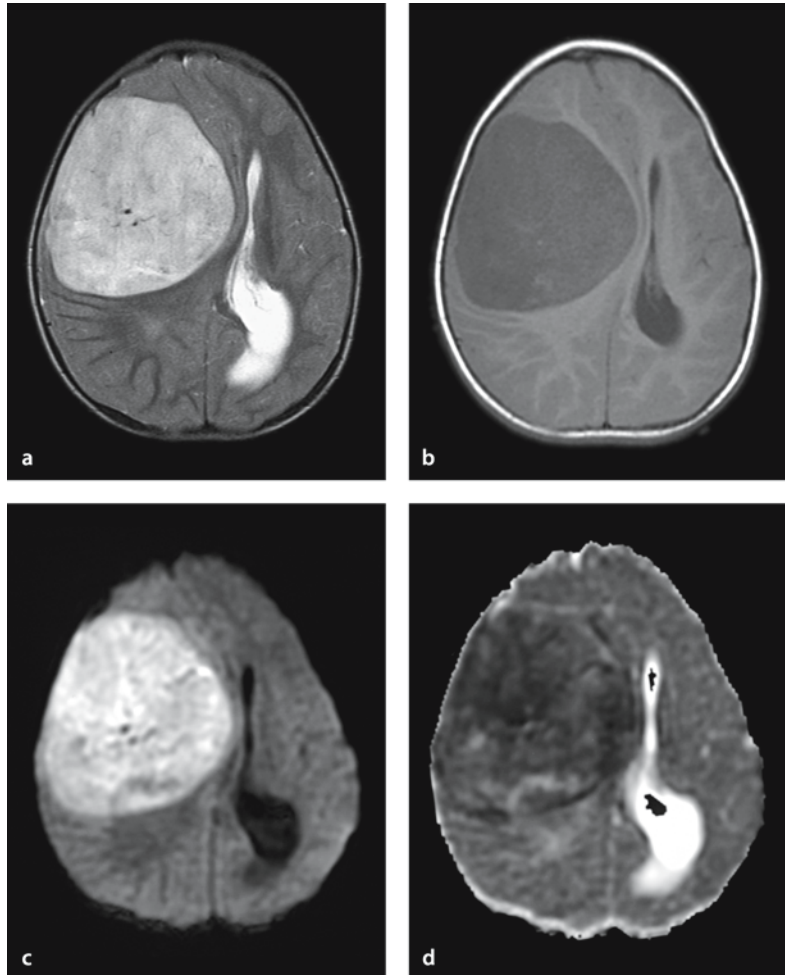
13.5 Meningiomas

The signal characteristics of meningiomas on DW images are variable [11, 12, 18, 36, 37]. Most benign meningiomas are isointense on DW images and ADC maps, but some are slightly hyperintense on both DW images and ADC maps (Fig. 13.11). Malignant or atypical meningiomas have markedly increased signal intensity on DW images and decreased ADC due to a high tumor cellularity [12, 18, 36]. However, other factors, such as multifocal areas of necrosis, numerous abnormal mitoses and cytologic pleomorphism may also cause the high DW signal in atypical and malignant meningiomas (Fig. 13.12).
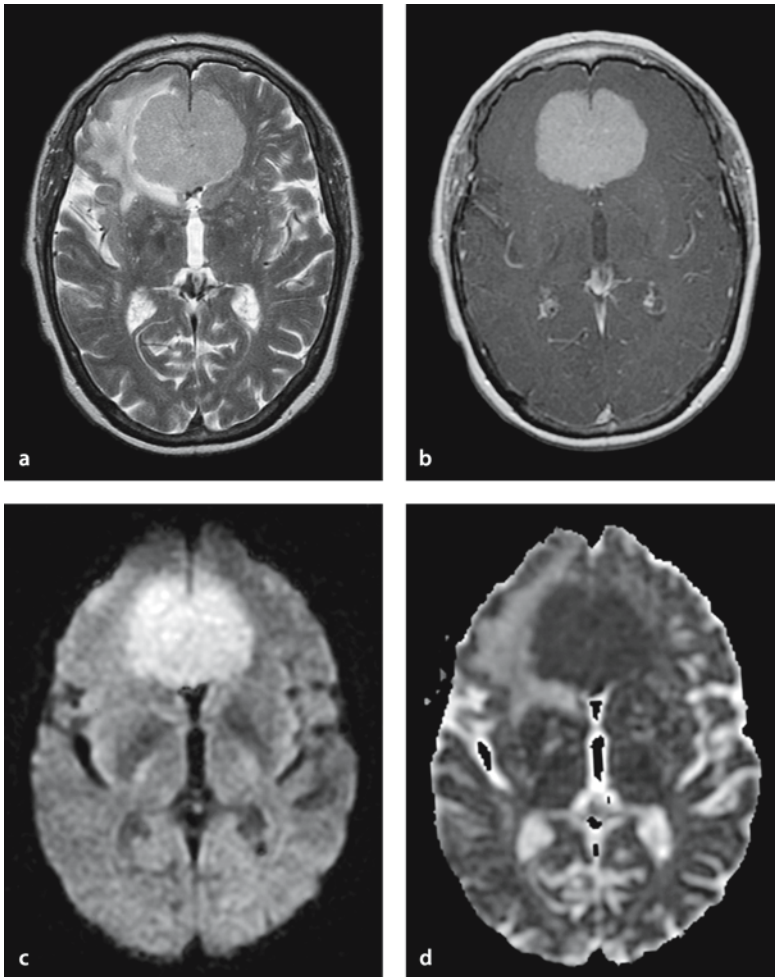
Figure 13.11 a–d

Benign meningioma (syncytial meningioma) in a 72-year-old female with a visual disturbance. **a** T2-weighted image shows a slightly hyperintense mass near the frontal aspect of the falx. **b** Gadolinium-enhanced T1-weighted image shows homogeneous enhancement. **c** DW image shows hyperintensity in the lesion. **d** ADC map shows mild hypointensity (0.73–0.78×10^{-3} mm^2/s)

Figure 13.12 a–d

Atypical meningioma in a 45-year-old female with headache. **a** T2-weighted image shows a heterogeneous intense mass in the temporal lobe (*arrows*). **b** Gadolinium-enhanced T1-weighted image shows heterogeneous enhancement (*arrows*). **c** DW image shows heterogeneous hyperintensity (*arrows*). **d** ADC map shows hypointensity, especially in the right side of the mass (0.51×10^{-3} mm^2/s; *arrows*)
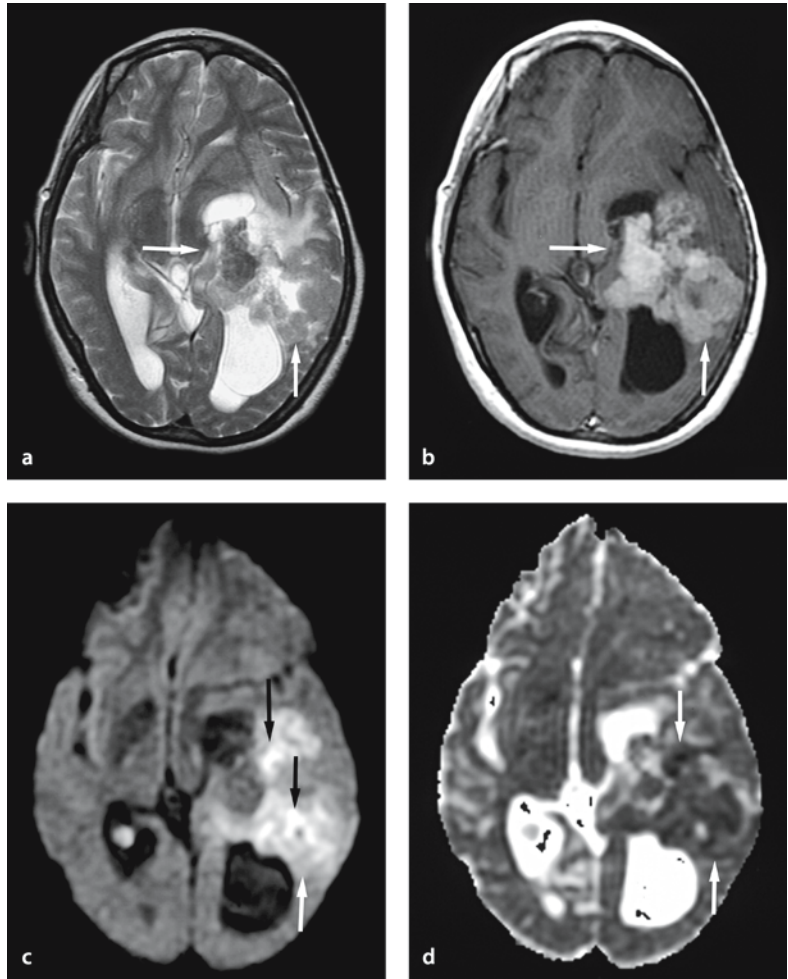
13.6 Malignant Lymphomas

Primary lymphomas of the central nervous system are rare malignant tumors, accounting for less than 1% of all brain tumors (Fig. 13.13). However, the incidence has been increasing subsequent to the spread of the acquired immunodeficiency syndrome [18, 38–41].

A majority of lymphomas are iso- or hypointense on T2-weighted images [18]. Most lymphomas show homogeneous enhancement in immunocompetent patients, but in immunosuppressed patients a rim enhancement is a more common finding [18, 38–40].

The enhancing components of lymphomas are generally hyperintense on DW images [16, 18, 41]. The ADC of lymphomas is often lower than that in high-grade gliomas [16]. As mentioned above, this corresponds to the hypercellularity and might help in differentiating between lymphomas and high-grade gliomas [16].
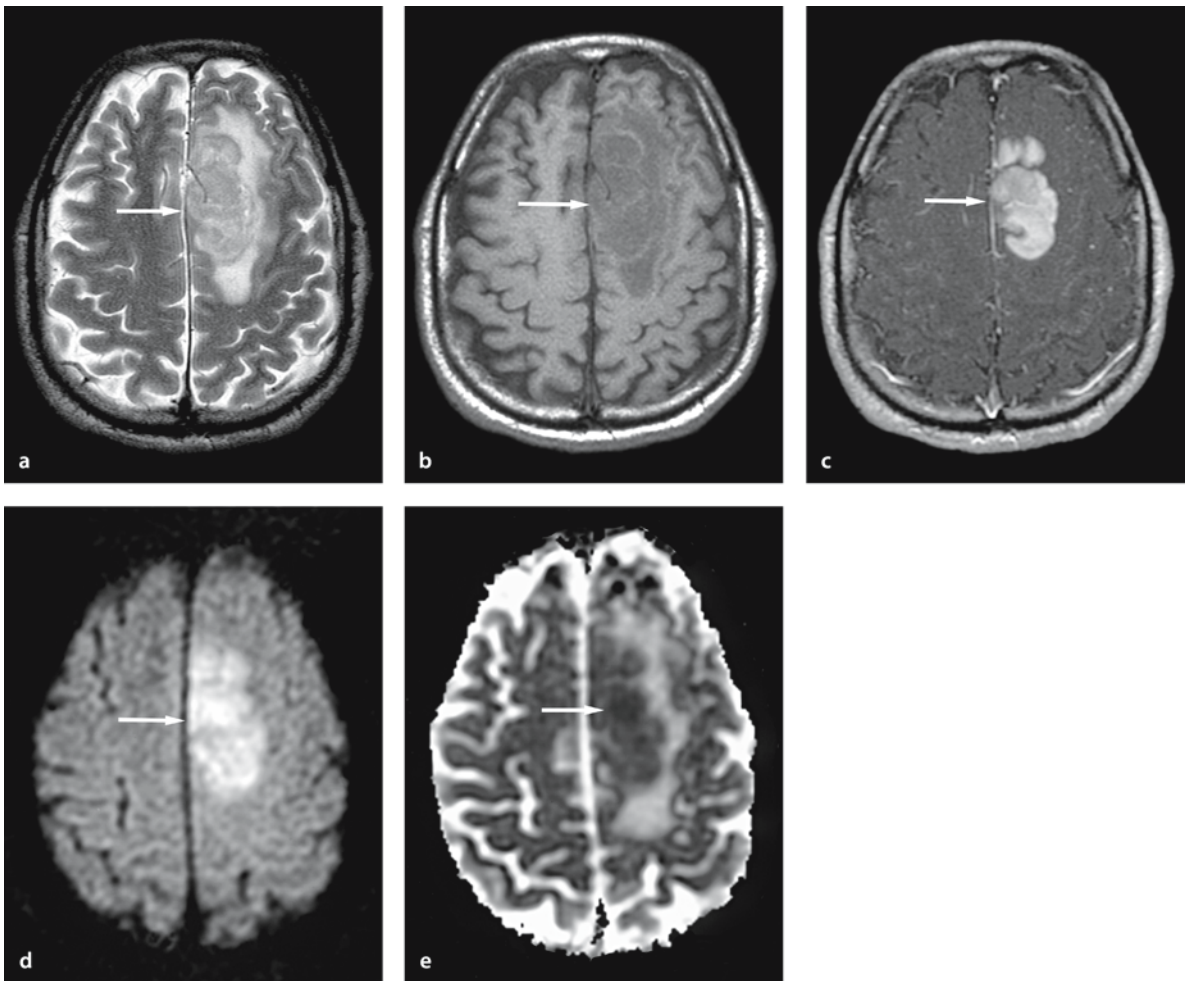
Figure 13.13 a–e

Lymphoma (diffuse large B cell type) in a 64-year-old male with seizure. a T2-weighted image shows a slightly hyperintense mass (*arrow*) with surrounding edema in the left frontal lobe. b T1-weighted image shows the hypointense mass (*arrow*) in the left frontal lobe. c Gadolinium-enhanced T1-weighted image shows the heterogeneously enhancing mass (*arrow*) in the left frontal lobe. d DW image shows hyperintensity in the lesion (*arrow*). e ADC map shows hypointensity in the lesion (0.51–0.71×10^{-3} mm^2/s; *arrow*)

13.7 Craniopharyngiomas

Craniopharyngiomas typically show a combination of contrast enhancement, cyst formation and calcifications (Fig. 13.14). Sener et al. reported hyperintensity on DW images, with increased ADC, corresponding to an increased diffusibility in the tumor [42] and a T2 shine-through effect.
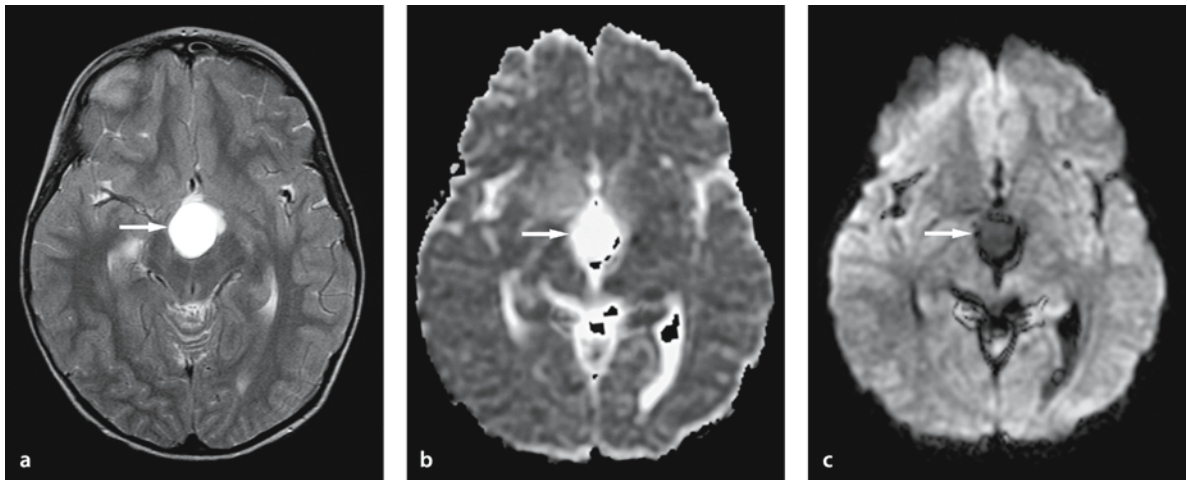
Figure 13.14 a–c

Craniopharyngioma in an 8-year-old male with panhypopituitarism. **a** T2-weighted image shows a hyperintense mass (*arrow*) in the suprasellar region. **b** DW image shows hypointensity in the mass (*arrow*). **c** ADC map shows hyperintensity (2.25–2.38×10^{-3} mm^2/s; *arrow*)

13.8 Metastases

The signal intensity of non-necrotic components of metastases on DW images is variable and depends on their T2 and ADC [2, 6, 11, 12, 18, 19, 30, 43–51]. DW imaging findings of solid components of metastasis are similar to those of gliomas, probably reflecting the cellularity of the primary tumor. The cellularity is a major determinant of their DW signal intensity [6, 11, 18, 30].

The common signal intensity of necrotic/cystic components of cerebral metastases may relate to an increase in free water, showing hypointensity on DW images and increased ADC. However, in the presence of extracellular met-hemoglobin and/or increased viscosity, DW images can show hyperintensity with decreased ADC (Figs. 13.15 and 13.16) [18, 43–51]. This condition is rare, but it should be considered as one differential diagnosis of pyogenic abscesses.
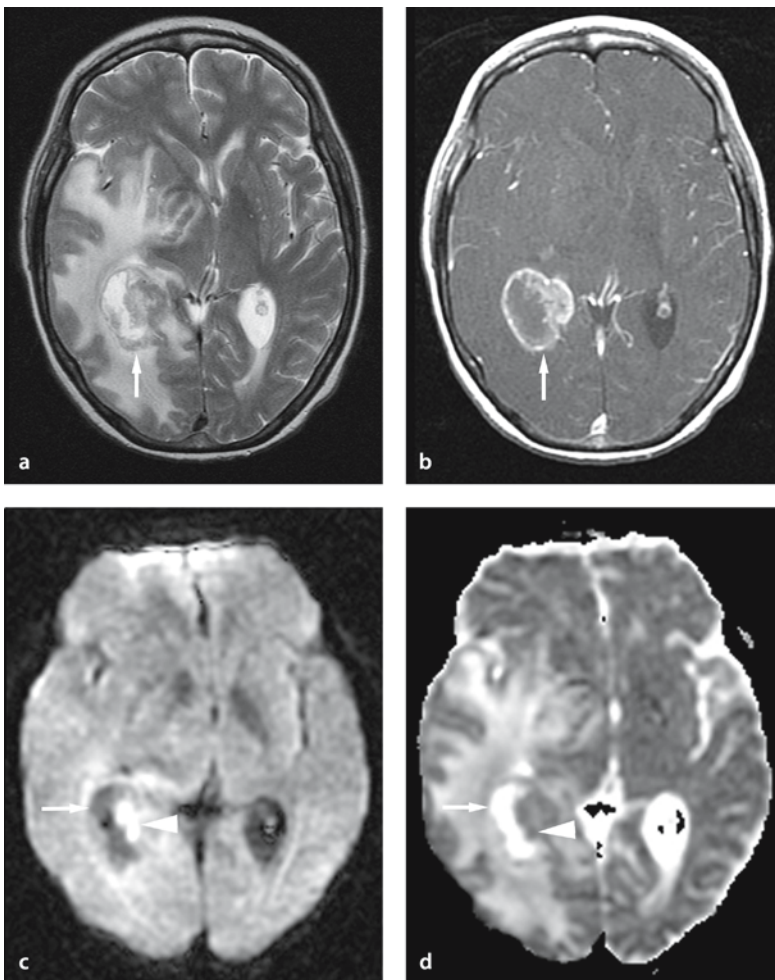
Figure 13.15 a–d

Metastasis (lung cancer) in a 59-year-old female with adenocarcinoma of the lung. **a** T2-weighted image shows heterogeneous intensity of a mass (*arrow*) with surrounding edema in the right temporal lobe. **b** Gadolinium-enhanced T1-weighted image shows heterogeneous ring-like enhancement (*arrow*). **c** DW image shows hyperintensity in the solid portion (*arrowhead*) and hypointensity in the cystic/necrotic portion (*arrow*). **d** ADC map shows hypointensity in the solid portion (0.97–1.00×10^{-3} mm^2/s; *arrowhead*) and hyperintensity (2.21–2.35×10^{-3} mm^2/s; *arrow*). Hyperintensity in the surrounding edema, consistent with vasogenic edema, is also seen
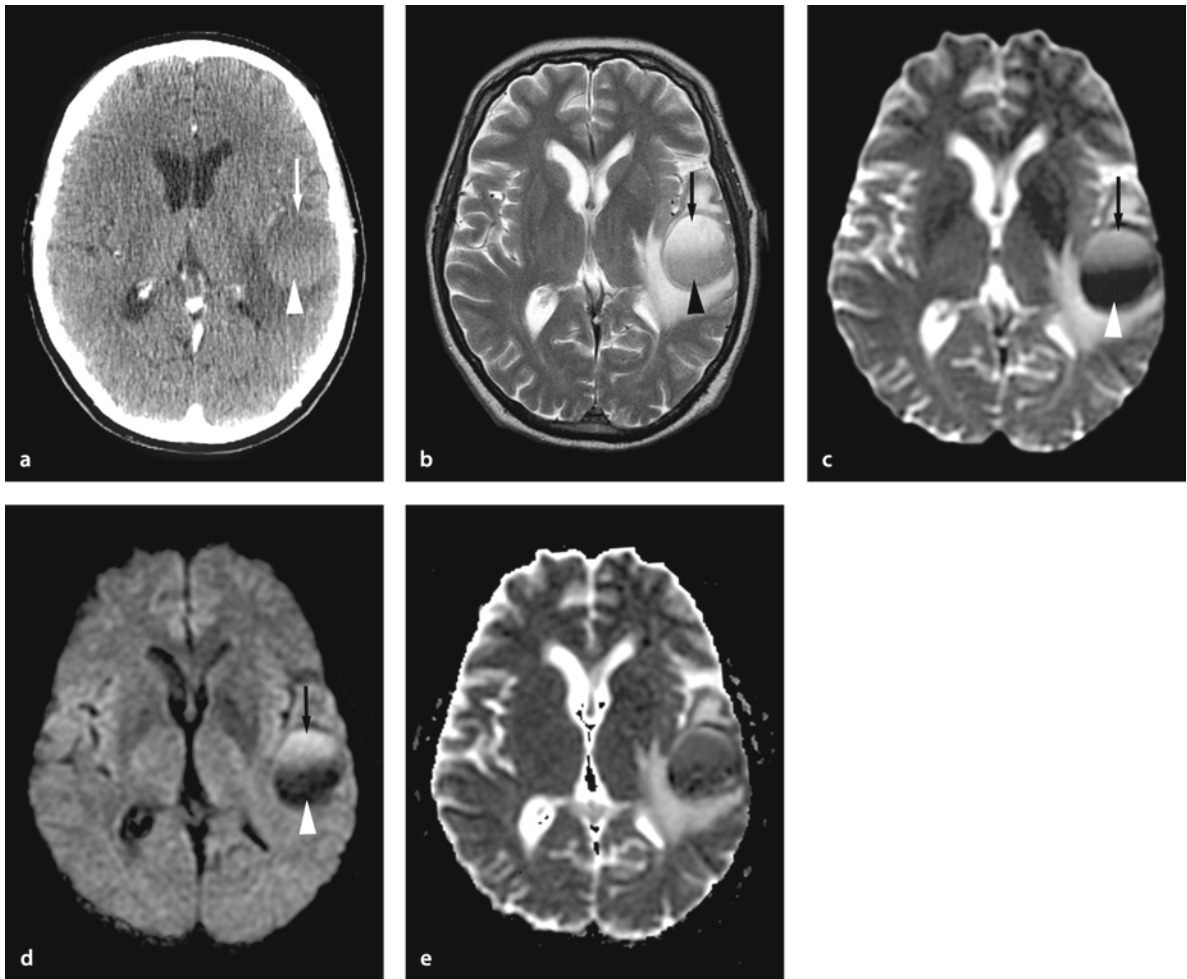
Figure 13.16 a–e

Metastasis (melanoma) in a 56-year-old male with metastatic melanoma. **a** Postcontrast computed tomography shows a heterogeneous density mass, which shows hypodensity (*arrow*) in the anterior portions and hyperdensity (*arrowhead*) in the posterior portions. **b** T2-weighted image shows the heterogeneous intense mass, which contains anterior hyperintense portion (*arrow*) and posterior hypointense portion (*arrowhead*) with surrounding edema in the left temporal lobe. **c** b_0 image also shows anterior hyperintense portion (*arrow*) and posterior hypointense portion (*arrowhead*). **d** DW image again shows anterior hyperintense portion (*arrow*) and posterior hypointense portion (*arrowhead*). **e** ADC map shows iso- to hypointensity in the lesion. The accurate calculation of ADC in the hemorrhage is difficult

13.9 Conclusion

Diffusion-weighted imaging can provide valuable information about tumor cellularity and help in the characterization and grading of tumors of the brain. In most situations, it is difficult to differentiate between specific tumors and to determine tumor infiltration. Future studies will show whether diffusion tensor imaging can improve our ability to characterize and grade brain tumors on imaging studies.

References

1. LeBihan D, Breton E, Lallemand D, Grenier P, Cabanis E, Laval-Jeantet M (1986) MR imaging of intravoxel incoherent motions: application to diffusion and perfusion in neurologic disorders. Radiology 161:401–407
2. Hajnal JV, Doran M, Hall AS, et al. (1991) MR imaging of anisotropically restricted diffusion of water in the nervous system: technical, anatomic, and pathologic considerations. J Comput Assist Tomogr 15:1–18
3. Tien RD, Felsberg GJ, Friedman H, Brown M, MacFall J (1994) MR imaging of high-grade cerebral gliomas: value of diffusion-weighted echoplanar pulse sequences. AJR Am J Roentgenol 162:671–677
4. Eis M, Els T, Hoehn-Berlage M, Hossmann KA (1994) Quantitative diffusion MR imaging of cerebral tumor and edema. Acta Neurochir Suppl (Wien) 60:344–346
5. Brunberg JA, Chenevert TL, McKeever PE, et al. (1995) In vivo MR determination of water diffusion coefficients and diffusion anisotropy: correlation with structural alteration in gliomas of the cerebral hemispheres. AJNR Am J Neuroradiol 16:361–371
6. Krabbe K, Gideon P, Wagn P, Hansen U, Thomsen C, Madsen F (1997) MR diffusion imaging of human intracranial tumours. Neuroradiology 39:483–489
7. Gupta RK, Sinha U, Cloughesy TF, Alger JR (1999) Inverse correlation between choline magnetic resonance spectroscopy signal intensity and the apparent diffusion coefficient in human glioma. Magn Reson Med 41:2–7
8. Sugahara T, Korogi Y, Kochi M, et al. (1999) Usefulness of diffusion-weighted MRI with echo-planar technique in the evaluation of cellularity in gliomas. J Magn Reson Imaging 9:53–60
9. Gupta RK, Cloughesy TF, Sinha U, et al. (2000) Relationships between choline magnetic resonance spectroscopy, apparent diffusion coefficient and quantitative histopathology in human glioma. J Neurooncol 50:215–226
10. Castillo M, Smith JK, Kwock L, Wilber K. (2001) Apparent diffusion coefficients in the evaluation of high-grade cerebral gliomas. AJNR Am J Neuroradiol 22:60–64
11. Stadnik TW, Chaskis C, Michotte A, et al. (2001) Diffusion-weighted MR imaging of intracerebral masses: comparison with conventional MR imaging and histologic findings. AJNR Am J Neuroradiol 22:969–976
12. Kono K, Inoue Y, Nakayama K, et al. (2001) The role of diffusion-weighted imaging in patients with brain tumors. AJNR Am J Neuroradiol 22:1081–1088
13. Gauvain KM, McKinstry RC, Mukherjee P, et al. (2001) Evaluating pediatric brain tumor cellularity with diffusion-tensor imaging. AJR Am J Roentgenol 177:449–454
14. Sinha S, Bastin ME, Whittle IR, Wardlaw JM (2002) Diffusion tensor MR imaging of high-grade cerebral gliomas. AJNR Am J Neuroradiol 23:520–527
15. Bastin ME, Sinha S, Whittle IR, Wardlaw JM (2002) Measurements of water diffusion and T1 values in peritumoural oedematous brain. Neuroreport 13:1335–1340
16. Guo AC, Cummings TJ, Dash RC, Provenzale JM (2002) Lymphomas and high-grade astrocytomas: comparison of water diffusibility and histologic characteristics. Radiology 224:177–183
17. Yang D, Korogi Y, Sugahara T, et al. (2002) Cerebral gliomas: prospective comparison of multivoxel 2D chemical-shift imaging proton MR spectroscopy, echoplanar perfusion and diffusion-weighted MRI. Neuroradiology 44:656–666
18. Stadnik TW, Demaerel P, Luypaert RR, et al. (2003) Imaging tutorial: differential diagnosis of bright lesions on diffusion-weighted MR images. Radiographics 23:E7–7
19. Bulakbasi N, Kocaoglu M, Ors F, Tayfun C, Ucoz T (2003) Combination of single-voxel proton MR spectroscopy and apparent diffusion coefficient calculation in the evaluation of common brain tumors. AJNR Am J Neuroradiol 24:225–233
20. Chenevert TL, McKeever PE, Ross BD (1997) Monitoring early response of experimental brain tumors to therapy using diffusion magnetic resonance imaging. Clin Cancer Res 3:1457–1466
21. Chenevert TL, Stegman LD, Taylor JM, et al. (2000) Diffusion magnetic resonance imaging: an early surrogate marker of therapeutic efficacy in brain tumors. J Natl Cancer Inst 92:2029–2036
22. Mardor Y, Roth Y, Lidar Z, et al. (2001) Monitoring response to convection-enhanced taxol delivery in brain tumor patients using diffusion-weighted magnetic resonance imaging. Cancer Res 61:4971–4973
23. Asao C, Korogi Y, Kitajima M Nishimura R, Baba Y, Kochi M, Yamashita Y (2003) Diffusion-weighted MR imaging of radiation-induced brain injury: the usefulness for differentiation from tumor recurrence. American Society of Neuroradiology 41st annual meeting 2003 proceedings 19:16
24. Tsuruda JS, Chew WM, Moseley ME, Norman D (1990) Diffusion-weighted MR imaging of the brain: value of differentiating between extraaxial cysts and epidermoid tumors. AJNR Am J Neuroradiol 11:925–931
25. Tsuruda JS, Chew WM, Moseley ME, Norman D (1991) Diffusion-weighted MR imaging of extraaxial tumors. Magn Reson Med 19:316–320
26. Maeda M, Kawamura Y, Tamagawa Y (1992) Intravoxel incoherent motion (IVIM) MRI in intracranial, extraaxial tumors and cysts. J Comput Assist Tomogr 16:514–518
27. Laing AD, Mitchell PJ, Wallace D (1999) Diffusion-weighted magnetic resonance imaging of intracranial epidermoid tumours. Australas Radiol 43:16–19
28. Dechambre S, Duprez T, Lecouvet F, Raftopoulos C, Gosnard G (1999) Diffusion-weighted MRI postoperative assessment of an epidermoid tumour in the cerebellopontine angle. Neuroradiology 41:829–831

29. Chen S, Ikawa F, Kurisu K, Arita K, Takaba J, Kanou Y (2001) Quantitative MR evaluation of intracranial epidermoid tumors by fast fluid-attenuated inversion recovery imaging and echo-planar diffusion-weighted imaging. AJNR Am J Neuroradiol 22:1089–1096

30. Bergui M, Zhong J, Bradac GB, Sales S (2001) Diffusion-weighted images of intracranial cyst-like lesions. Neuroradiology 43:824–829

31. Annet L, Duprez T, Grandin C, Dooms G, Collard A, Cosnard G (2002) Apparent diffusion coefficient measurements within intracranial epidermoid cysts in six patients. Neuroradiology 44:326–328

32. Kotsenas AL, Roth TC, Manness WK, Faerber EN (1999) Abnormal diffusion-weighted MRI in medulloblastoma: does it reflect small cell histology? Pediatr Radiol 29:524–526

33. Klisch J, Husstedt H, Hennings S, von Velthoven V, Pagenstecher A, Schumacher M (2000) Supratentorial primitive neuroectodermal tumours: diffusion-weighted MRI. Neuroradiology 42:393–398

34. Wilke M, Eidenschink A, Muller-Weihrich S, Auer DP (2001) MR diffusion imaging and 1H spectroscopy in a child with medulloblastoma. A case report. Acta Radiol 42:39–42

35. Erdem E, Zimmerman RA, Haselgrove JC, Bilaniuk LT, Hunter JV (2001) Diffusion-weighted imaging and fluid attenuated inversion recovery imaging in the evaluation of primitive neuroectodermal tumors. Neuroradiology 43:927–933

36. Filippi CG, Edgar MA, Ulug AM, Prowda JC, Heier LA, Zimmerman RD (2001) Appearance of meningiomas on diffusion-weighted images: correlating diffusion constants with histopathologic findings. AJNR Am J Neuroradiol 22:65–72

37. Bitzer M, Klose U, Geist-Barth B (2002) Alterations in diffusion and perfusion in the pathogenesis of peritumoral brain edema in meningiomas. Eur Radiol 12:2062–2076

38. Jack CR Jr, Reese DF, Scheithauer BW (1986) Radiographic findings in 32 cases of primary CNS lymphoma. AJR Am J Roentgenol 146:271–276

39. Hochberg FH, Miller DC (1988) Primary central nervous system lymphoma. J Neurosurg 68:835–853

40. Poon T, Matoso I, Tchertkoff V, Weitzner I Jr, Gade M (1989) CT features of primary cerebral lymphoma in AIDS and non-AIDS patients. J Comput Assist Tomogr 13:6–9

41. Chang L, Ernst T (1997) MR spectroscopy and diffusion-weighted MR imaging in focal brain lesions in AIDS. Neuroimaging Clin N Am 7:409–426

42. Sener RN, Dzelzite S, Migals A (2002) Huge craniopharyngioma: diffusion MRI and contrast-enhanced FLAIR imaging. Comput Med Imaging Graph 26:199–203

43. Noguchi K, Watanabe N, Nagayoshi T, et al. (1999) Role of diffusion-weighted echo-planar MRI in distinguishing between brain abscess and tumour: a preliminary report. Neuroradiology 41:171–174

44. Park SH, Chang KH, Song IC, Kim YJ, Kim SH, Han MH (2000) Diffusion-weighted MRI in cystic or necrotic intracranial lesions. Neuroradiology 42:716–721

45. Holtas S, Geijer B, Stromblad LG, Maly-Sundgren P, Burtscher IM (2000) A ring-enhancing metastasis with central high signal on diffusion-weighted imaging and low apparent diffusion coefficients. Neuroradiology 42:824–827

46. Tung GA, Evangelista P, Rogg JM, Duncan JA 3rd (2001) Diffusion-weighted MR imaging of rim-enhancing brain masses: is markedly decreased water diffusion specific for brain abscess? AJR Am J Roentgenol 177:709–712

47. Hartmann M, Jansen O, Heiland S, Sommer C, Munkel K, Sartor K (2001) Restricted diffusion within ring enhancement is not pathognomonic for brain abscess. AJNR Am J Neuroradiol 22:1738–1742

48. Geijer B, Holtas S (2002) Diffusion-weighted imaging of brain metastases: their potential to be misinterpreted as focal ischaemic lesions. Neuroradiology 44:568–573

49. Chang SC, Lai PH, Chen WL, et al. (2002) Diffusion-weighted MRI features of brain abscess and cystic or necrotic brain tumors: comparison with conventional MRI. Clin Imaging 26:227–236

50. Lai PH, Ho JT, Chen WL, Hsu SS, Wang JS, Pan HB, Yang CF (2002) Brain abscess and necrotic brain tumor: discrimination with proton MR spectroscopy and diffusion-weighted imaging. AJNR Am J Neuroradiol 23:1369–1377

51. Guzman R, Barth A, Lovblad KO, et al. (2002) Use of diffusion-weighted magnetic resonance imaging in differentiating purulent brain processes from cystic brain tumors. J Neurosurg 97:1101–1107

Pediatrics

14.1 Water Content of the Pediatric Brain

The water content of the pediatric brain is considerably higher than that of the adult brain. This makes it more difficult to diagnose ischemic and other lesions in pediatric patients using computed tomography (CT) and MR imaging. Diffusion-weighted (DW) imaging is sensitive to alteration in diffusion of water molecules, and this technique can help overcome some of these difficulties [1]. DW imaging is primarily useful for detecting and characterizing ischemic lesions, but also for evaluation of myelinization by demonstrating anisotropy of the white matter earlier than conventional MR imaging [2, 3].

14.2 Normal Structures

Diffusion-weighted imaging characteristics of a normal brain in young infants are different from those in adults [4]. Apparent diffusion coefficient (ADC) values in both gray and white matter of newborns are considerably higher than in adults. This reflects the high water content of the pediatric brain [5]. For the same reason, the deep white matter in the newborn normally shows hypointensity on DW imaging associated with increased ADC (Fig. 14.1). With increasing age, there is a relative decrease in water content of a pediatric brain. This is more evident in the white matter than in the gray matter. The decrease in water content is caused by myelinization replacing water during normal white matter development [2].
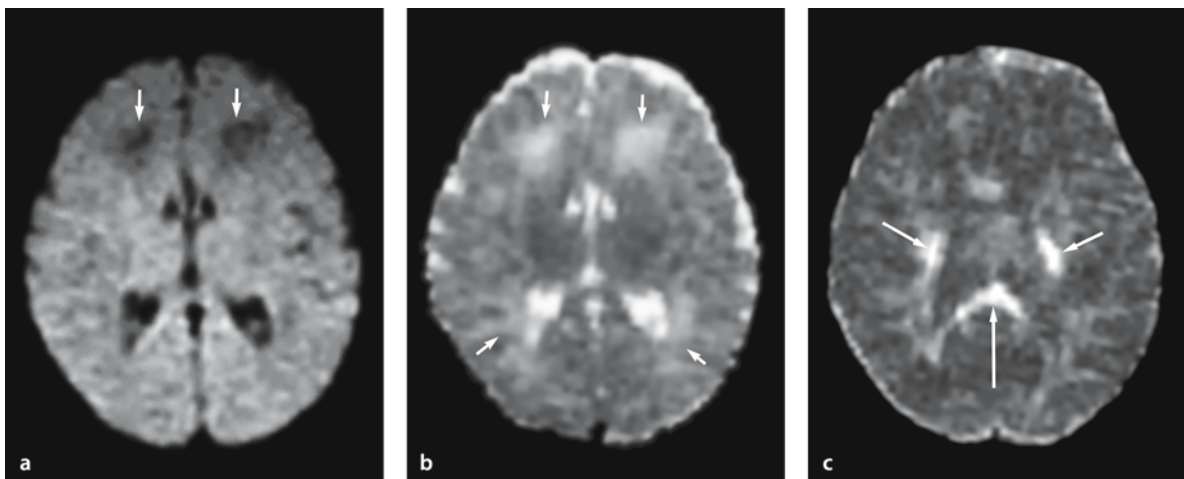
Figure 14.1 a–c

Normal pediatric DW imaging in a 2-day-old boy. **a** Low signal intensity and **b** increased ADC in the deep white matter are normal in this age group (*arrows*). **c** Fractional anisotropy map demonstrates anisotropy along the anterior and posterior limbs of the internal capsules (*arrows*), the corpus callosum (*long arrow*), and the temporo-parieto-occipital white matter earlier than regular T1- and T2-weighted images

14.3 Anisotropy

Normally anisotropy is much less evident in the immature brain than in the adult. One exception is corpus callosum, where anisotropy is already visible by DW imaging as early as the 28th gestational week. This occurs although the corpus callosum is composed of non-myelinated fibers. The phenomenon has been called premyelination anisotropy [3]. The anisotropic effect in the immature brain is thought to be related to structural changes of the axonal membrane. In general, anisotropy in the white matter of newborns is lower than in adults (Fig. 14.1). The anisotropic pattern can vary depending on the irregularity of axonal orientation as well as the degree of myelination.

14.4 Infarction and Ischemia

Ischemic infarctions in children are uncommon when compared with adults and they have different etiologies. They can be caused by thrombosis, embolism, arterial dissection, vasculitis, Moyamoya disease, sickle cell disease, child abuse, etc. (Figs. 14.2, 14.3, 14.4 and 14.5) [6, 7]. Hyperacute and acute infarctions are characterized by cytotoxic edema. Vasogenic edema occurs later and is typically seen in the subacute phase. DW imaging is useful for early detection of infarction in children, but also to differentiate between acute/subacute infarctions and chronic infarctions or ischemic gliosis.
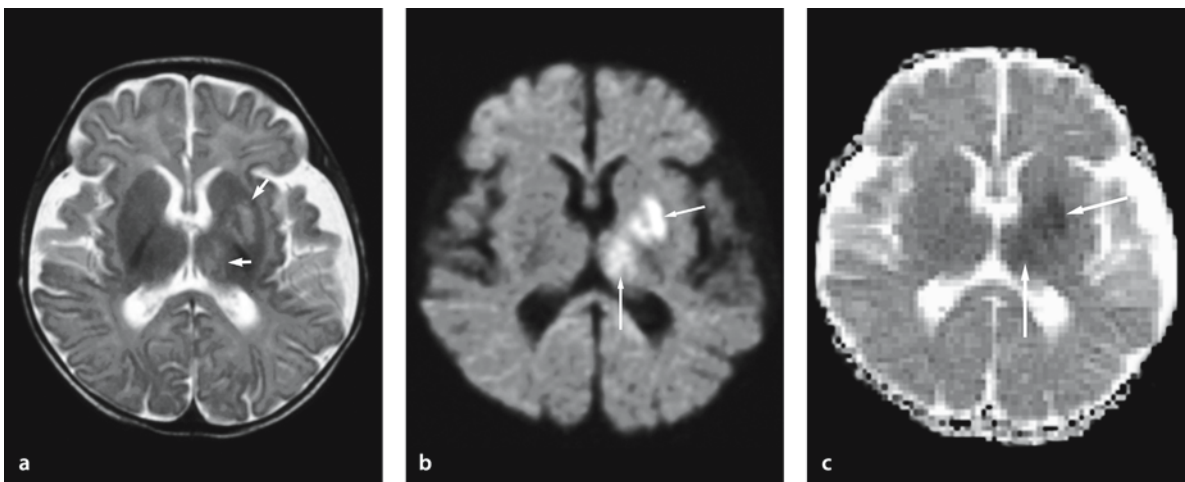
Figure 14.2 a–c

Cerebral infarction due to embolism in a 3-month-old boy. He had Down syndrome and ventricular septal defect. **a** T2-weighted image shows mild high signal lesions in the left putamen and thalamus (*arrows*). **b** DW image shows these lesions as high signal intensity (*arrows*). **c** ADC is decreased (*arrows*), consistent with acute infarcts
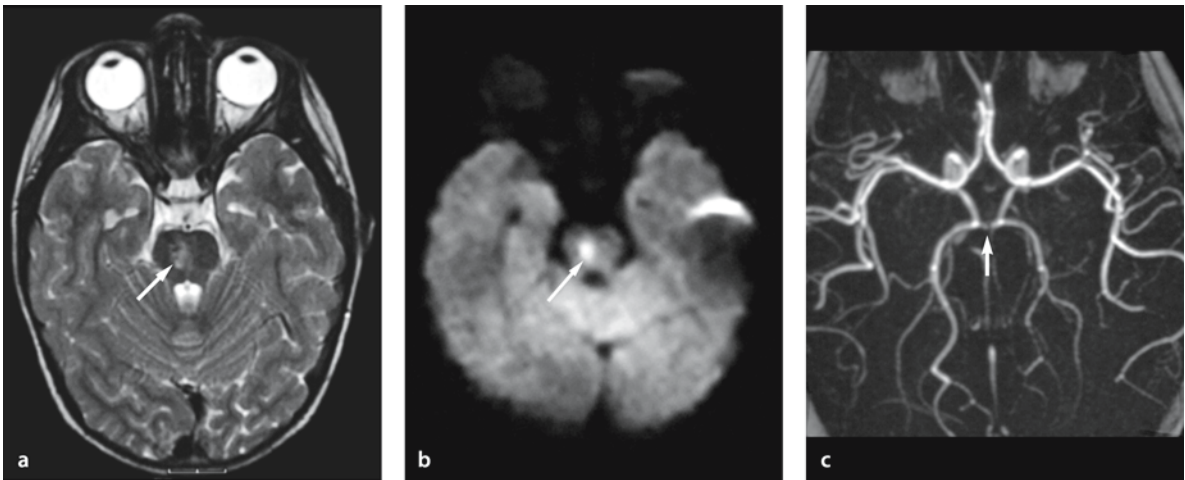
Figure 14.3 a–c ▲

Dissection of the vertebrobasilar arteries and infarction in a 4 year-old girl. **a** T2-weighted image shows high signal lesion in the right medial side of the pons (*arrow*). **b** DW image shows this lesion as hyperintense with decreased ADC (not shown), representing an acute infarct (*arrow*). **c** On MR angiography the vertebrobasilar arteries are absent due to dissection of the vertebrobasilar arteries (*arrow*). The posterior cerebral arteries are supplied from the anterior circulation
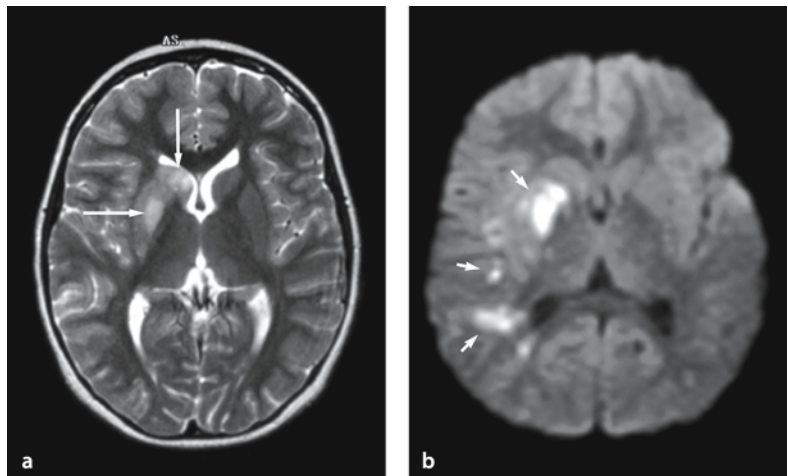
Figure 14.4 a–c

"Probable" Moyamoya disease in a 7-year-old girl. **a** T2-weighted image shows mild high signal lesions in the right basal ganglia. **b** DW image shows ischemic lesions not only in the basal ganglia but also in the parieto-occipital region as high signal, representing acute infarcts (*arrows*). **c** MR angiography shows occlusion of the right middle cerebral artery and stenosis of the right internal carotid artery (*arrows*) and bilateral posterior cerebral arteries (*arrowheads*).
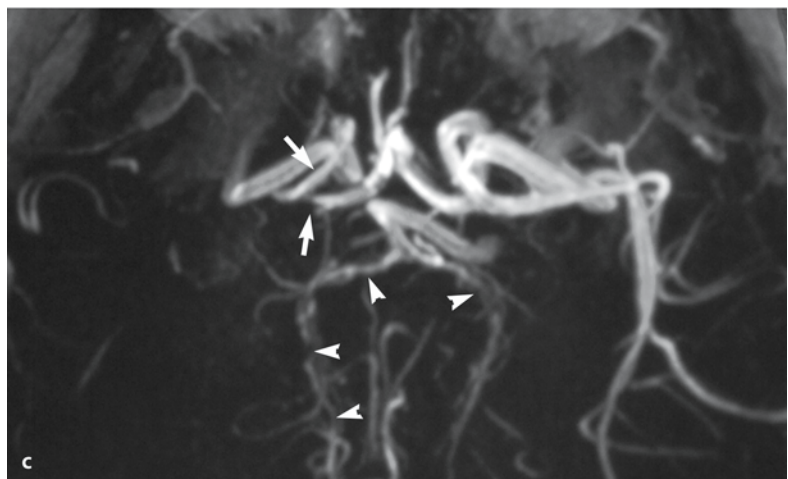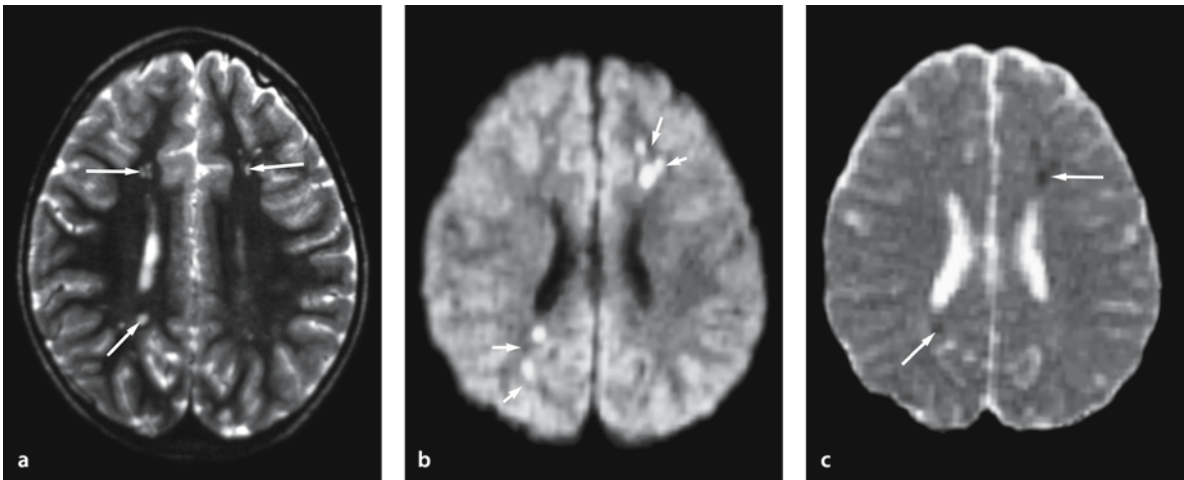
Figure 14.5 a–c

Sickle cell disease in a 4-year-old boy presenting with severe headache. **a** T2-weighted image shows multiple high signal spots in the white matter (*arrows*). **b** DW image shows some of these spots as very high signal intensity, representing small acute infarcts (*arrows*). **c** ADC map shows decreased ADC of these lesions consistent with small ischemic lesions (*arrows*). (From [49]).

14.4.1 Moyamoya Disease

Moyamoya disease is a chronic cerebrovascular occlusive disease of unknown origin that occurs predominantly in East Asia. In children it is characterized by progressive arterial stenosis with cerebral infarctions. The stenosis involves primarily the circle of Willis and the supraclinoid portion of the internal carotid arteries. Typically the internal carotid arteries are occluded bilaterally. In so-called "probable" Moyamoya disease, there is unilateral occlusion of one of the carotid arteries in its supraclinoid portion. DW imaging is useful for early detection of cerebral ischemia in this disease (Fig. 14.4) [6].

14.4.2 Sickle Cell Disease

About 5–8% of patients with sickle cell disease develop symptomatic cerebrovascular disease [7]. The risk of stroke is greatest during thrombotic crises and during the first 15 years of life. Stenosis or occlusion of both large and small vessels can cause cerebral infarction. Sickle cell disease results in vasculopathy, which in many respects is similar to Moyamoya dis-

ease. Cortical and white matter watershed ischemia is common; however, patients with sickle cell disease often also demonstrate multiple ischemic white matter lesions. These lesions can occur in spite of normal MR angiography and conventional angiography (Fig. 14.5). They are thought to be due to small vessel ischemic gliosis, similar to what is seen in small vessel disease of older patients.

14.4.3 Hypoxic Ischemic Encephalopathy

Hypoxic ischemic encephalopathy is the result of decreased global perfusion or oxygenation. It is generally due to neonatal anoxia, hypoglycemia, suffocation, cardiac arrest or child abuse. Whether produced by ischemia, anoxia or hypoglycemia, it is remarkably similar to infarcted brain in its appearance.

Diffusion-weighted imaging often depicts acute or subacute ischemic lesions when MR imaging and CT scans are normal or show only subtle abnormalities (Fig. 14.6) [8–13]. Diffuse hyperintensity on DW imaging with decreased ADC in the corpus callosum, and along the pyramidal tract in the internal capsules and the brain stem is occasionally seen. This is pre-

Figure 14.6 a–d

Hypoxic ischemic encephalopathy secondary to intrauterine cerebrovascular accident in a 2-day-old term girl. **a** T2-weighted image appears normal. **b** Fluid-attenuated inversion-recovery (FLAIR) image shows partially slightly high signal in the white matter (*arrows*). **c** DW image shows bilateral hyperintense lesions in the temporo-occipital cortices, white matter and corpus callosum (*arrows*), representing ischemic lesion and cytotoxic edema. **d** ADC map shows corresponding decreased ADC values
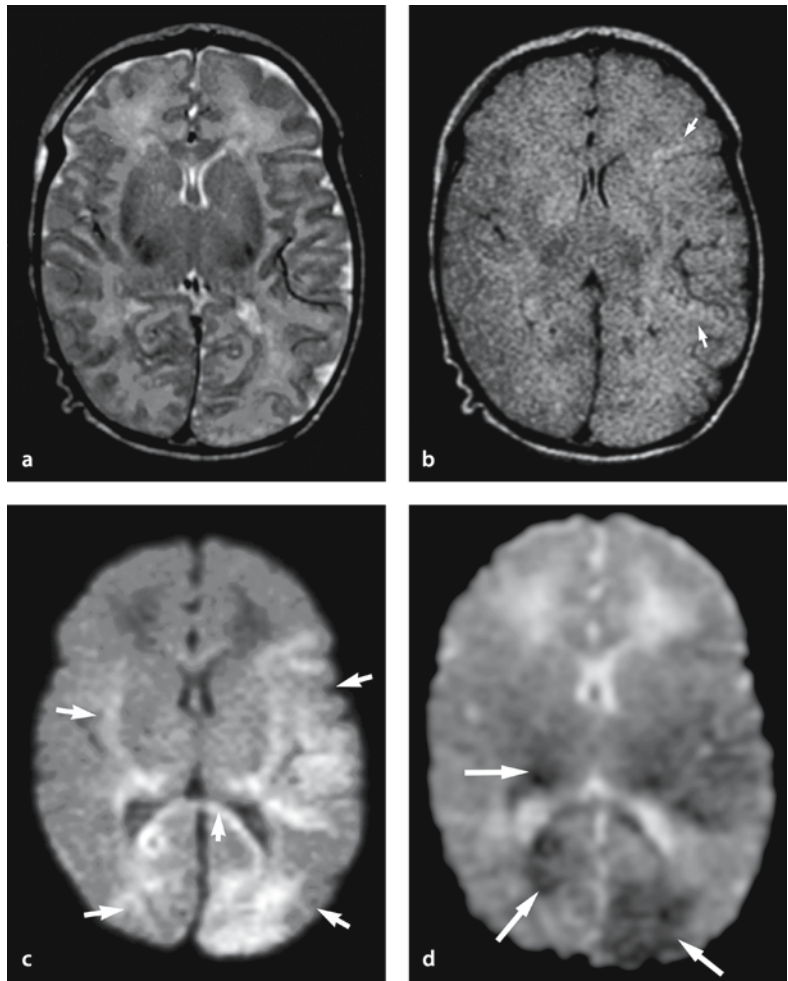
sumably due to cytotoxic edema of the glial cells, axons and myelin sheaths [14]. The prognosis of hypoxic ischemic encephalopathy depends on the extension of the cytotoxic edema, which is seen as hyperintensity on DW imaging. Hypoxic ischemic injury with cytotoxic edema is usually irreversible. DW imaging is helpful in establishing both the diagnosis and the prognosis, but also in the management of hypoxic ischemic encephalopathy.

14.5 Trauma

14.5.1 Battered Child Syndrome

In the USA, there are an estimated 3,000 deaths per year from non-accidental injuries. The pathogenesis of these brain parenchyma injuries is unknown, but unmyelinated white matter may be more vulnerable to shearing stress [15]. Young infants have a relatively large head, weak neck muscles and a thin skull, making them extremely vulnerable to traumatic injuries. In experimental studies of acute subdural hematomas in the infant rat, the glutamate concentration in the extracellular fluid of cortex was increased more than seven times over the basal level [16]. This suggests that the primary increased release of glutamate from the pre-synaptic terminal following traumatic stimuli and the primary decreased re-uptake of glutamate from the synapse following hypoxic or ischemic events are related to brain parenchymal injuries.

Histologic similarities have been observed in child abuse victims and infants with hypoxic ischemic encephalopathy. However, a history of apnea suggesting hypoxic–ischemic injury was only found in 57% of the child abuse cases. In a neuropathology study it was noted that diffuse axonal injuries were rare among child abuse victims, only seen in three out of 53 cases [17].

The distribution of widespread parenchymal injuries is often not related to the vascular territories or the location and size of acute subdural hematomas on CT and MRI (Fig. 14.7). However, it can be difficult to detect brain parenchyma injuries on CT as well as on routine MRI.

Diffusion-weighted imaging has a significant role in recognizing the extent of brain parenchymal injury. The parenchymal lesions can be unexpectedly extensive and caution is needed to window DW imaging optimally (Fig. 14.8). Quantifying the ADC value is especially useful to detect extensive parenchyma abnormalities.

The severity of DW imaging abnormality correlates with the patient's outcome [18]. However, MR spectroscopy may be better in evaluating the severity of trauma, as this will show decreased N-acetyl aspartate (NAA) (decreased neuronal activity), increased lactate (metabolic acidosis) and increased glutamate/glutamine (increased extracellular glutamate); the degree of these changes seems to be related to the severity of brain damage (Fig. 14.7) [19]. This grading may become important in the future since neuroprotective effects have been reported with several kinds of selective glutamate receptor antagonists in animal studies [20–22].
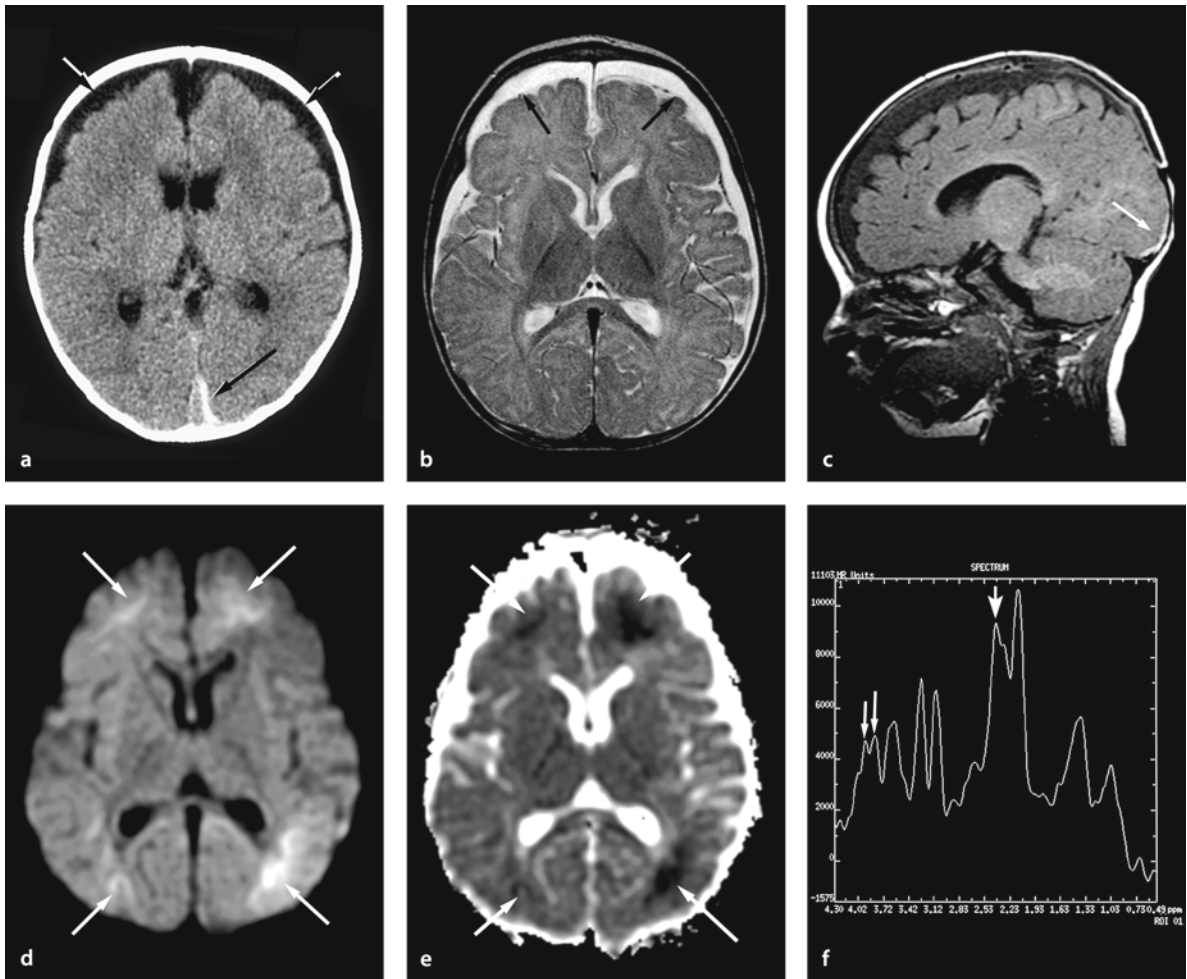
Figure 14.7 a–f

Battered child syndrome in a 6-month-old boy. **a** CT shows high density area representing acute subdural hematoma in the left occipital region (*long arrow*), and bilateral subdural fluid collections in the frontal region (*short arrows*). **b** T2-weighted image also shows bilateral subdural fluid collection and no apparent abnormalities in the brain parenchyma. **c** Sagittal T1-weighted image shows acute subdural hematoma as small linear hyperintensity in the occipital area (*arrow*). **d**, **e** DW image shows the extent of parenchymal abnormality as hyperintense lesions with decreased ADC in bilateral fronto-parieto-occipital white matter (*arrows*). This distribution is related to the hypoxic–ischemic encephalopathy rather than the subdural hematoma. **f** MR spectroscopy (TE 30 ms) shows an increased glutamate/glutamine peak (*arrow*) that may represent increased glutamate release or decreased glutamate re-uptake
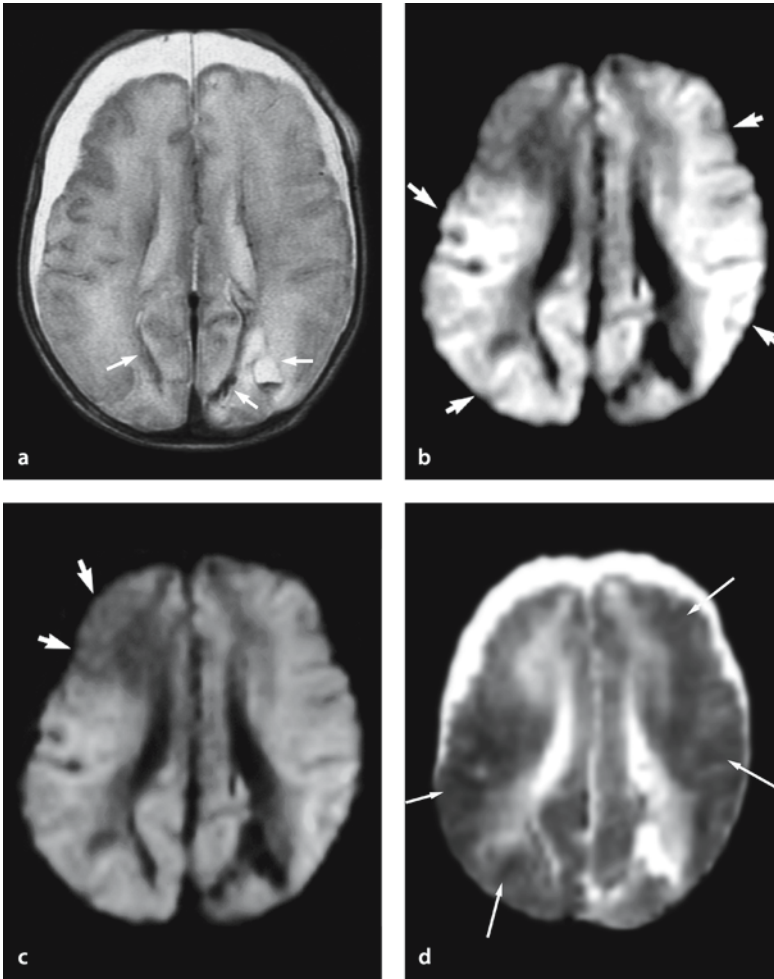
Figure 14.8 a–d

Battered child syndrome in a 2-month-old boy. **a** T2-weighted image shows intracranial hemorrhages with shearing injury (*arrows*) and bilateral chronic subdural hematomas in the bilateral frontal region. **b** DW image shows diffusely increased signal in both hemispheres (*arrows*) with sparing of only the right frontal area. **c** DW image filmed with incorrect window and level setting, suggesting wrongly that the low signal in the right frontal area is abnormal (*arrows*), when indeed this is the only normal portion of the brain. Correct window and levels are critical, as is comparison with findings on other sequences. **d** ADC values are decreased (0.31 x 10^{-3}/mm^2 per s) in the diffuse parenchymal abnormalities (*arrows*)
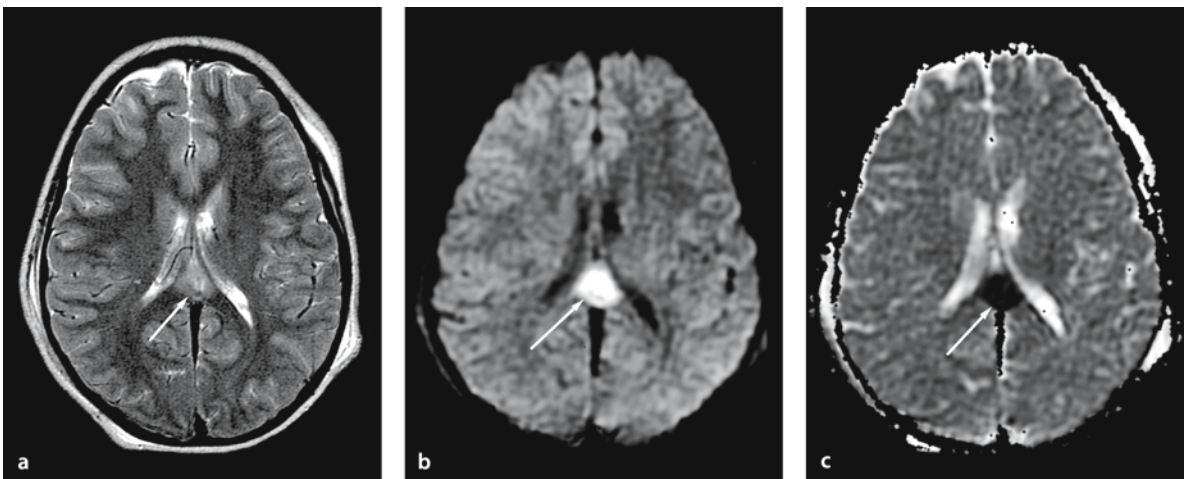
14.5.2 Diffuse Axonal Injury and Brain Contusion

It was once considered that edema following brain contusion or diffuse axonal injury was vasogenic. Recent experimental studies using DW imaging have shown that edematous regions following injury consist of both vasogenic and cytotoxic edema [23, 24]. DW imaging shows diffuse axonal injury as hyperintense, presumably due to cytotoxic edema (Fig. 14.9). It should be noted, however, that hemorrhagic components often accompany these brain injuries, which will affect the signal intensity on DW imaging. Brain contusions near the skull base are also often overlooked on DW imaging due to susceptibility artifacts.

14.6 Encephalopathies

14.6.1 Mitochondrial Encephalopathy

Mitochondrial encephalopathies show various patterns of central nervous system involvement. These include multiple infarcts in the cortex, white matter or basal ganglia. Infarcts are related to the type of mitochondrial encephalopathy and do not usually follow vascular territories. Other features of mitochondrial encephalopathy are spongy encephalopathy or demyelination with intramyelinic edema [25] and atrophy. DW imaging is useful for detecting the active ischemic changes (Fig. 14.10) [26].

Figure 14.10 a,b

Mitochondrial encephalomyopathy in a 20-month-old girl with seizures. **a** T2-weighted image shows multiple high signal lesions in bilateral basal ganglia and fronto-parieto-occipital cortex not corresponding to a vascular territory (*arrows*). **b**, **c** DW image shows multiple high signal intensity lesions associated with decreased ADC (*arrows*)

Figure 14.9 a–c

Diffuse axonal injury in an 11-year-old boy injured in a motor vehicle accident. **a** T2-weighted image shows a mildly hyperintense lesion in the corpus callosum (*arrow*). **b** DW image demonstrates this lesion as hyperintense (*arrow*). **c** ADC map shows decreased ADC of this lesion (*arrow*), probably representing cytotoxic edema associated with diffuse axonal injury

◄

14.6.2 Acute Necrotizing Encephalopathy

Acute necrotizing encephalopathy is a clinicopathological entity recently separated from acute encephalopathy of unknown etiology. It frequently occurs in East Asia. The hallmark of acute necrotizing encephalopathy is multiple, bilateral symmetric brain lesions showing necrosis, petechiae and cytotoxic edema without inflammatory cell infiltration [27]. These lesions are mainly seen in the thalamus and tegmentum (Fig. 14.11). The prognosis is generally poor.

14.6.3 Hypertensive Encephalopathy

Hypertensive encephalopathy occurs most often secondary to renal diseases in children. It also occurs in children treated for myeloproliferative disorders [28]. In children, convulsions are often accompanied by severe headache and restlessness. The most common abnormality on MR imaging is bilateral high signal intensity in parieto-occipital subcortical white matter. These lesions can also occur in the frontal lobes and gray matter, including basal ganglia, thalamus, cerebellum and brain stem. The mechanism of the disease is thought to be vasogenic edema from failure of autoregulation and/or a cytotoxic edema triggered by severe vasospasm. DW imaging can distinguish irreversible ischemic changes from reversible conditions with vasogenic edema (Fig. 14.12) [29].
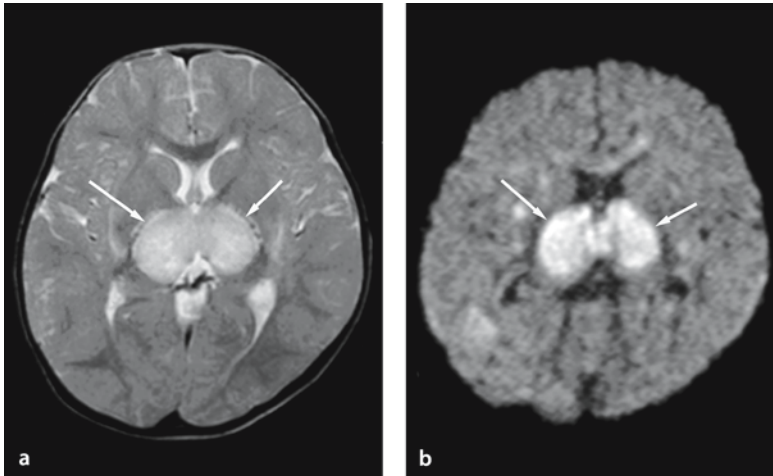
Figure 14.11 a,b

Acute necrotizing encephalopathy in a 1-year-old boy with seizure. **a** T2-weighted image shows multiple hyperintense lesions in bilateral thalami and right temporo-occipital region (*arrows*). **b** DW image also shows these lesions (*arrows*) as hyperintense associated with decreased ADC (not shown). (Courtesy of Ida M, M.D. Ekara Municipal Hospital, Japan)
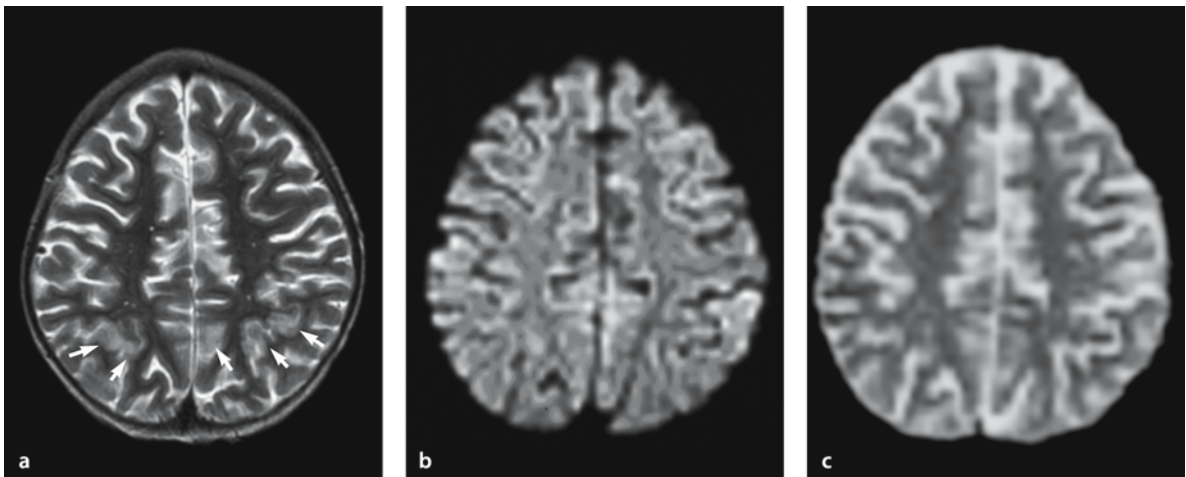
14.7 Infections

14.7.1 Encephalitis

Diffusion-weighted imaging can detect early encephalitic changes [30] and is generally more sensitive than conventional MR imaging. Herpes encephalitis demonstrates pathologically severe edema including both cytotoxic and vasogenic edema and massive tissue necrosis with petechial or confluent hemorrhage. Herpes simplex type 1 encephalitis in older children and adults usually involves the medial temporal lobe, inferior frontal lobes and insula (Fig. 14.13). Neonatal herpes simplex type 2 encephalitis involves the cortex and white matter extensively (Fig. 14.14). The early detection by DW imaging is valuable for early institution of treatment
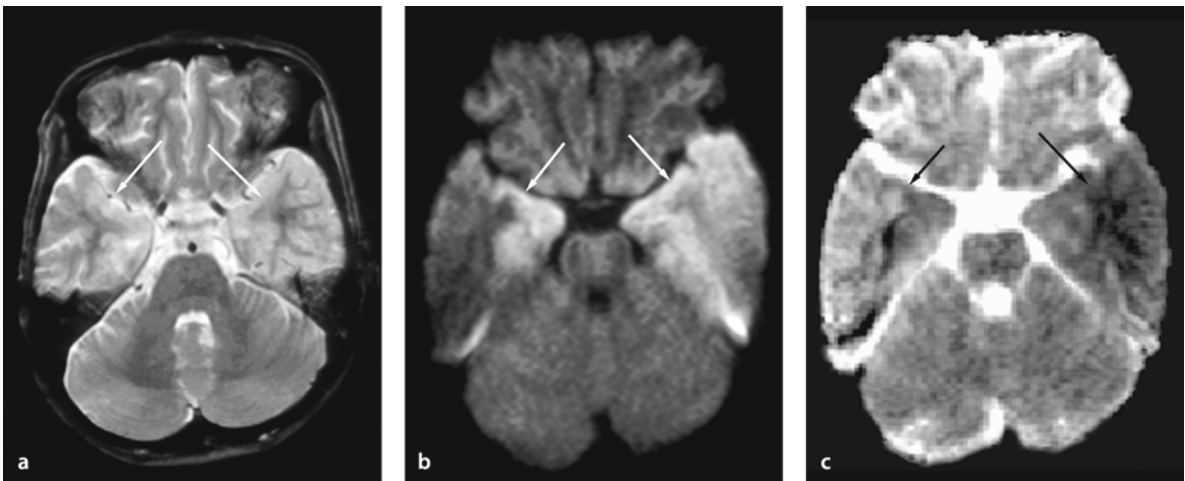
Figure 14.13 a–c

Herpes simplex type 1 encephalitis in an 11-year-old boy. **a** T2-weighted image shows hyperintense lesions in bilateral temporal lobes (*arrows*). **b** DW image clearly shows these lesions as hyperintense (*arrows*). **c** ADC map shows decreased ADC of these lesions (*arrows*)

Figure 14.12 a–c

Hypertensive encephalopathy in a 5-year-old girl with acute lymphoblastic leukemia during chemotherapy presenting with seizure. **a** T2-weighted image shows hyperintense lesions in bilateral parieto-occipital cortex (*arrows*). This high signal seems to be due to subtle vasogenic edema rather than frank ischemia. **b, c** DW image and ADC map show no apparent abnormal signal intensities

◄
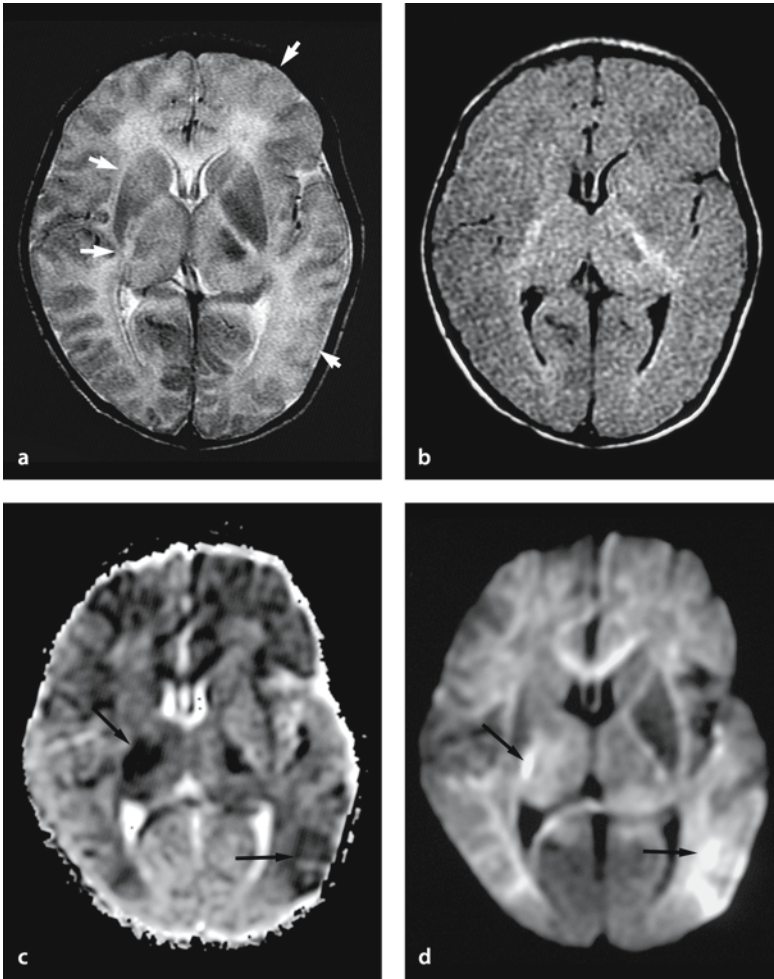
Figure 14.14 a–d

Herpes simplex type 2 encephalitis in a 2-week-old girl. **a** T2-weighted images show asymmetric hyperintense lesions in the thalami and right basal ganglia and cerebral cortices (*arrows*). The precise extent of the lesions is difficult to determine. **b** FLAIR image appears normal. **c, d** DW image shows asymmetric but extensive hyperintense lesions (*arrows*) with decreased ADC in the thalamus and gray and white matter of both hemispheres

14.7.2 Brain Abscess

Abscesses in the brain are potentially fatal, but may be successfully treated by early medical or surgical intervention. DW imaging can discriminate a brain abscess from a cystic or necrotic tumor, which is often difficult with conventional MR imaging [31]. The brain abscess shows very high signal on DW imaging associated with decreased ADC (Fig. 14.15). Pus usually consists of both dead and still viable neutrophils, along with necrotic tissue and bacteria, as well as exuded plasma. A possible explanation for the high signal on DW imaging is limited water mobility, presumably due to the high viscosity of continuous coagulative necrosis and hypercellularity of polynucleated neutrophils in the pus.
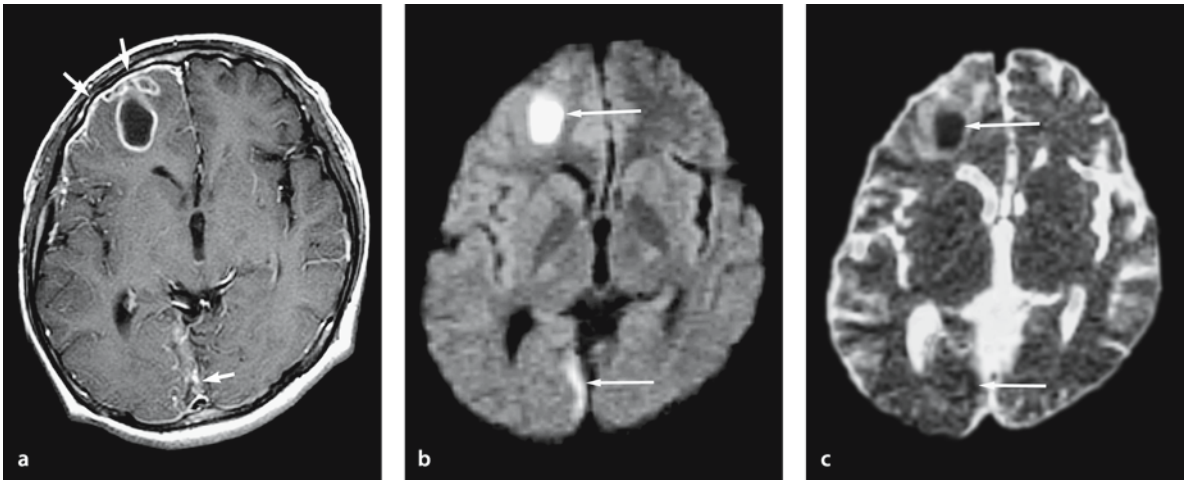
Figure 14.15 a–c

Brain abscess and subdural abscess in a 16-year-old male with high fever and headache. **a** Gadolinium-enhanced T1-weighted image shows thin-walled ring or rim-enhancing lesions with pachymeningeal enhancement in the right frontal lobe and right medial occipital region (*arrows*). **b** DW image shows cystic component of the right frontal and occipital lesion as very hyperintense (*arrows*). **c** ADC map shows decreased ADC in these cystic components (*arrows*). (Courtesy of Morikawa M, M.D., Nagasaki University, School of Medicine, Japan)

14.8 Brain Tumor

The signal intensity on DW imaging and the ADC values of brain tumors are variable and related to the architecture of the tumor. Malignant brain tumors, such as medulloblastoma (Fig. 14.16), primitive neuroectodermal tumor, glioma and lymphoma [32–35], often show high signal intensity on DW imaging associated with decreased ADC. The decreased ADC value is caused by increased intracellular water, hypercellularity and/or decreased extracellular water in tumor interstitium. Other brain tumors, either benign or malignant, show hyperintensity associated with increased ADC, indicating a T2 shine-through effect (Fig. 14.17).
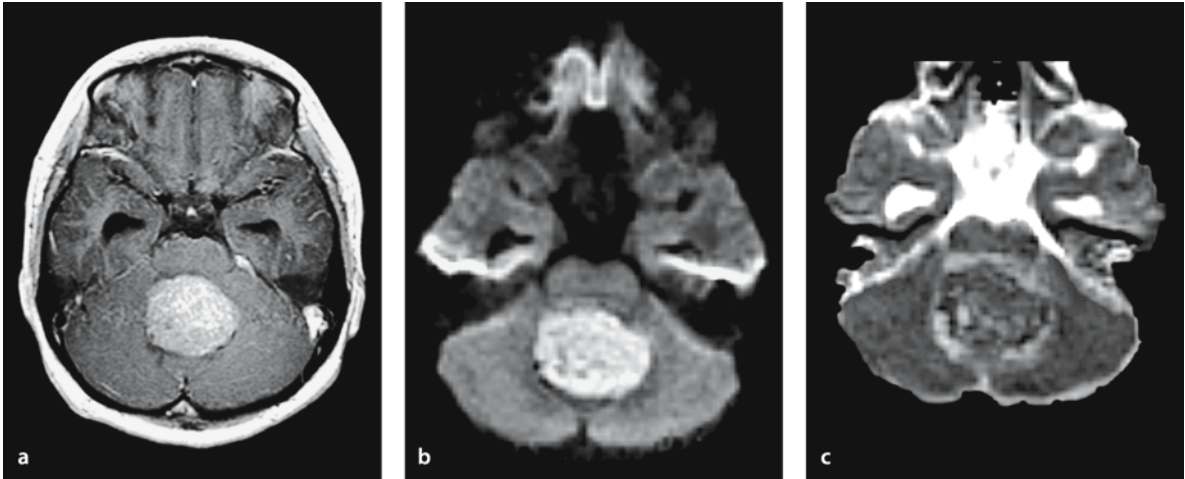
Figure 14.16 a–c

Medulloblastoma in a 10-year-old boy. **a** Gadolinium-enhanced T1-weighted image shows a solid mass with enhancement in the cerebellar vermis. **b** DW image shows this solid mass as hyperintense. **c** ADC map shows decreased ADC of this mass. This is due to high cellular density causing restricted diffusion. (Courtesy of Morikawa M, M.D., Nagasaki University, School of Medicine, Japan)
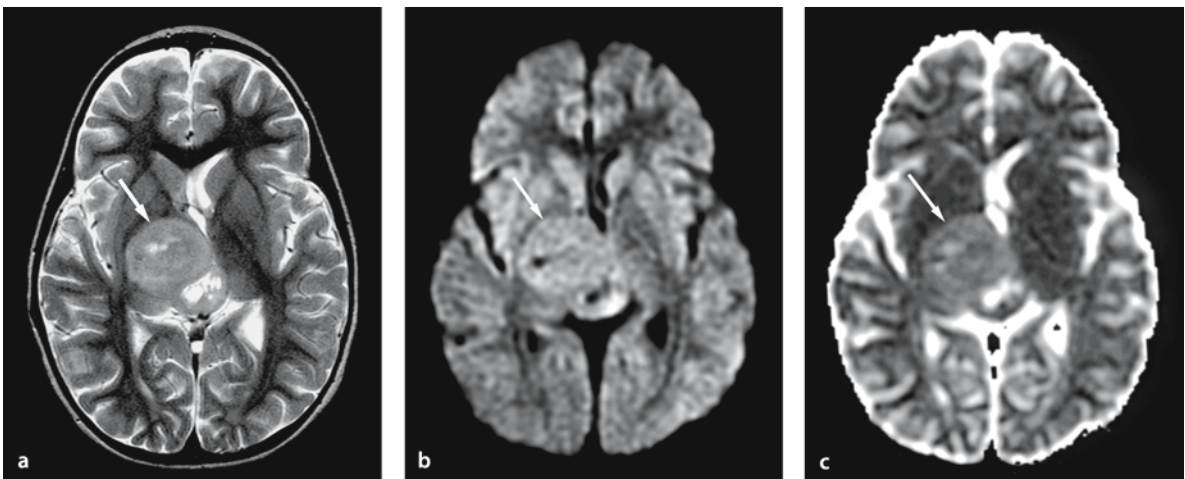
14.9 Dysmyelination and Demyelination

Diffusion-weighted imaging is useful in differentiating between white matter diseases in pediatric patients.

14.9.1 Pelizaeus–Merzbacher Disease

Pelizaeus–Merzbacher disease, one of the typical dysmyelination disorders, pathologically shows hypo- or amyelination and spares the axon. Despite hypo- or amyelination in Pelizaeus–Merzbacher disease, DW imaging shows normal diffusional anisotropy in the white matter (Fig. 14.18) [36]. This finding suggests that anisotropy is primarily related to structural changes of the axonal membrane in the immature brain.

Figure 14.18 a,b

Pelizaeus–Merzbacher disease in a 7-year-old boy with developmental delay. **a** T2-weighted image shows diffuse white matter hyperintensity extending into the U-fibers due to hypo- or amyelination (*arrows*). **b** DW image (*z axis*) demonstrates isointensity in the white matter and essentially normal anisotropy in the corpus callosum. ADC values are diffusely slightly increased in the white matter (not shown) (From [46]).
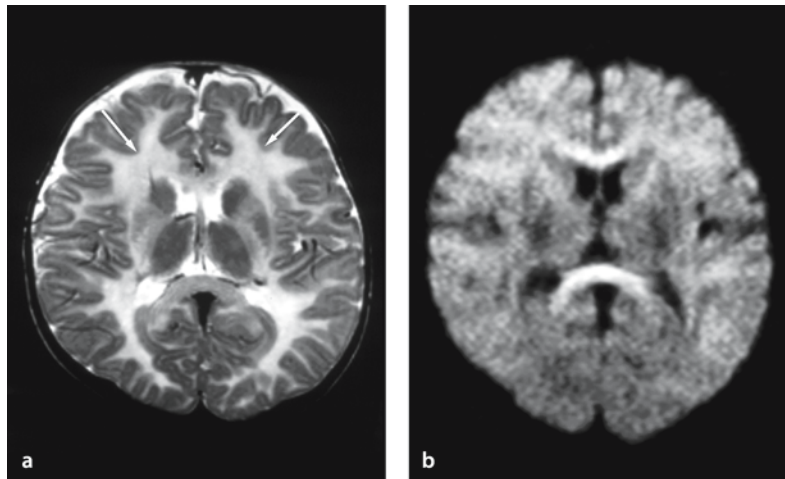
Figure 14.17 a–c

 Pilocytic astrocytoma in a 4-year-old girl. **a** T2-weighted images show a hyperintense mass lesion in the right thalamus (*arrow*). **b** DW image shows this solid mass as hyperintense (*arrow*). **c** ADC map shows slightly increased ADC of this mass. Hyperintensity on DW imaging is due to T2 signal effect, which is called T2 shine-through effect

◄

14.9.2 Vanishing White Matter Disease

Leukoencephalopathy with vanishing white matter is a newly recognized dysmyelinating disease of unknown etiology. In the late stage of this disease there is demyelination or hypomyelination and extensive cystic degeneration of the white matter associated with reactive changes. DW imaging shows low signal intensity, presumably representing cystic degeneration (Fig. 14.19).

14.9.3 Metabolic or Toxic Leukoencephalopathies

Some metabolic or toxic leukoencephalopathies such as phenylketonuria (Fig. 14.20), adrenoleukodystrophy, metachromatic leukodystrophy, L-2 hydroxyglutaric acidurig (Chap. 10), infantile neuronaldystrophy and Canavan's disease (Fig. 14.21) can show hyperintense lesions associated with decreased ADC on DW imaging [37–42]. One possible explanation for the hyperintense lesion is intramyelinic edema, which is one form of cytotoxic edema selectively occurring in myelin sheaths.
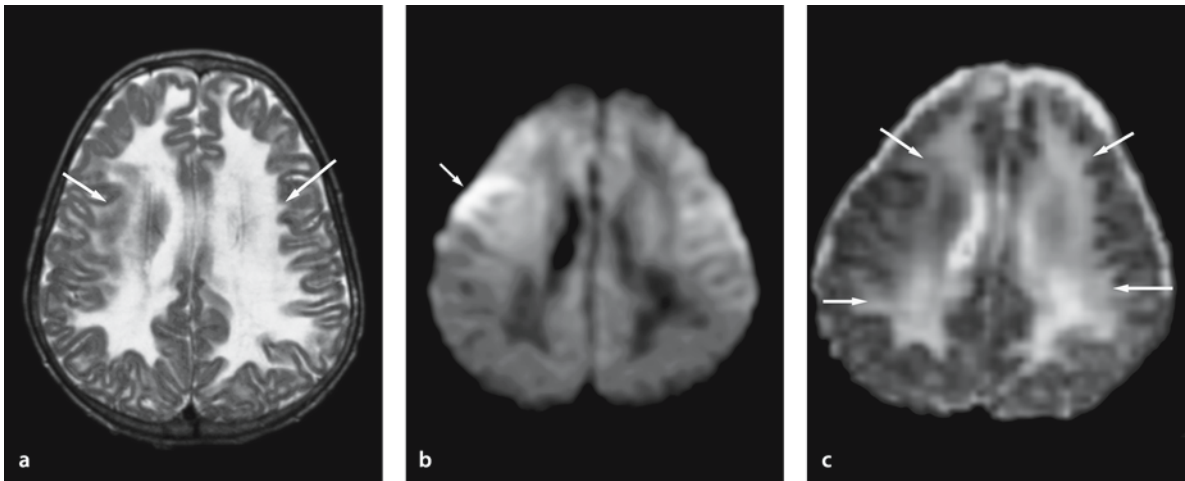
Figure 14.19 a–c

Vanishing white matter disease in an 8-year-old boy with progressive leukoencephalopathy. **a** T2-weighted image shows diffuse white matter hyperintensity extending into the U-fibers (*arrows*). **b** DW image demonstrates diffuse low signal intensity in the white matter. High signal intensity along right frontal lobes is magnetic susceptibility artifact due to the field heterogeneity (*arrow*). **c** ADC map shows diffusely increased ADC in the white matter, presumably due to cystic changes (*arrows*)

14.9.4 Multiple Sclerosis

Multiple sclerosis occasionally occurs in pediatric patients. Hyperintense plaques on DW imaging with decreased ADC are rare in multiple sclerosis (Fig. 14.21) [39]. When present, a possible explanation for the hyperintense, cytotoxic multiple sclerosis plaques may be intramyelinic edema.

14.9.5 Osmotic Myelinolysis

Osmotic myelinolysis also occurs in pediatric patients and can result in hyperintense lesions on DW imaging associated with decreased ADC (Fig. 14.22) [40].
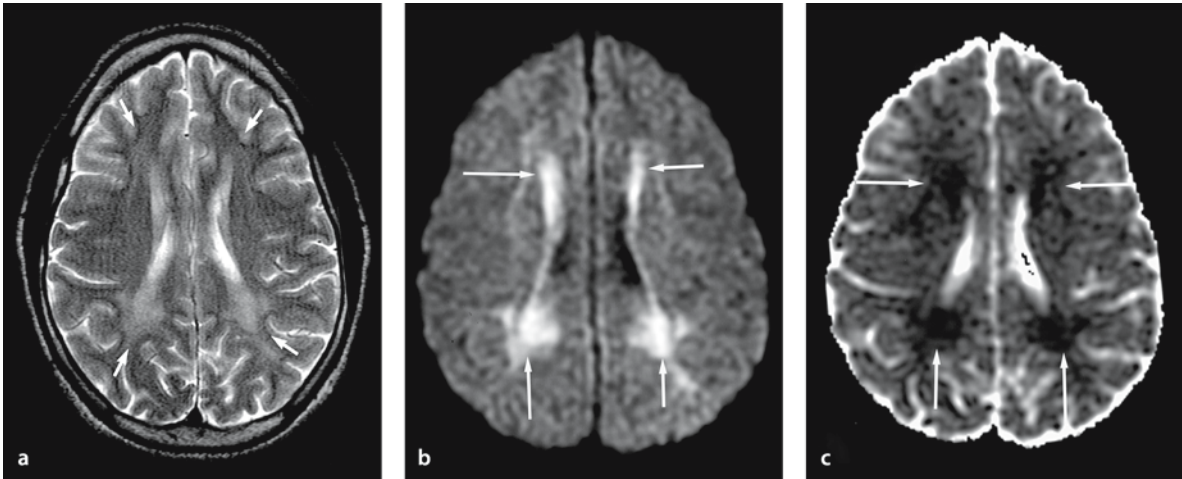
Figure 14.20 a–c

Phenylketonuria in a 36-year-old male **a** T2-weighted image shows hyperintense lesions in the periventricular white matter (*arrows*). **b** DW image shows these lesions as hyperintense (*arrows*). **c** These hyperintense lesions have decreased ADC representing cytotoxic edema, especially intramyelinic edema (*arrows*)

Figure 14.21 a,b

Canavan disease. 15-month-old boy presented with delayed psychomotor development seizures, and spasticity. **a** T2-weighted image reveals high signal in peripheral white matter, globi pallidi and thalami. Note diffuse atrophy and thinning of the cortex. **b** DW image shows high signal changes in the peripheral white matter and globi pallidi with mildly decreased ADC partially (not shown). (From Prof. Dr R. Nuri Sener, Department of Radiology, Ege University Hospital, Turkey, Journal of Computer Assisted Tomography 27, 2003, [42] with permission)
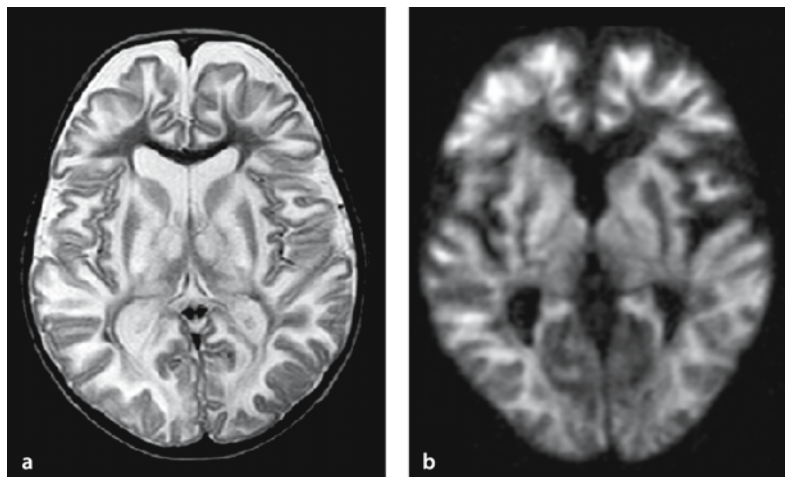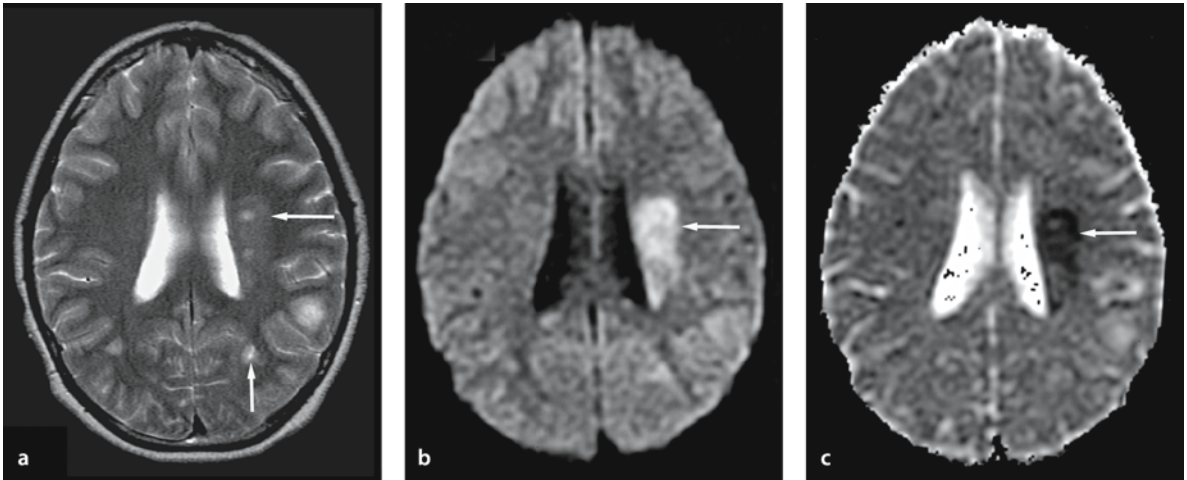
Figure 14.22 a–c

Acute multiple sclerosis in a 13-year-old female. **a** T2-weighted image shows multiple hyperintense lesions in the periventricular and subcortical white matter (*arrows*). **b, c** DW image shows a hyperintense plaque with decreased ADC (*arrows*) in the left corona radiata. This is a cytotoxic plaque, presumably mainly composed of intramyelinic edema
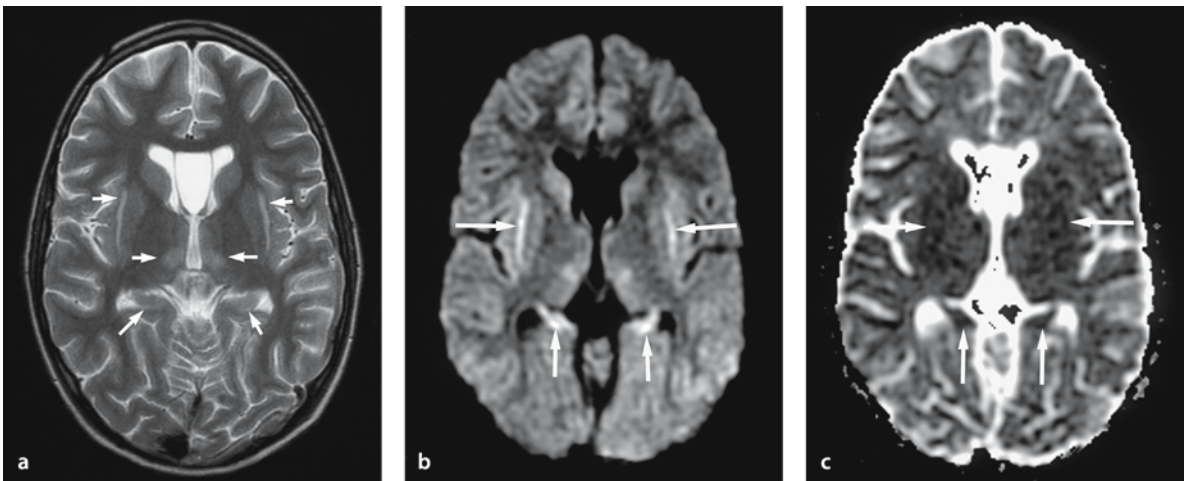
Figure 14.23 a–c

Osmotic myelinolysis (extrapontine myelinolysis) in an 11-year-old boy. **a** T2-weighted image shows symmetrical multiple slightly hyperintense lesions in the external capsules, hippocampi and medial thalami (*arrows*). **b, c** DW image shows these lesions (*arrows*) as hyperintense with decreased ADC, representing cytotoxic edema

14.10 Conclusion

Diffusion-weighted imaging plays an important role in the diagnosis of various pathological conditions in the pediatric brain, which has a high water content . DW imaging can also depict acute or subacute ischemic changes in children when conventional MR imaging or CT is normal or shows only subtle abnormalities. DW imaging is useful in differentiating white matter diseases and in differentiating between tumor and abscess. The calculation of ADC maps or fractional anisotropic images is quantitative and demonstrates the water content or anisotropy more precisely than DW imaging. However, recognition of imaging pitfalls is important for optimal interpretation of DW imaging.

References

1. Roley HA, Grant PE, Roberts TPL (1999) Diffusion MR imaging. Theory and applications. Neuroimaging Clin N Am 9:343–361
2. Neil JJ, Shiran SI, McKinstry RC, et al. (1998) Normal brain in human newborns: apparent diffusion coefficient and diffusion anisotropy measured by using diffusion tensor MR imaging. Radiology 209:57–66
3. Wimberger DM, Roberts TP, Barkobich AJ, et al. (1995) Identification of "premyelination" by diffusion-weighted MRI. JCAT 19:28–33
4. Tanner SF, Ramenghi LA, Ridgway JP, et al. (2000) Quantitative comparison of intrabrain diffusion in adults and preterm and term neonates and infants. AJR Am J Roentgenol 174:1643–1649
5. Morris MC, Zimmerman RA, Bilaniuk LT, et al. (1999) Changes in brain water diffusion during childhood. Neuroradiology 41:929–934
6. Yamada I, Himeno Y, Nagaoka T, et al. (1999) Moyamoya disease: evaluation with diffusion-weighted and perfusion echo-planar MR imaging. Radiology 212:340–347
7. Moran CJ, Siegel MJ, DeBaun MR (1998) Sickle cell disease: imaging of cerebrovascular complications. Radiology 206:311–321
8. Phillips MD, Zimmerman RA (1999) Diffusion imaging in pediatric hypoxic ischemia injury. Neuroimaging Clin N Am 9:41–52
9. Robertson RL, Ben-Sira L, Barnes PD, et al. (1999) MR line-scan diffusion-weighted imaging of term neonates with perinatal brain ischemia. AJNR Am J Neuroradiol 20:1658–1670
10. Johnson AJ, Lee BC, Lin W (1999) Echoplanar diffusion-weighted imaging in neonates and infants with suspected hypoxic-ischemic injury: correlation with patient outcome. AJR Am J Roentgenol 172:219–226
11. Inder T, Huppi PS, Zientara GP, et al. (1999) Early detection of periventricular leukomalacia by diffusion-weighted magnetic resonance imaging techniques. J Pediatr 134:631–634
12. Forbes KP, Pipe JG, Bird R (2000) Neonatal hypoxic-ischemic encephalopathy: detection with diffusion-weighted MR imaging. AJNR Am J Neuroradiol 21:1490–6
13. Wolf RL, Zimmerman RA, Clancy R, Haselgrove JH (2001) Quantitative apparent diffusion coefficient measurements in term neonates for early detection of hypoxic-ischemic brain injury: initial experience. Radiology 218:825–33
14. Rumpel H, Nedelcu J, Aguzzi A, et al. (1997) Late glial swelling after acute cerebral hypoxic-ischemia in the neonatal rat: a combined magnetic resonance and histochemical study. Pediatr Res 42:54–59
15. Chen CY, Zimmerman RA, Rorke LB (1999) Neoroimaging in child abuse: a mechanism-based approach. Neuroradiology 41:711–722
16. Bullock R, Butcher SP, Chen MH, et al. (1991) Correlation of the extracellular glutamate concentration with extent of blood flow reduction after subdural hematoma in the rat. J Neurosurg 74:794–802
17. Geddes JF, Hackshaw AK, Vowles GH, et al. (2001) Neuropathology of inflicted head injury in children. Patterns of brain damage. Brain 124:1290–1298
18. Suh DY, Davis PC, Hopkins KL, et al. (2001) Nonaccidental pediatric head injury: diffusion-weighted imaging findings. Neurosurgery 49:309–320
19. Holshouser BA, Ashwal S, Luh G, et al. (1997) Proton MR spectroscopy after central nervous system injury: outcome prediction in neonates, infants, and children. Radiology 202:487–496
20. Duhaime AC, Gennarelli LM, Boardman C (1996) Neuroprotection by dextromethorphan in acute experimental subdural hematoma in the rat. J Neurotrauma 13:79–84
21. Ikonomidou C, Qin Y, Labruyere J, Kirby C, et al. (1996) Prevention of trauma-induced neurodegeneration in infant rat brain. Pediatr Reseach 39:1020–1027
22. Smith SL, Hall ED (1998) Tirilazad widens the therapeutic window for riluzole-induced attenuation of progressive cortical degeneration in an infant rat model of the shaken baby syndrome. J Neurotrauma 15:707–719
23. Barzo P, Marmarou A, Fatouros P, et al. (1997) Contribution of vasogenic and cellular edema to traumatic brain swelling measured by diffusion-weighted imaging. J Neurosurg 87:900–907
24. Liu AY, Maldjian JA, Bagley LJ, Sinson GP, et al. (1999) Traumatic brain injury: diffusion-weighted MR imaging findings. AJNR Am J Neuroradiol 20:1636–1641
25. Ellison D, Love S (1998) Toxic injury of the CNS. In: Neuropathology, 1st edn. London: Mosby 25:5
26. Yonemura K, Hasegawa Y, Kimura K, Minematsu K, Yamaguchi T (2001) Diffusion-weighted MR imaging in a case of mitochondrial myopathy, encephalopathy, lactic acidosis, and strokelike episodes. AJNR Am J Neuroradiol 22:269–72
27. Yagishita A, Nakano I, Ushioda T, Otsuki N, Hasegawa A (1995) Acute encephalopathy with bilateral thalamotegmental involvement in infants and children: imaging and pathology findings. AJNR Am J Neuroradiol 16:439–447

28. Cooney MJ, Bradly WG, Symko SC, et al. (2000) Hypertensive encephalopathy: complication in children treated for myeloproliferative disorders: report of three cases. Radiology 214:711–716

29. Schwartz RB, Mulkern RV, Gudbjartsson H, et al. (1998) Diffusion-weighted MR imaging in hypertensive encephalopathy: clues to pathogenesis. AJNR Am J Neuroradiol 19:859–862

30. Tsuchiya K, Katase S, Yoshino A, et al. (1999) Diffusion-weighted MR imaging of encephalitis. AJR Am J Roentgenol 173:1097–1099

31 Ebisu T, Tanaka C, Umeda M, et al. (1996) Discrimination of brain abscess from necrotic or cystic tumors by diffusion-weighted echo planar imaging. Magn Reson Imaging 14:1113–1116

32. Kotsenas AL, Roth TC, Manness WK, et al. (1999) Abnormal diffusion-weighted MRI in medulloblastoma: does it reflect small cell histology? Pediatr Radiol 29:524–526

33. Erdem E, Zimmerman RA, Haselgrove JC, Bilaniuk LT, Hunter JV (2001) Diffusion-weighted imaging and fluid attenuated inversion recovery imaging in the evaluation of primitive neuroectodermal tumors. Neuroradiology Nov; 43(11):927–933

34. Tien RD, Felsberg GJ, Friedman H, et al. (1993) MR imaging of high-grade cerebral gliomas: value of diffusion-weighted echoplanar pulse sequence. AJR Am J Roentgenol 162:671–677

35. Guo AC, Cummings TJ, Dash RC, Provenzale JM (2002) Lymphomas and high-grade astrocytomas: comparison of water diffusibility and histologic characteristics. Radiology 224:177–183

36. Ono J, Harada K, Sakurai K, et al. (1994) MR diffusion imaging in Pelizaeus-Merzbacher disease. Brain Dev 16:219–223

37. Ono J, Harada K, Mano T, et al. (1997) Differentiation of dys- and demyelination using diffusion anisotropy. Pediatr Neurol 16:63–66

38. Eichler FS, Itoh R, Barker PB, et al. (2002) Proton MR spectroscopic and diffusion tensor brain MR imaging in X-linked adrenoleukodystrophy; initial experience. Radiology 225: 245–252

39. Sener RN (2002) Metachromatic leukodystrophy: diffusion MR imaging findings. AJNR Am J Neuroradiol 23: 1424–1426

40. Sener RN (2003) L-2 hydroxyglutaric aciduria: proton magnetic resonance spectroscopy and diffusion magnetic resonance imagimg findings. J Comput Assis Tomogr 27: 38–43

41. Sener RN (2003) Diffusion magnetic resonance imaging in infantile neuroaxonal dystrophy. J Comput Assis Tomogr 27: 34–37

42. Sener RN (2003) Canavan disease: diffusion magnetic resonance imaging findings. J Comput Assist Tomogr 27:30–33

43. Rovira A, Pericot I, Alonso J, Rio J, et al. (2002) Serial diffusion-weighted MR imaging and proton MR spectroscopy of acute large demyelinating brain lesions: case report. AJNR Am J Neuroradiol Jun-Jul; 23(6):989–994

44. Cramer SC, Stegbauer KC, Schneider A, et al. (2001) Decreased diffusion in central pontine myelinolysis. AJNR Am J Neuroradiol Sep; 22(8):1476–1479

45. Moritani T, Numaguchi Y, Lerner NB, et al. (2003) Sickle Cell Cerebrovascular Disease: usual and unusual findings on MR Imaging and MR Angiography, Clin Imaging. In press.

46. Moritani T, Shrier DA, Numaguchi Y, et al. (2000) Diffusion-weighted echo-planar MR imaging: clinical applications and pitfalls – a pictorial essay. Clin Imaging. 24: 181–192

How to Use This Book

In collaboration with A. Hiwatashi

Most textbooks related to imaging are organized into chapters based on the disease or the conditions that are described. This traditional way of organizing an imaging book, namely from the disease to the images, provides a firm structure and allows the author or editor to present all the imaging characteristics of a specific disease condition with its typical, atypical and specific features in one place. This book is no different and is also organized in this traditional way.

For the clinician using the book as an aid to solve a clinical case, this traditional approach is not practical. To match the imaging characteristics of your specific clinical case you essentially have to go through the entire book to find all the images that match the imaging features of your specific patient. To overcome this problem of a disease-oriented imaging book, we developed this chapter: here we turned the organization around, proceeding from the images to the disease/diagnosis. In this chapter we have prepared the material based on the imaging characteristics and grouped all conditions with similar imaging features together in seven tables. We used DW imaging, ADC and T2 characteristics to create seven tables with conditions that appeared similar on MR imaging.

The clinician can go directly to this chapter, determine if the lesion in question has a high, intermediate or low DW imaging signal intensity and then determine the same with regard to the ADC and T2 characteristics. He or she can then go to the table in Chap 15 that lists conditions with these imaging features. Each table is essentially a list of differential diagnosis for conditions with similar imaging characteristics. When combined with the knowledge of patient symptomatology and demographic criteria, the radiologist will be able to narrow the differential diagnosis to a few conditions.

These tables take into account that the same condition may have variable imaging characteristics; for this reason, several conditions are listed in more than one table. Moreover, within the tables there are variations as to the degree of a specific imaging feature, which allows the clinician to match his/her clinical case to the best table and condition. Chapter 15 makes direct reference to other chapters of the book, where a full description is then provided.

Table 1

Differential diagnoses for lesions with a **high diffusion** signal associated with **low ADC** and **iso intense T2** signal
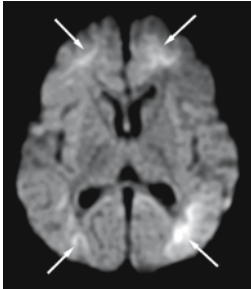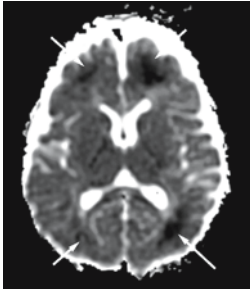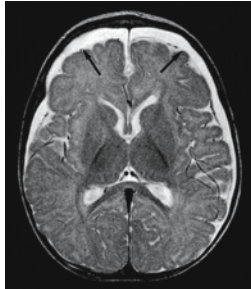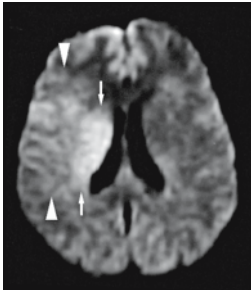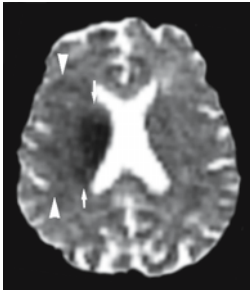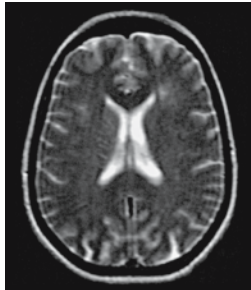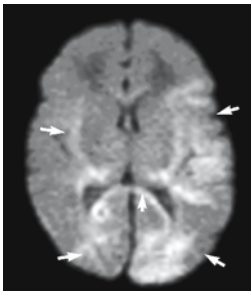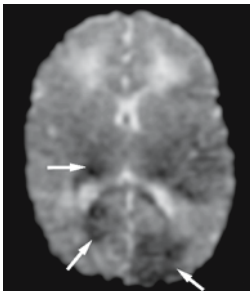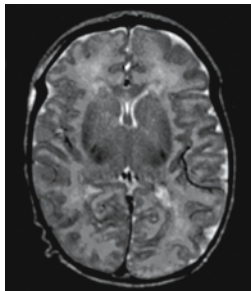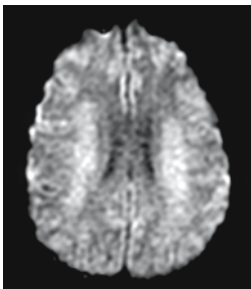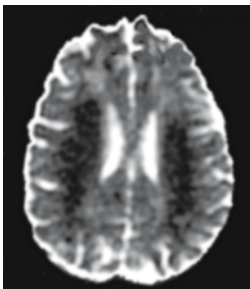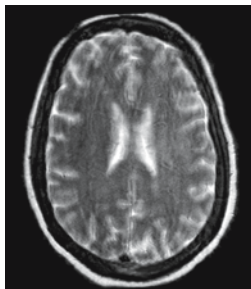
Diagnose	Reference images		
	DWI high	**ADC low**	**T2WI iso**

Infarction/hypoxia

Battered child	Fig. 14.7 d	Fig. 14.7 e	Fig. 14.7 b
Hyperacute infarction	Fig. 5.1 b	Fig. 5.1 c	Fig. 5.1 a
Hypoxic ischemic encephalopathy	Fig. 14.6 c	Fig. 14.6 d	Fig. 14.6 a

Toxic/metabolic

Methotrexate toxicity	Fig. 10.1 b	Fig. 10.1 c	Fig. 10.1 a

Table 2

Differential diagnoses for lesions with a **high diffusion** signal associated with **iso-high ADC** and a **high intense T2** signal
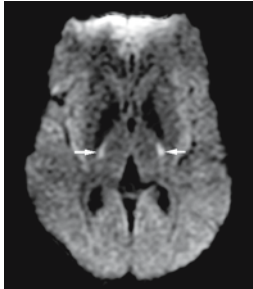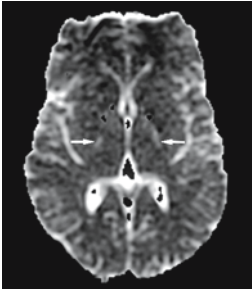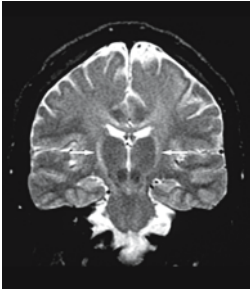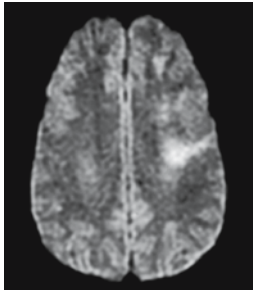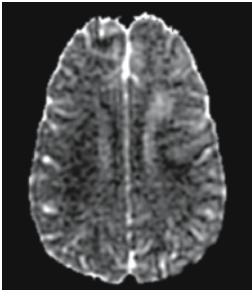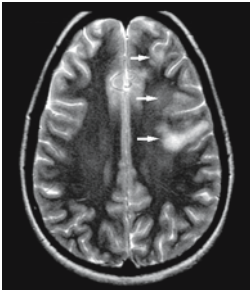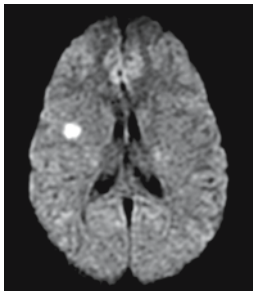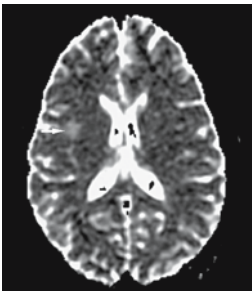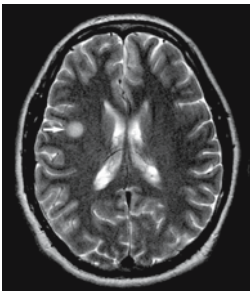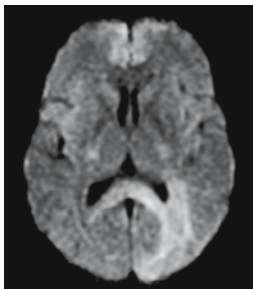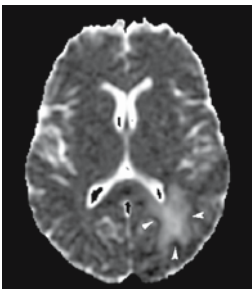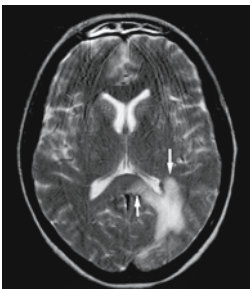
Diagnose	Reference images		
	DWI high	**ADC iso-high**	**T2 high**
Degeneration			
Amyotrophic lateral sclerosis (ALS)	Fig. 9.10 b	Fig. 9.10 c	Fig. 9.10 a
Demyelination			
Acute disseminated encephalomyelopathy (ADEM)	Fig. 9.5 c	Fig. 9.5 d	Fig. 9.5 a
Multiple sclerosis (MS)	Fig. 9.1 c	Fig. 9.1 d	Fig. 9.1 a
Progressive multiple leukoencephalophaty (PML)	Fig. 9.6 b	Fig. 9.6 c	Fig. 9.6 a

Table 2

Differential diagnoses for lesions with a **high diffusion** signal associated with **iso-high ADC** and a **high intense T2** signal
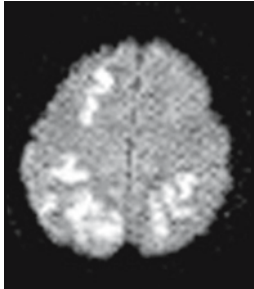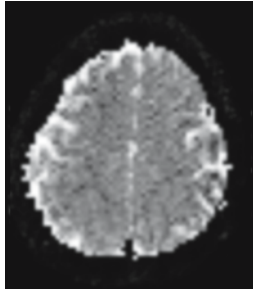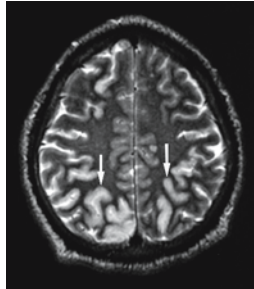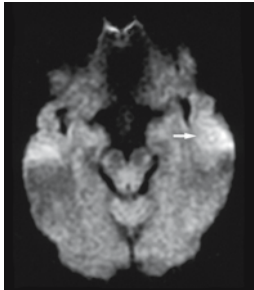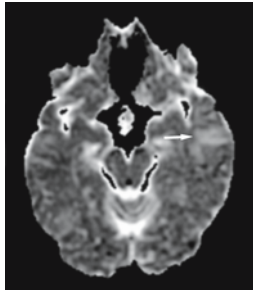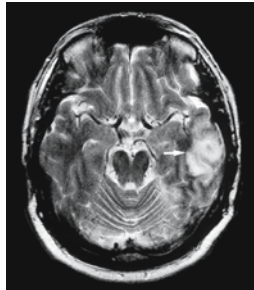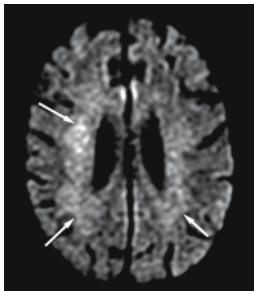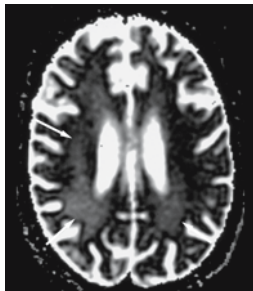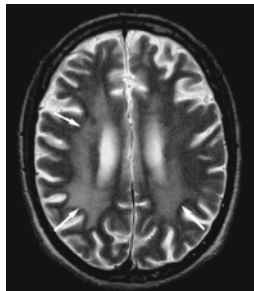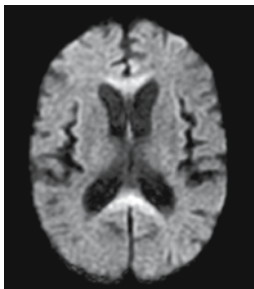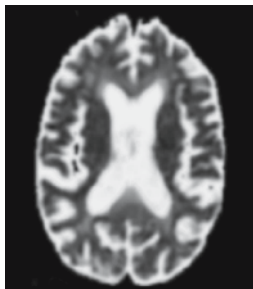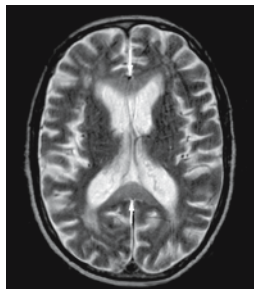
Diagnose	Reference images		
	DWI high	ADC iso-high	T2 high
Epilepsy			
Postictal	Fig. 8.4 d	Fig. 8.4 e	Fig. 8.4 a
Infarction			
Venous infarction	Fig. 5.7 c	Fig. 5.7 d	Fig. 5.7 b
Infection			
Human immunodeficiency virus (HIV)	Fig. 11.18 b	Fig. 11.18 c	Fig. 11.18 a
Toxic/metabolic			
Marchiafava-Bignami disease	Fig. 10.7 c	Fig. 10.7 d	Fig. 10.7 a

Table 2

Differential diagnoses for lesions with a **high diffusion** signal associated with **iso-high ADC** and a **high intense T2** signal
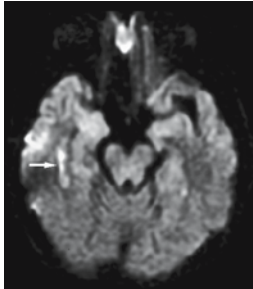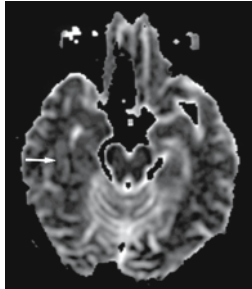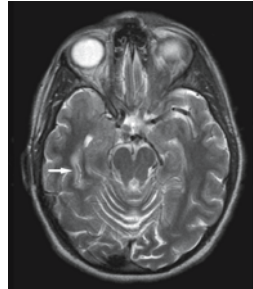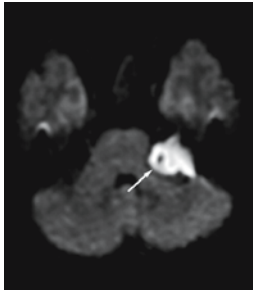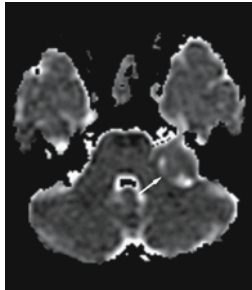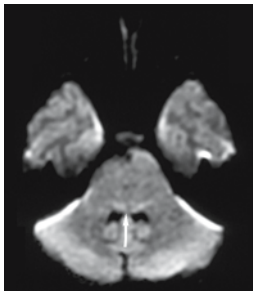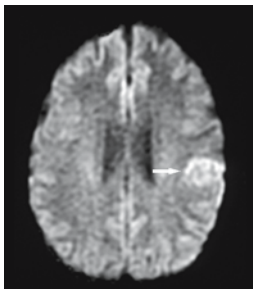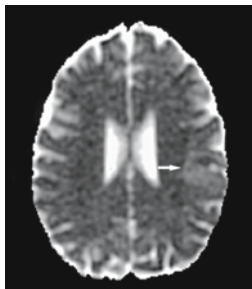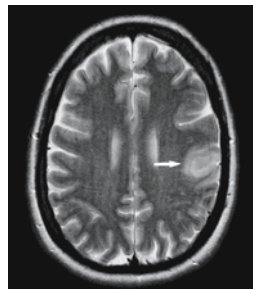
Diagnose	Reference images		
	DWI high	**ADC iso-high**	**T2 high**

Mitochondrial myopathy, encephalophathy, latic acidosis and stroke-like episodes (MELAS

Fig. 10.8 c   **Fig. 10.8 d**   **Fig. 10.8 a**

Tumor

Epidermoid

Fig. 11.12 c   **Fig. 11.12 d**   **Fig. 11.12 a**

Brain stem glioma

Fig. 13.5 d   **Fig. 13.5 e**   **Fig. 13.5 a**

Anaplastic astrocytoma

Fig. 3.2 c   **Fig. 3.2 d**   **Fig. 3.2 a**
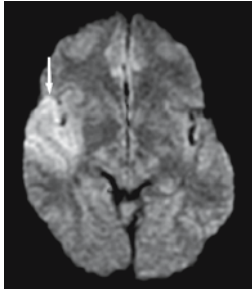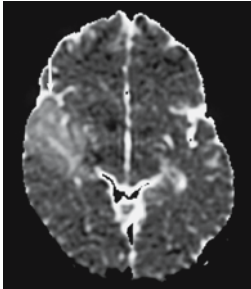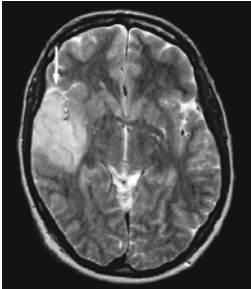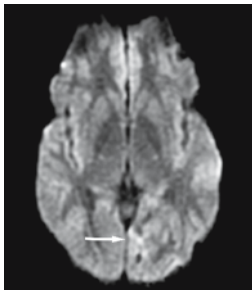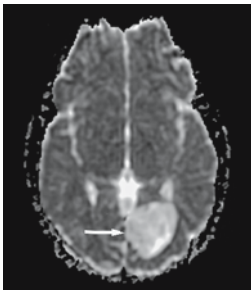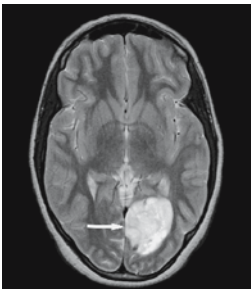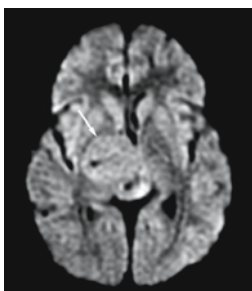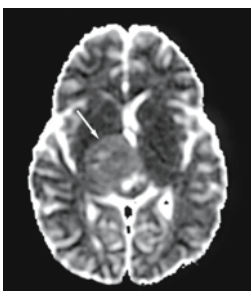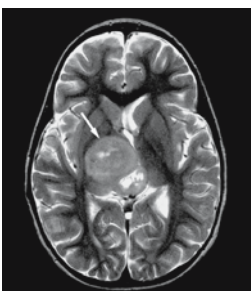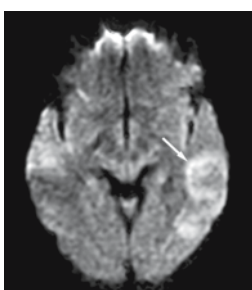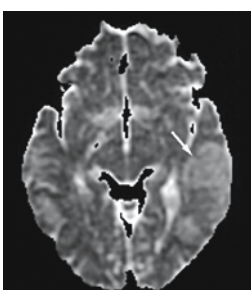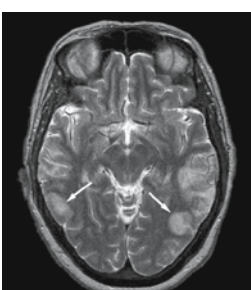
Diagnose	Reference images		
	DWI high	**ADC iso-high**	**T2 high**
Low-grade oligoastrocytoma	Fig. 13.6 c	Fig. 13.6 d	Fig. 13.6 a
Ganglioglioma	Fig. 13.7 c	Fig. 13.7 d	Fig. 13.7 a
Pilocytic astrocytoma	Fig. 14.17 b	Fig. 14.17 c	Fig. 14.17 a
Vasculitis/vasculopathy			
Primary angitis of central nervous system (PACNS)	Fig. 7.2 c	Fig. 7.2 d	Fig. 7.2 a

Table 2

Differential diagnoses for lesions with a **high diffusion** signal associated with **iso-high ADC** and a **high intense T2** signal
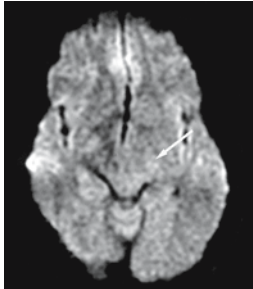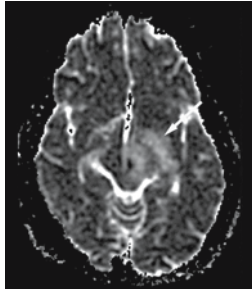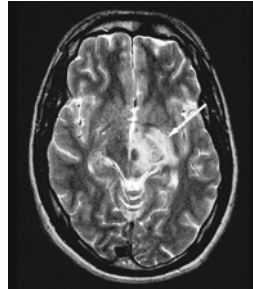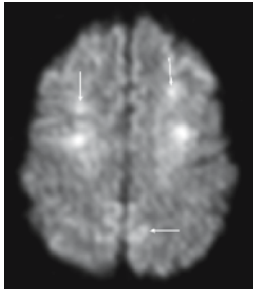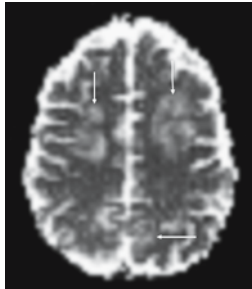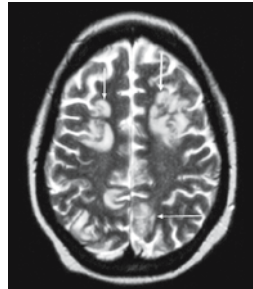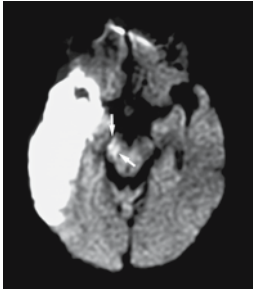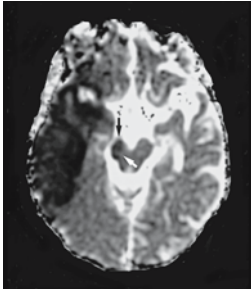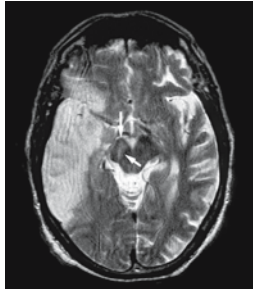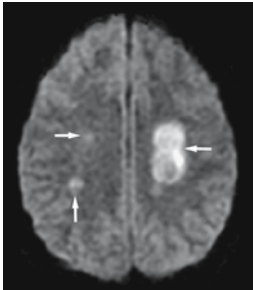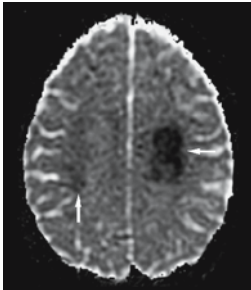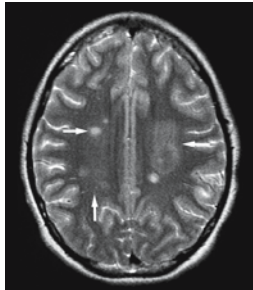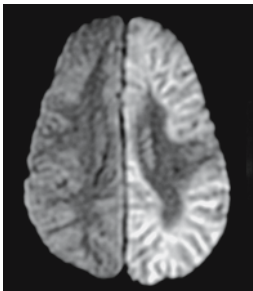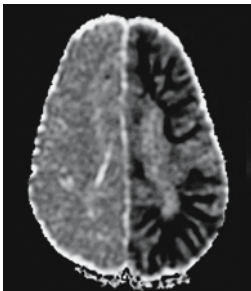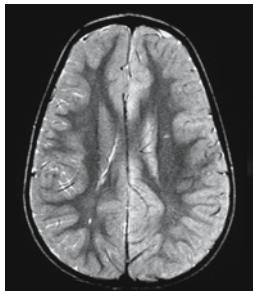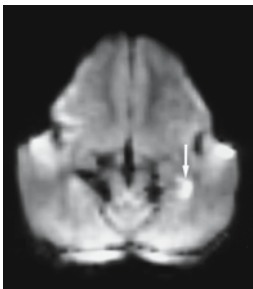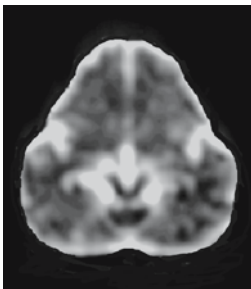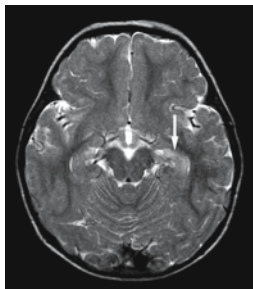
Diagnose	Reference images		
	DWI high	ADC iso-high	T2 high

Neuro-Behchet's disease

Fig. 7.7 c   **Fig. 7.7 d**   **Fig. 7.7 a**

Tacrolimus neurotoxicity
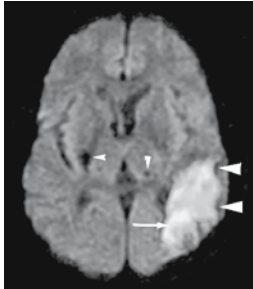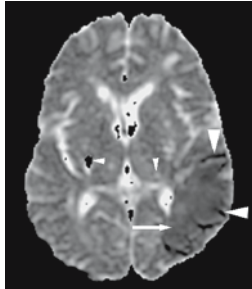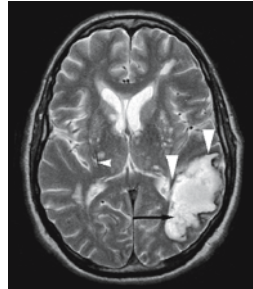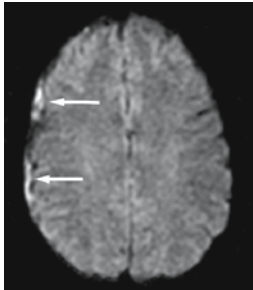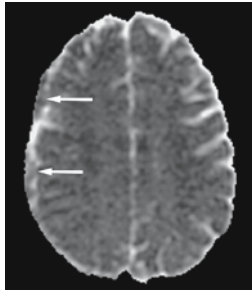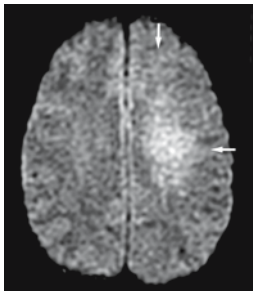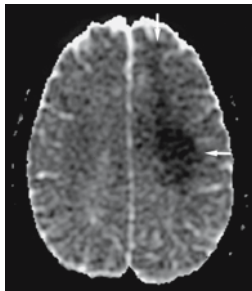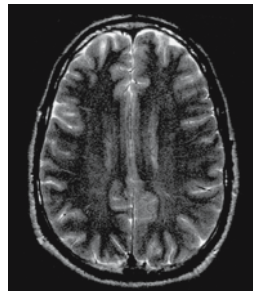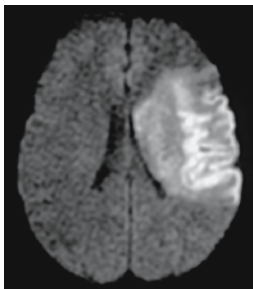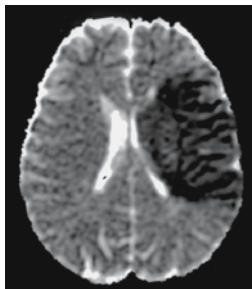
Fig. 7.17 b   **Fig. 7.17 c**   **Fig. 7.17 a**

Table 3

Differential diagnoses for lesions with a **high diffusion** signal associated with a **low ADC** and **high intense T2** signal

Diagnose	Reference images		
	DWI high	**ADC low**	**T2 high**
Degeneration			
Wallerian degeneration	Fig. 9.7 c	Fig. 9.7 d	Fig. 9.7 b
Demyelination			
Multiple sclerosis (MS)	Fig. 9.4 b	Fig. 9.4 c	Fig. 9.4 a
Epilepsy			
Status epileptics	Fig. 4.8 b	Fig. 4.8 c	Fig. 4.8 a
Postictal	Fig. 8.5 c	Fig. 8.5 d	Fig. 8.5 a
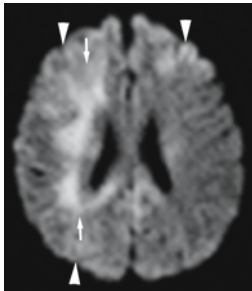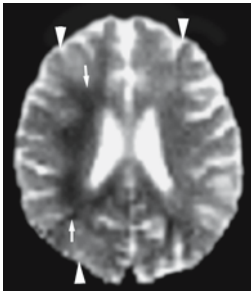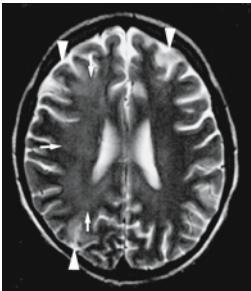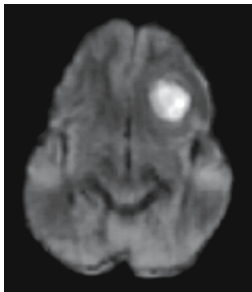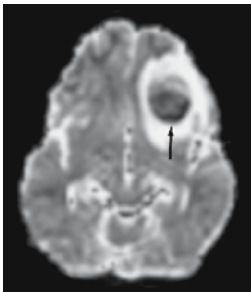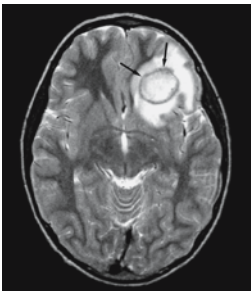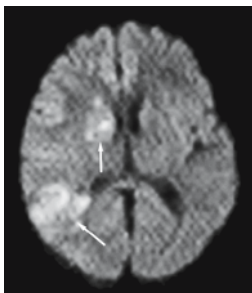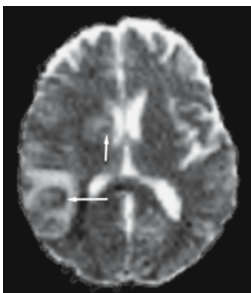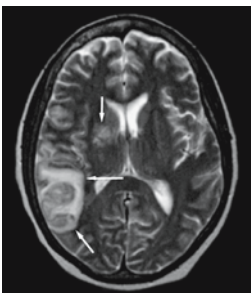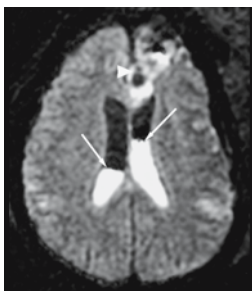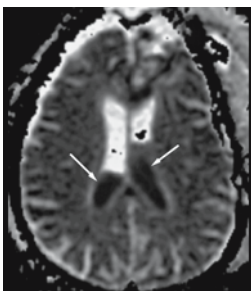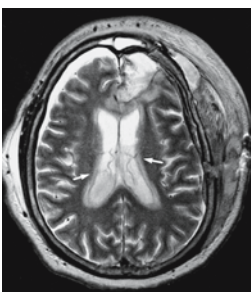
Table 3

Differential diagnoses for lesions with a **high diffusion** signal associated with a **low ADC** and **high intense T2** signal

Diagnose	Reference images		
	DWI high	**ADC low**	**T2 high**

Hematoma

Late subacute hematoma
(Extracellular methemoglobin)

Fig. 6.4 c   **Fig. 6.4 e**   **Fig. 6.4 a**

Subdural hematoma (SDH)

Fig. 6.6 c   **Fig. 6.6 e**   **Fig. 6.6 d**

Infarction/Ischemia

Hyperacute reversible ischemia (2 h)

Fig. 5.5 b   **Fig. 5.5 c**   **Fig. 5.5 a**

Acute infarction (24 h)

Fig. 3.3 d   **Fig. 3.3 e**   **Fig. 3.3 c**

Table 3

Differential diagnoses for lesions with a **high diffusion** signal associated with a **low ADC** and **high intense T2** signal

Diagnose	Reference images		
	DWI high	**ADC low**	**T2 high**
Subacute infarction (10 day)	Fig. 5.3 c	Fig. 5.3 d	Fig. 5.3 a

Infection

Abscess	Fig. 11.1 c	Fig. 11.1 d	Fig. 11.1 a
Septic emboli	Fig.11.2 b	Fig.11.2 c	Fig.11.2 a
Ventriculitis	Fig. 11.10 c	Fig. 11.10 d	Fig. 11.10 b

Table 3

Differential diagnoses for lesions with a **high diffusion** signal associated with a **low ADC** and **high intense T2** signal
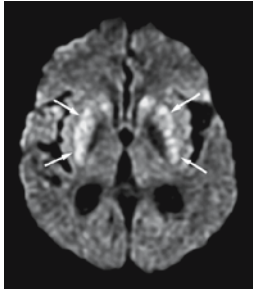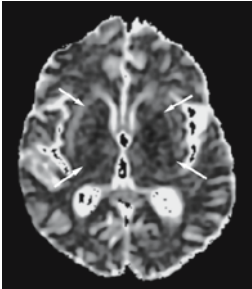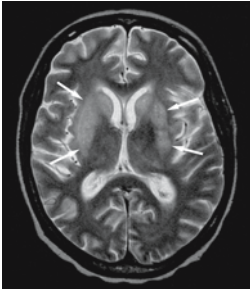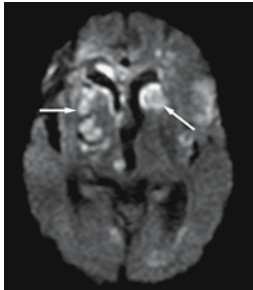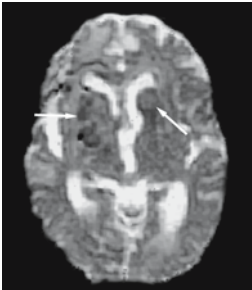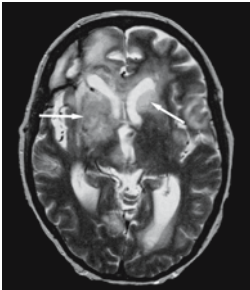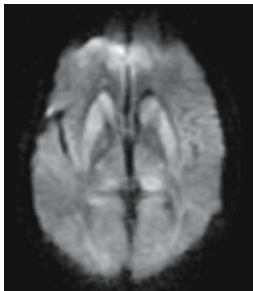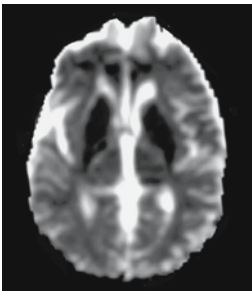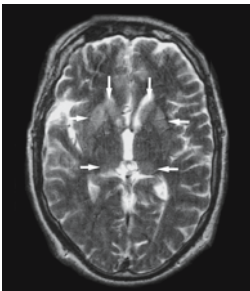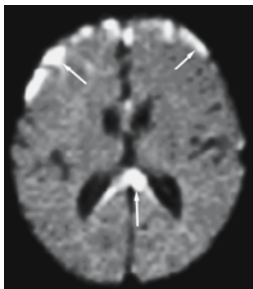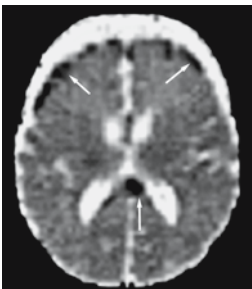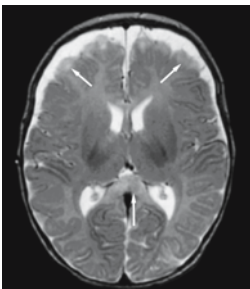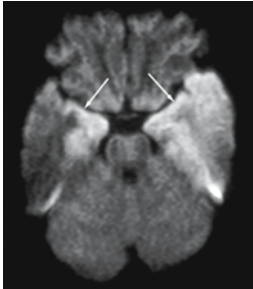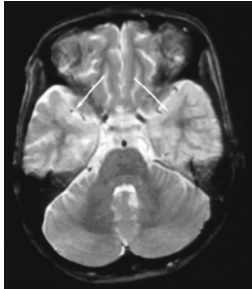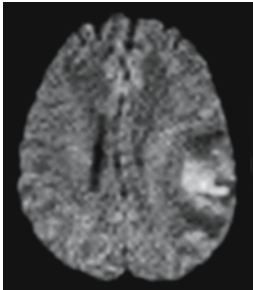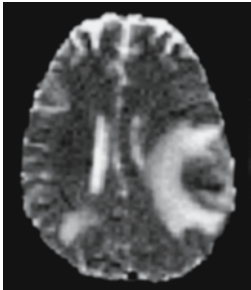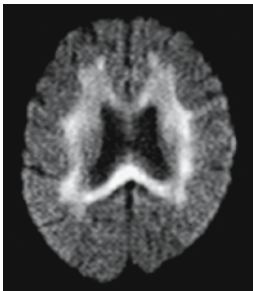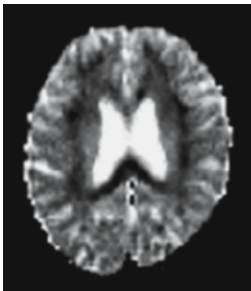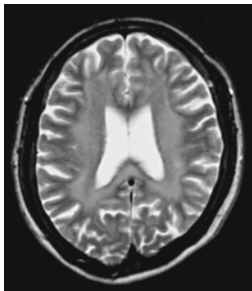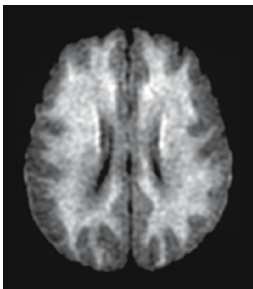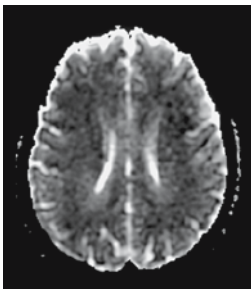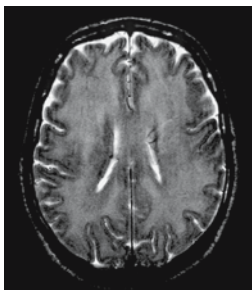
Diagnose	Reference images		
	DWI high	**ADC low**	**T2 high**
Acquired immunodeficiency syndrome (AIDS)	\nFig. 11.19. b	\nFig. 11.19. c	\nFig. 11.19. a
Aspergillosis (disseminated)	\nFig.11.16 b	\nFig.11.16 c	\nFig.11.16 a
Creutzfeldt-Jakob disease (CJD)	\nFig. 9.9 b	\nFig. 9.9 c	\nFig. 9.9 a
Group B Streptococcus meningitis	\nFig. 11.13 b	\nFig. 11.13 c	\nFig. 11.13 a

Table 3

Differential diagnoses for lesions with a **high diffusion** signal associated with a **low ADC** and **high intense T2** signal

Diagnose	Reference images		
	DWI high	**ADC low**	**T2 high**
Herpes simplex virus	Fig. 14.13 b	Fig. 14.13 c	Fig. 14.13 a
Toxoplasmosis	Fig. 4.16 b	Fig. 4.16 c	Fig. 4.16 a
Toxic/metabolic			
Carmofur	Fig.10.2 b	Fig.10.2 c	Fig.10.2 a
Heroin	Fig. 10.3 b	Fig. 10.3 c	Fig. 10.3 a

Table 3

Differential diagnoses for lesions with a **high diffusion** signal associated with a **low ADC** and **high intense T2** signal
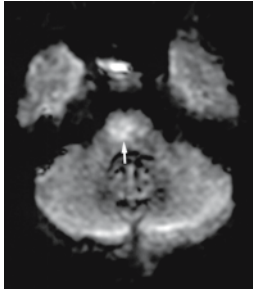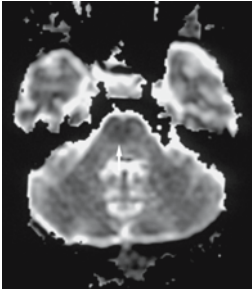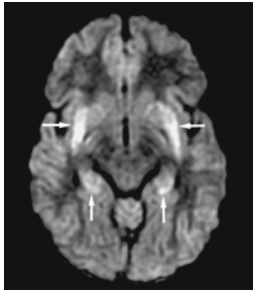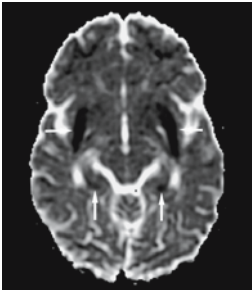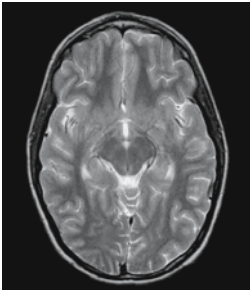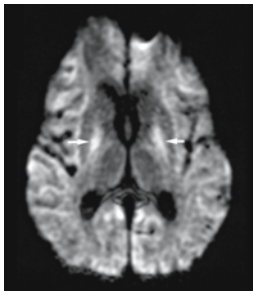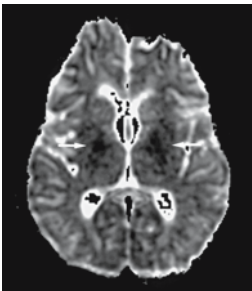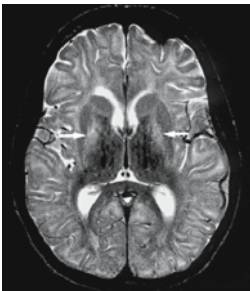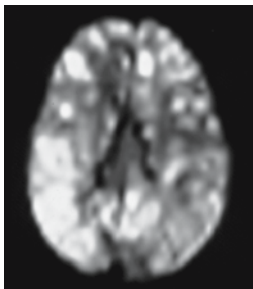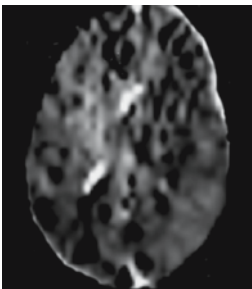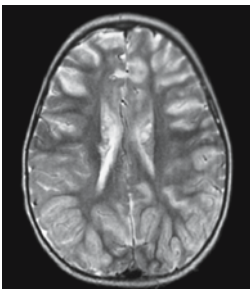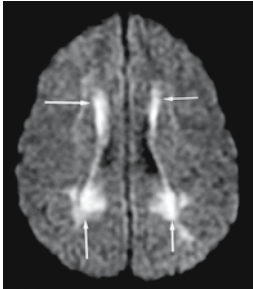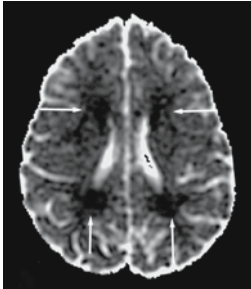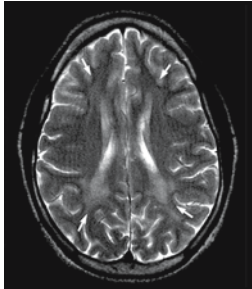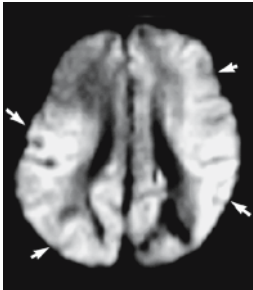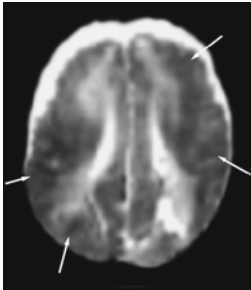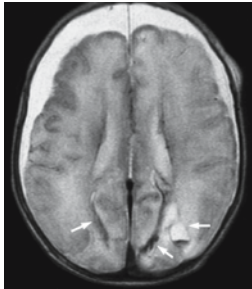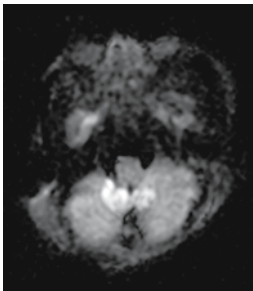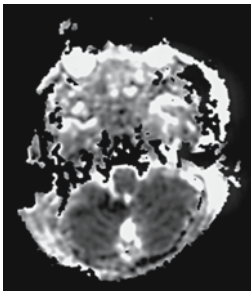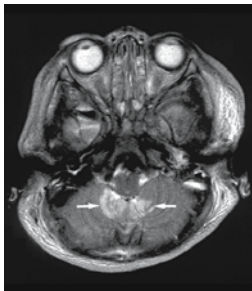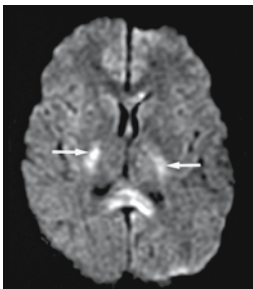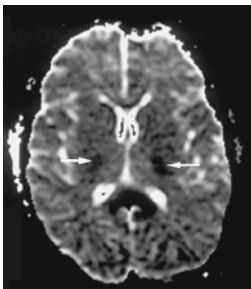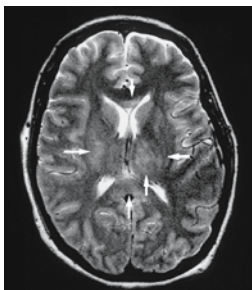
Diagnose	Reference images		
	DWI high	ADC low	T2 high
Central pontine myelinolysis (CPM)	Fig. 10.4. b	Fig. 10.4. c	Fig. 10.4. a
Extrapotine meyelinolysis (EPM)	Fig. 10.5 b	Fig. 10.5 c	Fig. 10.5 a
Glutaric aciduria	Fig.10.11 b	Fig.10.11 c	Fig.10.11 a
Mitochondrial encephalomyopathy	Fig. 10.9. b	Fig. 10.9. c	Fig. 10.9. a

Table 3

Differential diagnoses for lesions with a **high diffusion** signal associated with a **low ADC** and **high intense T2** signal

Diagnose	Reference images		
	DWI high	**ADC low**	**T2 high**
Phenylketonuria (PKU)	Fig. 14.20 b	Fig. 14.20 c	Fig. 14.20 a
Trauma			
Battered child	Fig. 14.8 b	Fig. 14.8 d	Fig. 14.8 a
Contusion	Fig.12.9 b	Fig.12.9 c	Fig.12.9 a
Diffuse axonal injury (DAI)	Fig. 12.2 c	Fig. 12.2 d	Fig. 12.2 a

Table 3

Differential diagnoses for lesions with a **high diffusion** signal associated with a **low ADC** and **high intense T2** signal
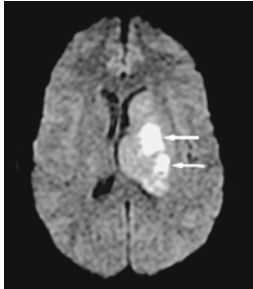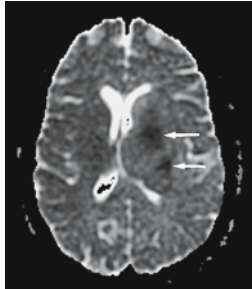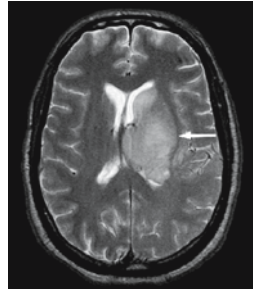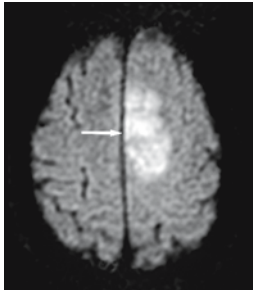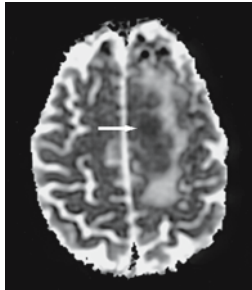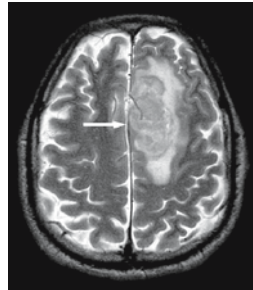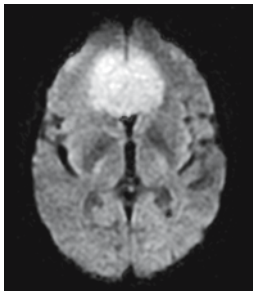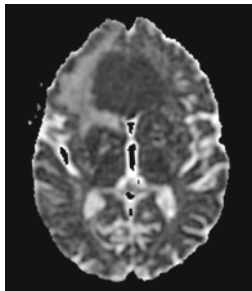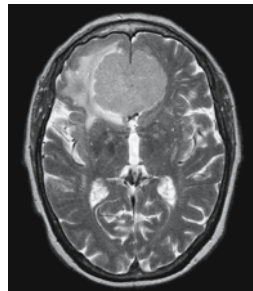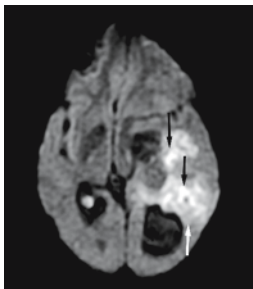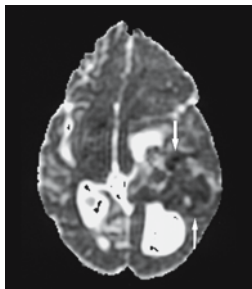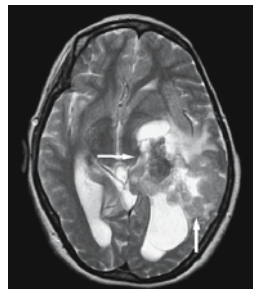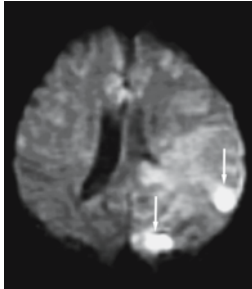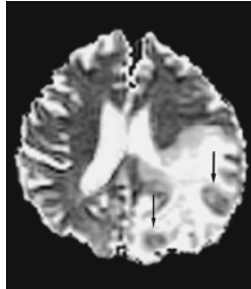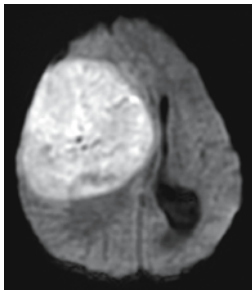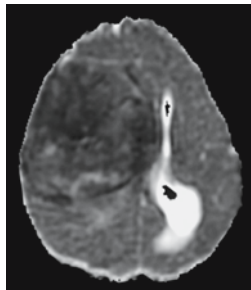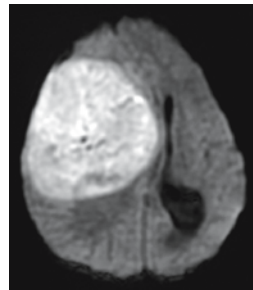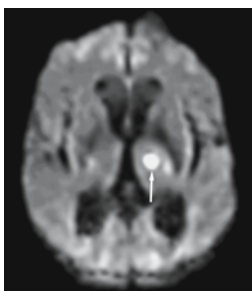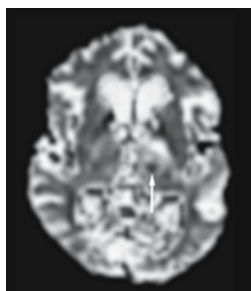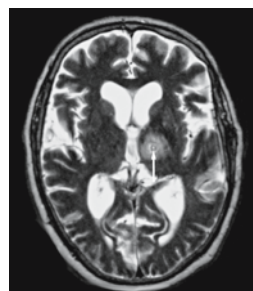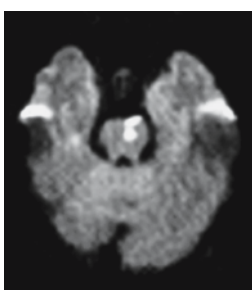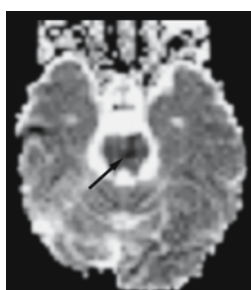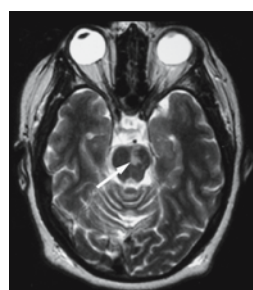
Diagnose	Reference images		
	DWI high	**ADC low**	**T2 high**

Tumor

Glioblastoma multiforme (GBM) (solid)

Fig. 13.2 d   Fig. 13.2 e   Fig. 13.2 a

Lymphoma

Fig. 13.13 d   Fig. 13.13 e   Fig. 13.13 a

Meningioma (syncytial)

Fig.13.11 c   Fig.13.11 d   Fig.13.11 a

Meningioma (atypical)

Fig. 13.12 c   Fig. 13.12 d   Fig. 13.12 a

Table 3

Differential diagnoses for lesions with a **high diffusion** signal associated with a **low ADC** and **high intense T2** signal

Diagnose	Reference images		
	DWI high	**ADC low**	**T2 high**
Metastasis	Fig. 11.6 c	Fig. 11.6 d	Fig. 11.6 a
Primitive neuroectodermal tumor (PNET)	Fig. 13.10 c	Fig. 13.10 d	Fig. 13.10 a
Radiation necrosis	Fig.11.7 b	Fig.11.7 c	Fig.11.7 a
Vasculitis			
Primary angitis of central nervous system (PACNS)	Fig. 7.3 e	Fig. 7.3 f	Fig. 7.3 b

Table 3

Differential diagnoses for lesions with a **high diffusion** signal associated with a **low ADC** and **high intense T2** signal
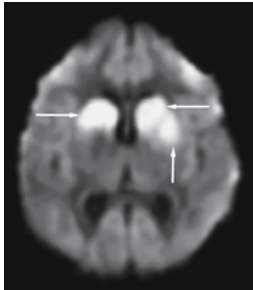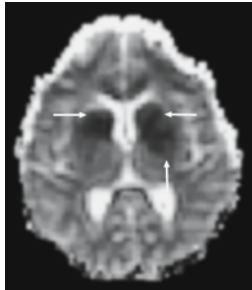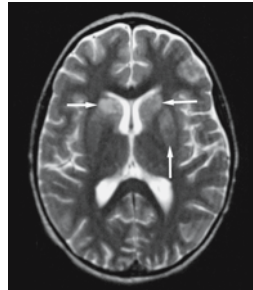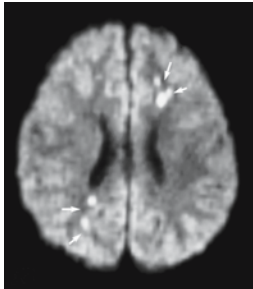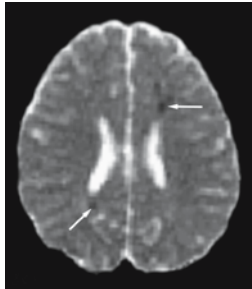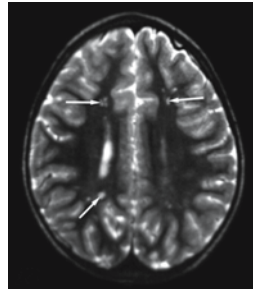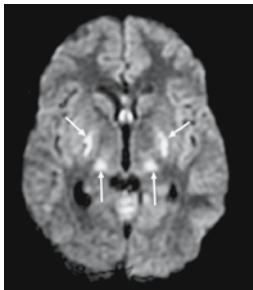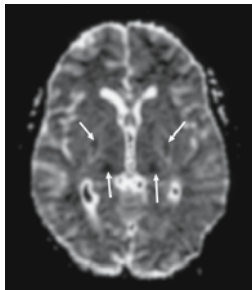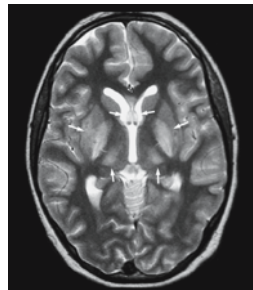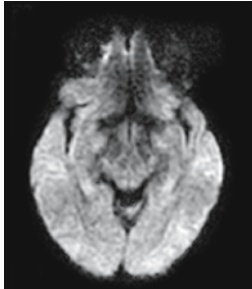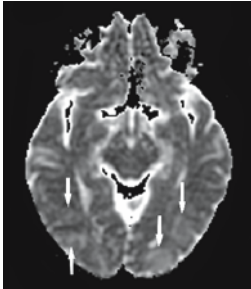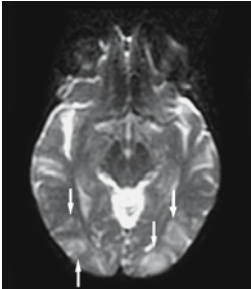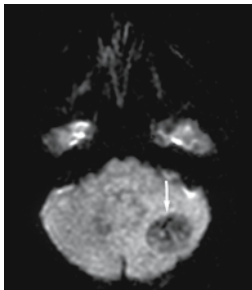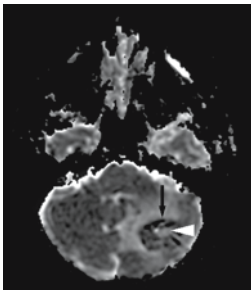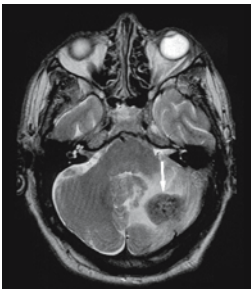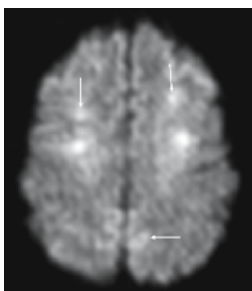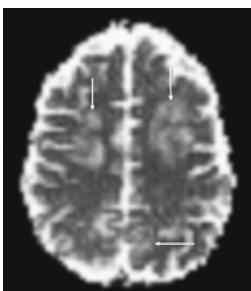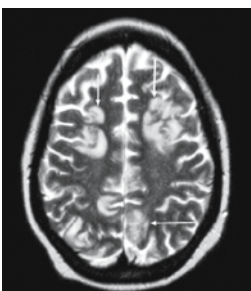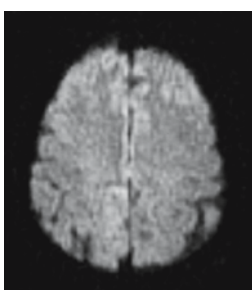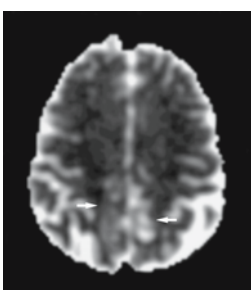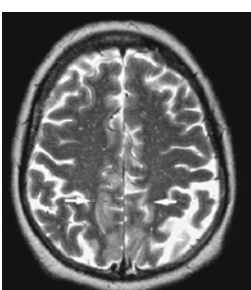
Diagnose	Reference images		
	DWI high	**ADC low**	**T2 high**

Pneumococcal meningitis and vasculitis

Fig. 7.8 b **Fig. 7.8 c** **Fig. 7.8 a**

Sickle cell disease

Fig. 14.5 b **Fig. 14.5 c** **Fig. 14.5 a**

Hemolytic uremic syndrome (HUS)

Fig.7.19 b **Fig.7.19 c** **Fig.7.19 a**
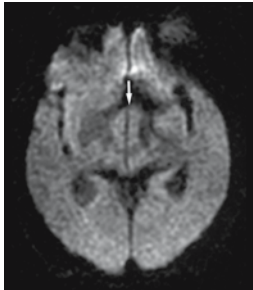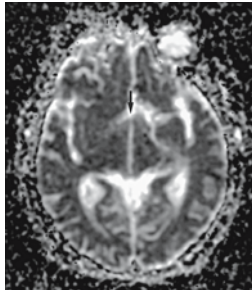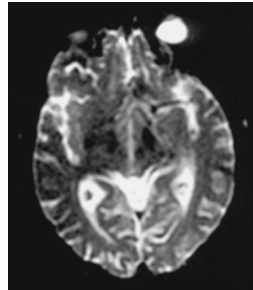
Table 4

Differential diagnoses for lesions with an **iso diffusion** signal associated with a **high ADC** and **high intense T2** signal

Diagnose	Reference images		
	DWI iso	**ADC high**	**T2 high**

Vasculitis/Vasculopathy

Posterior reversible encephalopathy synsdrome (PRES)

Fig. 3.4 c

Fig. 3.4 d

Fig. 3.4 b

Vasogenic edema (metastasis)

Fig. 3.5 e

Fig. 3.5 d

Fig. 3.5 a

Tacrolimus neurotoxicity

Fig. 7.17 b

Fig. 7.17 c

Fig. 7.17 a

Postictal

Fig. 8.2 d

Fig. 8.2 e

Fig. 8.2 a
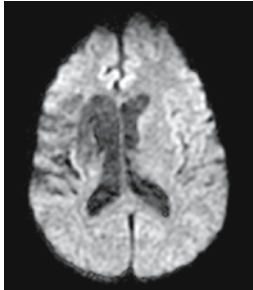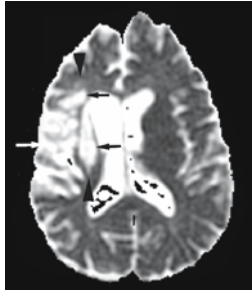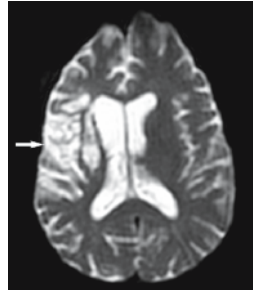
Table 4

Differential diagnoses for lesions with an **iso diffusion** signal associated with a **high ADC** and **high intense T2** signal

Diagnose	Reference images		
	DWI iso	ADC high	T2 high
Metabolic disease			
Wernicke			
	Fig. 10.6 b	Fig. 10.6 c	Fig. 10.6 a

Table 5

Differential diagnoses for lesions with a **low diffusion** signal associated with a **high ADC** and **high intense T2** signal

Diagnose	Reference images		
	DWI low	ADC high	T2 high
Infarction			
Chronic infarction (10 months)			
	Fig. 5.4 c	Fig. 5.4 d	Fig. 5.4 b
Tumor			
GBM (necrosis)			
	Fig. 11.5 c	Fig. 11.5 d	Fig. 11.5 a
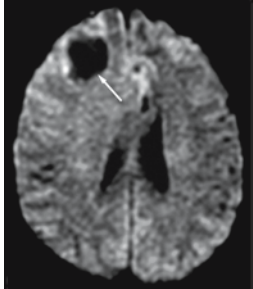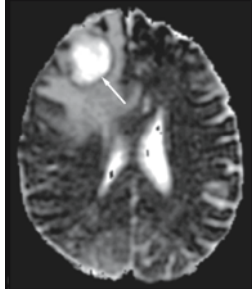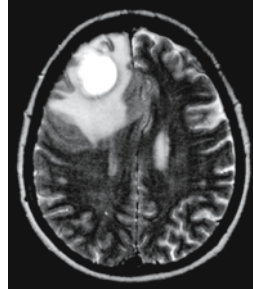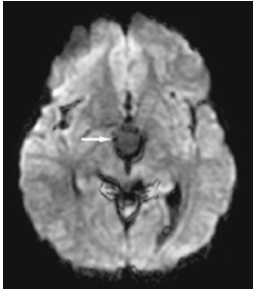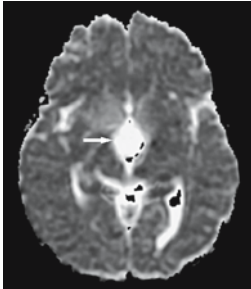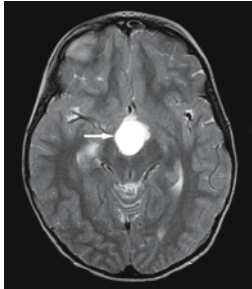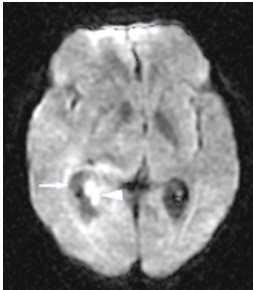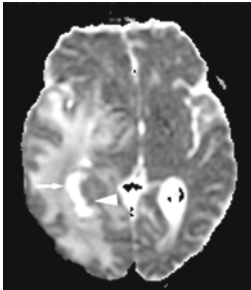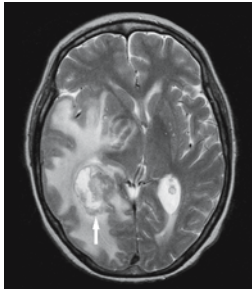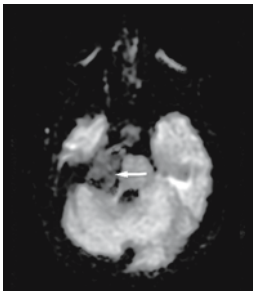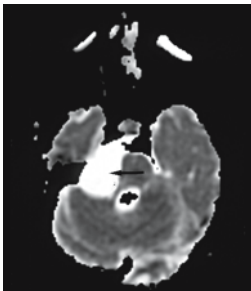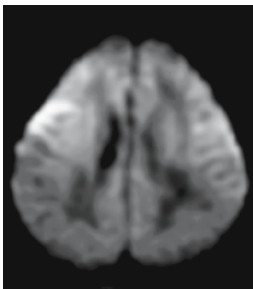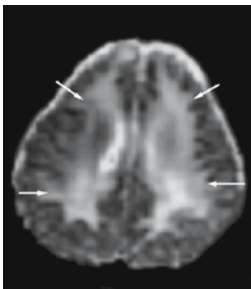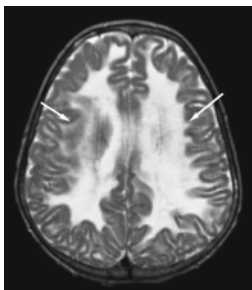
Table 5

Differential diagnoses for lesions with a **low diffusion** signal associated with a **high ADC** and **high intense T2** signal

Diagnose	Reference images		
	DWI low	**ADC high**	**T2 high**
Craniopharyngioma	Fig. 13.14 c	Fig. 13.14 b	Fig. 13.14 a
Matastasis (lung)	Fig. 13.15 c	Fig. 13.15 d	Fig. 13.15 a
Arachnoid cyst	Fig. 13.9 c	Fig. 13.9 d	Fig. 13.9 a
Vanishing white matter disease	Fig. 14.19 b	Fig. 14.19 c	Fig. 14.19 a

Table 5

Differential diagnoses for lesions with a **low diffusion** signal associated with a **high ADC** and **high intense T2** signal

Diagnose	Reference images		
	DWI low	ADC high	T2 high
van der Knaap disease	Fig. 10.12 b	Fig. 10.12 c	Fig. 10.12 a
Vasogenic edema (toxo)	Fig. 4.16 b	Fig. 4.16 c	Fig. 4.16 a
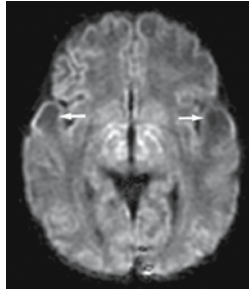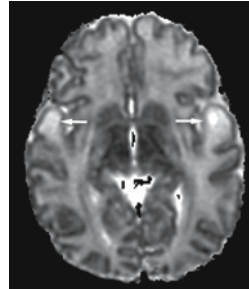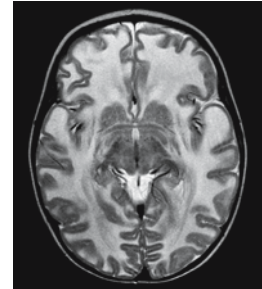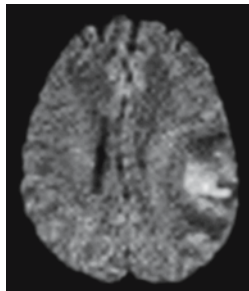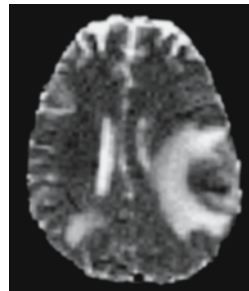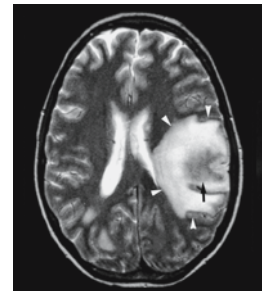
Table 6

Differential diagnoses for lesions with a **low diffusion** signal associated with a **high ADC** and **iso intense T2** signal

Diagnose	Reference images		
	DWI low	ADC high	T2 iso
Normal	Fig. 2.3 a	Fig. 2.3 b	Fig. 2.3 c

Neonate

Table 7

Differential diagnoses for lesions with **artifacts**

Diagnose	Reference images		
	DWI	ADC	T2
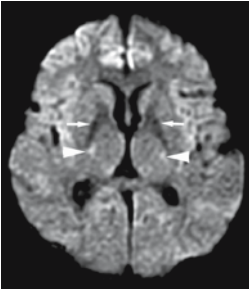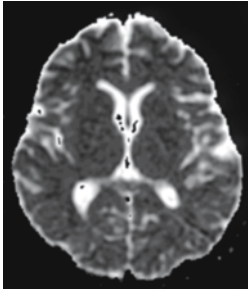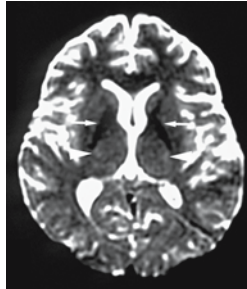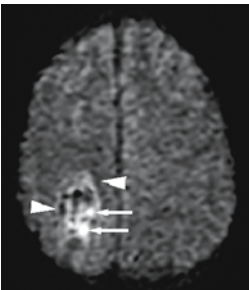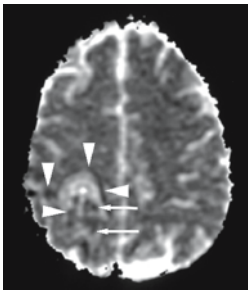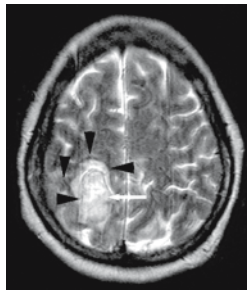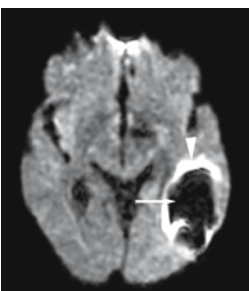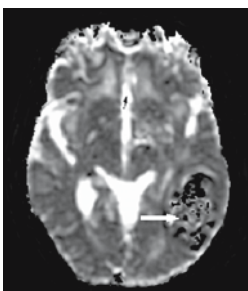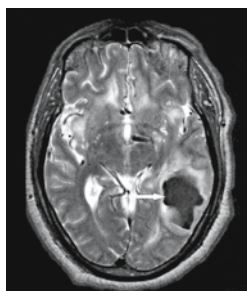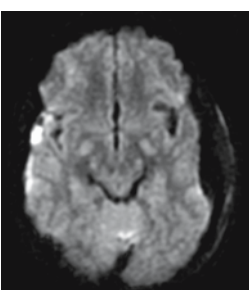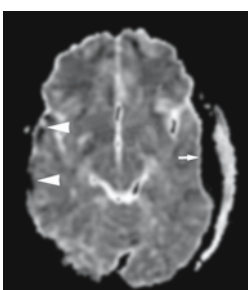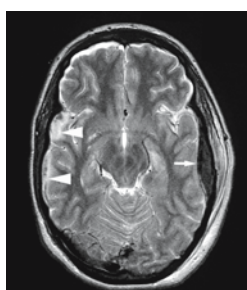
Diagnose	Reference images		
Susceptibility/Artifact **Normal iron deposition** **Hematoma**	 Fig. 2.1 a	 Fig. 2.1 b	 Fig. 2.1 c
Oxy/deoxy hemoglobin	 Fig. 6.2 d	 Fig. 6.2 f	 Fig. 6.2 b
Deoxy, IC met	 Fig. 6.3 c	 Fig. 6.3 e	 Fig. 6.3 a
Epidural hematoma (EDH)	 Fig. 12.10 c	 Fig. 12.10 d	 Fig. 12.10 b

Table 7

Differential diagnoses for lesions with **artifacts**
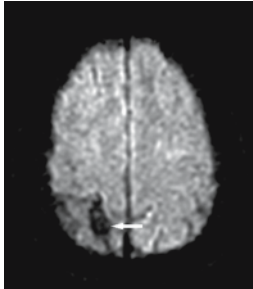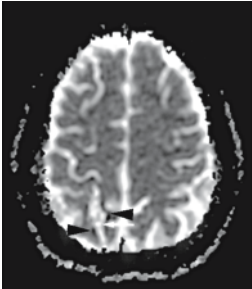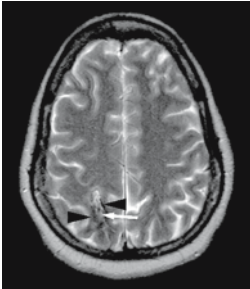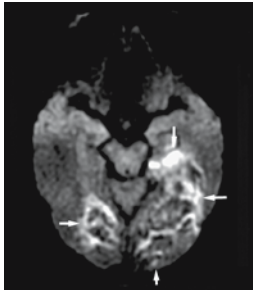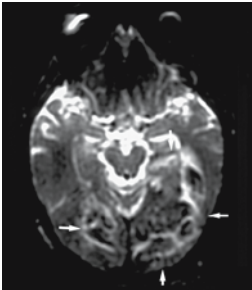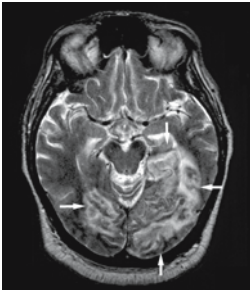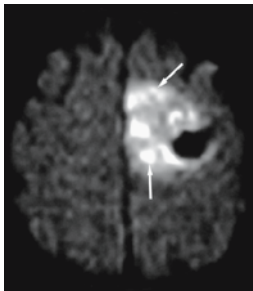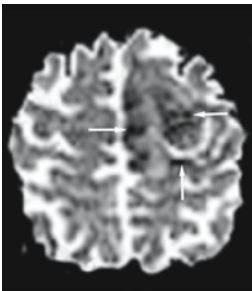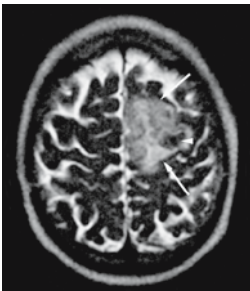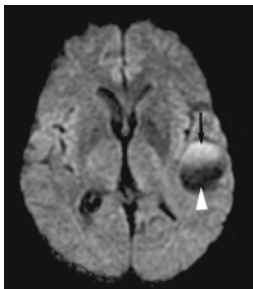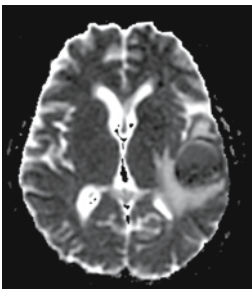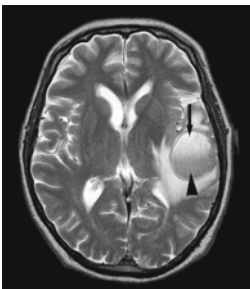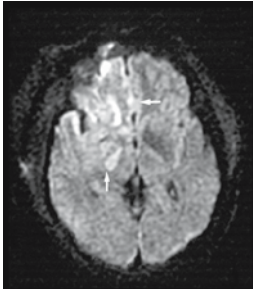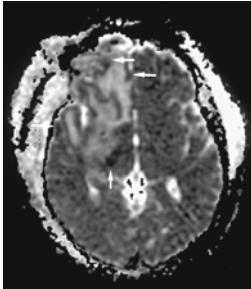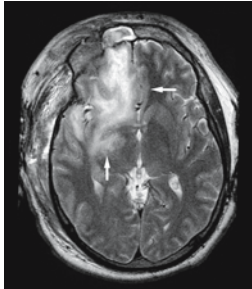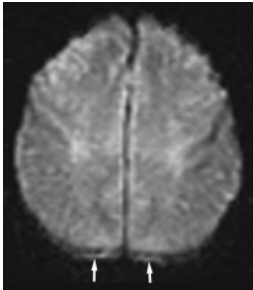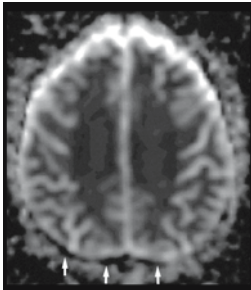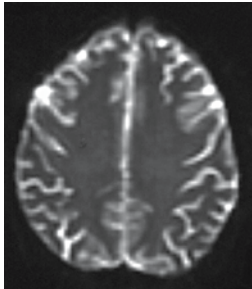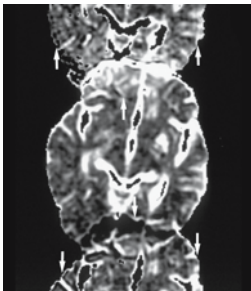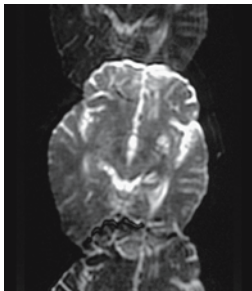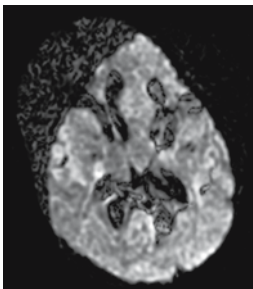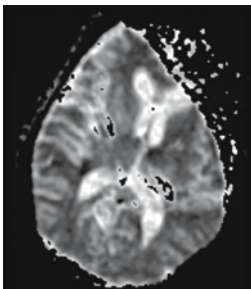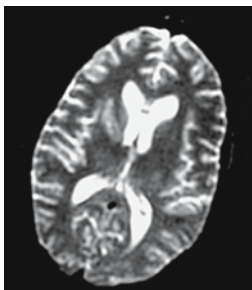
Diagnose	Reference images		
	DWI	ADC	T2
Hemosiderin/ferritin	Fig. 6.2 k	Fig. 6.2 m	Fig. 6.2 i
Hemorrhagic infarction	Fig. 5.11 b	Fig. 5.11 c	Fig. 5.11 a
Disseminated aspergillosis	Fig. 7.9 c	Fig. 7.9 d	Fig. 7.9 a
Metastasis (melanoma)	Fig. 13.16 d	Fig. 13.16 e	Fig. 13.16 b

Table 7

Differential diagnoses for lesions with **artifacts**

Diagnose	Reference images		
	DWI	ADC	T2
Contusion	Fig. 12.7 c	Fig. 12.7 d	Fig. 12.7 b
Eddy current artifacts	Fig. 3.7 a	Fig. 3.7 b	Fig. 3.7 c
N/2 ghosting artifacts	Fig. 3.10 a	Fig. 3.10 b	Fig. 3.10 c
Motion artifacts	Fig. 3.12 a	Fig. 3.12 b	Fig. 3.12 c

Subject Index